EARTHQUAKE PROBABILITIES FOR THE WASATCH FRONT REGION IN UTAH, IDAHO, AND WYOMING

by Working Group on Utah Earthquake Probabilities

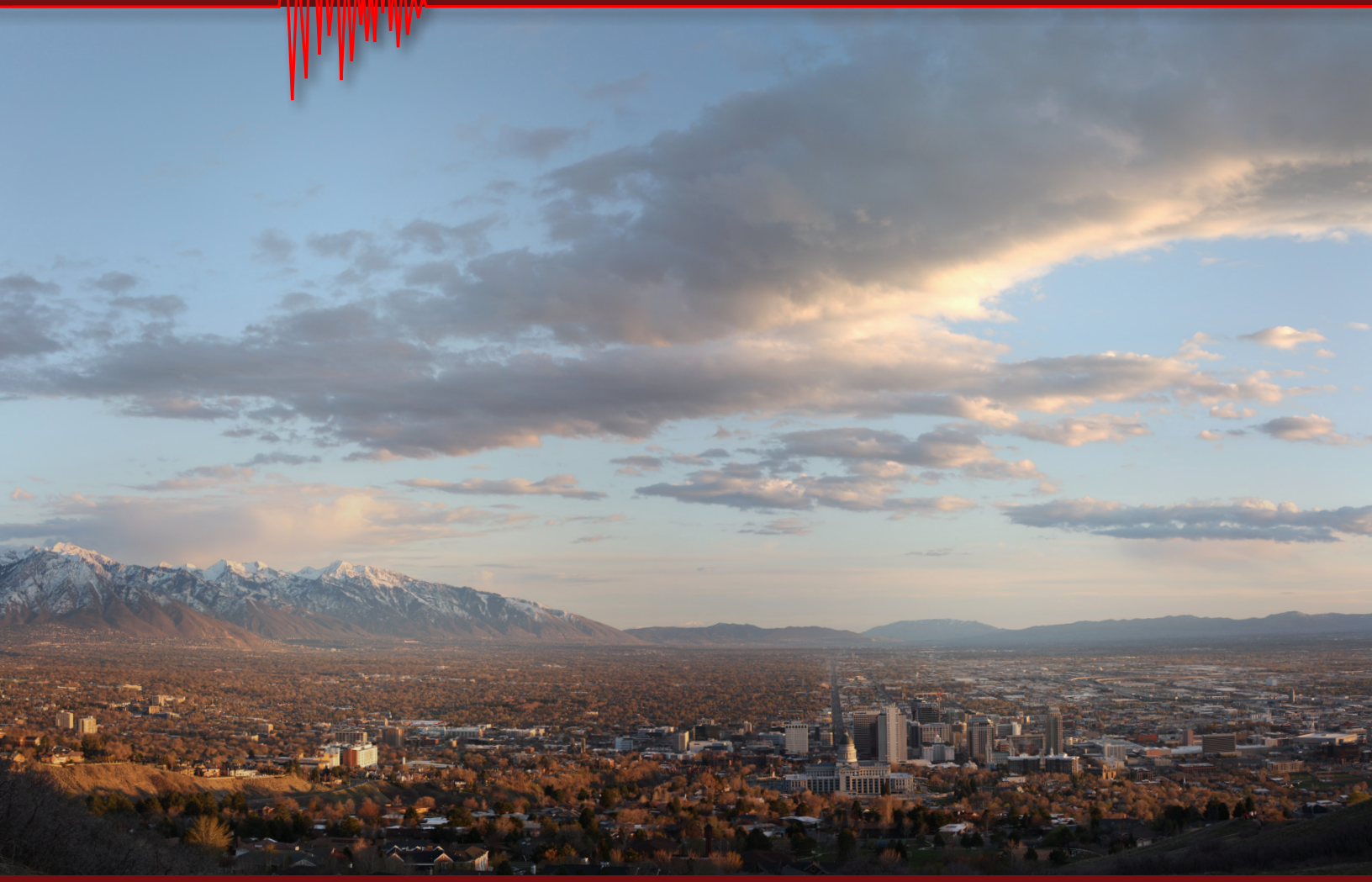

MISCELLANEOUS PUBLICATION 16-3
UTAH GEOLOGICAL SURVEY
a division of
UTAH DEPARTMENT OF NATURAL RESOURCES
in cooperation with
U.S. Geological Survey
2016

EARTHQUAKE PROBABILITIES FOR THE WASATCH FRONT REGION IN UTAH, IDAHO, AND WYOMING

by Working Group on Utah Earthquake Probabilities

Ivan Wong [1,8], William Lund [2], Christopher DuRoss [3,9], Patricia Thomas [1], Walter Arabasz [4], Anthony Crone [5], Michael Hylland [3], Nicolas Luco [5], Susan Olig [1,10], James Pechmann [4], Steve Personius [5], Mark Petersen [5], David Schwartz [6], Robert Smith [7], and Steve Bowman [3]

Cover photo: *The spectacular relief of the Wasatch Range east of Salt Lake City is the result of recurrent large earthquakes associated with movement on the Wasatch fault zone, Utah's longest and most active fault.*

ISBN 978-1-55791-923-6

[1] *URS Corporation (now AECOM), Seismic Hazards Group, 1333 Broadway, Suite 800, Oakland, CA 94612*
[2] *Utah Geological Survey, 646 North Main, Cedar City, UT 84721*
[3] *Utah Geological Survey, 1594 West North Temple, Salt Lake City, UT 84116*
[4] *University of Utah Seismograph Stations, Department of Geology and Geophysics, Salt Lake City, UT 84112*
[5] *U.S. Geological Survey, P.O. Box 25046, MS 966, Denver, CO 80225*
[6] *U.S. Geological Survey, 345 Middlefield Road, MS 977, Menlo Park, CA 94025*
[7] *University of Utah, Department of Geology and Geophysics, Salt Lake City, UT 84112*
[8] *Now at Lettis Consultants International, Inc., 1981 N. Broadway, Walnut Creek, CA 94596*
[9] *Now at U.S. Geological Survey, P.O. Box 25046, MS 966, Denver, CO 80225*
[10] *Now at Olig Seismic Geology, Inc., 519 Francis Drive, Martinez, CA 94553*

MISCELLANEOUS PUBLICATION 16-3
UTAH GEOLOGICAL SURVEY
a division of
UTAH DEPARTMENT OF NATURAL RESOURCES
in cooperation with
U.S. Geological Survey
2016

STATE OF UTAH
Gary R. Herbert, Governor

DEPARTMENT OF NATURAL RESOURCES
Michael Styler, Executive Director

UTAH GEOLOGICAL SURVEY
Richard G. Allis, Director

PUBLICATIONS
contact
Natural Resources Map & Bookstore
1594 W. North Temple
Salt Lake City, UT 84116
telephone: 801-537-3320
toll-free: 1-888-UTAH MAP
website: mapstore.utah.gov
email: geostore@utah.gov

UTAH GEOLOGICAL SURVEY
contact
1594 W. North Temple, Suite 3110
Salt Lake City, UT 84116
telephone: 801-537-3300
website: geology.utah.gov

Suggested citation:

Working Group on Utah Earthquake Probabilities (WGUEP), 2016, Earthquake probabilities for the Wasatch Front region in Utah, Idaho, and Wyoming: Utah Geological Survey Miscellaneous Publication 16-3, 164 p., 5 appendices.

Although this product represents the work of professional scientists, the Utah Department of Natural Resources, Utah Geological Survey, makes no warranty, expressed or implied, regarding its suitability for a particular use. The Utah Department of Natural Resources, Utah Geological Survey, shall not be liable under any circumstances for any direct, indirect, special, incidental, or consequential damages with respect to claims by users of this product.

Any use of trade, firm, or product names is for descriptive purposes only and does not imply endorsement by the U.S. Government or the State of Utah.

TABLE OF CONTENTS

Acronyms and Abbreviations xii
Executive Summary 1
1 Introduction 6
1.1 Background 6
1.2 Scope of Study 9
1.3 Review Process 10
1.4 Key Products 10
1.5 Report Organization 11
2 Methodology and Models 12
2.1 Wasatch Front Seismic Source Model 12
2.1.1 Fault Model 12
2.1.2 Background Earthquake Model 12
2.2 Deformation Model 13
2.3 Earthquake Rate Model 13
2.4 Probability Models 14
2.5 Treatment of Epistemic Uncertainties 14
3 Fault Characterization 15
3.1 Segmentation 15
3.2 Dips of Normal Faults 18
3.3 Depth of Seismogenic Faulting 19
3.4 Recurrence Models 22
3.5 Calculating Mean Recurrence Intervals and Rates 24
3.5.1 Time-Independent Poisson Mean Recurrence Rates 24
3.5.2 Time-Dependent BPT Mean Recurrence Intervals 25
3.5.3 Impact of Paleoseismic Data Uncertainty 25
3.6 Calculating Characteristic Magnitudes 26
3.6.1 Fault Length- Versus Displacement-Based Magnitudes 27
3.6.2 Magnitude Regressions 29
3.6.3 Regression Weights 29
4 Characterization of Wasatch Front Region Faults 32
4.1 Wasatch Fault Zone Central Segments 32
4.1.1 Paleoseismic Data Sources 33
4.1.2 Surface-Faulting Earthquake Histories 34
4.1.3 Earthquake Recurrence and Coefficient of Variation 34
4.1.4 Vertical Displacement and Slip Rate 36
4.1.5 Rupture Models and Geometries 38
4.1.6 Segment Boundary Uncertainties 40
4.1.7 Characteristic Magnitudes 41
4.2 Wasatch Fault Zone End Segments 42
4.2.1 Paleoseismic Data Sources 45
4.2.2 Earthquake Recurrence, Displacement, and Slip Rates 45
4.2.3 Rupture Models and Characteristic Magnitudes 47
4.3 Oquirrh–Great Salt Lake Fault Zone 48
4.3.1 Paleoseismic Data Sources 52
4.3.2 Analyses and Fault Source Parameters 57
4.4 Antithetic Fault Pairs 59
4.4.1 Analysis 62
4.4.2 Results 63
4.4.3 Model Parameters for Subsidiary Faults 65
4.5 Other Modeled Faults 67
4.6 Estimated Surface-Faulting Earthquakes < 18 ka in the WGUEP Wasatch Front Region 70
5 Historical Seismicity Catalog and a Background Earthquake Model 82
5.1 Overview 82
5.2 Steps in Developing a Unified Earthquake Catalog 82

5.2.1 Spatial Extent of the Catalog ... 82
5.2.2 Data Sources for the Unified Catalog ... 83
5.3 Uniform Moment Magnitude and Magnitude Uncertainty ... 83
5.3.1 Uniform Moment Magnitude ... 83
5.3.2 Magnitude Uncertainty ... 84
5.4 Best-Estimate Moment Magnitude (BEM) Catalog ... 84
5.4.1 Identification and Removal of Dependent Events (Declustering) ... 85
5.4.2 Periods of Completeness ... 85
5.5 Estimation of Unbiased Recurrence Parameters ... 85
5.5.1 Methodology to Correct for Magnitude Uncertainty ... 86
5.5.2 Rounding ... 87
5.6 Seismicity Rate Parameters of the Background Earthquake Model ... 87
6 Comparison of Geodetic and Geological/Seismological Moment Rates ... 89
6.1 Previous Work ... 89
6.2 Geodetic Data ... 92
6.3 Methodology ... 98
6.4 Geodetic Moment Rates ... 99
6.5 Geological/Seismological Moment Rates ... 100
6.6 Comparison of Geodetic and Geological/Seismological Moment Rates ... 100
6.7 Discussion: The Moment Rate Discrepancy ... 102
6.7.1 The Levan and Fayette Segments ... 102
6.7.2 Faults Omitted From the WGUEP Model ... 104
6.7.3 The Sevier Desert Detachment ... 106
6.7.4 Other Possible Explanations ... 109
6.8 Conclusions ... 109
7 Calculating Earthquake Probabilities ... 110
7.1 Methodology ... 110
7.1.1 Rupture Source Rates ... 110
7.1.2 Segment Rates ... 111
7.1.3 Magnitude Threshold for Probability Calculations ... 113
7.1.4 Magnitude-Frequency Distributions ... 113
7.1.5 Antithetic Faults ... 120
7.1.6 Segment Moment Rates ... 123
7.1.7 Implied Slip Rates ... 123
7.1.8 Probability Calculations ... 127
7.1.9 Calculation Sequence ... 127
7.2 Probability Models ... 127
7.2.1 Time-Independent – Poisson Model ... 130
7.2.2 Time-Dependent – BPT Model ... 131
7.2.3 Time-Independent versus Time-Dependent Weights ... 134
8 Earthquake Probabilities ... 135
8.1 Earthquake Probabilities in the Wasatch Front Region ... 135
8.1.1 50-Year Probabilities ... 135
8.1.2 30-Year, 100-Year, and Background Seismicity Probabilities ... 135
8.2 Probabilities for Individual Faults and Fault Segments ... 137
8.3 Sensitivity of Results to Models and Parametric Uncertainty ... 141
8.3.1 Fault Rupture Models ... 141
8.3.2 Probability Models ... 143
8.3.3 Magnitude Relations ... 146
9 Future Directions and Limitations ... 148
9.1 Characteristic Earthquake Model and Fault Segmentation ... 148
9.2 Fault Interactions ... 149
9.3 Use of Geodetic Data ... 149
9.4 Estimating Characteristic Magnitudes ... 149
9.5 COV ... 149
9.6 Time-Dependent Model Weights ... 149
10 Acknowledgments ... 150
11 References ... 150

APPENDICES

Appendix A Moment-Magnitude Regressions Considered by the WGUEP
Appendix B Holocene Paleoseismology of the Central Segments of the Wasatch Fault Zone, Utah
Appendix C Oquirrh–Great Salt Lake Fault Zone
Appendix D Other Fault Parameter Database
Appendix E A Uniform Moment Magnitude Earthquake Catalog and Background Seismicity Rates for the Wasatch Front and Surrounding Utah Region

FIGURES

ES-1 Probabilities of one or more earthquakes of **M** 6.0 and 6.75 or greater in the next 50 years in the Wasatch Front region 3
ES-2 Probabilities of one or more earthquakes of **M** 6.75 or greater in the next 50 years for selected faults and fault segments..... 5
1-1 Wasatch Front region as defined for this study 7
1-2 Segments of the WFZ in southern Idaho and northern Utah 8
3.1-1 Segmentation models for normal faults 17
3.2-1 Schematic diagram showing the non-linear increase in fault area with decreasing dip angles 18
3.3-1 Map of the Wasatch Front region showing the epicenters of 2523 earthquakes with well-constrained focal depths that occurred in this region between October 1974 and September 2011 20
3.3-2 East-west cross sections of the hypocenters with well-constrained focal depths in Figure 3.3-1 21
3.4-1 Maximum magnitude recurrence model 23
3.4-2 DTGR magnitude recurrence model 23
3.5-1 An example of a continuous gamma probability distribution for mean recurrence rate and its discrete five-point approximation calculated according to the CEUS-SSC report 24
3.5-2 An example of discretized five-point probability distributions of mean recurrence interval for the time-dependent BPT model, calculated according to the CEUS-SSC report 25
3.5-3 Examples of the effect of including uncertainty in the time interval over which past earthquakes have occurred 26
3.6-1 Average vertical displacement (D_{ave}) versus fault length (L; SRL or Lseg) for the central WFZ compared to historical scaling relations developed by Wells and Coppersmith (1994), Stirling *et al*. (2002), and Wesnousky (2008) 27
3.6-2 **M** for single- and multi-segment ruptures on the central WFZ based on estimates of M_0, which compares well with the censored-instrumental SRL-**M** regression of Stirling *et al*. (2002) 28
3.6-3 Comparison of several historical regressions on **M** with six historical large-magnitude normal-faulting earthquakes 30
4.1-1 Central segments of the WFZ showing paleoseismic research sites 33
4.1-2 Single-segment rupture model for the central WFZ 40
4.1-3 Intermediate rupture models for the central WFZ 41
4.1-4 Multi-segment rupture model for the central WFZ consisting of single-segment ruptures and multi-segment ruptures..... 42
4.1-5 Rupture lengths and segment-boundary uncertainties for single-segment ruptures on the WFZ central segments..... 43
4.1-6 Segment-boundary uncertainties for multi-segment ruptures on the central WFZ 44
4.2-1 Rupture lengths and segment-boundary uncertainties for single-segment ruptures on the WFZ end segments, and a LS-FS multisegment rupture 49
4.3-1 Segments of the OGSLFZ 51
4.4-1 Antithetic fault pairs in the Wasatch Front region 64
4.4-2 Graphical summary of antithetic-fault-pair metrics 65
5.2-1 Sketch map of catalog domains 83
5.4-1 Epicenter maps of earthquakes in the BEM catalog, 1850 through September 2012 84
5.5-1 Schematic frequency-magnitude diagram showing how unbiased ("true") recurrence rates can be determined by making appropriate corrections in either the x-direction in terms of magnitude or in the y-direction in terms of rate 86
5.6-1 Background earthquake model 87
6.1-1 Map of the Wasatch Front region showing surface traces of faults and fault segments considered in the earthquake forecast and subregions for comparisons of geodetic and geological/seismological moment rates 90
6.1-2 Comparison of observed and predicted velocity vectors, relative to stable North America, for the Wasatch Front region and the surrounding area 91
6.1-3 Comparison of fault slip rates from geological data and from the geodetic inversion of Zeng and Shen (2014) for faults in the Wasatch Front region 92
6.2-1 Color-coded map of maximum horizontal principal strain rate, $\dot{\epsilon}_1$ (extension positive) 95

6.2-2 Plot of N. 86° E. (mean $\dot{\epsilon}_1$-weighted $\dot{\epsilon}_1$ azimuth) velocity versus distance east for GPS stations in the Wasatch Front region 97
6.2-3 Same as Figure 6.2-2, but for the subregions shown in Figure 6.1-1 97
6.3-1 Block diagram of a normal fault 99
6.7-1 Map of the west-central part of the L-F subregion 105
7.1-1 Calculation of rupture source rates 111
7.1-2 Mean and ± 2σ cumulative magnitude-frequency relationships for the WFZ, OGSLFZ, background seismicity, and "other modeled faults" 121
7.1-3 Cumulative magnitude-frequency relationships for the "other modeled faults" 121
7.1-4 Mean incremental magnitude-frequency relationships for the WFZ, OGSLFZ, background seismicity, "other modeled faults," and total of all sources 122
7.1-5 Mean incremental magnitude-frequency relationships for the "other modeled faults" 122
7.1-6 Segment moment rates for the WFZ central segments and the single-segment rupture fault model 124
7.1-7 Segment moment rates for the WFZ central segments and all fault rupture models 124
7.1-8 Distribution of moment to segments from the unsegmented rupture model for the WFZ 125
7.1-9 Segment moment rates for the WFZ 125
7.1-10 Segment moment rates for the OGSLFZ 126
7.1-11 Distribution of moment to segments from the unsegmented rupture model for the OGSLFZ. 126
7.2-1 Illustration of the calculation of conditional probability from a PDF 131
7.2-2 BPT model 132
8.1-1 Probabilities of one or more earthquakes of **M** 6.0 and 6.75 or greater in the next 50 years in the Wasatch Front region 136
8.2-1 Probabilities of one or more earthquakes of **M** 6.75 or greater in the next 50 years for selected faults and fault segments 139

TABLES

2-1 WGUEP fault model components 13
3.2-1 Change in fault area for varying values of fault dip calculated for a fault length of 30 km and a seismogenic crustal thickness of 15 km 18
3.3-1 Focal depth percentiles 22
3.6-1 Average displacement per fault length relations 28
3.6-2 Moment-magnitude regressions and weights for Wasatch Front faults 30
4.1-1 Summary of earthquake timing data for the central WFZ 35
4.1-2 Mean recurrence intervals for the central WFZ 35
4.1-3 Summary of displacement per rupture source on the central WFZ 37
4.1-4 Summary of vertical slip rates for the central WFZ 37
4.1-5 Summary of rupture models and weights for the central WFZ 39
4.1-6 M_{char} distributions for central WFZ rupture sources 44
4.2-1 Displacement, slip rate, and recurrence for the WFZ end segments 46
4.2-2 Slip-rate model distributions for the WFZ end segments 47
4.2-3 Rupture lengths for the WFZ end segments 50
4.2-4 M_{char} distributions for WFZ end-segment rupture sources 50
4.3-1 Paleoearthquake times and estimated earthquake recurrence intervals for the Great Salt Lake fault 54
4.3-2 Timing of surface-faulting earthquakes on segments of the OGSLFZ 57
4.3-3 Rupture models for the OGSLFZ 58
4.3-4 Lengths for the OGSLFZ rupture sources 59
4.3-5 Modeled vertical displacement distributions for selected rupture sources of the OGSLFZ 59
4.3-6 Characteristic magnitude distributions for the OGSLFZ rupture sources 60
4.3-7 Poisson rate distributions for OGSLFZ rupture sources 60
4.3-8 Brownian Passage Time recurrence interval distributions for the Antelope Island and Fremont Island rupture sources of the OGSLFZ 62
4.4-1 Summary of antithetic-fault-pair metrics 66
4.4-2 Model parameters for subsidiary antithetic faults 66
4.5-1 Quaternary-active faults/fault segments in the Wasatch Front region removed from further consideration in the WGUEP earthquake forecast 68
4.5-2 Other modeled faults—Quaternary-active faults/fault segments in the Wasatch Front region, other than the WFZ and OGSLFZ, retained in the WGUEP fault model 69

4.5-3 Fault/fault segment parameters from USGS (2013) ... 69
4.6-1 Estimated surface-faulting earthquakes < 18 ka for the WGUEP Wasatch Front region ... 71
5.2-1 Boundaries of catalog domains (inclusive) ... 83
5.4-1 Data for seismicity rate calculations, WGUEP Region (BEM catalog, declustered) ... 85
5.6-1 Cumulative rates of independent background earthquakes ... 88
6.2-1 GPS velocity vectors for the Wasatch Front region ... 93
6.2-2 Average strain rates for the Wasatch Front region and subregions ... 96
6.5-1 Geological/seismological moment rates for Wasatch Front region seismic sources ... 101
6.5-2 Geological/seismological moment rates for the Wasatch Front region and subregions ... 102
6.6-1 Comparison of geodetic and geological/seismological moment rates ... 102
6.7-1 Faults in the L-F subregion that are not included in the WGUEP fault model ... 104
7.1-1 Recurrence intervals of characteristic events for the WFZ central segment models ... 112
7.1-2 Rupture source rates (Poisson) for the WFZ end segment and unsegmented fault models ... 113
7.1-3 Recurrence intervals for characteristic events and rupture source rates (Poisson) for OGSLFZ fault models ... 114
7.1-4 Rupture source rates (Poisson) for "other modeled faults" included in Wasatch Front region fault models ... 116
7.1-5 Segment rupture rates (Poisson) for the WFZ central segment fault models ... 117
7.1-6 Segment rupture rates (Poisson) for the WFZ end segment fault models ... 117
7.1-7 Segment rupture rates (Poisson) for the WFZ unsegmented fault model ... 118
7.1-8 Segment rupture rates (Poisson) for the WFZ ... 118
7.1-9 Segment rupture rates (Poisson) for OGSLFZ fault models ... 119
7.1-10 Segment rupture rates (Poisson) for the OGSLFZ ... 120
7.1-11 Segment rupture rates (Poisson) for other segmented faults in the Wasatch Front region ... 120
7.1-12 Segment moment rates ... 128
7.1-13 Implied slip rates for the WFZ central segments using a single-segment rupture model ... 130
7.1-14 Correlation of inputs ... 130
7.2-1 Recurrence intervals for time-dependent (BPT) calculations for the WFZ central segments ... 133
7.2-2 Recurrence intervals for time-dependent (BPT) calculations for the OGSLFZ ... 133
7.2-3 Equivalent Poisson rupture rates for time-dependent (BPT) rupture sources of the WFZ ... 133
7.2-4 Equivalent Poisson rupture rates for time-dependent (BPT) rupture sources of the OGSLFZ ... 133
8.1-1 Wasatch Front region 50-year probabilities ... 137
8.1-2 Wasatch Front region 30-year probabilities ... 137
8.1-3 Wasatch Front region 100-year probabilities ... 137
8.1-4 Background seismicity probabilities ... 137
8.2-1 WFZ segment 50-year probabilities ... 138
8.2-2 OGSLFZ segment 50-year probabilities ... 138
8.2-3 "Other modeled fault" 50-year probabilities ... 140
8.2-4 WFZ segment 30-year probabilities ... 141
8.2-5 OGSLFZ segment 30-year probabilities ... 141
8.2-6 "Other modeled fault" 30-year probabilities ... 142
8.2-7 WFZ 100-year probabilities ... 143
8.2-8 OGSLFZ segment 100-year probabilities ... 143
8.2-9 "Other modeled fault" 100-year probabilities ... 144
8.3-1 Sensitivity to fault rupture models of the WFZ central segments, **M** ≥ 6.75 in 50-year probabilities ... 145
8.3-2 Sensitivity to fault rupture models of the OGSLFZ segments, **M** ≥ 6.75 in 50-year probabilities ... 145
8.3-3 WFZ central segments, all fault models, **M** ≥ 6.75 probabilities ... 145
8.3-4 WFZ central segments, single-segment rupture model, **M** ≥ 6.75 probabilities ... 145
8.3-5 Sensitivity to COV: WFZ central segments, single-segment rupture model, **M** ≥ 6.75 in 50-year probabilities ... 146
8.3-6 OGSLFZ, single-segment rupture model, **M** ≥ 6.75 probabilities ... 146
8.3-7 Sensitivity to COV: OGSLFZ, single-segment rupture model, **M** ≥ 6.75 in 50-year probabilities ... 146
8.3-8 Sensitivity to magnitude relations: WFZ central segments, **M** ≥ 6.75 in 50-year probabilities ... 147
8.3-9 Sensitivity to magnitude relations: OGSLFZ, **M** ≥ 6.75 in 50-year probabilities ... 147
8.3-10 Sensitivity to magnitude relations: East Cache and Eastern Bear Lake faults, **M** ≥ 6.75 in 50-year probabilities ... 147

ACRONYMS AND ABBREVIATIONS

A	rupture area
AF	American Fork
AFP	antithetic fault pairs
AI	Antelope Island segment
A-M	area–magnitude
AMRT	apparent mean residence time
AMS	accelerator mass spectrometry
A_{IV}, A_V, A_{VI}, and A_{VII}	area shaken at or greater than MMI IV, V, VI, and VII
BC	Bowden Canyon
BCS	Brigham City segment
BEC	Box Elder Canyon
BEM	best-estimate moment magnitude
B.P.	before present (1950)
BPT	Brownian Passage Time
BRP	Basin and Range Province
BRPEWG	Basin and Range Province Earthquake Working Group
BRPEWGII	Basin and Range Province Earthquake Working Group II
^{14}C	radiocarbon
CEUS	central and eastern U.S.
CMS	Clarkston Mountain segment
COV	coefficient of variation
CR	conversion relationship
CRC	cumulative recurrence curve
CS	Collinston segment
D_{ave}	average displacement
D_{max}	maximum displacement
DC	Deep Creek
DEM	digital elevation model
DOE	U.S. Department of Energy
DTGR	doubly truncated Gutenberg-Richter
EBR	extended border region
ECFZ	East Cache fault zone
E[M]	uniform estimate of moment magnitude
EO	East Ogden
EPRI	Electric Power Research Institute
ERZ	standard vertical hypocentral error
ET	East Tintic segment
ETMF	East Tintic Mountains fault
FA	total felt area
FI	Fremont Island segment
FS	Fayette segment
GC	Garner Canyon
GEM	Global Earthquake Model
GPS	Global Positioning Satellite
GSLFZ	Great Salt Lake fault zone
HC	Hansen Canyon
IRSL	infrared stimulated luminescence
I_0	intensity at the epicenter
ISB	Intermountain Seismic Belt
K	Kaysville
ka	thousand years ago
KC	Kotter Canyon
K-S	Kolmogorov-Smirnov
kyr	thousand years
LCC	Little Cottonwood Canyon

LS	Levan segment
L_{seg}	linear segment length
L_{sub}	linear subsurface rupture length
L-F	Levan and Fayette segments
M	moment magnitude
Ma	million years ago
m_b	body-wave magnitude
M_C	coda magnitude
M_{char}	characteristic magnitude
MCS	Malad City segment
MD	duration magnitude
M_L	Richter local magnitude
mm/yr	millimeters per year
MMI	Modified Mercalli Intensity
MN	Mapleton North
M_0	seismic moment
M_{obs}	observed moment magnitude
MRE	most recent earthquake
MS	Mapleton South
MSR	multi-segment rupture
M_T	threshold magnitude
N*	effective number of earthquakes
NASA	National Aeronautics and Space Administration
NC	North Creek
NEHRP	National Earthquake Hazards Reduction Program
NEPEC	National Earthquake Prediction Evaluation Council
NO	Northern Oquirrh segment
NRC	Nuclear Regulatory Commission
NS	Nephi segment
NSHM	National Seismic Hazard Maps
nstr/yr	nanostrains per year
NVTD	net vertical tectonic displacement
OFZ	Oquirrh fault zone
OGSLFZ	Oquirrh-Great Salt Lake fault zone
OSL	optically stimulated luminescence
P(a)	probability of activity
PC	Pearsons Canyon
PD	Penrose Drive
PDF	probability density function
PP	Pole Patch
PS	Provo segment
PSHA	probabilistic seismic hazard analysis
PY	Promontory segment
RC	Rice Creek
REC	Red Canyon
ROC	Rock Canyon
RZ	Rozelle segment
SFDC	South Fork Dry Creek
SLCS	Salt Lake City segment
SO	Southern Oquirrh segment
SOMFZ	Southern Oquirrh Mountains fault zone
SP	Skinner Peaks
SQ	Santaquin
SR	slip rate
SRL	surface-rupture length
SRL-**M**	surface rupture length–magnitude
SSC	seismic source characterization

SSR	single-segment rupture
TH	Topliff Hill segment
THFZ	Topliff Hills fault zone
UCERF	Unified California Earthquake Rupture Forecast
UGS	Utah Geological Survey
ULFF	Utah Lake faults and folds
UQFPWG	Utah Quaternary Fault Parameters Working Group
USGS	U.S. Geological Survey
UTR	Utah Region
UTREXT	Extended Utah Region
UU	University of Utah
UUSS	University of Utah Seismograph Stations
WC	Willow Creek
WFZ	Wasatch fault zone
WGCEP	Working Groups on California Earthquake Probabilities
WGUEP	Working Group on Utah Earthquake Probabilities West
WVFZ	Valley fault zone

EARTHQUAKE PROBABILITIES FOR THE WASATCH FRONT REGION IN UTAH, IDAHO, AND WYOMING

by Working Group on Utah Earthquake Probabilities

EXECUTIVE SUMMARY

In a letter to *The Salt Lake Daily Tribune* in September 1883, U.S. Geological Survey (USGS) geologist G.K. Gilbert warned local residents about the implications of observable fault scarps along the western base of the Wasatch Range. The scarps were evidence that large surface-rupturing earthquakes had occurred in the past and more would likely occur in the future. The main actor in this drama is the 350-km-long Wasatch fault zone (WFZ), which extends from central Utah to southernmost Idaho. The modern Wasatch Front urban corridor, which follows the valleys on the WFZ's hanging wall between Brigham City and Nephi, is home to nearly 80% of Utah's population of 3 million. Adding to this circumstance of "lots of eggs in one basket," more than 75% of Utah's economy is concentrated along the Wasatch Front in Utah's four largest counties, literally astride the five central and most active segments of the WFZ.

Since the late 1960s, abundant paleoseismic data on the timing and size of prehistoric surface-rupturing earthquakes have been collected on the WFZ and other faults in Utah's Wasatch Front region, which extends into southeastern Idaho and southwestern Wyoming (Figure ES-1). Motivated in part by the recent development of improved methods to analyze paleoseismic data, the Working Group on Utah Earthquake Probabilities (WGUEP) was formed in January 2010, under the auspices of the Utah Geological Survey (UGS) and the USGS, to evaluate the probabilities of future occurrence of moderate-to-large earthquakes in the Wasatch Front region. The working group consisted of 14 geologists, seismologists, and engineers affiliated with diverse Federal, State, academic, and consulting organizations.

The WGUEP's goal was to develop probabilistic earthquake forecasts for the Wasatch Front region that include: (1) combined time-dependent and time-independent probabilities of large earthquakes for the five central segments of the WFZ and two segments of the Great Salt Lake fault zone, (2) time-independent probabilities for less well-studied faults, and (3) estimates of the time-independent probabilities of background earthquakes not associated with known or mapped faults in the moment magnitude (**M**) 5.0 to 6.75 range.

The WGUEP provides these forecasts with the hope that they will help heighten the public's awareness and understanding of the region's seismic hazards, just as the forecasts of the Working Groups on California Earthquake Probabilities (WGCEP) have successfully done. Our consensus-based time-dependent and time-independent earthquake probabilities in the Wasatch Front region are not only useful for regional hazard analyses, they also provide a robust basis for site-specific probabilistic seismic hazard analyses (PSHAs) for the safe design and evaluation of critical structures and facilities. Further, our time-dependent probabilities for fault ruptures can be incorporated into the PSHAs that will underpin urban seismic hazard maps planned by the USGS for the Wasatch Front region. Additionally, our earthquake forecasts can aid in developing public policies leading to more effective, sustained earthquake mitigation efforts in the Wasatch Front region.

Similar to the approach used by the 2008 WGCEP, the WGUEP methodology relies on four basic model components: a seismic source model, a deformation model, an earthquake rate model, and a probability model. In general, the seismic source model characterizes the physical geometry of the known faults; the deformation model gives recurrence intervals and/or slip rates for each fault segment and/or fault; the earthquake rate model gives the long-term rate of all earthquakes throughout the region above a specified threshold (in this case **M** 5.0 and greater); and the probability model gives a probability for earthquakes of different size over a specified time period. However, some significant differences exist between the WGUEP and the 2008 WGCEP model components; the WGUEP counterparts are much simpler due in large part to the availability of robust paleoseismic data for the WFZ and other faults in the Wasatch Front region.

Our probability model describes how earthquakes are distributed in time. The simplest version is the time-*independent* Poisson (memoryless) model, which assumes that each earthquake is completely independent of the timing of all other events. For example, with this model it makes no difference in the forecast for the Salt Lake City segment whether its last rupture occurred yesterday or 1000 years ago. Following the lead of the 2008 WGCEP, we have used only one time-*dependent* model, the Brownian Passage Time (BPT) model. The BPT model is a stress-renewal model that computes the probability of each segment rupturing conditioned on the length of time since the last event.

The WGUEP seismic source model consists of six groups of seismic sources: (1) the five central segments of the WFZ, (2) the end segments of the WFZ, (3) the combined Oquirrh–Great Salt Lake fault zone (OGSLFZ), (4) antithetic fault pairs (two faults that intersect each other at depth and may rupture coseismically), (5) significant other faults

in the Wasatch Front region, and (6) crustal background earthquakes. Background earthquakes are defined as those events less than **M** 6.75 ± 0.25 that cannot be associated with a known fault. A classic example of a background earthquake within the Wasatch Front region is the 1975 **M** 6.0 Pocatello Valley, Idaho, earthquake.

The 350-km-long WFZ consists of 10 segments that are thought to have ruptured repeatedly and independently in large magnitude (**M** ≥ 6.75) earthquakes. The five central segments from north to south are the Brigham City, Weber, Salt Lake City, Provo, and Nephi segments (Figure ES-1). These central segments are thought to be the most hazardous, because each segment has had multiple large Holocene (past 11,700 yrs) earthquakes that have produced surface rupture. Detailed geologic investigations at 23 paleoseismic sites on these segments have yielded data on the timing of past earthquakes and/or measured single-event fault displacements. The resulting data show that at least four to five earthquakes large enough to cause surface rupture have occurred on each central segment in the past ~6000 years. Despite the abundant paleoseismic data, a number of important questions needed to be considered in the WGUEP forecast. For example, although the paleoseismic data generally support the prevailing segmentation model for the WFZ, is it possible that adjacent segments have ruptured together, in whole or part, during a single large earthquake? To address the questions and reduce uncertainties in the sizes and timing of past events, we extensively and systematically reviewed and analyzed all of the available paleoseismic data for the five central segments.

At least 22 surface-faulting earthquakes have ruptured the central segments of the WFZ since about 6000 years ago, based on our analysis of all of the paleoseismic data and assuming that each earthquake ruptured a single segment of the fault zone. Using our revised surface-faulting earthquake histories for each segment, we calculated inter-event and mean recurrence intervals, which indicate a moderately periodic pattern of earthquake recurrence on the central WFZ as a whole: inter-event times for the segments range from 700 to 2700 years, and mean recurrence intervals range from 900 to 1500 years, similar to a composite mean recurrence interval for the central WFZ of about 1200 years.

Although we favor single-segment ruptures as the dominant earthquake process on the WFZ, we addressed uncertainties in the model by constructing rupture models that include both single- and multi-segment ruptures and by defining spatial uncertainties in the segment-boundary locations. We developed the models following our evaluation of possible multi-segment ruptures, which relied mostly on per-segment earthquake timing and displacement data. A companion *unsegmented* model allows potential "floating" ruptures along the WFZ that ignore the location of segment boundaries, thus complementing the range of possible ruptures included in the segmented models. The single-segment rupture model received more weight than those including multi-segment ruptures based on the significant timing differences in the youngest and best-constrained earthquakes along the fault, unique surface-faulting histories per segment, displacement-per-event data, and the presence of prominent bends or stepovers in the fault trace and/or basin depth changes at the segment boundaries. Characteristic magnitudes for the central WFZ segments range from a best-estimate **M** 7.1 for the Brigham City segment to **M** 7.3 for the Provo segment.

In addition to examining the central WFZ segments, we reviewed and evaluated paleoseismic data for other faults in the region to develop rupture models, characteristic earthquake, and rate information (earthquake timing and/or fault slip rates) for input into the WGUEP forecasts. These other faults included: (1) the end segments of the WFZ; (2) the OGSLFZ, particularly the Antelope Island and Fremont Island segments of the Great Salt Lake fault; (3) antithetic fault pairs such as the West Valley fault zone and the Salt Lake City segment of the WFZ; and (4) 45 other faults and fault segments in the Wasatch Front region.

Paleoseismic data for the five central segments of the WFZ as well as the Antelope Island and Fremont Island segments of the Great Salt Lake fault zone are sufficiently robust that we analyzed them in both a time-dependent and time-independent manner. The WFZ end segments, the Oquirrh fault zone, and all other faults were treated solely in the traditional time-independent manner due to insufficient information for a time-dependent analysis.

The background earthquake model depicts the fraction of future mainshocks in the Wasatch Front region that are expected to occur on seismic sources other than faults identified in the WGUEP fault model. For purposes of the WGUEP forecast, the background earthquake model provides rates for future mainshocks of **M** 5.0 or greater up to a maximum of **M** 6.75 ± 0.25. The probabilities for background earthquakes were treated only in a time-independent manner.

We compiled and processed an up-to-date historical and instrumental earthquake catalog for the background earthquake model that meets the needs of state-of-practice seismic hazard analysis, namely a catalog that: (1) is complete in terms of accounting for all known earthquakes in the magnitude range of interest; (2) assigns a uniform moment magnitude to each event; (3) identifies "dependent" events (foreshocks, aftershocks, and the smaller events of earthquake swarms) in earthquake clusters that can be removed for statistical analysis of mainshock recurrence parameters; (4) excludes non-tectonic seismic events such as blasts and mining-induced seismicity; and (5) quantifies the uncertainty and rounding error associated with the assigned magnitude of each earthquake.

Geodetic data were used in the most recent WGCEP forecasts and are increasingly being used in probabilistic seismic hazard analyses to estimate fault slip rates. Because of

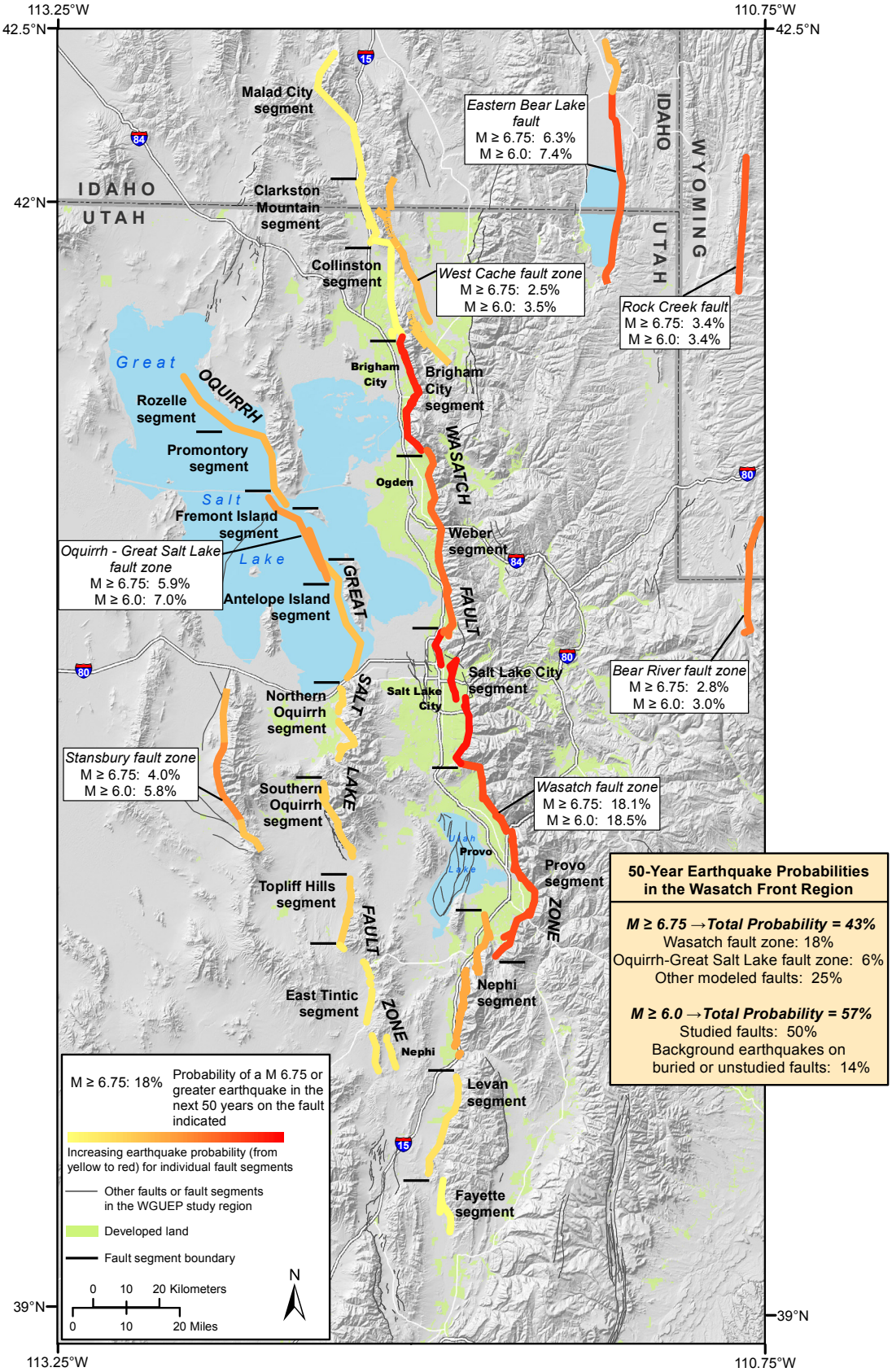

Figure ES-1. Probabilities of one or more earthquakes of **M** 6.0 and 6.75 or greater in the next 50 years (2014–2063) in the Wasatch Front region. "Other modeled faults" are those faults other than the Wasatch and the Oquirrh–Great Salt Lake fault zones. "Studied faults" include the Wasatch and Oquirrh–Great Salt Lake fault zones and the other modeled faults. Shaded topography generated from 90-m digital elevation data (https://eros.usgs.gov/elevation-products).

discrepancies observed in previous studies between geodetic moment rates and geological/seismological moment rates in the Wasatch Front region, we compared these rates for both the Wasatch Front region as a whole and four subregions. The geodetic moment rates for the Wasatch Front region, and for three of its four subregions, are consistent with the geological/seismological moment rates calculated for the WGUEP earthquake rate model. The geodetic moment rates are not consistent with the WGUEP earthquake rate model in the fourth subregion, an area that encompasses the Levan and Fayette segments of the WFZ. Further work is needed to identify the cause of this moment rate discrepancy; however, regardless of the cause of the discrepancy, we do not expect it to significantly affect the WGUEP forecast for the Wasatch Front region as a whole.

Based on the inputs summarized above, Figures ES-1 and ES-2 summarize earthquake probabilities in the Wasatch Front region in the next 50 years. The probability of one or more large (**M** ≥ 6.75) earthquakes occurring in the Wasatch Front region in the time period of 2014 to 2063 is 43%. This regional probability is for earthquakes on all of the characterized faults and the background seismicity. The probability of one or more earthquakes of **M** 6.0 or larger in the Wasatch Front region in the next 50 years is 57% (Figure ES-1). In addition to the probabilities shown on Figures ES-1 ans ES-2, the probability of one or more earthquakes of **M** 5.0 or larger in the Wasatch Front region in the next 50 years is 93%.

A significant contribution to these total probabilities comes from the WFZ and OGSLFZ. The total probability of at least one earthquake of **M** 6.75 or larger on either of these two fault zones is 23% in the next 50 years. The total probability from the other modeled faults is 25% due in part to some significant contributions from faults with higher slip rates such as the Eastern Bear Lake and Stansbury fault zones (Figure ES-1). The Eastern Bear Lake fault has a probability of 6.3% for one or more earthquakes of **M** 6.75 or larger in the next 50 years (Figure ES-1). For one or more earthquakes of **M** 6.0 or larger on the other faults, the 50-year probability is 34%. For background earthquakes of **M** 6.0 or larger on buried or unknown faults, the 50-year probability is 14%.

Figure ES-2 shows the 50-year probabilities for earthquakes of **M** 6.75 or larger on selected fault segments. For example, the probabilities on the Salt Lake City, Brigham City, Provo, and Weber segments are 5.8%, 5.6%, 3.9%, and 3.2%, respectively. The 50-year probability on the Nephi segment is relatively low at only 1.8% because its most recent rupture occurred only about 300 years ago. Although these individual probabilities might seem small, the total probability for an earthquake of **M** 6.75 or larger somewhere on the WFZ in the next 50 years is 18%. In the next 100 years, the probability increases to 33%. Such a large earthquake occurring anywhere along the WFZ will result in significant damage to communities in the Wasatch Front region and to the economy of the region as a whole (e.g., see Earthquake Engineering Research Institute, 2015).

Considering that the average age of Utah's citizens is the youngest in the nation with a median age of 29.2 years, there is a realistic chance that many current residents of the Wasatch Front region will experience a large earthquake in their lifetimes. Preparing for earthquakes requires an awareness that even earthquakes in the **M** 5 range can cause significant localized damage in urbanized areas, and the probability of earthquakes of this size occurring in the coming decades is very high.

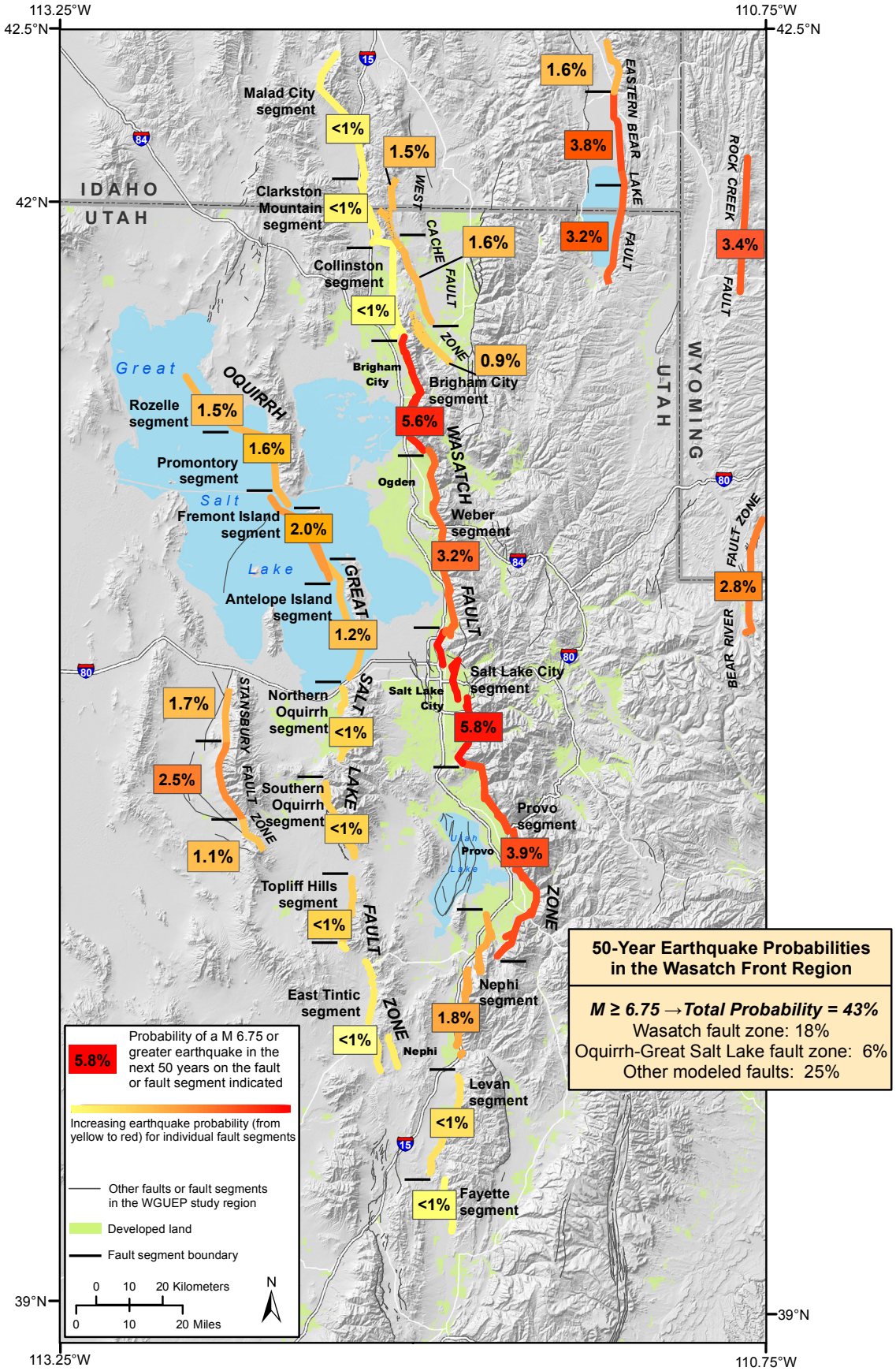

Figure ES-2. Probabilities of one or more earthquakes of **M** 6.75 or greater in the next 50 years for selected faults and fault segments. Shaded topography generated from 90-m digital elevation data (https://eros.usgs.gov/elevation-products).

1 INTRODUCTION

On July 24, 1847, when Mormon pioneers first viewed the Salt Lake Valley, Brigham Young famously pronounced, "This is the right place"—the place of destiny and refuge they had been seeking. By the time of Young's death in 1877, Mormon pioneers had extensively colonized most of what we now recognize as Utah's main seismic belt, notably along the Wasatch Front, the western escarpment of the Wasatch Range that forms the eastern topographic boundary of the Basin and Range Province (BRP). The dramatic topographic expression of the Wasatch Front signals active tectonic forces inexorably at work.

In his classic letter to *The Salt Lake Daily Tribune* in September 1883, G.K. Gilbert, then a senior geologist with the newly formed U.S. Geological Survey (USGS), warned local residents about the implications of observable fault scarps along the western base of the Wasatch Range—large surface-rupturing earthquakes had occurred before Mormon settlement and more would occur in the future. The main actor in this drama of course is the 350-km-long Wasatch fault zone (WFZ), which extends from central Utah to southernmost Idaho (Figure 1-1). The modern Wasatch Front urban corridor, which follows the valleys on the WFZ hanging wall between Brigham City and Nephi, is home to nearly 80% of Utah's population of 3 million. Adding to this circumstance of "lots of eggs in one basket," more than 75% of Utah's economy is concentrated along the Wasatch Front in Utah's four largest counties, literally astride the five central and most active segments of the WFZ.

In the past two decades, estimates of the probabilities of large earthquakes occurring in a specified time period in California have been developed by special working groups. Studies have been done for the San Francisco Bay area (Working Group on California Earthquake Probabilities [WGCEP], 1988, 1990, 1999, 2003), for southern California (WGCEP, 1995), and most recently, for California statewide as part of the Unified California Earthquake Rupture Forecast (UCERF) (WGCEP, 2008, 2014). The purpose of these studies was to calculate time-dependent probabilities of large earthquakes on major faults where requisite information was available on the expected mean frequency of earthquakes and the elapsed time since the most recent large earthquake (MRE). Where such information was lacking on less well-studied faults, time-independent probabilities were estimated. The key to making reliable earthquake probabilistic forecasts has been the availability of the requisite data.

The WGCEP reports have found a broad audience. Their probabilities have been successfully used to heighten public awareness of earthquake hazards, as a basis for lifeline infrastructure agencies to set priorities for retrofitting their systems, as motivation for municipalities to adopt unreinforced masonry retrofit ordinances, and for setting earthquake insurance rates. The characterization of earthquake sources has also provided the seismic source characterization input for California in the USGS National Seismic Hazard Maps (NSHMs). Similar to what has occurred in California, an authoritative consensus-based estimate of earthquake probabilities, developed and reviewed by the earth science community, can be incorporated into public policies in the Wasatch Front region that can help drive greater and more sustained earthquake mitigation efforts.

The level of information on past earthquakes on the WFZ and to a lesser extent on other regional faults, along with available information on regional seismicity, is now sufficiently robust to provide the requisite data for making probabilistic estimates of future large earthquakes along the WFZ and within the Wasatch Front region as defined on Figure 1-1. The methodologies necessary to estimate such probabilities have been developed and refined by the various California working groups and can now be applied in Utah. Previous estimates of WFZ earthquake probabilities, using information available at the time, have been made by Nishenko and Schwartz (1990), McCalpin and Nishenko (1996), McCalpin (2002) (Salt Lake City segment only), and Wong *et al*. (2002). The updated probabilities in this report supersede estimates made in these earlier studies.

A consensus-based earthquake forecast for the Wasatch Front region can have varied practical value beyond raising earthquake awareness and influencing public policy-making. The authoritative model components of the forecast provide a robust foundation for up-to-date probabilistic seismic hazard analyses (PSHA), both regional and site-specific. A principal regional application will be the incorporation of the model components into the next generation of NSHMs, which are the basis for building code provisions of the National Earthquake Hazards Reduction Program (NEHRP). On a finer scale, our time-dependent earthquake probabilities can be an important element of the PSHAs that will underpin urban seismic hazard maps for parts of the Wasatch Front region that are planned by the USGS for the Wasatch Front region. Site-specific PSHAs for critical structures and facilities can directly build upon the model components of the forecast.

1.1 Background

The WFZ is the most studied Quaternary normal fault in the world (e.g., Swan *et al*., 1980; Lund *et al*., 1991; Machette *et al*., 1991, 1992; Black *et al*., 1996; Lund and Black, 1998; Lund, 2005; Nelson *et al*., 2006; Olig *et al*., 2006; Machette *et al*., 2007; DuRoss *et al*., 2008, 2009, 2012; Personius *et al*., 2012). Paleoseismic evidence indicates that the fault is separated into seismogenic segments with relatively persistent boundaries between prehistoric surface ruptures (Schwartz and Coppersmith, 1984; Machette *et al*., 1991; DuRoss, 2008) (Figure 1-2). Repeated Holocene surface-faulting earthquakes are well documented along the five central segments,

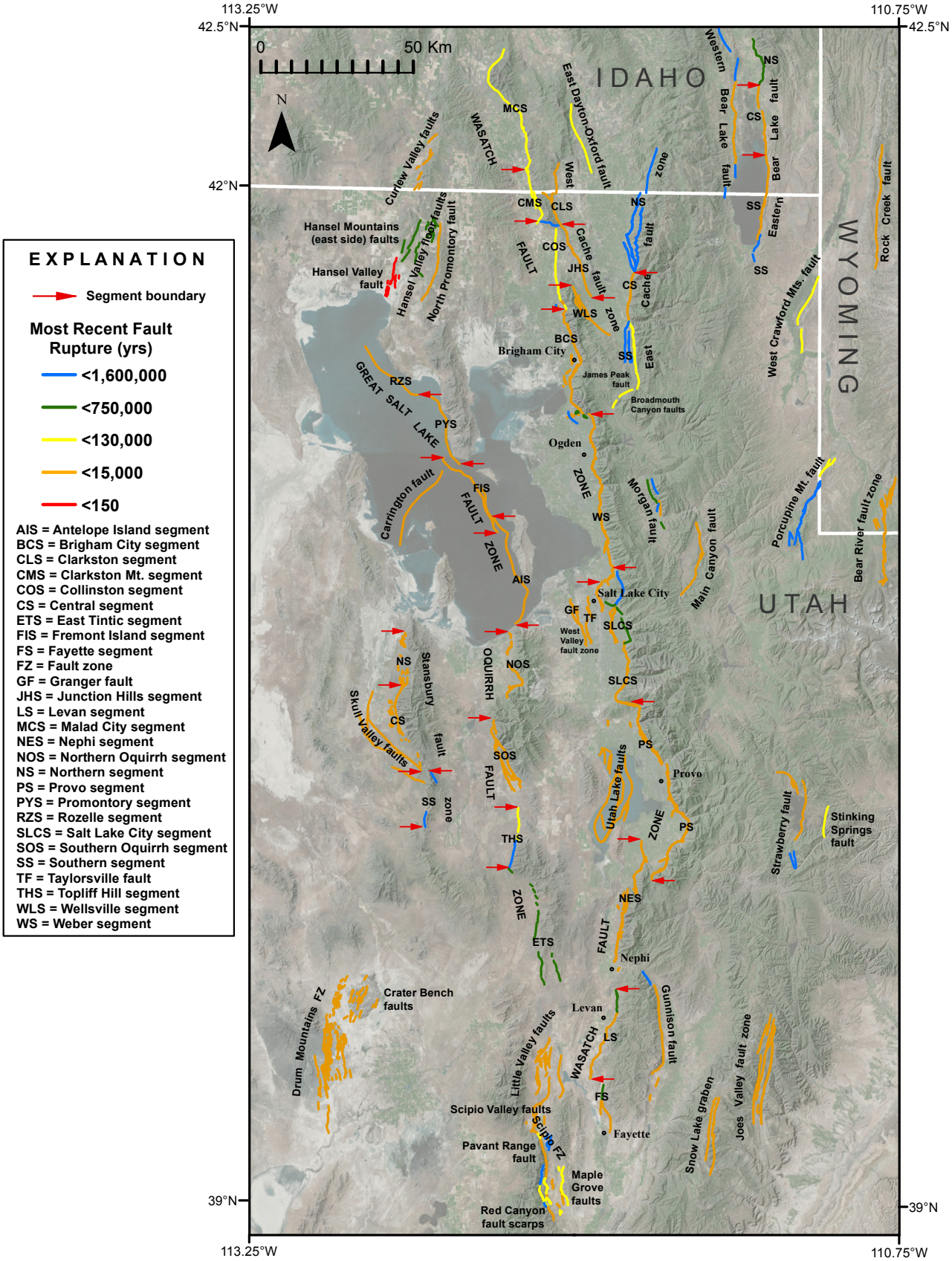

Figure 1-1. Wasatch Front region as defined for this study, which extends from 39.0° to 42.5°N latitude and 110.75° to 113.25°W longitude. Faults and fault segments shown are considered in the WGUEP probabilistic earthquake forecast. Base imagery from the USGS and National Aeronautics and Space Administration (NASA) (http://imagery.arcgisonline.com).

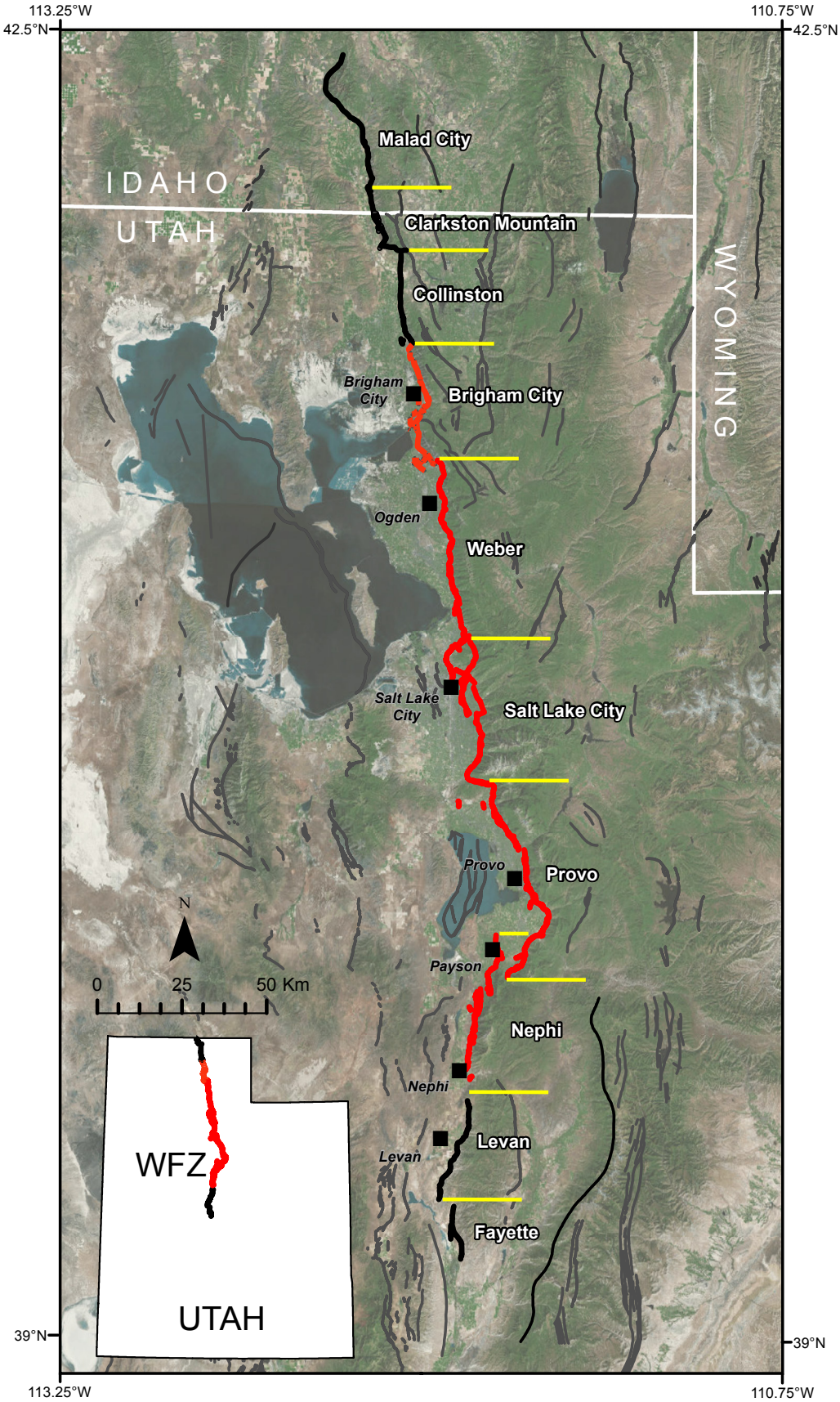

Figure 1-2. Segments of the WFZ in northern Utah and southern Idaho. The central WFZ, which has evidence of repeated Holocene surface-faulting earthquakes, is shown in red; end segments of the WFZ are shown in black. Other Quaternary faults in northern Utah are shown in dark gray. Fault traces from Black *et al*. (2003); base map is true-color satellite image (http://visibleearth.nasa.gov/view.php?id=55874).

which bound the valleys where most of Utah's population resides, and recurrence intervals are typically between one and a few thousand years (Machette *et al*., 1992; Lund, 2005). For the central segments, the Utah Quaternary Fault Parameters Working Group (UQFPWG) assigned consensus recurrence rates based on paleoseismic trenching information available up to 2005 (Lund, 2005). Since 2005, new data have become available for the Provo segment (Olig *et al*., 2006), the Nephi segment (DuRoss *et al*., 2008; Machette *et al*., 2007; Crone *et al*., 2014), the Weber segment (Nelson *et al*., 2006; DuRoss *et al*., 2009), and the Brigham City segment (DuRoss *et al*., 2012; Personius *et al*., 2012). Additionally, detailed paleoseismic trenching studies have been completed for the northern part of the Salt Lake City segment (DuRoss *et al*., 2014), the subparallel West Valley fault zone (Hylland *et al*., 2014), and the Nephi segment (DuRoss, 2014). The Salt Lake City segment and the Brigham City segment have the highest time-dependent hazard of the WFZ segments based on the long elapsed times since their most recent earthquakes (Wong *et al*., 2002).

Using then-available data and methods, McCalpin and Nishenko (1996) calculated both time-dependent and time-independent probabilities for the central WFZ. For the WFZ as a whole, they calculated Poisson (time-independent) probabilities of an earthquake of moment magnitude (**M**) 7.0 and larger to be 13% for 50 years and 25% for 100 years. Their time-dependent estimates for the Brigham City and Salt Lake City segments range up to 26% and 25%, respectively, in a 50-year period, and 46% and 57%, respectively, in a 100-year period. Time-dependent probabilities for the Weber, Provo, and Nephi segments were low (< 0.03) because each of those segments produced a large earthquake fairly recently (McCalpin and Nishenko, 1996). Wong *et al*. (2002), following the approach of the WGCEP (1999), calculated time-dependent probabilities and equivalent Poisson recurrence intervals (Section 7.2.2) that could be incorporated into hazard analyses for the Salt Lake City and Brigham City segments. They assumed a log-normal renewal model to calculate time-dependent probabilities for the next 50 years. The Brigham City segment is characterized by relatively short equivalent Poisson recurrence intervals due to its long elapsed time of 2,100 years compared to the mean recurrence interval of 1280 years over the past approximately 9,000 yr B.P. (Wong *et al*., 2002). The elapsed time on the Salt Lake City segment is close to the mean recurrence over the past 6,000 yr B.P., so its equivalent Poisson intervals are also relatively short. The time-dependent hazard along the Wasatch Front has been continually updated since 2002 by URS Corporation (URS), and the results have been presented at professional meetings although not published (Olig *et al*., 2005; Wong *et al*., 2007, 2009).

1.2 Scope of Study

In response to the need for a forecast of earthquake probabilities in the Wasatch Front region, 14 selected expert geologists, seismologists, and engineers from Federal and State organizations, academia, and the private sector joined together under the auspices of the Utah Geological Survey (UGS) and the USGS to form the Working Group on Utah Earthquake Probabilities (WGUEP). The WGUEP members are:

Ivan Wong (Chair)	URS Corporation (now at Lettis Consultants International, Inc.)
William Lund (Coordinator)	UGS
Walter Arabasz	University of Utah Seismograph Stations (UUSS)
Anthony Crone (USGS liaison)	USGS
Christopher DuRoss	UGS (now at USGS)
Michael Hylland	UGS
Nicolas Luco	USGS
Susan Olig	URS Corporation (now at Olig Seismic Geology, Inc.)
James Pechmann	UUSS
Steve Personius	USGS
Mark Petersen (NSHM liaison)	USGS
David Schwartz	USGS
Robert Smith	University of Utah (UU)
Patricia Thomas	URS Corporation (now AECOM)

The goal of the WGUEP was to develop an earthquake forecast for the Wasatch Front region (Figure 1-1) that includes the following earthquake probability estimates:

- Segment-specific time-dependent and time-independent probabilities of characteristic earthquakes on the five central segments of the WFZ.
- Time-dependent and time-independent probabilities for the whole WFZ for earthquakes of **M** ≥ 6.0 and **M** ≥ 6.75.
- Segment-specific and fault-specific time-dependent and time-independent probabilities for earthquakes of **M** ≥ 6.0 and **M** ≥ 6.75 on the two southern segments of the Great Salt Lake fault zone.
- Time-independent probabilities for earthquakes of **M** ≥ 6.0 and **M** ≥ 6.75 on other significant faults in the Wasatch Front region.
- Time-independent probabilities for background earthquakes in the Wasatch Front region for a range of magnitudes starting at **M** ≥ 5.0.
- Time-dependent and time-independent probabilities for all earthquake sources in the Wasatch Front region for a range of magnitudes starting at **M** ≥ 5.0.

Note that in the WGCEP approach, no fault was assigned a time-dependent model with a weight of 1.0. Some weight was always given to a time-independent model.

In addition to the WFZ and the Oquirrh–Great Salt Lake fault zone (OGSLFZ), 45 other faults and fault segments in the Wasatch Front region (Figure 1-1) were systematically treated as part of the earthquake forecast for this study (Section 4.5). The quantity and quality of available paleoseismic information for these other modeled faults is highly variable (see for instance Black *et al*., 2003; Lund, 2005), and many have no paleoseismic trenching data. Available data were only sufficient to make a time-independent earthquake forecast for these faults.

The WGCEP emphasized 30-year probabilities, which is an appropriate time interval given the high fault slip rates along the San Andreas transform plate boundary. In contrast, deformation rates in the Wasatch Front region are an order of magnitude lower than in California. Consequently, the WGUEP calculated the probabilities for a range of intervals ranging from 30 to 100 years although we emphasize the 50-year values (Section 8).

The WGUEP employed a methodology (Section 7) that is similar in some respects to that used in the UCERF process (WGCEP, 2008). Four model components were implemented in our effort (Section 2): a fault model, a deformation model, an earthquake rate model, and a probability model. We computed probabilities using two probability models: Poisson (time-independent) and Brownian Passage Time (BPT; time-dependent), which were also employed by the various WGCEPs (Section 2.4). We explicitly addressed epistemic (lack-of-knowledge) uncertainties in all input parameters through the use of logic trees (Section 2.5). We chose an approach similar to that taken by the WGCEPs; that is, we convened a series of meetings to review and develop model components. The WGUEP meetings are listed below.

Summaries of the WGUEP meetings are available on the UGS website (http://geology.utah.gov/hazards/earthquakes-faults/utah-earthquake-working-groups/utah-earthquake-probabilities/). The WGUEP extensively discussed and reviewed all the model components to arrive at a consensus. Limitations in the probability forecast were clearly defined.

1.3 Review Process

Because this report is a product of USGS and UGS support and was coauthored by members of both organizations, it was internally reviewed by both organizations and by the National Earthquake Prediction Evaluation Council (NEPEC). Reviewers are acknowledged in Section 10.

1.4 Key Products

Central to this report is a summary of the earthquake probabilities calculated for the Wasatch Front region by the WGUEP. Other key products include:

(1) A revised chronology of large surface-faulting earthquakes that have occurred along the central segments of the WFZ in the middle to late Holocene (past ~7000 years).

(2) Estimates of mean recurrence intervals, vertical displacements, and slip rates for rupture sources on the WFZ central segments.

(3) Models of single and multi-segment rupture behavior for the WFZ central segments.

(4) Estimates of the characteristic earthquake magnitudes and their uncertainties for the WFZ central segments.

(5) Estimates of characteristic magnitudes and slip rates for other significant faults in the Wasatch Front region.

Meeting	Date	Main Topic
1	10–11 February 2010	WGUEP formation and development of scope and methods
2	21–22 July 2010	Develop approach for characterization of the WFZ fault central segments
3	1–2 December 2010	Characterization of WFZ and other faults
4	16–17 February 2011	BRPEWG* II recommendations
5	28–29 June 2011	Strawman characterization of WFZ central segments
6	17–18 November 2011	Final data needs
7	16–17 February 2012	Preliminary results version 1
8	8–9 August 2012	Preliminary results version 2
9	13–14 February 2013	Preliminary results version 3
10	12–13 September 2013	Final results
11	5–6 February 2014	Review of draft final report
12	11 February 2015	Discussion on final report, rollout, and by-products

*Basin and Range Province Earthquake Working Group

(6) An updated historical and instrumental earthquake catalog for the Wasatch Front region (**M** ≥ 2.85) with uniform moment magnitude and quantified magnitude uncertainty together with a derivative catalog of independent earthquakes.

(7) Recurrence estimates for background earthquakes (**M** < 6.75) in the Wasatch Front region based on the catalog of independent earthquakes and corrected for bias due to magnitude uncertainty.

(8) A comparison of historical seismicity, geologic, and geodetic moment rates across the Wasatch Front region.

1.5 Report Organization

This report is divided into nine main sections, followed by acknowledgments, a list of references, and five appendices. In this introduction (Section 1) we have provided the background, objectives, scope of work, and key products of this study. Section 2 outlines the methodology that was used and the model components that were developed for the Wasatch Front region; the treatment of epistemic and aleatory uncertainties is also described. Section 3 describes the framework for the seismic source characterization of faults in the Wasatch Front region, including segmentation, depth of seismogenic faulting, recurrence models, calculation of recurrence intervals, and calculation of magnitudes. The characterization of specific faults in the Wasatch Front region is then described in Section 4, wherein the faults are divided into five groups, based on their treatment in this study: the WFZ central segments, the end segments of the WFZ, the OGSLFZ, antithetic fault pairs, and other significant faults. Section 5 describes the development of the earthquake catalog for the Wasatch Front region and its analysis to develop a background earthquake model. The evaluation of geodetic data in the Wasatch Front region and how the data were considered in this study is described in Section 6. Section 7 explains how earthquake probabilities were calculated using both a time-independent Poisson model and a time-dependent BPT model. Section 8 presents the earthquake probability results for the Wasatch Front region, both for the region as a whole and separately for the WFZ, the OGSLFZ, other modeled faults, and background earthquakes. Finally, in Section 9 we discuss the limitations of this study and suggest targets for future research in the Wasatch Front region.

2 METHODOLOGY AND MODELS

Similar to the approach used by the WGCEP (2008), the WGUEP methodology relies on four basic model components: a seismic source model, deformation model, earthquake rate model, and probability model. In general, the seismic source model gives the physical geometry of the known faults; the deformation model gives slip rates for each fault segment and/or fault segment; the earthquake rate model gives the long-term rate of all earthquakes throughout the region above a selected threshold (in this case **M** 5.0 and greater); and the probability model gives a probability for each event over a specified time period. There are some significant differences between the WGUEP and the WGCEP (2008) model components, with the WGUEP counterparts being much simpler in concept. The following section describes each model component of the methodology. Acronyms and abbreviations are defined on pages xii to xiv.

2.1 Wasatch Front Seismic Source Model

The Wasatch Front seismic source model consists of six groups of seismic sources (Section 4): the central WFZ, the end segments of the WFZ, the OGSLFZ, antithetic fault pairs, other significant faults, and crustal background earthquakes. Background earthquakes are defined as those events less than **M** 6.75 ± 0.25 that cannot be associated with known faults. A classic example of a background earthquake is the 1975 **M** 6.0 Pocatello Valley, Idaho, earthquake (Arabasz *et al*., 1981).

2.1.1 Fault Model

The Wasatch Front fault model is fundamentally a geologic model in that both fault geometry and long-term behavior are defined and constrained by geologic observations. The model incorporates complexity that leads to a wide spectrum of earthquake sizes and includes fault-specific constraints on the frequency of occurrence of those earthquakes. We adopt the basic elements and terminology of WGCEP (2003) in the fault model as shown in Table 2-1.

Several fault characteristics are described in more detail in Section 3. All faults are dominantly normal-slip faults that were modeled as planes. Some faults (e.g., the WFZ) have paleoseismic data in support of segmentation, where structural segment boundaries have likely served as relatively persistent rupture boundaries, confining prehistoric surface ruptures to particular sections of the faults (Section 3.1) (e.g., Machette *et al*., 1992; Lund, 2005). These faults lack known prehistoric rupture boundaries, and thus we used structural segment boundaries and available paleoseismic data to define their surface rupture characteristics. For these faults, we address epistemic uncertainties in rupture length by defining single- and multi-segment fault models and segment boundary uncertainties. Low weight was also given to an unsegmented model where ruptures were allowed to "float" along the fault regardless of segment boundaries. For other faults, the evidence is more ambiguous as to whether persistent rupture segment boundaries exist (e.g., Stansbury fault). For these faults, we gave higher weight to the unsegmented model. Most faults are included as single, independent (unsegmented) planar sources, unless the available data suggest otherwise. We note that the rupture behavior of many of the faults in this region is poorly understood and may actually be more complex than our simplistic assumptions. Alternatives to the single-plane, independent fault model are segmented faults and linked faults. Potentially linked faults may experience coseismic rupture along strike; individual segments of potentially segmented faults may rupture independently of each other.

We modeled faults as planar sources that extend the full depth of the seismogenic crust, with the exception of subsidiary faults in antithetic pairs. For subsidiary faults, which are truncated at depth by the master fault, maximum depth is a function of the dips of both faults and separation distance between the faults. Fault dips for all of these rupture models are averages estimated over the full depth of the seismogenic crust. For most typical range-bounding normal faults, we assumed preferred dips to be 50° with a range in uncertainty of ± 15° (Section 3.2).

In assigning probabilities of activity, P(a), for each fault source, we considered both the likelihood that the structure is capable of independently generating earthquakes (i.e., is seismogenic), and the likelihood that it is still active within the modern stress field. We incorporated many factors in assessing these likelihoods, such as: orientation in the modern stress field, fault geometry (length, continuity, depth extent, and dip), relation to other faults, age of youngest movement, geomorphic expression, amount of cumulative offset, rates of activity, and any evidence for a non-tectonic origin. We generally assigned faults with definitive evidence for repeated Quaternary activity a P(a) of 1.0 (Section 4.5). Exceptions include faults that may be secondary and dependent on other faults (e.g., the Utah Lake faults), or fault features that may have a non-seismogenic origin, and faults that may be too short (≤ 10 km) to independently generate significant earthquakes. The P(a) for faults that do not show definitive evidence for repeated Quaternary activity was individually judged based on the available data and the criteria explained above. Resulting values range from 0.5 to 1.0 (Section 4.5).

2.1.2 Background Earthquake Model

In most of the western U.S., particularly the BRP, the maximum magnitude for earthquakes not associated with known faults usually ranges from **M** 6 to 6.75. Repeated events larger than these magnitudes probably produce recognizable fault- or fold-related features at the earth's surface (e.g., Doser, 1985; dePolo, 1994). In this study, the WGUEP adopted a value of **M** 6.75 ± 0.25 after considerable discussion. The issue at hand was the completeness of the inventory of faults, which

Table 2-1. WGUEP fault model components.

Fault Segments
Some faults in the WGUEP model are segmented. Segments are based on prominent structural complexities along the fault and paleoseismic data, if available. These segments are the basic building blocks for earthquake ruptures on each fault. Each fault segment has length *L*, width *W*, dip, and slip rate and/or recurrence interval.
Rupture Sources
Individual faults or segments serve as rupture sources. For models including the simultaneous rupture of two or more adjacent segments, each possible combination of segments is a rupture source. However, some combinations of adjacent segments are deemed unlikely and are not modeled. A characteristic magnitude (M_{char}) is computed for each rupture source based on its rupture length *L* and rupture area *A*, and for some faults, average event displacement.
Floating Earthquakes
To address the uncertainty in fault segmentation, floating earthquakes of some specified magnitude or rupture length, without a fixed location, are used. Floating earthquakes, which allow for the fact that some earthquakes may not be constrained by fault segmentation, are also classified and treated as rupture sources.
Fault Rupture Models
A fault rupture model is a combination of the rupture sources for a fault, each combination representing one possibility for the long-term behavior of the fault. Logic tree weights are determined by expert judgment.

have a surficial signature. The WGUEP judged that repeated occurrences of **M** 6.75 ± 0.25 earthquakes on a fault would be identifiable in the surface geology and that all such faults are known within the Wasatch Front region. The best-estimate value and uncertainties were weighted in a logic tree similar to M_{char} for the faults. The background earthquake model depicts the frequency-magnitude distribution of mainshocks from **M** 5.0 to 6.75 expected to occur on seismic sources other than the faults included in the Wasatch Front fault model.

We calculated the rate of background seismicity from the historical seismicity catalog (Section 5). Typically, the seismicity associated with faults already included in the analysis was removed. However, in the case of the Wasatch Front region, few historical or instrumentally located earthquakes can be definitively associated with mapped surface faults—including the WFZ (e.g., Arabasz *et al*., 1992, 2007). Most background earthquakes appear to reflect seismicity on buried or unmapped secondary faults.

2.2 Deformation Model

In the WGCEP (2008) forecast, the deformation model assigns a slip rate and an aseismic slip factor plus their uncertainties to each fault segment or fault. The slip rates estimated by WGCEP (2008) were generally based on geologic data, but in some cases, geodetic data were used to constrain slip rates. In the Wasatch Front region, there is no evidence for aseismic slip (interseismic fault creep) and so no aseismic slip factor was used for any of the faults. WGUEP evaluated, but did not consider, geodetic data to constrain fault slip rates because of differences in geodetically-derived moment rates and rates based on geology and the historical seismicity record (Section 6).

Depending on the available data, we used recurrence intervals and/or slip rates to characterize rates of activity, generally preferring the former based on arguments in Wong and Olig (1998). For some faults, including the WFZ and OGSLFZ, we used both recurrence intervals and slip rates in the forecast (Section 4). For other faults, which generally lack individual earthquake times and robust mean recurrence estimates, we used slip rates in the forecast. All recurrence intervals and slip rates were depicted as distributions on logic trees with associated weights. We incorporated all available long- (≤ 1.6 Ma) and short-term (≤ 130 ka) data in developing slip rate or recurrence distributions, but we generally preferred short-term data when they were available. In addition to the time period, we also considered the type and quality of data in determining slip or recurrence rates. We converted vertical slip rates to net slip rates for most faults by assuming 100% dip-slip and using the preferred fault dips. For a typical range-bounding normal fault with a preferred dip of 50°, this results in a 30% increase when converting vertical slip rates to dip slip rates. Variations in displacement along strike can significantly affect the calculation of slip rates (Wong and Olig, 1998), but unfortunately there are very few faults for which we have enough data to calculate average rates for the entire fault. More typically there are only a few data points at one or two sites along the fault or no fault-specific data at all.

2.3 Earthquake Rate Model

The earthquake rate model consists of rates on faults (fault rupture model) and the background earthquakes. A fault-rupture model gives the long-term rate of all possible earthquakes above a selected threshold. The primary challenge in developing such a model is to satisfy all available constraints with full recognition of the uncertainties (Section 2.5): slip rate

data, paleoseismic event-rate constraints at particular locations, event-date correlations between sites, magnitude-area relationships, how slip varies along the length of each rupture, and any other geologic insight into what features might influence the distribution of ruptures (WGCEP, 2008). Similar to the WGCEP (2008), WGUEP rupture models were developed for the WFZ and OGSLFZ. Each rupture model consists of single-segment, multi-segment, and floating earthquake ruptures. The number of models ranged from two to five.

An integral part of the earthquake rate model is the choice of recurrence models and their weights. Both the maximum magnitude (truncated Gaussian) and truncated exponential models were used for faults. A truncated exponential model was used for the background earthquakes. The models used by the WGUEP are discussed in detail in the appropriate sections.

2.4 Probability Models

A probability model describes how events are distributed in time. The simplest model is the time-independent Poisson (memoryless) model that has been assumed appropriate in PSHA for decades (McGuire, 2004). The Poisson model assumes that each earthquake is completely independent of the timing of all other events. Hence with this model, it does not make a difference in the forecast for the Salt Lake City segment whether the most recent earthquake occurred yesterday or 1400 years ago.

Following the lead of WGCEP (2008), we have used only one time-dependent model, the BPT model. Other models were evaluated by WGCEP (2008), including the suite of models used by WGCEP (2003) and the traditional lognormal model and Weibull distribution, but they were found to be deficient in one or more aspects. The BPT model is a stress-renewal model that computes the probability of each segment rupturing conditioned on the date of the last event. Details on the probability models can be found in Section 7.

We treated the five central segments of the WFZ, as well as the Antelope Island and Fremont Island segments of the Great Salt Lake fault zone, in both a time-dependent and time-independent manner. The WFZ end segments, the Oquirrh fault zone, and all other faults were treated solely in the traditional time-independent manner due to lack of sufficient information for a time-dependent approach. We treated the probabilities for background earthquakes only in a time-independent manner (Section 5).

2.5 Treatment of Epistemic Uncertainties

WGUEP devoted considerable effort to defining uncertainties in the data, models, and parameters and tracking them throughout the calculations. Any model may have two types of uncertainty: aleatory uncertainty (variability) and epistemic uncertainty (unknowns). Aleatory uncertainty refers to the random variability that occurs in the natural world. The throwing of dice is the classic example. Epistemic uncertainty refers to what we do not know about the natural world, for example our ignorance of how the Earth works to produce earthquakes of a certain size at a certain place and time. To the extent a process is knowable, its epistemic uncertainty is reducible. Aleatory uncertainty, on the other hand, although quantifiable through direct observation, is irreducible. WGUEP used models to calculate quantities, and these models are defined by parameters that must be estimated. Both the choice of models and the estimation of their parameters have uncertainty associated with them. These model uncertainties and parameter uncertainties are, in general, of both the aleatory and epistemic types. Finally, WGUEP used expert judgment to decide a number of issues in this study, particularly the weighting of alternative interpretations or estimates. Differing expert judgment also represents uncertainty. Insofar as such differences arise from differing evaluations or perceptions of available but incomplete knowledge, this uncertainty is epistemic.

We treated almost all of the uncertainty considered in this study, including that arising from diverse expert judgment, as epistemic uncertainty. The only exceptions were the event-to-event variability that we associated with magnitude distributions and the aleatory component of the uncertainty in our time-dependent probability models. Confronted with a range of possibilities for a parameter (for example, the length of a fault segment) or a relation (for example, the relation between segment area and earthquake magnitude) or a probability model, WGUEP used logic trees with alternative interpretations or estimates with weights assigned to reflect the uncertainty. From the calculations of all possible alternatives at the ends of the logic tree branches, a distribution results that has mean values (for example, long-term rupture rates or 50-year earthquake probabilities) and their 5% and 95% confidence intervals.

In general, three values for each parameter were weighted and used in the analysis. Statistical analyses by Keefer and Bodily (1983) indicated that a three-point distribution of 5th, 50th, and 95th percentiles weighted 0.185, 0.63, and 0.185 (rounded to 0.2, 0.6, and 0.2), respectively, is the best discrete approximation of a continuous distribution. Alternatively, they found that the 10th, 50th, and 90th percentiles weighted 0.3, 0.4, and 0.3, respectively, can be used when limited available data make it difficult to determine the extreme tails (i.e., the 5th and 95th percentiles) of a distribution. Asymmetric distributions were also used when judged appropriate to do so. Note that the weights associated with the percentiles are not equivalent to probabilities for these values, but rather are weights assigned to define the distribution. We generally applied these guidelines in developing distributions for seismic source parameters with continuous distributions unless the available data suggested otherwise. Estimating the 5th, 95th, or even 50th percentiles is typically challenging and involves subjective judgment given limited available data.

3 FAULT CHARACTERIZATION

The following describes the parameters used in the fault models considered in the WGUEP forecast: segmentation, fault dips, depth of seismogenic faulting, recurrence models, recurrence intervals, and magnitudes. Acronyms and abbreviations are defined on pages xii to xiv.

3.1 Segmentation

From a perspective of historical worldwide surface faulting, an updated catalog of historical ruptures in shallow continental crust (Wells, 2013) lists 65 normal and normal-oblique surface ruptures out of a set of 267 total ruptures (all fault types). Rupture lengths for the normal and normal-oblique ruptures are typically 15 to 40 km. The longest is 95 to 101 km for the 1887 Sonora, Mexico (Pitaycachi, Tevas, and Otate faults) earthquake (Suter, 2008; 2015). In the BRP, the longest historical surface rupture is 62 km for the 1915 Pleasant Valley, Nevada, event (Wallace, 1984). The idea that long normal fault zones can be subdivided into rupture segments shorter than the full fault length is supported by the 1983 Borah Peak, Idaho, earthquake, in which a section of the 120-km long Lost River fault zone in Idaho, now called the Double Springs Pass segment, ruptured for 34 km (Crone *et al*., 1987). A similar interpretation was reached regarding the late Quaternary rupture histories of the adjacent Lemhi, Beaverhead, and Tendoy ranges (Crone and Haller, 1991). The WFZ, which has not ruptured historically, is 350 km long with a continuous 260 km central section. Given both worldwide and BRP observations, the expectation is that the next event or events along the WFZ will occur on identifiable shorter sections of the fault, which are termed rupture segments. These rupture segments are the principal sources of future WFZ earthquakes. The lengths of individual rupture segments along the WFZ in our analysis vary from 40 to 65 km. These lengths are consistent with, and toward the higher end of, historical normal fault surface ruptures. Fault segmentation is a primary assumption in characterization of the 350-km-long WFZ and associated faults of the Wasatch Front region, and in the quantification of earthquake probability.

The concept of fault segmentation has developed as an important component of fault characterization and seismic-hazard analysis, particularly for estimating rupture location and the magnitude of future earthquakes on a fault or fault zone (Schwartz, 1988). The concept is based, in part, on the observation from historical ruptures that fault zones, especially long ones such as the WFZ, have not ruptured along their entire length during an individual earthquake (Schwartz and Coppersmith, 1986; Schwartz, 1989). From a paleoseismic perspective, a combination of rupture timing, information on slip per event, and the location of timing variability relative to physical features such as major geometric changes, play key roles in developing an understanding of fault-specific segmentation. These earthquake-timing differences typically occur across prominent structural segment boundaries, which serve to arrest or significantly modulate fault slip (e.g., Crone *et al*., 1987; Personius *et al*., 2012). Although event timing is the most common type of paleoseismic information, analysis of historical and paleoseismic records of faults in shallow continental crust has provided examples of repeated similar amounts of displacement at a point or points on a fault (e.g., Klinger *et al*., 2011, and a summary of worldwide observations by Hecker *et al*., 2013). This suggests that the extent of many repeated ruptures may be similar. An implication is that there are physical features in a fault zone that control the length of a rupture and can divide a fault into distinct rupture segments. These rupture barriers may persist through repeated earthquake cycles (Aki, 1979, 1984; Elliott *et al*., 2015). While faults in all tectonic settings are segmented to varying degrees, paleoseismic observations (Schwartz and Coppersmith, 1984; Schwartz, 1988; Machette *et al*., 1992; Benedetti *et al*., 2013) suggest that segmented rupture behavior may be better developed and more persistent on normal faults than strike-slip faults (Biasi and Weldon, 2009; Schwartz *et al*., 2012; Scharer *et al*., 2014). In the absence of defined fault-rupture termination data, previously defined fault segmentation models provide the basis for characterizing potential earthquake ruptures and quantifying earthquake probabilities for segmented faults in the study region.

Fault segmentation models have been used in probabilistic forecasts dating back to the first regional probabilistic estimates for California in 1988 (WGCEP, 1988). The WGCEP (1988) developed segmentation models for the San Andreas fault and a limited number of major branches in northern and southern California. The model for the San Francisco Bay Area was modified following the 1989 Loma Prieta earthquake to include the Rodgers Creek fault and revise segmentation of the San Andreas fault (WGCEP, 1990). The WGCEP (1995) focused on southern California, maintaining the WGCEP (1988) San Andreas segmentation model and adding segmentation models for other strike-slip faults in southern California including the San Jacinto and Elsinore faults. The segmentation in each of these early probability models was relatively simple and was based primarily on the location along a fault where a historical rupture had occurred (or was believed to have occurred), locations where the amount of slip was considered to have changed during a historical rupture (this was the basis for segmenting both the 1906 and 1857 San Andreas rupture of the San Andreas fault), and general changes in fault geometry (particularly changes in strike). The WGCEP (1990) report was the first to include uncertainty in rupture segment end points.

More recent segmentation models, such as those for the San Andreas fault system in the San Francisco Bay Region (WGCEP, 1999 and particularly WGCEP, 2003), and for faults throughout California with high slip rates and substantial geologic information associated with them (called A-faults in UCERF2) by the WGCEP (2008), have improved segmentation modeling. In these probability studies, segments are sections of faults that are considered to be capable of failing

independently to produce an earthquake (for example, the southern Hayward fault segment is the source of the 1868 rupture) or join in multi-segment ruptures such as those of the 1857 and 1906 ruptures on the San Andreas fault. These rupture segments and their extent (surface length and crustal width) were developed on each fault from behavioral and kinematic observations. The behavioral considerations, primarily the difference in timing of events on adjacent parts of a fault either from paleoseismic observations or the extent of historical surface rupture, provide the strongest basis for segmentation. Locations of changes in slip rate (common at fault branches), the transition from locked to creeping sections of a fault or changes in the rate of creep along a fault, and the distribution of microearthquake activity provide additional behavioral bases for segmentation. Kinematic considerations are related to aspects of fault geometry that could affect rupture propagation. These considerations include changes in strike, bends and steps, branching or intersection points, changes in fault trace complexity, and variation in lithology along a fault. The WGCEP (2003) recognized that ruptures may not stop at preferred segment end points, and therefore defined zones of uncertainty based on the range of available observations. The zones of uncertainty were sometimes asymmetric and typically 10 to 20 km in length. The boundaries provide mean, maximum, and minimum fault segment rupture lengths. In contrast, the WGCEP (2008) defined specific segment endpoints with no uncertainty.

The segmentation models noted above were developed by groups of experts with specific knowledge of the faults they were analyzing. In the most recent fault characterization study for California (UCERF3), Field *et al*. (2013) adopted a different approach. In order to develop rupture models for all faults in California, as opposed to prescribing segmentation for a limited subset of faults for which there are fault behavioral data, they generated fault ruptures using an algorithm guided by a set of geometrically-based rules. The algorithm includes distances between fault endpoints (no rupture propagation beyond a separation distance of 5 km), limiting angular relations between faults (no rupture propagation across an intersection angle larger than 60 degrees), and a Coulomb stress analysis to eliminate rupture propagation in an unfavorable direction. This approach produced fault-to-fault jumps, multiple fault ruptures, and a range of rupture lengths for all faults in the model. A mathematical inversion with a set of seven equations, including constraining slip rate and paleoevent information, was then used to set the long-term rates of each rupture. To some degree, segmentation was developed in the UCERF3 inversion where slip-rate changes occur along strike, but it was not used explicitly in the California fault characterization. From the WGUEP perspective, the UCERF3 approach was developed largely from data and behavior of strike-slip faults, and its applicability for normal faulting is uncertain. Also, in the formulation of rupture lengths, it does not employ the paleoseismic observations on timing and slip from paleoearthquakes that are available for the WFZ and associated faults.

For the WFZ, as well as for other normal faults in the Wasatch Front region and in the broader BRP, the primary basis for defining potential rupture segments is the difference in the timing of paleoearthquakes along the length of the fault. Clear differences in earthquake timing, especially for the best constrained most recent earthquakes (Appendix B), occur across prominent structural segment boundaries (e.g., figure B-3 in Appendix B). There is very little microseismicity or fault creep, which are two behavioral features of many faults in California. Where changes in timing of past events can be associated with structural or geometric changes along range fronts (salients, re-entrants, complex fault branching, and gaps in surface rupture), the WGUEP considers the case for identification of a rupture segment boundary to be strengthened. Measurements of net displacement during individual paleoearthquakes along the WFZ add additional information for interpreting past fault rupture length and, therefore, segment length.

Many of the basic concepts regarding fault segmentation, in general and on normal faults in particular, developed from early paleoseismic studies on the WFZ. The segmentation model used by the WGUEP for the WFZ in the present analysis has been developed and refined over the past 30 years. Schwartz and Coppersmith (1984) initially suggested six segments, each a seismogenic source, based on differences in timing of the most recent rupture at a limited number of sites and on general structural changes along the Wasatch Range front. With additional paleoseismic investigation along the length of the WFZ (Section 4), the initial segmentation model was modified and the present model of 10 segments, each an independent seismogenic source, was developed (Machette *et al*., 1992). Since then, additional paleoseismic investigations (summarized by Lund, 2005; DuRoss, 2008; and the present report) have led to the development of a chronology of surface-faulting earthquakes for the central five segments that is considered complete for the past approximately 6000 years. The interpretation of this paleoseismic chronology provides the support for the segmentation model. However, consistent with Chang and Smith (2002) and DuRoss (2008), we constructed rupture scenarios that include two- to three-segment ruptures and also defined segment-boundary uncertainties that allow for both partial and spillover ruptures. The five central segments (Nephi, Provo, Salt Lake City, Weber, and Brigham City) (Figure 1-1) are the focus of the probability estimates presented here. The end segments (the Malad City, Collinston, and Clarkston Mountain segments to the north and the Levan and Fayette segments to the south) are discussed in Section 4.2.

The repeated difference in timing is a basis for independently rupturing segments (Figure 3.1-1a). Figure 3.1-1b shows independent segments having events that are closely spaced in time, making the distinction of separate events difficult within the resolution of common dating techniques (e.g., radiocarbon and luminescence). Overlapping earthquake time ranges permit the interpretation of multi-segment ruptures (Figure 3.1-1c), similar to those developed for strike-slip faults in the

California probability reports (e.g., WGCEP, 2008). In contrast, a subsegment may occasionally fail as an independent event (Figure 3.1-1d). Figure 3.1-1e shows that rupture on one segment may extend into or trigger slip on an adjacent segment, which itself fails independently at a later time. Typically, locations of low slip, especially near segment boundaries, do not fill in during subsequent events; thus, cumulative displacement and long-term slip rates vary along strike and are frequently lowest near segment boundaries (often coincident with the ends of mountain ranges).

For the five central segments of the WFZ (Brigham City to Nephi; Section 4), which have paleoseismic evidence of repeated Holocene surface-faulting earthquakes, unique earthquake chronologies per segment support independent rupture (Machette *et al*., 1992; Section 4.1; Figure 3.1-1a). Prominent structural segment boundaries, which bound separate hanging-wall basins along the trace of the fault (e.g., Salt Lake and Utah Valleys), provide further evidence for segmentation of the WFZ. These boundaries consist of complex (e.g., diffuse) faulting and/or decreased structural throw across the fault compared to the segment. Despite evidence for single-segment ruptures on the WFZ, overlapping earthquake times on adjacent segments permit multi-segment ruptures. Alternative rupture models, which include multi-segment ruptures involving two to as many as four segments and having combined lengths of 90 to 200 km, and their weights are described in Section 4.1 and Appendix B.

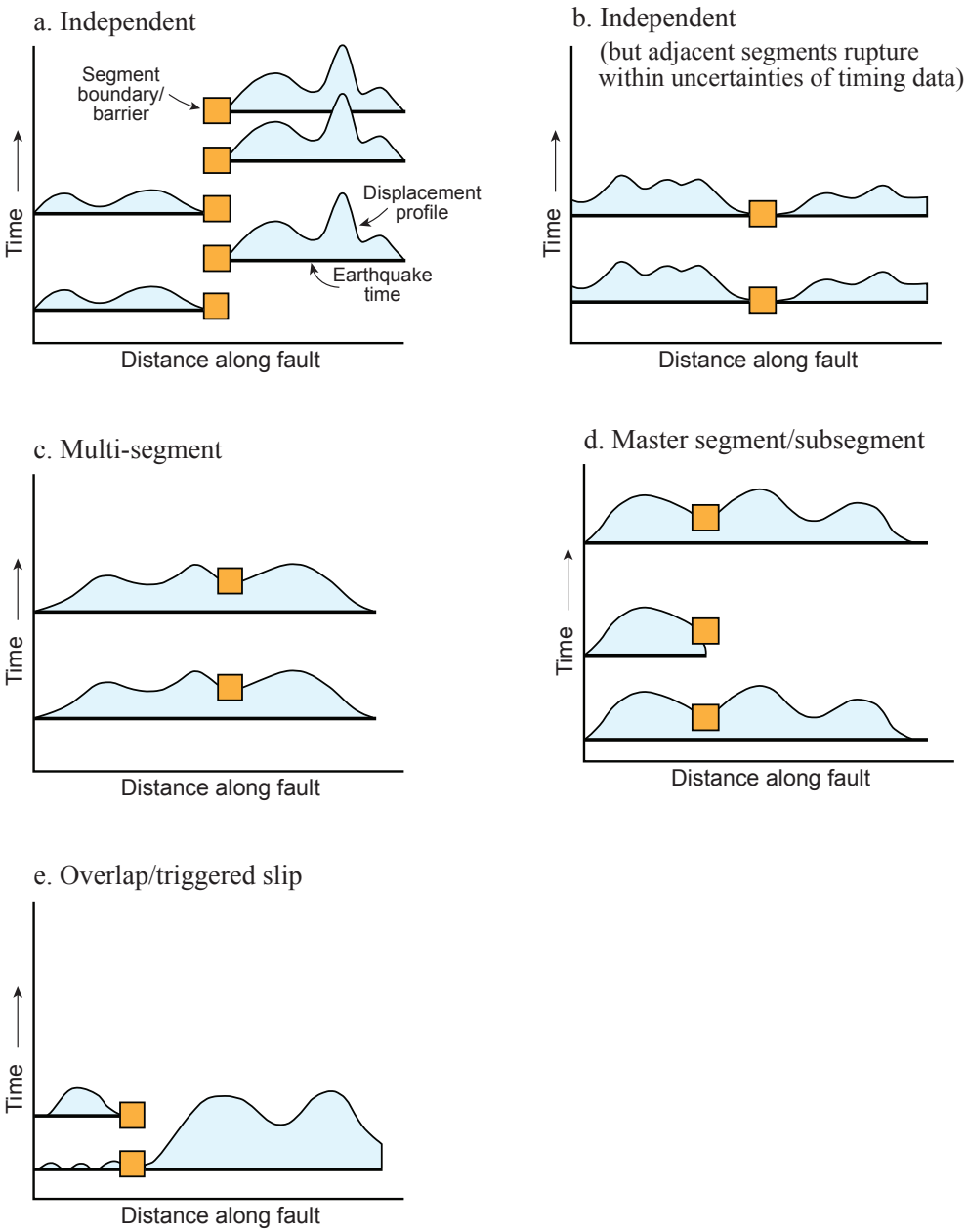

Figure 3.1-1. Segmentation models for normal faults: (a) independent, (b) independent (but adjacent segments rupture within uncertainties of timing data), (c) multi-segment, (d) master segment/subsegment, and (e) overlap/triggered slip.

3.2 Dips of Normal Faults

Models of fault sources require information about fault segmentation to estimate the length of fault ruptures (Section 3.1) and the downward extension of the fault to develop a geometric model of the potential rupture area on the fault plane. In these models, the dip assigned to a fault is a critical parameter because, for a given thickness of the seismogenic crust (Section 3.3), the change from a steep to shallower dip results in a non-linear increase in the fault area. Because the fault relationship between fault dip and area is a trigonometric function, this non-linear effect becomes more pronounced as the fault dips decrease to progressively shallower angles (Figure 3.2-1, Table 3.2-1).

The dip of normal-slip, Quaternary faults in the BRP has been the subject of considerable discussion (Lund, 2006, 2012) particularly because of the impact that fault dip has on the calculated hazard. Seismological data from large historical earthquakes on normal faults are the source of much of the information regarding the dip of active Quaternary faults. The 1983 Borah Peak earthquake is a representative model of a large earthquake that could occur on the WFZ. This **M** 6.9 earthquake produced 36.4 km of surface rupture on the Lost River fault zone (Crone *et al*., 1987). The well-defined pattern of aftershocks and geodetic data indicates that the earthquake occurred on a planar fault dipping about 45° to 47° through the seismogenic crust (Stein and Barrientos, 1985; Richins *et al*., 1987). In August 1984, a late aftershock (Richter local

Table 3.2-1. Change in fault area for varying values of fault dip calculated for a fault length of 30 km and a seismogenic crustal thickness of 15 km.

Dip angle (degrees)	Fault area (km^2)	Change in fault area (km^2) from prior dip angle	Increase in area from prior dip angle (%)	Change in fault area (km^2) from 60° dip	Increase in area from 60° dip (%)
60	519.6	—	—	—	—
50	587.4	67.8	13.0	67.8	13.0
40	700.1	112.7	19.2	180.5	34.7
30	900.0	199.9	28.6	380.4	73.2

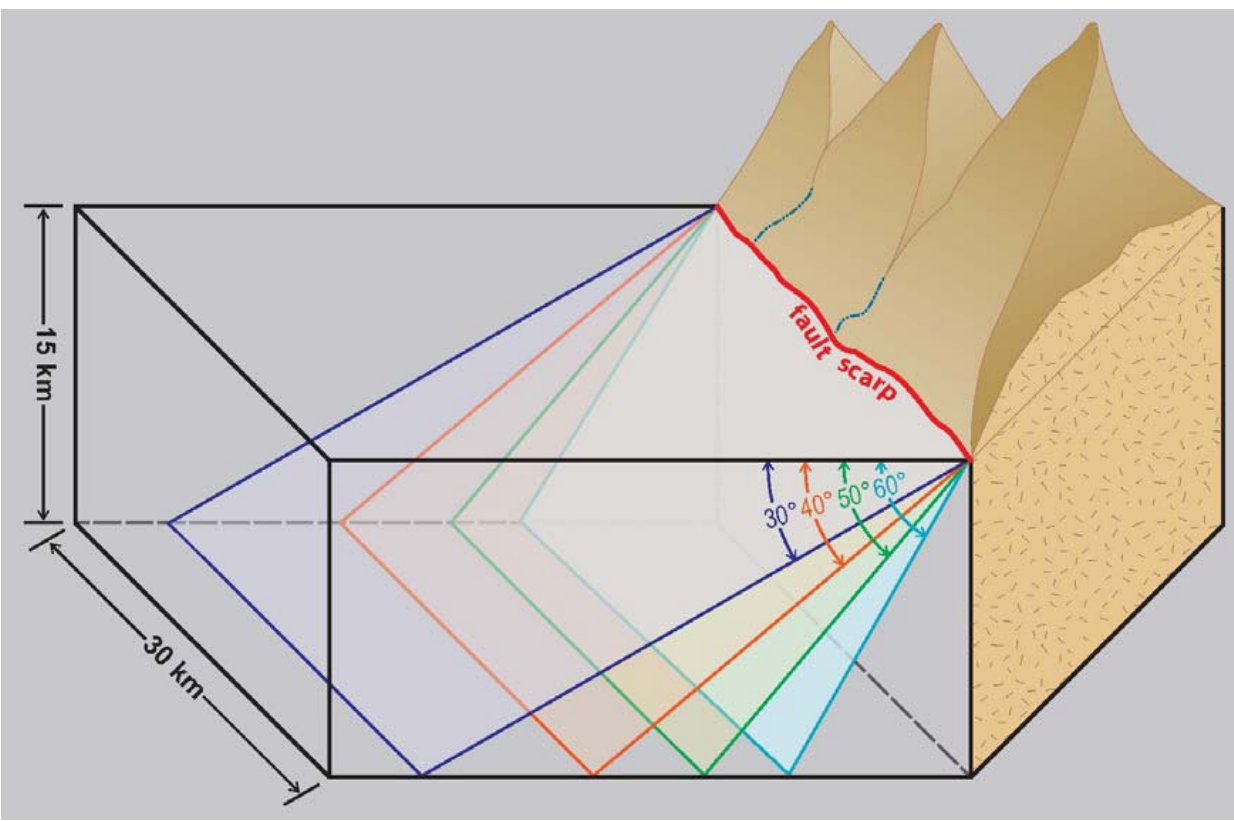

Figure 3.2-1. Schematic diagram showing the non-linear increase in fault area with decreasing dip angles.

magnitude [M_L] 5.8) occurred to the northwest of the mainshock, and the locations of 237 additional aftershocks suggest that this section of the Lost River fault zone has a dip of about 75° and the adjacent antithetic Lone Pine fault has a dip of about 58° (Payne *et al*., 2004).

The 1959 **M** 7.3 Hebgen Lake, Montana, earthquake was the largest historical earthquake in the Intermountain West and produced a complex rupture pattern on two faults. The analysis of P-waves indicated a preferred fault plane that dipped 54° ± 8° (Ryall, 1962), and the analysis of subevents of the mainshock and three significant aftershocks indicated that the earthquake may have first ruptured faults dipping 60° ± 5° (Doser, 1985). Barrientos *et al*. (1987) modeled the surface deformation caused by the earthquake and showed that faults with dips of 45° to 50° provide the best statistical fit to the deformation data.

Studies of other historical earthquakes and Quaternary normal faults in the BRP also indicated the faults have dips in the range of about 40° to 70°. Romney (1957) analyzed P-wave, first motions from the 1954 Fairview Peak, Nevada, earthquake and concluded that the causative fault had a dip of 62°. Slemmons (1957) reported that bedrock faults that slipped during the 1954 Dixie-Valley-Fairview Peak earthquakes had dips of 55° to 75°. Arabasz *et al*. (1981) analyzed data from the mainshock and 587 aftershocks of the M_L 6.0 Pocatello Valley, Idaho, earthquake and noted that the mainshock nodal plane had a dip of 39°, cross sections of the aftershock hypocenters suggest a dip of about 50°, and dislocation modeling indicated a fault dip of 60°. They noted that all of these data illustrate the uncertainty in defining the fault at depth and observed that their data do not preclude the possibility that the fault might be listric, that is, it flattens with depth.

Several studies have attempted to define the dip of the WFZ at depth. Zoback (1992) combined data from surface geology, gravity measurements, and petroleum exploration wells with a 30-km-long seismic-reflection profile near Nephi, Utah, and concluded that the WFZ in this area is a relatively planar feature with a dip of 50° to 55°. Bruhn *et al*. (1987) conducted a detailed structural analysis of the Salt Lake City segment based on slickenside data and details of the fault's orientation. They concluded that dip values along this part of the fault range from 35° to 65°. Smith and Bruhn (1984) examined more than 1500 km of seismic-reflection data across the WFZ and in adjacent parts of the BRP. They concluded that their data show steep to low angles and that low-angle and listric faulting may be associated with movement on pre-existing (reactivated) low-angle thrust faults. More recently, Chang and Smith (2002) and Chang *et al*. (2006) used geodetic data to analyze contemporary deformation and the associated seismic hazard along the Wasatch Front. They concluded that a dip of 55° yielded the best results for their stress modeling and provided the best agreement between geodetic and geologic deformation rates.

Doser and Smith (1989) evaluated source parameters for 50 earthquakes that have occurred throughout the Western Cordillera of the United States in the mainly extensional domain that exists between the San Andreas fault system on the west and the Great Plains on the east. In addition to normal-slip earthquakes, their regional analysis included earthquakes that had a large amount of strike-slip motion. From this analysis, they concluded that earthquakes in the region are likely to occur on planar faults that dip between 40° and 70°.

In a more global analysis of normal faulting in areas of continental extension, Jackson and White (1989) and Collettini and Sibson (2001) analyzed seismological data from more than 125 historical earthquakes. Jackson and White (1989) concluded that the vast majority of normal fault dips range between 30° and 60°. Collettini and Sibson (2001) updated the work of Jackson and White (1989) to include 13 additional intracontinental normal-slip ruptures. They concluded that these normal-slip ruptures unambiguously occurred on faults that have dips between 30° and 65° and that the distribution of fault angles has a clear peak at 45°. They also stated that no normal-slip earthquakes of **M** 5.5 or greater have occurred on faults dipping less than 30°.

The range of dips for normal faults summarized above emphasized that the WGUEP analysis needed to consider a wide range of fault dips. Based on the evaluation of these published studies and the recommendations of the BRPEWG (Lund, 2012), we used a value of 50° ± 15° for the preferred dip of range-bounding normal faults in the Wasatch Front fault model. For simplicity, following Bruhn and Schultz (1996), we also modeled antithetic faults (e.g., the West Valley fault zone, which is antithetic to the WFZ in Salt Lake Valley) using the same preferred dip value and associated uncertainty.

3.3 Depth of Seismogenic Faulting

We calculated the fault widths in the Wasatch Front fault model using the assumed dips, 50° ± 15° for most faults, and an estimated maximum depth of seismogenic faulting. For the maximum faulting depths, we used a weighted distribution based on consideration of maximum earthquake focal depths in the Wasatch Front region and also the maximum rupture depths for two large historical earthquakes elsewhere in the Intermountain West.

To analyze maximum earthquake focal depths in the Wasatch Front region, we used earthquakes in the UUSS catalog that meet the following criteria for focal depth quality: (1) epicentral distance to the nearest station less than or equal to the focal depth or 5 km, whichever is larger, and (2) standard vertical hypocentral error (ERZ) of 2 km or less, as calculated by the location program. Figure 3.3-1 is a map of the Wasatch Front region showing the epicenters of all of the earthquakes that meet these criteria and occurred between October 1974 and September 2011. The start of the time period corresponds to the start of telemetered seismic network recording at the

UUSS, which enabled a large increase in the number of stations (Arabasz *et al*., 1992). All of the seismic events in the dashed polygon at the lower right of Figure 3.3-1 were excluded from our analysis, because nearly all of the events in this area appear to be coal-mining related. The remaining 2523 events with good quality focal depths are primarily within a 75- to 100-km-wide zone roughly centered on the WFZ. This uneven distribution of events within the Wasatch Front region reflects the concentration of seismicity along the north-south trending Intermountain Seismic Belt ([ISB]; Smith and Arabasz, 1991; Pankow *et al*., 2009), but is partially a consequence of the focal depth criteria and the distribution of seismic stations in the region. The station distribution mimics the earthquake distribution, since most of the stations are located along the ISB in the central part of the study area and relatively few stations are in the eastern and western parts of the Wasatch Front region (Arabasz *et al*., 1992, 2010).

Figure 3.3-2 shows four east-west, ~210-km-long cross sections of the hypocenters in Figure 3.3-1. Each cross section is centered on an even degree of latitude and includes hypocenters within ±0.5 degrees latitude. For reference, we show on each cross section the locations of the surface trace of the WFZ and longitude 111° 50′ W (vertical dashed line). This longitude approximates the general east-west location of the WFZ surface trace (Figure 3.3-1). As best seen in cross sec-

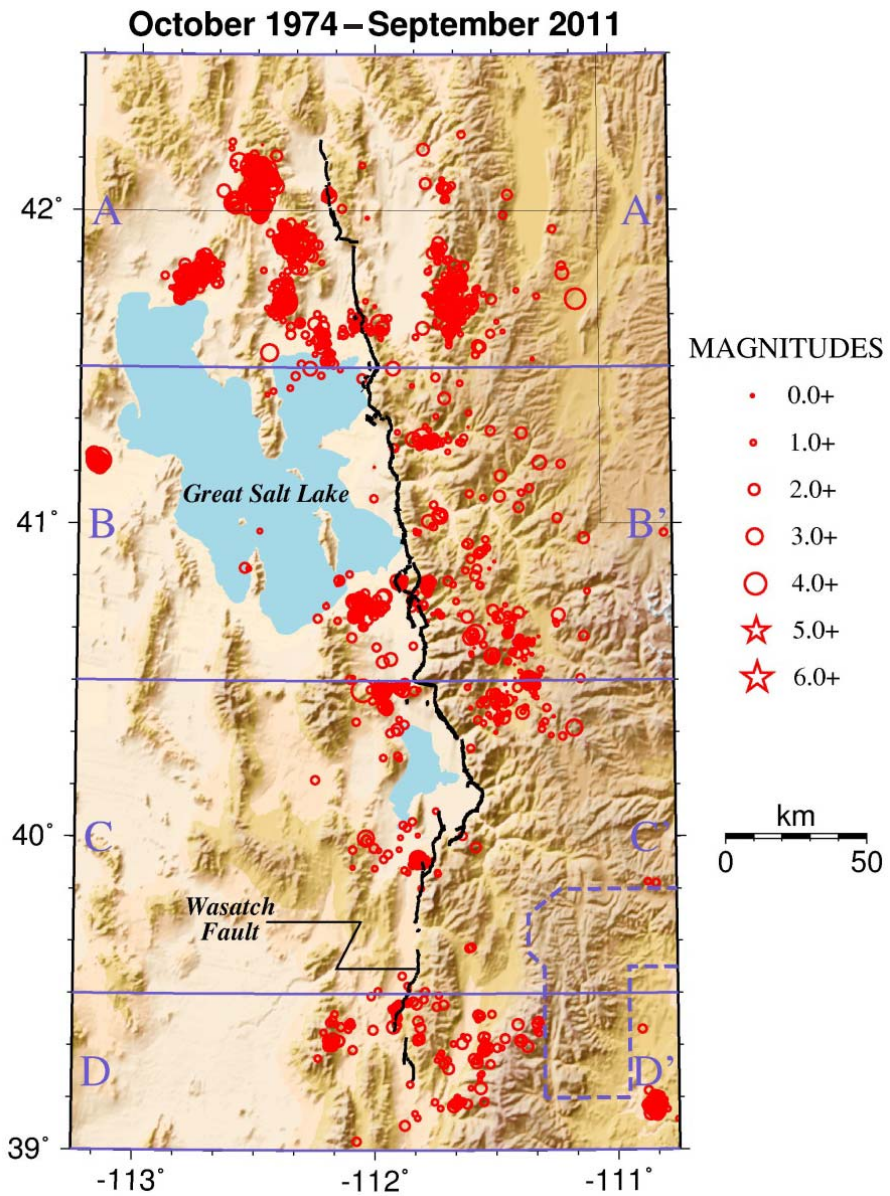

Figure 3.3-1. Map of the Wasatch Front region showing the epicenters of 2523 earthquakes with well-constrained focal depths that occurred in this region between October 1974 and September 2011. All seismic events in the blue dashed polygon at the lower right were excluded as probable mining-induced events. Blue lines and letters show areas of cross sections in Figure 3.3-2. Note that the earthquake magnitudes used for plotting this map and the cross sections are not the same as the magnitudes used for the recurrence analysis (Section 5). Shaded relief map constructed from USGS digital elevation data (http://nationalmap.gov).

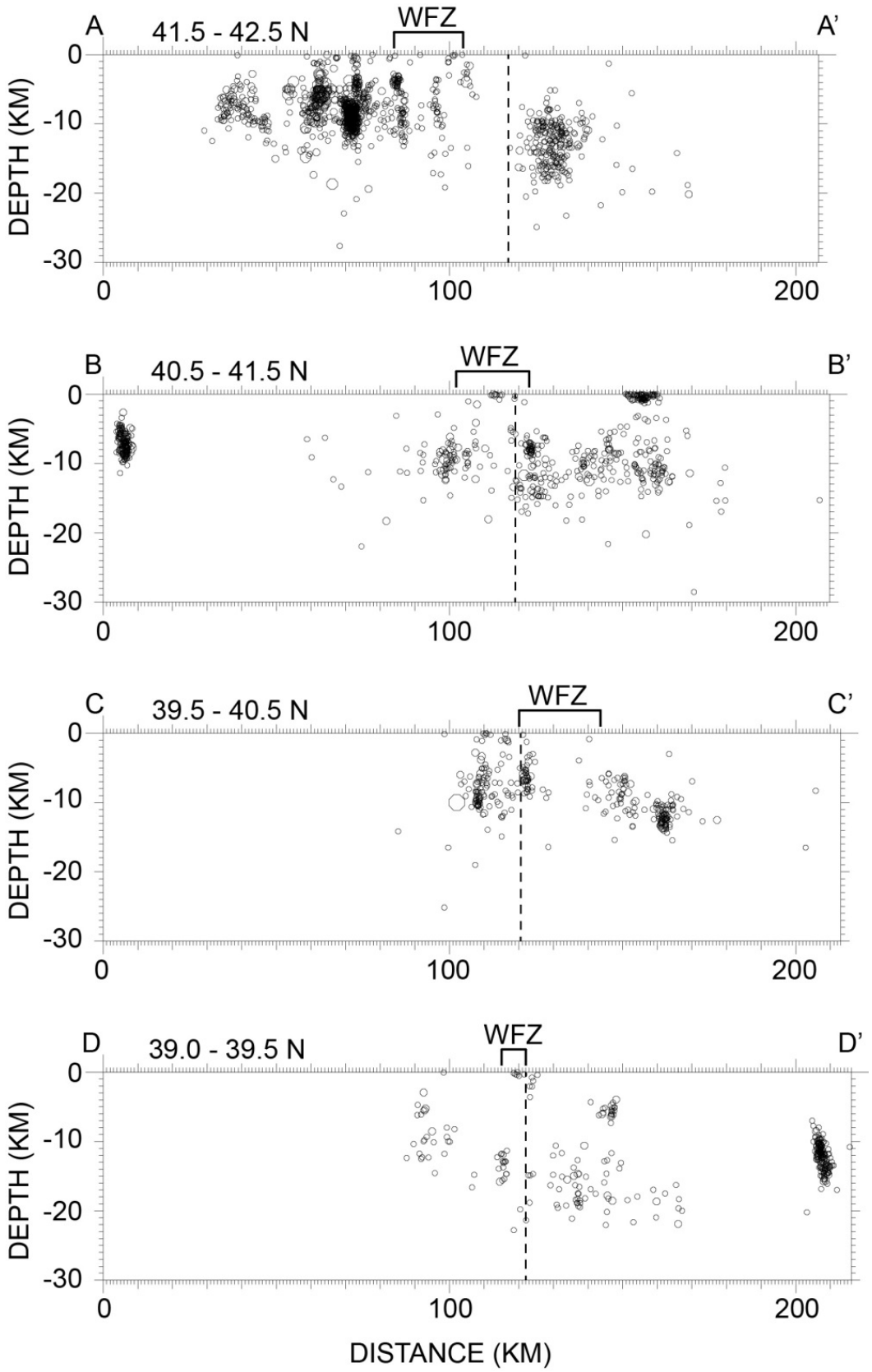

Figure 3.3-2. East-west cross sections of the hypocenters with well-constrained focal depths in Figure 3.3-1. The latitude range of the events and the locations of the Wasatch fault zone (WFZ) and longitude 111° 50′ W (vertical dashed line) are indicated on each cross section. Vertical exaggeration is 2:1.

tions A-A′, B-B′, and D-D′, maximum focal depths appear to be systematically greater by about 5 to 6 km to the east of the WFZ than to the west of it, and the change occurs over a distance of 20 km or more in the vicinity of the WFZ. The WFZ marks the eastern physiographic boundary of the BRP. The eastward increase in maximum focal depths across this boundary is at least qualitatively consistent with the well-known increase in crustal thickness and decrease in heat flow moving eastward from the BRP into the adjoining Middle Rocky Mountains and Colorado Plateau Provinces (e.g., Smith *et al*., 1989; Lowry and Perez-Gussinye, 2011).

Apparent variations in focal depths observed on hypocentral cross sections can be artifacts of sampling, because a larger sample of earthquakes is more likely to contain extreme focal depth values. To test the validity of the apparent eastward increase in focal depths observed on the cross sections in Figure 3.3-2, we computed 90th and 95th percentile focal depths for the parts of the Wasatch Front region to the east and west of 111° 50′ (Table 3.3-1). The results confirm the observations from the cross sections that the maximum focal depths are greater to the east of this line than to the west of it. Depending on whether the 90th or 95th percentile focal depth is chosen, the maximum focal depths increase from 11–12 km in the western part of the Wasatch Front region, to 16–18 km in the eastern part, with most of the change occurring near the WFZ at the eastern edge of the BRP. The average maximum focal depth for the region as a whole is 14 to 16 km.

In addition to the earthquake focal depth analysis presented here, detailed studies of two large, surface-faulting earthquakes in the ISB provide information on the expected maximum depth of seismogenic faulting in the Wasatch Front region. The 1959 **M** 7.3 Hebgen Lake, Montana, earthquake consisted of two subevents that nucleated at depths of 10 and 15 km, as indicated by the teleseismic body wave modeling of Doser (1985). The second subevent was the main event and had the deeper hypocenter. Barrientos *et al*. (1987) modeled the geodetic data from the Hebgen Lake earthquake with two *en echelon* fault planes of comparable seismic moment, extending to depths of 8.5 ± 2.5 km and 11 ± 3 km. The 1983 **M** 6.9 Borah Peak, Idaho, earthquake nucleated at a depth of 16 ± 4 km, as determined by modeling of teleseismic body waves by Doser and Smith (1985) and Barrientos *et al*. (1985). The fault break is inferred to have propagated unilaterally northwestward and upward from the hypocenter based on the aftershock distribution (Richins *et al*., 1987) and inversions of leveling data, which show slip on a 49°-dipping planar fault extending to a depth of 14 km (Barrientos *et al*., 1987). These studies suggest that the faulting in both the Borah Peak and Hebgen Lake earthquakes extended to a depth of around 15 km (Smith and Arabasz, 1991).

Considering all of the available information, the WGUEP decided to use a seismogenic depth of 15 ± 3 km for the Wasatch Front fault model and to apply location-dependent weights as follows. For the WFZ and faults to the west, the assigned weighting is 12 km (0.2), 15 km (0.7), and 18 km (0.1). For faults to the east of the WFZ, the weighting is 12 km (0.1), 15 km (0.7), and 18 km (0.2). The preferred seismogenic depth of 15 km is based primarily on the maximum rupture depths of the Hebgen Lake and Borah Peak earthquakes, but is also consistent with the 90th and 95th percentile focal depths of 14.1 and 16.0 km, respectively, for the Wasatch Front region as a whole (Table 3.3-1). The uncertainty limits of 12 and 18 km and their location-dependent weights are based mostly on the 95th percentile focal depths for the regions east and west of 111° 50′ W, but also account reasonably well for the uncertainties in the maximum rupture depths of the Borah Peak and Hebgen Lake earthquakes.

3.4 Recurrence Models

We modeled the magnitude-frequency relationships for the Wasatch Front region faults using the maximum magnitude and Gutenberg-Richter truncated exponential recurrence models, similar to the approach used by the USGS in the NSHMs (Petersen *et al*., 2008) (Figure 3.4-1). We weighted these models to represent our judgment on their applicability to the fault. For the background earthquakes, we assumed that only a Gutenberg-Richter truncated exponential recurrence relationship is appropriate.

The maximum magnitude model can be regarded as an extreme version of the traditional "characteristic" model. We adopted the model proposed by Wesnousky (1986). In the maximum magnitude model, there is no exponential portion of the recurrence curve and the characteristic magnitude (M_{char}) is distributed using a normal distribution defined by the mean magnitude and standard deviation of 0.12 magnitude unit (Frankel *et al*., 2002; Figure 3.4-1). The normal distribution is truncated at ± 2σ.

Table 3.3-1. Focal depth percentiles.

	West of 111° 50′	East of 111° 50′	Entire Region
Number of Events	1505	1018	2523
90th Percentile Depth (km)	11.1	16.2	14.1
95th Percentile Depth (km)	12.4	18.0	16.0

The recurrence rates for the fault sources are defined by either the slip rate or the average recurrence interval for the characteristic event. The slip rate is used to calculate the moment rate on the fault using the following equation defining the seismic moment:

$$M_0 = \mu A D \qquad (3\text{-}1)$$

where M_0 is the seismic moment, μ is the shear modulus (3.0 x 10^{11} dyne/cm^2), A is the area of the rupture plane, and D is the slip on the plane. Dividing both sides of the equation by time results in the moment rate as a function of slip rate:

$$\dot{M}_0 = \mu A S \qquad (3\text{-}2)$$

where $\dot{M}_0$ is the moment rate and S is the slip rate. M_o has been related to moment magnitude, **M**, by Hanks and Kanamori (1979):

$$\mathbf{M} = 2/3 \log M_0 - 10.7 \qquad (3\text{-}3)$$

Using this relationship and the relative frequency of different magnitude events from the recurrence model, the slip rate can be used to estimate the absolute frequency of different magnitude events.

We used the general approach of Molnar (1979) and Anderson (1979) to arrive at the recurrence for the Gutenberg-Richter truncated exponential model. The number of events exceeding a given magnitude, *N(m)*, for the truncated exponential relationship is

$$N(m) = \alpha(m^o)\frac{10^{-b(m-m^o)} - 10^{-b(m^u-m^o)}}{1-10^{-b(m^u-m^o)}} \qquad (3\text{-}4)$$

where $\alpha(m^o)$ is the annual frequency of occurrence of earthquakes greater than the minimum magnitude, m^o; *b* is the Gutenberg-Richter parameter defining the slope of the recurrence curve; and m^u is the upper-bound magnitude event that can occur on the source.

The m^o for the faults is **M** 6.75, which is the maximum magnitude for background earthquakes. We use a distribution that extends from **M** 6.75 to M_{char} with a *b*-value of either 0.0 or 1.0 (Figure 3.4-2). For the remainder of this report, we refer to this model as the doubly truncated Gutenberg-Richter (DTGR) magnitude recurrence model. This model is essentially a characteristic model similar to the model used by the USGS in the NSHM (Frankel *et al*., 2002). For segmented faults, the maximum magnitude model is used for the segmented rupture models and the DTGR model is used for the unsegmented rupture models. The absence of historical and instrumental seismicity that can be associated with the WFZ, particularly **M** 5.0 and greater (Arabasz *et al*., 1992) is consistent with the maximum magnitude model. All other faults in the Wasatch Front region are less well studied in terms of associating contemporary seismicity, but the pattern observed for the WFZ is probably true for those faults as well. For all simple, unsegmented faults, we weighted the maximum magnitude and DTGR models 0.7 and 0.3, respectively. For the DTGR model, b-values of 0.0 and 1.0 are equally weighted for these simple faults. If M_{char} is less than **M** 6.75, we assigned the maximum magnitude recurrence model a weight of 1.0 allowing magnitudes of M_{char} ± 0.24. For the background earthquakes, we used a truncated exponential model with a *b*-value that is derived from the historical seismicity record (Section 5.7).

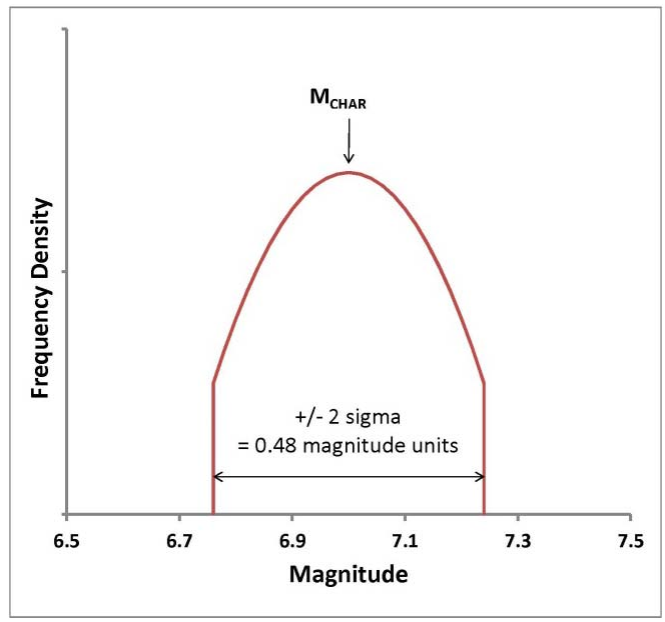

Figure 3.4-1. Maximum magnitude recurrence model.

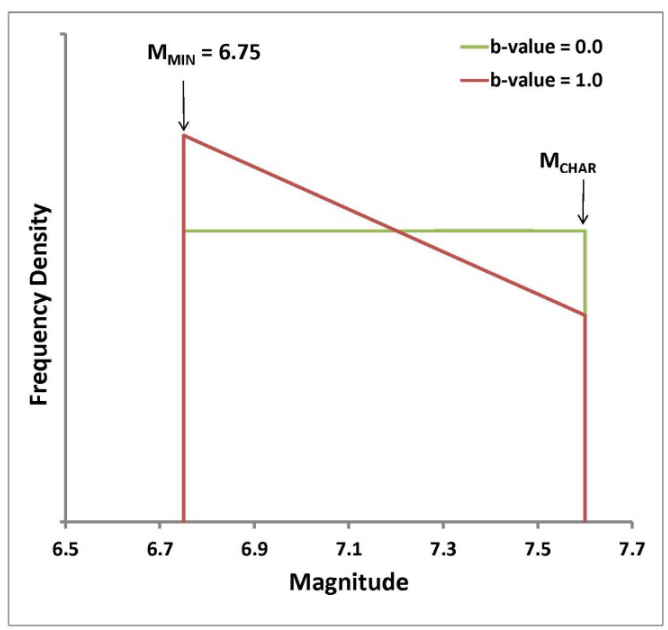

Figure 3.4-2. DTGR magnitude recurrence model.

3.5 Calculating Mean Recurrence Intervals and Rates

For faults with paleoseismic data (namely the WFZ central segments and the OGSLFZ), we calculated mean recurrence intervals/rates via the approaches described in the Central and Eastern U.S. (CEUS) Seismic Source Characterization (SSC) for Nuclear Facilities (EPRI/DOE/NRC, 2012). The CEUS-SSC approaches resulted in discrete five-point approximations to continuous probability distributions of mean recurrence intervals and rates that define weighted branches of the WGUEP logic tree. As discussed in the CEUS-SSC report and below, these probability distributions quantify the uncertainty in the mean recurrence intervals/rates that arise from relatively small samples sizes (i.e., small numbers) of past earthquakes. As an example, the five-point approximation for the Southern Oquirrh segment of the OGSLFZ is shown in Figure 3.5-1.

3.5.1 Time-Independent Poisson Mean Recurrence Rates

More specifically, to calculate mean recurrence rates for the time-independent Poisson model, denoted λ, we applied the approaches described in Sections 5.3.3.1.1 (Earthquake Count in a Time Interval) and 5.3.3.1.2 (Earthquake Recurrence Intervals) of the CEUS-SSC report. The latter was followed for the faults with paleoseismic data that include estimated occurrence times of past earthquakes, whereas the former was followed when the only available information is an estimated number of past earthquakes in an estimated time interval. Among the faults with paleoseismic data, all except the Southern Oquirrh segment of the OGSLFZ include estimated occurrence times of past earthquakes. Hence, we followed the approach of Section 5.3.3.1.2 of the CEUS-SSC report for all of the faults except the Southern Oquirrh segment. As mentioned in the CEUS-SSC report, for both types of paleoseismic data the continuous probability distribution of λ is a gamma distribution. In the case that the only available information is an estimated number of earthquakes, N, in an estimated time interval, T, the gamma distribution is that with a mean of $(N+1)/T$ and a mode of N/T (i.e., a shape parameter of $N+1$ and a rate parameter of $1/T$). In the case that estimated occurrence times are available (including the open interval of time since the most recent earthquake), as well as any estimated open interval of time before the oldest earthquake during which no other earthquake occurred, for a total estimated time interval of T, the gamma distribution is that with a mean of N/T and a mode of $(N-1)/T$ (i.e., a shape parameter of N and a rate parameter of $1/T$). Note that the availability of an open time interval before the oldest earthquake is not considered in the CEUS-SSC report (Section 5.3.3.1.2), but its inclusion here does not change the aforementioned gamma distribution. For either type of paleoseismic data, the continuous gamma

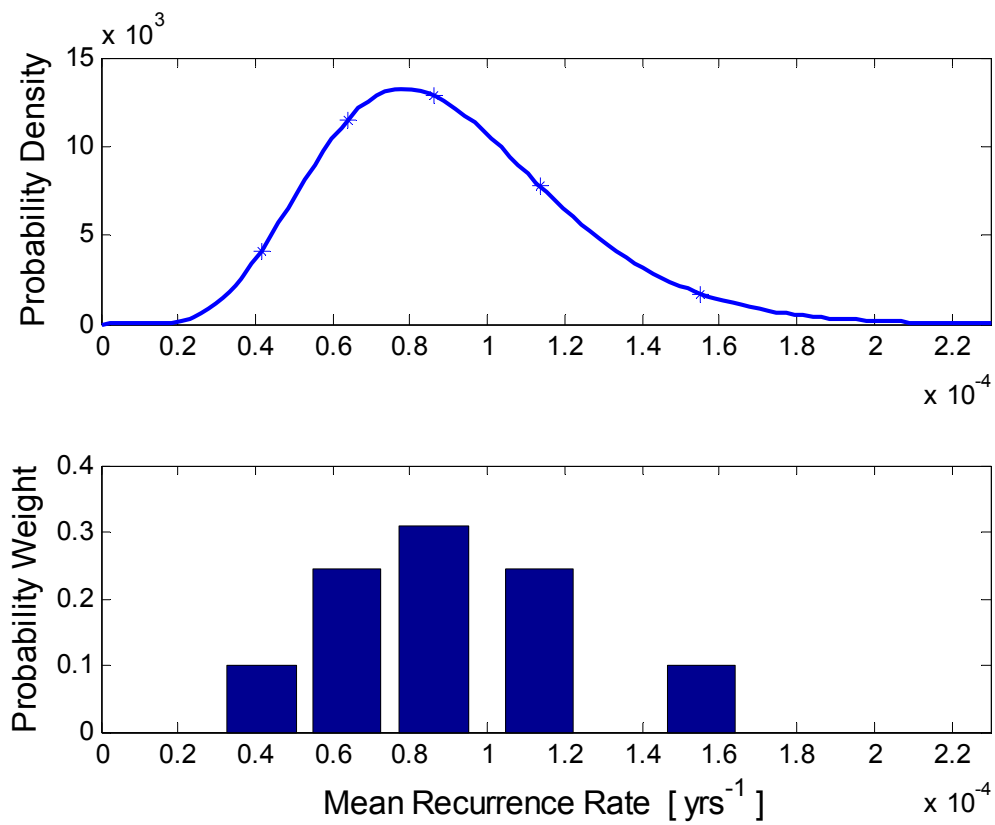

Figure 3.5-1. An example of a continuous gamma probability distribution for mean recurrence rate (top panel) and its discrete five-point approximation (bottom panel) calculated according to the CEUS-SSC report (EPRI/DOE/NRC, 2012, Section 5.3.3.1.1). This example is for the Southern Oquirrh segment of the OGSLFZ, assuming that there have been seven earthquakes in 89,011 years.

distribution was discretized into a five-point approximation like that shown in Figure 3.5-1, following Section 5.3.3.1.3 of the CEUS-SSC report. The five cumulative probabilities from the continuous distribution used to obtain mean recurrence rates/intervals for the discretized distribution are 0.034893, 0.211702, 0.5, 1-0.211702=0.788298, and 1-0.034893=0.965107. The five probability weights for the discrete approximation are 0.101, 0.244, 0.310, 0.244, and 0.101.

3.5.2 Time-Dependent BPT Mean Recurrence Intervals

To calculate mean recurrence intervals for the time-dependent BPT model, denoted μ, we applied the approach described in Section 5.3.3.2 (Estimation of Occurrence Rates for a Renewal Model) of the CEUS-SSC report. In addition to the required estimates of occurrence times, we considered any estimate of time before the oldest earthquake during which no other earthquakes occurred, as we did for the time-independent Poisson model discussed in the preceding paragraph. We did so in the same manner that the CEUS-SSC included the estimated open interval of time since the most recent earthquake (which we also considered). The results are five-point approximations to continuous probability distributions of μ for each of the three coefficients of variation of recurrence intervals (or aperiodicity coefficients) considered, namely 0.3, 0.5, and 0.7. As an example, the five-point approximation for the Salt Lake City segment of the WFZ is shown in Figure 3.5-2.

3.5.3 Impact of Paleoseismic Data Uncertainty

In our calculations of mean recurrence rates/intervals, we did not incorporate (with one exception described below) the input uncertainties discussed in Section 5.3.3.3 (Incorporating Uncertainty in the Input) of the CEUS-SSC report—namely uncertainties in the time interval T over which past earthquakes have occurred or in the earthquake occurrence times. We find the impacts of incorporating these uncertainties on the probability distributions of mean recurrence rates/intervals to be negligible in comparison to the uncertainty arising from the relatively small sample sizes of past earthquakes. For example, Figure 3.5-3(a) shows a comparison of the probability distributions of Poisson mean recurrence rates with and without incorporation of uncertainty in T, for the Weber segment of the WFZ, where both the uncertainty in T and the sample size of past earthquakes is relatively large (see Table 4.1-2). For the other fault segments with paleoseismic data, the differences between the probability distributions

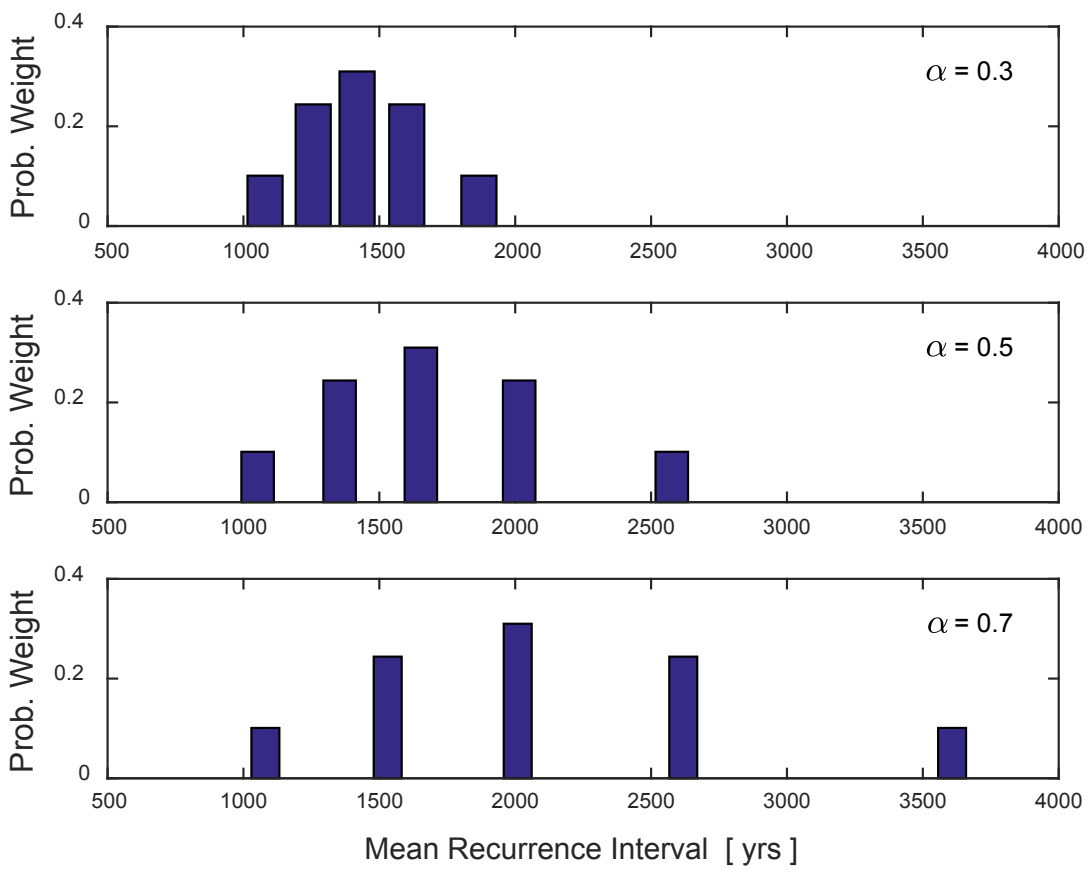

Figure 3.5-2. An example of discretized five-point probability distributions of mean recurrence interval for the time-dependent BPT model, calculated according to the CEUS-SSC report (Section 5.3.3.2). The three probability distributions correspond to the three aperiodicity coefficients (α's) considered. This example is for the Salt Lake City segment of the WFZ, assuming that it ruptured 1343, 2160, 4147, and 5250 years before 1950.

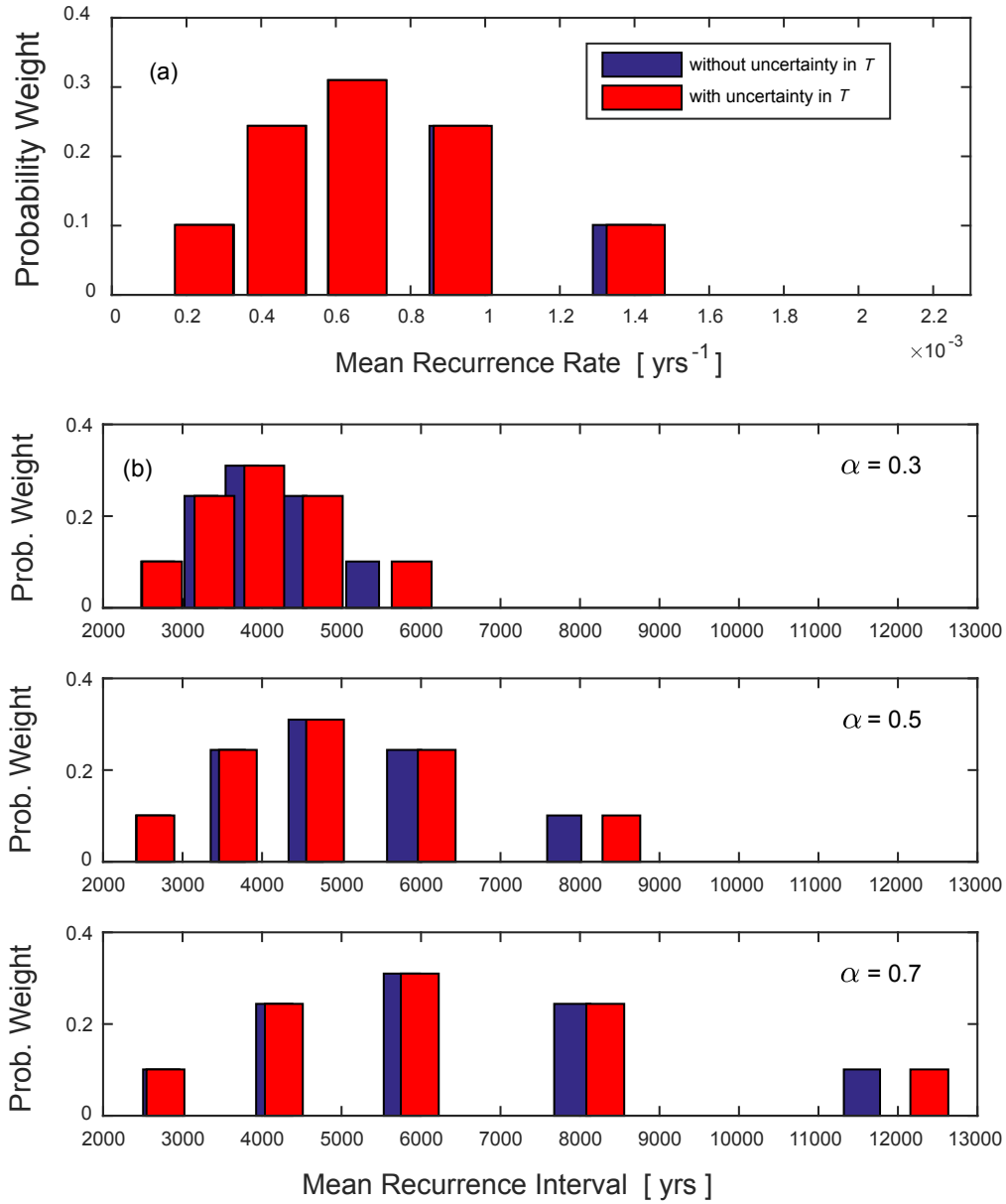

Figure 3.5-3. Examples of the effect of including uncertainty in the time interval, *T*, over which past earthquakes have occurred or in the earthquake occurrence times. The panel (a) example is for the Weber segment of the WFZ, where the effect of including uncertainty in *T* is largest relative to the other fault segments with paleoseismic data. The panel (b) example is for the Fremont Island segment of the OGSLFZ, where the effect of including relatively large uncertainty in the time of the oldest earthquake is incorporated. The changes in the time-independent Poisson mean recurrence rates illustrated in panel (a) are less than 3%, whereas those in the time-dependent BPT mean recurrence intervals of panel (b) are up to 12%.

with and without input uncertainty are even smaller, with the following exception illustrated in Figure 3.5-3(b): for the Fremont Island segment of the OGSLFZ, the uncertainty in the time of the oldest earthquake is 1000–5015 years before the penultimate event, with a uniform probability distribution. We incorporated this uncertainty by calculating a continuous probability distribution of BPT mean recurrence interval for each of the possible times of the oldest earthquake, and then applying the total probability theorem to calculate a continuous distribution (for each aperiodicity coefficient) that incorporates this timing uncertainty, in addition to the uncertainty arising from a small sample size of past earthquakes.

3.6 Calculating Characteristic Magnitudes

To calculate M_{char} for faults in the Wasatch Front region, we evaluated 19 historical regressions on **M** (Appendix A). These regressions relate **M** to one (or more) of many fault parameters, including linear surface-rupture length (SRL), linear segment length (L_{seg}), linear subsurface rupture length (L_{sub}), average displacement (D_{ave}), maximum displacement (D_{max}), rupture area (A; product of down-dip rupture width [W] and L_{sub}), seismic moment (M_0), and slip rate (SR). For segmented faults, we consider L_{seg} to be a reasonable estimate of SRL,

although SRL may exceed L_{seg} in some cases (e.g., Carpenter *et al*., 2012; discussed below). For calculating A, we used L_{seg} or SRL in place of L_{sub}, which is the average subsurface rupture length over the depth of the rupture, typically defined using historical aftershock data (e.g., Wells and Coppersmith, 1994). For segmented faults, we calculated A using:

$$A = L_{seg}\ W \qquad (3\text{-}5)$$

and for unsegmented faults, we use A equal to:

$$A = SRL\ W \qquad (3\text{-}6)$$

Although Wells and Coppersmith (1994) show that SRL is on average about 75% of L_{sub}, we use L_{seg} or SRL as a proxy for L_{sub} because (1) there is considerable scatter in the Wells and Coppersmith (1994) plot of SRL versus L_{sub} (their Figure 3), and (2) at larger magnitudes, the ratio of SRL to L_{sub} increases, making SRL a more reliable estimator of L_{sub} (Wells and Coppersmith, 1994). Finally, on the WFZ, decreased throw at prominent segment boundaries (forming fault salients) suggests that L_{sub} does not greatly exceed L_{seg} when averaged over several earthquake cycles. M_0 is defined by the equation:

$$M_0 = \mu\ D_{ave}\ A \qquad (3\text{-}7)$$

(Hanks and Kanamori, 1979), where μ is crustal rigidity (3 x 10^{11} dyne/cm^2), D_{ave} is the average fault-parallel displacement over the surface of the fault rupture, and A is defined by the fault length (L) and down-dip width (W), assuming a 50° fault dip and maximum rupture depth of 15 km. However, for consistency with SRL regressions, we assume a planar fault in the M_0 calculation (equations 3-5 and 3-6) and thus, calculated M_0 as follows:

$$M_0 = D_{ave}\ L_{seg}\ W \qquad (3\text{-}8)$$

$$M_0 = D_{ave}\ SRL\ W \qquad (3\text{-}9)$$

We did not consider regressions based on earthquake catalogs predating Wells and Coppersmith (1994) (e.g., Bonilla *et al*., 1984) or regressions calculated using only strike-slip- or reverse-faulting earthquakes.

For segmented faults lacking detailed paleoseismic displacement data, and thus, estimates of D_{ave} necessary for calculating M_0, we estimated D_{ave} using an L-D_{ave} linear regression calculated for the central WFZ (Figure 3.6-1), where:

$$D_{ave} = 0.044\ L \qquad (3\text{-}10)$$

Equation 3-10 is based on L_{seg} and the mean vertical displacement for each of the central five segments (Appendix A). The mean displacement per segment is the mean of several modeled displacement profiles calculated for individual ruptures (Table B-9). Although the minimum and maximum displacement ranges show considerable scatter in the data, the mean values show a consistent scaling of D_{ave} with L_{seg} at the segment lengths considered (35 to 59 km). Our L-D_{ave} relation predicts larger D_{ave} per fault length than relations by Wells and Coppersmith (1994; all fault types) and Wesnousky (2008; normal faults), and similar D_{ave} to the censored-instrumental SRL-D_{ave} relation of Stirling *et al*. (2002), although the Stirling *et al*. (2002) relation predicts larger D_{ave} at more moderate (35 to 45-km-long) SRLs (Figure 3.6-1; Table 3.6-1).

3.6.1 Fault Length- Versus Displacement-Based Magnitudes

Significant epistemic uncertainties complicate the determination of **M** for BRP normal faults. For example, for the central WFZ, a discrepancy exists where **M** based on D_{ave} or M_0 exceeds that based on SRL or A (average difference of 0.2 **M** units for single-segment ruptures using M_0 and SRL regressions; Figure 3.6-2). This **M** discrepancy affects

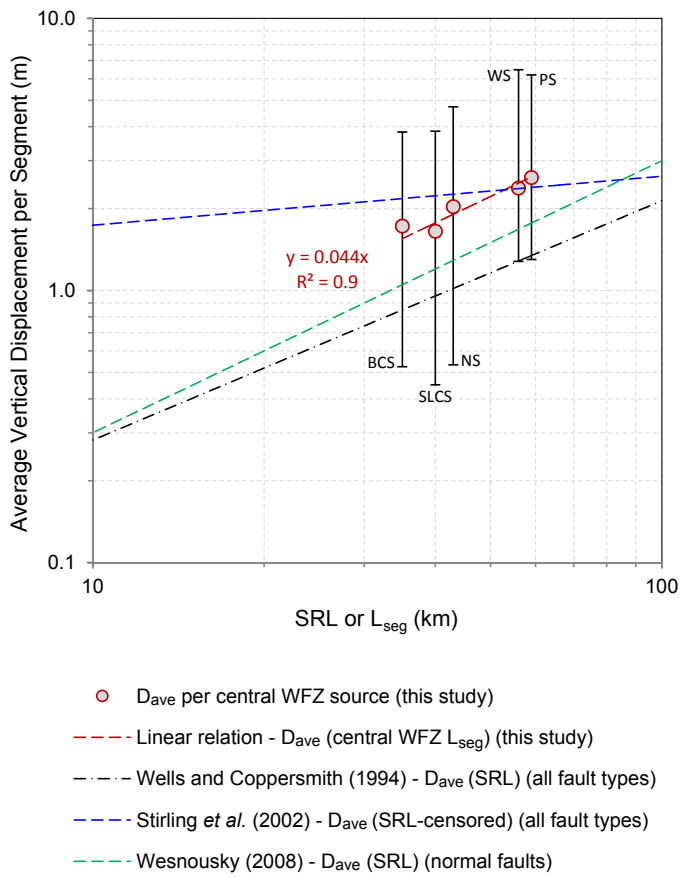

Figure 3.6-1. Average vertical displacement (D_{ave}) versus fault length (L; SRL or L_{seg}) for the central WFZ compared to historical scaling relations developed by Wells and Coppersmith (1994), Stirling *et al*. (2002), and Wesnousky (2008). Red dashed line indicates the linear fit to the D_{ave} per segment (mean of several modeled displacement profiles calculated for individual ruptures), where D_{ave} = 0.044*L (see Section 4 for discussion). Error bars indicate range in individual rupture displacements per segment.

Table 3.6-1. Average displacement per fault length relations.

SRL or L_{seg}[1] (km)	Wells and Coppersmith (1994) – D_{ave} (SRL)[2] (m)	Stirling *et al.* (2002) – D_{ave} (SRL-censored)[3] (m)	Wesnousky (2008) – D_{ave} (SRL)[4] (m)	This study – D_{ave} (L_{seg} for central WFZ)[5] (m)
25	0.6	2.0	0.8	1.1
35	0.8	2.2	1.1	1.5
59	1.3	2.4	1.8	2.6
100	2.1	2.6	3.0	4.4
128	2.7	2.7	3.8	5.6

[1] SRL values correspond with central WFZ segment median rupture lengths: 25 km is included as a possible partial-segment rupture, based on 50% of the mean segment length (L_{seg}) for the central WFZ (about 50 km); 35 km for Brigham City segment (shortest central segment); 59 km for Provo segment (longest central segment); 100 km for a possible two-segment rupture (mean $2xL_{seg}$), and 128 km for the longest (three-segment) rupture considered on the WFZ, based on paleoseismic data.

[2] Log(average vertical displacement [D_{ave}]) = 0.88log(SRL) – 1.43, based on an all-fault-type dataset (n = 66; Wells and Coppersmith, 1994).

[3] Log(D_{ave}) = 0.18log(SRL) + 0.06, based on censored-instrumental all-fault-type data (n = 50; Stirling *et al*., 2002).

[4] D_{ave} = 0.03*SRL, based on a normal fault dataset (n = 7; Wesnousky, 2008).

[5] D_{ave} = 0.044*L_{seg}, based on central WFZ data (n = 6 for single-segment ruptures; this study). D_{ave} values for multi-segment ruptures (100 and 128 km SRLs) are less well constrained because our D_{ave} relation is based on L_{seg} rather than SRL.

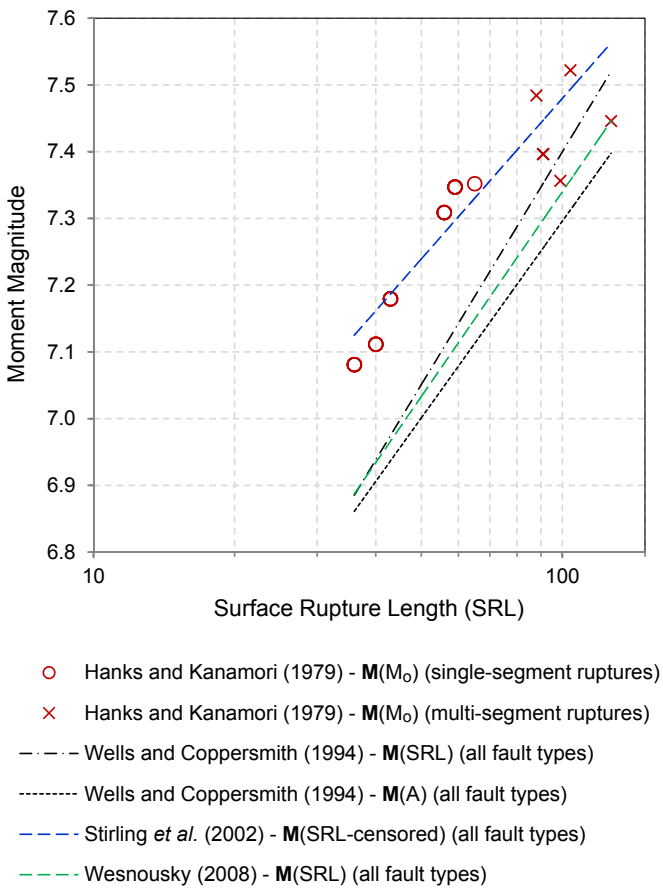

Figure 3.6-2. **M** for single- and multi-segment ruptures on the central WFZ based on estimates of M_0 (using regression of Hanks and Kanamori, 1979), which compares well with the censored-instrumental SRL-**M** regression of Stirling *et al*. (2002). For single-segment ruptures, these **M** estimates are on average about 0.2 units greater than those based on SRL-**M** and A-**M** regressions developed by Wells and Coppersmith (1994) and Wesnousky (2008).

estimates of M_0 release on the central WFZ, and thus, moment-balanced models of earthquake recurrence. For example, smaller magnitudes predicted by SRL and A regressions yield moment-balanced recurrence intervals that are significantly less than (about one-third of) those calculated using M_0-based magnitudes or the extensive WFZ paleoseismic data (Section 4). This discrepancy in **M** is possibly related to: (1) consistently larger vertical displacements (and thus moment release) per segment rupture length than expected from the empirical regressions (high stress drop earthquakes?), (2) rupture lengths extending beyond the mapped segment boundaries (e.g., Hemphill Haley and Weldon, 1999; Carpenter *et al*., 2012; DuRoss *et al*., 2012; Personius *et al*., 2012), (3) an incorrect bias in regressions because the datasets are dominated by strike-slip, reverse, and megathrust earthquakes in plate-boundary tectonic environments, and/or (4) different scaling relations for different strain-rate environments (Anderson *et al*., 1996) or large versus small to moderate earthquakes (Stirling *et al*., 2002).

The possibility that large, prehistoric earthquakes may have a SRL-**M** scaling relation different than that for small to moderate historical earthquakes stems from Stirling *et al*. (2002), who recognized a small-earthquake bias inherent in the Wells and Coppersmith (1994) SRL-**M** and A-**M** regressions. Stirling *et al*. (2002) addressed this bias by censoring an updated version of the Wells and Coppersmith (1994) earthquake dataset for SRL < 10 km, A < 200 km^2, D_{ave} < 2 m, and **M** < 6.5. Regressions generated from the censored-instrumental data of Stirling *et al*. (2002) predict larger **M** per SRL or A than Wells and Coppersmith (1994) (Figure 3.6-1), consistent with regressions based on the Stirling *et al*. (2002) preinstrumental data (which consist of large historical earthquakes predating 1900 and paleoseismic data). On the central WFZ, the censored-instrumental SRL-**M** regression predicts mag-

nitudes that are very similar to those based on M_0 (average difference of 0.04 **M** units for single-segment ruptures; Figure 3.6-2) and yields moment-balanced recurrence intervals consistent with paleoseismic data. Although, not originally intended for source-modeling applications, the Stirling *et al*. (2002) regressions fit the central WFZ data exceptionally well and are of particular interest to other segmented faults in the Wasatch Front region that lack D_{ave} information necessary to calculate **M** as a function of M_0. Thus, we applied the Stirling *et al*. (2002) SRL-**M** (censored instrumental) regression to these faults with the assumption that they have similar displacement-length scaling relations as the central WFZ, and thus, a similar amount of moment release per SRL.

Hemphill-Haley and Weldon (1999) and Carpenter *et al*. (2012) at least partially explain the discrepancy in displacement versus length-based **M** on limitations in measuring prehistoric SRL. Hemphill-Haley and Weldon (1999) suggested that displacement is a better indicator of prehistoric earthquake **M** than SRL. Using displacement profiles from 14 historical ruptures (multiple fault types), they developed parameters for scaling D_{ave} for use in the Wells and Coppersmith (1994) D_{ave}-**M** regression. Their D_{ave}-scaling parameters are based on the number of paleoseismic displacement observations available and the percent of the fault length that they cover; however, they recommended that at least five to ten displacement observations be used, which limit the practical application of their relations. Carpenter *et al*. (2012) cited examples of historical earthquake SRL in excess of L_{seg} and used seven historical earthquakes (multiple fault types) to generate L_{seg}-**M** regressions. For the WFZ, Lost River, and Lemhi fault segments, the L_{seg}-**M** relations predicted larger magnitudes that are more consistent with displacement-based estimates. Importantly, the Hemphill-Haley and Weldon (1999) and Carpenter *et al*. (2012) regressions help explain the displacement versus length discrepancy in **M**, while taking different approaches to address it. These regressions yield larger **M** than SRL regressions (e.g., Wells and Coppersmith, 1994), and thus, lend support to the Stirling *et al*. (2002) censored-instrumental SRL regression. We prefer the Stirling *et al*. (2002) SRL regression over displacement-based regressions because it (1) is based on a more statistically robust earthquake dataset, (2) agrees with the central WFZ paleoseismic data but avoids D_{ave}-calculation issues, such as the number and type (e.g., fault-parallel versus vertical, horizontal, or net) of displacement observations necessary to calculate **M**, and (3) can be applied to all faults in the Wasatch Front region.

3.6.2 Magnitude Regressions

Of the 19 **M** regressions evaluated (Appendix A), we selected six to characterize earthquake magnitudes for Wasatch Front faults (Table 3.6-2). In evaluating and selecting regressions, our primary goal was to adequately represent epistemic uncertainties in **M** while logically and consistently using the best available and most up-to-date regressions. We found that **M** estimates (as a function of SRL) span about 0.3 to 0.4 units (Figure 3.6-3) owing to differences in the fault parameter used; age, quality, and size of historical earthquake databases; and fault type and region considered. We selected **M** regressions that (1) estimate **M** and characterize the upper and lower bounds of the **M** uncertainty (Figure 3.6-2), (2) are based on the fundamental definition of Mo (e.g., Hanks and Kanamori, 1979), (3) are widely accepted and commonly used for BRP faults (e.g., SRL and A regressions of Wells and Coppersmith, 1994), (4) include the most up-to-date and well-vetted earthquake datasets (Stirling *et al*., 2002; SRL regression of Wesnousky, 2008), and (5) yield relatively large magnitudes consistent with the central WFZ paleoseismic data (Hanks and Kanamori, 1979; Stirling *et al*., 2002). Although the Wells and Coppersmith (1994) regressions are arguably out of date, we included the regressions (albeit with low weight) considering their common use in the BRP. Further, updated versions of the regressions (unpublished, but presented by Wells, 2015) have similar regression trends and statistical results to Wells and Coppersmith (1994) results. We had less confidence in regressions that (1) are based on limited earthquake datasets ($N < 20$), such as the normal-fault-type regressions of Wells and Coppersmith (1994) and Wesnousky (2008), and also Carpenter *et al*. (2012), (2) use fault parameters such as D_{ave}, D_{max}, or slip rate (SR) (Wells and Coppersmith, 1994; Anderson *et al*., 1996; Mason, 1996; Hemphill-Haley and Weldon, 1999), which are not well resolved for most BRP faults, or (3) include earthquake types (e.g., megathrust events; Leonard, 2010) that are not applicable to the BRP. As a result, our preference was for the most statistically robust regressions stemming from global, all-fault-type earthquake data (Table 3.6-2).

3.6.3 Regression Weights

We weighted our preferred **M** regressions according to fault type (Table 3.6-2). For *A*, *B*, and *C* faults, we used two SRL regressions that yield smaller **M** per length, the Wells and Coppersmith (1994) and Wesnousky (2008) SRL-**M** regressions, and two that yield larger **M** per length, the SRL regression based on the censored instrumental data of Stirling *et al*. (2002) (herein SRL-censored) and the M_0 relation of Hanks and Kanamori (1979). For antithetic faults, which include a secondary fault truncated at depth by a master fault (e.g., the West Valley fault zone), we used the A regressions of Wells and Coppersmith (1994) and Stirling *et al*. (2002) weighted equally.

A faults include the central WFZ (Section 4.1) and the Northern and Oquirrh segments of the OGSLFZ (Section 4.3). These faults are segmented and have sufficient modeled displacement information (e.g., Table A-9) for calculating **M** as a function of M_0. Because sensitivity studies showed that M_0 and SRL-censored regressions yield moment-balanced recurrence intervals that are generally consistent with paleoseismic earthquake-timing and recurrence data, we heavily weighted (0.9, divided equally) these regressions. To account for epistemic uncertainties in **M**, we included SRL regressions, but gave them low weight (0.1, divided equally). These

Table 3.6-2. Moment-magnitude regressions and weights for Wasatch Front faults.

Magnitude regression[1]			Regression parameters[2]			Wasatch Front fault category[3]			
			N	R	σ	*A*	*B*	*C*	AFP
Hanks and Kanamori (1979)	M_0, all	$2/3\log(M_0)-10.7$	NR	NA	NA	0.45	0.4	0	-
Stirling *et al.* (2002) (censored instrumental)	SRL, all	5.88+0.80log(SRL)	50	NR	0.3	0.45	0.4	0.34	-
Wesnousky (2008)	SRL, all	5.30+1.02log(SRL)	27	0.81	0.28	0.05	0.1	0.33	-
Wells and Coppersmith (1994)	SRL, all	5.08+1.16log(SRL)	77	0.89	0.28	0.05	0.1	0.33	-
Stirling *et al.* (2002) (censored instrumental)	A, all	5.09+0.73log(A)	47	NR	0.26	-	-	-	0.5
Wells and Coppersmith (1994)	A, all	4.07+0.98log(A)	148	0.95	0.24	-	-	-	0.5

[1] M_0 – seismic moment (μ*L*W*D_{ave}), A – rupture area (SRL*W; see text for discussion), SRL – linear surface rupture length. All – implies regressions based on strike-slip, normal, and reverse faulting earthquakes.
[2] N is number of earthquakes; R is regression coefficient; σ is standard deviation in magnitude. NA – not applicable. NR – not reported.
[3] Wasatch Front fault categories: *A* – segmented with good displacement data, *B* – segmented with limited displacement data, *C* – unsegmented with limited displacement data, AFP – antithetic fault pairs where the down-dip width of the secondary fault is truncated by the primary (master) fault at a relatively shallow seismogenic depth.

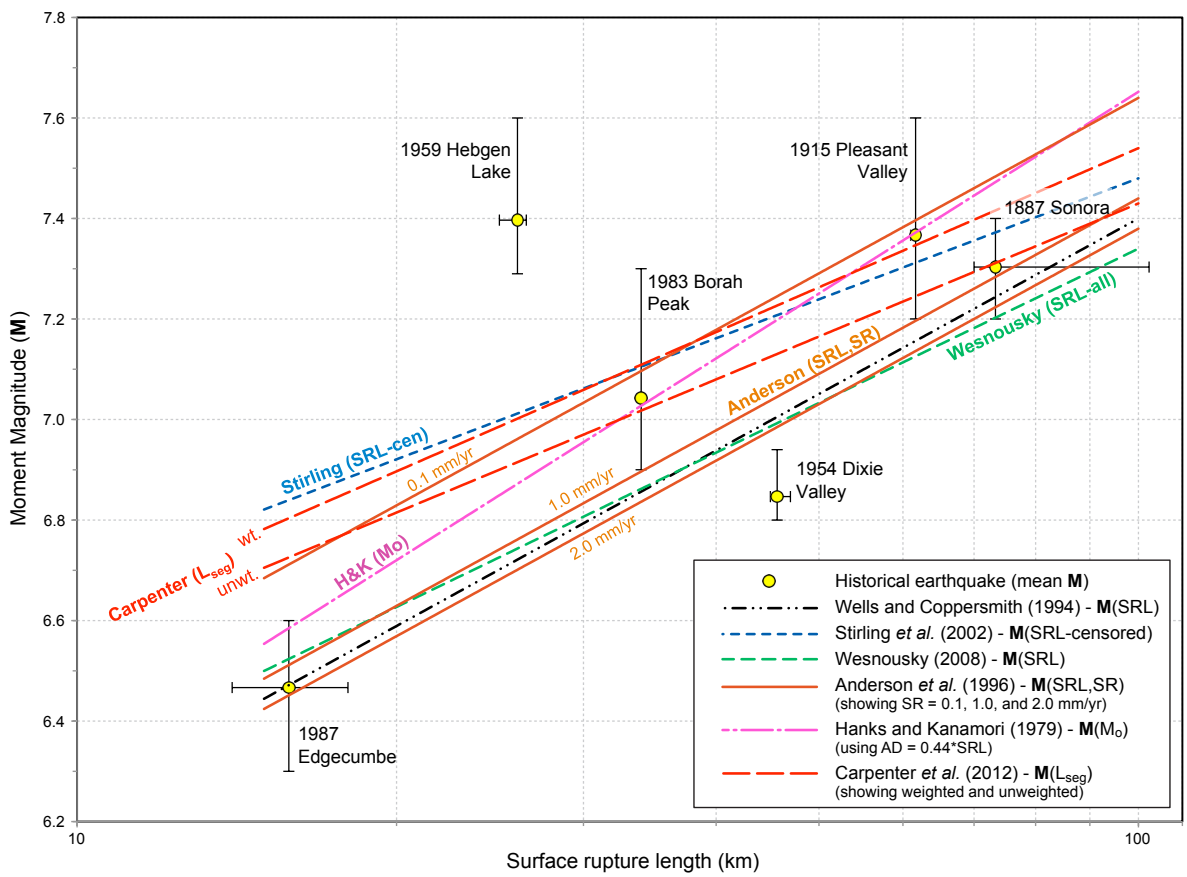

Figure 3.6-3. Comparison of several historical regressions on **M** with six historical large-magnitude normal-faulting earthquakes. The M_0-**M** curve of Hanks and Kanamori (1979) uses the L_{seg}-D_{ave} scaling relation developed for the central WFZ (this study; Figure 3.6-1). The **M** regressions based on both SRL and SR of Anderson *et al.* (1996) assumes SR values of 0.1, 1.0, and 2.0 mm/yr. For the L_{seg}-**M** regressions (Carpenter *et al.*, 2012), both weighted (wt.) and unweighted (unwt.) curves are shown. SRL and L_{seg} regressions are based on all-fault-type data. SRLs and **M**s for the historical earthquakes are based on values reported in Wells and Coppersmith (1994), Stirling *et al.* (2002), and Wesnousky (2008).

regressions and weights apply to both single- and multi-segment rupture models (Section 4).

B faults include five segmented faults that are generally less well studied, such as the end segments of the WFZ (Section 4.2) and the East and West Cache fault zones (Table D-1). *B* faults have total lengths ranging from about 45 to 86 km, including faults along the western edge of Scipio Valley and the eastern base of the Pavant Range that we include in a linked, 45-km long fault zone. Some *B* faults have limited displacement data, but additional analyses (e.g, constructing modeled displacement profiles) were not conducted for this study, and thus, we did not calculate D_{ave} or M_0. We considered using historical earthquake scaling relations (e.g., by Stirling *et al*., 2002 and Wesnousky, 2008) to determine D_{ave} for use in the M_0 calculation, but ultimately used our L-D_{ave} relation based on the central WFZ data, which corresponds reasonably well with the historical regressions (Figure 3.6-1). Although the central WFZ L–D_{ave} relation is based on limited data, we used this relation for *B* faults because we consider it likely that these long, segmented faults behave similarly to the WFZ, and have similar displacement-length scaling relations and M_0 release per SRL. Thus, similar to *A* faults, we gave substantial weight (0.8, divided equally) to the Stirling *et al*. (2002) SRL-censored and Hanks and Kanamori (1979) M_0 regressions. As *B* faults have generally received less paleoseismic study than *A* faults, we weighted the SRL regressions 0.2 total (0.1 each), which is slightly greater than that for *A* faults (0.1 total).

C faults include 17 unsegmented faults that generally lack paleoseismic displacement information (Table D-1). *C* faults range from 10 to 42 km long and include some relatively short, linked faults, such as those defining the 17-km long Morgan fault. The Joes Valley fault zone and Snow Lake graben are considered *C* faults in their deep-penetration models. In general, *C* faults have broadly constrained or unknown earthquake recurrence intervals and poorly constrained slip rates. Because *C* faults are relatively short and unsegmented and have very limited paleoseismic data, we are less confident that their rupture behavior (e.g., M_o release and **M** per SRL) is similar to that for *A* faults such as the WFZ. As a result, we chose not to estimate D_{ave} using our central WFZ L–D_{ave} relation, and thus, did not include the Hanks and Kanamori (1979) M_o regression. We weighted the remaining regressions equally (Stirling *et al*. (2002) 0.34 weight; Wells and Coppersmith (1994) 0.33 weight; Wesnousky (2008) 0.33 weight) because of uncertainty in whether regressions yielding larger or smaller **M** are more applicable to *C* faults, and to adequately bracket larger epistemic uncertainties in estimating **M** for these less well understood faults.

Antithetic faults include the Hansel Valley, West Valley, Western Bear Lake, and Utah Lake faults, all of which intersect master faults at relatively shallow depths (i.e., less than the seismogenic depth of about 12 to 18 km described in Section 3.2). For example, the West Valley fault zone, which is antithetic to the Salt Lake City segment of the WFZ, is likely truncated by the WFZ at a relatively shallow depth of about 7 km (depending on both the master and antithetic fault dips). This group also includes the Joes Valley fault zone and Snow Lake graben when modeled at shallow-penetration depths. To account for the reduced surface area relative to the length of these antithetic faults, we used the A regressions of Wells and Coppersmith (1994) and Stirling *et al*. (2002) weighted equally.

4 CHARACTERIZATION OF WASATCH FRONT REGION FAULTS

The following describes the characterization of the faults considered in the WGUEP forecast. Much of the forecast region was occupied by pluvial Lake Bonneville, which produced numerous shoreline features in the latest Pleistocene that provide datums useful for characterizing the amounts and timing of prehistoric earthquakes. The two most prominent features are the Bonneville highstand shoreline, which was abandoned following the Bonneville Flood about 18 ka (Oviatt, 1997; Benson *et al*., 2011; Janecke and Oaks, 2011; Miller *et al*., 2013; Reheis *et al*., 2014) after which the lake stabilized about 100 m lower at the Provo shoreline. The age of the Provo phase is still the focus of ongoing research, but the most recent published estimates of the timing of retreat from the Provo level are ~16.5–15 ka (Godsey *et al*., 2011; Miller *et al*., 2013). Both of these features are used in our analysis of long-term slip rates along the central segments of the WFZ (Section 4.1.4; Appendix B) and the timing of paleoearthquakes on the Oquirrh–Great Salt Lake fault zone (Section 4.3). Acronyms and abbreviations are defined on pages xii to xiv.

4.1 Wasatch Fault Zone Central Segments

The WFZ is Utah's longest and most active normal-slip fault, extending about 350 km from southern Idaho to central Utah, and forming a prominent structural boundary between the BRP to the west and the relatively more stable Middle Rocky Mountain and Colorado Plateau provinces to the east. The WFZ has a complex trace that comprises ten segments (Figure 1-2) thought to generally rupture as seismogenically independent parts of the fault zone (Machette *et al*., 1992). This segmentation model is supported by (1) well-defined fault salients, marked by complex and diffuse faulting and shallow bedrock (indicating decreased fault displacement), which separate adjacent hanging-wall basins, and (2) along-strike changes in fault geometry and range-front morphology, and timing of most recent surface faulting (Swan *et al*., 1980; Schwartz and Coppersmith, 1984; Machette *et al*., 1992; Wheeler and Krystinik, 1992). For the five central segments (Brigham City to Nephi; Figure 4.1-1), which have paleoseismic evidence of repeated Holocene surface-faulting earthquakes, unique earthquake chronologies per segment support independent rupture (Machette *et al*., 1992; Lund, 2005; DuRoss, 2008; DuRoss *et al*., 2016). Thus, in the absence of well-defined rupture boundaries for prehistoric ruptures of the WFZ, we used the structural boundaries, together with paleoseismic earthquake timing and displacement data, as the basis for defining the fault's surface rupture characteristics and uncertainties. Additional discussion of paleoseismic data in the context of structural complexities along the WFZ is included in DuRoss *et al*. (2016). The central WFZ segments are the focus of this section; the end segments, including the Malad City, Collinston, and Clarkston Mountain segments to the north and the Levan and Fayette segments to the south (Figure 1-2), are discussed in Section 4.2.

The central segments of the WFZ are characterized by prominent fault scarps displacing late Holocene to latest Pleistocene geomorphic surfaces, and have been the focus of numerous paleoseismic fault-trench investigations. To date, 23 research trench sites (excluding those for pre-development fault-setback and educational purposes that have not culminated in peer-reviewed trench logs or papers) have yielded earthquake timing and/or displacement data. These data indicate that at least four to five Holocene earthquakes have occurred on each central segment (Machette *et al*., 1992; Lund, 2005; DuRoss, 2008), yielding mean recurrence times of ~1.3 to 2.5 thousand years (kyr) (post ~6 thousand years ago [ka]) per segment (Lund, 2005), a mean per-event vertical displacement of about 2 m for the central WFZ (DuRoss, 2008), and mean vertical slip rates for the segments of ~0.5 to 2.2 mm/yr (Machette *et al*., 1992; Friedrich *et al*., 2003; Lund, 2005). However, despite these paleoseismic data, important questions remained regarding earthquakes on the central segments at the time of this analysis. For example, should original paleoseismic data be superseded by or integrated with the results of more recent paleoseismic studies, which have generally yielded smaller earthquake-timing uncertainties due to improved sampling and dating methods? How complete are the paleoseismic data for each segment, and what methods should be used to calculate earthquake recurrence values and fault slip rates? Finally, how robust is the segmentation model for the fault? Although paleoseismic data generally support the segmentation model of Machette *et al*. (1992), should alternative (e.g., multi-segment-rupture) models permitted by uncertainties in the earthquake-timing and displacement data (e.g., Chang and Smith, 2002; DuRoss, 2008) be included?

To address these questions, we systematically examined previous paleoseismic data for the WFZ central segments to characterize their surface-faulting earthquake histories and rates of activity. For each segment, we reviewed and compiled published paleoseismic data from each trench site (generally excluding incomplete and unpublished data), and constructed time-stratigraphic OxCal models (e.g., Bronk Ramsey, 2008; Lienkaemper and Bronk Ramsey, 2009), which yielded earthquake-timing probability density functions (PDFs) for each site. We used the revised site PDF data to construct earthquake histories for each segment by correlating and combining the per-site earthquake-timing PDFs along the segment (after DuRoss *et al*., 2011). Because of the detailed nature of this work, discussions of the paleoseismic data, OxCal models, and segment-wide earthquake chronologies (and methods used to derive them) are included in Appendix B. These data are also discussed by DuRoss *et al*. (2011), Personius *et al*. (2012), and Crone *et al*. (2014). Using the revised earthquake histories per segment, we calculated inter-event and mean earthquake recurrence intervals, coefficients of variation (COVs) on recurrence, and vertical slip rates, which use per-event displacements and the recurrence-interval data. Final-

ly, we constructed several fault-rupture models that address epistemic uncertainties in fault segmentation and earthquake rupture extent. The fault and earthquake parameters and rupture models are summarized here; expanded discussions, including detailed descriptions of our methods and results, are included in Appendix B.

In this analysis, we compared and combined site-earthquake data (i.e., paleoseismic trench data) for each segment separately. That is, we did not systematically compare site earthquakes along the fault (i.e., on adjacent segments) to exhaustively allow for all possible rupture combinations (e.g., Biasi and Weldon, 2009). The assumption of single-segment ruptures on the central WFZ is consistent with Machette *et al.* (1992), Lund (2005), and DuRoss (2008), but affects the determination of the segment chronologies and recurrence intervals. Ultimately, we considered the potential for rupture beyond the segment boundaries and defined rupture uncertainties to account for more flexibility in the segmentation of the fault, but considered the treatment of the fault in a fully unsegmented manner outside the scope of this work.

4.1.1 Paleoseismic Data Sources

The central segments of the WFZ consist of (north to south) the Brigham City segment (BCS), Weber segment (WS), Salt Lake City segment (SLCS), Provo segment (PS), and Nephi segment (NS) (Figure 4.1-1). Most segments comprise two to three subsections, which we define as separate fault strands or continuous zones of faulting along the segment identified on the basis of along-strike changes in fault geometry, such as fault step-overs, gaps, or changes in orientation. These segments have been the subject of numerous paleoseismic investigations, which have yielded estimates of surface-faulting earthquake timing and displacement (Appendix B).

The 35-km-long (all length measurements in this section are straight-line, end-to-end) BCS is the northernmost segment of the central WFZ that has evidence of Holocene surface rupture (Figure 4.1-1). Paleoseismic data for the BCS are from the north-central part of the segment at Bowden Canyon (BC; Personius, 1991a), Box Elder Canyon (BEC; McCalpin and Forman, 2002), Hansen Canyon (HC; DuRoss *et al.*, 2012), and Kotter Canyon (KC; DuRoss *et al.*, 2012), and the southern part at Pole Patch (PP; Personius, 1991b) and Pearsons Canyon (PC; DuRoss *et al.*, 2012) (paleoseismic site abbreviations in this section correspond with Figure 4.1-1 and Appendix B). Personius *et al.* (2012) used paleoseismic data from these sites to constrain the timing of four late Holocene earthquakes on the BCS (Appendix B).

The 56-km-long WS is the second longest WFZ segment (Figure 4.1-1). Paleoseismic data for the WS are from trench investigations on the south-central part of the segment at the Kaysville (K) site (Swan *et al.*, 1980, 1981; later reoccupied by McCalpin *et al.*, 1994), and the northern part of the WS at the East Ogden (EO; Nelson, 1988; Nelson *et al.*, 2006) and

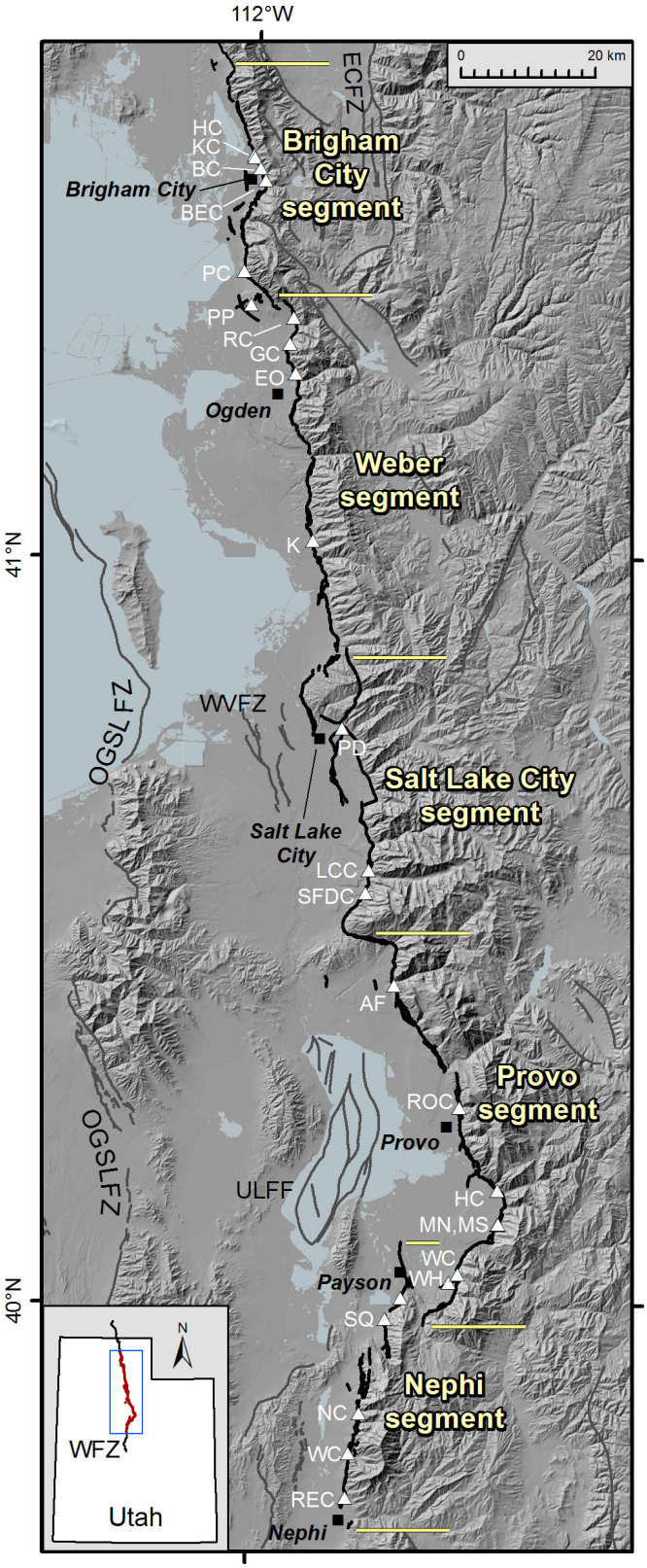

Figure 4.1-1. Central segments of the WFZ (from Black *et al.*, 2003) showing paleoseismic research sites (yellow triangles; see Appendix A for site abbreviations). ECFZ – East Cache fault zone, ETMF – East Tintic Mountains fault, OGSLFZ – Oquirrh–Great Salt Lake fault zone, ULFF – Utah Lake faults and folds, WVFZ – West Valley fault zone. Shaded topography generated from 10-m digital elevation data (https://lta.cr.usgs.gov/NED).

Rice Creek (RC; DuRoss *et al*., 2009) sites. Additional paleoseismic data are from a cut-slope excavation near East Ogden at the Garner Canyon (GC) site (Nelson, 1988; Forman *et al*., 1991; Nelson *et al*., 2006). Paleoseismic data from these sites contribute to the timing of five mid- to late Holocene earthquakes on the WS (DuRoss *et al*., 2011) (Appendix B).

The 40-km-long SLCS (Figure 4.1-1) comprises three subsections (separate fault strands) that are separated by prominent left steps: the Warm Springs, East Bench, and Cottonwood faults. Paleoseismic data for the SLCS are from fault-trench investigations at the Little Cottonwood Canyon (LCC; Swan *et al*., 1981; later reoccupied by McCalpin, 2002) and South Fork Dry Creek (SFDC; Schwartz and Lund, 1988; Black *et al*., 1996) sites, both on the Cottonwood fault. Paleoseismic data for the Penrose Drive (PD) site on the East Bench fault (DuRoss *et al*., 2014) were not available at the time of our analysis. Paleoseismic data from LCC and SFDC provide evidence of four late Holocene earthquakes on the SLCS (Appendix B).

The PS is the longest segment on the WFZ, which consists of three distinct subsections that have a total length of 59 km (Figure 4.1-1). Seven paleoseismic trench sites have been investigated along the PS, but only four of these sites had sufficient timing data available to be included in this analysis: the American Fork (AF) site (Forman *et al*., 1989; Machette *et al*., 1992) on the northern subsection, the Rock Canyon/Rock Creek (ROC) site (Lund and Black, 1998) on the central subsection, and the Mapleton South (MS; Lund *et al*., 1991) and Mapleton North (MN; Lund *et al*., 1991; later trenched by Olig *et al*., 2011) sites on the southern subsection. Based on data from these sites, at least five mid- to late Holocene earthquakes have occurred on the PS (Appendix B).

The NS is the southernmost segment of the central WFZ that has evidence of multiple Holocene surface-faulting earthquakes (Figure 4.1-1). The NS extends 43 km and comprises two subsections—a 17-km-long northern strand and a 25-km-long southern strand—which are separated by a 4 to 5-km-wide right step in bedrock. Paleoseismic data for the NS are from three trench sites on the southern strand at North Creek (NC; Hanson *et al*., 1981, 1982), Red Canyon (REC; Jackson, 1991), Willow Creek (WC; Machette *et al*., 2007; Crone *et al*., 2014), and one site on the northern strand near Santaquin (SQ; DuRoss *et al*., 2008). Crone *et al.* (2014) report four late Holocene earthquakes on the NS using data from these sites (Appendix B).

4.1.2 Surface-Faulting Earthquake Histories

At least 22 surface-faulting earthquakes have ruptured the central segments of the WFZ since about 6.0 ka (Table 4.1-1; Appendix B). Our revised surface-faulting earthquake histories per segment reflect important analytical steps, including the systematic analysis of previous paleoseismic data, OxCal modeling, and the correlation of site earthquakes along each segment. Although we summarize the data here, important and detailed discussions in Appendix B address (1) assumptions regarding the quality and completeness of the previous data, (2) the methods by which we combined the probabilistic earthquake timing data from OxCal into segment-wide earthquake chronologies, and (3) remaining uncertainties in the per-segment paleoseismic data and earthquake histories.

4.1.3 Earthquake Recurrence and Coefficient of Variation

We calculated individual (inter-event, e.g., B4–B3) and closed and open mean recurrence intervals for the central WFZ segments (Tables 4.1-1 and 4.1-2) by sampling our revised earthquake times (segment PDFs summarized in Table 4.1-1) in a Monte Carlo model (see Appendix B for discussion). Closed mean recurrence is the total elapsed time between the oldest and youngest earthquakes divided by the number of closed intervals between them (e.g., B4–B1 time divided by 3). Open mean recurrence intervals, or the number of events per unit time (*N*-in-*T*), use the total elapsed time from the maximum age constraint on the oldest event to the present (time of analysis, 2011) divided by the number of earthquakes that occurred in that period (e.g., 5.9 ± 0.4 ka divided by 4). Because the central segments have limited earthquake records, but similar mean recurrence estimates (Table 4.1-2), we grouped the individual recurrence intervals and calculated a composite mean recurrence interval for the central WFZ (using a Monte Carlo model discussed in Appendix B). The composite mean recurrence is a more statistically robust estimate because the inter-event recurrence sample size increases from 2 to 4 per segment to 16 for the central WFZ. These recurrence estimates do not account for sample-size uncertainties, which are discussed in Section 3.5.

The COV on recurrence, the standard deviation of inter-event recurrence intervals divided by their mean, is a measure of the periodicity of earthquakes on a fault, where smaller values indicate more periodic recurrence and a COV of 1.0 represents random timing. The WGCEP (2003, 2008) used a COV of 0.5 ± 0.2 based on a global dataset of repeating earthquake sequences (Ellsworth *et al*., 1999). To test the suitability of the global COV to the central WFZ, we calculated a composite COV for the central WFZ using grouped (composite) inter-event recurrence data. The basis for the composite COV is similar mean recurrence parameters for the individual segments. Similar to the composite mean recurrence interval, the composite COV is a more statistically robust estimate; however, the estimate does account for sample-size uncertainties (e.g., Section 3.5).

Inter-event intervals for the central WFZ segments show moderate variability (Table 4.1-1; Appendix B). For example, the youngest four earthquakes (B4 to B1) on the BCS yield consistent inter-event intervals of 1.0 to 1.1 kyr; however, about 2.5 kyr have elapsed since the most recent BCS earthquake, B1. Inter-event intervals for the WS, SLCS, PS, and NS are also irregular, ranging from about 0.7 kyr to 2.7 kyr, and varying by a factor of 2.4 to 3.5 per segment. For example, although two inter-event intervals for the WS are ~1.4

Table 4.1-1. Summary of earthquake timing data for the central WFZ.

Rupture[1]	**Earthquake Timing**[2] (ka)		**Inter-event recurrence**[3] (kyr)
	Mean ± 2σ	5th–50th–95th [mode]	
B1	2.4 ± 0.3	2.2–2.4–2.6 [2.4]	-
B2	3.5 ± 0.2	3.4–3.5–3.7 [3.4]	1.1 (B2–B1)
B3	4.5 ± 0.5	4.1–4.5–5.0 [4.5]	1.0 (B3–B2)
B4	5.6 ± 0.6	5.0–5.6–6.1 [5.6]	1.1 (B4–B3)
W1	0.6 ± 0.1	0.5–0.6–0.6 [0.5]	--
W2	1.1 ± 0.6	0.7–1.2–1.7 [1.3]	0.7 (W2–W1)
W3	3.1 ± 0.3	2.9–3.1–3.3 [3.1]	1.9 (W3–W2)
W4	4.5 ± 0.3	4.2–4.5–4.7 [4.5]	1.4 (W4–W3)
W5	5.9 ± 0.5	5.6–5.9–6.4 [5.6]	1.4 (W5–W4)
S1	1.3 ± 0.2	1.2–1.3–1.5 [1.3]	-
S2	2.2 ± 0.2	2.0–2.2–2.3 [2.2]	0.8 (S2–S1)
S3	4.1 ± 0.3	3.9–4.1–4.4 [4.1]	2.0 (S3–S2)
S4	5.3 ± 0.2	5.1–5.2–5.5 [5.2]	1.1 (S4–S3)
P1	0.6 ± 0.05	0.5–0.6–0.6 [0.6]	-
P2	1.5 ± 0.4	1.2–1.5–1.8 [1.7]	0.9 (P2–P1)
P3	2.2 ± 0.4	1.9–2.3–2.6 [2.3]	0.8 (P3–P2)
P4	4.7 ± 0.3	4.5–4.7–4.9 [4.7]	2.5 (P4–P3)
P5	5.9 ± 1.0	5.2–5.8–6.9 [5.6]	1.2 (P5–P4)
N1	0.2 ± 0.1	0.1–0.2–0.3 [0.2]	-
N2	1.2 ± 0.1	1.2–1.2–1.3 [1.2]	1.0 (N2–N1)
N3	2.0 ± 0.4	1.7–2.0–2.3 [2.0]	0.8 (N3–N2)
N4	4.7 ± 1.8	3.3–4.7–6.1 [5.8]	2.7 (N4–N3)

[1] Numerical values indicate youngest (e.g., B1) and progressively older earthquakes (e.g., B2–B4).
[2] Summary statistics based on integration of per-site earthquake-timing PDFs (derived from OxCal models; Appendix B) following the method of DuRoss *et al*. (2011). See Appendix B for PDF integration method and site PDFs contributing to the segment-wide rupture times. Earthquake times are in thousands of years before 1950.
[3] Individual recurrence interval (RI) is mean recurrence time between earthquakes (e.g., B4–B3 time); see Appendix B for uncertainties.

Table 4.1-2. Mean recurrence intervals for the central WFZ.

Segment	**Closed mean RI**[1] (kyr)	**Open mean RI (*N*-in-*T*)**[1] (kyr)	**Time since MRE**[2] (kyr)
BCS	1.1 ± 0.2 (B4–B1)	1.5 ± 0.1; 4 events < 5.9 ± 0.4 ka	2.5 ± 0.3
WS	1.3 ± 0.1 (W5–W1)	1.4 ± 0.3; 5 events < 7.1 ± 1.4 ka	0.6 ± 0.07
SLCS	1.3 ± 0.1 (S4–S1)	1.3 ± 0.09; 4 events < 5.2 ± 0.4 ka	1.4 ± 0.2
PS	1.3 ± 0.2 (P5–P1)	1.2 ± 0.03; 5 events < 6.1 ± 0.2 ka	0.6 ± 0.05
NS	0.9 ± 0.2 (N3–N1)	1.1 ± 0.04; 3 events < 3.2 ± 0.1 ka	0.3 ± 0.09

[1] Closed mean recurrence is elapsed time between oldest and youngest earthquakes per segment (e.g., B4–B1) divided by the number of closed intervals. Open mean recurrence is the time from the maximum constraining age on the oldest event (e.g., 5.9 ± 0.4 ka for B4) to the present (2011) divided by number of events. Recurrence values do not account for sample-size uncertainties (see Section 3.5). See text and Appendix B for additional discussion.
[2] Time (to the present; 2011) since the most recent earthquake (MRE).

kyr (W5–W4 and W4–W3), the longest interval of 1.9 kyr for W3–W2 is 2.9 times greater than the 0.7-kyr interval for W2–W1. These inter-event intervals are useful for understanding and comparing the variability in earthquake recurrence on the central WFZ, but they do not necessarily represent the longer-term mean recurrence for the segments.

Estimates of closed mean recurrence are similar for the five central segments (Table 4.1-2). With the exception of the NS, the mean intervals range from 1.1 kyr (BCS) to 1.3 kyr (WS, SLCS, and PS). These similar mean intervals reflect the most current earthquake data per segment and form the basis for our composite (grouped) central WFZ recurrence estimate. The NS has a shorter mean interval of 0.9 kyr, but this value is based on only two intervals between N3 and N1. The closed mean recurrence for the NS is 1.5 kyr if calculated using the N4–N1 time. However, we are not confident in this recurrence value because of the large uncertainty in the timing of N4 and concerns about the completeness of the earthquake record between N3 and N4 (Appendix B).

Open mean (*N*-in-*T*) recurrence intervals are very similar to the closed mean intervals (Table 4.1-2); differences are related to the elapsed time since the MRE or the time between the oldest earthquake and its maximum age constraint. The open mean recurrence values for the WS, SLCS, and PS are within about 0.1 kyr of the closed mean values. The BCS has the largest difference between the two values (~1.1 kyr—closed mean, ~1.5 kyr—open mean) because of the long elapsed time since its MRE (2.5 kyr). The NS has an intermediate (~0.2-kyr) difference in the recurrence values (~0.9 kyr—closed mean, ~1.1 kyr—open mean), which stems from the 1.2-kyr elapsed time between N3 (~2.0 kyr) and its maximum limiting age (~3.2 kyr).

The composite mean recurrence for the central WFZ is 1.2 ± 0.1 kyr (2σ), which represents the distribution of mean intervals calculated from 16 closed inter-event recurrence PDFs sampled in multiple simulations. We used the grouped inter-event recurrence data to calculate a composite COV for the central WFZ of 0.5 ± 0.1 (2σ), with a minimum–maximum range of about 0.3 to 0.7. Similar to the composite recurrence, the composite COV limits the variability in the per-segment COVs, which are based on only two to three inter-event recurrence estimates and range from 0.3 ± 0.4 (NS) to 0.6 ± 0.3 (PS) (Appendix B). Ultimately, we used the composite COV for the WFZ as a plausibility test of the global COV of 0.5 ± 0.2 used by the WGCEP (2003; 2008). The consensus of the WGUEP was to use a central WFZ COV of 0.5 ± 0.2 based on the global COV (Ellsworth *et al*., 1999), but supported by the composite COV mean (0.5) and possible range of uncertainty (± ~0.2) calculated here.

4.1.4 Vertical Displacement and Slip Rate

We compiled vertical displacement data per trench site to estimate mean vertical displacement per rupture and rupture source (e.g., individual segments; Table 2-1) on the central WFZ. Rupture sources include single-segment ruptures (e.g., the BCS or WS) and multi-segment ruptures (e.g., the BCS+WS), which are discussed in Section 4.1.5 and Appendix B. These data are derived from the original paleoseismic-data sources listed in Appendix B.

Using our correlation of site events along the segments (Tables B-1 to B-5), we combined individual vertical displacements per site into mean and minimum–maximum range displacements per rupture (e.g., earthquake B1). We modeled the mean displacement (and range) per rupture by fitting analytical (ellipse-shaped) displacement curves to the site data (after Chang and Smith, 2002; and Biasi and Weldon, 2009) based on the well-documented observation that displacement tapers toward the ends of a surface rupture (Hemphill-Haley and Weldon, 1999; Biasi and Weldon, 2006; Wesnousky, 2008). These per-rupture displacements were then used to calculate mean vertical displacement per rupture source (e.g., for the BCS; Table 4.1-3). The resulting source displacements are limited by assumptions regarding the position of the displacement observations along the individual ruptures (the WFZ segmentation model). For example, different results could be expected for ruptures having lengths significantly shorter or longer than the segment lengths used. Further, several ruptures are constrained by limited (e.g., one to two) point displacement observations. However, despite these limitations, per-rupture displacements are similar for each rupture source (Appendix B). Additional discussion of our displacement-modeling methods and results for both single- and multiple-segment ruptures is included in Appendix B.

We used the mean displacements per earthquake rupture and per single-segment rupture source, the individual earthquake times, and the open and closed mean recurrence intervals to calculate vertical slip rates for the central WFZ segments (Table 4.1-4; Appendix B) and for the central WFZ as a whole (composite slip rates). For each segment, we determined (1) a closed-interval slip rate using the modeled mean displacement for the segment (Table 4.1-3) divided by the segment's closed mean recurrence interval (Table 4.1-2), (2) an open-interval slip rate for which we used the total displacement (Appendix B) in the time period defined by the maximum limiting age for the oldest earthquake (Table 4.1-1) to the present, and (3) long-term rates based on the vertical offset of geomorphic surfaces related to the latest Pleistocene-age Provo phase (~15-18 ka) and highstand (~18 ka) of Lake Bonneville (Appendix B). We calculated composite slip rates comprising (1) a composite, long-term slip rate based on eight long-term (latest Pleistocene) slip rates (Appendix B), and (2) a composite, closed-interval, mean slip rate for which we used the mean of the average displacements per segment divided by the closed-interval mean composite recurrence interval for the central WFZ. We report a weighted mean slip rate per segment that uses these slip rates and a weighting scheme shown in Table 4.1-4 and discussed in Appendix B.

Table 4.1-3. Summary of displacement per rupture source on the central WFZ.

Rupture Source[1]	**Obs. D**[2] (m)	**Modeled D (displacement curves)**[3] (m)			**EQs obs.**[4]	**Disp. obs.**[4]
	μ	μ	min	max		
BCS	2.0	1.7	1.2	2.1	4	6
WS	2.1	2.4	1.1	4.1	5	16
SLCS	1.7	1.7	1.2	2.2	4	8
PS	2.5	2.6	1.3	3.6	4	6
NS	1.8	2.0	1.5	2.7	3	5-6
BCS+WS	2.2	2.0	1.7	2.4	3	13
WS+SLCS	1.9	2.7	2.4	2.9	1	6
SLCS+PS+NS	2.1	1.7	1.6	1.9	1	3
SLCS+PS	2.0	1.6	1.3	2.0	2	6
PS+NS	2.1	2.8	1.2	4.2	2	4

[1] Vertical displacement (D) for single-segment rupture sources, e.g., the BCS or WS, and multiple-segment rupture sources, e.g., the BCS and WS combined (BCS+WS). Multi-segment rupture sources are discussed in Section 4.1.5; see Appendix B for additional discussion.
[2] Mean (μ) of observed displacement per earthquake on the source (Appendix B). For example, mean observed displacement for BCS is mean of displacement estimates for B1, B2, B3, and B4 (Appendix B).
[3] Mean (μ) and minimum-maximum range of modeled displacement per earthquake on the source, using analytical displacement curves (Appendix B).
[4] EQs. obs. is total number of earthquakes on the source. Disp. obs. is the total number of site observations of displacement for the source.

Table 4.1-4. Summary of vertical slip rates for the central WFZ.

Slip Rate (SR):	**BCS**	**WS**	**SLCS**	**PS**	**NS**
	mm/yr [wt.]	mm/yr [wt.]	mm/yr [wt.]	mm/yr [wt.]	mm/yr [wt.]
Closed mean SR per segment[1]	1.6 (1.0–2.4) [0.2]	1.9 (1.1–2.9) [0.35]	1.3 (1.0–1.8) [0.35]	2.0 (1.2–3.0) [0.35]	1.7 (1.1–3.2) [0.2]
Open mean SR per segment[2]	1.2 (0.9–1.3) [0.2]	1.7 (1.2–2.3) [0]	1.3 (1.0–1.6) [0]	2.1 (1.9–2.4) [0]	1.5 (1.3–1.8) [0.2]
Composite closed mean SR[3]	1.7 (0.9–2.7) [0.3]	1.7 (0.9–2.7) [0.35]	1.7 (0.9–2.7) [0.35]	1.7 (0.9–2.7) [0.35]	1.7 (0.9–2.7) [0.3]
Composite long-term SR[4]	1.0 (0.6–1.4) [0.3]	1.0 (0.6–1.4) [0.3]	1.0 (0.6–1.4) [0.3]	1.0 (0.6–1.4) [0.3]	1.0 (0.6–1.4) [0.3]
Weighted mean SR [5]	**1.3 (0.8–2.0)**	**1.5 (0.9–2.4)**	**1.3 (0.8–2.0)**	**1.6 (0.9–2.4)**	**1.4 (0.9–2.2)**

[1] Closed-interval slip rate (SRs) are the average of mean, minimum, and maximum SRs based on (1) average displacement and recurrence and (2) elapsed time and total displacement.
[2] Open-interval SRs are based on the total displacement since the maximum limiting age for the oldest earthquake on the segment.
[3] The composite closed mean SR is based on the mean displacement per event and the composite closed recurrence interval for the central WFZ. See text and Appendix B for discussion.
[4] The composite long-term SR is based on long-term SRs per segment, which are based on the total net vertical tectonic displacement of latest Pleistocene-age geomorphic surfaces related to the Provo phase and highstand of Lake Bonneville and reported in Appendix B.
[5] Weighted mean SRs per segment are based on weighting scheme for per-segment and composite SRs (weights shown in brackets); see Appendix B for discussion.

The modeled mean displacements per source range from 1.7 m for the BCS and SLCS to 2.6 m for the PS. These yield a mean displacement for the central WFZ of 2.1 m, which is similar to the unmodeled mean of 2.0 m, and a mean of 2.2 m reported by DuRoss (2008).

The weighted mean slip rates are very similar for each segment ranging from 1.3 mm/yr for the BCS and SLCS (the shortest segments), to 1.5 and 1.6 mm/yr for the WS and PS, respectively (the longest segments) (Table 4.1-4). The similarity in these rates reflects the fairly consistent closed-interval slip rates (1.3 to 2.0 mm/yr) and open-interval slip rates (1.2 to 2.1 mm/yr), as well as the composite rates, which are included in the weighted-mean calculation for each segment. The composite long-term slip rate is 1.0 mm/yr (0.6 to 1.4 mm/yr range) based on both measured displacements across Provo-phase and Bonneville highstand surfaces of the Bonneville lake cycle. The composite closed-interval slip rate is 1.7 mm/yr (0.9 to 2.7 mm/yr range) using the mean of the mean displacements per segment (2.1 m) divided by the composite mean recurrence interval (1.2 ± 0.1 kyr).

4.1.5 Rupture Models and Geometries

Prominent structural segment boundaries along the central WFZ represent persistent (long-term) features that may act as barriers to lateral propagation of surface faulting (Machette *et al*., 1992). Support for the seismogenic independence of the segments stems from their unique late Holocene earthquake histories as well as significant differences in most recent earthquake timing across these complex structural boundaries (Schwartz and Coppersmith, 1984; Machette *et al*., 1992; Lund, 2005; DuRoss, 2008). However, similar to Machette *et al*. (1992), we cannot rule out the simultaneous rupture of adjacent segments (e.g., Chang and Smith, 2002) considering moderate to large uncertainties in earthquake timing and limited mid-Holocene earthquake records for the segments. Thus, we used the refined earthquake chronologies and displacement estimates per segment to identify possible and probable multi-segment ruptures on the central WFZ. These ruptures are included in rupture models (Table 4.1-5; Figures 4.1-2 to 4.1-5) that capture the range of possible earthquake rupture behavior on the central WFZ.

We constructed both single- and multi-segment rupture models for the central WFZ (Table 4.1-5; Figures 4.1-2 to 4.1-5) following an evaluation of possible multi-segment ruptures on the central WFZ (Appendix B). Our analyses relied mostly on the per-segment earthquake timing, using the degree of overlap in the segment PDFs (PDF overlap of Biasi and Weldon, 2009) and displacement data. Our analysis focused mostly on two-segment ruptures, which yield rupture lengths of about 90 to 100 km (consistent with the largest known historic normal slip earthquake in the BRP, the 1887 **M** 7.5 ± 0.3 Sonora, Mexico earthquake; Suter, 2006); however, we also considered ruptures as long as three adjacent segments if the paleoseismic data warranted it. Model development followed methods similar to those of the WGCEP (2003, 2008). Although our rupture models yield different rupture-source combinations, similar to WGCEP (2003), a significant difference is that they are based on paleoseismic data that span the middle to late Holocene, and thus encompass the behavior of the central WFZ over multiple earthquake cycles. Our rupture models are similar to the *a priori* maximum, geologic-insight, and minimum rupture models calculated by the WGCEP (2008) for UCERF2.

We modeled the central WFZ using a combination of single and multi-segment ruptures included in five rupture models. The basis for the WFZ rupture models and weights in Table 4.1-5 is briefly summarized as follows. Preference (model weight of 0.7) for the single-segment rupture model (Figure 4.1-2), where each segment acts as an independent source, is based on (1) prominent along-strike variations in fault geometry (e.g., fault step-overs, gaps, and changes in strike), complexity (e.g., areas of diffuse faulting), and structure (e.g., range-front morphology and relief) that define prominent fault salients, hanging-wall basins, and fault segments, (2) differences in the timing of the youngest surface-faulting earthquakes at sites along the WFZ (e.g., compare the timing of the youngest events along the BCS, WS, SLCS, and PS; Figure 3 in Appendix B), (3) unique late Holocene surface-faulting earthquake histories per segment (Figure 4.1-2), (4) differences in per-event vertical displacement across the segment boundaries (e.g., compare DuRoss *et al*., 2011 to Personius *et al*., 2012; see also DuRoss, 2008), (5) long-term (latest Pleistocene) slip deficits at the segment boundaries (Machette *et al*., 1992), and (6) paleoseismic evidence for at least one spillover rupture from the WS to the BCS (DuRoss *et al*., 2012; Personius *et al*., 2012), rather than the simultaneous rupture of both segments.

We also considered possible multi-segment ruptures on the WFZ, which we filtered using the segment earthquake timing and displacement data (see Appendix B for additional discussion). Two to three multi-segment ruptures that are most consistent with the per-segment earthquake timing and displacement data (e.g., having moderate overlap in segment PDFs; Appendix B) are included in a set of intermediate rupture models (Figure 4.1-3), whereas the multi-segment rupture model (Figure 4.1-4) includes the maximum number (n=7) of multi-segment ruptures permitted by the timing data alone (Table 4.1-5; Appendix B). We gave more weight to the intermediate models (combined weight of 0.175) compared to the multi-segment rupture model (weight of 0.025) because they include the most probable multi-segment ruptures. Although some of the two- (and three-) segment ruptures included in the multi-segment model may have occurred, we find it highly unlikely that all them occurred given the segmentation arguments discussed above. Although we cannot discount the occurrence of multi-segment ruptures, we found no observational basis to conclude that earthquakes on the central WFZ regularly rupture multiple segments, and thus assigned relatively low weights to the multi-segment

Table 4.1-5. Summary of rupture models and weights for the central WFZ.

Rupture Model[1]	Rupture Sources[2]	WGUEP Weight[3]	Earthquakes[4]	Notes
SSR	B, W, S, P, N	0.7	22 SSR	Only SSRs occur
Int. C	B, W, S, P, N, B+W	0.075	18 SSR, 2 MSR	SSRs, including B+W MSR
Int. A	B, W, S, P, N, B+W, S+P	0.05	16 SSR, 3 MSR	SSRs, including most-probable MSRs
Int. B	B, W, S, P, N, B+W, P+N	0.05	16 SSR, 3 MSR	SSRs, including most-probable MSRs
MSR	B, W, S, P, N, B+W, W+S, S+P, P+N, S+P+N	0.025	7 SSR, 7 MSR	All possible MSRs occur
-	Unsegmented[†]	0.1	-	-

[1] Rupture models include (1) all single-segment ruptures (SSRs) (SSR model; Figure 4.1-3), (2) combinations of SSRs and multi-segment ruptures (MSRs) we consider most probable (Intermediate [Int.] A, B, and C; Figure 4.1-4), and (3) all possible MSRs (MSR model; Figure 4.1-5). See text and Appendix B for discussion of model development.
[2] Rupture sources: B–BCS, W–WS, S–SLCS, P–PS, N–NS; combinations of these indicate multi-segment-rupture sources (*e.g.*, B+W).
[†] The unsegmented model accounts for possible multi-segment and/or partial-segment ruptures not included in these models.
[3] Consensus weight of the WGUEP.
[4] Number of earthquakes included in each rupture model; see Appendix B for timing information for individual earthquakes.

and intermediate rupture models (total weight of 0.2 compared to the single-segment rupture model weight of 0.7). These model weights are consistent with the differences in most-recent earthquake timing across the prominent segment boundaries (Figure B-3), as well as paleoseismic evidence for at least one spillover rupture on the central WFZ (Personius *et al*., 2012), which represents a more likely mode of segment-boundary failure.

An unsegmented rupture model was implemented in the WGUEP forecast to account for ruptures on the central WFZ and the WFZ as a whole, irrespective of the fault segmentation model and defined rupture boundaries. This model uses a distribution of magnitudes (as opposed to rupture lengths) ranging from **M** 6.75 to 7.6 (Section 3.4). To some degree, this model accounts for a level of partial-segment rupture and rupture across a segment boundary (spillover rupture) greater than that allowed by the segment boundary uncertainties (Section 4.1.6). We assigned a relatively low weight (0.1) to the unsegmented model because the central WFZ is characterized by prominent segment boundaries and because the paleoseismic data suggest that ruptures on the central WFZ are not spatially random (e.g., the youngest earthquakes on the BCS are significantly older than those on the adjacent WS). Furthermore, we account for many multi-segment ruptures in our multi-segment and intermediate models, where those ruptures honor available paleoseismic earthquake timing and displacement data. Rates for the unsegmented model are based on the central WFZ closed-mean slip rate (~1.7 mm/yr; 0.2 weight) and long-term slip rate (~1.0 mm/yr; 0.3 weight), as well as the broad range in slip rates for the northernmost end segments (Section 4.2.2).

Together, the single-segment, intermediate, and multi-segment rupture models highlight possible modes of rupture along the central WFZ. However, our analyses are limited by modeling assumptions and poorly constrained mid-Holocene earthquake data. For example, although our analysis of the site PDF data by segment is consistent with the body of work indicating a segmented fault (e.g., Schwartz and Coppersmith, 1984; Machette *et al*., 1992; Lund, 2005; DuRoss, 2008; Personius *et al*., 2012) and serves to help constrain the per-segment earthquake chronologies (e.g., DuRoss *et al*., 2011), it does limit our ability to define and evaluate all possible rupture permutations. We have addressed this limitation by constructing multi-segment and unsegmented rupture scenarios and by defining segment-boundary uncertainties (Section 4.1.6), which allow for both partial-segment and spillover ruptures (i.e., coseismic rupture across a "leaky" segment boundary; Crone and Haller, 1991; see for example, Crone *et al*., 1987; DuRoss *et al*., 2012; Personius *et al*., 2012) not specifically accounted for in the rupture models. Ultimately, our treatment of the WFZ is consistent with the hybrid characteristic slip model of DuRoss (2008) in which "large-displacement single-segment ruptures dominate the fault history but are interrupted by anomalously small- and large-displacement events (i.e., possible partial- and multi-segment ruptures, respectively)." However, the possibility of ruptures across WFZ segment boundaries needs to be evaluated using the site earthquake data to yield a more comprehensive suite of rupture models (e.g., Biasi and Weldon, 2009). Finally, although the youngest earthquakes along the WFZ are consistent with a segmented fault, poorly constrained mid-Holocene earthquakes allow for longer rupture lengths. Additional mid- to early Holocene paleoseismic data for the central WFZ would aid in evaluating which of these multi-segment ruptures are most plausible.

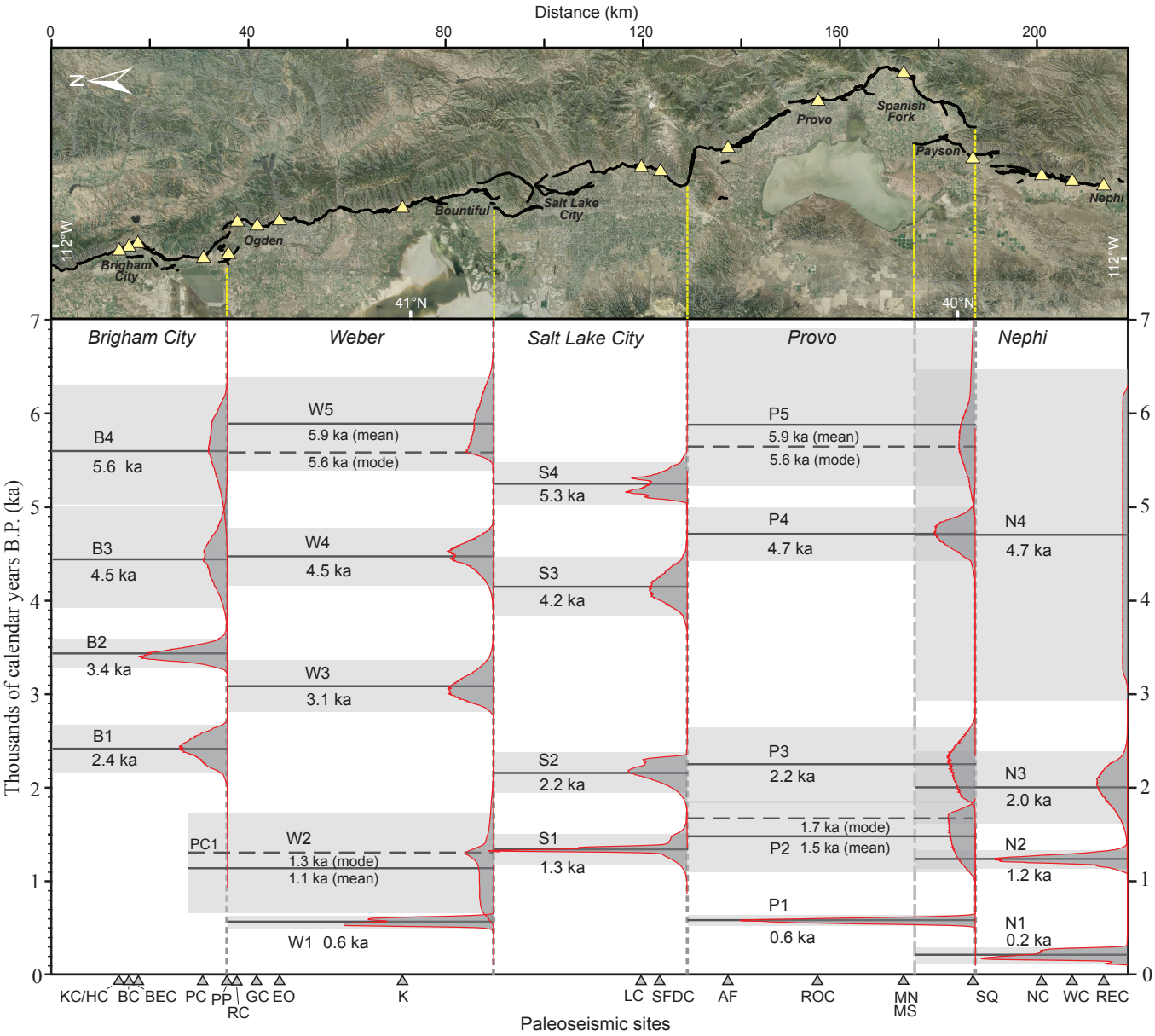

Figure 4.1-2. Single-segment rupture model for the central WFZ. Upper panel shows map of the central segments; yellow triangles show locations of paleoseismic study sites. Lower panel shows times of earthquakes on each segment. Solid horizontal lines indicate mean earthquake times (dashed lines indicate modal times for select earthquakes); gray boxes show 2σ time ranges. Red lines with gray-shaded fill are earthquake-timing PDFs derived from our integration of site paleoseismic data (see Appendix B for discussion and explanation of site abbreviations). Base map is aerial imagery (https://gdg.sc.egov.usda.gov/) overlain on shaded topography generated from 10-m digital elevation data (https://lta.cr.usgs.gov/NED).

4.1.6 Segment Boundary Uncertainties

To define segment-boundary uncertainties for the central WFZ (Figure 4.1-5), we considered the geometry and extent of Holocene faulting near the ends of the segments, and, if available, paleoseismic data from sites close to the segment boundaries (Figure 4.1-1; Appendix B). Most segment boundaries are moderately well constrained (3 to 8 km); however, we include large uncertainties (13 to 17 km) for the complex overlapping fault step-over between the PS and NS. The best-constrained boundary is the BCS–Collinston segment (CS) boundary (±3 km) based on the extent of Holocene surface faulting on the BCS, the apparent lack of Holocene rupture on the CS, and 3 km of spillover rupture from the BCS onto the southern CS (Personius, 1990; Personius *et al*., 2012). We applied asymmetric uncertainties for several segment boundaries. The uncertainty for the BCS and WS is 3 to 8 km (depending on the segment; Figure 4.1-5), which accounts for the spillover rupture that occurred during earthquake W2 (DuRoss *et al*., 2012; Personius *et al*., 2012). An asymmetric uncertainty for the PS and NS (+4, -13 km for the southern PS and +5, -17 km for the northern NS) is based on overlap between the two segment traces, the total length of the northern strand of the Nephi segment. See Appendix B for

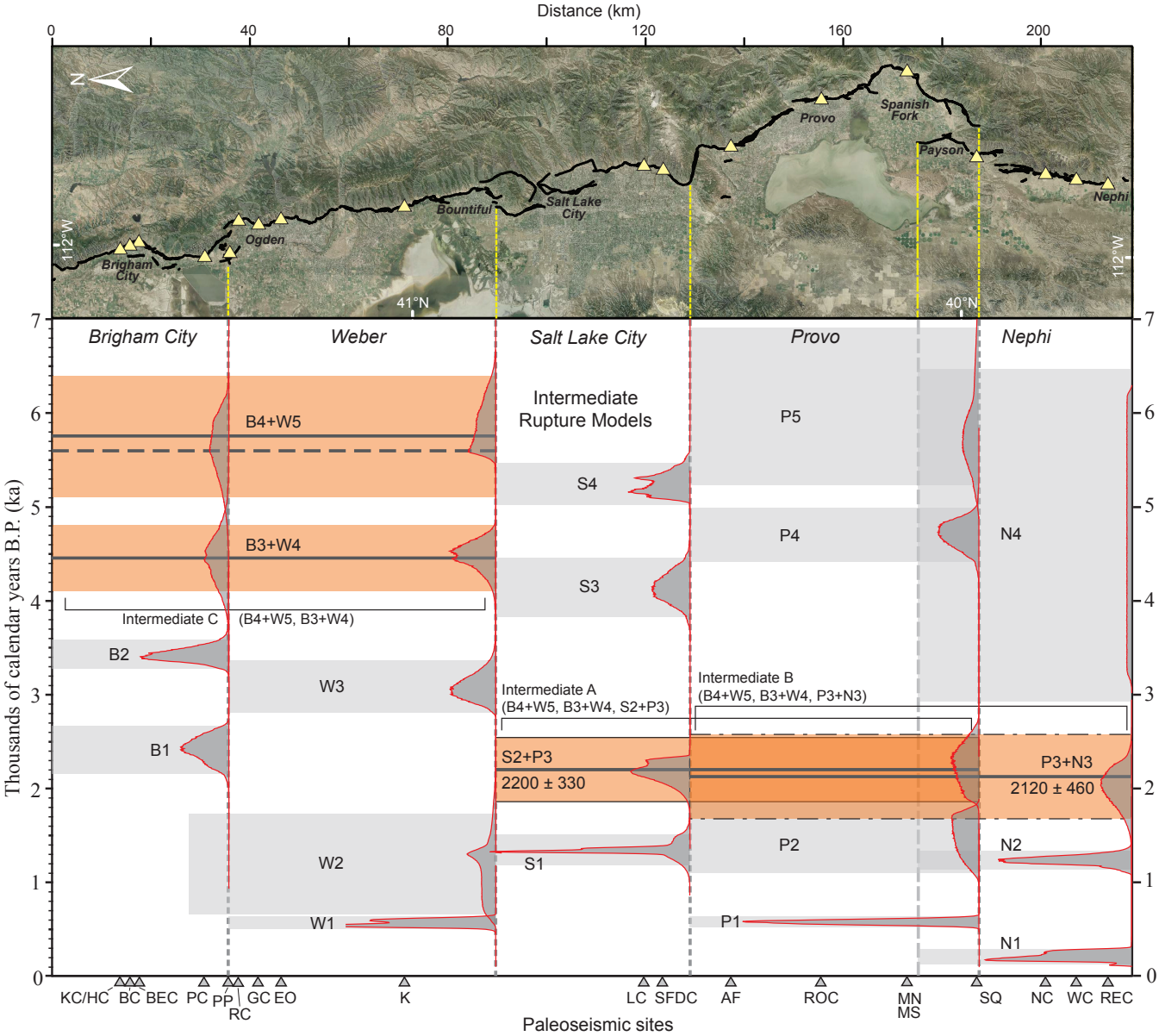

Figure 4.1-3. Intermediate rupture models for the central WFZ. Upper panel is the same as in Figure 4.1-2. Intermediate model A consists of single-segment ruptures (gray boxes showing 2σ ranges) and multi-segment ruptures B4+W5, B3+W4, and S2+P3 (orange boxes showing 2σ ranges). Intermediate model B includes P3+N3 in place of S2+P3. Intermediate model C has single-segment ruptures as well as multi-segment ruptures B4+W5 and B3+W4. Solid horizontal lines indicate mean earthquake times (dashed lines indicate modal times for select earthquakes). Red lines with gray-shaded fill are earthquake-timing PDFs derived from our integration of site paleoseismic data (see Appendix B for discussion and explanation of site abbreviations). Base map is aerial imagery (https://gdg.sc.egov.usda.gov/) overlain on shaded topography generated from 10-m digital elevation data (https://lta.cr.usgs.gov/NED).

additional descriptions of geologic data used to constrain the segment-boundary uncertainties. We used these uncertainties to define a range of rupture-lengths for both single- and multi-segment ruptures (Figures 4.1-5 and 4.1-6; Table 4.1-6); see Appendix B for additional discussion.

4.1.7 Characteristic Magnitudes

We calculated M_{char} for central WFZ rupture sources (e.g., single segments or combinations of segments) using four earthquake-magnitude regressions for Type A faults included in Table 4.3-5 (Section 3.5). Weighted mean estimates of M_{char} range from **M** 7.1 to 7.5 (Table 4.1-6), including estimates of **M** 7.1 to 7.3 for single-segment rupture sources and **M** 7.4 to 7.5 for multi-segment rupture sources. We used SRL–**M** and M_0–**M** regressions to define M_{char} for both single and multi-segment rupture sources. Estimates of **M** based on SRL account for median and range SRL (Table B-16) determined using the segment-boundary uncertainties (Table B-17). Estimates of **M** as a function of M_0 include uncertainties in SRL, down-dip rupture length, and fault-parallel displacement. Down-dip rupture length is a function of fault dip

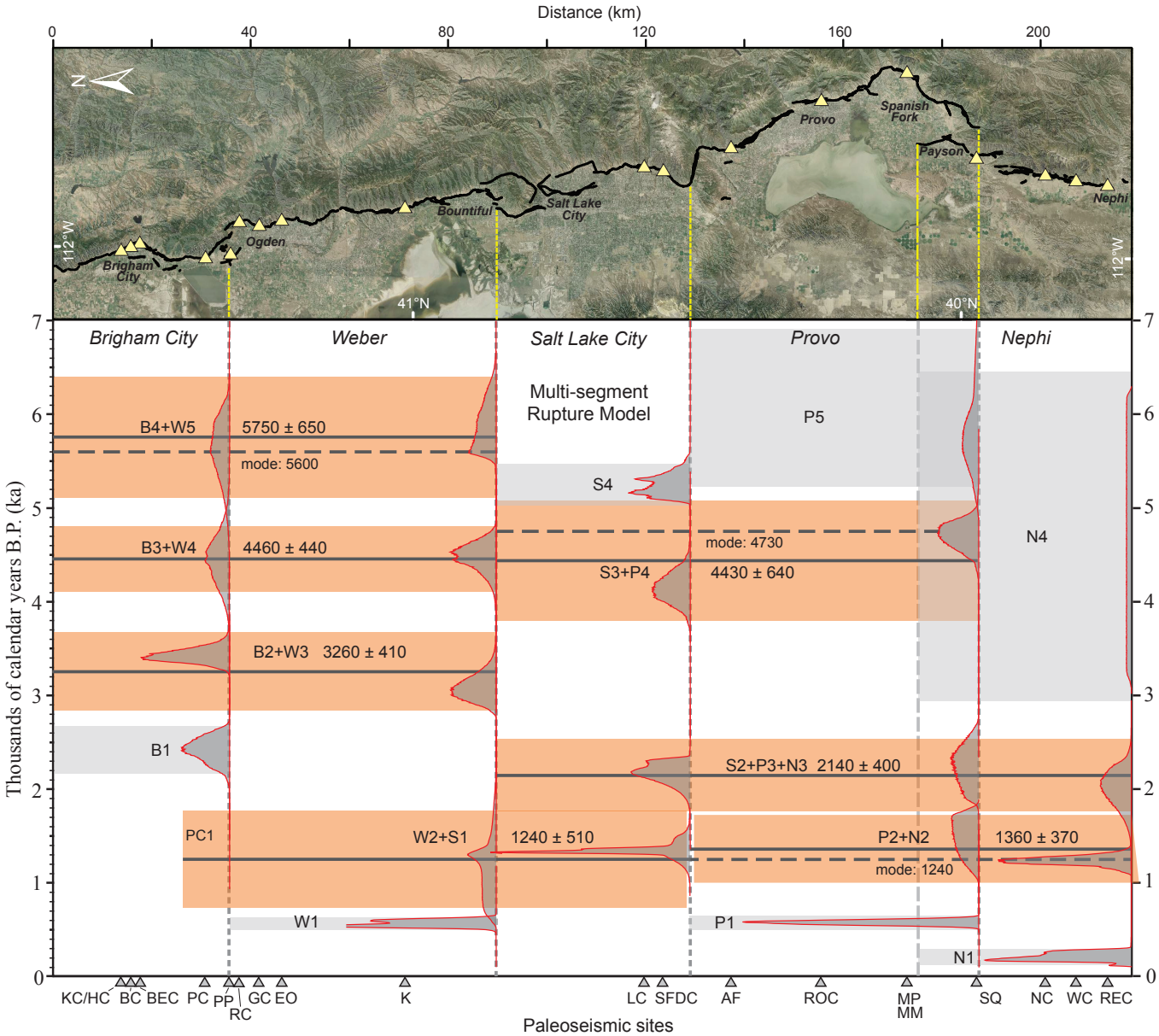

Figure 4.1-4. Multi-segment rupture model for the central WFZ consisting of single-segment ruptures (gray boxes showing 2σ ranges) and multi-segment ruptures (orange boxes showing 2σ ranges). Solid horizontal lines indicate mean earthquake times (dashed lines indicate modal times for select earthquakes). Red lines with gray-shaded fill are earthquake-timing PDFs derived from our integration of site paleoseismic data (see Appendix B for discussion and explanation of site abbreviations). Base map is aerial imagery (https://gdg.sc.egov.usda.gov/) overlain on shaded topography generated from 10-m digital elevation data (https://lta.cr.usgs.gov/NED).

(50° ± 15°; Section 2.1.1) and seismogenic depth (12 to 18 km; Section 3.2). Displacements included in the M_0 calculations are the mean, minimum, and maximum values per source determined using the modeled displacement profiles (Table 4.1-3). For the single-segment rupture sources, M_{char} ranges from **M** 6.9 to 7.1 (5th percentile values) to **M** 7.2 to 7.5 (95th percentile values), consistent with **M** estimates for historical BRP earthquakes (the 1915 Pleasant Valley, 1954 Dixie Valley, 1959 Hebgen Lake, and 1983 Borah Peak earthquakes) ranging from **M** 6.8 to 7.6 (Wells and Coppersmith, 1994; Stirling *et al*., 2002; Wesnousky, 2008).

4.2 Wasatch Fault Zone End Segments

We classify five segments of the WFZ as end segments: the Collinston (CS), Clarkston Mountain (CMS), and Malad City (MCS) segments on the north, and the Levan (LS) and Fayette (FS) segments on the south (Figure 1-2). Although the end segments show evidence for late Quaternary surface faulting, they are distinguished from the central segments by significantly lower rates of activity, and only the LS and FS have fault scarps on latest Pleistocene to Holocene-aged deposits (post-Lake Bonneville highstand). On-trend with the BCS, the CS extends northward 30 km from the seg-

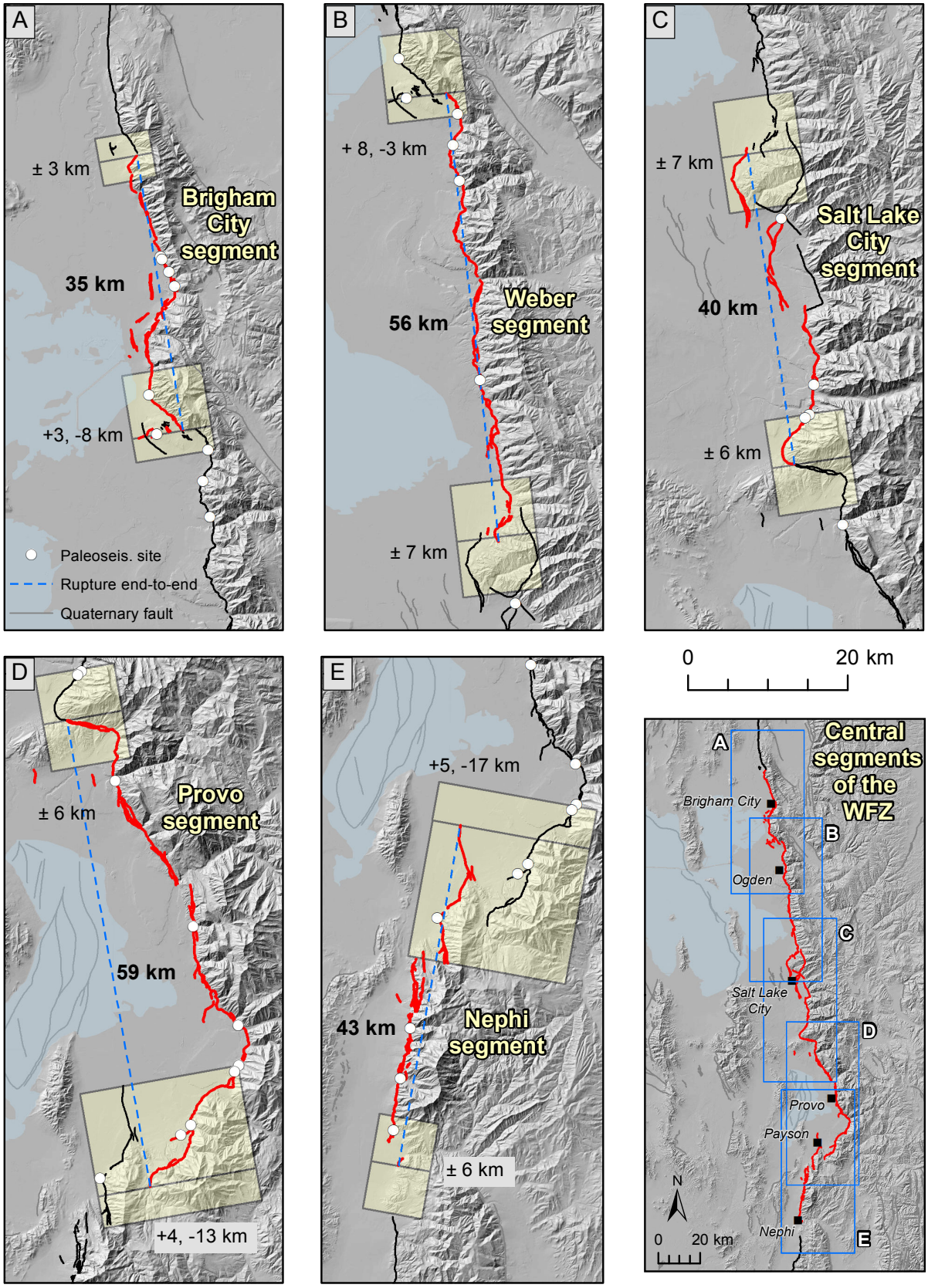

Figure 4.1-5. Rupture lengths (red) and segment-boundary uncertainties for single-segment ruptures on the WFZ central segments. Yellow boxes correspond to segment-boundary uncertainties defined using the geometry and timing of faulting and paleoseismic data (Appendix B). White dots show paleoseismic sites, and blue dashed lines are straight-line length measurements (between rupture ends) showing median rupture lengths (e.g., 35 km for the BCS). See text and Table B-17 (Appendix B) for discussion of individual segment-boundary uncertainties. Shaded topography generated from 10-m digital elevation data (https://lta.cr.usgs.gov/NED).

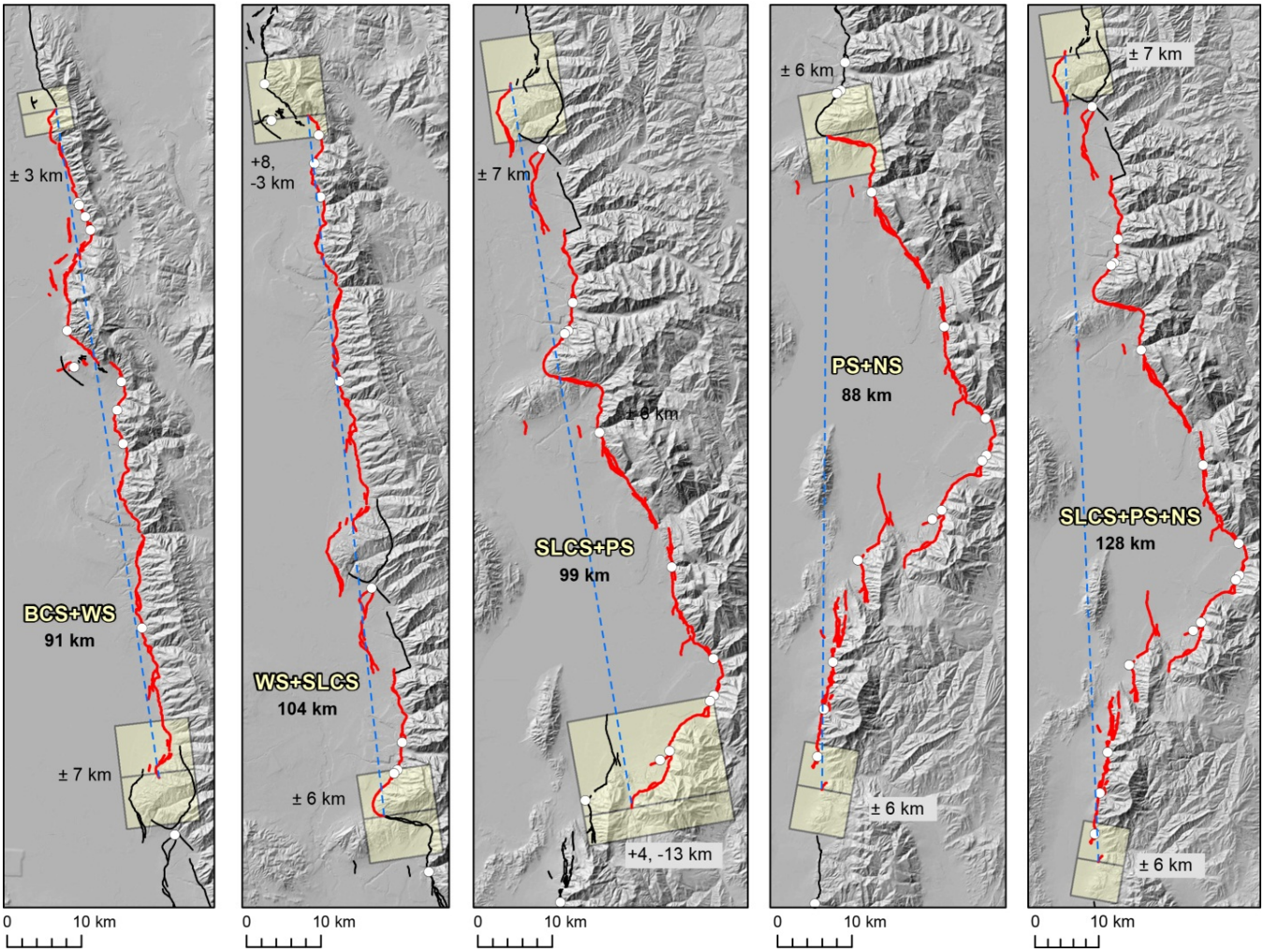

Figure 4.1-6. Segment-boundary uncertainties for multi-segment ruptures (red) on the central WFZ. Yellow boxes correspond to segment-boundary uncertainties defined using the geometry and timing of faulting and paleoseismic data, and are the same as those defined for single-segment ruptures (Figure 4.1-5). White dots show paleoseismic sites, and blue dashed lines are straight-line length measurements (between rupture ends) showing median rupture lengths (e.g., 91 km for the BCS+WS multi-segment rupture source). See text and Appendix B for discussion of individual segment-boundary uncertainties. Shaded topography generated from 10-m digital elevation data (https://lta.cr.usgs.gov/NED).

Table 4.1-6. M_{char} distributions for central WFZ rupture sources.

Rupture Source	Wt. Mean M_{char}	5th Percentile M_{char}	95th Percentile M_{char}
Brigham City (BCS)	7.06	6.87	7.24
Weber (WS)	7.28	7.04	7.50
Salt Lake City (SLCS)	7.12	6.91	7.28
Provo (PS)	7.29	7.07	7.51
Nephi (NS)	7.14	6.92	7.35
BCS+WS	7.42	7.27	7.56
SLCS+PS	7.41	7.22	7.52
WS+SLCS	7.50	7.37	7.69
PS+NS	7.44	7.22	7.65
SLCS+PS+NS	7.52	7.35	7.62

Weighted (Wt.) mean characteristic magnitude (M_{char}) and 5th–95th percentile ranges are based on the weighting of four SRL–**M** and M_0–**M** regressions discussed in Section 3.5 as well as fault-rupture parameters included in Section 4.1 and discussed in Appendix B. All rupture sources considered A faults.

ment boundary near Honeyville, Utah. At the northern end of the CS near Plymouth, Utah, the WFZ steps left 6 km along the transverse Short Divide fault to the southern end of the 19-km-long CMS, which extends about 8 km into Idaho. Machette *et al*. (1992) defined the CMS–MCS boundary as being at the Woodruff spur, a bedrock salient along the front of the Malad Range 14 km south of Malad City, Idaho. However, more recent mapping indicates that the CMS–MCS boundary is a relay ramp, characterized by a 3-km right step and 9 km of *en echelon* overlap (Long *et al*., 2004, 2006). The MCS terminates northward near Marsh Valley, Idaho (Haller and Lewis, 2004, citing geologic mapping of Pope *et al*., 2001), giving the segment a straight-line length of 48 km. At the southern end of the WFZ, the 31-km-long LS continues southward on-trend with the NS, but is separated from the NS by a 5-km gap in late Quaternary surface faulting. Like the CMS–MCS boundary, the LS–FS boundary is also a relay ramp, characterized by a 4-km left step and 10 km of *en echelon* overlap (Hylland and Machette, 2008). The 22-km-long FS terminates near the town of Fayette, Utah.

4.2.1 Paleoseismic Data Sources

Paleoseismic data are very limited for the WFZ end segments, and only a single fault trench study (on the LS [Jackson, 1991]) has been conducted. After an initial aerial photography evaluation and reconnaissance of the northern end segments by Cluff *et al*. (1974) to as far north as the vicinity of Malad City, Idaho (42.229° N.), subsequent reconnaissance led to segmentation models being proposed by Schwartz and Coppersmith (1984) and later refined by Machette *et al*. (1992). Hylland (2007a) conducted additional paleoseismic reconnaissance of the CS and CMS, including scarp profiling in the Honeyville area (CS–BCS boundary) and at Elgrove Canyon (CMS). Also in the Honeyville area, Personius (1990) measured vertical scarp offsets during surficial geologic mapping of the BCS and southern CS. M.D. Hylland and W.M. Phillips (Idaho Geological Survey) conducted an aerial reconnaissance of the entire MCS and limited ground reconnaissance of scarps near Elkhorn Mountain in 2012, but no other neotectonic work has been done on the MCS since the scarp and lineament mapping of Cluff *et al*. (1974).

On the LS and FS, an initial aerial photography evaluation and reconnaissance by Cluff *et al*. (1973) was followed by paleoseismic reconnaissance and scarp profiling by Machette *et al*. (1992), additional scarp profiling and diffusion-equation modeling by Hylland (2007b), and surficial geologic mapping by Hylland and Machette (2008). Also, Crone (1983a) and Schwartz and Coppersmith (1984) reported radiocarbon dating results for charcoal collected from faulted fan alluvium that constrained timing of the most recent surface-faulting earthquake on the LS. Finally, Jackson (1991) supplemented his paleoseismic data from the Skinner Peaks trench site on the LS with logging of a natural exposure of the fault at Deep Creek, including thermoluminescence dating of a buried soil beneath scarp-derived colluvium.

4.2.2 Earthquake Recurrence, Displacement, and Slip Rates

The low rates of activity on the WFZ end segments generally preclude determining recurrence intervals. Earthquake timing is constrained by numerical ages for only two surface-faulting earthquakes; both of these were on the LS, and large uncertainty in the time of the penultimate earthquake results in a poorly constrained recurrence estimate for just a single seismic cycle. Timing of the most recent surface faulting on the CMS and FS can be estimated from geologic relations, but no other earthquake timing data exist for the FS and three northern end segments, so earthquake recurrence cannot be determined.

The three northern WFZ end segments are characterized by steep, abrupt range-front escarpments and steep, linear gravity gradients parallel to the fault zone (Zoback, 1983), indicating overall structural continuity and late Quaternary fault activity. However, fault scarps are generally absent on deposits of Lake Bonneville age (30–12 ka) and younger (Personius, 1990; Machette *et al*., 1992; Hylland, 2007a). The only documented fault scarps on Quaternary deposits along these segments include possible scarps on "older" alluvium on the MCS (Cluff *et al*., 1974), a scarp on late Pleistocene alluvium at the mouth of Elgrove Canyon on the CMS (Biek *et al*., 2003; Hylland, 2007a), and scarps on various deposits of middle Quaternary age and younger in the Coldwater Canyon reentrant near Honeyville (CS–BCS boundary) (Personius, 1990). These latter scarps include small fault scarps on Bonneville lake cycle deposits and Provo-aged (Bonneville regressive phase) fan alluvium, and have been interpreted as being associated with the northern extent of surface faulting on the BCS, and not with CS surface faulting (Personius, 1990; Hylland, 2007a). Outside of the Coldwater Canyon area, much of the inferred trace of the northern WFZ end segments lies at or closely below the elevation of Lake Bonneville's highstand shoreline, so the unfaulted lake deposits date to around the time of the lake's highstand (~18 ka). Therefore, the timing of most recent surface faulting on the three northern end segments can only be constrained as predating the Lake Bonneville highstand, and the timing of earlier surface-faulting earthquakes is unknown.

For the northern end segments, per-event vertical displacement can be determined only for the CMS. Hylland (2007a) estimated a per-event vertical displacement of 2 m for the CMS based on scarp-profile analysis and geomorphic evidence for two surface-faulting events at Elgrove Canyon. This displacement value and a minimum elapsed time since the most recent surface-faulting earthquake of 18 kyr yield a maximum geologic (open-ended) vertical slip rate of 0.1 mm/yr (Hylland, 2007a; Table 4.2-1). The latest Pleistocene–Holocene slip rate for the CS is likely similar, assuming a displacement value similar to that of the CMS (similar also to the mean vertical displacement of 2.2 m for the six central WFZ segments; DuRoss, 2008). A maximum of 12 m of net geomorphic surface offset of fan

Table 4.2-1. Displacement, slip rate, and recurrence for the WFZ end segments.

Segment	Timing of Most Recent Surface Faulting	Net Displ. or Surface Offset (m)	Time Interval (kyr)	Slip Rate (mm/yr)	WGUEP Slip Rate Consensus Range (mm/yr)	Recurrence Interval (kyr)
MCS[1]	Late Pleistocene	≤ 1.5 (est.)	> 18	< 0.08	0.01–0.1	NA
CMS[2]	Late Pleistocene	2.0	> 18	< 0.1	0.01–0.1	NA
CS[3]	Late Pleistocene	2 (est.)	> 18	< 0.1	0.01–0.1	NA
	Long term[4]:	≤ 12	300	≤ 0.04		
LS[5]	≤ 1.0 ± 0.2 ka	1.8	> 4.8–9.8	< 0.2–0.4	0.1–0.6	> 3 & < 12**
	1.0–1.5 ka	1.8–3.0	> 1.3–3.3	< 0.5–2.3		
		–	–	< 0.3±0.1*		
		–	–	0.1–0.6**		
	Long term[4]:	≤ 4.8	100–250	≤ 0.02–0.05		
FS[6]	Early(?) Holocene (SW strand)	0.8–1.6	< 11.5	> 0.07–0.1	0.01–0.1	NA
	Latest Pleistocene (SE strand)	0.5–1.3	< 18	> 0.03–0.07		
	Early(?) or middle (?) Pleistocene (N strand)	No data	> 250	NA		
	Long term[4]:	≤ 3.0	100–250	≤ 0.01–0.03		

NA, not applicable.

[1] Data from Machette *et al*. (1992), this report.
[2] Data from Hylland (2007a).
[3] Data from Personius (1990), Hylland (2007a).
[4] Long-term slip rate based on maximum measured scarp heights and estimated age of soil developed on faulted deposits.
[5] Data from Jackson (1991), Hylland (2007b), Hylland and Machette (2008); * – Preferred value of Hylland and Machette (2008), ** – Utah Quaternary Fault Parameters Working Group consensus range (Lund, 2005).
[6] Data from Hylland (2007b), Hylland and Machette (2008).

alluvium estimated to be approximately 300 ka based on soil development (Personius, 1990) yields a longer-term (middle Pleistocene–Holocene) maximum slip rate for the CS of about 0.04 mm/yr (Table 4.2-1). On average, per-event vertical displacement on the MCS may be smaller than on segments to the south, given the position of the MCS at the northernmost extent of the WFZ. This assumption is supported by surface-offset measurements on the FS (discussed below) at the southernmost extent of the WFZ. An estimated maximum vertical displacement of 1.5 m and a minimum elapsed time since the most recent surface-faulting earthquake (MRE) of 18 kyr yield a maximum geologic (open-ended) vertical slip rate for the MCS of 0.08 mm/yr (Table 4.2-1).

For the LS, a net vertical tectonic displacement (NVTD) measurement of 1.8 m for the MRE has been obtained from the Deep Creek natural exposure (Jackson, 1991; Machette *et al*., 1992; Hylland, 2007b). This displacement is similar to the 1.2 to 2.0 m (average 1.6 m) of net geomorphic surface offset determined from 10 profiles across single-event scarps along the LS (Hylland, 2007b). The MRE on the LS occurred shortly after 1.0 ± 0.2 ka based on thermoluminescence and radiocarbon age constraints (Jackson, 1991; Hylland and Machette, 2008). Timing of the penultimate event is poorly constrained but likely sometime before 6.0 to 10.6 ka (see discussion in Hylland and Machette, 2008), indicating an inter-event time interval of at least 4.8 to 9.8 kyr. This time interval and a displacement value of 1.8 m yield a maximum vertical slip rate of 0.2 to 0.4 mm/yr (Table 4.2-1). Timing and displacement data from the Skinner Peaks trench (Jackson, 1991) yield higher, but likely unrealistic, maximum slip rates of 0.5 to 2.3 mm/yr (Hylland and Machette, 2008). A maximum of 4.8 m of net geomorphic surface offset of fan alluvium estimated to be approximately 100 to 250 ka based on soil development (Hylland and Machette, 2008) yields a longer-term (middle Pleistocene–Holocene) maximum slip rate of 0.02 to 0.05 mm/yr. The UQFPWG agreed on a consensus slip rate for the LS of 0.1 to 0.6 mm/yr and a poorly constrained recurrence range of > 3 to < 12 kyr (Lund, 2005).

Based on analysis of 12 profiles across single-event scarps, the vertical displacements and timing of surface faulting vary for the three different strands of the FS (Hylland, 2007b). Geologic relations and profile data indicate that the most recent surface faulting occurred in mid- to early Holocene

time on the southwestern strand, latest Pleistocene time on the southeastern strand, and prior to ~250 ka on the northern strand (Hylland, 2007b). The displacement range for the southwestern and southeastern strands of 0.5 to 1.6 m and maximum estimated constraining earthquake times of 18 to 11.5 ka yield a minimum vertical slip rate for the FS of 0.03 to 0.1 mm/yr (Table 4.2-1). A maximum of 3 m of net geomorphic surface offset (measured on the southestern strand) of fan alluvium estimated to be approximately 100 to 250 ka based on soil development (Hylland and Machette, 2008) yields a longer-term (middle Pleistocene–Holocene) maximum slip rate of 0.01 to 0.03 mm/yr.

The limited earthquake-specific timing data generally precludes calculation of meaningful recurrence estimates for the WFZ end segments, so modeling of these segments uses slip-rate data instead. Based on the estimated slip rates, the WGUEP established consensus slip-rate ranges (5th to 95th percentile) of 0.01 to 0.1 mm/yr for the MCS, CMS, CS, and FS, and 0.1 to 0.6 mm/yr for the LS (Tables 4.2-1 and 4.2-2). For the LS and FS, these ranges represent total slip rates that result from both single-segment and multi-segment ruptures. As discussed in Section 4.2.3, we included both single-segment and multi-segment rupture models to address the aleatory variability of LS and FS ruptures, and we split the total slip rates evenly between the two models. In other words, the slip-rate distributions in Table 4.2-2 for the LS single-segment rupture and the LS+FS multi-segment rupture each generally represent one-half of the WGUEP consensus LS total slip-rate values. However, we assigned a 5th percentile LS+FS multi-segment slip rate that is less than one-half of the 5th percentile LS consensus slip rate so that the sum of the 5th percentile LS+FS multisegment slip rate (0.005 mm/yr) and FS single-segment slip rate (0.005 mm/yr) equals the FS total single-segment slip rate value of 0.01 mm/yr. The slip-rate distribution for the FS single-segment rupture represents one-half of the WGUEP consensus FS total slip-rate values, but the sum of the 95th percentile single-segment and multi-segment values is greater than the maximum value of the WGUEP consensus range; however, the consensus range is derived from minimum slip-rate values, so we consider the summed values to be acceptable. In a qualitative sense, the slip-rate distributions seem reasonable: the FS total slip-rate values are less than the LS total slip-rate values (by roughly a factor of 2) and greater than the northern end-segment slip-rate values (by roughly a factor of 3), which lack evidence for any Holocene surface faulting.

We also include the end segments in the unsegmented WFZ rupture model as described in Section 4.1.5. This model allows for ruptures along the entire WFZ, irrespective of segment boundaries. That is, ruptures that include part of the central segments, end segments, or both are allowed. For the unsegmented model slip rate, we used the composite slip rates for the central segments (Table 4.1-4) and the broad WGUEP consensus range of slip rates (0.01 to 0.1 mm/yr) for the end segments (Table 4.2-2).

4.2.3 Rupture Models and Characteristic Magnitudes

In the absence of both earthquake-specific paleoseismic data and continuous scarps on latest Quaternary deposits, large uncertainties exist regarding surface rupture lengths on the three northern WFZ end segments. The segment lengths for

Table 4.2-2. Slip-rate model distributions for the WFZ end segments.

Segment	WGUEP Slip Rate Consensus Range[1] (mm/yr)	Slip Rate Distribution (5th–50th–95th percentile) (0.2–0.6–0.2 weight)
Malad City (MCS)	0.01 – 0.1	0.01 – 0.05 – 0.1
Clarkston Mountain (CMS)	0.01 – 0.1	0.01 – 0.05 – 0.1
Collinston (CS)	0.01 – 0.1	0.01 – 0.05 – 0.1
MCS+CMS[2]	–	–
MCS+CMS+CS[3]	–	–
Levan (LS), single-segment	–	0.05 – 0.15 – 0.3
Fayette (FS), single-segment	–	0.005 – 0.025 – 0.05
LS+FS	–	0.005 – 0.15 – 0.3
LS total; single-segment + (LS+FS)	0.1 – 0.6[4]	0.055 – 0.3 – 0.6[5]
FS total; single-segment + (LS+FS)	0.01 – 0.1[4]	0.01 – 0.175 – 0.35[5]

[1] See Table 4.2-1 for slip-rate data.
[2] Used for floating rupture length in multi-segment model.
[3] Cumulative length for multi-segment model; not modeled rupture length.
[4] Total slip rates (single-segment + multi-segment rupture); see text for discussion.
[5] Summed 5th, 50th, and 95th percentile values (single-segment + multi-segment rupture) for comparison with WGUEP consensus ranges only; values not used in model.

the northern segments shown on Figure 4.2-1 and listed in Table 4.2-3 relate primarily to along-strike changes in fault geometry coincident with transverse structural features; whether or not these lengths typify "characteristic" ruptures is unknown. For the MCS, the median rupture length is the straight-line distance between the northern end of the segment as mapped by Pope *et al*. (2001) and the southern end of the segment as mapped by Long *et al*. (2004). Location uncertainties for both rupture ends are symmetrical (± 3 km). For the CMS, Hylland (2007a) used the empirical relations of Wells and Coppersmith (1994) between vertical displacement and surface rupture length to evaluate CMS rupture length relative to the 2-m per-event displacement determined from a fault scarp at Elgrove Canyon. Hylland (2007a) concluded that the actual surface rupture length may have been considerably longer than the segment's 19 km median rupture length, possibly as long as 30 km. To account for this possible extra length, location uncertainties for both rupture ends are asymmetrical (+5, -3 km), and the +5 km uncertainties result in a maximum rupture length of 29 km. For the CS, the median rupture length is the distance between the western end of the transverse Short Divide fault on the north and the southern end of the segment as mapped by Personius (1990). Location uncertainty for the north end of the segment is asymmetrical (+3, -6 km) to account for possible rupture termination on the main north-trending trace of the segment south of the Short Divide fault. Location uncertainty for the south end of the CS is symmetrical (± 3 km) and is based on the distance of BCS rupture spill-over onto the CS (Personius, 1990; Hylland, 2007a). Given the large uncertainties in rupture lengths, we modeled the northern end segments as both segmented and unsegmented equally weighted. In the unsegmented model, we used a floating earthquake having a 60-km-long rupture (essentially equal to a combined MCS-CMS rupture), a minimum magnitude of **M** 6.75 ± 0.25 (from the DTGR magnitude recurrence model; see Section 3.4), and an M_{char} commensurate with a 60-km median surface rupture length. M_{char} model distributions for the northern WFZ end segments are shown in Table 4.2-4.

Geologic and scarp-profile data from the LS and FS indicate a variety of possible rupture scenarios, including partial and multi-segment ruptures. Composite scarp morphology on the southern 15 km of the LS indicates surface faulting during both the MRE and penultimate paleoearthquakes; the lack of composite scarp morphology on the northern part of the LS indicates the penultimate earthquake did not rupture this part of the segment (i.e., partial-segment rupture; Hylland, 2007b). Similarly, differences in scarp morphology and age of faulted deposits indicate differences in the timing of surface faulting on all three strands of the FS (i.e., partial-segment ruptures; Hylland, 2007b). Hylland and Machette (2008) interpreted fault scarps and lineaments on Quaternary deposits in the LS–FS overlap zone as being associated with structures accommodating a left-stepping transfer of displacement within a relay ramp, and these structures likely facilitate synchronous rupture between the two segments (Hylland, 2007b; Hylland and Machette, 2008). Using the empirical relations of Wells and Coppersmith (1994) between average displacement, maximum displacement, and surface rupture length, Hylland (2007b) showed that measured displacements for latest Pleistocene to Holocene ruptures on the short southwestern and southeastern strands (6–10 km) of the FS appear to require part of the LS to contribute length to those ruptures (i.e., spill-over ruptures). Finally, given the overlapping geometry of the LS and FS and an end-to-end (straight-line) combined length of 46 km (Figure 4.2-1 and Table 4.2-3), we cannot discount the possibility of a full-length multi-segment rupture, and include this in our modeling of the LS and FS.

Because of the possibility of partial-segment rupture of the LS on one hand, and coseismic rupture of subsidiary faults in the LS and FS overlap zone on the other hand, location uncertainties for both rupture ends of the LS are asymmetrical (Figure 4.2-1, Tables 4.2-2 and 4.2-3). The uncertainty at the north end of the LS (+6, -8 km) accounts for the gap in late Quaternary surface faulting between the LS and NS, as well as the mapped northern extent of the MRE rupture on the LS. The uncertainty at the south end of the segment (+8, -3 km) accounts for the length of subsidiary faults in the LS and FS overlap area that could rupture coseismically with the LS. Location uncertainties for both ends of the FS are symmetrical (± 3 km); the uncertainties at the north end encompass the northern extent of composite scarps on the south end of the LS, which possibly indicate spill-over of mid- to early Holocene surface faulting on the Fayette segment (Hylland, 2007b).

We modeled the southern end segments using both single-segment and multi-segment (LS+FS) rupture sources. Slip rates for each of the rupture sources were determined assuming the segments rupture individually about half the time and together about half the time. The single-segment and multi-segment rupture models were each given a weight of 1.0, and the slip rate was split evenly between the two models (see discussion in Section 4.2.2). For the multi-segment rupture, we used the combined length of the LS and FS (46-km median rupture length) and assigned a minimum magnitude of **M** 6.75 ± 0.25 (from the DTGR magnitude recurrence model; see Section 3.4) and an M_{char} commensurate with a 46-km median surface rupture length. M_{char} model distributions for the LS, FS, and LS+FS ruptures are shown in Table 4.2-4.

4.3 Oquirrh–Great Salt Lake Fault Zone

The OGSLFZ is the next major range-bounding fault zone west of the WFZ (Figure 4.3-1). Similar to the WFZ, the OGSLFZ is a down-to-the-west zone of normal faults that strikes north-south through the ISB in central Utah. After the WFZ, the OGSLFZ is the longest and most active fault zone in the Wasatch Front urban corridor (Wong *et al*., 1995, 2002; Youngs *et al*., 2000). However, in contrast to the WFZ, the OGSLFZ has not been studied as thoroughly or in its entirety. For example, the OGSLFZ is not included in the *Quaternary*

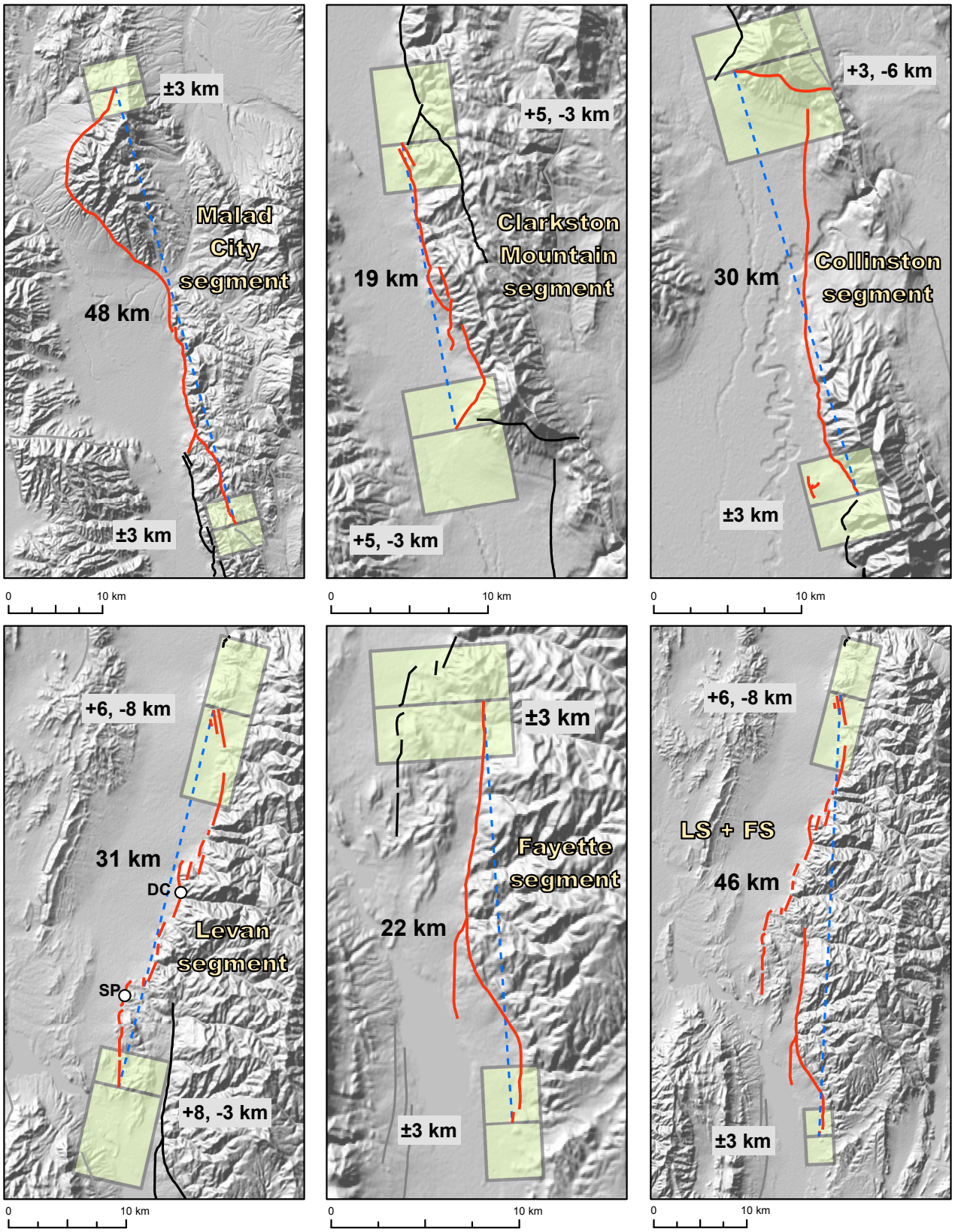

Figure 4.2-1. Rupture lengths and segment-boundary uncertainties for single-segment ruptures on the WFZ end segments, and a LS-FS multisegment rupture (LS+FS). Yellow boxes correspond to segment-boundary uncertainties defined using neotectonic data and best judgment. Blue dashed lines are straight-line length measurements (between rupture ends) showing median rupture lengths (e.g., 48 km for the MCS). White dots on Levan segment show paleoseismic sites: DC, Deep Creek; SP, Skinner Peaks. See text for discussion of individual segment-boundary uncertainties. Note that scale varies among the six maps. Shaded topography generated from 10-m digital elevation data (https://lta.cr.usgs.gov/NED).

Table 4.2-3. Rupture lengths for the WFZ end segments.

Rupture	Median SRL[1] (km)	SRL uncert.[2] (km)		Min SRL[3] (km)	Max SRL[3] (km)	Notes
		North	South			
Malad City segment (MCS)	48	±3	±3	42	54	Based on geologic mapping.
Clarkston Mountain segment (CMS)	19	+5, -3	+5, -3	13	29	Based on geologic mapping; +10 km uncertainty based on empirically derived segment length using 2 m maximum displacement value (Hylland, 2007a).
Collinston segment (CS)	30	+3, -6	±3	21	36	Based on geologic mapping, plus scarp-profile data at southern segment boundary.
MCS+CMS[4]	60	±3	+5, -3	54	68	Used for floating rupture length in unsegmented model.
MCS+CMS+CS[4]	87	±3	±3	81	93	Cumulative length for unsegmented model; not modeled rupture length.
Levan segment (LS)	31	+6, -8	+8, -3	20	45	Based on geologic mapping and scarp-profile data.
Fayette segment (FS)	22	±3	±3	16	28	Based on geologic mapping and scarp-profile data.
LS+FS[4]	46	+6, -8	±3	35	55	–

[1] Median SRL per rupture source based on the linear distance between mapped segment ends.
[2] SRL uncertainties at the northern and southern rupture ends based on segment-boundary uncertainties (Figure 4.2-1). Two values indicate asymmetric uncertainties about median value. End segment uncertainties are weighted 0.2, 0.6, and 0.2.
[3] Minimum and maximum possible SRL per rupture source based on segment-boundary uncertainties.
[4] Cumulative multi-segment lengths avoid double-counting segment lengths that overlap.

Table 4.2-4. M_{char} distributions for WFZ end-segment rupture sources.

Rupture Source	Fault Type	Wt. Mean M_{char}	5th Percentile M_{char}	95th Percentile M_{char}
Malad City	B	7.19	7.01	7.39
Clarkston Mtn	B	6.77	6.49	6.98
Collinston	B	6.97	6.76	7.12
Northern Floating	B	7.29	7.11	7.52
Levan	B	6.99	6.72	7.19
Fayette	B	6.83	6.59	7.00
Levan+Fayette	B	7.16	6.97	7.37

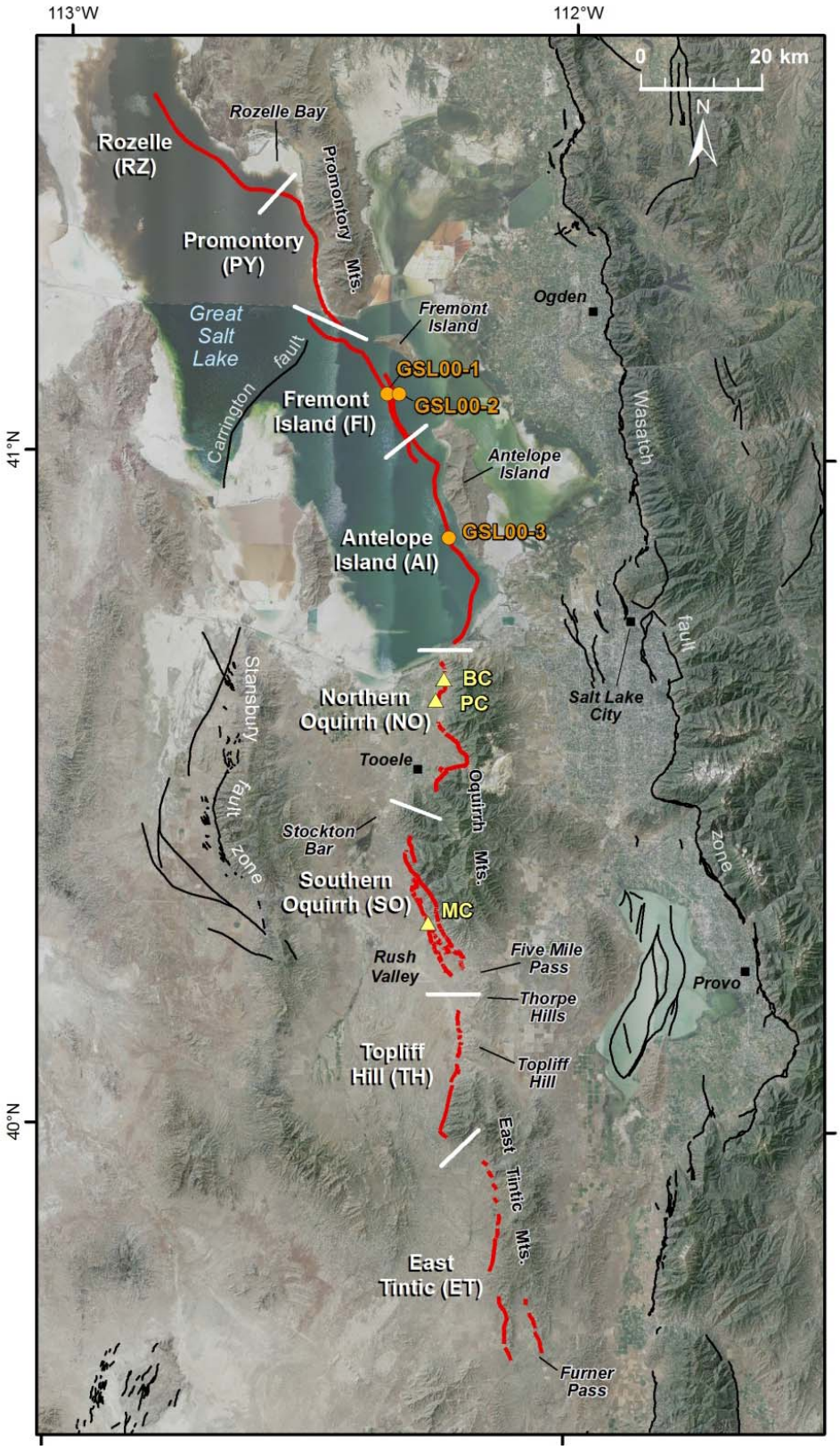

Figure 4.3-1. Segments of the OGSLFZ, shown in red, from north to south (map sources follow in brackets): RZ – Rozelle, PY – Promontory, FI – Fremont Island, and AI – Antelope Island segments of the Great Salt Lake fault [Dinter and Pechmann, 2012]; NO – northern Oquirrh segment [Solomon, 1996]; SO – southern Oquirrh segment (SO) [Olig *et al*., 1999a, 1999b]; (4) TH – the Topliff Hill segment [Black and Hecker, 1999a]; and, ET – East Tintic segment [Black and Hecker, 1999b]. White lines indicate segment boundaries, triangles show paleoseismic trench sites, and circles show borehole locations. Base map is aerial imagery (https://gdg.sc.egov.usda.gov/) overlain on shaded topography generated from 10-m digital elevation data (https://lta.cr.usgs.gov/NED).

Fault and Fold Database of the United States (USGS, 2013) as a single fault zone with sections, like the WFZ to the east and the Stansbury fault zone to west. Instead, the OGSLFZ is included in the database as several separate, individual faults: the East Great Salt Lake fault zone, the Oquirrh fault zone, the Southern Oquirrh Mountains fault zone, the Topliff Hill fault zone, and the East Tintic Mountains (west side) faults. Additionally, not all of the OGSLFZ was included in the 2008 NSHM (i.e., the Topliff Hill and East Tintic faults were excluded; Petersen *et al*., 2008). Nonetheless, the along-strike continuity of fault traces that separate mountain ranges to the east from basins to the west, prompted Youngs *et al*. (1987, 2000) to first consider the OGSLFZ as a single, but likely segmented, fault zone in their PSHA of the Wasatch Front. Subsequent PSHAs in the region have generally followed this approach (e.g., Wong *et al*., 1995, 2002), and the WGUEP decided to do so as well based on the along-strike alignment and continuity of faults, their similarity in slip direction, and considering their relative similarity to the adjacent WFZ and Stansbury fault zone, which are also being treated as single zones with potential individual rupture segments.

The OGSLFZ is about 216 km long (straight line, end-to-end), extending from north of Rozel Bay in the Great Salt Lake, south to Furner Pass (Figure 4.3-1). The fault zone is characterized by a series of discontinuous Quaternary fault scarps along the west side of the Promontory Range, Fremont Island, Antelope Island, Oquirrh Mountains, Thorpe Hills, Topliff Hill, and East Tintic Mountains. Nomenclature for the OGSLFZ is inconsistent and warrants explanation. As defined here, the OGSLFZ includes from north to south: (1) the Rozelle (RZ), Promontory (PY), Fremont Island (FI), and Antelope Island (AI) segments (which form the Great Salt Lake fault of Dinter and Pechmann, 2012); and (2) the northern Oquirrh segment (NO); (3) the southern Oquirrh segment (SO); (4) the Topliff Hill segment (TH); and (5) the East Tintic segment (ET) (Figure 4.3-1).

The Great Salt Lake fault was previously referred to as the East Great Salt Lake fault zone by Dinter and Pechmann (1999, 2000) following Cook *et al*. (1980). This simple nomenclature contrasts with that for the southern part of the OGSLFZ (Oquirrh fault zone and segments to the south), which reflects various interpretations of fault geometry and segmentation. Cook and Berg (1961) referred to the southern OGSLFZ collectively as the Oquirrh-Boulter-Tintic fault zone. The NO segment was previously referred to as the Oquirrh marginal fault by Everitt and Kaliser (1980), the northern Oquirrh fault zone by Barnhard and Dodge (1988) and Olig *et al*. (1994), and the Oquirrh fault zone by Barnhard and Dodge (1988), Olig *et al*. (1996), and Solomon (1996). The SO segment includes the Mercur, Soldier Canyon, West Eagle Hill, and Lakes of Kilarney faults and was previously referred to as the northern Oquirrh-Boulter-Tintic fault zone by Everitt and Kaliser (1980) and as the Southern Oquirrh Mountains fault zone by Wu and Bruhn (1994) and Olig *et al*. (1999a, 1999b, 2001). The TH segment was previously referred to as the southern Oquirrh Boulter Tintic fault zone by Everitt and Kaliser (1980) and the Topliff Hill fault zone of Barnhard and Dodge (1988). The ET segment was previously referred to as the East Tintic Mountains fault zone by Bucknam and Anderson (1979) and the East Tintic Mountains (west side) faults by Black and Hecker (1999b) and Hecker (1993).

4.3.1 Paleoseismic Data Sources

Although the OGSLFZ has not been as thoroughly studied as the WFZ, various geological, geophysical, and paleoseismic studies have been conducted and were considered by the WGUEP for modeling the fault zone. We briefly summarize these data and interpretations below, focusing on the geometry, kinematics, and paleoseismic characteristics (timing, size and rate of paleoearthquakes) of the fault zone. Unlike the WFZ, the OGSLFZ has not been discussed collectively as a seismic source in any detail in previous publications. Therefore, we have included more detail here, particularly regarding the paleoseismic data used in the WGUEP model.

Previous studies of the OGSLFZ generally fall into two groups: (1) those of the segments of the Great Salt Lake fault, which are submerged underwater and have been studied collectively by geophysical and borehole investigations; and, (2) those of the Oquirrh fault zone and segments to the south, which are terrestrial and were studied by more conventional paleoseismic methods. For convenience, we generally follow that organization below. Additional important data sources included Hecker (1993), Black *et al*. (2003), and Lund (2005). Lund (2005) previously summarized paleoseismic data and consensus parameters for the Great Salt Lake fault, and the NO and SO segments of the Oquirrh fault zone. Both Hecker (1993) and Black *et al*. (2003) included all of the faults (albeit with different names) in their Quaternary fault compilations. Finally, steep gravity gradients, with lows over basins and highs over ranges, are variously associated with the different segments of the OGSLFZ (Cook and Berg, 1961; Everitt and Kaliser, 1980; Cook *et al*., 1989), partly reflecting long-term along-strike variations in fault behavior; we considered these Bouger gravity data in developing rupture models and assigning weights for the fault zone.

Great Salt Lake Fault

Numerous seismic reflection and other geophysical studies have helped define the geometry of the Great Salt Lake fault and its segments (e.g., Mikulich and Smith, 1974; Cook *et al*., 1980; Viveiros, 1986; Mohapatra and Johnson, 1998; Dinter and Pechmann, 2000; Coleman *et al*., 2002; Dinter and Pechmann, 2005). From interpretation of hundreds of kilometers of high-resolution seismic reflection profiles in the south arm of the Great Salt Lake, along with oil company seismic reflection data for both the north and south arms (Bortz *et al*., 1985; Viveiros, 1986; Mohapatra and Johnson, 1998), Dinter and Pechmann (1999, 2000, 2005) originally identified

three segments for the fault: the (old) Promontory, Fremont, and Antelope Island segments (USGS, 2013, fault numbers 2369a, 2369b, and 2369c, respectively). This segmentation model was largely based on along-strike changes in fault trace geometry and the heights of lake-bottom fault scarps. This model was compiled in Black *et al*. (2003) and used in the 2008 NSHM (Petersen *et al*., 2008). However, subsequent collection of bathymetry and high-resolution seismic reflection data in the north arm of the Great Salt Lake has provided evidence for a previously unrecognized segment boundary in Rozelle Bay, which is near the middle of the old Promontory segment (Dinter and Pechmann, 2012). This evidence includes the observation that the lake bottom scarps in the north arm are significantly larger south of Rozel Bay, suggesting that this section of the fault ruptured more recently than the section of the fault to the north and that the Great Salt Lake fault comprises four, instead of three segments (Dinter and Pechmann, 2014). Based on these data and interpretations, we have broken out the new RZ segment and revised the PY segment accordingly. From north to south, the approximate end to end segment lengths are: RZ-25 km, PY-25 km, FI-25 km, and AI- 35 km (Figure 4.3-1).

The dip of the Great Salt Lake fault affects slip rate and other important seismic source parameters. Some interpretations of seismic reflection data show a listric geometry for parts of the Great Salt Lake fault zone, with near surface dips of about 60° that shallow to less than 20°–30° by depths of 3 to 4 km (Smith and Bruhn, 1984; Viveros, 1986; Mohapatra and Johnson, 1998). However, we do not consider these interpretations to be definitive because other interpretations are possible (e.g., Smith and Bruhn, 1984), and moderately-dipping faults within the crystalline basement can be difficult to image with the seismic reflection method.

Evidence for prehistoric earthquakes on the Great Salt Lake fault includes stratigraphic displacements, subsidiary fault terminations, and differential tilting interpreted from high-resolution seismic reflection profiles, with age information from radiocarbon dates from event horizons sampled in drill cores along the FI and AI segments. These data indicate at least three large earthquakes occurred since about 12 ka on each of these segments, yielding an average recurrence interval of 4200 ± 1400 years (with 2σ uncertainties; Dinter and Pechmann, 2000, 2005). Table 4.3-1 summarizes the specific paleoearthquake timing data and calculated recurrence intervals. With the exception of the youngest event on the AI segment, limiting ages for the FI and AI are from terrestrial charcoal extracted from a single core interval spanning the event horizon (typically ~10 cm long). For the youngest event on the AI segment, an age of about 0.6 ± 0.2 ka was interpolated from terrestrial charcoal dates from two 4-cm core intervals, one above and one below the event horizon. This event is much younger than the youngest event on the FI segment at about 3.2 ± 0.2 ka. The timing of the youngest events on the AI and FI is consistent with bathymetry data, which show a prominent and youthful scarp for the AI segment in contrast to a more subdued and partially buried scarp for the FI segment (Baskin and Allen, 2005; Dinter and Pechmann, 2005). In contrast, the dates of the two older events identified on each segment appear to overlap at 2σ (Table 4.3-1). The paleoearthquake dates in Table 4.3-1 have not been fully documented in a peer-reviewed publication. However, the WGUEP reviewed the supporting seismic, stratigraphic, and radiocarbon dating information for these paleoearthquake dates and decided that the data were reliable enough to use in both time-dependent and time-independent probability calculations.

Based on their review of paleoseismic data for the Great Salt Lake fault, the UQFPWG assigned consensus recurrence values of 4200 ± 2400 years, with the increased range intended to help account for the uncertainty resulting from the limited number of observations (Lund, 2005). At the time of this study, segment-specific paleoseismic data are not available for the PY and RZ segments. However, preliminary analysis of displacements observed in new reflection seismic profiles acquired in the north arm of the lake suggests that rates of activity for these segments may be similar to the AI and FI segments (Dinter and Pechmann, 2012).

Net vertical tectonic displacements (NVTDs) interpreted to be for the youngest event along the AI segment were measured at 17 profile locations and integrated to estimate an along-strike average NVTD of 2.3 ± 0.6 m (J.C. Pechmann and D.A. Dinter, University of Utah, written communication to UQFPWG; reported in Lund, 2005). NVTD accounts for antithetic faulting and backtilting, which can be significant along normal faults (Swan *et al*., 1980) like the Great Salt Lake fault. Based on this estimate and their consensus recurrence intervals, the UQFPWG recommended a vertical slip rate distribution of 0.3-0.6-1.6 mm/yr (estimated 5th, preferred value 50th, and estimated 95th percentiles, respectively) for the Great Salt Lake fault zone (Lund, 2005).

Northern Oquirrh Segment

Gilbert (1890) first identified west-facing fault scarps on Lake Bonneville deposits along the west side of the northern and southern Oquirrh Mountains. Much later, based on 1:50,000-scale geologic mapping, Everitt and Kaliser (1980) split the fault into two separate zones (essentially the NO and SO segments) along the northern and southern parts of the Oquirrh Mountains in Tooele and Rush Valleys, respectively. Bucknam (1977) and Barnhard and Dodge (1988) separately mapped both the NO and SO segments (at 1:250,000 scale), and profiled fault scarps on unconsolidated deposits. Along the NO segment (USGS, 2013, fault number 2398), Barnhard and Dodge (1988) measured scarp heights of 2.9 to 10.8 m and surface offsets of 1.3 to 7.3 m for mostly compound scarps on late Quaternary sediments. Solomon (1996) mapped the surficial geology along the fault zone at a 1:24,000 scale. All of these studies recognized two major sections for the NO segment: a northern section characterized by nearly continuous

Table 4.3-1. Paleoearthquake times and estimated earthquake recurrence intervals for the Great Salt Lake fault[1].

Earthquake Pairs	Timing (terrestrially calibrated[2], residence corrected[3], cal yr B.P.[4])[5]	Recurrence Interval (yr)[5]
Antelope Island segment		
EH-A3	586 +201/-241	5584 +219/-172
EH-A2	6170 +236/-234	
EH-A2	6170 +236/-234	3728 +223/-285
EH-A1	9898 +247/-302	
Fremont Island segment		
EH-F3	3150+235/-211	3262 +151/-184
EH-F2	6412 +209/-211	
EH-F2	6412 +209/-211	<5015 +587/-424
EH-F1	<11,427 +605/-449	
Average single-segment recurrence interval = 4200 ± 1400 years[6]		

[1] Dinter and Pechmann (2005).
[2] Radiocarbon years converted to calendar years using Stuiver *et al*. (1998) terrestrial calibration (CALIB v. 4.3; Stuiver and Reimer, 1993).
[3] Correction for carbon residence time in provenance area prior to deposition = 321+191/-171 cal yr, the difference between the terrestrially calibrated ^{14}C date of Mazama ash interval at Site GSL00-3 (=7994+170/-128 cal yr B.P.) and terrestrial calibration (=7673+113/-86 cal yr B.P.) of published Mazama ^{14}C age (6845±50 ^{14}C yr B.P.; Bacon [1983]).
[4] Calendar years before 1950.
[5] 2σ confidence limits.
[6] The mean, with 2σ confidence limits, for the three closed recurrence intervals.

fault scarps in alluvium, and a southern section characterized by a prominent slope break at the bedrock-alluvial fault contact at the base of the range front.

The end-to-end length of 21 km for the nearly continuous mapped fault length of the NO segment contrasts to the range front length of about 30 km, and leaves a gap in latest Quaternary scarps along the base of the range front between the NO and SO segments (Figure 4.3-1; Everitt and Kaliser, 1980; Barnhard and Dodge, 1988; Solomon, 1996; Olig *et al*., 1999a, 1999b). This gap is coincident with the Stockton Bar salient (Figure 4.3-1), which has been interpreted as forming a segment boundary between the NO and SO segments (e.g., Everitt and Kaliser, 1980; Olig *et al*., 1994; Youngs *et al*., 2000; Wong *et al*., 2002). The Stockton Bar is a prominent sandbar deposited during the Lake Bonneville highstand (Gilbert, 1890) on a bedrock and topographic high that forms a salient between Tooele Valley to the north and Rush Valley to the south (Cook and Berg, 1961; Everitt and Kaliser, 1980; Cook *et al*., 1989). The Stockton Bar salient is near Kelsey Peak (elevation 3162 m), an adjacent high point in the Oquirrh Mountains, and appears similar in some respects to the Traverse Mountains salient of the SLCS of the WFZ. The location of these salients may have been influenced by older pre-existing structures (Smith and Bruhn, 1984; Helm, 1995). At the northern end of the NO segment, newly identified fault scarps that lie under Great Salt Lake north of Lakepoint (D.A. Dinter, University of Utah, written communication, January 2010) are considered here to be part of the NO segment (and its 21 km length) because of their along-strike alignment and proximity to the rest of the NO segment.

Olig *et al*. (1994, 1996) conducted detailed paleoseismic trench studies at two sites along the northern portion of the NO segment at Big and Pole Canyons (Figure 4.3-1). At Big Canyon, three trenches revealed structural and stratigraphic evidence for one event with 2.2 m (2.0 to 2.7 m) of NVTD (inferred from colluvial-wedge thickness and accounting for antithetic faulting, drag folding, and backtilting) between 4800 and 7900 cal yr B.P. based on three radiocarbon ages (Olig *et al*., 1994; 1996). Lake Bonneville deposits showed no evidence for additional faulting events, so apparently no other events occurred since about 20 ka.

At Pole Canyon, a single trench exposed structural and stratigraphic evidence for two events with indirect evidence for a third older event. Based on stratigraphic correlations, the youngest event at Pole Canyon was inferred to correlate to the event exposed at Big Canyon and resulted in 2.7 m (2.2 to 3.3 m) of NVTD, measured on offset tufa-cemented regressive beach deposits. Three radiocarbon ages, along with Lake Bonneville stratigraphy, constrained the timing of the penultimate event between 20,300 and 26,400 ^{14}C yr B.P. and the antepenultimate event to before 32,800 ^{14}C yr B.P. (Olig *et al*., 1994, 1996). Note that at the time of Olig *et al*.'s (1994, 1996) study, only radiocarbon ages, not calibrated ages, were reported for the penultimate event because the calendar calibration curve (Stuiver and Reimer, 1993) did not extend

back to the time of the penultimate event. Based on colluvial wedge thickness and comparison to the MRE wedge, Olig *et al*. (1994, 1996) estimated 2.3 m (1.9 to 2.9 m) of NVTD for the penultimate event, a recurrence interval of 13,300 to 22,100 ^{14}C years, and vertical slip rates ranging from 0.1 mm/yr (2.2 m/22,100 years) to 0.2 mm/yr (2.7 m/13,300 years) for the interval between the most recent and penultimate earthquakes. In comparison, their estimates of open-ended vertical slip rates since the time of the penultimate event at Pole Canyon range from 0.19 mm/yr (5.0 m/26,400 ^{14}C years) to 0.25 mm/yr (5.0 m/ 20,300 ^{14}C years).

Based on their review of all of the paleoseismic data, the UQFPWG recommended a consensus vertical slip rate distribution of 0.05-0.2-0.4 mm/yr for the NO segment (Lund, 2005). Their census recurrence interval distribution for the NO segment is 5-20-50 kyr.

Southern Oquirrh Segment

Gilbert (1890) observed scarps along the southern Oquirrh Mountains that he interpreted to be related to post-Lake Bonneville faulting, similar to those along the northern Oquirrh Mountains. Atwood (1916) disagreed that the southern part of the range was faulted, but Gilluly (1928, 1932) provided conclusive evidence for the SO segment (USGS, 2013, fault number 2399), including fault exposures, stratigraphic offsets, structural relief, and topographic relief. He estimated a cumulative throw of 915 to 1524 m across the four, main, north-northwest-striking, down-to-the-west, normal faults (Soldier Canyon, Lakes of Kilarney, Mercur, and West Eagle Hill faults; Figure 2 in Olig *et al*., 2001) that together form the boundary between Rush Valley to the west and the southern Oquirrh Mountains to the east.

The SO segment is characterized by discontinuous, *en echelon*, and overlapping bedrock and late Quaternary fault scarps that extend from Soldier Canyon on the north, to near Fivemile Pass on the south, for an end-to-end total length of about 25 km (Figure 4.3-1; Wu and Bruhn, 1994; Olig *et al*., 1999a, 1999b). Measurements of fault orientations and striations on bedrock faults indicate dominantly dip-slip on two sets of faults (Wu and Bruhn, 1994). Based on scarp profiles and their structural analysis, Wu and Bruhn (1994) suggested that the two sets of faults have grown together through time, forming a convex fault trace pattern in map view with the maximum along-strike displacements (both cumulative and in the late Quaternary) occurring at the apex (i.e., near the middle of the SO segment on the Mercur fault).

Olig *et al*. (1999b) conducted detailed mapping of fault scarps on Quaternary surfaces, mostly on the Mercur and West Eagle Hill faults, including scarp profiling and soil studies to help differentiate scarp ages. Their observations of along-strike displacement patterns also generally support linkage and possible coseismic rupture of the faults. However, NVTDs are clearly younger and larger on the Mercur fault than on the West Eagle Hill fault, respectively averaging 5.8 ± 0.5 m versus 1.5 ± 0.5 m on intermediate age late Quaternary surfaces, and ranging from 6 to 10 m versus 3 to 4 m on older late Quaternary surfaces (unit af2 in Olig *et al*., 1999b). Furthermore, although range crest elevations and Quaternary displacements taper to the south on both faults, neither fault appears to taper to the north, suggesting that perhaps the SO and NO rupture coseismically and/or slip could be transferred to bedrock faults such as the Lakes of Kilarney and Soldier Canyon faults (Olig *et al*., 1999a, 1999b), or perhaps slip patterns are complicated by younger sediments draping pre-existing larger scarps. Regardless, it is noteworthy that although the Rush Valley basin geometry tapers to the north, with a structural, topographic, and gravity high at South Mountain, to the south the basin does not taper and the basin fill actually appears thickest, estimated to exceed 3000 ft (914 m) at the SO-TH segment boundary (Everitt and Kaliser, 1980).

Early attempts to determine the timing of youngest faulting on the SO segment came to conflicting conclusions. Everitt and Kaliser (1980) excavated a shallow trench across the southern end of the Mercur fault below the Bonneville shoreline. The trench exposed a 12-m wide graben and Lake Bonneville deposits, which they interpreted to be faulted based on the presence of shear fabric and warping of contacts (B.L. Everitt, personal communication, 1995). In contrast, Barnhard and Dodge (1988) re-interpreted the exposure and suggested that faulting pre-dated the transgression of Lake Bonneville at 17 to 18 ka, which was consistent with their scarp-profile data. Wu and Bruhn (1994) also suggested faulting was pre-Bonneville based on their scarp-profile data.

Olig *et al*. (2001) excavated trenches across three *en echelon* fault scarps of the Mercur fault on older late Quaternary fan deposits north of Mercur Canyon (Figure 4.3-1). The trenches revealed stratigraphic and structural evidence for five to seven earthquakes, which vertically offset pre-Bonneville fan deposits 9.25 to 11.1 m. Two charcoal AMS radiocarbon ages and six infrared stimulated luminescence (IRSL) ages for fan sediment (including loess) help constrain the timing of events, all of which occurred after 86–92 ka. This timing constraint includes a previously unpublished IRSL age for sample MCET2-L5Y, which we report here as 85.6 ± 6.1 ka.

Four of the events at the Mercur Canyon site occurred on the main westernmost trace since 75 ± 10 ka, including the youngest event shortly after 4430 to 4830 cal yr B.P., but well before 1295 to 1530 cal yr B.P. (Olig *et al*., 2001). The age of this youngest event compares favorably with cosmogenic ^{14}C ages determined for a bedrock scarp of the northern Lakes of Kilarney fault, which suggest that faulting occurred around 4360 ± 1220 cal yr B.P. (Handwerger *et al*., 1999). Additionally, the 75 ka age, which is an average of two IRSL ages for an A_v soil horizon on loess predating the western scarp, compares favorably with ^{10}Be/^{26}Al cosmogenic dating of

quartzite boulders on the upthrown fan surface that suggest a minimum age of 75 ± 5 ka (Mattson and Bruhn, 2001).

Olig *et al*. (2001) estimated an average recurrence interval for the past five to seven events of 12 to 25 kyr. They estimated average vertical displacements per event of 1.3 to 2.2 m and an average vertical slip rate of 0.09 to 0.14 mm/yr since 92 ka at Mercur Canyon. In comparison, Mattson and Bruhn (2001) estimated a slip rate of ~0.1 mm/yr since 50–60 ka based on their diffusion modeling of the formation of the western fault scarp at Mercur Canyon. From review of all the paleoseismic data, the UQFPWG recommended rates for the SO segment that were similar to the NO segment, with a consensus vertical slip rate distribution of 0.05-0.2-0.4 mm/yr (Lund, 2005). Similarly, their consensus recurrence-interval distribution for the SO segment is: 5-20-50 kyr.

Topliff Hill Segment

The TH segment extends south of the SO segment along the southeastern margin of Rush Valley (Figure 4.3-1). The TH segment was first mapped by Bucknam (1977) and was also included on the geologic map of Moore and Sorrenson (1979), but it has not been trenched and remains poorly understood. As included here, the TH segment (USGS, 2013, fault number 2407) is characterized by discontinuous, down-to-the-west scarps that overall trend north-south for about 20 km along the margin between Rush Valley to the west and the Thorpe Hills, Topliff Hill, and the northern end of the East Tintic Mountains to the east (Figure 4.3-1; Black and Hecker, 1999a). Much of the southern portion of the TH segment along the East Tintic Mountains is characterized by a sharp, linear bedrock-alluvial contact with a faceted range-front and active alluvial apron, although some short scarps on an alluvial fan surface were mapped by Everitt and Kaliser (1980; southern end of Plate IIIc) and Black and Hecker (1999a).

Scarps of the TH segment are generally above the Bonneville shoreline, but a notable exception is at a site along the northwest margin of Topliff Hill, site #1106 of Everitt and Kaliser (1980). They found that scarps are generally higher on older surfaces, and observed smaller scarp heights (4.5 to 10 feet) for those faults below the Bonneville shoreline than for fault scarps above the shoreline (heights of 22 to 25 feet), suggesting repeated faulting "into post-Bonneville time." They interpreted the faulted fan surface at this site as post-Bonneville highstand (that is ≤ 18,000 cal yr B.P. after Reheis *et al*., 2014). They also augered three holes (shown in their Figure 11 but not discussed in the text), which show elevation differences for subrounded gravels across the fault; however, these elevation differences are ambiguous because they could be either fault-related or depositional.

In contrast, Barnhard and Dodge (1988) re-interpreted faulting on the TH segment to be older than the Bonneville shoreline at site #1106. They interpreted the alluvial-fan surface to be wave-etched by the Bonneville highstand and thus pre-Bonneville in age. They also inferred an older age for the TH scarp compared to the Bonneville highstand based on a quantitative comparison of scarp morphologies.

Based on review of all the data and interpretations, we found the surficial relations ambiguous regarding whether faulting on the TH segment predates or postdates the Bonneville highstand. The fan at site #1106 is clearly pre-Bonneville for the reasons noted by Barnhard and Dodge (1988), but below the shoreline the fan surface is also clearly eroded into and thus is also post-Bonneville. As the scarp appears smaller below the shoreline, but is still preserved (and not eroded away by transgression of the lake), faulting could have occurred after the shoreline was formed as Everitt and Kaliser (1980) originally interpreted. Alternatively, the scarp could be smaller below the shoreline because it has been partially eroded by transgression of the lake, although this seems less likely given the prominent scarp morphology visible in Google Earth imagery. Importantly, Barnhard and Dodge (1988) interpreted pre-Bonneville faulting for the SO segment based on scarp morphology data, and yet trenching revealed evidence for much younger Holocene faulting. Regardless, the age of youngest faulting along the TH segment remains unclear and needs additional subsurface investigation.

Slip rate and recurrence data are lacking for the TH segment. Barnhard and Dodge (1988) measured scarp heights of less than 2 m to over 7 m on unconsolidated deposits. Hecker (1993) gave a maximum displacement of 5.8 m, but she did not report the measurement location, whether the measurement represents surface offset or vertical displacement, or an associated age of faulted deposits. The USGS (2013) categorizes the TH segment as having a slip rate of less than 0.2 mm/yr, but also emphasizes that scarp ages are uncertain.

East Tintic Segment

The ET segment is the southernmost segment of the OGSLFZ (Figure 4.3-1). Although scarps were originally identified by Goode (1959) and included on geologic maps by Morris (1975, 1987), the ET segment is even more poorly understood than the TH segment and has not been trenched. As included here, the ET segment (USGS, 2013, fault number 2420) is characterized by isolated and highly dissected remnants of scarps that overall trend north-south for about 41 km along the western range front of the East Tintic Mountains. The ET segment also includes overlapping, subparallel traces along Furner Ridge, as well as an apparent along strike 4-km gap in faulting (Figure 4.3-1; Black and Hecker, 1999b).

Little is known about rates of activity on the ET segment. Unlike other Quaternary scarps in the Delta 1°x 2° quadrangle, Bucknam and Andersen (1979) did not profile scarps of the ET segment, but suggest that their appearance on aerial photographs implies "that they are among the oldest scarps

that we have recognized in western Utah" because they are highly dissected and largely buried by alluvium of several different ages. The USGS (2013) categorizes the ET segment as having a slip rate of less than 0.2 mm/yr.

4.3.2 Analyses and Fault Source Parameters

This section describes the fault parameters assigned to the OGSLFZ by the WGUEP, including distributions and weights. Details of some of the supporting analyses are included in Appendix C.

Timing of Surface Faulting Earthquakes

To augment the data on timing of paleoearthquakes previously discussed in Section 4.3.1, the WGUEP conducted OxCal analyses of the paleoseismic trench data for the NO and SO segments (Appendix C). These analyses allowed all of the radiocarbon ages to be calendar calibrated for the NO segment, allowed inclusion of a previously unpublished age for the SO segment, reduced uncertainties in the timing of several events, and provided probability density functions of ages for comparison and further rate analyses (as discussed in Section 3.4). The OxCal analyses were conducted using a similar approach to the WFZ, but were greatly simplified because of the limited number of trench sites and data; therefore, additional analyses were not needed to compare the PDFs for the timing of events between different sites. Appendix C-1 shows the input OxCal models and Appendix C-2 shows the results for the NO and SO segments.

Table 4.3-2 summarizes the timing of events identified on the various segments of the OGSLFZ, including the revised timing of events from the OxCal analysis of the trench data for the NO and SO segments. The mean timing of events on the NO and SO segments did not significantly change, but uncertainties are generally reduced and in particular the timing for the most recent events on the NO and SO segments no longer overlap in the 5th to 95th percentile range. The paleoearthquake times on the AI and FI segments include 2σ ranges based on the calibrated radiocarbon ages from Dinter and Pechmann (2005).

Table 4.3-2. Timing of surface-faulting earthquakes on segments of the OGSLFZ[1].

	Fault Segment	Youngest Event	Penultimate Event	Older Events
Great Salt Lake fault[2]	Rozelle (RZ)	Holocene (?)	unknown	unknown
	Promontory (PY)	Holocene (?)	unknown	unknown
	Fremont Island (FI)	3150 (+240, -210)	6410 (±210)	> 7410[3] < 11,430 (+610, -450)
	Antelope Island (AI)	590 (+200, -240)	6170 (+240, -230)	9,900 (+250, -300)
	Northern Oquirrh (NO)[4]	6320 (±1600) [4970 to 7640]	27,600 (±3840) [24,430 to 30,800]	> > 33,000
	Southern Oquirrh (SO)[5]	3030 (±1880) [1460 to 4580]	Roughly 5 to 31 ka	Two additional events since about 75 ka; or three to five additional events since about 92 ka
	Topliff Hills (TH)	> 18,000[6] or < 18,000[7]	unknown	unknown
	East Tintic (ET) [8]	middle and late Pleistocene (?)	unknown	unknown

[1] Updated from Olig *et al*. (2001) as noted. Mean ages in calendar calibrated radiocarbon years before 1950 (cal yr B.P.), rounded to the nearest decade, with 2-σ errors in parentheses and 5th and 95th percentiles in brackets, except as noted.
[2] Timing data from Dinter and Pechmann (2005), except as described in footnote 3.
[3] The antepenultimate event occurred within a 12-m-thick salt and sapropel unit. The maximum age for this event is from radiocarbon dating of charcoal from sediments immediately underlying the salt and sapropel unit (Dinter and Pechmann, 2005). The minimum age comes from a conservative time estimate of at least 1000 yrs between the penultimate event horizon and the top of the salt and sapropel unit, based on measurements of sediment thicknesses between these two horizons and sedimentation rates estimated for the overlying sediments.
[4] From analysis in Appendix C, using data from previous studies of the Big Canyon and Pole Canyon trench sites (Olig *et al*., 1994; 1996). For comparison, previously the 5th and 95th percentiles of the youngest and penultimate events on the NO segment were respectively estimated to be 4800 to 7900 cal yr B.P., and 20,300 to 26,400 ^{14}C yr B.P. Note that a mean age of 30,910 cal yr B.P. was calculated for sample OFPC-RC3 (Table C-1) and used in rate calculations for the NO segment (Table 4.3-7).
[5] From analysis in Appendix C, using previous timing data for the Mercur fault from Mercur Canyon trench site (Olig *et al*., 2001) and an additional unpublished IRSL age (see text for discussion). For comparison, previously the 5th and 95th percentiles of the youngest event on the SO segment were estimated to be 1300 to 4830 cal yr B.P. Note that the mean of the combined age for the Unit 2a loess of 88,950 cal yr B.P. (Table C-2) was used as the maximum age constraint in rate calculations for the SO segment (see Table 4.3-7).
[6] Modified from Barnhard and Dodge (1988) based on Lake Bonneville highstand age from Reheis *et al*. (2014).
[7] Modified from Everitt and Kaliser (1980) based on Lake Bonneville highstand age from Reheis *et al*. (2014); see text for discussion.
[8] From Bucknam and Anderson (1979).

Rupture Models and Geometries

Early PSHAs developed a single-segmentation model for the OGSLFZ that included 5 segments (Wong *et al*., 1995; Youngs *et al*., 2000). More recently, rupture models for the OGSLFZ have become more complex to better address uncertainties and incorporate new data (e.g., Wong *et al*., 2002).

Based on expert opinion and consensus, the WGUEP agreed on the rupture models and weights for the OGSLFZ in Table 4.3-3. These five rupture models and weights were based on the data sources discussed in Section 4.3.1 and the timing data summarized in Table 4.3-2. We tried to include more epistemic uncertainty than past models, but not all possibilities and combinations were explicitly included. To keep the model manageable, we included those rupture sources judged to be more likely (with weights of 0.1 or greater), and accounted for the rest by an unsegmented model with a weight of 0.2.

The basis for each of the OGSLFZ rupture models and weights in Table 4.3-3 is briefly summarized as follows. Rupture model 2, where each segment is an independent source, was favored with a weight of 0.4 because of strong differences or variations in (1) along-strike fault trace geometry between segments, including gaps, changes in strike, and step-overs, (2) structural relief, including footwall-range topography and hanging wall-basin geometry, (3) the timing of the most recent faulting event (although this is poorly constrained for some segments), and (4) rates of activity among segments (in many but not all cases). We gave the floating unsegmented rupture (rupture model 5) the next highest weight of 0.2 for the OGSLFZ, slightly higher than for the WFZ, because the OGSLFZ has fewer paleoseismic data and larger uncertainties. In the unsegmented model, we assumed the maximum length of the floating rupture to be three times the average segment length, allowing for ruptures as long as 87 km. Rupture model 1 includes coseismic rupture of the NO+SO segments and is weighted 0.15. This model is consistent with Gilbert's (1890) original interpretation of faults bounding the Oquirrh Mountains and the absence of a decrease in range elevation at the NO-SO boundary. It is also supported by the large displacements per event given the relatively short individual NO and SO lengths, the apparent large displacements at the northern end of the SO segment based on scarp profiles, the similar slip rates of the two segments, and the overlap in ages of older events (although these ages are poorly constrained). Rupture model 3 includes coseismic rupture of the FI and AI segments and is also weighted 0.15. Model 3 is supported by the large displacements per event on the AI segment relative to its short length, the overlap in timing of the penultimate events on the two segments, and the similar rates of activity of the two segments. Finally, rupture model 4 includes coseismic rupture of the SO and TH segments and is weighted 0.1. Model 4 is supported by the basin geometry of Rush Valley (with its deepest point at the SO-TH boundary), the possibility that the timing of the youngest events overlap (given the uncertainty for the TH segment), and the large displacements per event given the relatively short length of the SO segment.

Table 4.3-4 shows the preferred lengths and uncertainties for all the earthquake sources (segments and combinations of segments) of the OGSLFZ. Similar to the WFZ, the ranges of uncertainties were guided by gaps, overlaps, step-overs and other fault trace complexities. For rupture endpoints with apparent gaps or overlaps in fault scarps on Quaternary deposits, we have generally assumed the median boundary to be at the midpoint. Similar to the central WFZ, the uncertainties in lengths are correlated with those of the adjacent segments and multisegment sources have the same coordinates and uncertainties as the respective segment endpoints (for example, the northern end of FI+AI source has the same coordinates as the northern end of the FI source).

As per our default distribution for normal faults (Section 3.2), we used a dip distribution of 50° ± 15° W, weighted 0.6 ± 0.2, for the entire OGSLFZ. Although Wu and Bruhn (1994) measured slightly steeper dips for bedrock faults of the SO segment, and seismic reflection profiles suggest a listric geometry and perhaps shallower average dip for the segments of the Great Salt Lake fault zone (Smith and Bruhn, 1984; Viveros, 1986; Mohapatra and Johnson, 1998), we adopted the default range-bounding, normal-fault distribution for the entire zone for simplicity.

Displacements

We calculated per event displacement distributions for the NO, SO, and NO+SO sources using the displacement data discussed in Section 4.3.1 and the same method used for the WFZ (fixed and/or best-fit ellipses to the data—see Appendix

Table 4.3-3. Rupture models for the OGSLFZ*.

Rupture Model	Rupture Sources	Weight
1	RZ, PY, ***FI***, ***AI***, NO+SO, TH, ET	0.15
2	RZ, PY, ***FI***, ***AI***, NO, SO, TH, ET	0.4
3	RZ, PY, FI+AI, NO, SO, TH, ET	0.15
4	RZ, PY, ***FI***, ***AI***, NO, SO+TH, ET	0.1
5	Unsegmented (floating)	0.2

* Rupture sources shown in bold and italics indicate a time-dependent model (weighted 0.8) was also included in the analysis.

Table 4.3-4. Lengths for the OGSLFZ rupture sources[1].

Rupture Source	Median SRL (km)	Northern Endpoint Uncertainties	Southern Endpoint Uncertainties	Min SRL (km)	Max SRL (km)
RZ	26.5	+5; -2	±2	22.8	33.1
PY	22.2	±2	+2.7, -3.3	18.4	26.2
FI	25.6	+2.7, -3.3	+2.3, -2.1	20.0	29.8
AI	33.7	+2.3, -2.1	+2.9, -2.5	29.6	37.9
NO	29.7	+2.9, -2.5	+10, -4.5	19.7	34.4
SO	30.7	+10, -4.5	+2.9, -3.2	24.2	37.9
TH	23.3	+2.9, -3.2	+2, -8.7	18.2	31.1
ET	39.7	+2, -8.7	+2, -3	31.3	43.7
FI+AI	57.8	+2.7, -3.3	+2.9, -2.5	52.0	62.3
NO+SO	56.7	+2.9, -2.5	+2.9, -3.2	51.9	62.7
SO+TH	52.1	+10, -4.5	+2, -8.7	47.2	63.2
Floating	87	--	--	80.8	92.8

[1]All SRL measured straight-line, end-to-end.

Table 4.3-5. Modeled vertical displacement distributions for selected rupture sources of the OGSLFZ (see Appendix C-4 for details).

Rupture Source	Pref D[1] (m) (weighted 0.6)	Min D (m) (weighted 0.2)	Max D (m) (weighted 0.2)	No. of Obs.	Notes
SO	1.56	0.62	2.65	5	Average of fixed ellipses from five events (P1-P5)
NO	2.075	1.61	2.67	3	Average of best-fit ellipse from P1 (n=2) and fixed ellipse from P2
SO+NO	2.055	1.68	2.52	5	Average of best-fit ellipses from P1 and P2

[1] Vertical displacement (D).

B for detailed discussion). Inputs are shown in Appendix C-3. Resulting modeled outputs are shown in Appendix C-4 and are summarized in Table 4.3-5. Preferred values range from 1.6 to 2.1 m, whereas the full range is from 0.6 to 2.7 m.

Characteristic Magnitudes

Using the displacement distributions in Table 4.3-5, we treated the NO, SO and NO+SO sources as Type A faults (see Section 3.5) for calculating M_{char}. We treated all other sources for the OGSLFZ (RZ, PY, AI, FI, AI+FI, SO+TH, TH, ET, and floating) as Type B faults for calculating M_{char}. Table 4.3-6 shows the M_{char} distributions for the various rupture sources of the OGSLFZ.

Recurrence and Slip Rates

As described in Section 3, we used a variety of different approaches to characterize rate distributions and available data for the OGSLFZ rupture sources, which included timing data in Table 4.3-2 and the slip rate and other paleoseismic data discussed in Section 4.3.1. The approaches, Poisson rate distributions, and weights are summarized in Table 4.3-7. Also included are brief notes on input data, the approaches used, and weights.

We used a time-dependent BPT model for the FI and AI rupture sources with a weight of 0.8. As fault-specific data are lacking, we assumed a COV distribution similar to the central WFZ (Section 4.1.3). Because rates are much lower for the NO and SO segments than for the central WFZ and AI and FI segments, a BPT model was not used for the NO and SO segments. BPT rate distributions for the FI and AI sources are shown in Table 4.3-8.

4.4 Antithetic Fault Pairs

The Wasatch Front region contains a number of antithetic fault pairs-subparallel normal faults that dip toward each other and are separated by horizontal distances that, depending on fault dip, could allow the faults to intersect within seis-

Table 4.3-6. Characteristic magnitude distributions calculated for the OGSLFZ rupture sources.

Rupture Source	Fault Type	Wt. Mean M_{char}	5th Percentile M_{char}	95th Percentile M_{char}
RZ	B	6.92	6.73	7.06
PY	B	6.83	6.61	7.01
FI	B	6.89	6.68	7.04
AI	B	7.03	6.84	7.19
NO	A	7.03	6.79	7.25
SO	A	7.01	6.74	7.20
TH	B	6.86	6.63	7.04
ET	B	7.09	6.91	7.28
FI+AI	B	7.27	7.10	7.50
NO+SO	A	7.27	7.09	7.44
SO+TH	B	7.24	7.05	7.44
Floating	B	7.47	7.28	7.74

Table 4.3-7. Poisson rate distributions for OGSLFZ rupture sources.[1]

Source	Approach (weight)	Recurrence (in yrs) or Vertical Slip Rate (in mm/yr)[2]	Notes
RZ segment	Recurrence Intervals (1.0)	14,103 (0.101) 6300 (0.244) 3724 (0.310) 2377 (0.244) 1468 (0.101)	No segment-specific slip rate or event timing data available. Assumed similar rates to the AI segment.
PY segment	Recurrence Intervals (1.0)	14,103 (0.101) 6300 (0.244) 3724 (0.310) 2377 (0.244) 1468 (0.101)	No segment-specific slip rate or event timing data available. Assumed similar rates to the AI segment.
FI segment[3]	Recurrence Intervals (1.0)	13,680 (0.101) 6024 (0.244) 3521 (0.310) 2222 (0.244) 1348 (0.101)	From approach 2 with $N = 3$ and $T = 11{,}488$ yrs (Table 4.3-1).[4]
AI segment[3]	Recurrence Intervals (1.0)	14,103 (0.101) 6300 (0.244) 3724 (0.310) 2377 (0.244) 1468 (0.101)	From approach 2 with $N = 3$ and $T = 9959$ yrs (Table 4.3-1).
NO segment	Recurrence Intervals (0.6)	106,538 (0.101) 36,153 (0.244) 18,453 (0.310) 10,613 (0.244) 5983 (0.101)	From approach 2 with $N = 2$ and $T = 30{,}971$ yrs (Appendix C-2 and Table 4.3-2).
	Slip Rates (0.4)	***0.05 (0.2)*** ***0.2 (0.6)*** ***0.4 (0.2)***	Consensus slip rates from the UQFPWG (Lund, 2005).

Table 4.3-7. Continued.

Source	Approach (weight)	Recurrence (in yrs) or Vertical Slip Rate (in mm/yr)[2]	Notes
SO segment	Recurrence Intervals (0.6)	37,291 (0.101) 22,366 (0.244) 15,698 (0.310) 11,433 (0.244) 8004 (0.101)	From approach 1 with $N = 5$ and $T = 89{,}011$ yrs (Appendix C-2 and Table 4.3-2). This alternative of five events is weighted 0.5.
		24,106 (0101) 15,704 (0.244) 11,606 (0.310) 8817 (0.244) 6441 (0.101)	From approach 1 with $N = 7$ and $T = 89{,}011$ yrs (distribution weighted 0.5) (see Appendix C-2 and Table 4.3-2). This alternative of seven events is weighted 0.5.
	Slip Rates (0.4)	***0.05 (0.2)*** ***0.2 (0.6)*** ***0.4 (0.2)***	Consensus slip rates from the UQFPWG (Lund, 2005).
TH segment	Slip Rates (1.0)	***0.05 (0.2)*** ***0.2 (0.6)*** ***0.4 (0.2)***	No segment-specific paleoseismic data. Assumed rates similar to the NO and SO segments based on descriptions of scarps and arguments in Everitt and Kaliser (1980).
ET segment	Slip Rates (1.0)	***0.025 (0.3)*** ***0.1 (0.4)*** ***0.2 (0.3)***	Assumed half the rates of the NO and SO segments, but with broader weights due to larger uncertainties, based on relatively poor geomorphic expression for this end segment (Black and Hecker, 1999b).
FI+AI segments	Recurrence Intervals (1.0)	14,103 (0.101) 6300 (0.244) 3724 (0.310) 2377 (0.244) 1468 (0.101)	Used rate distribution of AI segment as it is better constrained and rate distributions are similar.
NO+SO segments	Slip Rates (1.0)	***0.05 (0.2)*** ***0.2 (0.6)*** ***0.4 (0.2)***	Used slip rate and not recurrence because slip rate distributions are the same for each segment, whereas the timing of the youngest event on each segment does not overlap at 2σ, and the timing of earlier events is broad.
SO+TH segments	Slip Rates (1.0)	***0.05 (0.2)*** ***0.2 (0.6)*** ***0.4 (0.2)***	Used slip rate distribution of the SO segment as it is better constrained.
Floating	Slip Rates (1.0)	GSLF segments: ***0.3 (0.2)*** ***0.6 (0.6)*** ***1.6 (0.2)*** Other segments: ***0.05 (0.2)*** ***0.2 (0.6)*** ***0.4 (0.2)***	Similar to the WFZ, we used two rate distributions with higher rates for the portion including the Great Salt Lake fault segments, and lower rates for the portion including the other segments. Rates are consensus slip rates from the UQFPWG (Lund, 2005).

[1] The time intervals for these calculations are years before 2011: cal yr B.P. ages (yrs before 1950) plus 61 yrs.
[2] Followed by weights in parentheses.
[3] Time dependent approach also used for this source with Poisson model weighted 0.2, and BPT model weighted 0.8 (Table 7.2-2 for BPT rate distributions).
[4] Note added in proof: The Poisson recurrence intervals used in the probability calculations for the Fremont Island segment were incorrect. The effect of this error was to increase some of the 50-yr probabilities listed for this segment in Table 8.2-2 by 0.1%. The correct recurrence intervals (with their weights) are as follows: 16,269 (0.101), 7267 (0.244), 4296 (0.310), 2742 (0.244), and 1694 (0.101).

Table 4.3-8. BPT recurrence interval distributions for the Antelope Island and Fremont Island rupture sources of the OGSLFZ.

Source	Recurrence (yrs)			Weights	Input (yrs)
	α = 0.3	α = 0.5	α = 0.7		
FI segment	2742	2659	2784	0.101	t_0 = 3211 = lapse time (until 2011)
	3401	3696	4274	0.244	t_1 = 3262 = inter-event time 1
	4028	4793	5984	0.310	t_2 = inter-event time 2, uniform probability
	4764	6197	8318	0.244	distribution from $1000 \leq t_2 \leq 5015$
	5885	8521	12,395	0.101	$t_f = 5015 - t_2$
					= open interval before earliest event
	4112	5029	6461	Weighted Mean	
AI segment	3410	3095	3028	0.101	t_0 = 647 = lapse time (until 2011)
	4210	4381	4868	0.244	t_1 = 5584 = inter-event time 1
	4976	5765	7062	0.310	t_2 = 3728 = inter-event time 2
	5877	7546	10,083	0.244	t_f = 0
	7232	10,464	15,302	0.101	= open interval before earliest event
	5079	6067	7689	Weighted Mean	

mogenic depths. Some of these fault pairs are major range-front, graben-bounding faults, whereas others consist of a major range-front fault paired with a subsidiary intrabasin fault. Important issues when modeling the seismic hazard presented by antithetic fault pairs are evaluating the potential for one fault to be truncated at depth by the other fault, and determining which fault is the non-truncated (master) fault and which is the truncated (subsidiary) fault. This issue was discussed by the Basin and Range Province Earthquake Working Group II (BRPEWGII; Lund, 2012) in the context of providing recommendations to the USGS for the 2014 update of the NSHMs. At that meeting, Geologic Issue G2 was stated as: How should antithetic fault pairs be modeled in the NSHMs? For example, what is the relation and seismogenic significance of antithetic fault pairs such as the East and West Cache faults, and strands of the Salt Lake City segment of the WFZ and the West Valley fault zone?

The BRPEWGII developed recommendations for evaluating antithetic fault pairs on the NSHMs (Lund, 2012), several of which apply to our modeling efforts. These recommendations include the following:

- Explore using metrics to guide selection of master and subsidiary faults.
  - Evaluate dataset for overlapping relations to select the master fault based on length.
  - Evaluate using aspect ratio (length/width) for individual antithetic fault pairs.
  - Where data allow, structural throw should be used rather than topographic relief.
  - Evaluate using the product of length and throw as a parameter for selecting the master fault.
- Use subsurface data (e.g., seismic reflection) where available to guide master fault selection.
- Where available data do not give a clear indication of the master versus subsidiary fault, model both alternatives using a logic tree approach.
- Use rupture area (rather than surface rupture length) to determine magnitude for truncated faults.

Each of the three primary metrics (fault length, overlap, and structural throw/topographic relief) used to identify the master versus subsidiary fault in an antithetic fault pair can potentially indicate which fault has been the dominant structure over time (i.e., master fault). Fault length serves as a proxy for fault maturity, overlapping relations provide a comparative indicator of controlling structure, and structural throw/topographic relief serves as a proxy for long-term slip rate (Haller and Harmsen, 2011).

4.4.1 Analysis

We initially considered six antithetic fault pairs within the Wasatch Front region for analysis per the BRPEWGII recommendations:

(1) West Valley fault zone–Salt Lake City segment of the WFZ

(2) Utah Lake faults–Provo segment of the WFZ

(3) Hansel Valley fault–North Promontory fault

(4) West Cache fault zone–East Cache fault zone

(5) Western Bear Lake fault–Eastern Bear Lake fault

(6) Joes Valley fault zone (west side)–Joes Valley fault zone (east side)

After reviewing available geologic and paleoseismic information for each fault pair, we eliminated the West Cache–East Cache fault zones and Joes Valley fault zone from the antithet-

ic fault pair analysis. In the case of the West and East Cache fault zones, surficial geologic mapping (McCalpin, 1989; Solomon, 1999) and paleoseismic studies (McCalpin, 1994; Black *et al*., 2000; Evans and McCalpin, 2012) indicated differences in surface-faulting chronologies among the various segments of the two fault zones, which suggest independent activity. Accordingly, we modeled the West Cache and East Cache fault zones as independent sources, each extending to full seismogenic depth (see Appendix D). In the case of the Joes Valley fault zone, structural interpretation of seismic reflection profiles (Anderson, 2008) and the narrow width (< 5 km) of the Joes Valley graben indicate that the Joes Valley faults are linked structures. Accordingly, we modeled the Joes Valley fault zone as a single source. Based on their similarity to the Joes Valley fault zone, the Snow Lake graben faults were also modeled as a single source (see Appendix D).

For the four remaining fault pairs (Figure 4.4-1), we attempted to identify master and subsidiary faults by comparing fault length, percent overlap, and topographic relief (data were insufficient to allow us to use structural throw rather than topographic relief). Fault length is the straight-line, end-to-end length of the mapped surface trace of the fault or segment, and with the exception of the Hansel Valley and Western Bear Lake faults, length values are from USGS (2013). The Hansel Valley–Promontory and Western–Eastern Bear Lake fault pairs are both graben-bounding fault pairs, and where the graben-bounding system comprises multiple faults or segments, we used the combined length of the entire fault system (e.g., combined length of the Hansel Valley, Hansel Mountains [east side], and Hansel Valley [valley floor] faults; combined length of Western Bear Lake and Bear Lake [west side] faults; and combined length of the Northern, Central, and Southern sections of the Eastern Bear Lake fault). In general, greater length can be an indication of the master fault. Percent overlap shows how much of the length of one fault or segment is overlapped by the other fault or segment of the pair; smaller percent overlap can be an indication of the master fault. Topographic relief reflects the difference in elevation between the fault and topographic high points in the footwall of the fault, and includes both maximum and "average" relief. The mean elevation of five footwall points equally spaced along the length of the fault, generally on or near a drainage divide, was used to calculate the "average" topographic relief. Greater relief can be an indication of the master fault. Finally, we used the product of length and average relief to evaluate the fault pairs; a larger product can be an indication of the master fault. Figure 4.4-2 and Table 4.4-1 summarize the antithetic-fault-pair metrics.

4.4.2 Results

Our analysis of antithetic fault pairs using metrics recommended by the BRPEWGII produced mixed results. For the West Valley fault zone–Salt Lake City segment (WFZ) and Utah Lake faults–Provo segment (WFZ) pairs, metrics values differed substantially between each of the paired faults, providing a strong indication of master versus subsidiary fault. Also, these results were consistent with other geologic and geophysical data related to fault geometry. For the Hansel Valley fault–North Promontory fault and Western Bear Lake fault–Eastern Bear Lake fault pairs, differences between metrics values for each of the paired faults were relatively small, and the somewhat equivocal indications of master versus subsidiary fault based on the metrics conflicted with other available geologic and geophysical data and assumptions based on regional observations. Ultimately, our identification of master and subsidiary faults used the metrics to provide initial results, but we modified these results when other information provided a compelling reason to do so.

West Valley fault zone–Salt Lake City segment: The metrics for the West Valley fault zone–Salt Lake City segment pair indicate the Salt Lake City segment of the WFZ is the master fault. The Salt Lake City segment is longer than the West Valley fault zone, the entire length of the West Valley fault zone is overlapped by the Salt Lake City segment, and the West Valley fault zone has almost no relief compared to the Salt Lake City segment (Figure 4.4-2, Table 4.4-1).

Utah Lake faults–Provo segment: The metrics for the Utah Lake faults–Provo segment pair indicate the Provo segment of the WFZ is the master fault. Relations among the metrics for the Utah Lake faults–Provo segment pair are very similar to those for the West Valley fault zone–Salt Lake City segment pair (Figure 4.4-2, Table 4.4-1).

Hansel Valley fault–North Promontory fault: The metrics for the Hansel Valley (+ Hansel Mountains [east side] + Hansel Valley [valley floor]) fault–North Promontory fault pair are equivocal, but give a slight indication of the Hansel Valley fault being the master fault (Figure 4.4-2, Table 4.4-1). However, given the distributed nature of the Hansel Valley fault system versus the more continuous, single trace of the North Promontory fault, the association of the North Promontory fault with a significant mountain range, and the regional pattern of major faults bounding the eastern margins of individual basins in the eastern Great Basin (see, for example, Arabasz *et al*., 1992), our consensus is that the North Promontory fault is very likely the master fault.

Western Bear Lake–Eastern Bear Lake faults: Similar to the Hansel Valley–North Promontory fault pair, the metrics for the Western Bear Lake (+ Bear Lake [west side]) fault–Eastern Bear Lake (Northern, Central, and Southern sections) fault pair are somewhat equivocal and slightly favor the Western Bear Lake fault as the master fault (Figure 4.4-2, Table 4.4-1). However, structural interpretation of seismic reflection profiles (Smith and Bruhn, 1984; Evans, 1991), as well as the regional pattern of major faults bounding the eastern margins of individual basins in the eastern Great Basin, indicates the Eastern Bear Lake fault system is likely the master fault.

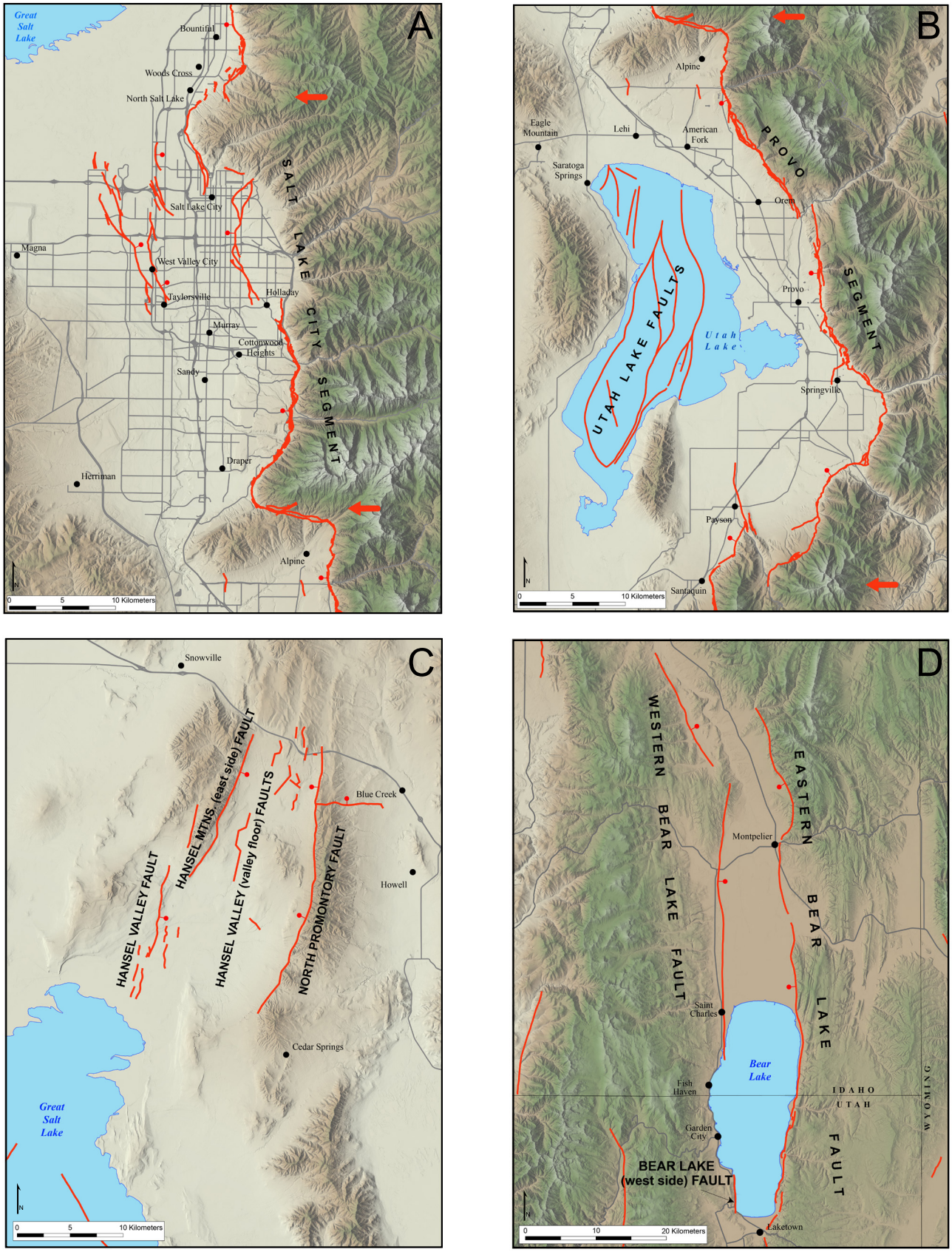

Figure 4.4-1. Antithetic fault pairs in the Wasatch Front region. Arrows indicate segment boundaries. (A) West Valley fault zone and SLCS of the WFZ. (B) Utah Lake faults and Provo segment of the WFZ. (C) Hansel Valley (+ Hansel Mountains [east side] + Hansel Valley [valley floor]) faults and North Promontory fault. (D) Western Bear Lake (+ Bear Lake [west side]) faults and Eastern Bear Lake fault. Note that scale varies among the four maps. Shaded topography generated from 10-m digital elevation data (https://lta.cr.usgs.gov/NED).

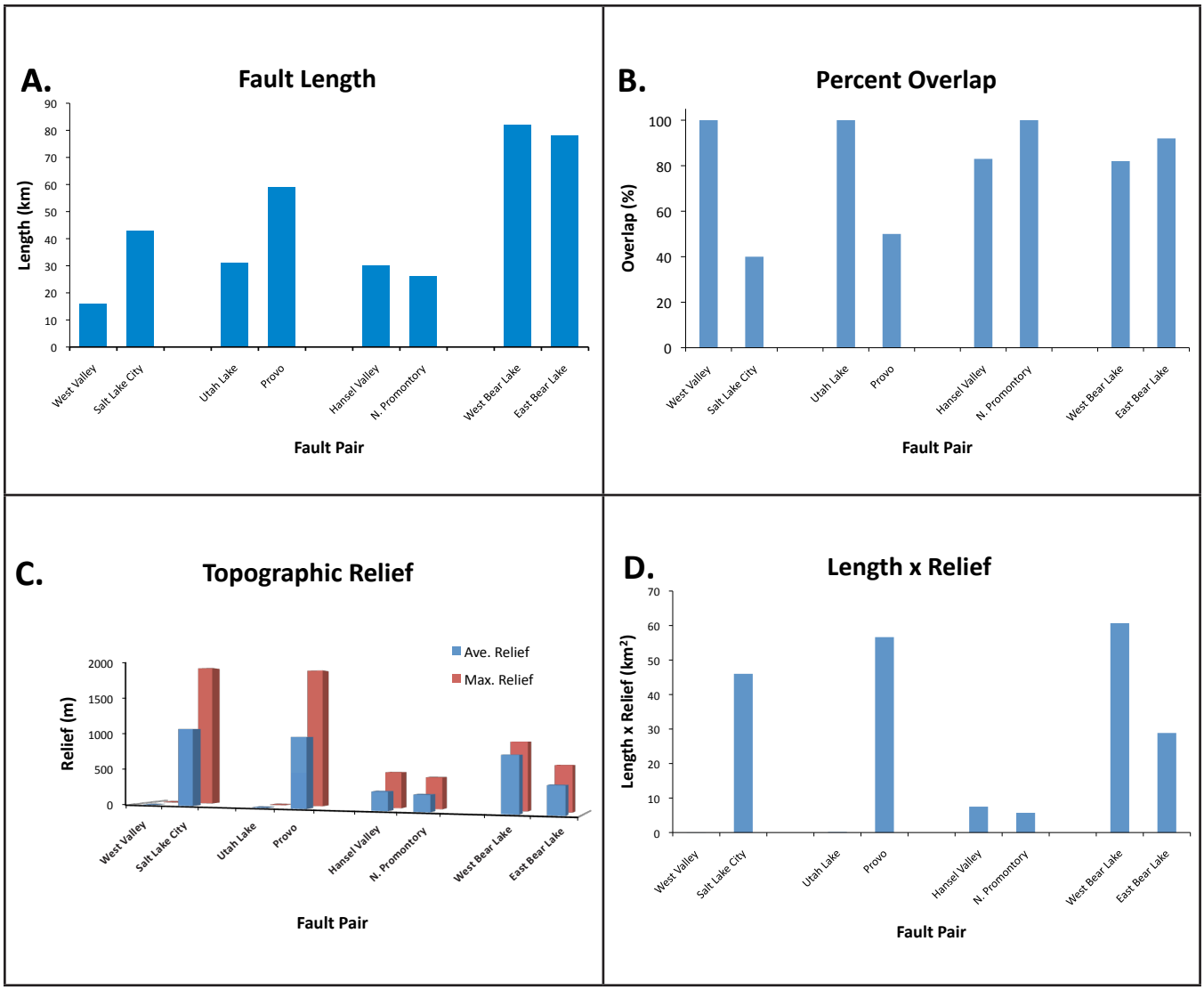

Figure 4.4-2. Graphical summary of antithetic-fault-pair metrics. (A) Fault surface-trace length from USGS (2013) except as noted in text discussion. Greater length can be considered an indication of the master fault (i.e., reflecting fault maturity). (B) Percent of fault length overlapped by the other fault in pair. Smaller percent overlap can be considered an indication of the master fault (i.e., larger, controlling structure). (C) Footwall relief. Greater relief can be considered an indication of the master fault (i.e., higher slip rate). (D) Length multiplied by average relief. Larger product can be considered an indication of the master fault (i.e., reflecting fault maturity and/or higher slip rate).

4.4.3 Model Parameters for Subsidiary Faults

Table 4.4-2 summarizes the model parameters used for the subsidiary faults of the four antithetic fault pairs evaluated, including minimum, average, and maximum fault separation distances (used in conjunction with fault dip to calculate truncation depths for subsidiary faults, and hence rupture area for earthquake magnitude calculations). Minimum and maximum truncation depths are 0.7 and 10 km for the West Valley fault zone, 2 and 22 km for the Utah Lake faults, 0.5 and 15 km for the Hansel Valley fault, and 1.4 and 9.3 km for the Western Bear Lake fault. Although the maximum truncation depth for the Utah Lake faults exceeds the seismogenic depth parameter used in the modeling (15 ± 3 km), we did not account for this minor discrepancy in the modeling given the small contribution of the Utah Lake faults to the forecast probabilities.

Table 4.4-2 also shows rupture models for each subsidiary fault (i.e., independent versus simultaneous rupture) and our consensus weights. For the West Valley fault zone, higher weight (0.75) is given to the simultaneous rupture model, as paleoseismic earthquake timing data (DuRoss and Hylland, 2014) and mechanical modeling constraints (e.g., Xiao and Suppe, 1992; Bruhn and Schultz, 1996) indicate a high potential for synchronous rupture (Hylland *et al*., 2014). Weights for the Utah Lake faults are 0.50/0.50, as sparse data preclude a sound basis for weighting one model higher than the other. The higher weight (0.60) for independent rupture of the Hansel Valley fault stems from the possibility that the 1934 Hansel Valley earthquake (M_L 6.6) may have nucleated on this fault, based on the presence of surface deformation along the fault (Walter, 1934; Shenon, 1936; dePolo *et al*., 1989), and the absence of documented surface rupture along the master(?)

Table 4.4-1. Summary of antithetic-fault-pair metrics.[1]

Fault or Segment	Length[2] (km)	Percent Overlap	Max. Relief (m)	Ave. Relief (m)	Length x Relief[3] (km^2)	Metrics-based Classification[4]	WGUEP Consensus Classification[3]
West Valley	16	100	6	2	0.0	Subsidiary	**Subsidiary**
Salt Lake City	43	40	1950	1070	46.0	Master	**Master**
Utah Lake	31	100	5	4	0.1	Subsidiary	**Subsidiary**
Provo	59	50	1880	960	56.6	Master	**Master**
Hansel Valley[5]	30	83	480	250	7.5	Master	**Subsidiary**
N. Promontory	26	100	420	220	5.7	Subsidiary	**Master[6]**
W. Bear Lake[7]	82	82	900	740	60.7	Master	**Subsidiary**
E. Bear Lake[8]	78	92	600	370	28.9	Subsidiary	**Master[6]**

[1] Shaded cells indicate data suggesting master fault.
[2] Length from USGS (2013) except as noted in text discussion.
[3] Rupture length multiplied by average footwall relief and rounded to the nearest 0.1 km.
[4] Subsidiary fault assumed to be truncated at depth by master fault.
[5] Includes Hansel Valley fault, Hansel Mountains (east side) faults, and Hansel Valley (valley floor) faults (see Figure 4.4-1C).
[6] Selection of master fault based on subsurface data and regional observations rather than metrics; see discussion in text.
[7] Includes Western Bear Lake and Bear Lake (west side) faults (see Figure 4.4-1D).
[8] Includes Northern, Central, and Southern sections.

Table 4.4-2. Model parameters for subsidiary antithetic faults.

Fault or Segment	Rupture Model	SRL[1] (km)	Dip (Degrees)	Fault Separation Distance (min., ave., max.) (km)
West Valley	Independent (0.25)	16	50 ± 15	3, 9, 14
	Simultaneous (0.75)			
Utah Lake	Independent (0.50)	31	50 ± 15	9, 17, 31
	Simultaneous (0.50)			
Hansel Valley	Independent (0.60)	30	50 ± 15	2, 9, 14
	Simultaneous (0.40)			
W. Bear Lake	Independent (0.40)	26[2]	50 ± 15	6, 9, 13
	Simultaneous (0.60)	24[3]		
		19[4]		

[1] SRL, surface rupture length (straight-line, end-to-end).
[2] Maximum documented rupture length, used when modeled with a Southern section Eastern Bear Lake fault rupture (SRL = 35 km) or floating rupture (SRL = 39 km) in the unsegmented model for the Eastern Bear Lake fault.
[3] When modeled with a Central section Eastern Bear Lake fault rupture (24 km), the Western Bear Lake fault SRL is limited to the SRL of the Central section Eastern Bear Lake fault to avoid a subsidiary fault SRL that exceeds the master fault SRL.
[4] When modeled with a Northern section Eastern Bear Lake fault rupture (19 km), the Western Bear Lake fault SRL is limited to the SRL of the Northern section Eastern Bear Lake fault to avoid a subsidiary fault SRL that exceeds the master fault SRL.

North Promontory fault. However, regional and teleseismic waveform analysis indicates a strike-slip focal mechanism for the 1934 earthquake (Doser, 1989), and the structural and seismogenic relations between the North Promontory fault and Hansel Valley fault remain uncertain. For the Western Bear Lake fault, higher weight (0.60) is given to the simultaneous rupture model based on the fault's likely structural relation with the Eastern Bear Lake fault from interpretation of seismic reflection profiles (Smith and Bruhn, 1984; Evans, 1991).

4.5 Other Modeled Faults

The Wasatch Front region contains 105 Quaternary-active faults/fault segments in addition to the WFZ and OGSLFZ (Black *et al*., 2003; URS Corporation, written communication, 2010; USGS, 2013). The quantity and quality of paleoseismic information available for those faults/fault segments is highly variable, and many have no paleoseismic trenching data. The available data show that these faults/fault segments range from 2 to 104 km long, have vertical slip rates from < 0.2 mm/yr to > 1.0 mm/yr, and times of most recent deformation ranging from historical to Quaternary (< 1.6 Ma; USGS, 2013). The fact that these faults can be recognized and mapped at the ground surface indicates that they have experienced at least one surface-rupturing earthquake in the past.

Not all of the 105 Quaternary-active faults/fault segments possess sufficiently robust seismic parameters to affect a probabilistic earthquake forecast that ranges from annually to 100 years. The WGUEP established the following screening criteria to identify faults/fault segments that would not have a significant impact on the WGUEP earthquake forecast.

1. Faults categorized by their "most recent prehistoric deformation" by the USGS (2013) as late and middle Quaternary (< 750 ka) or Quaternary (< 1.6 Ma) if they could not be plausibly linked to more recently active faults. See http://earthquake.usgs.gov/hazards/qfaults/glossary.php for definitions of the four USGS (2013) prehistoric deformation timing categories.

2. Faults less than 15 km long, if they cannot be plausibly linked with other faults/fault segments to form longer linked fault zones. Faults less than 15 km long are considered unlikely to generate an earthquake of **M** ≥ 6.75 (low end of magnitude range assigned by the WGUEP to recurrence models used to characterize individual fault sources). Earthquakes smaller than **M** 6.75 are accommodated as background earthquakes in the WGUEP earthquake forecast.

3. Group consensus – which chiefly involved retaining short faults (< 15 km) that would have otherwise been eliminated from further consideration, but that could be linked to form longer fault zones, even though the shorter faults are individually mapped and reported in the literature.

Note, for purposes of this evaluation, criteria used to establish a plausible link between individual fault strands included (1) along-strike alignment and continuity, (2) common slip direction, (3) fault overlaps, and (4) gaps or stepovers along strike generally ≤ 5 km (Wesnousky, 2008; Field *et al*., 2013; Biasi and Wesnousky, 2015).

Application of these screening criteria identified 60 faults/fault segments in the Wasatch Front region considered unlikely to affect the WGUEP earthquake forecast (Table 4.5-1) These faults were removed from further consideration in the WGUEP fault model. Table 4.5-2 lists the remaining 45 faults/fault segments retained as earthquake sources for the WGUEP earthquake forecast (Figure 1-1). These retained fault/fault segments were subsequently characterized, and are hereafter referred to in the forecast as "other modeled faults." Faults/fault segments reported in Table 4.5-2 that are < 15 km long are linked to form longer composite fault zones (Appendix D); faults/fault segments that are linked in the forecast share a common superscript number in Table 4.5-2.

Summary parameters from the USGS (2013) for both retained and deleted faults/fault segments (Table 4.5-3) show that all of the deleted faults/fault segments except one (Martin Ranch fault) have slip rates < 0.2 mm/yr; conversely, 37 (80%) of the retained faults/fault segments have similarly low slip rates, so slip rate per se was not a discriminating factor for eliminating faults/fault segments from the WGUEP forecast. Four deleted faults have times of most recent prehistoric deformation of latest Quaternary (< 15 ka) and five had deformation times of late Quaternary (< 130 ka); however, all eight faults are < 15 km long, and none could be plausibly linked to other faults/fault segments. All retained faults with lengths < 15 km or times of most recent prehistoric deformation of late to middle Quaternary (< 750 ka) or Quaternary (< 1.6 Ma) could be linked with other faults/fault segments to form longer fault zones considered capable of generating a **M** ≥ 6.75 earthquake (Table 4.5-2).

Using available paleoseismic information, we characterized (modeled) the 45 faults/fault segments retained in the WGUEP earthquake forecast (Table 4.5-2, Appendix D) using the following criteria.

- Rupture Model: Includes independent (unsegmented), linked (multiple short faults combined to form a longer fault zone), segmented, coseismic (independent or synchronous rupture of antithetic fault pairs), and deep or shallow penetrating for the Joes Valley fault zone and Snow Lake graben.
- Probability of Activity: Likelihood that a fault/fault segment is a seismogenic source capable of generating an earthquake within the modern stress field. Probabilities of activity < 1.0 variously reflect the possible influence

Table 4.5-1 Quaternary-active faults/fault segments in the Wasatch Front region removed from further consideration in the WGUEP earthquake forecast.

Almy fault zone	Ogden Valley North Fork fault
Bald Mountain fault	Ogden Valley northeastern margin faults
Bear River Range faults	Ogden Valley southwestern margin faults
Big Pass fault	Pavant faults
Blue Springs Hills faults	Pleasant Valley fault zone, Dry Valley graben
Cedar Mountains (east side) faults	Pleasant Valley fault zone, graben
Cedar Valley (south side) fault	Pleasant Valley fault zone, unnamed faults
Clover fault zone	Puddle Valley fault zone
Cricket Mountains (north end) faults	Raft River Mountains fault
Deseret faults	Round Valley faults
Dolphin Island fracture zone	Ryckman Creek fault
Duncomb Hollow fault	Sage Valley fault
East Canyon fault (southern section)	Saint John Station fault zone
East Kamas fault	Saleratus Creek fault
East Lakeside Mountains fault zone	Sheeprock fault zone
East side Sublette Range fault	Sheeprock Mountains fault
Elk Mountain fault	Simpson Mountains faults
Frog Valley fault	Southern Joes Valley fault zone
Gooseberry graben faults	Spring Creek fault
Hyrum fault	Sublette Flat fault
Japanese and Cal Valleys faults	Sugarville area faults
Lakeside Mountains (west side) faults	The Pinnacle fault
Little Diamond Creek fault	Valley Mountains monocline
Long Ridge (northwest side) fault	Vernon Hills fault zone
Long Ridge (west side) fault	Wasatch monocline
Lookout Pass fault	Western Bear Valley faults
Mantua area faults	West Pocatello Valley fault
Martin Ranch fault	White Mountain area faults
North Bridger Creek fault	Whitney Canyon fault
North Promontory Mountains fault	Woodruff fault

of non-seismogenic salt tectonics, geophysical data indicating a fault soles into a detachment surface at shallow depth, or that the fault is related to a stress field no longer active in the study area.

- Fault Category: *A* – WFZ and OGLFZ (considered elsewhere in this report); *B* – segmented faults thought to behave in a manner similar to the WFZ; *C* – unsegmented faults and short linked faults; *AFP* – antithetic fault pairs where the down-dip width of the secondary fault is truncated by the primary (master) fault at a relatively shallow seismogenic depth.
- Surface Rupture Length: Measured straight-line, end-to-end fault/fault segment length reported in USGS (2013), unless otherwise noted in Appendix D.
- Dip: Range in crustal fault dip of 50 ± 15 degrees as recommended to the USGS for the 2014 update of the NSHMs by BRPEWGII (Lund, 2012) and adopted by the WGUEP for most normal faults in the Wasatch Front region (section 3.2). Dips are weighted 35° (0.3), 50° (0.4), 65° (0.3). Exceptions are the Joes Valley fault zone and Snow Lake graben, which based on seismic-profile information and structural relations, are assigned a dip of 70° ± 15° weighted 55 (0.3), 70 (0.4), 85 (0.3).
- Seismogenic Depth: Range of seismogenic depths adopted by the WGUEP of 15 ± 3 km weighted 12 km (0.1), 15 km (0.7), 18 km (0.2) east of the WFZ, and 12 km (0.2), 15 km (0.7), 18 km (0.1) west of the WFZ, unless noted otherwise in Appendix D (Section 3.2).
- Vertical Slip Rate: Depending on available paleoseismic data, two types of vertical slip rates may be reported in Appendix D. The first and most common type is termed a "geologic slip rate" (USGS, 2013), which

Table 4.5-2 Other modeled faults—Quaternary-active faults/fault segments in the Wasatch Front region, other than the WFZ and OGSLFZ, retained in the WGUEP fault model. Superscripts indicate linked faults.

Bear River fault zone	Morgan fault
Broadmouth Canyon faults[1]	North Promontory fault
Carrington fault	Pavant Range fault[4]
Crater Bench fault[2]	Porcupine Mountain fault
Crawford Mountains (west side) fault	Red Canyon fault scarps[4]
Curlew Valley faults	Rock Creek fault
Drum Mountains fault zone[2]	Scipio fault zone[4]
East Cache fault zone	Scipio Valley faults[4]
Northern segment	Skull Valley (mid valley) faults
Central segment	Snow Lake graben
Southern segment[1]	Stansbury fault
East Dayton–Oxford faults	Northern segment
Eastern Bear Lake fault	Central segment
Northern segment	Southern segment
Central segment	Stinking Springs fault
Southern segment	Strawberry fault
Gunnison fault	Utah Lake faults
Hansel Valley fault[3]	West Cache fault zone
Hansel Mountains (east side) faults[3]	Clarkston fault
Hansel Valley (valley floor) faults[3]	Junction Hills fault
James Peak fault[1]	Wellsville fault
Joes Valley fault zone	West Valley fault zone
Little Valley faults	Granger fault[5]
Main Canyon fault	Taylorsville fault[5]
Maple Grove faults[4]	Western Bear Lake fault

Table 4.5-3. Fault/fault segment parameters from USGS (2013) for Quaternary-active faults/fault segments other than the WFZ and OGSLFZ in the Wasatch Front region.

Parameters		**Retained Faults**	**Excluded Faults**
Total[1]	105	45	60
Slip Rate			
< 0.2 mm/yr		37	59
> 0.2 mm/yr < 1.0 mm/yr		7	1
> 1.0 mm/yr < 5.0 mm/yr		1	0
Timing of Most Recent Movement			
Historical		1	0
Latest Quaternary < 15 ka		32	4
Late Quaternary < 130 ka		7	5
Late and Middle Quaternary < 750 ka		3	21
Quaternary < 1.6 Ma		2	30
Length			
0 – 10 km		4	29
11 – 20 km		15	17
21– 30 km		11	6
31 – 40 km		6	5
> 40 km		9	3

[1] Excludes the WFZ and OGSLFZ.

is typically determined from offset geologic features whose age can be estimated or measured. These rates usually average slip over a few to many earthquake cycles. The second type is calculated on the basis of known times and amounts of slip for two or more prehistoric earthquakes. Those data are generally obtained from detailed paleoseismic trenching investigations. This type of high-quality data is sparse for the "other modeled faults" in the Wasatch Front region.

- Recurrence Interval: Average time interval between surface-rupturing earthquakes. Intervals may be based on numerical dating (e.g., radiocarbon, optically stimulated luminescence, dendrochronology), or non-numerical methods (such as stratigraphy or geomorphology) (USGS, 2013). Similar to vertical slip-rate data, high-quality recurrence-interval data are sparse for the "other modeled faults" in the Wasatch Front region.
- Characteristic Magnitude: M_{char} is the characteristic magnitude for a rupture source, which assumes full rupture of the source and is computed from magnitude relations relating fault length, area, or seismic moment to magnitude. The "other modeled faults" in the WGUEP fault model for the Wasatch Front region (Table 4.5-2) are either *B*, *C*, or *AFP* faults (see section 3.6), the magnitude relations and weights used to determine M_{char} for the "Other" faults are presented in Table 3.6-2.

We used the fault parameter data summarized in Appendix D to help construct the WGUEP fault model (section 2.1.1). The fault model uses geologic observations (kinematic and paleoseismic data) to constrain fault geometry and long-term fault behavior. The model accommodates fault-specific complexities that allow analysis of a wide spectrum of earthquake sizes and rates in the Wasatch Front region. The data in Appendix D help address issues of fault segmentation, single versus multi-segment ruptures, frequency of earthquake occurrence, and appropriate M_{char} values for individual faults other than the WFZ and OGSLFZ in the WGUEP earthquake forecast.

The paleoseismic information used to characterize the faults/fault segments in Table 4.5-2 comes chiefly from the UQFPWG consensus preferred recurrence-interval and vertical slip-rate estimates for Utah Quaternary faults having paleoseismic trenching data (Lund, 2005), URS Corporation seismic-source parameter data for faults/fault segments in the Wasatch Front region (URS Corporation, written communication, 2010), the USGS (2013), and geologic literature available for individual faults/fault sections (see Appendix D for additional notes on information sources).

In addition to the weights assigned to the preferred ranges of crustal dips and seismogenic depths (see above), we also assigned weights where appropriate to alternative rupture models, to probability of activity, and to vertical slip-rate and recurrence-interval ranges. These weights reflect the consensus of the WGUEP based upon the available geologic and paleoseismic information available for the 45 faults/fault segments retained in the WGUEP model (Table 4.5-2).

4.6 Estimated Surface-Faulting Earthquakes < 18 ka in the WGUEP Wasatch Front Region

This section presents an estimate (minimum/preferred/maximum) of surface-faulting earthquakes in the WGUEP Wasatch Front region (Figure 1-1) for the past 18 kyr (Table 4.6-1). Hecker (1993) made a similar earthquake estimate for the past 15 kyr in the Wasatch Front region as defined by Arabasz *et al*. (1992). The boundaries of the Arabasz *et al*. (1992) region are approximately the same as the WGUEP region on the north, west, and south, but extend an additional 96 to 112 km farther east to the western part of the Uintah Basin (Hecker, 1993, Figure 8). Hecker (1993) evaluated 37 faults or fault segments believed to exhibit evidence of latest Pleistocene (< 15 ka) displacement. Time of faulting was chiefly evaluated based on the relation (younger or older) of fault displacement with Lake Bonneville highstand deposits, then thought to be 15 kyr old. Subsequent research has revised the time of the Bonneville highstand to 18 ka (Reheis *et al*., 2014); therefore, < 18 ka is the time interval used for the WGUEP surface-faulting-earthquake estimate. However, both the Hecker (1993) and WGUEP time intervals are based largely on the age of Lake Bonneville highstand deposits, and essentially represent the same time period.

The WGUEP surface-faulting-earthquake estimate includes 53 faults, fault segments, and composite fault zones (Table 4.6-1) that together comprise the WGUEP fault model. Differences between the Hecker (1993) and WGUEP fault models are chiefly due to (1) the greater amount of paleoseismic information now available for many Utah faults, and (2) the subsequent segmentation characterization of many longer Utah faults. Among the faults/fault segments in the WGUEP model not included in the Hecker (1993) estimate are the (1) three northern segments of the WFZ (Malad City, Clarkston Mountain, and Collinston), (2) four segments of the Great Salt Lake fault zone (Rozelle, Promontory, Fremont Island, Antelope Island), (3) the Northern segment of the East Bear Lake fault zone, (4) the East Tintic segment of the Oquirrh fault zone, (5) three segments of the East Cache fault zone (Northern, Central, Southern), (6) three segments of the Stansbury fault (Northern, Central, Southern), (7) three faults that comprise the West Cache fault zone (Clarkston, Junction Hills, Wellsville), and (8) the Carrington, Crawford Mountains (west side), Curlew Valley, Little Valley, Main Canyon, Porcupine Mountain, Rock Creek, Skull Valley, and Stinking Springs faults. Faults in the Hecker (1993) evaluation not in the WGUEP fault model include the Big Pass, Puddle Valley, Clear Lake, Tabernacle, Cricket Mountains, and Mantua area faults. The WGUEP either considered these faults not sufficiently active to affect the WGUEP earthquake probability forecast (Section 4.5), or they are outside the WGUEP Wasatch Front region.

Table 4.6-1. Estimated surface-faulting earthquakes < 18 ka for the WGUEP Wasatch Front region.

WASATCH FAULT ZONE								
Segment Name	**Most Recent Deformation**	**Quantity/ Quality Paleoseismic Data[2]**	**WGUEP Slip Rate (mm/yr)**	**WGUEP Recurrence Interval (kyr)**	**Displacement (m)**	**Documented Paleoearthquakes < 18 ka**	**Estimated Number Earthquakes (*N*) < 18 ka min/pref/max**	**Comments**
Malad City	> 18 kyr[1]	3	0.01 – 0.1[1]	–	≤ 1.5[1]	_	0/0/1	No known scarps on latest Pleistocene or Holocene deposits. Allow for the possibility of a single surface-faulting earthquake since 18 ka.
Clarkston Mountain	> 18 kyr[1]	3	0.01 – 0.1[1]	–	2.0[1]	_	0/0/1	No known scarps on latest Pleistocene or Holocene deposits. Allow for the possibility of a single surface-faulting earthquake since 18 ka.
Collinston	> 18 kyr[1]	3	0.01 – 0.1[1]	–	≤ 2.0[1]	_	0/0/1	No known scarps on latest Pleistocene or Holocene deposits. Allow for the possibility of a single surface-faulting earthquake since 18 ka.
Brigham City	Holocene	1	0.6/1.0/1.4[3]	1.5 ± 0.1[4]	1.2/1.7/2.1[5]	4 < 5.9 ± 0.4 ka[4]	6/11/15	*N* estimated from long-term slip rate and average displacement. Minimum number from paleoseismic trench observations.
Weber	Holocene	1	0.6/1.0/1.4[3]	1.4 ± 0.3[4]	1.1/2.4/4.1[5]	5 < 7.1 ± 1.4 ka[4]	5/8/11	*N* estimated from long-term slip rate and average displacement. Minimum number from paleoseismic trench observations.
Salt Lake City	Holocene	1	0.6/1.0/1.4[3]	1.3 ± 0.09[4]	1.2/1.7/2.2[5]	9< 16.5 ± 1.9 ka	9/9/10	Paleoseismic trench data (DuRoss *et al*., 2014).
Provo	Holocene	1	0.6/1.0/1.4[3]	1.2 ± 0.03[4]	1.3/2.6/3.6[5]	5< 6.1 ± 0.2 ka[4]	5/7/10	*N* estimated from long-term slip rate and average displacement. Minimum number from paleoseismic trench observations.
Nephi	Holocene	1	0.6/1.0/1.4[3]	1.1 ± 0.04[4]	1.5/2.0/2.7[5]	3< 3.2 ± 0.1 ka[4]	5/9/13	*N* estimated from long-term slip rate and average displacement. Minimum number from paleoseismic trench observations.
Levan	Holocene	2	0.1 – 0.6[1]	> 3 & < 12[1]	1.8 – 3.0[1]	1	1/3/4	Interpolated to mid-range displacement and slip-rate values to obtain preferred earthquake estimate.
Fayette	Holocene	3	0.01 – 0.1[1]	–	0.8 – 1.6[1]	–	1/2/3	Based on Hylland (2007b) and Hylland and Machette (2008)
						Totals	**32/49/69**	

Table 4.6-1. Continued.

OQUIRRH–GREAT SALT LAKE FAULT ZONE									
Segment Name	**Most Recent Deformation**	**Quantity/ Quality Paleoseismic Data[2]**	**WGUEP Slip Rate (mm/yr)**	**WGUEP Recurrence Interval (kyr)**	**WGUEP Length (km)**	**D_{ave} = 0.044L[6] (m)**	**Documented Paleoearthquakes < 18 ka**	**Estimated Number Earthquakes (*N*) < 18 ka min/pref/max**	**Comments**
Rozelle	Holocene	3	–	_	25	1.10	_	3/4/10	Assume similar recurrence interval as the Antelope Island segment (Dinter and Pechmann, 2012).
Promontory	Holocene	3	–	_	25	1.10	_	3/4/10	Assume similar recurrence interval as the Antelope Island segment (Dinter and Pechmann, 2012).
Fremont Island	Holocene	2	–	4.2 ± 2.4 ka	25	1.10	3	3/4/10	Based on WGUEP recurrence interval.
Antelope Island	Holocene	2	0.3/0.6/1.6	4.2 ± 2.4 ka	35	1.54	3	3/4/10	Based on WGUEP recurrence interval.
Northern Oquirrh	Holocene	2	0.05/0.2/0.4	–	30	1.32	1	1/1/1	Paleoseismic trench data (Olig *et al.*, 1994, 1996).
Southern Oquirrh	Holocene	2	0.05/0.2/0.4	–	31	1.36	1	1/1/1	Similar to Northern Oquirrh segment, one documented event post 18 ka, penultimate event likely > 20 ka (Olig *et al.*, 1999a, 1999b, 2001).
Topliff Hills	?	2	0.05/0.2/0.4	–	23	1.01	?	0/0/1	Timing of most recent surface faulting earthquake pre- or post-Bonneville is ambiguous (Everitt and Kaliser, 1980; Barnhard and Dodge, 1988).
East Tintic	Middle-Late Pleistocene	3	0.025/0.1/0.2	–	40	1.76	_	0/0/2	*N* estimated from slip-rate and average-displacement data.
							Totals	**14/18/45**	

Table 4.6-1. Continued.

OTHER MODELED FAULTS									
Fault Name	**Most Recent Deformation[7]**	**Quantity/ Quality Paleoseismic Data[2]**	**WGUEP Slip Rate (mm/yr)**	**WGUEP Recurrence Interval (kyr)**	**WGUEP Length (km)**	**D_{ave} = 0.044L[6] (m)**	**Documented Paleoearthquakes < 18 ka**	**Estimated Earthquakes (*N*) < 18 ka min/pref/max**	**Comments**
Bear River fault zone	Latest Quaternary (< 15 ka)	2	–	1.0/2.3/3.5	35	–	2	2/2/2	Paleoseismic trench data (West, 1994). Geologically young fault with no associated range front and only two documented surface-faulting earthquakes.
Carrington fault	Latest Quaternary (< 15 ka)	3	–	1.8/4.2/6.6	~28	–	_	3/4/10	Assumed similar recurrence interval as the Antelope Island segment.
Crater Bench fault and Drum Mountains fault zone	Latest Quaternary (< 15 ka)	2	0.01/0.04/0.2	–	52	2.29	1?	0/1/2	Fault displaces the Provo shoreline of Lake Bonneville so has experienced at least one Latest Quaternary (< 15 ka) surface-faulting earthquake (Crone, 1983b).
Crawford Mountains (west side) fault	Late Quaternary (< 130 ka)	3	0.01/0.02/0.04	–	25	1.10	–	0/0/1	Low slip-rate fault reported to show evidence for late Pleistocene activity (USGS, 2013). Allow for the possibility of a single surface-faulting earthquake since 18 ka.
Curlew Valley faults	Latest Quaternary (< 15 ka)	3	0.1/0.3/0.8	–	20	0.88	–	2/6/16	Large scarps (≤ 24 m) likely cut Lake Bonneville lacustrine deposits. *N* estimated from slip-rate and average-displacement data.
East Cache fault zone									
Northern section	Quaternary (< 1.6 Ma)	3	0.04/0.1/0.2	–	41	1.80	–	0/1/2	*N* estimated from slip-rate and average-displacement data.
Central section	Latest Quaternary (< 15 ka)	2	0.04/0.2/0.4	4/10/15	17	0.75	2	2/2/2	Paleoseismic trenching data (McCalpin and Forman, 1991; McCalpin, 1994).
Southern section – includes the Broadmouth Canyon faults and James Peak fault	Late Quaternary (< 130 ka)	2	0.01/0.03/0.07	10/50/100	29	1.28	–	0/0/0	Paleoseismic trenching data (McCalpin and Evans (2012). Most recent surface-faulting earthquake is at least 26 ka.

Table 4.6-1. Continued.

Fault Name	Most Recent Deformation[7]	Quantity/ Quality Paleoseismic Data[2]	WGUEP Slip Rate (mm/yr)	WGUEP Recurrence Interval (kyr)	WGUEP Length (km)	D_{ave} = 0.044L[6] (m)	Documented Paleoearthquakes < 18 ka	Estimated Earthquakes (*N*) < 18 ka min/pref/max	Comments
East Dayton – Oxford faults	Late Quaternary (< 130 ka)	3	0.01/0.05/0.1	–	23	1.01	–	0/0/2	*N* estimated from slip-rate and average-displacement data. No documented evidence of Latest Quaternary fault scarps, but steep mountain front abruptly terminates Quaternary deposits. Allow for the possibility of two surface-faulting earthquakes since 18 ka.
Eastern Bear Lake fault									
Northern section	Middle and Late Quaternary (< 750 ka)	3	0.1/0.3/0.8	–	19	0.84	–	2/6/17	*N* estimated from slip-rate and average-displacement data.
Central section	Latest Quaternary (< 15 ka)	3	0.2/0.6/1.6	–	24	1.06	–	3/10/27	*N* estimated from slip-rate and average-displacement data, assigned same slip rate as the Southern section.
Southern section	Latest Quaternary (< 15 ka)	2	0.2/0.6/1.6	3/8/15	35	1.54	2	2/2/3	Earthquake estimate based on paleoseismic trenching information presented in McCalpin (2003) and Lund (2005). Note that the preferred and maximum earthquake counts for the Southern section based on trenching data are significantly less than those for the Central and Northern sections, which are based on slip rate and average per event displacement.

Table 4.6-1. Continued.

Fault Name	Most Recent Deformation[7]	Quantity/ Quality Paleoseismic Data[2]	WGUEP Slip Rate (mm/yr)	WGUEP Recurrence Interval (kyr)	WGUEP Length (km)	D_{ave} = 0.044L[6] (m)	Documented Paleoearthquakes < 18 ka	Estimated Earthquakes (*N*) < 18 ka min/pref/max	Comments
Faults along the western edge of Scipio Valley and eastern base of the Pavant Range. From south to north includes the Red Canyon fault scarps, Maple Grove faults, Pavant Range fault, Scipio fault zone, and Scipio Valley faults.	Latest Quaternary (< 15 ka) to Late Quaternary (< 130 ka)	3	0.02/0.1/0.4	–	45	1.98	–	1/1/4	Several north-striking, individually short faults along the north side of the Pavant Range and the western side of Scipio Valley that are in close alignment, some show evidence for at least one Latest Quaternary surface-faulting earthquake (Anderson and Bucknam, 1979; Bucknam and Anderson, 1979). Maximum earthquake estimate based on slip rate and average displacement.
Gunnison fault	Late Quaternary (< 130 ka)	3	0.02/0.1/0.4	–	42	1.85	–	1/1/4	Assigned similar slip rate as faults along the west side of Scipio Valley and the north side of the Pavant Range. *N* estimated from slip-rate and average-displacement data.
Hansel Valley fault, Hansel Mountains (east side) faults, and Hansel Valley (valley floor) faults	Historic to Late Quaternary (< 130 ka)	2	0.06/0.1/0.2	–	30	1.32	2	2/2/3[8] 1/1/2[9]	Antithetic to the North Promontory fault, independent rupture given 60% weight (Table 4.4-2). The fault exhibits an irregular pattern of surface faulting with inter-event intervals ranging from possibly as little as 1-2 kyr to more than 30 kyr, indicating that earthquake recurrence has been highly variable through time (McCalpin *et al.*, 1992). The Hansel Valley fault produced Utah's only historical surface-faulting earthquake. Maximum earthquake estimate based on slip rate and average displacement.

Table 4.6-1. Continued.

Fault Name	Most Recent Deformation[7]	Quantity/ Quality Paleoseismic Data[2]	WGUEP Slip Rate (mm/yr)	WGUEP Recurrence Interval (kyr)	WGUEP Length (km)	D_{ave} = 0.044L[6] (m)	Documented Paleoearthquakes < 18 ka	Estimated Earthquakes (*N*) < 18 ka min/pref/max	Comments
Joes Valley fault zone (combined)	Latest Quaternary (< 15 ka)	2	–	5/10/50	37	1.63	1	1/1/4	Available paleoseismic information indicates one surface-faulting earthquake post ~15 ka. Maximum earthquake estimate based on recurrence interval.
Little Valley faults	Latest Quaternary (< 15 ka)	3	0.02/0.1/0.4	–	20	0.88	–	0/2/8	Assigned similar slip rate as faults along the west side of Scipio Valley and the north side of the Pavant Range. *N* estimated from slip-rate and average-displacement data.
Main Canyon fault (formerly East Canyon east side faults)	Latest Quaternary (< 15 ka)	2	0.01/0.02/0.04	–	26	1.14	1	1/1/2	Paleoseismic trenching data (Piety *et al.*, 2010).
Morgan fault	Latest Quaternary (< 15 ka) to Middle and late Quaternary (< 750 ka)	2	0.01/0.02/0.04	25/100	17	0.75	1	1/1/1	Sullivan *et al.* (1988) and Sullivan and Nelson (1992) report evidence for a Latest Quaternary (< 15 ka) surface-faulting earthquake. Allow for the possibility of a single surface-faulting earthquakes since 18 ka.
North Promontory fault	Latest Quaternary (< 15 ka)	2	0.1/0.2/0.5	–	26	1.14	1	1/1/8	McCalpin *et al.* (1992) state that all that can be said with confidence is that fault has sustained surface rupture at least once since Bonneville time (< 18 ka) and several times since either oxygen isotope stage 4 or 6 time. Maximum earthquake estimate based on slip rate and average displacement.

Table 4.6-1. Continued.

Fault Name	Most Recent Deformation[7]	Quantity/ Quality Paleoseismic Data[2]	WGUEP Slip Rate (mm/yr)	WGUEP Recurrence Interval (kyr)	WGUEP Length (km)	D_{ave} = 0.044L[6] (m)	Documented Paleoearthquakes < 18 ka	Estimated Earthquakes (*N*) < 18 ka min/pref/max	Comments
Porcupine Mountain fault	Late Quaternary (< 130 ka)	3	0.01/0.02/0.04	–	35	1.54	–	0/0/1	Low slip-rate fault offsets apparently young (Holocene-latest Pleistocene?) alluvial fans (Jon King, Utah Geological Survey, written communication, 2000). Allow for the possibility of a single surface-faulting earthquake since 18 ka.
Rock Creek fault	Latest Quaternary (< 15 ka)	2	0.2/0.6/1.0	0.6/4/10	41	1.80	2	2/2/8	Minimum and preferred earthquake estimates based on paleoseismic trenching data (McCalpin and Warren, 1992). Maximum earthquake estimate based on slip rate and average displacement, but account for a most recent event on the fault at about 3.6 ± 0.3 ka.
Skull Valley (mid valley) faults	Latest Quaternary (< 15 ka)	2	0.05/0.3/0.5	–	34	1.50	–	0/3/6	*N* estimated from slip-rate and average-displacement data.
Snow Lake graben	Latest Quaternary (< 15 ka)	3	–	5/10/50	26	1.14	–	1/2/4	Assigned similar recurrence interval range as the Joes Valley fault zone. Lacks paleoseismic trenching data to refine minimum and preferred earthquake estimates.
Stansbury fault									
Northern segment	Latest Quaternary (< 15 ka)	3	0.07/0.4/1.0	–	24	1.06	–	1/7/17	*N* estimated from slip-rate and average-displacement data.
Central segment	Latest Quaternary (< 15 ka)	3	0.07/0.4/1.0	–	33	1.45	–	1/5/12	*N* estimated from slip-rate and average-displacement data.
Southern segment	Quaternary (< 1.6 Ma)	3	0.07/0.4/1.0	–	17	0.75	–	1/10/24	*N* estimated from slip-rate and average-displacement data.

Table 4.6-1. Continued.

Fault Name	Most Recent Deformation[7]	Quantity/ Quality Paleoseismic Data[2]	WGUEP Slip Rate (mm/yr)	WGUEP Recurrence Interval (kyr)	WGUEP Length (km)	D_{ave} = 0.044L[6] (m)	Documented Paleoearthquakes < 18 ka	Estimated Earthquakes (*N*) < 18 ka min/pref/max	Comments
Stinking Springs fault	Late Quaternary (< 130 ka)	3	0.03/0.1/0.3	–	10[10]	0.44	–	1/4/12	Assume similar slip-rate distributions as the Strawberry fault. Fault disappears beneath Strawberry reservoir, so total fault length is unknown. Estimated from slip-rate and average-displacement data.
Strawberry fault	Latest Quaternary (< 15 ka)	2	0.03/0.1/0.3	–	32	1.41	2?	1/2/3	Earthquake timing displacement data are lacking for the main fault. Trenches across a subsidiary fault exposed evidence for two to three earthquakes displacing alluvial-fan deposits estimated to be 15 to 30 ka based on soil development (Nelson and Martin, 1982; Nelson and Van Arsdale, 1986; Lund, 2005).
Utah Lake faults	Latest Quaternary (< 15 ka)	3	0.1/0.4/0.6	–	31	1.36	–	1/5/8[8] 0/3/4[9]	Antithetic to the Provo segment of the Wasatch fault zone, independent rupture given 50% weight (Table 4.4-2). Assigned same slip-rate range as the West Valley fault zone. *N* estimated from slip-rate and average-displacement data.
West Cache fault									
Clarkston fault	Latest Quaternary (< 15 ka)	2	0.1/0.4/0.7	–	21	0.92	1	1/2/3	Paleoseismic trench data (Black *et al.*, 2000).
Junction Hills fault	Latest Quaternary (< 15 ka)	2	0.05/0.1/0.2	–	24	1.06	1	1/1/1	Paleoseismic trench data (Black *et al.*, 2000).
Wellsville fault	Latest Quaternary (< 15 ka)	2	0.05/0.1/0.2	–	20	0.88	1	1/1/2	Paleoseismic trench data (Black *et al.*, 2000).

Table 4.6-1. Continued.

Fault Name	Most Recent Deformation[7]	Quantity/ Quality Paleoseismic Data[2]	WGUEP Slip Rate (mm/yr)	WGUEP Recurrence Interval (kyr)	WGUEP Length (km)	D_{ave} = 0.044L[6] (m)	Documented Paleoearthquakes < 18 ka	Estimated Earthquakes (*N*) < 18 ka min/pref/max	Comments
West Valley fault zone (combined Taylorsville and Granger faults)	Latest Quaternary (< 15 ka)	2	0.1/0.4/0.6	–	16	0.70	6	6/6/6[8] 2/2/2[9]	Antithetic to the Salt Lake City segment of the Wasatch fault zone, independent rupture given 25% weight (Table 4.4-2). Paleoseismic trench data (Hylland *et al*., 2014).
Western Bear Lake fault	Latest Quaternary (< 15 ka)	2	0.1/0.5/0.8	–	26	1.14	2	2/2/13[8] 1/1/5[9]	Antithetic to the Eastern Bear Lake fault, independent rupture given 40% weight (Table 4.4-2). Minimum and preferred earthquake estimates based on paleoseismic trench data (McCalpin, 1990, 2003). Maximum earthquake estimate based on slip rate and average displacement, and the fact that paleoseismic data are only available for one of the two major strands of this fault.
							Total Total adjusted for antithetic faults	44/106/238 **37/98/221**	
							Total estimated surface-faulting earthquakes < 18 ka for the WGUEP Wasatch Front region	83/165/335	
							Regional recurrence interval	217/109/54 yrs	

[1] Table 4.2-1.
[2] (1) High-quality paleoseismic data from multiple trenching investigations. (2) Limited or poor quality paleoseismic data from trenching investigations. (3) No paleoseismic trenching data.
[3] Table 4.1-4, Composite long-term slip rate related to the latest-Pleistocene Provo phase and highstand of Lake Bonneville (~15–18 ka).
[4] Table 4.1-2, Open mean recurrence interval (*N*-in-*T*)
[5] Table 4.1-3, Modeled D (displacement curves), mean (μ) value used to estimate number of earthquakes.
[6] For segmented faults lacking detailed paleoseismic displacement data, the WGUEP estimated average displacement (AD) using an L-AD linear regression calculated for the central WFZ (Figure 3.6-1), where AD = 0.044, and L = Lseg. Lacking displacement data for most of the "other modeled faults" in the WGUEP fault model, this relation was adopted here to determine an AD for those faults, segmented or not, for which little or no displacement data were available.
[7] From the *Quaternary Fault and Fold Database of the United States* (USGS, 2013).
[8] Earthquake estimate if fault is an independent seismic source.
[9] Earthquake estimate if an antithetic fault, percentage of independent ruptures based on Table 4.4-2.
[10] Part of fault lies beneath Strawberry reservoir, so total fault length unknown.

Paleoseismic information available for the 53 faults, fault segments, and composite fault zones in the WGUEP fault model is highly variable, ranging from a likely complete or nearly complete surface-faulting record since 16.5 ± 1.9 ka for the Salt Lake City segment of the WFZ (DuRoss *et al*., 2014), to no paleoseismic data at all for several faults (e.g., Rozelle and Promontory segments of the Great Salt Lake fault zone). In almost every case, even for faults with paleoseismic information, the surface-faulting record rarely extends beyond middle- to early-Holocene time, so little information exists regarding surface faulting in the Wasatch Front region from ~6 to 18 ka. Table 4.6-1 provides a numerical ranking of the general quality and completeness of the paleoseismic data available for the faults in the WGUEP fault model.

Because paleoseismic data are lacking or incomplete for many faults in the WGUEP fault model, estimating the number of surface-faulting earthquakes over the past 18 kyr in the Wasatch Front region required making several assumptions about fault behavior (particularly for faults with little or no paleoseismic data), and interpolating mostly late- to middle-Holocene paleoseismic data into the past. Key assumptions made for the WGUEP surface-faulting-earthquake estimate include:

1. A single, long-term (18 kyr) slip-rate range of 0.6/1.0/1.4 mm/yr is applicable to the five central segments of the WFZ (Section 4.1.4).
2. Except where long-term slip-rate or recurrence-interval data indicate otherwise, WGUEP consensus slip rates (Appendix D) are applicable for the past 18 kyr.
3. For faults with little or no displacement data, the formula $D_{ave} = 0.044\ L$, where D_{ave} = average displacement and L = fault/fault segment length, was used to estimate average per event displacement. The WGUEP originally developed this relation for segmented faults (Section 3.6), but its use is extended here to all faults/fault segments with no or limited displacement data.
4. Except where long-term recurrence data permit, average displacement and consensus WGUEP slip-rate (SR) values were used to estimate average surface-faulting recurrence (D_{ave}/SR = average recurrence).
5. Faults with no paleoseismic data act like other, similar faults for which data are available. The explicit assumptions made are the following:
    a. The Rozelle and Promontory segments of the Great Salt Lake fault zone and the Carrington fault behave like the Antelope Island segment of the Great Salt Lake fault zone (Section 4.3 and Appendix D).
    b. The Southern Oquirrh fault segment behaves like the Northern Oquirrh fault segment (Section 4.3).
    c. The Central section of the Eastern Bear Lake fault behaves like the Southern section of the fault (Appendix D).
    d. The Gunnison and Little Valley faults behave like the faults along the western side of Scipio Valley and the north side of the Pavant Range (Appendix D).
    e. The Snow Lake graben behaves like the Joes Valley fault zone (Appendix D).
    f. The Stinking Springs fault behaves like the Strawberry fault (Appendix D).
    g. The Utah Lake faults behave like the West Valley fault zone (Appendix D).
6. Faults in the WGUEP fault model identified as antithetic to master faults (Section 4.4) produce independent earthquakes at rates stipulated by the total rate multiplied by the weight for the independent rupture model in Table 4.4-2. Only independent ruptures on antithetic faults were included in the WGUEP surface-faulting-earthquake estimate.

Using available paleoseismic data and considering the assumptions above, we estimate the following numbers of surface-faulting earthquakes (minimum/preferred/maximum): 32/49/69 for the WFZ, 14/18/45 for the Oquirrh–Great Salt Lake fault zone, and 37/98/221 for the "other modeled faults" in the WGUEP fault model (includes only independent events on antithetic faults) (Table 4.6-1). Summed earthquake values for the Wasatch Front region as a whole are 83/165/335. Note that only 30% of the preferred number of earthquakes in the Wasatch Front region over the past 18 kyr occurred on the WFZ. The WGUEP surface-faulting-earthquake estimate is higher than the Hecker (1993) estimate (50/85/120) chiefly because the WGUEP fault model includes more faults/fault segments, 53 versus 37, and a longer time period, 18 versus 15 kyr. However, the WGUEP maximum earthquake estimate is approximately three times larger than the Hecker (1993) maximum estimate, which is significantly greater than would be expected based only on the larger number of faults and longer time period of the WGUEP estimate. The approximate three-fold increase in the maximum number of earthquakes between the Hecker (1993) and WGUEP surface-faulting-earthquake estimates reflects the broad range of the slip-rate values assigned by the WGUEP to faults with limited or no paleoseismic data to capture uncertainty in faults behavior.

High slip rates result in short average recurrence intervals and a correspondingly greater number of surface-faulting earthquakes for a given time interval. The calculated maximum earthquake numbers for several faults in the Wasatch Front region are intuitively too high, e.g., 24 surface-faulting earthquakes on the Southern segment of the Stansbury fault. However, given the broad slip-rate range assigned to that fault segment (0.07/0.4/1.0 mm/yr), and the estimated average per event displacement (0.75 m) (Table 4.6-1), the fault segment theoretically could produce 24 surface-faulting earthquakes in 18 kyr. High maximum earthquake values for several no or low-data faults in Table 4.6-1 are included in the WGUEP surface-faulting-earthquake estimate to honor the WGUEP

consensus slip-rate values. In instances where a long-term earthquake record is available (e.g., Central segment of the East Cache fault zone, Southern section of the Eastern Bear Lake fault), the maximum number of documented earthquakes in the past 18 kyr is significantly less than maximum values determined from average displacement and slip rate. The exceptions are the five central segments of the WFZ which have comparatively good paleoseismic data. There, better constrained average displacement data result in earthquake counts for the Brigham City, Weber, Provo, and Nephi segments that approximate the long-term paleoseismic record for the Salt Lake City segment (i.e., where available, good data provide better estimates).

Based on a surface-faulting-earthquake estimate of 50/85/120 since 15 ka, Hecker (1993) reported regional surface-faulting recurrence intervals of 300/175/125 years. The WGUEP surface-faulting-earthquake estimate (83/165/335) results in regional surface-faulting recurrence values of 217/109/54 years since 18 ka (Table 4.6-1). The short minimum recurrence interval (54 yr) reflects the high maximum number of surface-faulting earthquakes for the WGUEP Wasatch Front region that results from the broad slip-rate ranges assigned by the WGUEP to low/no data faults, and indicates that the WGUEP maximum earthquake number is a conservative high estimate.

5 HISTORICAL SEISMICITY CATALOG AND A BACKGROUND EARTHQUAKE MODEL

This section describes the principal aspects of the construction and analysis of an earthquake catalog that serves as the basis for a background earthquake model for the Wasatch Front region. Further details of the catalog and its analysis are provided in Appendix E. Acronyms and abbreviations are defined on pages xii to xiv.

5.1 Overview

As introduced in Section 2.1.2, *background earthquakes* are those not associated with known faults and of a size generally below the threshold of surface faulting. The background earthquake model depicts the frequency-magnitude distribution of future mainshocks in the study region expected to occur on seismic sources other than the faults included in the WGUEP fault model (Section 2.1.1). For the purposes of the probability estimates in this report, the background earthquake model provides rates of future mainshocks of **M** 5.0 or greater up to a maximum of **M** 6.75 ± 0.25. This analysis of background seismicity in the Wasatch Front region is distinguished from earlier ones, such as those of Youngs *et al*. (1987, 2000) and Pechmann and Arabasz (1995), by more thorough and rigorous treatments of the earthquake record, magnitude estimates, and magnitude uncertainties.

Our desired background earthquake model requires an up-to-date earthquake catalog that meets the needs of state-of-practice seismic hazard analysis, namely, a catalog that: (1) is complete in terms of accounting for all known earthquakes in the magnitude range of interest, (2) assigns a uniform moment magnitude to each event, (3) identifies "dependent" events (foreshocks, aftershocks, and the smaller events of earthquake swarms) in earthquake clusters that can be removed for statistical analysis of mainshock recurrence parameters, (4) excludes non-tectonic seismic events such as blasts and mining-induced seismicity, and (5) quantifies the uncertainty and rounding error associated with the assigned magnitude of each earthquake.

Two U.S. studies exemplify the rigorous development and treatment of earthquake catalogs for calculating background seismicity rates: EPRI/DOE/NRC (2012) for the central and eastern U.S., and Felzer (2007) for California. We have used the former study, first, as a *general* guide in developing an earthquake catalog with uniform moment magnitude for the Wasatch Front region and, second, for methodology guidance in handling magnitude uncertainties for calculating unbiased seismicity rate parameters. In Appendix E, we explain how we depart from the EPRI/DOE/NRC (2012) methodology.

Section 5.2 outlines the steps taken to develop an earthquake catalog for the Wasatch Front region that unifies existing catalogs of the two primary agents of seismic monitoring within the study region: the University of Utah Seismograph Stations (UUSS) and the USGS. In Section 5.3, we explain the handling of various size measures in the earthquake record together with magnitude conversions to uniform moment magnitude, and we explain the importance of magnitude uncertainty. The resulting earthquake catalog is described in Section 5.4, including its "declustering" to achieve a catalog of independent mainshocks and how we assessed periods of completeness for different magnitude ranges. Finally, in Sections 5.5 and 5.6 we summarize the calculation of unbiased seismicity rate parameters that constitute the background earthquake model for the Wasatch Front region.

5.2 Steps in Developing a Unified Earthquake Catalog

To develop a unified earthquake catalog with uniform moment magnitude, we carried out the following basic steps:

- Selection of a catalog region large enough for effective declustering around the edges of the region of interest.
- Merging, chronological sorting, and editing of individual line entries from diverse UUSS and USGS source catalogs—accounting for all reported earthquakes, removing duplicates and non-tectonic events, and selecting the line entry with the preferred time and location for each unique earthquake.
- Compilation and evaluation of available size measures for each event in the master catalog.
- Assessment of magnitude uncertainties and rounding errors for individual magnitudes.
- Tabulation of available instrumental measurements of moment magnitude, **M**, for earthquakes in the catalog region.
- Determination of conversion relationships between **M** and other available size measures using general orthogonal regression (for comparison, corresponding ordinary least-squares regressions were also performed).
- Assignment of a uniform moment magnitude to each earthquake in the master catalog, based on either direct measurement or conversion from other size measures (duly accounting for the propagation of uncertainties).

To give the reader a general understanding of the makeup of the master catalog, we next describe its spatial extent and the data sources (see Appendix E for more detail).

5.2.1 Spatial Extent of the Catalog

The Wasatch Front region defined for the WGUEP probabilistic earthquake forecast (Figure 1-1) is termed the WGUEP Region here. We chose a larger region for compiling a master earthquake catalog for two reasons. First, when applying a declustering algorithm to an earthquake catalog, the bounds of the catalog should be larger than the target region to avoid

possible edge effects. Second, anticipating other applications, it was desirable to develop a unified UUSS-USGS catalog that covers the entire Utah Region—the standard region (UTR, Table 5.2-1) for which the UUSS has the responsibility for seismic monitoring and catalog reporting as part of the Advanced National Seismic System.

Table 5.2-1. Boundaries of catalog domains (inclusive).

	UTREXT	UTR	WGUEP
North	43.50° N	42.50° N	42.50° N
South	36.00° N	36.75° N	39.00° N
West	115.00° W	114.25° W	113.25° W
East	108.00° W	108.75° W	110.75° W

The region selected for the master catalog compilation, termed the Extended Utah Region (UTREXT), encompasses an area larger than the Utah Region (UTR) and its embedded WGUEP Region. The geographic boundaries of these regions are specified in Table 5.2-1 and spatial relations are shown in Figure 5.2-1. A fourth domain, termed the Extended Border Region (EBR), consists of the UTREXT minus the UTR.

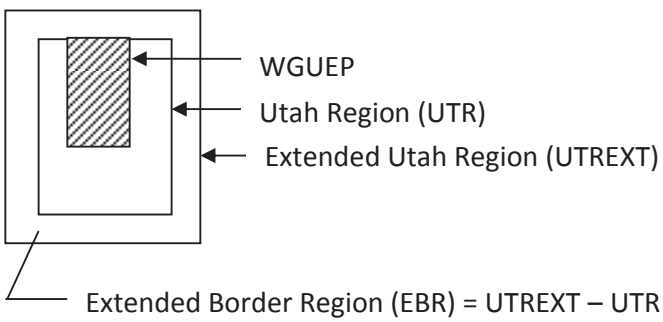

Figure 5.2-1. Sketch map of catalog domains.

5.2.2 Data Sources for the Unified Catalog

In aiming for a unified UUSS-USGS catalog, emphasis was placed on authoritative source catalogs compiled or produced directly by the UUSS and the USGS. For historical earthquakes, these catalogs are compilations based on various primary and secondary sources and documented by USGS and UUSS researchers. For instrumentally recorded earthquakes, the source catalogs consist of tabulations directly resulting from regional seismic monitoring by the UUSS since mid-1962 and from national-scale seismic monitoring by the USGS since 1973 (or in earlier decades by the U.S. Coast and Geodetic Survey).

5.3 Uniform Moment Magnitude and Magnitude Uncertainty

The primary purpose for compiling the earthquake catalog was to develop unbiased estimates of seismicity rate parameters for the background earthquake model. Key methodology steps are the assignment of a uniform moment magnitude to each earthquake in the catalog, assessment of magnitude uncertainties, and the application of bias corrections based on those uncertainties to estimate unbiased recurrence parameters.

5.3.1 Uniform Moment Magnitude

We require an earthquake catalog in which a uniform size measure is specified for each event in terms of **M**, defined by Hanks and Kanamori (1979):

$$\mathbf{M} = 2/3 \log M_0 - 10.7 \qquad (5.3\text{-}1)$$

where M_0 is the earthquake's scalar seismic moment in dyne-cm. **M** is used in state-of-practice seismic hazard analyses for consistency with modern ground-motion prediction equations. Moreover, **M** has become the size measure preferred by seismologists because it is the best indicator of an earthquake's true relative size and can be directly tied to physical properties of the earthquake source.

Our culled master catalog for the Extended Utah Region contains more than 5300 earthquakes larger than about magnitude 2.5, but direct instrumental measurements of **M** are available for only 107 of those. Using the observed values of **M**, together with some supplementary data, 18 conversion relationships to **M** (16 new, 2 revised) were developed for the WGUEP forecast for an assortment of shaking-intensity size measures and instrumental magnitudes that varied with time and reporting agency. The principal instrumental magnitudes in the source catalogs are Richter local magnitude (M_L), coda or duration magnitude (M_C, MD), and body-wave magnitude (m_b). The non-instrumental size measures that were converted to **M** are: the maximum value of Modified Mercalli Intensity, MMI (I_0); total felt area (FA); and the extent of area shaken at or greater than MMI IV, V, VI, and VII (A_{IV}, A_V, A_{VI}, and A_{VII}). Where multiple size measures were available for an individual earthquake, we computed a weighted mean of these measures using inverse-variance weighting to get a best estimate of **M**.

Different approaches can be utilized to transform an earthquake catalog with a minor fraction of direct instrumental measurements of **M** into one with "uniform moment magnitude." In the methodology of EPRI/DOE/NRC (2012), the uniform estimate of moment magnitude is E[**M**], the "expected value of moment magnitude," given uncertainty in either the observed value of **M** or in the value of **M** estimated from one or more other size measures. For reasons explained in Appendix E, we decided not to use "E[**M**]" for uniformly estimating moment magnitude. We call the alternative uniform moment magnitude used to construct our catalog a "best-estimate" moment magnitude. Our Best-Estimate Moment Magnitude (BEM) catalog assigns a value of moment magnitude to each earthquake that either is directly observed ($\mathbf{M}_{obs}$), is

based on magnitude conversion to **M** using general orthogonal regression(s), or is a reported value of magnitude which we assume to be equivalent to **M**.

5.3.2 Magnitude Uncertainty

Quantifying magnitude uncertainty (defined presently) is important to three aspects of our analysis of background seismicity: (1) correcting for bias in earthquake recurrence rates (see Musson, 2012, and references therein), (2) specifying the error-variance ratio between dependent and independent variables when using general orthogonal regression for magnitude conversions, which is favored by many experts (e.g., Castellaro *et al*., 2006, Castellaro and Bormann, 2007, Lolli and Gasperini, 2012), and (3) using inverse-variance weighting when combining different size measures to get a robust estimate of moment magnitude for an individual earthquake.

The magnitude of an earthquake is generally taken as the mean value of magnitude determinations of the same type made at multiple recording stations. In the absence of systematic and discretization (rounding) errors, the mean value of the event magnitude can be viewed as having random errors that are normally distributed with zero mean and standard deviation, σ (Tinti and Mulargia, 1985; Veneziano and Van Dyke, 1985). Following these cited authors, we define the latter statistic σ as the *magnitude uncertainty.* This term is equivalent to "magnitude accuracy" used by Kagan (2002, 2003). Determinations of σ for the various magnitudes in the master catalog are given and explained in Appendix E—including the assessment of uncertainties in original magnitude scales and the propagation of uncertainties in regressions and in inverse-variance weighting.

5.4 Best-Estimate Moment Magnitude (BEM) Catalog

Our unified and uniform earthquake catalog for the Extended Utah Region, i.e., the BEM catalog (Appendix E), contains 5388 earthquakes (~2.5 ≤ **M** ≤ 6.63) covering the time period from 1850 through September 30, 2012. The complete BEM catalog (Figure 5.4-1a) includes mainshocks,

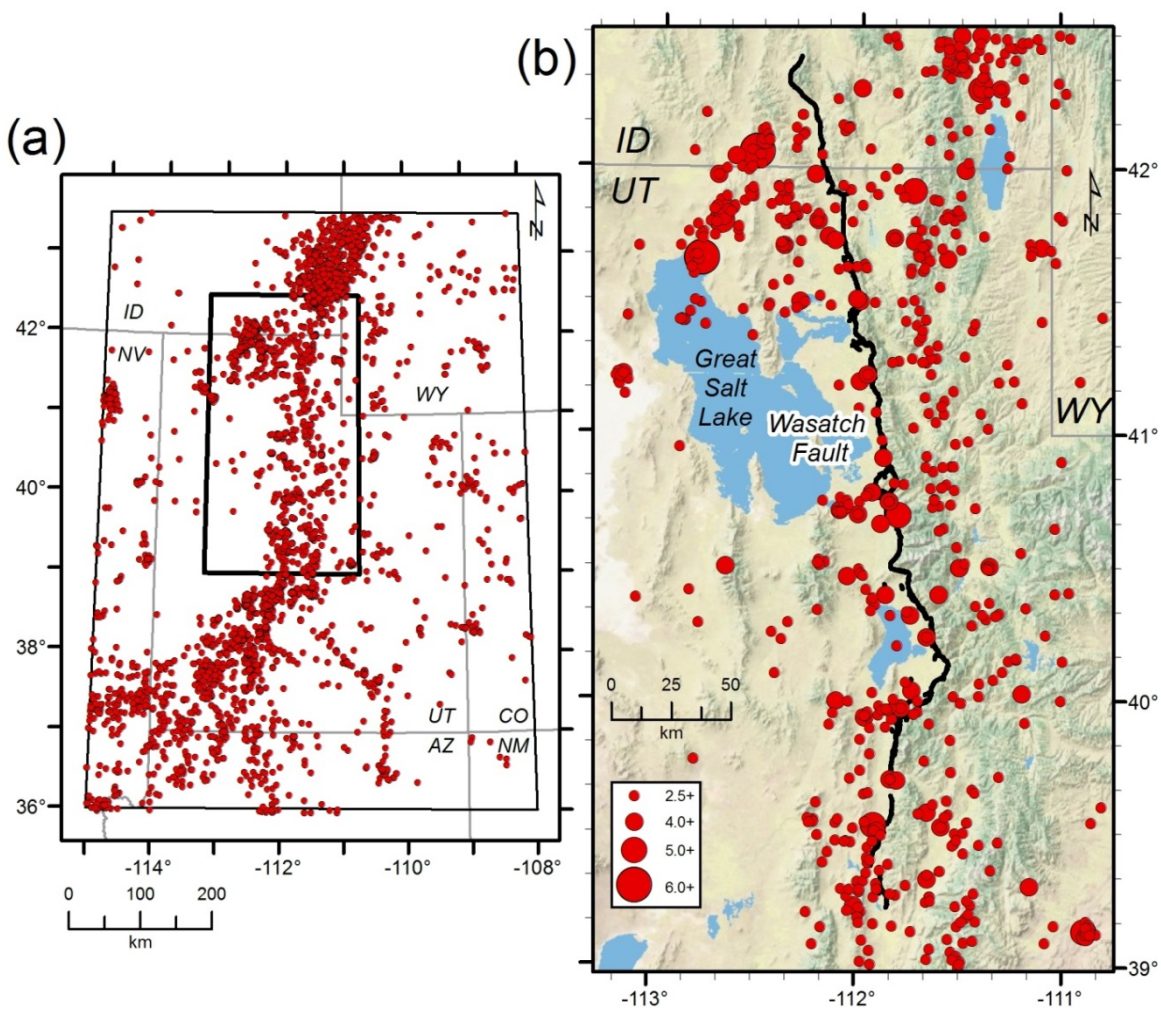

Figure 5.4-1. Epicenter maps of earthquakes in the BEM catalog, 1850 through September 2012. (a) Total catalog (clustered) for the UTREXT. (b) Declustered catalog of independent mainshocks in the WGUEP Region, outlined in the inset in (a). Base map is U.S. National Park Service Natural Earth physical map (http://goto.arcgisonline.com/maps/World_Physical_Map).

foreshocks, aftershocks, and earthquake swarms. Non-tectonic seismic events such as blasts and mining-induced seismicity are excluded from the Utah Region but not the Extended Border Region. Injection-induced earthquakes were retained in the BEM catalog but not used in the calculations for earthquake rates in the present study. Our background earthquake model assumes the occurrence of independent earthquakes following a Poisson distribution, which requires the identification and removal of dependent events from the earthquake catalog.

5.4.1 Identification and Removal of Dependent Events (Declustering)

Spatial and temporal clustering is common in natural seismicity. Statistical techniques are required to decompose or "decluster" an earthquake catalog into "main" events that are random and independent in a statistical sense and "dependent" events (foreshocks, aftershocks, and the smaller events of earthquake swarms) that relate non-randomly to the main events. Declustering algorithms variously use magnitude-dependent space-time windows, specific cluster models, or stochastic approaches to remove dependent events from an earthquake catalog (e.g., van Stiphout *et al*., 2012).

For conformity with procedures used by the USGS in earthquake catalog processing for the NSHMs (see Petersen *et al*., 2008), we used the computer program *cat3w* developed by Dr. Charles Mueller of the USGS. The program implements the declustering method of Gardner and Knopoff (1974), in which smaller earthquakes within fixed time and distance time windows of larger shocks are identified as dependent events. The effectiveness of using *cat3w* to decluster our BEM catalog was verified by (1) comparing space-time plots of the original and declustered versions of the catalog, and (2) using the Kolmogorov-Smirnov (K-S) test to analyze data in critical magnitude bins. The declustered catalog for the WGUEP Region contains 660 independent mainshocks ($2.50 \leq \mathbf{M} \leq 6.59$), shown in the epicenter map of Figure 5.4-1b.

5.4.2 Periods of Completeness

To determine the completeness period, T_C, associated with different magnitude thresholds in the declustered catalog, we used cumulative recurrence curves (CRCs) together with general information on the space-time evolution of seismographs, population, and newspapers. A CRC is a plot of the cumulative number of earthquakes above a given magnitude threshold versus time. The use of a probabilistic approach, which allows the analysis and use of variable completeness throughout an entire earthquake record (see, for example, EPRI/DOE/NRC, 2012, or Felzer, 2007) was beyond the scope of this study. According to Grünthal *et al*. (1998, as quoted in and cited by Hakimhashemi and Grünthal, 2012), the CRC method is "very simple but rather robust."

Ultimately, the parameter of the background earthquake model of primary concern to the WGUEP is the annual rate of occurrence of independent mainshocks of $\mathbf{M} \geq 5.0$ within the *entire* WGUEP Region. Accordingly, this region was treated as a single domain for assessing the completeness periods summarized in Table 5.4-1. Our primary objective in selecting the starting point for each T_C was to bracket a completeness period for which the earthquake rate is convincingly uniform and reliable, particularly for magnitude thresholds below 4.95. The completeness periods in Table 5.4-1 are conservative minimum values of T_C. For the three magnitude thresholds below 4.95, statistical tests of rate changes allow earlier start dates for T_C; thus, our conservatively selected start dates do not necessarily mark when network sensitivity changed to enable uniform reporting above those magnitude threshold (see Appendix E).

5.5 Estimation of Unbiased Recurrence Parameters

Our approach to estimating earthquake recurrence parameters involves a standard procedure used in PSHA—namely, the use of the Weichert (1980) maximum-likelihood algorithm to fit a truncated exponential distribution to earthquake

Table 5.4-1. Data for seismicity rate calculations, WGUEP Region (BEM catalog, declustered).

Magnitude Range	Year (Start)[1]	Year (End)	*t* (years)	No. of Earthquakes	Sum *N** [2]
$2.85 \leq \mathbf{M} < 3.55$	**1986**	2012.75	26.75	183	170.721
$3.55 \leq \mathbf{M} < 4.25$	**1979**	2012.75	33.75	39	37.553
$4.25 \leq \mathbf{M} < 4.95$	**1963**	2012.75	49.75	9	8.532
$4.95 \leq \mathbf{M} < 5.65$	***1908***	2012.75	104.75	4	3.158
$5.65 \leq \mathbf{M} < 6.35$	***1880***	2012.75	132.75	2	1.926
$6.35 \leq \mathbf{M} < 7.00$	*1850*	2012.75	162.75	1	0.769

[1] Bold date indicates the start of the completeness period, T_C, based on a pick from a cumulative recurrence curve (CRC); italicized date, based on other arguments; bold italicized date, CRC plus other arguments.

[2] *N** is the effective number of earthquakes, corrected for magnitude uncertainty on an earthquake-by-earthquake basis and summed (Sum *N**) for the specified magnitude interval.

counts in magnitude bins (see, for example, EPRI/DOE/NRC, 2012). Two known potential sources of bias that can affect the seismicity-rate calculations are magnitude uncertainty and the discretization or rounding of magnitude values to some specified nearest decimal value.

5.5.1 Methodology to Correct for Magnitude Uncertainty

The effect of magnitude uncertainty on calculations of earthquake rate parameters is described by Musson (2012), who reviews different approaches to correct for bias in frequency-magnitude relations. He also underscores the complexity of the issue. Basically, because of the exponential distribution of magnitude, observed magnitudes (measured with normally distributed errors) together with their counts in discrete bins can have "apparent" values that differ from their "true" values—typically shown using simulated earthquake catalogs.

As a conceptual guide, Figure 5.5-1 illustrates the equivalence of approaches proposed independently by Tinti and Mulargia (1985) and Veneziano and Van Dyke (1985) to correct for magnitude uncertainty σ in calculating unbiased ("true") seismicity rates. Without dwelling on the mathematical equations (Appendix E), the following key points can be grasped from this figure. First, in a frequency-magnitude plot, bias caused by magnitude uncertainty can equivalently be corrected either in the *x*-direction using an adjusted magnitude called **M*** ("M-star") or in the y-direction using an adjusted rate called *N** ("N-star"). Second, the sign of the necessary corrections depends on whether the starting data lie along the line based on values of $\mathbf{M}_{obs}$ or its equivalent, as is the case for the BEM catalog, or along the line based on values of E[**M**], as is the case for an E[**M**] catalog developed following the equations and steps of the EPRI/DOE/NRC (2012) methodology.

EPRI/DOE/NRC (2012) showed that for catalogs with variable levels of completeness as a function of magnitude, the *N** approach performs better than the **M*** approach. Accordingly, we used the *N** approach in this study. We followed the EPRI/DOE/NRC (2012) steps of (1) calculating *N** from σ on an earthquake-by-earthquake basis (using $N^* = \exp\{-(b \ln(10))^2\sigma^2/2\}$), (2) summing *N** for earthquakes within specified magnitude intervals (Table 5.4-1), (3) dividing each *N** sum by the period of completeness for its respective magnitude interval, and (4) using a maximum-likelihood approach to compute seismicity rate parameters from the effective *N** counts (Figure 5.6-1). For the *N** calculations, a *b*-value of 1.05 assessed from preliminary processing of the BEM catalog was used.

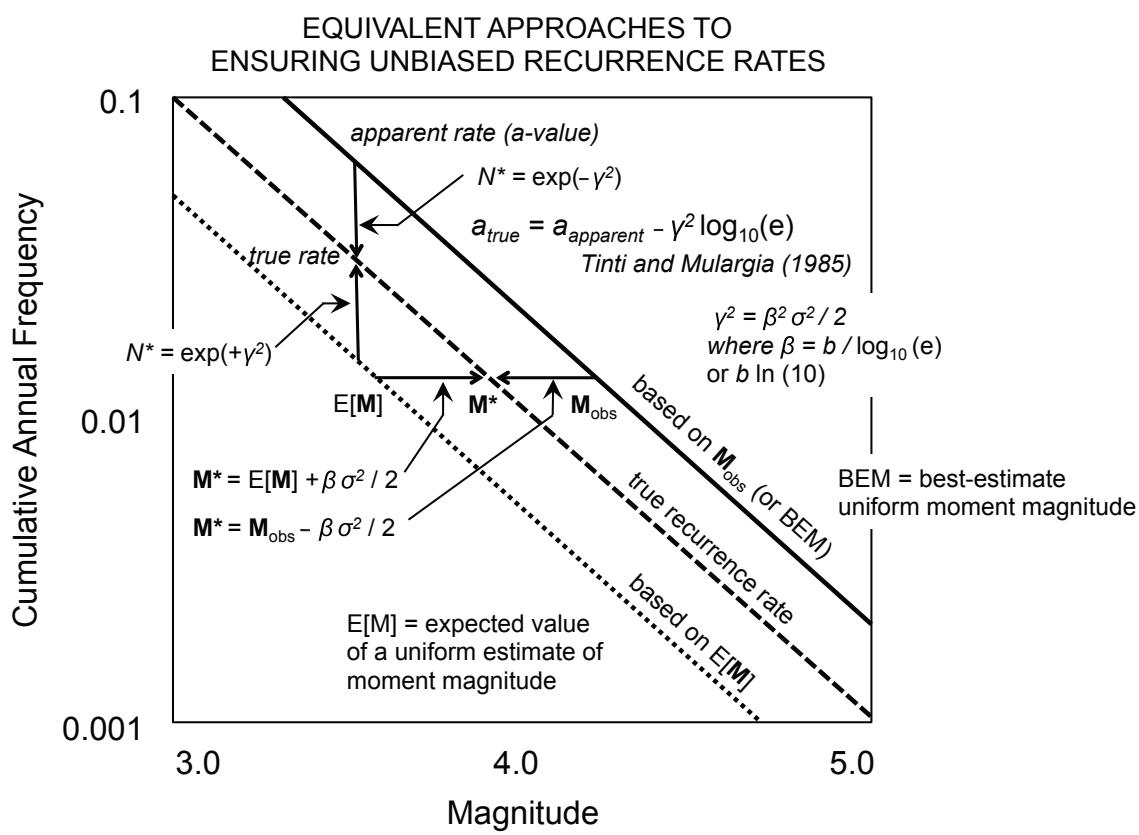

Figure 5.5-1. Schematic frequency-magnitude diagram showing how unbiased ("true") recurrence rates can be determined by making appropriate corrections in either the *x*-direction in terms of magnitude, **M**, or in the *y*-direction in terms of rate, expressed here as the annual rate, *a*, of earthquakes ≥ **M**. Adapted from EPRI/DOE/NRC (2012). *N** as defined on the figure is the equivalent count assigned to an individual earthquake.

5.5.2 Rounding

The potential overestimation of seismicity rates due to the rounding of reported magnitudes in an earthquake catalog was examined by Felzer (2007). It should be noted that the object of her study, an earthquake catalog for California, involved a substantial proportion of events in the early to mid-1900s that had assigned magnitudes (M_L) rounded to the nearest 0.5. Further, because of an assumed equivalence between M_L and **M**, rounded values of M_L (except where a measured value of **M** was also available) translated directly into similarly rounded values of **M** in her moment-magnitude catalog, thus motivating the need for correction. In the EPRI/DOE/NRC (2012) study, the potential impact of rounding of data to the nearest 0.1 magnitude unit was examined using simulated data sets, and statistical tests showed that the effect of the rounding could be ignored.

In this study, the effect of rounded magnitude values was judged to be insignificant in our calculations and was ignored. All values of **M** entering into our final seismicity-rate calculations for the WGUEP Region are uniformly rounded to the nearest 0.01 magnitude unit as the result of calculating **M** either from a measured value of scalar seismic moment or from magnitude-conversion relationships, in which case the effects of rounding in original size measures are subsumed in the regressions.

5.6 Seismicity Rate Parameters of the Background Earthquake Model

The culmination of all the described preceding steps was the calculation of seismicity rate parameters for the background earthquake model. This was done using the data of Table 5.4-1 and the maximum-likelihood algorithm of Weichert (1980) to solve for unbiased recurrence parameters for the WGUEP Region. The Weichert algorithm has the virtue of handling binned magnitude data with variable periods of completeness as well as truncation of the exponential magnitude distribution at an upper limit, m_u. Figure 5.6-1 shows the fit to the data for an m_u of 7.00 corresponding to the upper limit of the largest magnitude bin in Table 5.4-1 and consistent with a maximum magnitude of **M** 6.75 ± 0.25. We tested alternative values of m_u from 6.75 to 8.00 and determined that both the seismicity rates and *b*-value were insensitive to the change.

In mathematical form, the truncated exponential distribution shown on Figure 5.6-1 can be expressed (see Youngs and Coppersmith, 1985, Equation 9) as

$$N(m) = N(m_0)\,\frac{10^{-b(m - m_0)} - 10^{-b(m_u - m_0)}}{1 - 10^{-b(m_u - m_0)}} \qquad (5.6\text{-}1)$$

where $N(m)$ is the number of earthquakes per year of magnitude m or larger, m_0 is the minimum magnitude, and m_u is the upper bound magnitude. For the background earthquake model, based on N^*, the cumulative annual rate of independent mainshocks greater than or equal to m_0 = 2.85 is 7.70 with a standard error of 0.52. The *b*-value determined for the model is 1.06 with a standard error of 0.06. Table 5.6-1 provides rate information for **M** ≥ 5.0 and other magnitude ranges, calculated using these parameters and Equation 5.6-1.

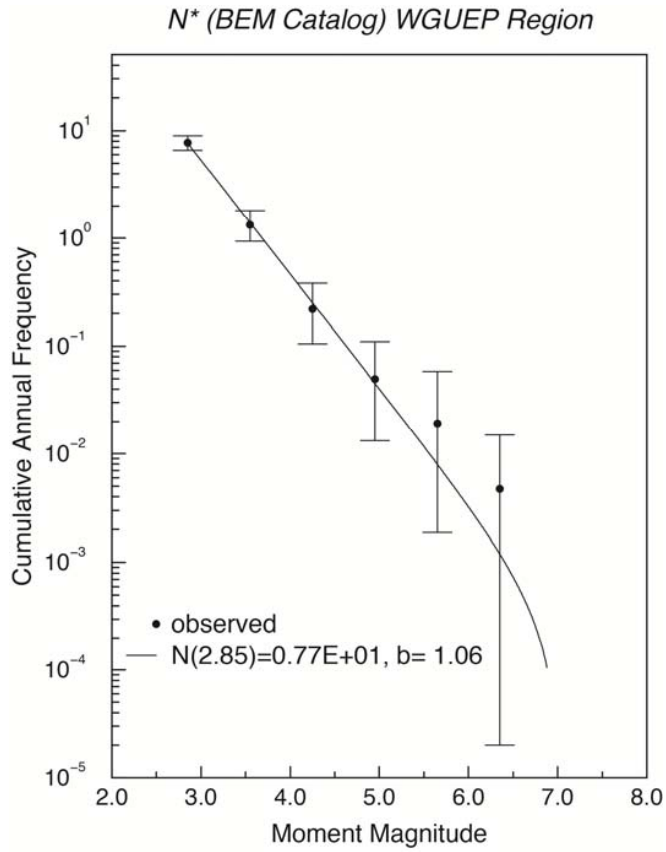

Figure 5.6-1. Background earthquake model. Frequency-magnitude distribution of declustered background earthquakes (**M** ≥ 2.85) in the WGUEP Region, corrected for magnitude uncertainty and calculated using the maximum-likelihood algorithm of Weichert (1980).

The confidence limits on the seismicity rates in Table 5.6-1 are based on a 25-point discrete probability distribution for paired $N(m_0)$ and *b*-values that Robert R. Youngs of AMEC Foster Wheeler (written communication, March 16, 2014) determined for us using the data in Table 5.4-1, and the same likelihood model used to calculate the best-fit $N(m_0)$ and *b*-values. We used this discrete probability distribution to calculate the confidence limits in Table 5.6-1, which are 5th and 95th percentile values. This procedure appropriately accounts for the correlation between the uncertainties of $N(m_0)$ and *b*. Based on the probability distribution provided by R. R. Youngs for our data set (with m_0 = 2.85 and m_u = 7.00), one can estimate the 90% confidence limits on $N(m)$ for other magnitude ranges above **M** ≥ 5.0 (e.g., **M** ≥ 5.25) by using the following paired values in Equation 5.6-1: $N(m_0)$ = 7.89 events/yr and b = 1.18 for the 5th percentile rate and $N(m_0)$ = 8.61 events/yr and b = 1.00 for the 95th percentile rate (see Appendix E).

Table 5.6-1. Cumulative rates of independent background earthquakes.

Magnitude Range	Rate (events/yr)	90% Confidence Limits on Rate	
		Lower (events/yr)	Upper (events/yr)
M ≥ 3.00	5.34	4.72	5.92
M ≥ 3.50	1.58	1.30	1.83
M ≥ 4.00	0.465	0.344	0.586
M ≥ 4.50	0.137	0.089	0.192
M ≥ 5.00	0.0402	0.0228	0.0606
M ≥ 5.50	0.0116	0.0058	0.0188
M ≥ 6.00	0.00322	0.00141	0.00552
M ≥ 6.50	0.000734	0.000289	0.001328

6 COMPARISON OF GEODETIC AND GEOLOGICAL/SEISMOLOGICAL MOMENT RATES

This section compares seismic moment rates estimated from crustal deformation measurements, commonly referred to as "geodetic moment rates," with geological/seismological moment rates predicted by the Wasatch Front seismic source model developed in this study. We compare these moment rates for both the Wasatch Front region as a whole and for the four subregions shown in Figure 6.1-1. We defined the subregion boundaries to coincide with selected segment boundaries interpreted for the WFZ, taking into account the distribution of the Global Positioning System (GPS) velocity vectors shown in Figure 6.1-2. Each subregion spans two or more segments of the WFZ and extends across the entire east-west extent of the Wasatch Front region. The purpose of this analysis is to determine whether or not the characterization of earthquake rates and magnitudes developed for the WGUEP forecast is consistent with geodetic measurements of crustal deformation in the Wasatch Front region. Acronyms and abbreviations are defined on pages xii to xiv.

The results show that geodetic moment rates agree with geological/seismological moment rates calculated from the WGUEP model, within the uncertainty limits, for the Wasatch Front region as a whole and for three of the four subregions. In the fourth and southernmost subregion, which includes the Levan and Fayette segments of the WFZ (L-F, Figure 6.1-1), the geodetic moment rate is five times larger than the geological/seismological moment rate with no overlap in the 90% confidence limits. This discrepancy exists because the strain rate in the L-F subregion is similar to the strain rate in the three subregions to the north, but the geological moment rate predicted for the known faults in the L-F area is much lower. At the present time, we do not have a satisfactory explanation for the larger-than-expected strain rate in the southernmost Wasatch Front region.

6.1 Previous Work

Previous studies have used a variety of techniques to compare the observed crustal deformation rates in the Wasatch Front region with predicted rates based on geological and seismological data, with mixed results. Friedrich *et al*. (2003) compared horizontal extension rates to Holocene cumulative vertical fault slip rates along an east-west profile just south of Great Salt Lake and found that they were in good agreement. Niemi *et al*. (2004) used two kinematic block models, intended to bound a range of simple elongation (pure shear) strain accumulation models, to compare geodetic and maximum geological horizontal extension rates on an east-west profile across the southern end of the Wasatch Front region between 39° and 39.6° N. Their late Quaternary maximum velocity field agrees well with their geodetic velocity field, but their Holocene maximum velocity field is more than a factor of two larger. Chang (2004) used a nonlinear optimization algorithm to find best-fitting strain accumulation models for GPS velocity measurements across the five central segments of the WFZ. His preferred model has a fault plane that dips 27° and creeps 7 mm/yr between 9 and 20 km depth. The vertical component of the slip rate for this model is 3.2 mm/yr, which is about twice as large as the weighted mean slip rates for the central segments of the WFZ (Table 4.1-4). Chang *et al*. (2006) interpreted GPS data across the WFZ with a coseismic deformation model. They concluded that the GPS data were consistent with geological measurements of vertical component slip rates if the dip of the WFZ is steeper than 30°. Velasco *et al*. (2010) modeled crustal deformation around the central part of the WFZ using a strain accumulation model similar to that of Chang (2004). Their best-fit model to GPS data corrected for glacial isostatic rebound has creep of 3.3 ± 0.2 mm/yr below a locking depth of 10 ± 3 km on a surface dipping 19° ± 7°.

One of the most recent efforts to jointly analyze geodetic and geological data for the Wasatch Front region is the fault slip rate inversion by Zeng and Shen (2014), which provides the starting point for the analysis presented in this section. Their inversion was one of two fault-based geodetic inversion models that were utilized in the source characterizations for the 2014 NSHMs (Petersen *et al*., 2014). Zeng and Shen (2014) inverted geodetic data for slip rates on the faults used in the hazard calculations for the 2008 NSHMs, which are shown on Figure 6.1-2. They fixed the dips of these faults to the preferred values used in the 2008 NSHMs, which are 50° for all of the faults on Figure 6.1-2 (Haller and Wheeler, 2008). Zeng and Shen's (2014) model for the faults within the map area of Figure 6.1-2 assumes that each fault creeps on a planar extension of the fault in the lower crust at a rate equal to the long-term slip rate. They constrained their model to match as closely as possible the geological slip rates used for these faults in the 2008 NSHMs (Haller and Wheeler, 2008), with some modifications. The slip rates that they obtained for faults in the Wasatch Front region are in good agreement with the geologically determined slip rates with one notable exception: the Levan segment of the WFZ (Figure 6.1-3). The modeled slip rate for this segment is 1.56 mm/yr compared to the geologic slip rate of 0.31 mm/yr (computed from recurrence data in Haller and Wheeler, 2008). Fault slip rates from the Zeng and Shen (2014) inversion and a similar inversion by Bird (2014) were each given a weight of 0.1 in the 2014 NSHM probabilistic hazard calculations for the western U.S. outside of California. The incorporation of these geodetic models into the calculations increased the mapped hazard by about 15% to 20% in some areas, including the area around the Levan segment of the WFZ (Petersen *et al*., 2014).

The WGUEP model for earthquake sources in the Wasatch Front region is much more comprehensive and up-to-date than the information that was used for any of the previous geodetic analyses, including that of Zeng and Shen (2014). Therefore, we revisit the question of compatibility between

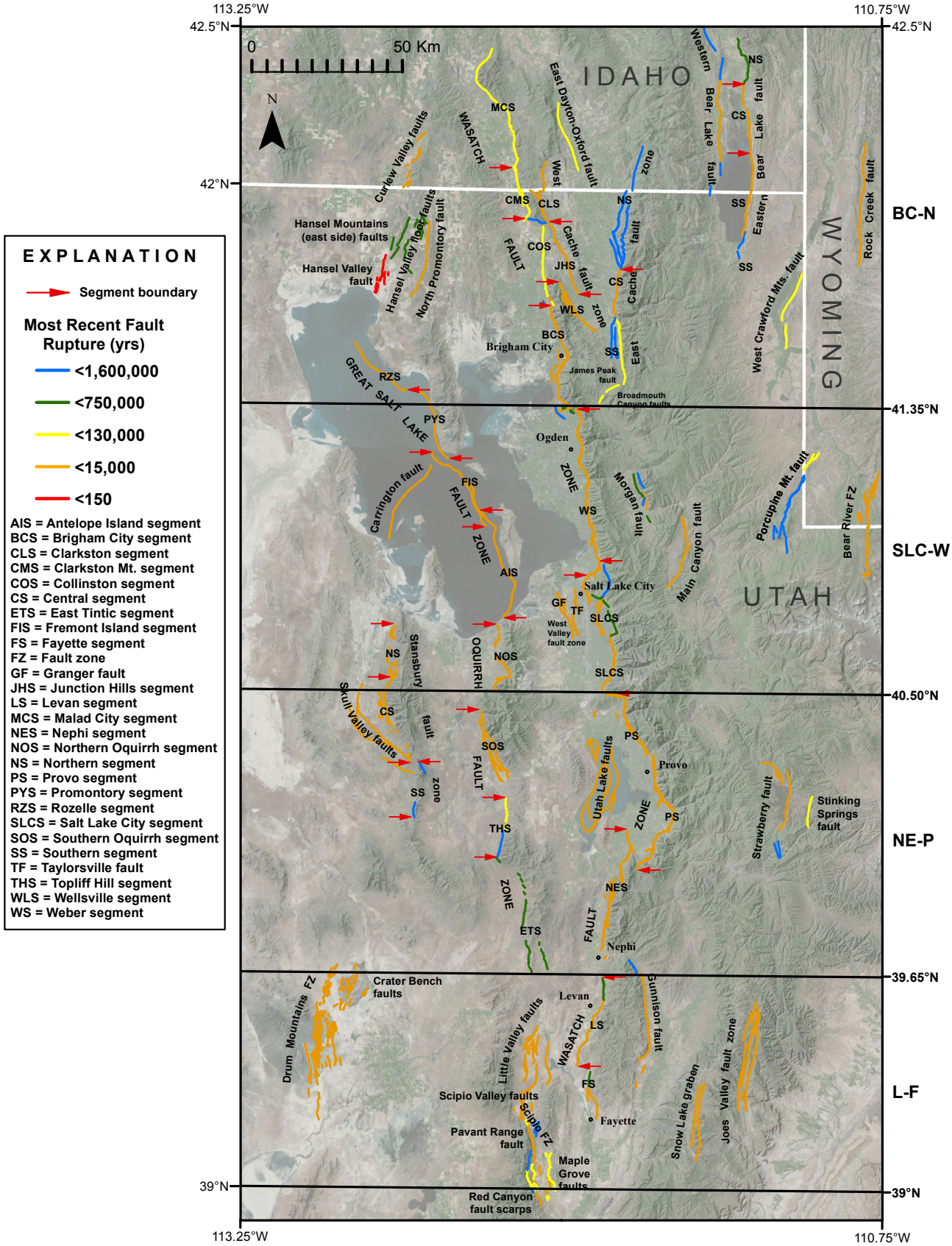

Figure 6.1-1. Map of the Wasatch Front region showing surface traces of faults and fault segments considered in the earthquake forecast and subregions for comparisons of geodetic and geological/seismological moment rates. The subregion names come from the abbreviations for the WFZ segments that they encompass: BC-N, Brigham City segment and north; SLC-W, Salt Lake City and Weber segments; NE-P, Nephi and Provo segments; and L-F, Levan and Fayette segments. Base imagery from the USGS and NASA (http://imagery.arcgisonline.com).

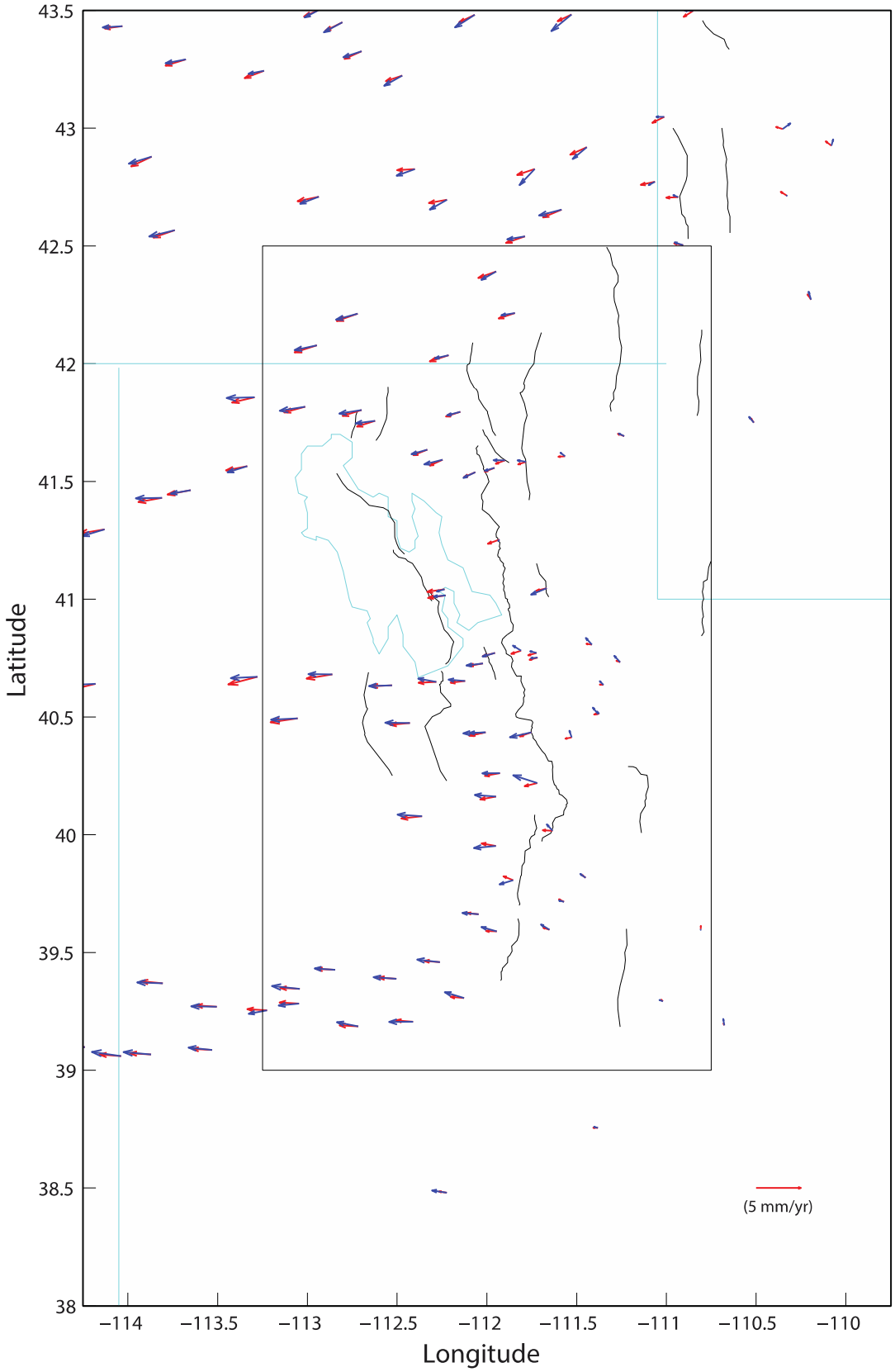

Figure 6.1-2. Comparison of observed (blue) and predicted (red) velocity vectors, relative to stable North America, for the Wasatch Front region (box) and the surrounding area. The irregular blue line shows the outline of the Great Salt Lake; the straight blue lines show state boundaries. The black lines show the surface traces of Quaternary faults used in the 2008 NSHMs and in the Zeng and Shen (2014) fault slip inversion. The mean of the 90% confidence limits on the observed velocity vectors (1.645 std. dev., Table 6.2-1) is a circle of radius 0.6 mm/yr, which is approximately the width of the arrowheads on the vectors. Figure provided by Yuehua Zeng, USGS.

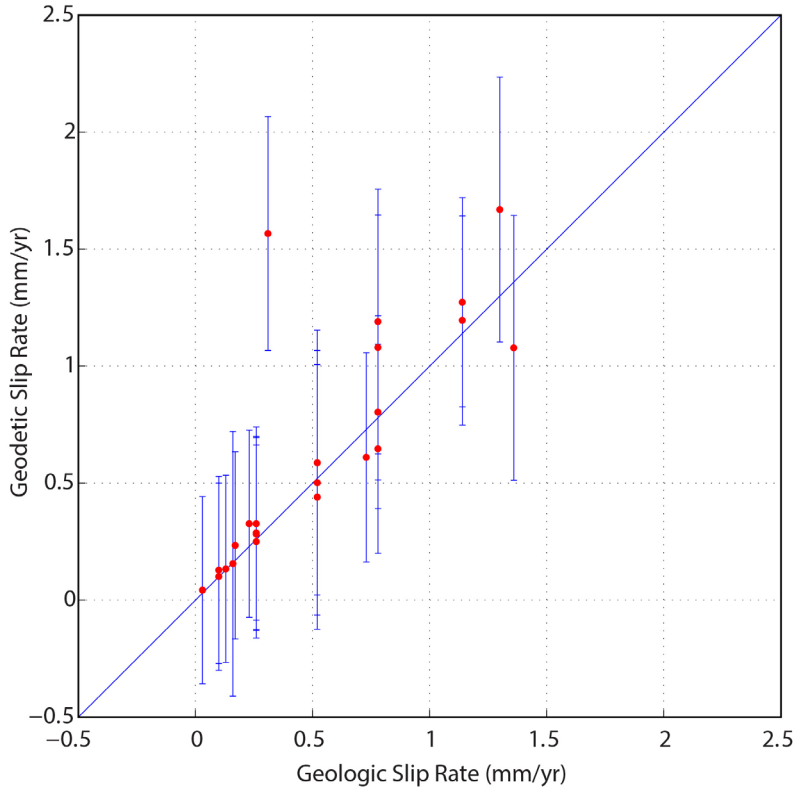

Figure 6.1-3. Comparison of fault slip rates from geological data and from the geodetic inversion of Zeng and Shen (2014) for faults in the Wasatch Front region. The blue vertical bars represent one standard deviation uncertainties on the slip rates from the geodetic inversion. The diagonal blue line represents perfect agreement between the two slip rates. The data point farthest from this line is for the Levan segment of the WFZ. Figure modified from Zeng and Shen (2014) by Yuehua Zeng, USGS.

geodetic measurements of strain rates and the earthquake rates predicted from geological and seismological data. We chose not to use the geodetic data directly in constructing the WGUEP source model because of the high level of uncertainty involved in converting measured crustal deformation rates to earthquake rates in the Wasatch Front region. Two of the primary contributors to this uncertainty are (1) questions regarding the applicable strain accumulation model for normal faults in this region, and (2) the difficulty of resolving slip rates on the individual faults and fault segments in the WGUEP model, especially with the relatively sparse distribution of GPS stations in the Wasatch Front region. In part because of these issues, geodetically based source models were assigned a fairly low weight of 20% in the 2014 NSHM hazard calculations for the western U.S. outside of California. An additional factor that entered into our choice of geodetic analysis methods was that the geodetic models developed for the 2014 NSHMs did not become available until after the source characterization work for the WGUEP project was largely completed.

6.2 Geodetic Data

The basic data that we used for our geodetic analysis are the velocity vectors for the western U.S. that Zeng and Shen (2014) used for their fault slip inversion for the 2014 NSHMs (Figure 6.1-2). These velocity vectors are the result of the reprocessing of data from several networks of GPS stations by several different groups. The velocity vector solutions from the different groups were rotated into a common North American reference frame by McCaffrey *et al*. (2014). Zeng and Shen (2014) edited the McCaffrey *et al*. (2014) data set to remove velocity vectors that they judged to be problematic for reasons explained in their report. Most of the data from within the Wasatch Front region (Table 6.2-1) came from networks of permanent GPS stations installed and operated by the University of Utah and by the National Science Foundation EarthScope project. Most, but not all, of the velocity vectors that Zeng and Shen (2014) used for the stations in this region are averages of solutions from three different groups: Shen and Wang (2012), the Plate Boundary Observatory (2011), and the Scripps Orbit and Permanent Array Center (2012).

The blue and red arrows in Figure 6.1-2 show observed and predicted GPS velocity vectors, respectively, from the Zeng and Shen (2014) study for a region extending one degree in latitude and longitude beyond the boundaries of the Wasatch Front region (box). The velocity vectors in the eastern one-third of the Wasatch Front region show minimal motion relative to stable North America. The velocity vectors in the western part of this region show westward motion, relative to stable North America, which begins at about the longitude of the WFZ and increases rapidly westward to 2 to 3 mm/yr. This deformation

Table 6.2-1. GPS velocity vectors for the Wasatch Front region.

Station	Latitude[1] (deg)	Longitude[1] (deg)	E Velocity, V_E (mm/yr)	N Velocity, V_N (mm/yr)	Std Dev V_E (mm/yr)	Std Dev V_N (mm/yr)
0H64	40.1617	-111.9494	-2.420	0.130	0.500	0.500
1S2E	40.7522	-111.7167	-0.750	-0.060	0.400	0.400
A121	40.2190	-111.7195	-2.720	0.640	0.600	0.600
BAIR	41.5393	-112.0641	-1.280	-0.480	0.400	0.500
BATI	42.2152	-111.8429	-1.450	-0.200	0.488	0.502
BENN	41.0419	-112.2351	-0.860	-0.180	0.300	0.400
CAPS	39.6622	-112.0465	-1.900	0.120	0.600	0.500
CEDA	40.6807	-112.8605	-2.693	0.060	0.300	0.300
COON	40.6526	-112.1210	-1.870	0.103	0.300	0.300
DCUT	40.4128	-111.5276	-0.270	0.560	0.552	0.552
DOWN	42.3910	-111.9481	-1.570	-0.705	0.740	0.800
DRUF	42.0359	-112.2125	-1.450	-0.260	0.370	0.400
ELBE	39.9519	-111.9500	-2.510	-0.170	0.400	0.400
EOUT	41.2532	-111.9289	-0.127	-0.130	0.300	0.300
F230	39.2538	-113.2236	-2.170	-0.220	0.800	0.900
F250	39.2829	-113.0458	-2.370	-0.110	0.500	0.500
F291	39.2064	-112.4116	-2.770	0.010	0.500	0.500
FORE	40.5119	-111.3803	-0.613	0.527	0.300	0.300
H100	39.2933	-111.0204	-0.480	0.060	0.300	0.300
HEBE	40.5141	-111.3727	-0.300	0.157	0.300	0.300
HWUT	41.6072	-111.5651	-0.458	0.275	0.300	0.300
LMUT	40.2614	-111.9281	-2.005	-0.020	0.431	0.388
LTUT	41.5921	-112.2468	-1.990	-0.380	0.300	0.300
MONC	39.8066	-111.8529	-1.600	-0.370	0.500	0.600
MOUT	41.0462	-111.6656	-1.760	-0.560	0.400	0.400
MPUT	40.0156	-111.6336	-0.697	0.535	0.300	0.300
MUHA	40.7267	-112.0225	-1.850	-0.170	0.400	0.500
NAIU	41.0157	-112.2297	-1.303	-0.083	0.300	0.300
NGRI	42.0777	-112.9460	-2.415	-0.375	0.321	0.331
P016	40.0781	-112.3614	-2.775	0.162	0.303	0.300
P057	41.7566	-112.6231	-2.105	-0.180	0.300	0.300
P084	40.4940	-113.0540	-2.987	-0.073	0.300	0.300
P086	40.6488	-112.2821	-2.037	0.295	0.300	0.300
P088	40.7718	-111.7229	-0.725	0.125	0.303	0.300
P101	41.6923	-111.2360	-0.545	0.188	0.300	0.300
P103	39.3451	-113.0421	-3.213	0.293	0.300	0.300
P104	39.1861	-112.7171	-2.470	0.382	0.300	0.300
P105	39.3875	-112.5041	-2.660	0.163	0.300	0.300
P106	39.4590	-112.2623	-2.632	0.222	0.300	0.300
P108	39.5889	-111.9445	-1.813	0.382	0.300	0.300
P109	39.5975	-111.6508	-1.043	0.420	0.300	0.300
P110	39.7152	-111.5711	-0.605	0.080	0.354	0.348
P111	41.8173	-113.0122	-2.780	-0.300	0.300	0.300
P112	39.8169	-111.4500	-0.665	0.303	0.300	0.300
P114	40.6340	-112.5276	-2.592	-0.037	0.300	0.300
P115	40.4744	-112.4280	-2.795	0.050	0.310	0.310
P116	40.4340	-112.0142	-2.388	-0.067	0.310	0.308
P117	40.4352	-111.7514	-2.438	-0.445	0.303	0.300
P118	40.6355	-111.3499	-0.440	0.287	0.300	0.300
P119	40.7318	-111.2577	-0.647	0.510	0.337	0.300
P121	41.8034	-112.6983	-2.440	-0.263	0.300	0.300
P122	41.6354	-112.3319	-1.713	-0.372	0.300	0.300
P124	41.5576	-111.9574	-1.057	-0.263	0.300	0.300
P125	41.5890	-111.8989	-1.243	0.023	0.300	0.300
P126	41.5832	-111.7805	-0.910	0.107	0.300	0.300
P675	42.2122	-112.7188	-2.342	-0.480	0.308	0.305
P783	40.8074	-111.4149	-0.695	0.538	0.300	0.300
PUC1	39.5992	-110.8087	-0.080	-0.130	0.300	0.300
RBUT	40.7811	-111.8089	-0.928	0.430	0.300	0.300
SIDE	41.7950	-112.1483	-1.400	-0.280	0.500	0.500
SLCU	40.7722	-111.9550	-1.390	-0.300	0.300	0.300
SMEL	39.4256	-112.8449	-2.385	0.162	0.300	0.300
SPIC	39.3062	-112.1275	-2.250	0.517	0.300	0.300
WILI	40.4353	-112.0068	-1.830	-0.070	0.500	0.500
				Mean	0.363	0.369
				Mean 90% confidence limits	0.597	0.608

[1] NAD83

pattern is similar to that observed in a number of previous studies, including Friedrich *et al*. (2003), Niemi *et al*. (2004), Hammond and Thatcher (2004), Chang *et al*. (2006), and Velasco *et al*. (2010).

Table 6.2-1 lists the 64 velocity vectors that Zeng and Shen (2014) used from GPS stations in the Wasatch Front region (Yuehua Zeng, USGS, written communication, 2014). The standard deviations for the vector components are adopted from those reported by the original reprocessing groups, with some modifications. The original standard deviations are formal statistical uncertainty estimates from the fit of a constant secular velocity vector, relative to the stable North America reference frame, to time series of GPS position measurements. For the velocities that are average values from multiple processing groups, the standard deviations listed are also average values from the different solutions. For the purpose of the fault slip inversions of Zeng and Shen (2014), and other inversion studies that used the McCaffrey *et al*. (2014) data set (see Petersen *et al*., 2014), a lower limit of 0.3 mm/yr was imposed on the standard deviations of the east and north velocities. This lower limit was imposed to prevent sites with very low uncertainties from dominating the least-squares solutions and to account for some uncertainty in the reference frame corrections. Even though only one of the two reasons for these limits is strictly relevant here, we retain these lower limits in our own analyses of the GPS data.

The strain rates that we used in our analysis are spatially averaged values of the maximum horizontal principal strain rate, $\dot{\epsilon}_1$ (extension positive), derived from the following procedure: (1) interpolation of GPS velocity vectors from the whole western U.S. onto a uniform grid with 0.05° latitude and longitude spacing, (2) calculation of strain rates from the interpolated velocity vectors using a finite-difference method, and (3) averaging over the resulting grid of $\dot{\epsilon}_1$ values and associated azimuths to obtain mean values for the Wasatch Front region and the four subregions. Yuehua Zeng carried out the first two of these steps. Zeng also performed 400 Monte Carlo simulations to assess the effect of the velocity vector uncertainties, assumed to be normally distributed, on the mean $\dot{\epsilon}_1$ values for the various regions. For efficiency reasons, these simulations were done using a larger grid spacing of 0.1° and a smaller geographic area, which extended 4° beyond the Wasatch Front region. These differences were unimportant for the purpose of assessing mean strain rate uncertainties, as the mean $\dot{\epsilon}_1$ values from the Monte Carlo simulations were all within 3% of the values obtained by the three-step procedure outlined above.

Figure 6.2-1 is a color-coded map of the $\dot{\epsilon}_1$ grid showing the $\dot{\epsilon}_1$ azimuths as two-headed arrows with lengths proportional to the magnitude of $\dot{\epsilon}_1$. This map shows a zone of high strain rate centered on the WFZ south of Great Salt Lake, with the highest rates of up to 47 nanostrains per year (nstr/yr) occurring on the northern half of the Provo segment of the WFZ. In the latitude range spanned by the Great Salt Lake, the zone of high strain rate is more spread out, does not exceed ~30 nstr/yr, and is centered 15 to 40 km west of the WFZ. The different strain rate pattern in this latitude range may be partially an artifact of the lower density of GPS stations. However, the strain rate pattern is similar near the northern end of Great Salt Lake, where it is reasonably well constrained by a line of GPS stations crossing the northern part of the Brigham City segment of the WFZ (Figures 6.1-2 and 6.2-1). The variation in strain rate along the WFZ has no apparent relation to the dates of the last paleoearthquakes (Table 4.1-2). The maximum principal strain rate direction in the high-strain-rate areas ranges from ENE-WSW to ESE-WNW and has an average direction close to E-W. Deviations of the $\dot{\epsilon}_1$ azimuths from E-W tend to be towards the normals to the local fault strikes (Figure 6.2-1).

Table 6.2-2 lists the mean values of $\dot{\epsilon}_1$, the other horizontal principal strain rate $\dot{\epsilon}_2$, and the $\dot{\epsilon}_1$ azimuth for the Wasatch Front region and the four subregions. This table also lists the 90% confidence limits on the mean $\dot{\epsilon}_1$ values (± 1.645 std. dev.) obtained from the Monte Carlo simulations. The mean values for the $\dot{\epsilon}_1$ azimuths are weighted by the $\dot{\epsilon}_1$ magnitudes. If the area of each grid point was the same, and the azimuth of $\dot{\epsilon}_1$ was the same everywhere, then the mean of the $\dot{\epsilon}_1$ values at each grid point would equal the mean extensional strain over the whole region in the direction of the maximum horizontal extension. The variation in the grid point areas is only about 5%, which is negligible. There is some variability in the azimuth of $\dot{\epsilon}_1$, as noted above. However, we use the average of the scalar $\dot{\epsilon}_1$ values in our analysis in order to account, to some extent, for the correlated variations in $\dot{\epsilon}_1$ azimuths and fault normal directions in the Wasatch Front region.

As indicated in Table 6.2-2, the mean of the maximum horizontal principal strain rate, $\dot{\epsilon}_1$, for the Wasatch Front region (red box, Figure 6.2-1) is 11 nstr/yr (extensional). The mean $\dot{\epsilon}_1$ values for the four subregions are all positive (extensional), remarkably similar to each other, and within 10% of the value for the region as a whole. The mean $\dot{\epsilon}_2$ values for the Wasatch Front region and the subregions are all negative (compressional), and their absolute values are smaller than those of the corresponding $\dot{\epsilon}_1$ values by factors of 3.3 to 6.6. The mean $\dot{\epsilon}_1$-weighted $\dot{\epsilon}_1$ azimuths for the four subregions are all within 10° of the value for the region as a whole, which is 86°. Thus, to first order, the strain rate within the Wasatch Front region can be considered to be uniaxial E-W extension with an average value of 11 nstr/yr across the width of the region. The magnitudes of the average strain rates in Table 6.2-2 are, to some extent, arbitrary because the region boundaries are arbitrary and the strain rates vary considerably with each region (Figure 6.2-1). However, when we use these average strain rates we multiply them by the areas of the regions over which they were calculated, essentially converting them to an average velocity difference across the region times the north-south width of the region.

As a check on the average strain rates, we plot GPS-measured velocity versus distance east of the western edge of the

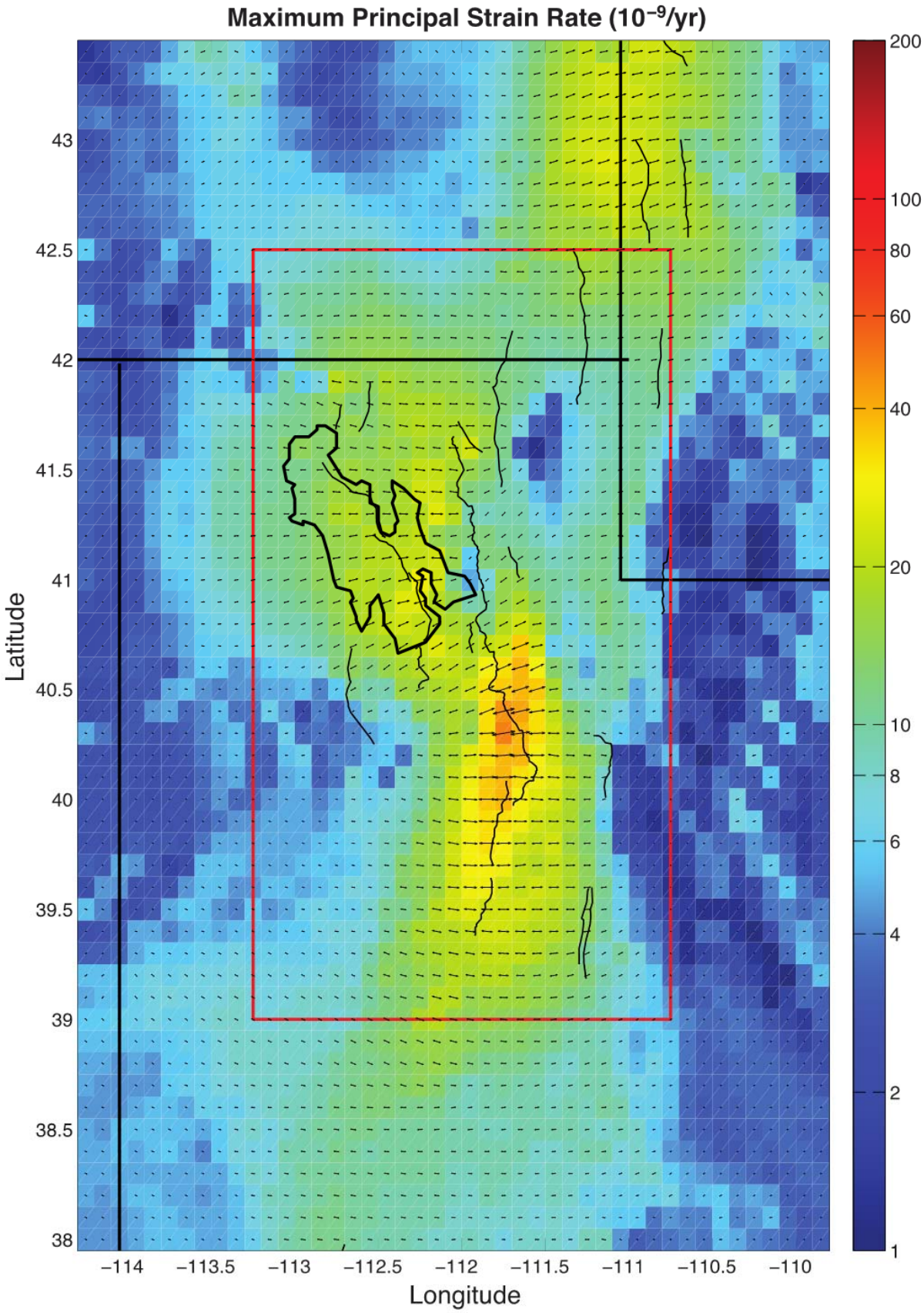

Figure 6.2-1. Color-coded map of maximum horizontal principal strain rate, $\dot{\epsilon}_1$ (extension positive). Note that the color scale is logarithmic. The two-headed arrows show the azimuth of $\dot{\epsilon}_1$ and have lengths proportional to the magnitude of $\dot{\epsilon}_1$. The other features shown on the map are the same as in Figure 6.1-2. Figure provided by Yuehua Zeng, USGS.

Table 6.2-2. Average strain rates for the Wasatch Front region and subregions.

Region	Latitude Range (deg)	Best Estimate				Alternative Estimate		
		$\dot{\epsilon}_1$ (nstr/yr)	90% CL[1] $\dot{\epsilon}_1$ (%)	$\dot{\epsilon}_2$ (nstr/yr)	$\dot{\epsilon}_1$ Az[2] (deg)	$\dot{\epsilon}_1'$ (nstr/yr)	90% CL $\dot{\epsilon}_1'$ (%)	$\dot{\epsilon}_1'/\dot{\epsilon}_1$
Wasatch Front	39.00–42.50	10.96	± 7	-2.47	86	12.33	± 17	1.13
BC-N	41.35–42.50	10.08	± 11	-3.01	90	10.17	± 24	1.01
SLC-W	40.50–41.35	11.90	± 9	-2.96	76	9.86	± 19	.83
NE-P	39.65–40.50	11.59	± 9	-1.89	88	10.50	± 18	.91
L-F	39.00–39.65	10.59	± 11	-1.60	93	12.22	± 20	1.15
Mean			± 9				± 20	1.00

[1] CL, confidence limit.

[2] Mean $\dot{\epsilon}_1$-weighted azimuth of $\dot{\epsilon}_1$.

Wasatch Front region (113.25° W) for (1) the whole Wasatch Front region (Figure 6.2-2), and (2) the four Wasatch Front subregions that we defined (Figure 6.2-3). The component of the velocity plotted is the component in the direction of the mean $\dot{\epsilon}_1$-weighted $\dot{\epsilon}_1$ azimuth for the region, as indicated in the vertical axis label. The error bars shown are 90% confidence limits (± 1.645 std. dev.), calculated from the standard errors in the east and north velocities in Table 6.2-1. The solid red line on each plot shows the velocity change across the region predicted by the strain rate model that we used to calculate the geodetic moment rates, which is uniaxial strain in the $\dot{\epsilon}_1$ direction. The solid red lines are not fit directly to the velocity vectors shown on the plots in Figures 6.2-2 and 6.2-3. Instead, these lines are calculated from the $\dot{\epsilon}_1$ grid (Figure 6.2-1) as follows. The change in velocity across each 0.05° longitude grid interval is computed by multiplying the mean $\dot{\epsilon}_1$ for that longitude, averaged over the latitude range for the region, by the distance across the grid interval measured in the mean $\dot{\epsilon}_1$ direction for the region. The absolute values of these predicted velocity curves are arbitrary, but they are positioned to match the observed velocities on the eastern ends of the regions. We consider the agreement between the predicted and observed velocities to be acceptable, considering that the strain rate model is a two-dimensional model that was fit to a larger data set than is shown on the plots.

The observed velocities in the average $\dot{\epsilon}_1$ directions are all west to west-southwest relative to stable North America, with the rate increasing westward by around 2.1 to 2.6 mm/yr across each of the regions shown in the plots. Most of the velocity increase takes place in the middle of the regions, in the vicinity of the WFZ, with relatively uniform velocities on the eastern and western ends. Consequently, as a check, alternative estimates for the average strain rates in the Wasatch Front region and the four subregions can be made from the difference in the average velocities on the eastern and western ends of each region.

The solid blue lines on each end of the five GPS velocity plots show inverse-variance weighted mean velocities from two to five GPS stations. The dotted lines show 5th and 95th percentile confidence limits on these mean velocities. The difference between the mean velocities on the two sides of a region divided by the distance across the region in the mean $\dot{\epsilon}_1$ direction gives the alternative estimates of the average strain rates in Table 6.2-2. These alternative average strain rate estimates are somewhat arbitrary, like the best estimates, because the widths of the regions are arbitrary. The ratios between the alternative strain rate estimates and the best estimates range from 0.83 to 1.15 and have a mean of 1.00. The 90% confidence limits on the alternative strain rate estimates range from 18% to 24% and have a mean value of 20% (Table 6.2-2). These 90% confidence limits might be overestimates because of the minimum values imposed on velocity vector uncertainties.

The results of the Monte Carlo simulations show 90% confidence limits on the best-estimate mean $\dot{\epsilon}_1$ values for the five regions of ± 7% to ± 11%, with an average value of ± 9% (Table 6.2-2). These confidence limits do not fully account for the effects of the uneven distribution of the GPS stations in and around the regions of interest (Figure 6.1-2). Furthermore, the ratios between the alternative and best-estimate maximum principal strain rates, and the 90% confidence limits for the former (Table 6.2-2), suggest that the actual uncertainties might be somewhat larger than those indicated by the Monte Carlo simulations. Considering all of the uncertainty information in Table 6.2-2, and also the ~2% to 3% effect of changing the grid size and area for computing the strain rates, we assume nominal 90% confidence limits of ± 15% for the mean $\dot{\epsilon}_1$ values determined for the Wasatch Front region and its four subregions. We note that because strain rate uncertainty is only one of three sources of uncertainty that we consider in calculating the geodetic moment rates (see Section 6.4), using 90% confidence limits of ± 20% instead of ± 15% does not noticeably affect the mean geodetic moment rates and changes their uncertainty ranges by less than 2%.

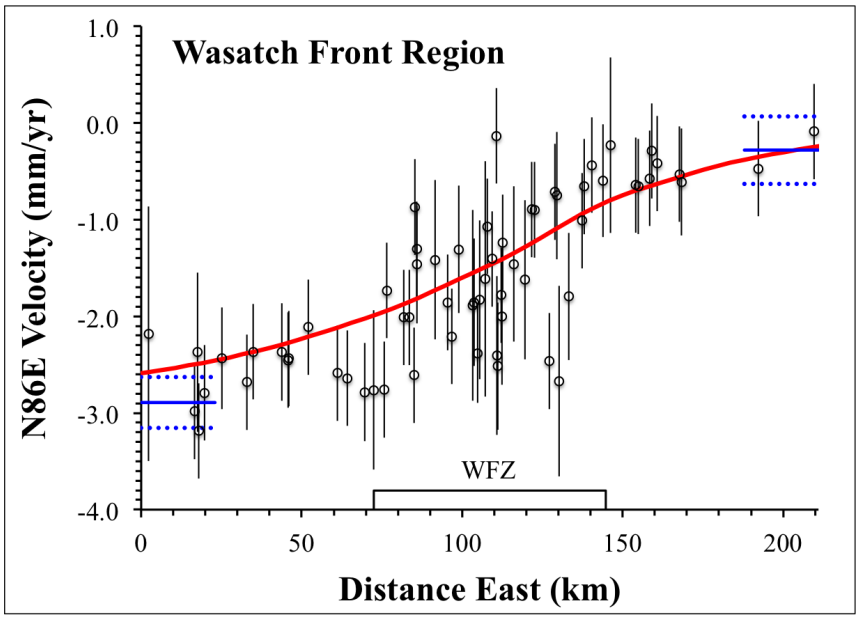

Figure 6.2-2. Plot of N. 86° E. (mean $\dot{\epsilon}_1$-weighted $\dot{\epsilon}_1$ azimuth) velocity versus distance east for GPS stations in the Wasatch Front region (box in Figure 6.1-2). Error bars are 90% confidence limits (± 1.645 std. dev.). The solid red line shows predicted velocity changes from the strain rate model, positioned to match the data on the east end. The blue lines show inverse-variance weighted mean velocities (solid) and 90% confidence limits (dotted) used to calculate the alternative strain rate estimate in Table 6.2-2. The WFZ spans the labeled distance range.

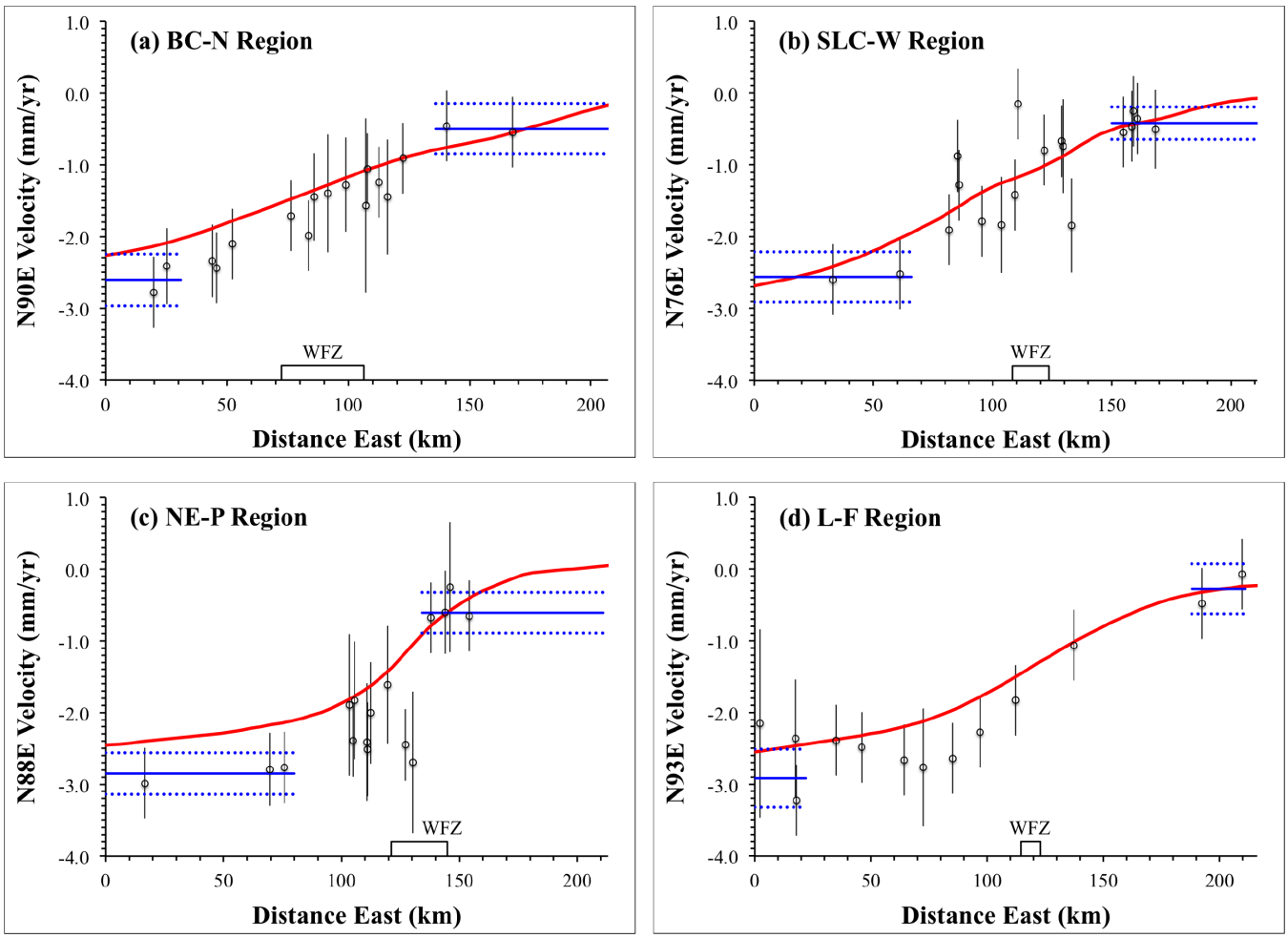

Figure 6.2-3. Same as Figure 6.2-2, but for the subregions shown in Figure 6.1-1.

6.3 Methodology

Following Ward (1994), we use an equation originally derived by Kostrov (1974) to convert the surface strain rates presented in the previous section into expected seismic moment rates for the Wasatch Front region and the four subregions shown in Figure 6.1-1. These expected moment rates, which are known as geodetic moment rates, are then compared to moment rates calculated from geological and seismological data for the same regions. The geodetic moment rates should be equal to the geological/seismological moment rates if, as assumed by Ward (1994), contemporary strain rates are equal to long-term deformation rates from earthquakes when averaged over sufficiently large regions and time intervals. Note that this assumption is only valid if the region of averaging is large enough to encompass all of the strain accumulation zones from the faults contained within the region. We consider this assumption to be reasonable, at least for the faults with the highest associated strain rates, because the strain rates along the eastern and western edges of the Wasatch Front region are generally much lower than those in the center of the region (Figures 6.2-1 to 6.2-3).

Kostrov's (1974) equation describes how movement in separate earthquakes along numerous randomly located fractures can be summed in a quasi-plastic deformation process. The equation is:

$$\dot{\epsilon}_{IJ} = \frac{1}{2\mu A H_s \Delta t} \sum_{\kappa} M_{0ij}^{(\kappa)} \qquad (6\text{-}1)$$

where $\dot{\epsilon}_{IJ}$ is the "mean tensor of the rate of deformation due to the seismic flow of rock mass," μ is the rigidity, A is the surface area of the region for the $M_{0ij}^{(\kappa)}$ summation, H_s is the thickness of the seismogenic layer, Δt is the time interval for the $M_{0ij}^{(\kappa)}$ summation, and $M_{0ij}^{(\kappa)}$ is the ij'th component of the moment tensor of the κ'th earthquake. If M_0 is the scalar moment, then for double-couple sources:

$$M_{0ij} = M_0(b_i n_j + b_j n_i) \qquad (6\text{-}2)$$

where b_i and b_j are the ith and jth components, respectively, of a unit vector in the displacement direction and n_i and n_j are the ith and jth components, respectively of a unit vector perpendicular to the fault plane.

To apply this equation to the Wasatch Front region, we select a coordinate system with the x_1-axis parallel to the direction of the maximum horizontal principal strain rate, $\dot{\epsilon}_{IJ}$, with extension positive. The x_2-axis is horizontal and normal to x_1, and the x_3-axis is directed upward. We also make the simplifying assumption that all of the seismic moment release is due to normal faulting on planes which strike in the x_2 direction and have a dip of δ. With this assumption, the nonzero moment tensor elements become $M_{011} = M_0 \sin 2\delta$, $M_{033} = -M_0 \sin 2\delta$, and $M_{013} = \pm M_0 \cos 2\delta$, with the sign of M_{013} depending on the dip direction. Substituting the first two of these moment tensor elements into Kostrov's equation gives

$$\dot{\epsilon}_{11} = -\dot{\epsilon}_{33} = \frac{\sin 2\delta}{2\mu A H_s \Delta t} \sum_{\kappa} M_0^{(\kappa)} \qquad (6\text{-}3)$$

where $M_0^{(\kappa)}$ is the scalar moment of the κ'th earthquake or, equivalently,

$$\dot{M}_0 = \frac{2\mu A H_s}{\sin 2\delta} \dot{\epsilon}_1 \qquad (6\text{-}4)$$

where $\dot{M}_0$ is the seismic ("geodetic") moment rate for the volume.

Ward (1994) similarly reduced Kostrov's original tensor equation to a scalar equation by replacing $\dot{\epsilon}_{IJ}$ with the largest principal strain rate and replacing $\frac{1}{\Delta t}\sum_{\kappa} M_{0ij}^{(\kappa)}$ by $\dot{M}_0$ for each of his subregions. Our particular application of Kostrov's equation assumes normal faulting on planes striking perpendicular to $\dot{\epsilon}_1$, but reduces to Ward's equation for the special case of $\delta = 45°$. Note that for a given $\dot{\epsilon}_1$, the geodetic moment rate $\dot{M}_0$ has a minimum value of $2\mu A H_s \dot{\epsilon}_1$ for $\delta = 45°$.

To provide some physical insight into Equation (6-4), we present here a second derivation of this equation for the special case of the simple block model shown in cross section in Figure 6.3-1. In this block model, all of the moment release occurs on a single normal fault of dip δ and length L that extends through the entire thickness of the seismogenic layer H_s. Let $\bar{d}$ be the average displacement on this fault in an earthquake, which is uniform across the fault surface in this block model, and let Δt be the average earthquake recurrence interval. From Figure 6.3-1 and the definition of seismic moment, the moment rate on the fault is given by

$$\dot{M}_0 = \mu L (H_s/\sin\delta)\, \bar{d}/\Delta t \qquad (6\text{-}5)$$

The permanent horizontal strain rate in the direction perpendicular to the fault is

$$\dot{\epsilon}_1 = \frac{\Delta W}{W \Delta t} = \frac{\bar{d}\cos\delta}{W \Delta t} \qquad (6\text{-}6)$$

where W is the width of the region under consideration and ΔW is the change in this width that occurs during an earthquake. Solving Equation (6-6) for $\bar{d}$ and substituting into equation (6-5) gives

$$\dot{M}_0 = \frac{\mu L W H_s}{\sin\delta\cos\delta} \dot{\epsilon}_1 = \frac{2\mu A H_s}{\sin 2\delta} \dot{\epsilon}_1 \qquad (6\text{-}7)$$

which is the same as Equation (6-4). From Equation (6-7) and Figure 6.3-1, it can be seen that the $1/\sin 2\delta$ factor in Equation (6-4) is the result of two competing factors. Consider Figure 6.3-1 with a given, fixed extension rate perpendicular to the fault and a fixed seismogenic zone thickness H_s. As the fault dip increases from 0° to 90°, the fault slip rate $\dot{\bar{d}}$ needed to produce the given extension rate $\Delta \dot{W} = \dot{\bar{d}} \cos\delta$ increases pro-

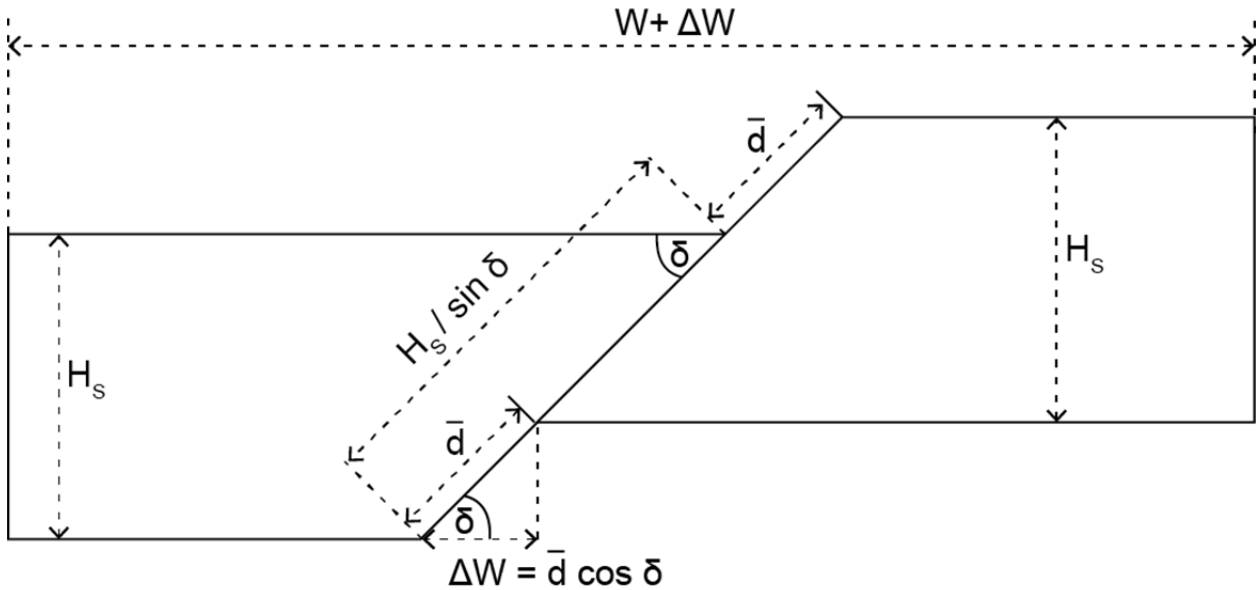

Figure 6.3-1. Block diagram of a normal fault. W is the width of the region under consideration, ΔW is the change in this width during an earthquake, H_s is the thickness of the seismogenic layer, δ is the fault dip, and $\bar{d}$ is the average displacement on the fault in an earthquake.

portional to 1/ cos δ. This increase in slip rate increases the moment rate on the fault. The competing factor is that as the fault dip increases, the fault width H_s / sin δ decreases proportional to 1/ sin δ because the bottom edge of the fault is fixed at the bottom of the seismogenic zone. This decrease in the fault width decreases the fault area, and hence, the moment rate on the fault. Because the moment rate is proportional to the product of the slip rate and the fault area, the change in the moment rate with the fault dip is proportional to 1/ sin δ cos δ = 2/ sin 2δ.

Although the derivation in the preceding paragraph is for a block model with a single normal fault, this derivation can clearly be generalized to a block model having multiple normal faults. Thus, this derivation shows that the moment rate Equation (6-4) is the same as that of a two-dimensional block model in which all of the moment release occurs on parallel normal faults of dip δ that break the whole seismogenic layer. In applying this equation to short-term measurements of $\dot{\epsilon}_1$, we are essentially assuming a two-dimensional strain accumulation model in which the seismogenic layer is being extended in the $\dot{\epsilon}_1$ direction at a rate equivalent to the long-term and large-scale permanent rate of deformation caused by earthquakes. Relatively steady extension of the seismogenic layer at the long-term rate could occur, for example, if the strain accumulation in this layer is driven by basal tractions produced by underlying ductile extension (see Bourne *et al*., 1998, and Niemi *et al*., 2004).

The simplifying assumptions that we made are reasonable for the Wasatch Front region. All of the major active faults in the region are normal faults. The average azimuth of the maximum horizontal extensional strain rate for the region as a whole, weighted by the principal strain rate magnitudes $\dot{\epsilon}_1$, is N. 86° E. (Table 6.2-2). This average azimuth is perpendicular to the approximately N-S average strike of the faults in the Wasatch Front region (Figure 6.1-1). The actual fault strikes vary, but generally range from SSW to SSE. The $\dot{\epsilon}_1$ azimuths generally range from ENE-WSW to ESE-WNW in the parts of the Wasatch Front region where $\dot{\epsilon}_1$ is above its average value of 11×10^{-9}. As noted earlier, in some places, such as along the central WFZ, there appears to be a tendency for the $\dot{\epsilon}_1$ azimuths to rotate to directions perpendicular to the local fault strikes (Figure 6.2-1).

6.4 Geodetic Moment Rates

We applied Equation (6-4) to calculate geodetic moment rates for the Wasatch Front region and the four subregions shown in Figure 6.1-1. The input parameters that we used are $\mu = 3 \times 10^{11}$ dynes/cm^2, A = surface area of the region, H_s = 15 ± 3 km (from Section 3.3), δ = 50° ± 15° (from Section 3.2), and the best estimate $\dot{\epsilon}_1$ values listed in Table 6.2-2, with assumed 90% confidence limits of ± 15% as discussed in Section 6.2. The uncertainty in μ is not considered here because the geodetic and the geological/seismological moment rates all depend linearly on μ and the same value of μ is used for all moment rate calculations. Consequently, the uncertainty in μ is irrelevant for the comparisons between geodetic and geological/seismological moment rates.

We used discrete probability distributions for H_s, δ, and $\dot{\epsilon}_1$ and a logic tree approach to determine mean, 5th percentile, and 95th percentile values for the geodetic moment rates. For H_s we initially used the two region-dependent three-point logic tree distributions from Section 3.3: 12 km (0.2), 15 km (0.7), and 18 km (0.1) for the WFZ and faults to the west and 12 km (0.1), 15 km (0.7), and 18 km (0.2) for faults to the east of

the WFZ. For δ, we used the following five-point distribution (based on Miller and Rice, 1983) rather than the three-point distribution employed in the WGUEP earthquake probability calculations in order to better account for the non-Gaussian distribution of the $1/(\sin 2\delta)$ factor in equation 6-4: 28.8° (0.101), 40.6° (0.244), 50° (0.310), 59.4° (0.244), and 71.2° (0.101). This five-point dip distribution, like the three-point dip distribution, approximates a normal distribution in which the 10th and 90th percentile dips are 35° and 65°, respectively. For $\dot{\epsilon}_1$, we approximate a normal distribution with 5th and 95th percentile values of $0.85\dot{\epsilon}_1$ and $1.15\dot{\epsilon}_1$, respectively, with a three-point distribution from Keefer and Bodily (1983): $0.85\dot{\epsilon}_1$ (0.2), $\dot{\epsilon}_1$ (0.6), and $1.15\dot{\epsilon}_1$ (0.2). After combining the discrete probability distributions for H_s, δ, and $\dot{\epsilon}_1$ together in a logic tree, we found that the geographic variation in the H_s weights had only a very minor effect on the mean and 5th and 95th percentile values for the geodetic moment rates. Given this fact, and the difficulty of identifying and separating the strain accumulation zones for the faults east and west of the WFZ, we decided to simply average the values from the two sets of H_s weights.

6.5 Geological/Seismological Moment Rates

Table 6.5-1 lists the mean, 5th percentile, and 95th percentile geological moment rates for all of the faults considered in the WGUEP's earthquake forecast plus the corresponding seismological moment rates for the background earthquake source. We calculated the mean moment rates using the seismic source models and associated logic trees developed in the preceding sections of this report, excluding the time-dependent models and assuming $\mu = 3 \times 10^{11}$ dynes/cm^2. The 5th percentile moment rates are zero for the independent ruptures on four faults that are modeled as subsidiary faults in an antithetic fault pair. These rates are zero because the antithetic fault pairs may also rupture coseismically and in that branch of the logic tree, all of the moment rate is assigned to the master fault. Table 6.5-1 also indicates how the moment rates from the various sources are partitioned among the four subregions shown in Figure 6.1-1. For the faults or fault segments that span two subregions, the moment rates are divided between the two subregions proportional to the percentage of the straight line end-to-end fault length that lies within each region. The relatively small moment rate from the background source, about 3% of the total, is subdivided proportional to the subregion areas.

Table 6.5-2 provides the total geological/seismological moment rates for the Wasatch Front region and its four subregions, plus subtotals for three groups of sources: the WFZ, all other faults including the OGSLFZ, and the background earthquakes. The mean moment rate for a group of sources is, to a good approximation, equal to the sum of the mean moment rates for its constituent sources. However, that is not true for the 5th and 95th percentile moment rates.

As indicated in Table 6.5-2, the mean total moment rate in the WGUEP source model for the whole Wasatch Front region is 6.31×10^{24} dyne-cm/yr. This rate is equivalent to the moment rate that would be produced by the occurrence of one **M** 5.8 earthquake per year. Two-thirds of the total moment rate for the region comes from the two central subregions, which have nearly equal moment rates and together occupy about half the area of the Wasatch Front region (Figure 6.1-1). One of these two central subregions, NE-P, includes the Nephi and Provo segments of the WFZ; the other, SLC-W, includes the Salt Lake City and Weber segments of the WFZ. The northernmost subregion, BC-N, has a somewhat smaller moment rate than the two central subregions despite its larger area, which covers about one-third the total area of the Wasatch Front region. The BC-N subregion includes the Brigham City segment of the WFZ and other WFZ segments farther north. The southernmost subregion, L-F, has a mean moment rate that is a factor of five or more smaller than that of all of the other subregions. The L-F subregion covers the north-south extent of the Levan and Fayette segments of the WFZ.

One of the most significant observations to be made from Table 6.5-2 is that the WFZ accounts for only about half of the estimated seismic moment rate for the Wasatch Front region. The other half comes primarily from the rest of the faults in the region, including the OGSLFZ, which have a combined moment rate comparable to that of the WFZ. This result is consistent with Hecker's (1993) tabulation of post-Bonneville surface-faulting earthquakes within a region very similar to the Wasatch Front region as defined in this report (Figure 6.1-1). Hecker's tabulation showed that only half of the estimated 50 to 120 post-Bonneville surface-faulting earthquakes within her study region that were recognized or suspected at the time of her study occurred on the WFZ. One implication of the moment rate subtotals in Table 6.5-2 is that it is very important for strain rate models for the Wasatch Front region to include the other faults in the region besides the WFZ. Some of the Wasatch Front strain rate models published to date do not, including Chang *et al*. (2006) and Velasco *et al*. (2010).

6.6 Comparison of Geodetic and Geological/Seismological Moment Rates

Table 6.6-1 compares geodetic moment rates to geological/seismological moment rates for the Wasatch Front region, and for the four subregions mapped in Figure 6.1-1. For the Wasatch Front region and the three northernmost subregions, the agreement between the two moment rates is reasonably good and well within the uncertainty limits. The geological/seismological moment rate for the Wasatch Front region as a whole is lower than the geodetic moment rate, by 31%, but there is substantial overlap in the uncertainty limits. For the SLC-W and NE-P subregions, which encompass the Salt Lake City, Weber, Nephi, and Provo segments of the WFZ, the mean values for the two moment rates agree within 15%. For the BC-N subregion, which includes the Brigham City

Table 6.5-1. Geological/seismological moment rates for Wasatch Front region seismic sources.

Source	Moment Rate (dyne-cm/yr)			% M_0 Rate in Subregion			
	Mean	5th Percentile	95th Percentile	L-F	NE-P	SLC-W	BC-N
Wasatch Fault Zone							
Fayette segment	2.71E+22	1.13E+21	7.23E+22	100			
Levan segment	7.23E+22	7.73E+21	1.82E+23	100			
Nephi segment	6.03E+23	1.29E+23	1.52E+24		100		
Provo segment	9.56E+23	2.91E+23	2.07E+24		100		
Salt Lake City segment	5.38E+23	1.47E+23	1.20E+24			100	
Weber segment	7.67E+23	2.25E+23	1.72E+24			100	
Brigham City segment	3.40E+23	9.59E+22	7.87E+23				100
Collinston segment	1.27E+22	1.64E+21	3.26E+22				100
Clarkston Mt segment	1.26E+22	1.47E+21	2.93E+22				100
Malad City segment	1.83E+22	2.31E+21	4.77E+22				100
Oquirrh-Great Salt Lake Fault Zone							
East Tintic segment	3.58E+22	5.67E+21	9.04E+22		100		
Topliff Hill segment	4.51E+22	7.15E+21	1.10E+23		100		
Southern Oquirrh segment	5.07E+22	9.53E+21	1.14E+23		100		
Northern Oquirrh segment	4.68E+22	6.14E+21	1.16E+23			100	
Antelope Island segment	1.51E+23	3.49E+22	3.70E+23			100	
Fremont Island segment	1.24E+23	2.34E+22	3.17E+23			100	
Promontory segment	9.45E+22	1.62E+22	2.43E+23			70	30
Rozelle segment	9.97E+22	2.39E+22	2.77E+23				100
Other Modeled Faults							
West Valley fault zone (ind ruptures)	5.57E+21	0.00E+00	2.63E+22			100	
Utah Lake faults (ind ruptures)	3.44E+22	0.00E+00	1.22E+23		100		
East Cache fault zone	1.26E+23	2.00E+22	3.19E+23				100
Bear River fault zone	1.84E+23	6.98E+22	5.68E+23			100	
Eastern Bear Lake fault	5.12E+23	1.12E+23	1.44E+24				100
Western Bear Lake fault (ind ruptures)	1.45E+22	0.00E+00	6.10E+22				100
North Promontory fault	9.07E+22	1.91E+22	2.43E+23				100
Hansel Valley fault (ind ruptures)	5.74E+21	0.00E+00	2.12E+22				100
Stansbury fault-Southern segment	6.37E+22	6.52E+21	1.92E+23		100		
Stansbury fault-Central segment	1.23E+23	1.25E+22	3.97E+23		90	10	
Stansbury fault-Northern segment	8.99E+22	9.20E+21	2.72E+23			100	
West Cache fault zone	1.53E+23	3.30E+22	3.56E+23				100
Rock Creek fault	2.33E+23	4.49E+22	5.61E+23				100
Carrington fault	8.57E+22	1.39E+22	1.99E+23			100	
Skull Valley faults	8.04E+22	9.82E+21	1.75E+23		100		
Scipio Valley and Pavant Range faults	5.62E+22	4.93E+21	1.97E+23	100			
Curlew Valley faults	5.51E+22	1.10E+22	1.75E+23				100
Gunnison fault	5.21E+22	4.60E+21	1.84E+23	90	10		
Strawberry fault	3.19E+22	7.36E+21	1.02E+23		100		
Little Valley faults	2.48E+22	2.19E+21	8.75E+22	100			
Crater Bench and Drum Mts fault zone	2.97E+22	2.85E+21	1.14E+23	100			
Joes Valley fault zone	2.11E+22	6.38E+20	6.07E+22	100			
East Dayton-Oxford faults	8.93E+21	1.26E+21	1.89E+22				100
Porcupine Mt fault	7.28E+21	1.92E+21	1.92E+22			100	
Main Canyon fault	5.37E+21	1.42E+21	1.42E+22			100	
West Crawford Mts fault	4.99E+21	1.37E+21	1.37E+22				100
Morgan fault	3.47E+21	8.20E+20	9.30E+21			100	
Stinking Springs fault	1.14E+22	1.84E+21	4.10E+22		100		
Snow Lake graben	1.32E+22	3.80E+20	3.98E+22	100			
Background Earthquakes	1.83E+23	8.15E+22	3.51E+23	19.0	24.6	24.2	32.3

Table 6.5-2. Geological/seismological moment rates for the Wasatch Front region and subregions (dyne-cm/yr).

Source		Region				
		Wasatch Front	L-F	NE-P	SLC-W	BC-N
Wasatch Fault Zone	Mean	3.33E+24	9.94E+22	1.56E+24	1.31E+24	3.84E+23
	5th Percentile	1.51E+24	1.01E+22	5.59E+23	4.98E+23	1.25E+23
	95th Percentile	6.21E+24	2.57E+23	3.16E+24	2.56E+24	8.24E+23
OGSLFZ Plus Other Faults	Mean	2.77E+24	1.92E+23	4.69E+23	7.82E+23	1.33E+24
	5th Percentile	1.88E+24	7.52E+22	2.23E+23	4.14E+23	7.47E+23
	95th Percentile	4.02E+24	3.74E+23	8.38E+23	1.33E+24	2.28E+24
Background Earthquakes	Mean	1.83E+23	3.48E+22	4.51E+22	4.44E+22	5.92E+22
	5th Percentile	8.15E+22	1.55E+22	2.01E+22	1.97E+22	2.63E+22
	95th Percentile	3.51E+23	6.67E+22	8.64E+22	8.50E+22	1.13E+23
Total	Mean	6.31E+24	3.26E+23	2.07E+24	2.13E+24	1.77E+24
	5th Percentile	4.18E+24	1.54E+23	1.02E+24	1.19E+24	1.09E+24
	95th Percentile	9.36E+24	5.58E+23	3.70E+24	3.54E+24	2.79E+24

Table 6.6-1. Comparison of geodetic and geological/seismological moment rates.

Region	Area (10^{14} cm^2)	Geodetic M_0 Rate (10^{24} dyne-cm/yr)			Geol/Seism M_0 Rate (10^{24} dyne-cm/yr)		
		Mean	5th Percentile	95th Percentile	Mean	5th Percentile	95th Percentile
Wasatch Front	8.21	9.13	6.53	13.28	6.31	4.18	9.36
BC-N	2.65	2.71	1.94	3.94	1.77	1.09	2.79
SLC-W	1.99	2.40	1.72	3.49	2.13	1.19	3.54
NE-P	2.02	2.37	1.70	3.45	2.07	1.02	3.70
L-F	1.56	1.67	1.20	2.43	0.33	0.15	0.56

segment and the three less active segments to the north, the geological/seismological moment rate is 35% below the geodetic moment rate. However, there is considerable overlap in the 5th and 95th percentile confidence limits for these moment rates.

In contrast, the geodetic moment rate for the L-F subregion, which spans the north-south extent of the Levan and Fayette segments of the WFZ, is a factor of five higher than the geological/seismological moment rate. This difference is significant at the 90% level, because the 5th percentile for the geodetic moment rate (1.20×10^{24} dyne-cm/yr) is more than a factor of two above the 95th percentile for the geological/seismological moment rate (0.56×10^{24} dyne-cm/yr). The large discrepancy between these two moment rates is consistent with the results of the Zeng and Shen (2014) fault slip rate inversion shown in Figure 6.1-3. The evidence for this discrepancy can be seen in the original data. The strain rate for the L-F subregion is about the same as in the other subregions, as shown in Table 6.2-2 and Figures 6.1-2 and 6.2-3. The geodetic moment rate for the L-F subregion is 62% to 70% of the rates in the other subregions, mostly due to the smaller area of the L-F subregion (Table 6.6-1). However, the geological moment rate on the WFZ in the L-F subregion is only one-fourth or less of the rates in the other subregions, and the geological moment rate on the other faults is less than half the values for other subregions (Table 6.5-2).

6.7 Discussion: The Moment Rate Discrepancy

6.7.1 The Levan and Fayette Segments

The underlying reason for the high geodetic moment rate in the L-F region compared to the geological/seismological moment rate is unknown. The highest strain rates in this region occur in the general vicinity of the Levan and Fayette segments of the WFZ (Figures 6.1-2 and 6.2-1). Is it possible that the WGUEP model underestimates the geological moment rates on these two segments? In the Zeng and Shen (2014) inversion solution, the slip rate on the Levan segment is a factor of five higher than the geologic slip-rate estimate of 0.31 mm/yr (Haller and Wheeler, 2008). The Fayette segment was not included in the Zeng and Shen (2014) inversion because this segment was not used in the hazard calculations for the 2008 NSHMs. If we multiply the moment rate on the Levan segment by five, the mean geological/seismological moment rate in the L-F region increases to 0.62×10^{24} dyne-cm/yr. However, this moment rate is still a factor of 2.7 below the mean geodetic moment rate.

The paleoseismic data for the Levan and Fayette segments are more limited than the data available for the five central segments of the WFZ to the north (Brigham City to Nephi).

Nevertheless, from the available data, the rate of earthquake activity on the Levan and Fayette segments is evidently much lower than on the five central segments. Paleoseismic studies of scarps, one trench, and one natural exposure on the Levan segment have found evidence for two surface-faulting earthquakes on this segment since sometime before 6000–10,600 cal yr B.P. (Section 4.4.2; Hylland, 2007b; Hylland and Machette, 2008). In contrast, four or five documented surface-faulting earthquakes occurred during the past ~6000 yrs on each of the five central segments of the WFZ (Table 4.1-1; Figure 4.1-2). On the Fayette segment, cross-cutting geologic relations and scarp profile data indicate that the most recent surface faulting occurred in the mid- to early Holocene on the southwestern strand, latest Pleistocene on the southeastern strand, and prior to ~250,000 ka on the northern strand. The times of earlier surface-faulting earthquakes on the Fayette segment are unknown due to the lack of trenching data (Section 4.2.2; Hylland, 2007b; Hylland and Machette, 2008).

The WGUEP model uses slip rates to quantify the rates of seismic activity on the Levan and Fayette segments. Holocene vertical slip-rate bounds from the trench and the natural exposure on the Levan segment are < 0.5 to 2.3 mm/yr and < 0.2 to 0.4 mm/yr, respectively, the latter value being considered the more reliable of the two (Table 4.2-1; Hylland and Machette, 2008). On the Fayette segment, vertical offsets measured from scarp profiles, in combination with maximum age estimates for the most recent event, provide Holocene slip rate bounds of > 0.07 to 0.1 mm/yr for the southwestern strand and latest Pleistocene slip rate bounds of > 0.03 to 0.07 mm/yr for the southeastern strand (Table 4.2-1). In the WGUEP segmented rupture model (weight 0.9), the total slip rate on the Levan and Fayette segments is equally partitioned between single-segment ruptures and combined Levan-Fayette segment ruptures (see Table 4.2-2 and the accompanying discussion). The sum of the median vertical slip rates assigned to these two types of ruptures is 0.3 mm/yr on the Levan segment and 0.175 mm/yr on the Fayette segment. For comparison, the closed mean vertical slip rates for the five central segments of the WFZ have preferred values ranging from 1.3 mm/yr to 2.0 mm/yr (Table 4.1-4).

The difference between the means of the geodetic moment rate and the geological/seismological moment rate for the L-F region is 1.34×10^{24} dyne-cm/yr. This difference is a factor of 13.5 larger than the sum of the mean moment rates on the Levan and Fayette segments in the WGUEP model, which is 9.94×10^{22} dyne-cm/yr. Therefore, to account for the moment rate discrepancy by changing the WGUEP slip rates for the Levan and Fayette segments, we would need to increase these slip rates by a factor of 14.5. The resulting vertical slip rates of 4.4 mm/yr on the Levan segment and 2.5 mm/yr on the Fayette segment are clearly unrealistic, as they are significantly larger than the preferred mean slip rates for the five central segments of the WFZ (Table 4.1-4). Also, a 4.4 mm/yr slip rate on the Levan segment would exceed both of the maximum slip rate estimates for this segment.

The geological moment rates in the WGUEP model are a function of the fault dips, which are assumed to be 50° ± 15° (90% confidence limits) for all faults. Some evidence suggests that the dips along the Levan and Fayette segments of the WFZ might be at or below the low end of the assumed dip range. Smith and Bruhn (1984) interpret a seismic reflection section across the northern Levan segment at the town of Levan (Figure 6.1-1) to show a WFZ dip of ~34° at 1.9 km depth. However, this dip measurement has a large uncertainty because of the poor quality of the seismic reflection data. Schelling *et al*. (2007) write that "south of the town of Nephi [Figure 6.1-1], the Wasatch fault dip decreases and seismic data indicate that this southern extension of the Wasatch fault merges with a detachment surface located within shales and evaporites of the Arapien Shale underneath Juab Valley." On a structural cross section that crosses the Levan segment 6.5 km NNE of Levan, Schelling *et al*. (2007) show the dip of the WFZ decreasing from ~40° near the surface to ~6° at ~3.6 km depth, at the base of the Arapien Shale. It is unclear from their cross section what happens to the WFZ beyond the western end of the 6°-dipping section, which is 9 km west of the surface trace. Unfortunately, we cannot evaluate Schelling *et al*.'s (2007) interpretation of the subsurface geometry of the Levan segment because they did not publish the seismic reflection data on which it is based. We are skeptical of their interpretation for various reasons, including the lack of supporting data, mechanical implausibility, and the difficulty of distinguishing Mesozoic thrust faults from superimposed Cenozoic normal faults. Nevertheless, the Schelling *et al*. (2007) and Smith and Bruhn (1984) studies motivate us to explore the effects of possible lower fault dips along the Levan and Fayette segments on the L-F region moment rate discrepancy.

For fixed values of μ, L, H_s, and vertical slip rate $\dot{d}_v$, substituting $\dot{d}_v / \sin\delta$ for $\bar{d}/\Delta t$ in Equation (6-5) shows that the moment rate on a normal fault is proportional to $1/(\sin\delta)^2$. Therefore, to estimate the moment rate for an assumed dip δ other than 50° ± 15°, we multiply the WGUEP moment rate by $(\sin 50°/\sin\delta)^2$. This dip adjustment is approximate because the original WGUEP moment rates are mean values calculated using discrete probability distributions for dip and other parameters. Recall that the geodetic moment rate is inversely proportional to sin 2δ (Equation [6-4]). Consequently, if the missing geodetic moment rate is assumed to be accommodated by normal faults with a dip other than 50°, we multiply it by sin 100°/sin 2δ. This adjustment is also approximate because our original geodetic moment rates are mean values calculated using discrete probability distributions for dip, seismogenic depth, and strain rate (Section 6.4).

The shallowest plausible dip for a seismogenic normal fault in the Wasatch Front region is 30°, based on both theoretical expectations and a worldwide compilation of fault plane dips for 25 shallow, continental, M > 5.5 normal-faulting earthquakes (Collettini and Sibson, 2001). This compilation shows a dip distribution extending from 30° to 65°, with a peak at

45°. As discussed in Section 3.2, the available data from large normal-faulting earthquakes in the Basin and Range Province are in agreement with the minimum dip of 30° observed in the worldwide data set. If we assume a dip of 30° instead of 50° on the Levan and Fayette segments, the dip adjustment discussed above increases their combined geologic moment rate to 2.33×10^{23} dyne-cm/yr. The geodetic moment rate in the L-F region that is unaccounted for by earthquake sources in the WGUEP model other than the Levan and Fayette segments is 1.44×10^{24} dyne-cm/yr for 50°-dipping faults and 1.64×10^{24} dyne-cm/yr for 30°-dipping faults. Therefore, in order to account for the missing moment rate on the Levan and Fayette segments, assuming 30° dips, their slip rates would need to be increased by a factor of 7.0. The resulting median slip rates of 2.1 mm/yr on the Levan segment and 1.2 mm/yr on the Fayette segment are still unrealistically high. We conclude that the Levan and Fayette segments could, at most, account for only a small part of the discrepancy between the geodetic and geological/seismological moment rates for the L-F region.

6.7.2 Faults Omitted From the WGUEP Model

Another possibility that must be considered is that the WGUEP fault model is missing one or more significant active faults in the L-F region. Table 6.7-1 summarizes information on 12 known or suspected Quaternary faults that are located at least partially within the L-F region but are not included in the WGUEP fault model (see also Figure 6.7-1). All are normal faults with northerly or southerly strikes. Eleven of these faults are in the *Quaternary Fault and Fold Database of the United States* (USGS, 2013; see also Black *et al*., 2003). All 11 are assigned to the database slip rate category of < 0.2 mm/yr, but the database does not cite specific slip-rate measurements for any of them. These 11 faults are not included in the WGUEP model because the WGUEP considered them unlikely to significantly affect the earthquake forecast, based primarily on their length and/or the age of their most recent surface deformation (see Section 4.5). For completeness, Table 6.7-1 includes another suspected Quaternary fault in the region that Cline and Bartley (2007) have named the Salina detachment (Figure 6.7-1). This feature is a Cenozoic-Jurassic contact on the eastern side of the Sevier Valley that Cline and Bartley (2007) interpret as an east-dipping rolling hinge normal fault (Buck, 1988; Wernicke and Axen, 1988). They argue that this fault is a southwestward continuation of the Gunnison fault (called the West Sanpete fault in their paper) that likely transfers displacement southward to the Elsinore and Sevier faults. The only evidence that the Salina detachment is active is its inferred connection to the Gunnison fault, which has had late Holocene movement (Fong, 1995; Black *et al*., 2003). If the Salina detachment is active, then its slip rate is likely to be in the < 0.2 mm/yr category like the Gunnison fault to the north and the Sevier and Elsinore faults to the south.

The cumulative length within the L-F region of all of the faults listed in Table 6.7-1 is 175 km. To estimate their combined moment rate, we assume that they are all pure normal faults with a dip of 50° that extend to 15 km depth. With these assumptions, and the previously assumed rigidity of 3×10^{11} dynes/cm^2, the maximum estimated slip rate for these faults of 0.2 mm/yr gives a maximum estimated moment rate of 2.68×10^{23} dyne-cm/yr. This maximum moment rate is a factor of five smaller than the missing moment rate.

Of course, it is possible that the length and/or slip rate has been underestimated for some of the faults in Table 6.7-1, or that there are other, unknown, active faults in the region. To put these possibilities into perspective, let us assume, for the sake of argument, that all of the missing moment rate occurs

Table 6.7-1. Faults in the L-F subregion that are not included in the WGUEP fault model.

Fault Name*	End-To-End Length (km)*	Length in L-F Region (km)	Time of Most Recent Deformation*
Clear Lake fault zone	36	26	Latest Quaternary (< 15 ka)
Cricket Mountains (north end) faults	3	3	Middle and late Quaternary (< 750 ka)
Cricket Mountains (west side) fault	41	7	Latest Quaternary (< 15 ka)
Deseret faults	7	7	Middle and late Quaternary (< 750 ka)
Gooseberry graben faults	23	4	Middle and late Quaternary (< 750 ka)
Japanese and Cal Valleys faults	30	30	Middle and late Quaternary (< 750 ka)
Pavant faults	30	26	Middle and late Quaternary (< 750 ka)
Pleasant Valley fault zone, unnamed	31	2	Quaternary (< 1.6 Ma)
Sage Valley fault	11	11	Quaternary (< 1.6 Ma)?
Salina detachment	80	38	Quaternary (< 1.6 Ma)?
Sugarville area faults	5	5	Latest Quaternary (< 15 ka)
White Mountain area faults	16	16	Quaternary (< 1.6 Ma)
Total	–	175	

*Information from USGS (2013), except for the Salina detachment (Cline and Bartley, 2007).

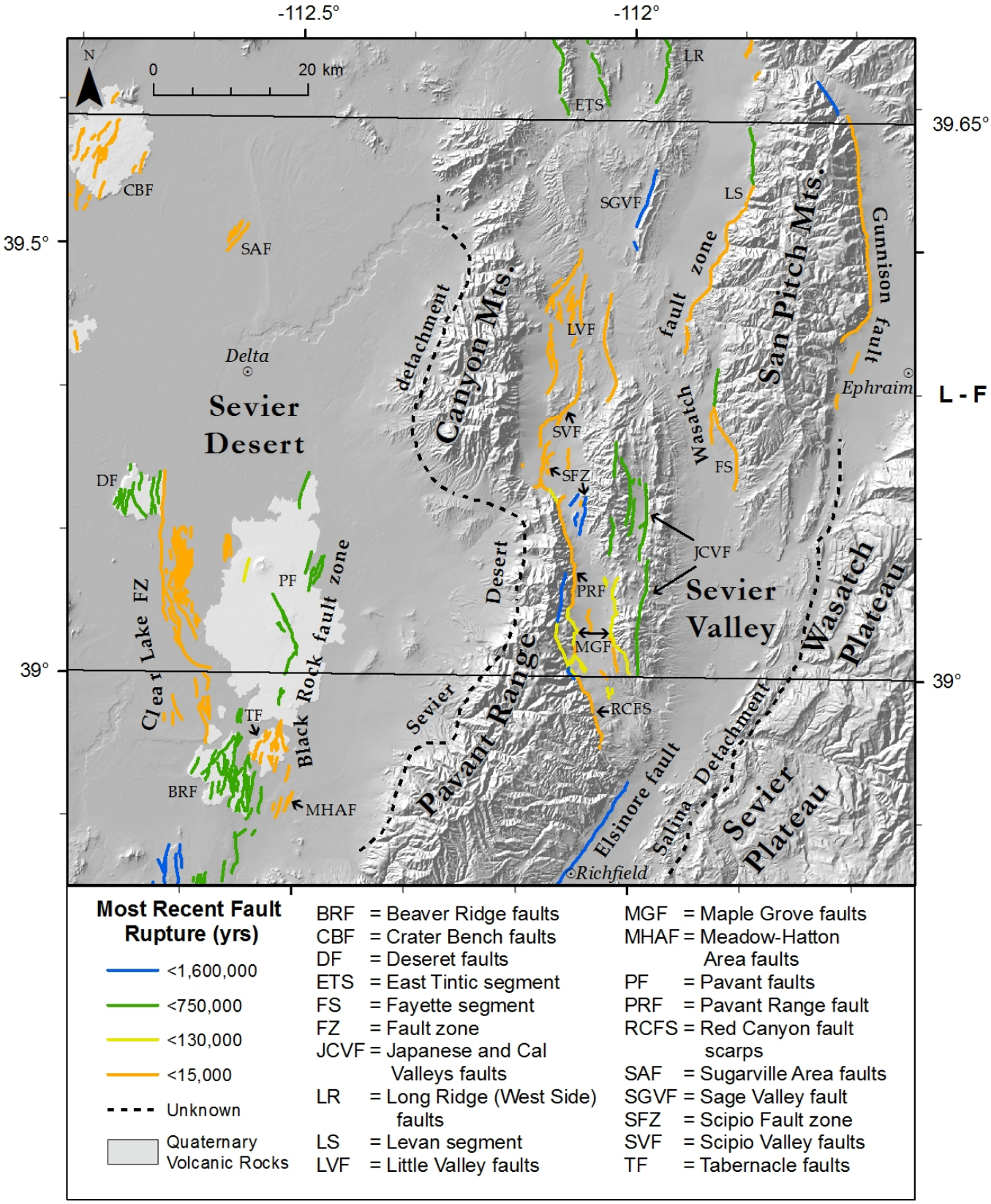

Figure 6.7-1. Map of the west-central part of the L-F subregion showing Quaternary volcanic rocks (Hecker, 1993) and the surface traces of faults in the *Quaternary Fault and Fold Database of the United States* (USGS, 2013), color-coded by age. The dashed black lines are the surface traces of two other possible Quaternary faults discussed in the text: the Salina detachment (Cline and Bartley, 2007) and the Sevier Desert detachment. The trace for the latter is the surface projection of the Sevier Desert reflector from Anders *et al*. (2001), shown over the north-south extent of the contour map of this reflector in Wills *et al*. (2005). Shaded topography generated from 60-m digital elevation data (http://nationalmap.gov).

on a north- or south-striking normal fault with a dip of 50° that extends the full north-south length of the L-F region (72.2 km) and has a depth extent of 15 km. With these assumptions and the assumed rigidity, the vertical component of the slip rate on the fault would need to be 2.4 mm/yr to account for the missing seismic moment. This slip rate is comparable to the maximum slip-rate estimates for the five central, most active segments of the WFZ (Table 4.1-4). It seems unlikely that a 72-km-long, moderately-dipping fault with a slip rate of 2.4 mm/yr, or even four such faults with slip rates of ~0.6 mm/yr, could exist in the L-F region and remain unrecognized. It is possible that there are unrecognized active faults buried beneath the late Pleistocene Lake Bonneville sediments that underlie much of the western third of the L-F region. However, during the 13 kyr time period since the youngest of these lake sediments were deposited (Reheis *et al*., 2014; Oviatt, 2015), a normal fault with a vertical-component slip rate of 0.6 mm/yr would be expected to produce multiple surface-faulting earthquakes and a total vertical displacement of ~7.8 m. A fault with 7.8 m of post-Bonneville displacement should be visible in the L-F region landscape.

If our hypothetical fault is assumed to have a dip of less than 50°, then it could accommodate the missing moment rate with a slip rate that has a vertical component of less than 2.4 mm/yr. If we assume a 30° dip for our hypothetical 72-km-long north- or south-striking normal fault, the vertical component of the slip rate required to account for the missing moment rate is 1.2 mm/yr. We consider it unlikely that an unrecognized fault having this length and slip rate exists in the L-F region.

6.7.3 The Sevier Desert Detachment

If our hypothetical fault is assumed to have a dip of 12°, then it could accommodate the missing moment rate with a slip rate having a vertical component of 0.43 mm/yr. If the arguments in the previous sections are temporarily set aside, the calculation for a 12° dip is potentially relevant because a number of investigators have interpreted a prominent, 11°- to 12°-west-dipping seismic reflector beneath the Sevier Desert in the L-F region to be a low-angle normal fault known as the Sevier Desert detachment (McDonald, 1976; Allmendinger *et al*., 1983; Von Tish *et al*., 1985; Planke and Smith, 1991; Coogan and DeCelles, 1996; McBride *et al*., 2010). This reflector projects to the surface along the western margins of the Canyon and Pavant Ranges (Figure 6.7-1; Anders *et al*., 2001; Niemi *et al*., 2004). Contour maps of the Sevier Desert reflector, constructed with data from reflection profiles and wells, show a minimum north-south extent of 75 to 85 km with the northern end located ~10–15 km south of the northern boundary of the L-F subregion (Von Tish *et al*., 1985; Planke and Smith, 1991; Wills *et al*., 2005). Perpendicular to strike, the reflector can be traced westward for more than 70 km from the near surface to a depth of 12 to 15 km (Allmendinger *et al*., 1983; Von Tish *et al*., 1985).

Interestingly, Niemi *et al*. (2004) attributed a maximum horizontal Holocene slip rate of 6.6 mm/yr to the Sevier Desert detachment, which they assumed to have an average dip of 12° based on seismic reflection profile interpretations by Allmendinger *et al*. (1983) and Von Tish *et al*. (1985). This detachment accounts for two-thirds of Niemi *et al*.'s estimated maximum Holocene geologic extension rate on an east-west profile across the L-F region. However, the Sevier Desert detachment is not included in the WGUEP seismic source model due to questions about whether or not this interpreted detachment is actually an active fault (discussed below) and the lack of evidence worldwide for normal-faulting earthquakes on faults of such shallow dip (discussed above and in Section 3.2). We note that there is no entry for the Sevier Desert detachment in the *Quaternary Fault and Fold Database of the United States* (USGS, 2013), although it is mentioned in the discussions of some other faults in the region.

The geological origin and seismogenic potential of the Sevier Desert reflector have been controversial for more than three decades (see Hintze and Davis, 2003, Christie-Blick *et al*., 2009, and McBride *et al*., 2010, for reviews). Anders and Christie-Blick (1994) and Anders *et al*. (2001) argue that the eastern part of this reflector is not a fault but an unconformity, based on their observation that cores and drill cuttings from two industry boreholes show no increase in microfractures and other forms of fault-related deformation near the reflector. They interpret the western part of the reflector to be a Cretaceous thrust fault that fortuitously aligns with the unconformity (see also Wills *et al*., 2005). The supporters of the detachment hypothesis consider the borehole data of Anders and Christie-Blick (1994) and Anders *et al*. (2001) to be unreliable due to the 3 m sampling interval (Allmendinger and Royce, 1995; Coogan and DeCelles, 2007). Otton (1995) proposed that a west-dipping, low-angle (18° to 24°) contact between Miocene conglomerates and underlying Cambrian and Precambrian rocks in the western Canyon Mountains is a surface exposure of the Sevier Desert detachment. However, based on their own field studies, Wills and Anders (1999) and also Hintze and Davis (2003, p. 205) interpret this contact as an unconformity rather than a fault.

Even if one accepts the interpretation of the Sevier Desert reflector as a low-angle normal fault, there is no compelling evidence that this fault is still active. No Quaternary fault scarps are mapped in the area where the Sevier Desert reflector projects to the surface (Figure 6.7-1; USGS, 2013). Various authors have proposed that some active fault traces farther west in the Sevier Desert are splays of the Sevier Desert detachment, most notably the east-dipping Clear Lake fault zone and the west-dipping Black Rock fault zone (Figure 6.7-1; Von Tish *et al*., 1985; Niemi *et al*., 2004; McBride *et al*., 2015). The Black Rock fault zone (Hoover, 1974; Oviatt, 1991) consists of the faults called the Pavant faults, Tabernacle faults, Beaver Ridge faults, and Meadow-Hatton Area faults in the *Quaternary Fault and Fold Database of the United States* (USGS, 2013). The Clear Lake and Black Rock fault

zones are close together at their southern ends and diverge northward to form a north-trending graben ~35 km long and up to 15 km wide, centered 25 to 35 km west of the surface projection of the Sevier Desert reflector (Figure 6.7-1; Niemi *et al*., 2004; McBride *et al*., 2015). This graben is imaged on a seismic reflection profile published by McDonald (1976, Plate III, at the intersection of lines 2 and 3). McDonald interpreted this graben to be bounded by listric normal faults that sole into the Sevier Desert detachment, based in part on his observation that these faults do not noticeably offset the detachment. On other seismic reflection lines across the Sevier Desert, McDonald (1976, Plate IV, line 20), Planke and Smith (1991, lines 2, 4, and 10), and Niemi *et al*. (2004, their Figure 7) interpreted an east-dipping listric normal fault or fault zone that projects upward to the Clear Lake fault scarps on the western side of the graben (the Western Basin-Bounding fault of Planke and Smith, 1991) and merges downward into the Sevier Desert detachment. However, in the opinion of McBride *et al*. (2015), "no published subsurface data clearly and definitively link" the Clear Lake fault and the Sevier Desert detachment. Wills *et al*. (2005, their Figure 10) presented an alternative interpretation of seismic reflection and well data for the Sevier Desert that shows the Clear Lake and Black Rock fault zones cutting the Sevier Desert reflector (which they refer to as the Paleozoic-Tertiary contact).

In their analysis of geological extension rates across the L-F region, Niemi *et al*. (2004) treated the Black Rock fault zone as the current primary surface trace of the Sevier Desert detachment. They assigned a maximum Holocene vertical slip rate of 1.4 mm/yr to this fault zone, based on Hoover's (1974) report that it displaces the 11 ka Tabernacle Hill basalt flow by 15.2 m along the Tabernacle faults section of this fault zone (TF on Figure 6.7-1). Niemi *et al*. (2004) considered this slip rate to be a maximum value because Hecker (1993, citing Oviatt, verbal communication, 1988) noted that the Tabernacle Hill flow appears to be draped over pre-existing fault scarps. If so, then some or all of the fault displacement could predate the flow. From this maximum vertical slip rate $\dot{d}_v$ on the Black Rock fault zone, Niemi *et al*. (2004) calculated a maximum Holocene horizontal slip rate $\dot{d}_h$ on the Sevier Desert detachment of 6.6 mm/yr using the simple geometrical relationship $\dot{d}_h = \dot{d}_v / \tan \delta$ and an average dip δ on the detachment of 12°. They did not consider the slip rate on the antithetic Clear Lake fault in their calculation, stating that "it is unclear how vertical slip rates on an antithetic fault that soles into the detachment relate to the slip rate on the detachment at depth." Replacement of Hoover's (1974) approximate age of 11 ka for the Tabernacle Hill basalt flow by a much better determined age of 18.2 ± 0.3 cal ka B.P. from Lifton *et al*. (2015) reduces the maximum vertical slip rate on the Black Rock fault zone to 0.84 mm/yr and the maximum horizontal slip rate on the Sevier Desert detachment to 4.0 mm/yr.

There are three issues with Niemi *et al*.'s (2004) assumption that the Black Rock and Clear Lake fault zones are the active surface traces of the Sevier Desert detachment, two of which they acknowledge. The first is that no significant topography has developed along either the Black Rock fault zone or the antithetic Clear Lake fault zone. The second is that the Black Rock fault zone is only about half as long as the mapped extent of the Sevier Desert detachment (Figure 6.7-1). These two facts are incompatible with the large middle and late Cenozoic displacements of 5.5–7.2 km (Planke and Smith, 1991) to 28–38 km (Von Tish *et al*., 1985) estimated for the Sevier Desert detachment, unless one assumes that the surface displacement on this detachment has only recently shifted to the Black Rock fault zone. Niemi *et al*. (2004) and others suggested that such a shift has occurred, but if so, then where are the older surface traces of the Sevier Desert detachment? The third issue is that the Black Rock fault zone cuts Quaternary volcanic rocks over most of its length and connects four Quaternary volcanic vents (Oviatt, 1989, 1991; McBride *et al*., 2015). This association with recent volcanism suggests that the displacements along the Black Rock fault zone and the nearby Clear Lake fault zone could be the result of local magma movement and/or subsidence over a magma chamber, rather than tectonic processes (Oviatt, 1989; Hecker, 1993; Black *et al*., 1999; Niemi *et al*., 2004).

Finally, there are some significant questions regarding the field observations on which Niemi *et al*.'s (2004) preferred Holocene slip rate for the Black Rock fault zone is based. The first, as mentioned above, is the question of whether or not the Tabernacle Hill basalt flow is cut by this fault zone or if it is draped over pre-existing fault scarps. The second question is whether or not the 15.2 m vertical displacement of this flow reported by Hoover (1974) is the net vertical displacement across the entire fault zone, which is the appropriate measurement to use for a slip-rate calculation. The Tabernacle faults section of the Black Rock fault zone is a complex zone of both east- and west-dipping normal faults that spans the entire 5-km width of the roughly circular Tabernacle flow (Figure 6.7-1; Oviatt and Nash, 1989; Oviatt, 1991). Hoover (1974) does not document where or how he measured his 15.2 m displacement on the Tabernacle faults or any of the other vertical displacements that he provides for the Black Rock fault zone. However, he writes that these displacements "were measured along the master fault or extensions of it," which suggests that they were measured across a single fault rather than the whole fault zone. With regard to the Tabernacle Hill flow, Oviatt and Nash (1989) state that "The outer rim of the basalt flow has a uniform altitude of 1,445 m" (4740 feet; see also Oviatt, 1991). They support this statement with a geologic map that shows the 1445 m elevation contour from the 1986 USGS topographic map of the area. This edition of the map has more detailed topographic contours than the 2014 edition and, with a 20 ft (6.1 m) contour interval, is comparable in resolution to the best available digital elevation model for this area (5 m). Although a contour interval of 6.1 m is marginal for resolving a 15.2 m elevation difference across the Tabernacle Hill flow, the topographic map shows no evidence for a linear 15.2-m elevation step on this flow. Considering the problems surrounding Hoover's (1974) reported

15.2-m offset of the Tabernacle Hill flow, the vertical slip rate on the Black Rock fault zone may be much smaller than the maximum value of 1.4 mm/yr that Niemi *et al*. (2004) used to calculate the maximum horizontal slip rate on the Sevier Desert detachment—and our revised maximum vertical slip rate of 0.84 mm/yr.

Niemi *et al*. (2004) provided three other maximum vertical slip-rate values for the Black Rock fault zone. All three rely heavily on Hoover (1974), and all are problematic in some way. Niemi *et al*. calculated a maximum late Holocene slip rate of ~2.0 mm/yr from a 6.1 m offset measured in the Ice Springs basalt flow and a basalt age of 3 to 4 ka based on "stratigraphic arguments," all attributed to Hoover (1974). The Ice Springs basalt flow is at the southern end of the Pavant faults (Figure 6.7-1). The actual age of this flow is < 660 ± 340 ^{14}C yr B.P. (Valastro *et al*., 1972; Oviatt, 1991), which converts to < 710 +290/-330 cal yr before 2014 (2 std. dev. uncertainties) using OxCal v. 4.2 (Bronk Ramsey and Lee, 2013) with the Reimer *et al*. (2009) terrestrial calibration curve. Combining this age with the 6.1 m offset gives a maximum slip rate of 8.6 +7.5/-2.5 mm/yr, which is clearly too high to be a useful limit. A more basic problem with this slip rate is Oviatt's (1991) observation that the Ice Springs basalt is not cut by faults but flowed over preexisting Quaternary fault scarps (see also USGS, 2013). Niemi *et al*. (2004) also determined a late Quaternary slip rate for the Black Rock fault zone based on Hoover's (1974) observation that it offsets 128 ka Pavant 1 lava flows by up to 18.3 m but not Bonneville shorelines (18 ka; see Reheis *et al*., 2014). This observation yields a maximum vertical slip rate of 0.17 mm/yr, which Niemi *et al*. (2004) round up to 0.2 mm/yr, but list incorrectly as 0.3 mm/yr in their Table 4. Hoover (1974) described his K-Ar age of 128 ka for the Pavant 1 lavas as a "statistical maximum" at the 95% confidence limit. However, it is unclear how he calculated this age and uncertainty limit. The 128 ka age is close to the average age for Hoover's (1974) oldest sample of Pavant basalt, for which he determined two poorly constrained ages of 93 ± 78 ka and 133 ± 97 ka (1 std. dev. uncertainties). These ages have very large uncertainties because of the small radiogenic argon content of the samples (Hoover, 1974; Francis H. Brown, personal communication, 2015). Finally, Niemi *et al*. (2004) calculated a maximum Quaternary slip rate for the Black Rock fault zone of ~0.1 mm/yr (rounded up from 0.07 mm/yr) based on Hoover's (1974) report of a maximum vertical displacement of 67 m on "a fault displacing the Beaver Ridge 1 lavas" and his reasonably well constrained "statistical average" K-Ar age of 918 ka for these lavas. The main problem with this slip-rate determination is that it comes from a displacement measurement on just one of many east- and west-dipping normal faults in the 10-km-wide Beaver Ridge faults section of the Black Rock fault zone (see Figure 6.7-1 and the geologic maps in Hoover, 1974, and Oviatt, 1991). If this fault zone is tectonic in origin, then the net displacement across all of the faults in the zone must be accounted for in any tectonic analysis. Another problem with this slip rate is that it is measured over a much longer time period than is generally considered suitable for use in earthquake hazard analysis.

Based on the above discussion, the only one of Niemi *et al*.'s (2004) slip rates for the Black Rock fault zone that appears to be based on a reliable displacement measurement is the late Quaternary maximum vertical slip rate of 0.17 mm/yr. This measurement is the offset of the Pavant 1 lavas by a maximum of 18.3 m along the Pavant faults (Devil's Kitchen) section of the fault zone, most of which is dominated by a single major fault trace (Figure 6.7-1). Despite the question about the uncertainty in the 128 ka age of the Pavant 1 lavas, which may be as large as the age itself, we consider Niemi *et al*.'s 0.17 mm/yr maximum late Quaternary slip rate to be the least problematic of their four slip rates. Interestingly, their estimate of the maximum late Quaternary vertical slip rate on the Clear Lake fault zone is comparable, 0.2 mm/yr over the past 4 Myr. Nevertheless, for the purpose of illustration, we follow Niemi *et al*. (2004) and use only the late Quaternary slip rate on the Black Rock fault zone to calculate the slip rate on the 12°-dipping Sevier Desert detachment. Balanced cross sections would be needed to properly account for the slip rate on the antithetic Clear Lake fault in this calculation.

Niemi *et al*.'s (2004) late Quaternary slip rate is a maximum rate because it is calculated from the maximum observed offset of the Pavant 1 lavas along the Pavant faults. Surface slip distributions compiled by Wesnousky (2008) for eight normal and oblique-normal faulting earthquakes have ratios of maximum slip to average slip that range from 1.9 to 4.7, with an average ratio of 3.2. We estimate an average late Quaternary slip rate for the Black Rock fault zone by dividing the maximum rate of 0.17 mm/yr (Hoover, 1974; Niemi *et al*., 2004) by three. To calculate a hypothetical moment rate from the resulting average slip rate of 0.06 mm/yr, we assume that the active portion of the Sevier Desert detachment is a planar surface dipping 12° west from the intersection with the Black Rock fault zone down to a depth of 15 km. We estimate that the depth of the intersection with the Black Rock fault zone is ~3 km based on the seismic reflection profile in Plate III of McDonald (1976) and an average Cenozoic rock P-wave velocity of 3.2 km/s (Anders *et al*., 1995). Using the resulting depth range of 3 to 15 km and an along-strike length within the L-F region of 62 km, based on the contour map in Wills *et al*. (2005), the late Quaternary slip rate gives a moment rate of 3.11×10^{23} dyne-cm/yr. The missing moment rate, adjusted for a fault dip of 12° instead of 50°, is more than a factor of 10 larger: 3.24×10^{24} dyne-cm/yr. To account for all of the missing moment rate on the Sevier Desert detachment with this assumed fault geometry, a vertical slip rate of 0.62 mm/yr would be required. This slip rate is less than the two maximum Holocene slip rates that Niemi *et al*. (2004) estimated from the work of Hoover (1974), but for reasons explained above the observational basis for both of these slip rates is problematic.

In summary, some or possibly all of the missing moment rate in the L-F region could potentially be accounted for by in-

cluding the Sevier Desert detachment as an active fault in the WGUEP probability model. However, including this fault in the model would require us to accept the following premises: (1) the Sevier Desert reflector is a detachment fault, not an unconformity, (2) the Sevier Desert detachment is active despite its low, mechanically unfavorable dip angle of 12° and the lack of evidence for any continental normal-faulting earthquakes on faults dipping less than 30° (Collettini and Sibson, 2001), and (3) the Black Rock fault zone is the current active surface trace of this detachment even though its connection to the detachment is uncertain, it has no significant topographic signature, its mapped length is only about half that of the detachment, and it displaces predominantly Quaternary basalts along an alignment of four Quaternary volcanic vents (Hecker, 1993; Niemi *et al*., 2004; USGS, 2013; McBride *et al*., 2015). We consider the combination of these assumptions to be too unlikely to warrant the inclusion of the Sevier Desert detachment in the WGUEP model. If we did include it, and if we used Niemi *et al*.'s (2004) late Quaternary (~100 ka) vertical slip rate on the Black Rock fault zone to calculate the moment rate on the Sevier Desert detachment, then this detachment would account for less than a tenth of the missing moment rate.

6.7.4 Other Possible Explanations

Other possible, but speculative, explanations for the moment rate discrepancy in the L-F region include postseismic relaxation from a large, unrecognized prehistoric earthquake in the region and aseismic deformation, perhaps related to salt tectonics. A critical examination of these alternative hypotheses for this moment rate discrepancy is beyond the scope of this report.

6.8 Conclusions

In conclusion, the geodetic moment rates for the Wasatch Front region, and for three of the four subregions that we defined, are consistent with the geological/seismological moment rates for these regions calculated for the WGUEP earthquake rate model. The geodetic moment rates are not consistent with the WGUEP earthquake rate model within the southernmost fifth of the Wasatch Front region, an area that encompasses the Levan and Fayette segments of the WFZ. Further work should be undertaken to try to identify the cause of this moment rate discrepancy.

One possible interpretation of the large moment rate discrepancy in the L-F subregion is that the WGUEP earthquake rate model is missing one or more important faults in this region or underestimates the earthquake rates on one or more of the faults included in the model. If this interpretation is correct, then the WGUEP forecast would underestimate the earthquake probabilities for the L-F region and, to a much smaller extent, for the Wasatch Front region as a whole. From Table 6.6-1, the excess geodetic moment rate in the L-F region is ~15% of the geodetic moment rate for the Wasatch Front region as a whole. The potential effects of this excess moment rate on the WGUEP forecast for the whole Wasatch Front region would be ~15% of the probability values, which is much less than the amount of uncertainty in these probabilities (Tables 8.8-1 to 8.1-3). Given this estimated effect, and the fact that the geodetic and geological/seismological moment rates for the Wasatch Front region agree within their uncertainty limits, we consider the geodetic data to be consistent with the WGUEP earthquake rate model for the Wasatch Front region as a whole.

7 CALCULATING EARTHQUAKE PROBABILITIES

In this section, we describe the details of the process of calculating earthquake probabilities using the Poisson and BPT probability models. Both time-independent and time-dependent probability calculations require the rate of rupture on all rupture sources. An overview of the methodology along with intermediate results, such as rupture rates, moment rates, and magnitude-frequency distributions, are provided in Section 7.1, followed by details on time-independent probability calculations (Section 7.2) and time-dependent probability calculations (Section 7.3). Acronyms and abbreviations are defined on pages xii to xiv.

7.1 Methodology

The identified faults and background seismicity within the Wasatch Front region produce a broad range of earthquake sizes at different rates of occurrence. The rates of occurrence of earthquakes on rupture sources are the primary inputs to the earthquake probability calculations. The development of rupture sources is described in Section 4. For well-defined and complex faults, such as the WFZ, rupture sources can be single-segments, combinations of segments, or floating ruptures. Other smaller faults may only be modeled with a single rupture source. A fault rupture model consists of one to many rupture sources that represent the long-term rupture behavior of the fault. In this study, rupture rates are developed directly for each rupture source and input into the rupture source probability calculations.

7.1.1 Rupture Source Rates

We calculated rupture source rates from recurrence intervals of characteristic events and/or geologic slip rates. For the central segments of the WFZ and several segments of the OGSLFZ, rates of characteristic events are developed directly based on paleoseismic data. The available paleoseismic data for these fault segments allows for calculation of recurrence intervals of characteristic events that include statistical uncertainty due to number of samples (Section 3.4). The rates of characteristic events, λ_{char}, are calculated for each of the rupture sources, not for individual segments, which eliminates the need to partition rate from segments to single and multi-segment ruptures. The relative distribution of magnitudes for ruptures in all segmented fault models is assumed to follow a Gaussian distribution (maximum magnitude recurrence model) as described in Section 3.4 and illustrated on Figure 3.4-1. For the maximum magnitude recurrence model, the mean rate, λ, is simply the rate of the characteristic event, λ_{char} (inverse of the recurrence interval of the characteristic event).

We also characterized some of the other smaller, less studied faults (Types C and AFP as defined in Section 3.6.3) using recurrence intervals of characteristic events (Appendix D), although we have not incorporated statistical uncertainty due to sample size for Type C and AFP faults. Both the maximum magnitude and DTGR magnitude recurrence models are used. The DTGR model contains a range of magnitudes from **M** 6.75 up to the characteristic event (Figure 3.4-2). When applying this model to a seismic source characterized with recurrence intervals, we assumed that the moment release rate is the same as implied by the maximum magnitude model. To obtain the mean rupture rate of the range of events in the DTGR model, the moment release rate implied for characteristic events using the maximum magnitude model (recurrence rate of the characteristic events multiplied by the mean moment of the characteristic events) is divided by the mean moment of events in the DTGR model:

$$\lambda = \frac{\lambda_{char} \times \overline{M_{0_{char}}}}{\overline{M_{0_{DTGR}}}} \qquad (7\text{-}1)$$

The mean moment of the characteristic events is a function of the its mean magnitude, $\overline{M_{char}}$, and the shape of the characteristic magnitude PDF. For a Gaussian magnitude distribution truncated at $\pm 2\sigma_m$, the moment is approximately lognormally distributed. The mean moment is calculated as in WGCEP (2003):

$$\overline{M}_{0char} = \frac{1}{\sqrt{2\pi}} \int_{-2}^{2} 10^{1.5(\boldsymbol{M}+\sigma_m x)+16.05} e^{-\frac{x^2}{2}} dx \qquad (7\text{-}2)$$

which can be approximated by the following equation:

$$\overline{M}_{0char} = 10^{1.5\overline{M}char+16.05-0.0481\sigma m+1.775\sigma m^2} \qquad (7\text{-}3)$$

For the Gutenberg-Richter magnitude distribution truncated at an upper and lower magnitude, the mean moment is

$$\frac{\beta \times 10^{(16.05\ \exp(\beta Mmin)) \times [\exp(t_i * Mchar) - \exp(t_i * Mmin)]}}{(1-\exp(-\beta * (Mchar - Mmin))) * t_i} \qquad (7\text{-}4)$$

where $\beta = \ln(10)b$ and $t_i = 1.5\ \ln(10) - \beta$.

For a source with M_{char}, the magnitudes modeled with the DTGR model (**M** 6.75 to M_{char}) are smaller than that of the maximum magnitude model ($M_{char} \pm 0.24$). Therefore, the mean moment of events in the DTGR model is lower. Thus, the resulting rate of events for the DTGR model is larger than in the maximum magnitude model.

For the WFZ end segments, several segments of the OGSLFZ, and most Type C and AFP faults, the limited historical and paleoseismic records are not sufficient to directly calculate or estimate earthquake recurrence rates. In these instances, we used geologic slip rates to estimate rates of seismic moment release on these faults. Estimation of earthquake rates is then made based on the moment release rate and size of earthquakes that release the moment.

The calculation of rupture source rates using slip rates is straightforward for the faults characterized with slip rates in

the Wasatch Front region. For each fault characterized with slip rates, each segment ruptures only as part of one rupture source, thus segment slip rates can be attributed fully to its rupture source without any partitioning to more than one type of rupture. The long-term moment release rate, which is estimated as shear modulus (3.0×10^{11} dyne/cm^2) times seismogenic fault area times slip rate, is assumed to be achieved by a repeating sequence of similar-sized earthquakes. The mean rupture source rate, λ, is simply the long-term moment release, $\dot{M}_0$, rate divided by the mean moment of the repeating earthquakes, $\overline{M_0}$. For the maximum magnitude recurrence model, $\overline{M_0}$ is $\overline{M_{0_{char}}}$ as defined in equation (7.3). For the DTGR model, $\overline{M_0}$ is $\overline{M_{0_{DTGR}}}$ as defined in equation (7.4). Some faults have both slip rate and recurrence intervals (e.g., Table 4.3-7). These two types of rates are separate branches on the logic tree with weights assigned. Figure 7.1-1 illustrates the calculation sequence for rupture source rates.

We computed the rates of characteristic events on rupture sources for the WFZ central segments based on paleoseismic data using the methods described in Section 3.4; these are listed in Table 7.1-1. As described in Section 3.4, the five discrete rates are approximations to continuous probability distributions of mean recurrence intervals/rates that define weighted branches of the WGUEP logic tree. Note that the inverse of a rupture source rate is equal to the recurrence interval of characteristic events, as only the maximum magnitude recurrence model is used for the segmented rupture models of the WFZ. Table 7.1-1 provides rates in terms of recurrence intervals for ease of comparison with recurrence intervals of other faults in the WGUEP region. Rupture source rates for the WFZ end segments and the unsegmented model for the central segments and the WFZ as a whole are based on geologic slip rates only (Sections 4.1.5 and 4.2.2). The resulting rupture source rates are listed in Table 7.1-2. These rates are computed based on the moment balancing of geologic slip rate as described above. The uncertainty reflects the uncertainty in not only the geologic slip rates, but also the uncertainty in fault area (from length, dip, and seismogenic thickness distributions) and characteristic (i.e., magnitude relations and their inputs) and recurrence models. For the OGSLFZ, we computed rupture source rates based on paleoseismic data using the methods described in Section 3.4 and/or geologic slip rates (Table 7.1 3).

For other faults within the Wasatch Front region, rupture source rates were based on geologic slip rates and/or recurrence intervals. Recurrence intervals were mostly based on consensus values from the UQFPWG (Lund, 2005). Sampling uncertainty was not formally incorporated using the methods of Section 3.5. The majority of effort in determining recurrence rates was focused on the WFZ and OGSLFZ. Future studies should consider including this uncertainty for faults with available paleoseismic data. Table 7.1-4 lists the rupture source rates for all other faults included in the study.

7.1.2 Segment Rates

We computed the rate of earthquakes for a fault segment in the model by summing the rate of rupture sources that involve the specified segment. We assumed floating ruptures to be uniformly distributed along the length of the fault restricting the rupture to within the ends of the fault. We computed the partitioned rate for a given segment based on the segment length, rupture length, total fault length, and location of segment along the fault trace. For instance, a large floating rupture on

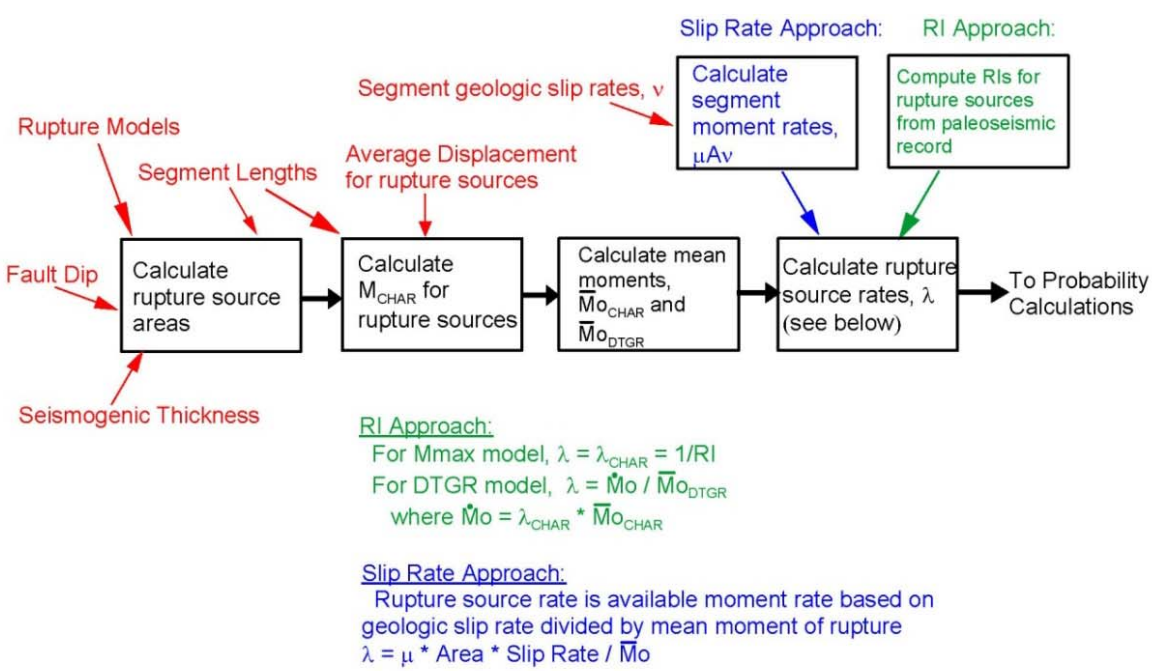

Figure 7.1-1. Calculation of rupture source rates.

Table 7.1-1. Recurrence intervals of characteristic events for the WFZ central segment models.

Fault Model	Rupture Source	Recurrence Intervals of Characteristic Events Determined from Paleoseismic Data[1]				
		$1/\lambda_{char96.51\%}$ (wt. = 0.101)	$1/\lambda_{char78.83\%}$ (wt. = 0.244)	$1/\lambda_{char50\%}$ (wt. = 0.31)	$1/\lambda_{char21.17\%}$ (wt. = 0.244)	$1/\lambda_{char3.49\%}$ (wt. = 0.101)
Single-Segment Rupture	BCS	722	1106	1630	2543	4935
	WS	732	1077	1525	2256	4003
	SLCS	641	981	1446	2256	4379
	PS	634	932	1319	1952	3465
	NS	477	772	1209	2044	4577
Intermediate A Rupture Model	BCS	1156	2051	3566	6986	20,588
	WS	1050	1700	2663	4505	10,084
	SLCS	783	1268	1986	3360	7521
	PS	744	1138	1678	2618	5081
	NS	477	772	1209	2044	4577
	B+W	1376	2440	4243	8313	24,496
	S+P	1837	3970	8891	25,908	173,526
Intermediate B Rupture Model	BCS	1156	2051	3566	6986	20,588
	WS	1050	1700	2663	4505	10,084
	SLCS	641	981	1446	2256	4379
	PS	744	1138	1678	2618	5081
	NS	624	1108	1926	3773	11,118
	B+W	1376	2440	4243	8313	24,496
	P+N	1837	3970	8891	25,908	173,526
Intermediate C Rupture Model	BCS	1156	2057	3566	6986	20,588
	WS	1050	1700	2663	4505	10,084
	SLCS	641	981	1446	2256	4379
	PS	634	932	1319	1952	3465
	NS	477	772	1209	2044	4577
	B+W	1376	2440	4243	8313	24,496
Multisegment Rupture Model	BCS	1784	3855	8635	25,160	168,514
	WS	2122	4587	10,273	29,935	200,499
	SLCS	1583	3421	7662	22,326	149,537
	PS	1191	2112	3672	7194	21,200
	NS	963	2082	4663	13,587	91,000
	B+W	1050	1700	2663	4505	10,084
	W+S	2122	4587	10,273	29,935	200,499
	S+P	1837	3970	8891	25,908	173,526
	P+N	1837	3970	8891	25,908	173,526
	S+P+N	1837	3970	8891	25,908	173,526

[1] $1/\lambda_{char}$ is shown for ease of comparison with recurrence intervals for faults. λ_{char} is the rate of characteristic events based on paleoseismic data as per Section 3.4.

Table 7.1-2. Rupture source rates (Poisson) for the WFZ end segment and unsegmented fault models.

Fault Model	Rupture Source	Rupture Source Rates[1,2]		
		$\lambda_{5th\%}$ ($1/\lambda_{5th\%}$)	λ_{mean} ($1/\lambda_{mean}$)	$\lambda_{95th\%}$ ($1/\lambda_{95th\%}$)
Segmented Rupture Model - Northern End Segments	Malad City	4.13×10^{-6} (242,000)	3.01×10^{-5} (33,200)	7.91×10^{-5} (12,600)
	Clarkston Mountain	5.53×10^{-6} (180,800)	5.42×10^{-5} (18,500)	1.32×10^{-4} (7580)
	Collinston	4.87×10^{-6} (205,300)	4.04×10^{-5} (24,800)	1.05×10^{-4} (9520)
Floating Rupture Model - Northern End Segments	Floating	1.49×10^{-5} (67,100)	1.09×10^{-4} (9170)	2.57×10^{-4} (3890)
Segmented Rupture Model - Southern Segments	Levan	2.42×10^{-5} (41,300)	1.22×10^{-4} (8200)	3.09×10^{-4} (3240)
	Fayette	2.67×10^{-6} (375,000)	2.49×10^{-5} (40,200)	6.18×10^{-5} (16,200)
	Levan + Fayette	2.16×10^{-6} (463,000)	9.03×10^{-5} (11,100)	2.43×10^{-4} (4150)
Unsegmented Rupture Model	Floating on BCS+WS+SLCS+PS+NS	1.35×10^{-3} (730)	4.04×10^{-3} (250)	8.08×10^{-3} (120)
	Floating on all 10 segments	2.95×10^{-5} (33,900)	2.38×10^{-4} (4200)	5.67×10^{-4} (1760)

[1] 1/Rate is shown for ease of comparison with recurrence intervals for faults.
[2] Rates determined from moment balancing geologic slip rate.

the WFZ that is longer than the average segment length will rupture central segments more frequently than end segments when distributed evenly along the fault trace. As the rupture length decreases to less than the average segment length, the partitioning of rate approaches the ratio of segment length to total fault length. The assumption of uniform distribution of ruptures on the fault implies that slip tapers to zero at the ends of the fault. The degree of tapering depends on the length of the rupture relative to the fault length.

Segment rates for all segmented faults in the Wasatch Front region are provided in Tables 7.1-5 to 7.1-11. Segment rates are provided for each fault model and for the weighted total of all fault models.

7.1.3 Magnitude Threshold for Probability Calculations

We computed probabilities for the occurrence of an event greater than a specified size. The magnitude of ruptures on faults and in the background is described by a recurrence model, which reflects the aleatory uncertainty in the size of an event. To compute rupture probabilities of events greater than a threshold magnitude (M_T), the probability that a given rupture will be larger than the M_T must be computed. The probability calculations require the rate of events larger than M_T:

$$\gamma_{char_i}(\mathbf{M}>M_T) = \Sigma_{i=1}^{Nrup}\ \gamma_{char_i} P_i(\mathbf{M}>M_T) \qquad (7\text{-}5)$$

where $P_i(\mathbf{M}>M_T)$ is the probability that the magnitude is greater than M_T, which we computed by integrating the magnitude recurrence PDF from M_T upwards:

$$P_i(\mathbf{M}>M_T) = \int_{M_T}^{\infty} f_{m_i}(m)\,dm \qquad (7\text{-}6)$$

We accommodated the epistemic uncertainty in rupture magnitude through the use of several magnitude relations used to determine M_{char}, as described in Section 3.6. In addition, there is uncertainty in inputs to these relations (fault length, width, dip, and average displacement). The 5th, mean, and 95th percentile M_{char} for rupture sources are provided in Section 4 (Tables 4.1-6, 4.2-4, and Appendix D).

7.1.4 Magnitude-Frequency Distributions

The long-term magnitude-frequency distributions for a fault can be calculated by combining the rate of earthquakes as a function of magnitude for all rupture sources within a given fault model. Figure 7.1-2 shows the cumulative magnitude-frequency distributions for the WFZ, OGSLFZ, background seismicity, and the "other modeled faults" combined. In addition, the observed seismicity and the background seismicity exponential recurrence curve are shown on Figure 7.1-2. Figure 7.1-3 shows the cumulative magnitude-frequency distributions for all the "other modeled faults" in the Wasatch Front region considered in this study. The incremental magnitude-frequency distributions are provided on Figures 7.1-4 and 7.1-5.

Table 7.1-3. Recurrence intervals for characteristic events and rupture source rates (Poisson) for OGSLFZ fault models.

Fault Model	Rupture Source	RI wt. / SR wt.	Recurrence Intervals of Characteristic Events Determined from Paleoseismic Data[1]					Rupture Source Rates[1,2]		
			$1/\lambda_{char96.51\%}$ (years) (wt. = 0.101)	$1/\lambda_{char78.83\%}$ (years) (wt. = 0.244)	$1/\lambda_{char50\%}$ (years) (wt. = 0.31)	$1/\lambda_{char21.17\%}$ (years) (wt. = 0.244)	$1/\lambda_{char3.49\%}$ (years) (wt. = 0.101)	$\lambda_{5th\%}$ ($1/\lambda_{5th\%}$)	λ_{mean} ($1/\lambda_{mean}$)	$\lambda_{95th\%}$ ($1/\lambda_{95th\%}$)
1	RZ	1.0 / 0.0	1468	2377	3724	6300	14,103	7.09×10^{-5} (14,100)	3.01×10^{-4} (3320)	6.81×10^{-4} (1470)
	PY	1.0 / 0.0	1468	2377	3724	6300	14,103	7.09×10^{-5} (14,100)	3.01×10^{-4} (3320)	6.81×10^{-4} (1470)
	FI	1.0 / 0.0	1348	2222	3521	6024	13,680	7.31×10^{-5} (13,680)	3.20×10^{-4} (3130)	7.42×10^{-4} (1350)
	AI	1.0 / 0.0	1468	2377	3724	6300	14,103	7.09×10^{-5} (14,100)	3.01×10^{-4} (3320)	6.81×10^{-4} (1470)
	NO+SO	0.0 / 1.0	NA	NA	NA	NA	NA	1.97×10^{-4} (50,800)	1.13×10^{-4} (8850)	2.58×10^{-4} (3880)
	TH	0.0 / 1.0	NA	NA	NA	NA	NA	2.64×10^{-5} (37,900)	1.91×10^{-4} (5240)	4.65×10^{-4} (2150)
	ET	0.0 / 1.0	NA	NA	NA	NA	NA	1.19×10^{-5} (84,000)	6.90×10^{-5} (14,500)	1.78×10^{-4} (5600)
2	RZ	1.0 / 0.0	1468	2377	3724	6300	14,103	7.09×10^{-5} (14,100)	3.01×10^{-4} (3320)	6.81×10^{-4} (1470)
	PY	1.0 / 0.0	1468	2377	3724	6300	14,103	7.09×10^{-5} (14,100)	3.01×10^{-4} (3320)	6.81×10^{-4} (1470)
	FI	1.0 / 0.0	1348	2222	3521	6024	13,680	7.31×10^{-5} (13,680)	3.20×10^{-4} (3130)	7.42×10^{-4} (1350)
	AI	1.0 / 0.0	1468	2377	3724	6300	14,103	7.09×10^{-5} (14,100)	3.01×10^{-4} (3320)	6.81×10^{-4} (1470)
	NO	0.6 / 0.4	5983	10,613	18,453	36,153	106,538	9.39×10^{-6} (106,500)	8.86×10^{-5} (11,300)	1.99×10^{-4} (5130)
	SO	0.6 / 0.4	6441 (0.5) 8004 (0.5)	8817 (0.5) 11,433 (0.5)	11,606 (0.5) 15,698 (0.5)	15,704 (0.5) 22,366 (0.5)	24,106 (0.5) 37,291 (0.5)	2.68×10^{-5} (37,300)	1.06×10^{-4} (9430)	3.00×10^{-4} (3330)
	TH	0.0 / 1.0	NA	NA	NA	NA	NA	2.64×10^{-5} (37,900)	1.91×10^{-4} (5240)	4.65×10^{-4} (2150)
	ET	0.0 / 1.0	NA	NA	NA	NA	NA	1.19×10^{-5} (84,000)	6.90×10^{-5} (14,500)	1.78×10^{-4} (5600)

Table 7.1-3. Continued

Fault Model	Rupture Source	RI wt. / SR wt.	Recurrence Intervals of Characteristic Events Determined from Paleoseismic Data[1]					Rupture Source Rates[1,2]		
			$1/\lambda_{char96.51\%}$ (years) (wt. = 0.101)	$1/\lambda_{char78.83\%}$ (years) (wt. = 0.244)	$1/\lambda_{char50\%}$ (years) (wt. = 0.31)	$1/\lambda_{char21.17\%}$ (years) (wt. = 0.244)	$1/\lambda_{char3.49\%}$ (years) (wt. = 0.101)	$\lambda_{5th\%}$ ($1/\lambda_{5th\%}$)	λ_{mean} ($1/\lambda_{mean}$)	$\lambda_{95th\%}$ ($1/\lambda_{95th\%}$)
3	RZ	1.0 / 0.0	1468	2377	3724	6300	14,103	7.09×10^{-5} (14,100)	3.01×10^{-4} (3320)	6.81×10^{-4} (1470)
	PY	1.0 / 0.0	1468	2377	3724	6300	14,103	7.09×10^{-5} (14,100)	3.01×10^{-4} (3320)	6.81×10^{-4} (1470)
	FI+AI	1.0 / 0.0	1468	2377	3724	6300	14,103	7.09×10^{-5} (14,100)	3.01×10^{-4} (3320)	6.81×10^{-4} (1470)
	NO	0.6 / 0.4	5983	10,613	18,453	36,153	106,538	9.39×10^{-6} (106,500)	8.86×10^{-5} (11,300)	1.99×10^{-4} (5130)
	SO	0.6 / 0.4	6441 (0.5) 8004 (0.5)	8817 (0.5) 11,433 (0.5)	11,606 (0.5) 15,698 (0.5)	15,704 (0.5) 22,366 (0.5)	24,106 (0.5) 37,291 (0.5)	2.68×10^{-5} (37,300)	1.06×10^{-4} (9430)	3.00×10^{-4} (3330)
	TH	0.0 / 1.0	NA	NA	NA	NA	NA	2.64×10^{-5} (37,900)	1.91×10^{-4} (5240)	4.65×10^{-4} (2150)
	ET	0.0 / 1.0	NA	NA	NA	NA	NA	1.19×10^{-5} (84,000)	6.90×10^{-5} (14,500)	1.78×10^{-4} (5600)
4	RZ	1.0 / 0.0	1468	2377	3724	6300	14,103	7.09×10^{-5} (14,100)	3.01×10^{-4} (3320)	6.81×10^{-4} (1470)
	PY	1.0 / 0.0	1468	2377	3724	6300	14,103	7.09×10^{-5} (14,100)	3.01×10^{-4} (3320)	6.81×10^{-4} (1470)
	FI	1.0 / 0.0	1348	2222	3521	6024	13,680	7.31×10^{-5} (13,680)	3.20×10^{-4} (3130)	7.42×10^{-4} (1350)
	AI	1.0 / 0.0	1468	2377	3724	6300	14,103	7.09×10^{-5} (14,100)	3.01×10^{-4} (3320)	6.81×10^{-4} (1470)
	NO	0.6 / 0.4	5983	10,613	18,453	36,153	106,538	9.39×10^{-6} (106,500)	8.86×10^{-5} (11,300)	1.99×10^{-4} (5130)
	SO+TH	0.0 / 1.0	NA	NA	NA	NA	NA	1.85×10^{-5} (54,000)	1.16×10^{-4} (8600)	3.19×10^{-4} (3140)
	ET	0.0 / 1.0	NA	NA	NA	NA	NA	1.19×10^{-5} (84,000)	6.90×10^{-5} (14,500)	1.78×10^{-4} (5600)
5	Floating on RZ+PY+FI+AI	0.0 / 1.0	NA	NA	NA	NA	NA	1.22×10^{-4} (8200)	7.60×10^{-4} (1320)	1.79×10^{-3} (560)
	Floating on all segments	0.0 / 1.0	NA	NA	NA	NA	NA	2.74×10^{-4} (3650)	8.91×10^{-4} (1120)	2.44×10^{-4} (410)

[1] 1/Rate is shown for ease of comparison with recurrence intervals for faults.
[2] Rates determined from moment balancing geologic slip rates. Geologic slip rates are provided on Table 4.3-7.

Table 7.1-4. Rupture source rates (Poisson) for "other modeled faults" included in Wasatch Front region fault models.

Fault	Fault Model	Rupture Source	Rupture Source Rates[1,2]		
			$\lambda_{5th\%}$ ($1/\lambda_{5th\%}$)	λ_{mean} ($1/\lambda_{mean}$)	$\lambda_{95th\%}$ ($1/\lambda_{95th\%}$)
Bear River	Unsegmented	Bear River	2.86×10^{-4} (3500)	6.03×10^{-4} (1660)	1.32×10^{-3} (760)
Carrington	Unsegmented	Carrington	7.09×10^{-5} (14,100)	3.35×10^{-4} (2990)	7.38×10^{-4} (1360)
Crater Bench and Drum Mtns	Unsegmented	Crater Bench and Drum Mtns	5.85×10^{-6} (170,900)	6.74×10^{-5} (14,800)	2.91×10^{-4} (3440)
Crawford Mtns	Unsegmented	Crawford Mtns	5.78×10^{-6} (173,000)	2.86×10^{-5} (35,000)	8.04×10^{-5} (12,400)
Curlew Valley	Unsegmented	Curlew Valley	5.29×10^{-5} (18,900)	4.43×10^{-4} (2260)	1.33×10^{-3} (750)
East Cache	Unsegmented	Floating	7.58×10^{-5} (13,200)	5.30×10^{-4} (1890)	1.23×10^{-3} (810)
	Segmented	North	1.83×10^{-5} (54,600)	1.35×10^{-4} (7400)	3.56×10^{-4} (2800)
		Central	3.90×10^{-5} (25,600)	2.18×10^{-4} (4590)	5.36×10^{-4} (1870)
		South	7.29×10^{-6} (137,200)	3.00×10^{-5} (33,300)	1.00×10^{-4} (10,000)
East Dayton-Oxford	Unsegmented	East Dayton-Oxford	5.81×10^{-6} (172,100)	5.79×10^{-5} (17,300)	1.45×10^{-4} (6900)
Eastern Bear Lake	Unsegmented	Floating	3.69×10^{-4} (2710)	1.79×10^{-3} (560)	4.77×10^{-3} (210)
	Segmented	North	6.41×10^{-5} (15,600)	3.88×10^{-4} (2580)	9.24×10^{-4} (1080)
		Central	1.22×10^{-4} (8200)	6.63×10^{-4} (1500)	1.55×10^{-3} (650)
		South	6.75×10^{-5} (14,800)	4.47×10^{-4} (2240)	1.26×10^{-3}(790)
Faults along the edge of Scipio Valley–Pavant Range	Unsegmented	Faults along the edge of Scipio Valley–Pavant Range	1.30×10^{-5} (76,900)	1.53×10^{-4} (6540)	5.97×10^{-4} (1680)
Gunnison	Unsegmented	Gunnison	1.37×10^{-5} (73,000)	1.55×10^{-4} (6450)	5.83×10^{-4} (1700)
Hansel Valley (Independent)[3]	Unsegmented	Hansel Valley	4.38×10^{-5} (22,830)	1.02×10^{-4} (9800)	4.14×10^{-4} (2400)
Joe's Valley	Unsegmented	Joe's Valley	2.00×10^{-5} (50,000)	1.11×10^{-4} (9000)	2.00×10^{-4} (5000)
Little Valley	Unsegmented	Little Valley	1.53×10^{-5} (65,400)	2.00×10^{-4} (5000)	6.65×10^{-4} (1500)
Main Canyon	Unsegmented	Main Canyon	5.85×10^{-6} (170,900)	2.90×10^{-5} (34,500)	9.05×10^{-5} (11,000)
Morgan	Unsegmented	Morgan	7.11×10^{-6} (140,600)	3.42×10^{-5} (29,200)	9.00×10^{-5} (11,100)
North Promontory	Unsegmented	North Promontory	5.73×10^{-5} (17,500)	3.16×10^{-4} (3170)	9.77×10^{-4} (1020)
Porcupine Mtn	Unsegmented	Porcupine Mtn	5.67×10^{-6} (176,400)	2.70×10^{-5} (37,000)	7.73×10^{-5} (12,900)
Rock Creek	Unsegmented	Rock Creek	1.00×10^{-4} (10,000)	7.04×10^{-4} (1420)	1.78×10^{-3} (560)
Skull Valley	Unsegmented	Skull Valley	4.03×10^{-5} (24,800)	3.35×10^{-4} (2990)	7.70×10^{-4} (1300)
Snow Lake Graben	Unsegmented	Snow Lake Graben	2.00×10^{-5} (50,000)	1.07×10^{-4} (9350)	2.00×10^{-4} (5000)
Stansbury	Unsegmented	Floating	1.25×10^{-4} (8000)	1.08×10^{-3} (920)	2.89×10^{-3} (350)
	Segmented	North	3.57×10^{-5} (28,000)	4.08×10^{-4} (2450)	1.04×10^{-3} (960)
		Central	3.44×10^{-5} (29,100)	3.61×10^{-4} (2770)	9.01×10^{-4} (1110)
		South	3.82×10^{-5} (26,200)	5.17×10^{-4} (1930)	1.27×10^{-3} (790)
Stinking Springs	Unsegmented	Stinking Springs	3.25×10^{-5} (30,800)	2.71×10^{-4} (3690)	8.33×10^{-4} (1200)
Strawberry	Unsegmented	Strawberry	3.04×10^{-5} (32,900)	1.25×10^{-4} (8000)	3.41×10^{-4} (2930)
Utah Lake (Independent)[3]	Unsegmented	Utah Lake	3.86×10^{-5} (25,900)	2.21×10^{-4} (4530)	9.03×10^{-4} (1110)
West Cache	Unsegmented	Floating	1.80×10^{-4} (5560)	9.72×10^{-4} (1030)	2.08×10^{-3} (480)
	Segmented	North	5.24×10^{-5} (19,100)	3.99×10^{-4} (2500)	1.01×10^{-3} (990)
		Central	2.55×10^{-5} (39,200)	1.00×10^{-4} (10,000)	2.36×10^{-4} (4240)
		South	2.64×10^{-5} (37,900)	1.13×10^{-4} (8850)	2.60×10^{-4} (3850)
West Valley (Independent)[3]	Unsegmented	West Valley	3.86×10^{-5} (25,900)	2.21×10^{-4} (4530)	1.49×10^{-3} (670)
Western Bear Lake (Independent)[3]	Unsegmented	Western Bear Lake	4.72×10^{-5} (21,200)	2.61×10^{-4} (3830)	1.48×10^{-3} (680)

[1] ($1/\lambda$) is shown for ease of comparison with recurrence intervals for faults.
[2] Geologic slip rates and recurrence intervals provided in Appendix D.
[3] Rates for subsidiary antithetic faults are for independent ruptures only and do not include the rate of simultaneous rupture with the master fault.

Table 7.1-5. Segment rupture rates (Poisson) for the WFZ central segment fault models.

Fault Model	Fault Segment	Segment Rupture Rates[1,2]		
		$\lambda_{5th\%}$ ($1/\lambda_{5th\%}$)	λ_{mean} ($1/\lambda_{mean}$)	$\lambda_{95th\%}$ ($1/\lambda_{95th\%}$)
Single-segment Rupture	BCS	2.03×10^{-4} (4930)	6.68×10^{-4} (1500)	1.39×10^{-3} (720)
	WS	2.50×10^{-4} (4000)	7.02×10^{-4} (1430)	1.37×10^{-3} (730)
	SLCS	2.28×10^{-4} (4390)	7.52×10^{-4} (1330)	1.56×10^{-3} (640)
	PS	2.89×10^{-4} (3460)	8.12×10^{-4} (1230)	1.58×10^{-3} (630)
	NS	2.18×10^{-4} (4590)	9.21×10^{-4} (1090)	2.10×10^{-3} (480)
Intermediate A Rupture Model	BCS	1.84×10^{-4} (5440)	6.11×10^{-4} (1640)	1.21×10^{-3} (830)
	WS	2.63×10^{-4} (3800)	6.97×10^{-4} (1440)	1.31×10^{-3} (760)
	SLCS	2.45×10^{-4} (4080)	7.25×10^{-4} (1380)	1.39×10^{-3} (720)
	PS	3.09×10^{-4} (3240)	8.10×10^{-4} (1240)	1.46×10^{-3}(690)
	NS	2.18×10^{-4} (4590)	9.21×10^{-4} (1090)	2.10×10^{-3} (480)
Intermediate B Rupture Model	BCS	1.84×10^{-4} (5440)	6.11×10^{-4} (1640)	1.21×10^{-3} (830)
	WS	2.63×10^{-4} (3800)	6.97×10^{-4} (1440)	1.31×10^{-3} (760)
	SLCS	2.28×10^{-4} (4390)	7.52×10^{-4} (1330)	1.56×10^{-3} (640)
	PS	3.09×10^{-4} (3240)	8.10×10^{-4} (1240)	1.46×10^{-3} (690)
	NS	2.02×10^{-4} (4950)	7.79×10^{-4} (1280)	1.72×10^{-3} (580)
Intermediate C Rupture Model	BCS	1.84×10^{-4} (5440)	6.11×10^{-4} (1640)	1.21×10^{-3} (830)
	WS	2.63×10^{-4} (3800)	6.97×10^{-4} (1440)	1.31×10^{-3} (760)
	SLCS	2.28×10^{-4} (4390)	7.52×10^{-4} (1330)	1.56×10^{-3} (640)
	PS	2.89×10^{-4} (3460)	8.12×10^{-4} (1230)	1.58×10^{-3} (630)
	NS	2.18×10^{-4} (4590)	9.21×10^{-4} (1090)	2.10×10^{-3} (480)
Multisegment Rupture Model	BCS	2.15×10^{-4} (4650)	5.84×10^{-4} (1710)	1.15×10^{-3} (870)
	WS	2.89×10^{-4} (3460)	6.99×10^{-4} (1430)	1.27×10^{-3} (790)
	SLCS	2.19×10^{-4} (4570)	6.51×10^{-4} (1540)	1.23×10^{-3} (810)
	PS	3.11×10^{-4} (3220)	8.08×10^{-4} (1240)	1.46×10^{-3} (690)
	NS	1.62×10^{-4} (6170)	6.31×10^{-4} (1590)	1.33×10^{-3} (750)

[1] ($1/\lambda$) is shown for ease of comparison with recurrence intervals for faults.
[2] These rates account for segment rupture as a single-segment and as part of a multi-segment rupture.

Table 7.1-6. Segment rupture rates (Poisson) for the WFZ end segment fault models.

Fault Model	Fault Segment	Segment Rupture Rates[1,2]		
		$\lambda_{5th\%}$ ($1/\lambda_{5th\%}$)	λ_{mean} ($1/\lambda_{mean}$)	$\lambda_{95th\%}$ ($1/\lambda_{95th\%}$)
Segmented Rupture Model - Northern End Segments	Malad City	4.13×10^{-6} (242,000)	3.01×10^{-5} (33,200)	7.91×10^{-5} (12,600)
	Clarkston Mountain	5.53×10^{-6} (180,800)	5.42×10^{-5} (18,500)	1.32×10^{-4} (7580)
	Collinston	4.87×10^{-6} (205,300)	3.95×10^{-5} (25,300)	9.97×10^{-5} (10,000)
Floating Rupture Model - Northern End Segments	Malad City	3.90×10^{-6} (256,400)	2.98×10^{-5} (33,600)	7.05×10^{-5} (14,200)
	Clarkston Mountain	5.19×10^{-6} (192,700)	3.96×10^{-5} (25,300)	9.38×10^{-5} (10,700)
	Collinston	7.08×10^{-6} (141,200)	5.40×10^{-5} (18,500)	1.28×10^{-4} (7810)
Segmented Rupture Model - Southern Segments	Levan	4.92×10^{-6} (203,000)	1.15×10^{-4} (8700)	3.03×10^{-4} (3300)
	Fayette	2.65×10^{-5} (37,700)	2.12×10^{-4} (4720)	5.43×10^{-4} (1840)

[1] ($1/\lambda$) is shown for ease of comparison with recurrence intervals for faults.
[2] These rates account for segment rupture as a single-segment and as part of a multi-segment rupture.

Table 7.1-7. Segment rupture rates (Poisson) for the WFZ unsegmented fault model.

Fault Model	Fault Segment	Segment Rupture Rates[1,2]		
		$\lambda_{5th\%}$ ($1/\lambda_{5th\%}$)	λ_{mean} ($1/\lambda_{mean}$)	$\lambda_{95th\%}$ ($1/\lambda_{95th\%}$)
Unsegmented Model	Malad City	3.90×10^{-6} (256,400)	2.98×10^{-5} (33,600)	7.05×10^{-5} (14,200)
	Clarkston Mountain	5.19×10^{-6} (192,700)	3.96×10^{-5} (25,200)	9.38×10^{-5} (10,700)
	Collinston	7.08×10^{-6} (141,200)	5.40×10^{-5} (18,500)	1.28×10^{-4} (7810)
	Brigham City	3.08×10^{-4} (3250)	8.62×10^{-4} (1160)	1.72×10^{-3} (580)
	Weber	7.30×10^{-4} (1370)	2.09×10^{-3} (480)	4.16×10^{-3} (240)
	Salt Lake City	7.36×10^{-4} (1360)	2.11×10^{-3} (470)	4.20×10^{-3} (240)
	Provo	7.92×10^{-4} (1260)	2.26×10^{-3} (440)	4.51×10^{-3} (220)
	Nephi	3.74×10^{-4} (2670)	1.05×10^{-3} (950)	2.10×10^{-3} (480)
	Levan	5.16×10^{-6} (193,800)	3.94×10^{-5} (25,400)	9.33×10^{-5} (10,700)
	Fayette	2.14×10^{-6} (467,300)	1.63×10^{-5} (61,400)	3.87×10^{-5} (25,800)

[1] These rates account for rate of segment participation in floating rupture.
[2] These rates account for segment rupture as a single-segment and as part of a multi-segment rupture.

Table 7.1-8. Segment rupture rates (Poisson) for the WFZ.

Fault Model	Fault Segment	Segment Rupture Rates[1]		
		$\lambda_{5th\%}$ ($1/\lambda_{5th\%}$)	λ_{mean} ($1/\lambda_{mean}$)	$\lambda_{95th\%}$ ($1/\lambda_{95th\%}$)
Weighted Total of All Fault Models	Malad City	4.44×10^{-6} (225,200)	5.42×10^{-5} (18,500)	1.55×10^{-4} (6450)
	Clarkston Mountain	8.81×10^{-6} (113,500)	6.44×10^{-5} (15,500)	1.63×10^{-4} (6140)
	Collinston	6.58×10^{-6} (152,000)	4.79×10^{-5} (20,900)	1.18×10^{-4} (8480)
	Brigham City	2.03×10^{-4} (4930)	6.78×10^{-4} (1480)	1.39×10^{-3} (720)
	Weber	2.50×10^{-4} (4000)	8.46×10^{-4} (1180)	1.80×10^{-3} (560)
	Salt Lake City	2.28×10^{-4} (4390)	8.85×10^{-4} (1130)	1.82×10^{-3} (550)
	Provo	2.89×10^{-4} (3460)	9.58×10^{-4} (1040)	1.95×10^{-3} (510)
	Nephi	2.18×10^{-4} (4590)	9.24×10^{-4} (1080)	2.10×10^{-3} (480)
	Levan	2.10×10^{-5} (47,600)	1.95×10^{-4} (5130)	2.24×10^{-4} (1910)
	Fayette	4.78×10^{-6} (209,200)	1.05×10^{-4} (9520)	2.95×10^{-4} (3390)

[1] These rates account for rupture as a single-segment and as part of multi-segment and floating ruptures.

Figure 7.1-2 shows a significant mismatch at the larger magnitudes (**M** ≥ 5.5) between (1) a straight line extrapolation of the recurrence model derived from the historical seismicity record (green), and (2) the total recurrence model, which is based on both historical seismicity data and geologic data (black). This mismatch is manifested by the upward "bulge" in the plot for the latter model, which is the mean cumulative frequency-magnitude relationship for all earthquake sources. The red box with the horizontal red line inside indicates the minimum (1/217), preferred (1/109), and maximum (1/54) rate of surface-faulting earthquakes during the past 18 kyr as determined in Section 4.6, plotted at the estimated minimum magnitude for such earthquakes of **M** 6.75 ± 0.25. This box serves as a check on the total recurrence model, because the estimated rate of surface-faulting earthquakes was determined using a simpler approach with fewer assumptions. The excellent agreement between the rate of surface-faulting earthquakes shown by the box and the total recurrence model (black line) provides some support for the interpretation of the bulge in the latter as a real feature, rather than as an artifact of the assumptions of the model. Interestingly, the observed earthquake rates (triangles, Figure 7.1-2) for the two highest magnitude bins, **M** ≥ 5.65 and **M** ≥ 6.35, are also higher than expected based on a linear extrapolation of the recurrence model derived from historical seismicity data. However, the rates for these magnitude bins have large uncertainties because the earthquake catalog has only three independent mainshocks of **M** ≥ 5.65 and one of **M** ≥ 6.35 (Table 5.4-1 and Figure 5.6-1).

Possible explanations for the bulge include the following: (1) Because of the restricted areal extent of our study region and its dominance by the WFZ (see Figure 5.4-1), earthquake recurrence data in the study region do not exhibit a Gutenberg-Richter relationship. (2) The relatively short historical earthquake record in the study region is not representative of long-term recurrence. (3) Our judgment that the maximum magnitude model is more appropriate than the truncated exponential model for modeling the recurrence of earthquakes on the major faults in the region may be incorrect and greater

Table 7.1-9. Segment rupture rates (Poisson) for OGSLFZ fault models.

Fault Model	Fault Segment	Segment Rupture Rates[1]		
		$\lambda_{5th\%}$ ($1/\lambda_{5th\%}$)	λ_{mean} ($1/\lambda_{mean}$)	$\lambda_{95th\%}$ ($1/\lambda_{95th\%}$)
1	RZ	7.09×10^{-5} (14,100)	3.01×10^{-4} (3320)	6.81×10^{-4} (1470)
	PY	7.09×10^{-5} (14,100)	3.01×10^{-4} (3320)	6.81×10^{-4} (1470)
	FI	7.31×10^{-5} (13,700)	3.20×10^{-4} (3130)	7.42×10^{-4} (1350)
	AI	7.09×10^{-5} (14,100)	3.01×10^{-4} (3320)	6.81×10^{-4} (1470)
	NO	9.39×10^{-6} (106,500)	8.86×10^{-5} (11,300)	1.99×10^{-4} (5030)
	SO	2.68×10^{-5} (37,300)	1.06×10^{-4} (9430)	3.00×10^{-4} (3330)
	TH	2.64×10^{-5} (37,900)	1.91×10^{-4} (5240)	4.65×10^{-4} (2150)
	ET	1.19×10^{-5} (84,000)	6.90×10^{-5} (14,500)	1.78×10^{-4} (5600)
2	RZ	7.09×10^{-5} (14,100)	3.01×10^{-4} (3320)	6.81×10^{-4} (1470)
	PY	7.09×10^{-5} (14,100)	3.01×10^{-4} (3320)	6.81×10^{-4} (1470)
	FI	7.31×10^{-5} (13,700)	3.20×10^{-4} (3130)	7.42×10^{-4} (1350)
	AI	7.09×10^{-5} (14,100)	3.01×10^{-4} (3320)	6.81×10^{-4} (1470)
	NO	9.39×10^{-6} (106,500)	8.86×10^{-5} (11,300)	1.99×10^{-4} (5130)
	SO	2.68×10^{-5} (37,300)	1.06×10^{-4} (9430)	3.00×10^{-4} (3330)
	TH	2.64×10^{-5} (37,900)	1.91×10^{-4} (5240)	4.65×10^{-4} (2150)
	ET	1.19×10^{-5} (84,000)	6.90×10^{-5} (14,500)	1.78×10^{-4} (5600)
3	RZ	7.09×10^{-5} (14,100)	3.01×10^{-4} (3320)	6.81×10^{-4} (1470)
	PY	7.09×10^{-5} (14,100)	3.01×10^{-4} (3320)	6.81×10^{-4} (1470)
	FI	7.09×10^{-5} (14,100)	3.01×10^{-4} (3320)	6.81×10^{-4} (1470)
	AI	7.09×10^{-5} (14,100)	3.01×10^{-4} (3320)	6.81×10^{-4} (1470)
	NO	9.39×10^{-6} (106,500)	8.86×10^{-5} (11,300)	1.99×10^{-4} (5130)
	SO	2.68×10^{-5} (37,300)	1.06×10^{-4} (9430)	3.00×10^{-4} (3330)
	TH	2.64×10^{-5} (37,900)	1.91×10^{-4} (5240)	4.65×10^{-4} (2150)
	ET	1.19×10^{-5} (84,000)	6.90×10^{-5} (14,500)	1.78×10^{-4} (5600)
4	RZ	7.09×10^{-5} (14,100)	3.01×10^{-4} (3320)	6.81×10^{-4} (1470)
	PY	7.09×10^{-5} (14,100)	3.01×10^{-4} (3320)	6.81×10^{-4} (1470)
	FI	7.31×10^{-5} (13,700)	3.20×10^{-4} (3130)	7.42×10^{-4} (1350)
	AI	7.09×10^{-5} (14,100)	3.01×10^{-4} (3320)	6.81×10^{-4} (1470)
	NO	9.39×10^{-6} (106,500)	8.86×10^{-5} (11,300)	1.99×10^{-4} (5130)
	SO	1.85×10^{-5} (54,100)	1.17×10^{-4} (8550)	3.10×10^{-4} (3230)
	TH	1.85×10^{-5} (54,100)	1.17×10^{-4} (8550)	3.10×10^{-4} (3230)
	ET	1.19×10^{-5} (84,000)	6.90×10^{-5} (14,500)	1.78×10^{-4} (5600)
5	RZ	1.81×10^{-4} (5530)	5.01×10^{-4} (2000)	1.19×10^{-3} (840)
	PY	3.02×10^{-4} (3310)	8.35×10^{-4} (1200)	1.98×10^{-3} (500)
	FI	3.39×10^{-4} (2950)	9.47×10^{-4} (1060)	2.22×10^{-3} (450)
	AI	2.73×10^{-4} (3660)	7.82×10^{-4} (1280)	1.77×10^{-3} (570)
	NO	4.66×10^{-5} (21,500)	2.94×10^{-4} (3400)	6.90×10^{-4} (1450)
	SO	4.43×10^{-5} (22,600)	2.79×10^{-4} (3580)	6.56×10^{-4} (1520)
	TH	3.58×10^{-5} (27,900)	2.26×10^{-4} (4430)	5.29×10^{-4} (1890)
	ET	2.53×10^{-5} (39,500)	1.59×10^{-4} (6290)	3.74×10^{-4} (2670)

[1] These rates account for segment rupture as a single-segment and as part of multi-segment and floating ruptures.

Table 7.1-10. Segment rupture rates (Poisson) for the OGSLFZ.

Fault Model	Fault Segment	Segment Rupture Rates[1]		
		$\lambda_{5th\%}$ ($1/\lambda_{5th\%}$)	λ_{mean} ($1/\lambda_{mean}$)	$\lambda_{95th\%}$ ($1/\lambda_{95th\%}$)
Weighted Total of All Fault Models	RZ	7.09×10^{-5} (14,100)	3.40×10^{-4} (2940)	6.81×10^{-4} (1470)
	PY	7.09×10^{-5} (14,100)	4.05×10^{-4} (2470)	1.02×10^{-3} (980)
	FI	7.31×10^{-5} (13,700)	4.46×10^{-4} (2240)	1.20×10^{-3} (830)
	AI	7.09×10^{-5} (14,100)	3.95×10^{-4} (2530)	9.51×10^{-4} (1050)
	NO	1.74×10^{-5} (57,500)	1.33×10^{-4} (7520)	4.08×10^{-4} (2450)
	SO	2.49×10^{-5} (40,200)	1.43×10^{-4} (6990)	4.12×10^{-4} (2430)
	TH	2.69×10^{-5} (37,200)	1.92×10^{-4} (5210)	4.80×10^{-4} (2080)
	ET	1.26×10^{-5} (79,400)	8.75×10^{-5} (11,400)	2.36×10^{-4} (4240)

[1] These rates account for segment rupture as a single-segment, multi-segment rupture and as part of a floating rupture.

Table 7.1-11. Segment rupture rates (Poisson) for other segmented faults in Wasatch Front region.

Fault	Fault Segment	Segment Rupture Rates[1]		
		$\lambda_{5th\%}$ ($1/\lambda_{5th\%}$)	λ_{mean} ($1/\lambda_{mean}$)	$\lambda_{95th\%}$ ($1/\lambda_{95th\%}$)
East Cache	North	2.06×10^{-5} (48,500)	1.83×10^{-4} (5460)	5.39×10^{-4} (1860)
	Central	4.12×10^{-5} (24,300)	2.57×10^{-4} (3890)	6.69×10^{-4} (1500)
	South	7.29×10^{-6} (137,200)	7.73×10^{-5} (12,900)	3.48×10^{-4} (2870)
Eastern Bear Lake	North	9.53×10^{-5} (10,500)	4.72×10^{-4} (2120)	1.23×10^{-3} (810)
	Central	1.76×10^{-4} (5680)	9.11×10^{-4} (1100)	2.72×10^{-3} (370)
	South	9.45×10^{-5} (10,600)	6.84×10^{-4} (1460)	2.21×10^{-3} (450)
Stansbury	North	5.09×10^{-5} (19,600)	4.49×10^{-4} (2230)	1.09×10^{-3} (920)
	Central	5.10×10^{-5} (19,600)	5.49×10^{-4} (1820)	1.86×10^{-3} (540)
	South	4.43×10^{-5} (22,600)	4.77×10^{-4} (2100)	1.24×10^{-3} (800)
West Cache	North	7.92×10^{-5} (12,600)	4.32×10^{-4} (2320)	1.06×10^{-3} (940)
	Central	3.64×10^{-5} (27,500)	3.61×10^{-4} (2770)	1.43×10^{-3} (700)
	South	3.78×10^{-5} (26,500)	2.25×10^{-4} (4440)	7.20×10^{-4} (1390)

[1] These recurrence rates are participation rates which account for segment rupture as a single-segment and as part of a multi-segment rupture.

weight should be given to the latter. (4) We have overestimated the geologic slip rates in the region. These potential explanations are not mutually exclusive. It is noteworthy that a bulge is also observed in the earthquake recurrence curve for California (Petersen *et al*., 2000; Field *et al*., 2009) and British Columbia (BCHydro, 2012). The bulge in the California recurrence has been removed in the UCERF3 model (Field *et al*., 2013). The USGS, as part of the National Seismic Hazard Mapping Project, compared the historical seismicity rates with the total predicted earthquake rates for the northern and central BRP, an area much larger than the Wasatch Front region (Mark Petersen, USGS, written communication, 2015). They too noted a bulge in the magnitude range **M** 5.5 to 7.0, although it was considerably smaller than the one in our recurrence model. The WGUEP acknowledges the possibility that the observed bulge for the Wasatch Front region may be due to an overprediction of earthquakes in the **M** 6 to 7 range, but the bulge may indeed be a real physical feature of earthquake recurrence in the region.

7.1.5 Antithetic Faults

The Wasatch Front region contains four antithetic fault pairs (Section 4.4). We modeled these faults either as independent faults or a system containing a master fault and a subsidiary fault. When modeled as a system, the rate of the subsidiary fault is set to the rate of the master fault (i.e., the subsidiary fault always ruptures with the master fault). For the probability calculations, we treated this as a single event. The magnitude of the event is based on the total moment release from both faults. Given a magnitude of an event on the master fault ($\mathbf{M}_m$), the moment of the master fault rupture ($M_{0,m}$) is computed as

$$M_{0,m} = 10^{(1.5 \times \mathbf{M}_m + 16.05)} \qquad (7\text{-}7)$$

The magnitude of the subsidiary fault rupture is determined from the subsidiary fault area and the magnitude-area relation (Section 3.6). We calculated the area of the subsidiary

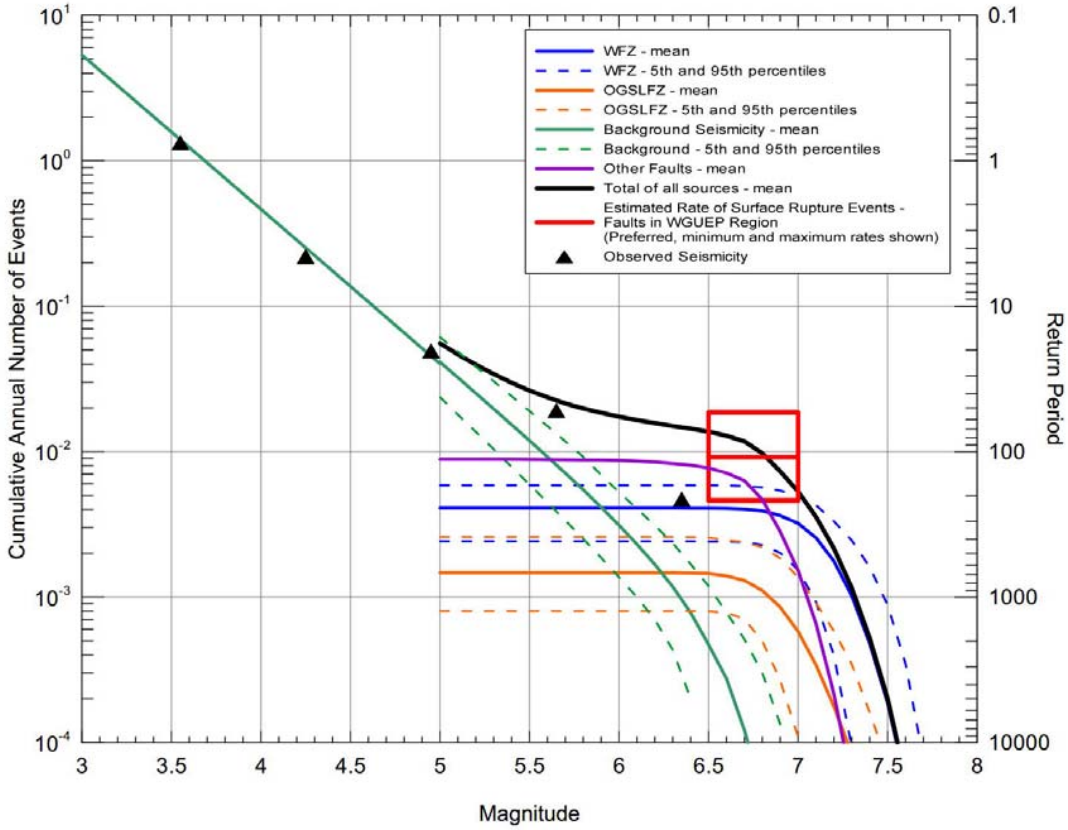

Figure 7.1-2. Mean and ± 2σ cumulative magnitude-frequency relationships for the WFZ, OGSLFZ, background seismicity, and "other modeled faults."

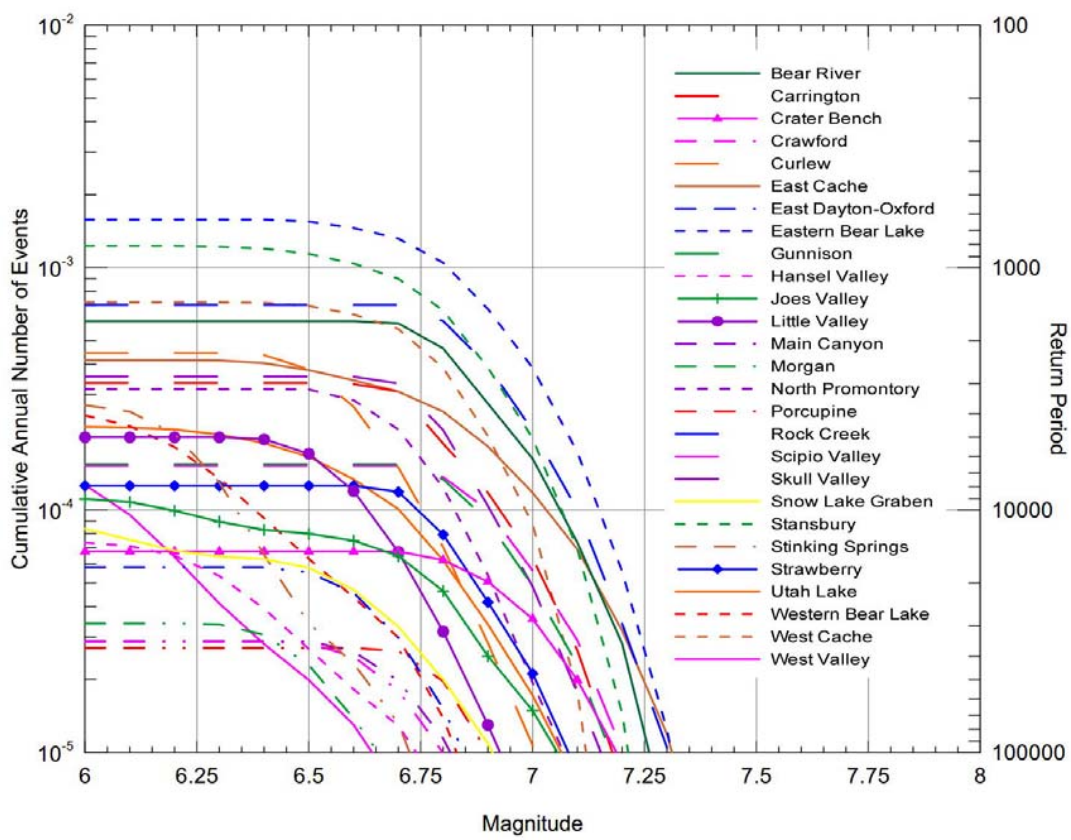

Figure 7.1-3. Cumulative magnitude-frequency relationships for the "other modeled faults."

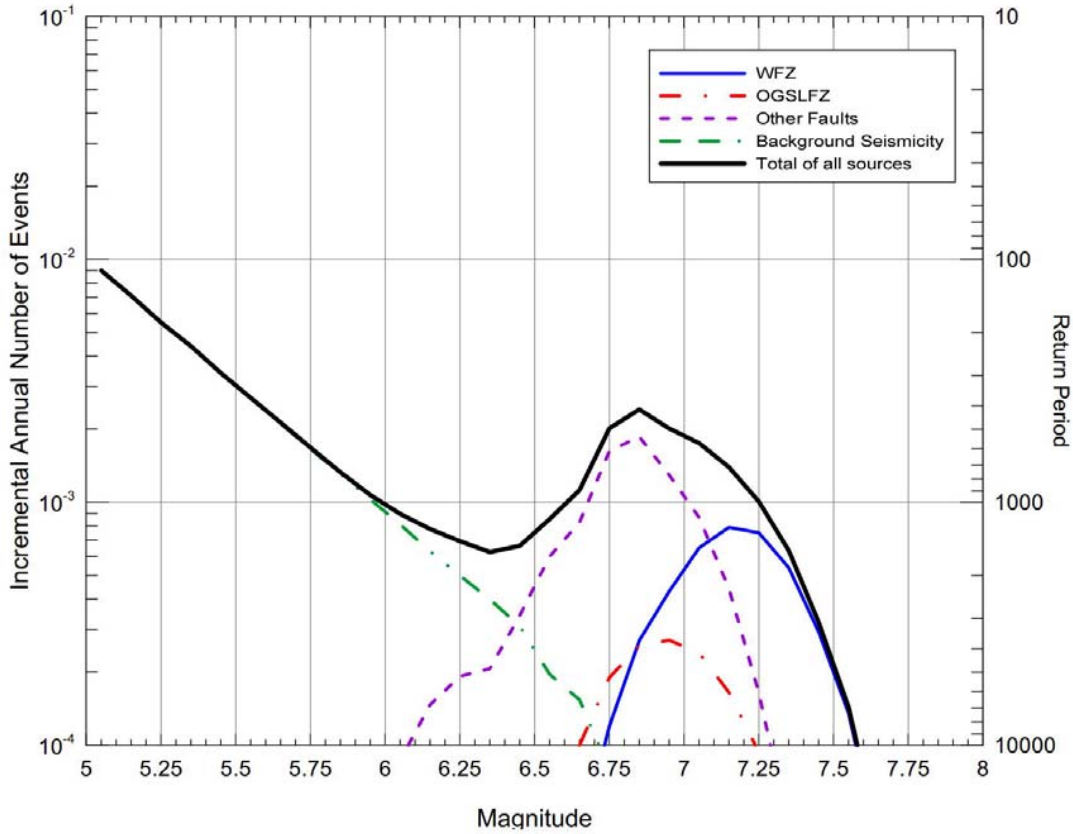

Figure 7.1-4. Mean incremental magnitude-frequency relationships for the WFZ, OGSLFZ, background seismicity, "other modeled faults," and total of all sources.

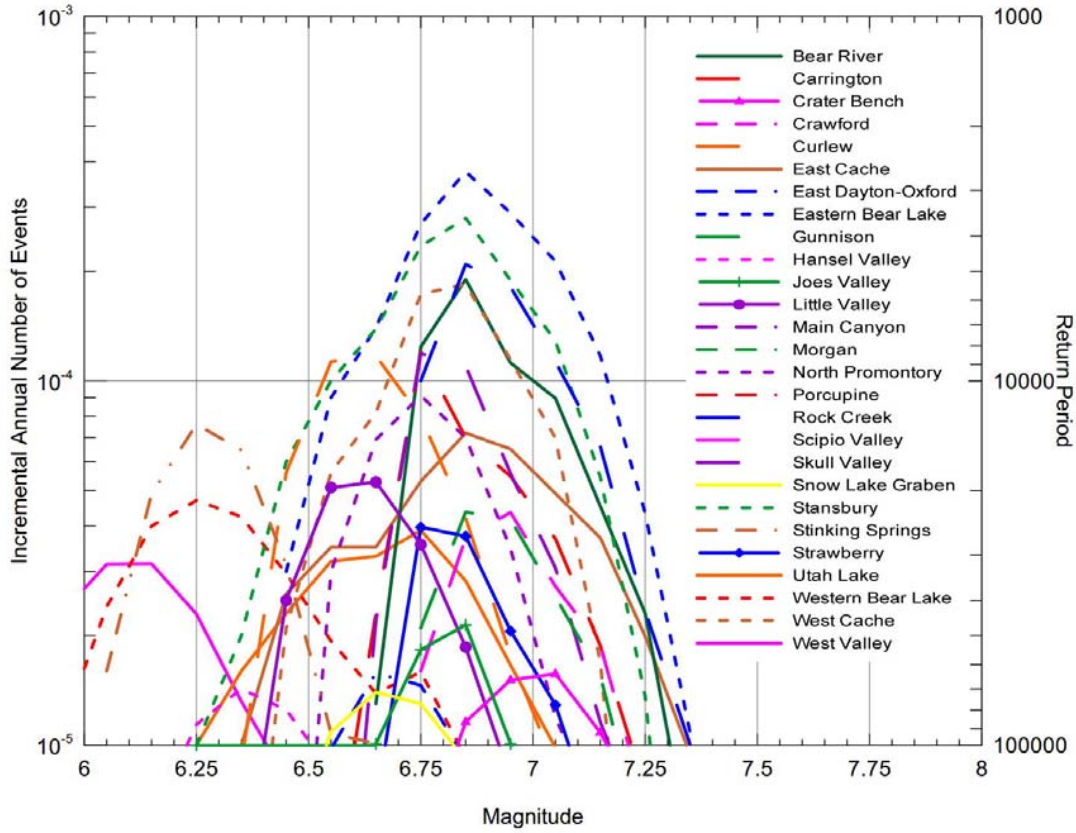

Figure 7.1-5. Mean incremental magnitude-frequency relationships for the "other modeled faults."

fault for each rupture based on the dips of both the master and subsidiary faults, separation distance, and seismogenic thickness. If the faults intersect for a given geometry, the subsidiary fault is truncated by the master fault. The moment of the subsidiary fault rupture, $M_{0,s}$, is determined using equation (7-7) and the magnitude of the subsidiary fault (the *m* subscript is replaced with an *s*). The magnitude of the coseismic event (M_{CS}) modeled for probability calculations is computed as

$$M_{CS} = \frac{2}{3} \times \log(M_{0,m}+M_{0,s}) - 10.7 \qquad (7\text{-}8)$$

7.1.6 Segment Moment Rates

Long-term moment rates for rupture sources can be computed based on the rupture source rates and the mean moment of events on these rupture sources. Each rupture source moment rate is partitioned to all segments involved in the rupture. The total moment rate for each segment is the sum of all partitioned moment rates from rupture sources containing the specified segment. For rupture sources consisting of more than one segment, the moment rate is partitioned to the segments proportional to the segment lengths. For floating ruptures, the moment rate is partitioned to the segments based on the relative rate of rupture on each segment. As discussed above, floating ruptures are distributed uniformly along the fault trace, thus the relative rate of rupture of each segment is a function of the rupture length, segment length, total fault length, and location of the segment along the fault trace.

For those faults characterized by recurrence intervals, it is useful to compare segment moment rates from each fault model to those based on geologic slip rate estimates. The fault models for the WFZ central segments and the Great Salt Lake fault zone are characterized using recurrence intervals based on paleoseismic data. Figure 7.1-6 shows the segment moment rates for the WFZ central segments for the preferred rupture model (SSR model) compared to those based on the geologic slip rates. The mean segment moment rates along with the 5th to 95th range is shown on Figure 7.1-6. The mean segment moment rates for each segment from this model (assuming Poisson behavior) compare well with those based on the segment slip rates. In general, the 5th to 95th percentile ranges of segment moment rates for the model exceed the ranges based on the geologic slip rates. The larger range for the model is likely due to the inclusion of sample size uncertainty in the distribution of rupture rates for the model (Section 3.4). Figure 7.1-7 compares the segment moment rates for the WFZ central segments for all fault models assuming Poisson behavior. In general, all of the segmented models for the WFZ central segments have similar mean segment model rates. The unsegmented model predicts a higher segment moment rate for the SLCS than the segmented models and the segment-specific geologic slip rate. This result is partially due to the assumption that floating ruptures are uniformly distributed along the fault. The SLCS, being in the center of the fault, is involved in the floating rupture more often than segments near the ends of the fault. Figure 7.1-8 shows the proportion of the moment rate from the floating ruptures in the unsegmented model attributed to each segment. Note that we modeled the unsegmented model for the WFZ with two floating ruptures—one that ruptures the entire fault and one the ruptures only the central segments—to accommodate higher geologic slip rates on the central segments. The largest magnitude modeled in the unsegmented model (**M** 7.6) has a rupture length of approximately 125 km. When distributed along the five central segments, the SLCS is always involved. When distributed along the entire fault, the SLCS is involved 66% of the time. Segment moment rates for all ten WFZ segments are shown on Figure 7.1-9. The larger mean moment rates for the central segments generally agree with those based on the geologic slip rates which are larger for the central segments. The unsegmented rupture model appears to underpredict moment rate for the southern end segments.

Figure 7.1-10 shows the segment moment rates for all models of the OGSLFZ assuming Poisson behavior. Where available, segment moment rates based on geologic slip rates are provided for comparison. Similar to the WFZ, the unsegmented model has two floating ruptures. One rupture floats on all segments. A second rupture floats only on the four segments of the Great Salt Lake fault zone to accommodate the higher geologic slip rates on those segments. Figure 7.1-11 shows the proportion of moment rate from the floating ruptures attributed to each segment. The unsegmented rupture model results in moment rates on the Fremont Island and Promontory segments that are significantly larger than the other rupture models indicating that the slip rates used for the floating rupture on the Great Salt Lake fault zone are inconsistent with the recurrence intervals for these segments used in the other models.

Moment rates for fault segments can also be useful in comparisons to geodetic rates (Section 6). Total moment rates (Poisson model) of fault segments for all faults characterized in the Wasatch Front region, as well as moment rates for background seismicity, are provided in Table 7.1-12.

7.1.7 Implied Slip Rates

For fault models characterized entirely by recurrence intervals, such as the WFZ central segments, an implied slip rate can be computed as

$$SR_{implied} = \frac{\dot{M}_0}{\mu A} \qquad (7\text{-}9)$$

where $\dot{M}_0$ is the segment moment rate described above, μ is the rigidity, and A is the segment area. Implied slip rates for the WFZ central segments using the preferred single-segment rupture models are provided in Table 7.1-13. We have converted them to vertical slip rates. The weighted mean geologic slip rates from Table 4.1-4 are shown for comparison.

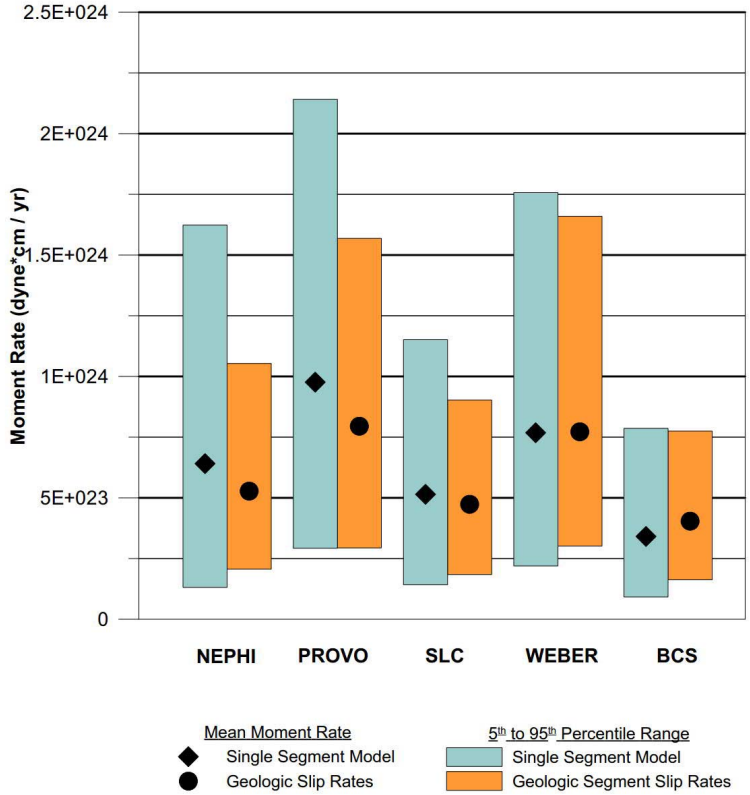

Figure 7.1-6. Segment moment rates for the WFZ central segments and the single-segment rupture fault model.

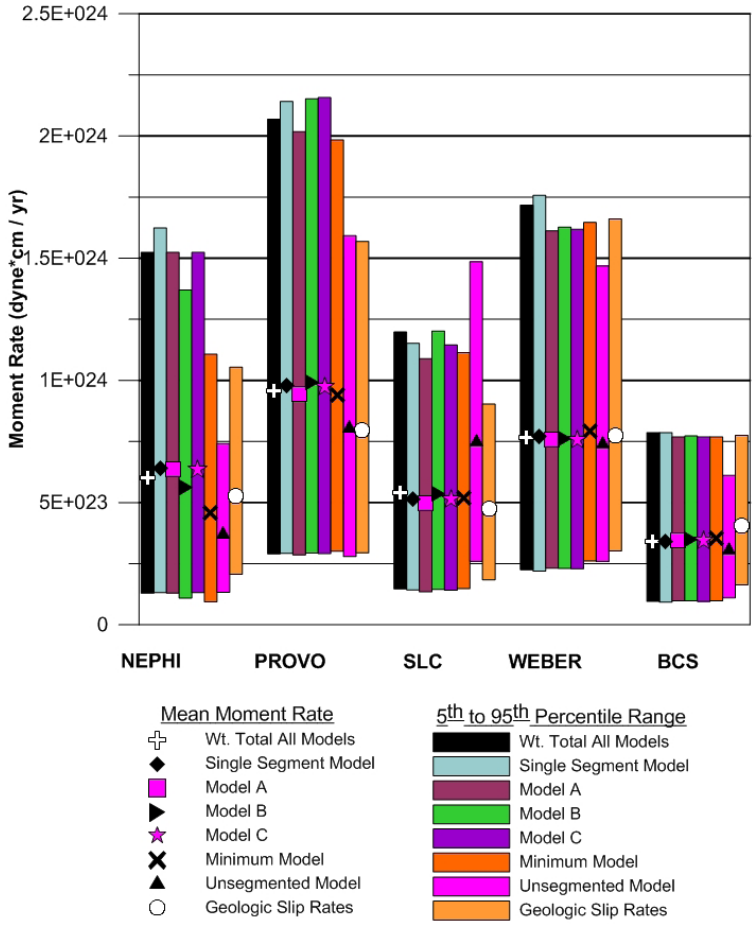

Figure 7.1-7. Segment moment rates for the WFZ central segments and all fault rupture models.

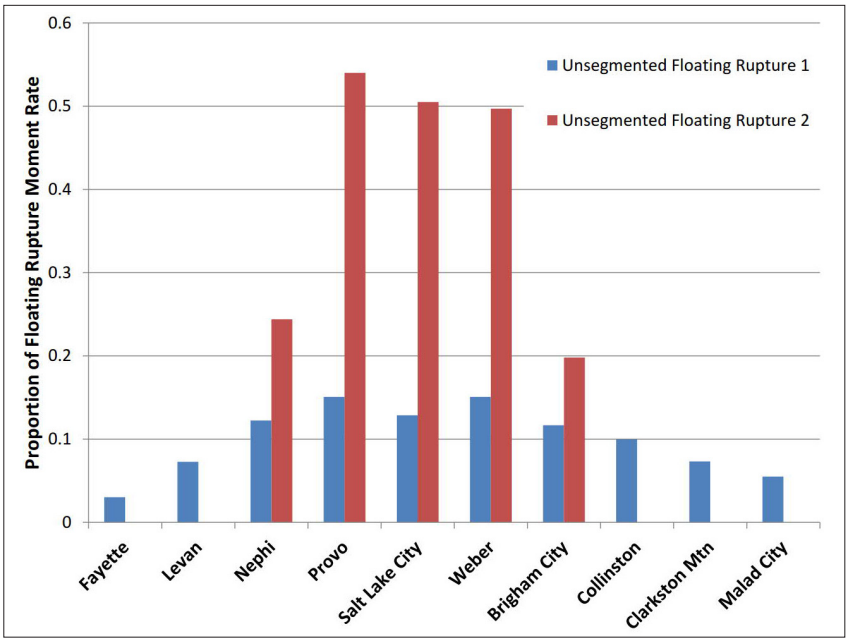

Figure 7.1-8. Distribution of moment to segments from the unsegmented rupture model for the WFZ.

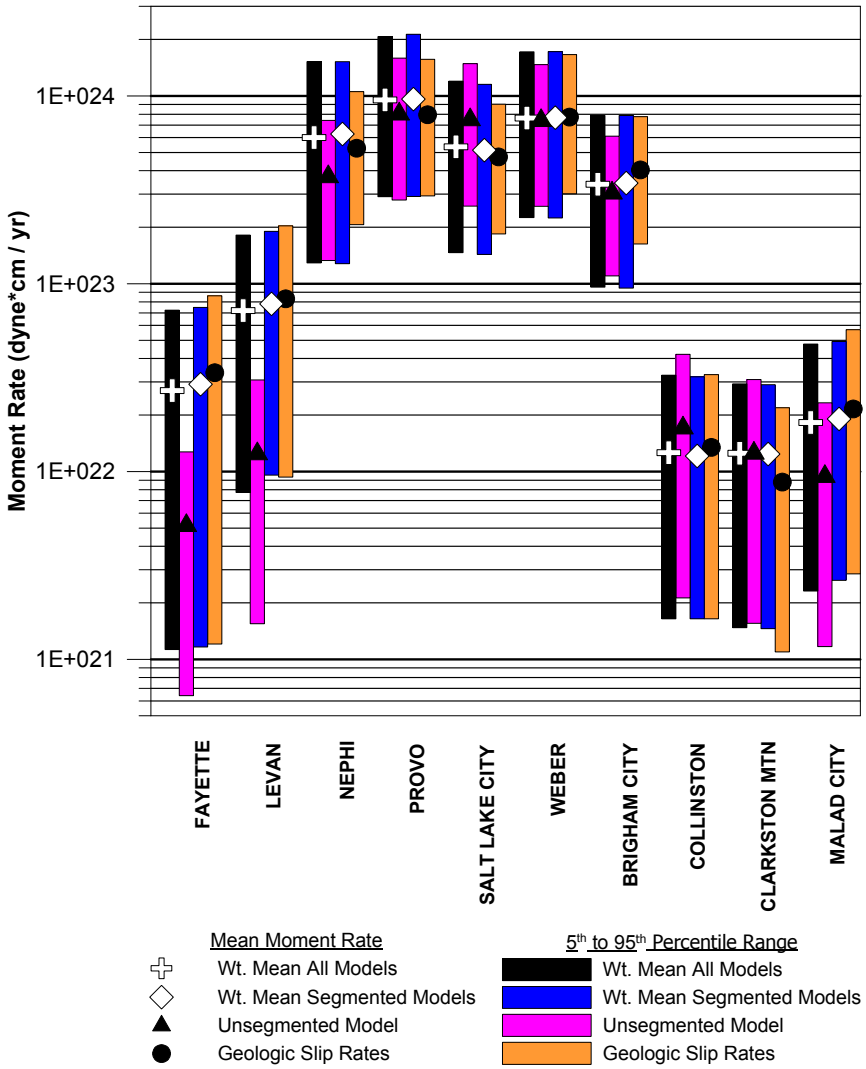

Figure 7.1-9. Segment moment rates for the WFZ.

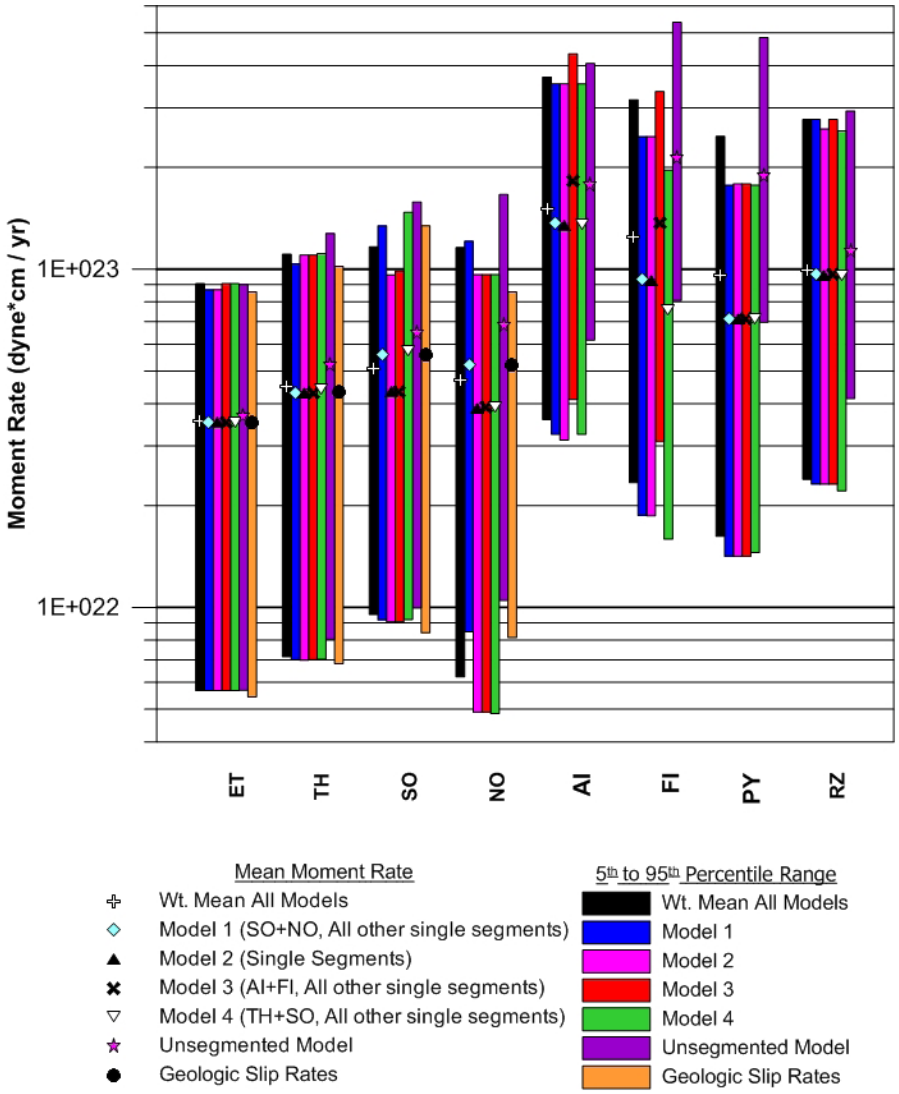

Figure 7.1-10. Segment moment rates for the OGSLFZ.

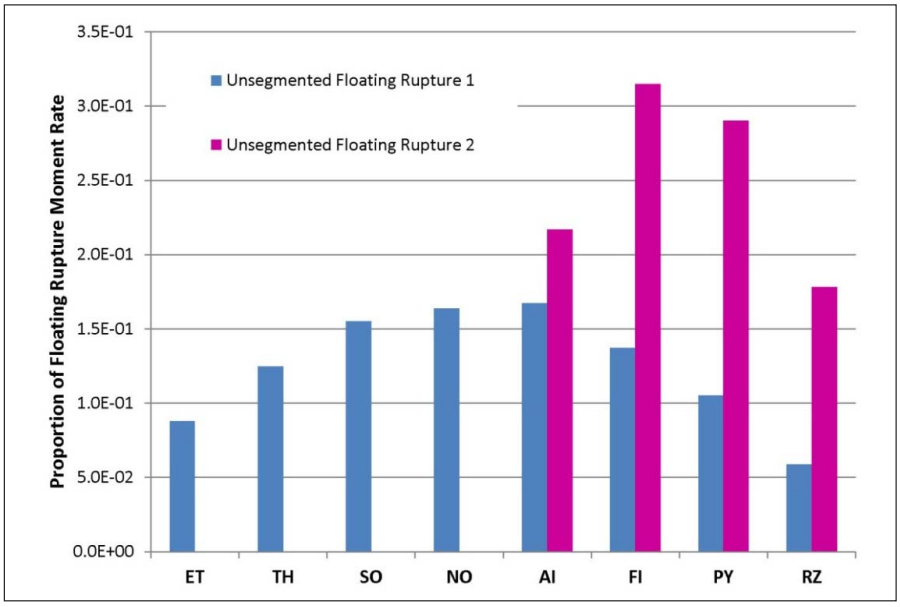

Figure 7.1-11. Distribution of moment to segments from the unsegmented rupture model for the OGSLFZ.

7.1.8 Probability Calculations

Rupture source probabilities are computed from the rupture source rates of exceeding the threshold magnitude (Section 7.2). For the time-dependent probabilities, the COV and the time since last event are also required (Section 7.3). Rupture source probabilities are then aggregated to obtain fault rupture probabilities. Segment rupture probabilities can also be obtained by combining all rupture sources containing the specified segment and the floating ruptures for the unsegmented model partitioned as described above. Rupture probabilities for background seismicity are computed from the long-term seismicity rates described in Section 5. Fault and background seismicity rupture probabilities are then aggregated to obtain the Wasatch Front regional probabilities.

The probabilities are calculated for a suite of time periods and threshold magnitudes. We selected the time periods and magnitudes to assist in the decisions in engineering design of a variety of structures, retrofit of structures, and earthquake policy. We calculated the probabilities for time periods of 30, 50, and 100 years beginning in 2014. Threshold magnitudes (M_T) are **M** 5.0, 6.0, and 6.75. The results presented in Section 8 include:

- The probabilities for a large earthquake on each rupture source characterized in the model.
- The probabilities that each fault segment will be ruptured by a large earthquake.
- The probability for a large earthquake on each fault characterized in the model.
- The probability of a background earthquake (i.e., an event not on one of the characterized faults).
- The probability that an earthquake will occur somewhere in the region.

7.1.9 Calculation Sequence

The calculation of rupture source rates and probabilities involve many models, relations, and parameters. Most of the uncertainty is treated as epistemic uncertainty. We assigned weights on different models (e.g., probability models or recurrence models) or relations (e.g., magnitude–fault length relations) based on the expert judgment of the WGUEP using logic trees. We also treated model and relation inputs using a logic tree approach, with a distribution represented by discrete values and weights. The combination of all input, relation, and model choices results in thousands of logic tree branches or combinations of input values, relations, and models. We sampled the distribution of logic tree branches using a Monte Carlo approach in a FORTRAN code. Mean, 5th, and 95th percentile probabilities (and selected computed parameters such as rates) were determined using the Monte Carlo sampling of the full logic tree. For the full Wasatch Front region model, the use of 50,000 samples produced stable mean, 5th, and 95th values.

Within the full logic tree, correlation exists between some inputs at the fault or regional level. For instance, for a given sampling of the full logic tree, we assumed seismogenic thickness to be the same for all faults within the same subregion (the Wasatch Front region was divided into two subregions to accommodate an increased possibility of thicker seismogenic crust to the east, as described in Section 3.3). The correlations between inputs are provided in Table 7.1-14. Note that the recurrence model for the WFZ is correlated at the sub-fault level. For computational reasons, we divided the WFZ into three sub-faults: northern end segments, central segments, and southern end segments for which fault models are not correlated.

7.2 Probability Models

The mean rupture source rates described in Section 7.1.1 represent the predicted long-term behavior. Calculating the conditional probability of an earthquake occurring in a specified time interval requires a probability model. Probability models describe how the earthquakes are distributed in time. Probability models may take into account various amounts of physics. The probability models selected for this study are the Poisson model and the BPT model.

Both of these models have the same underlying mathematical model for the calculation of probabilities. The probability of rupture for a rupture source is specified by a PDF, *f(t)*, that defines the chance that failure will occur in the interval from t to $t + \Delta t$, where t is the time measured from the date of the most recent earthquake (Figure 7.2-1). The area under *f(t)* between $t = 0$ and $t = \infty$ is 1, as it is assumed that there will be another earthquake. The area under *f(t)* between $t = T$ and $t = \infty$ defines the survivor function, F(T), which gives the probability that at least time T will elapse between successive events.

$$F(T) = \int_T^{\infty} f(t)dt \qquad (7\text{-}10)$$

For any probability model, $F(0) = 1$ and $F(\infty) = 0$. The hazard function, *h(t)*, is the ratio of the PDF to the survivor function. The hazard function is more useful in comparing different probability models. It gives the instantaneous rate of failure at time t conditional upon no event having occurred up to time t.

The probabilities computed in this study are conditional probabilities. They give the probability that an earthquake will occur on a defined rupture source (or in the background) during a specified time interval, conditional on it not having occurred by the year 2014. The conditional probability is calculated by dividing the area under the PDF in the interval of interest by the area of the density function at times equal

Table 7.1-12. Segment moment rates.

Fault or Fault Zone	Fault Segment	Segment Moment Rate (dyne *cm / yr)		
		Mean	5th Percentile	95th Percentile
WFZ	Malad City	1.83E+22	2.31E+21	4.77E+22
	Clarkston Mountain	1.26E+22	1.47E+21	2.93E+22
	Collinston	1.27E+22	1.64E+21	3.26E+22
	Brigham City	3.40E+23	9.59E+22	7.87E+23
	Weber	7.67E+23	2.25E+23	1.72E+24
	Salt Lake City	5.38E+23	1.47E+23	1.20E+24
	Provo	9.56E+23	2.91E+23	2.07E+24
	Nephi	6.03E+23	1.29E+23	1.52E+24
	Levan	7.23E+22	7.73E+21	1.82E+23
	Fayette	2.71E+22	1.13E+21	7.23E+22
OGSLFZ	RZ	9.97E+22	2.39E+22	2.77E+23
	PY	9.45E+22	1.62E+22	2.43E+23
	FI	1.24E+23	2.34E+22	3.17E+23
	AI	1.51E+23	3.49E+22	3.70E+23
	NO	4.68E+22	6.14E+21	1.16E+23
	SO	5.07E+22	9.53E+21	1.14E+23
	TH	4.51E+22	7.15E+21	1.10E+23
	ET	3.58E+22	5.67E+21	9.04E+22
Bear River	Bear River	1.84E+23	6.98E+22	5.68E+23
Carrington	Carrington	8.57E+22	1.39E+22	1.99E+23
Crater Bench and Drum Mountains	Crater Bench and Drum Mountains	2.97E+22	2.85E+21	1.14E+23
Crawford Mountains	Crawford Mountains	4.99E+21	1.37E+21	1.37E+22
Curlew Valley	Curlew Valley	5.51E+22	1.10E+22	1.75E+23
East Cache	North	7.29E+22	9.57E+21	1.71E+23
	Central	3.64E+22	5.22E+21	9.30E+22
	South	1.62E+22	2.18E+21	6.03E+22
East Dayton-Oxford	East Dayton-Oxford	8.93E+21	1.26E+21	1.89E+22
Eastern Bear Lake	North	9.17E+22	1.74E+22	2.51E+23
	Central	2.07E+23	4.06E+22	5.56E+23
	South	2.13E+23	4.08E+22	6.20E+23
Faults along the edge of Scipio Valley-Pavant Range	Faults along the edge of Scipio Valley-Pavant Range	5.62E+22	4.93E+21	1.97E+23
Gunnison	Gunnison	5.21E+22	4.60E+21	1.84E+23

Table 7.1-12. Continued.

Fault or Fault Zone	Fault Segment	Segment Moment Rate (dyne *cm / yr)		
		Mean	5th Percentile	95th Percentile
Hansel Valley[1]	Hansel Valley	5.74E+21	0.00E+00	2.12E+22
Joes Valley	Joes Valley	2.11E+22	6.38E+20	6.07E+22
Little Valley	Little Valley	2.48E+22	2.19E+21	8.75E+22
Main Canyon	Main Canyon	5.37E+21	1.42E+21	1.42E+22
Morgan	Morgan	3.47E+21	8.20E+20	9.30E+21
North Promontory	North Promontory	9.07E+22	1.91E+22	2.43E+23
Porcupine Mountain	Porcupine Mountain	7.28E+21	1.92E+21	1.92E+22
Rock Creek	Rock Creek	2.33E+23	4.49E+22	5.61E+23
Skull Valley	Skull Valley	8.04E+22	9.82E+21	1.75E+23
Snow Lake Graben	Snow Lake Graben	1.32E+22	3.80E+20	3.98E+22
Stansbury	North	8.99E+22	9.20E+21	2.72E+23
	Central	1.23E+23	1.25E+22	3.97E+23
	South	6.37E+22	6.52E+21	1.92E+23
Stinking Springs	Stinking Springs	1.14E+22	1.84E+21	4.10E+22
Strawberry	Strawberry	3.19E+22	7.36E+21	1.02E+23
Utah Lake[1]	Utah Lake	3.44E+22	0.00E+00	1.22E+23
West Cache	North	7.10E+22	1.15E+22	1.62E+23
	Central	5.12E+22	9.20E+21	1.75E+23
	South	3.12E+22	7.67E+21	8.81E+22
West Valley[1]	West Valley	5.57E+21	0.00E+00	2.63E+22
Western Bear Lake[1]	Western Bear Lake	1.45E+22	0.00E+00	6.10E+22
Background Seismicity		1.83E+23	8.15E+22	3.51E+23

[1] Moment rates for subsidiary antithetic faults are only for independent rupture. Moment rate for simultaneous rupture of both master and subsidiary faults is contained in master fault moment rate.

Table 7.1-13. Implied slip rates for the WFZ central segments using single-segment rupture model.

Fault Segment	Implied Slip Rate[1] (mm/year)							Geologic Slip Rate[2] (mm/yr)
	Single-Segment Model	Intermediate A Model	Intermediate B Model	Intermediate C Model	Minimum Model	Unsegmented Model	Wt. Mean All Models	Wt. Mean
BCS	1.25	1.28	1.28	1.27	1.29	1.05	1.25	1.38
WS	1.69	1.86	1.66	1.65	1.69	1.52	1.69	1.57
SLCS	1.44	1.43	1.44	1.44	1.46	2.21	1.44	1.38
PS	1.96	1.92	2.02	1.97	1.94	1.65	1.96	1.61
NS	1.94	1.94	1.72	1.94	1.45	1.11	1.94	1.50

[1] 100% Poisson branch
[2] Geologic slip rates from Table 4.1-1

Table 7.1-14. Correlation of inputs.

Input	Correlation Level
Segmentation boundary location (used to compute segment lengths)	Adjacent segments
Seismogenic thickness	Regional (entire Wasatch region divided into 2 regions – east and west)
Dip	Fault
Average displacement	None
Magnitude relation	All faults of the same fault type (A, B, C or D)
Geologic slip rate	Fault (low, medium, high)
Paleoseismic recurrence interval	None
Recurrence model	Fault[1]
Rate approach (recurrence intervals versus geologic slip rates)	None
Probability model	Region (when time-dependent probability model selected for region, faults without this branch use Poisson model)
COV	Region
Date of Last Event	None

[1] For computational reasons, recurrence models are not correlated between the northern end segments, southern end segments, and central segments of the WFZ.

or greater than the start of the interval of interest (Figure 7.2-1). The conditional probability is defined by

$$P(T \le t \le T + \Delta T \,|\, t > T) = \frac{F(T)\text{-}F(T + \Delta T)}{F(T)} \qquad (7\text{-}11)$$

7.2.1 Time-Independent – Poisson Model

The Poisson model describes the distribution of times between successive events for a homogeneous Poisson process (random occurrence) and is specified by the PDF

$$f_{Exp}(t) = \lambda e^{-\lambda t} \qquad (7\text{-}12)$$

where λ is the mean rate of events per unit time (reciprocal to the mean interval between events). In our calculations, λ is the mean rupture rate of each rupture source, as described in Section 7.1. The Poisson distribution has the important property that the hazard function is constant, $h_{\mathrm{Exp}}(t)$ λ. Thus, it has no "memory" of the time of the most recent event. An earthquake is just as likely to occur on a fault segment one day after the most recent event as it is to occur 200 years later. The conditional probability is also independent of the time of the most recent event.

The Poisson model is the standard model for PSHAs. This model is appropriate when no information other than the mean rate of earthquake production is known; it can be viewed as the "least-informative" model or simplest, depending on one's perspective. However, the Poisson model fails to incorporate the most basic physics of the earthquake process, whereby the tectonic stress released when a fault fails must rebuild before the next earthquake can occur at that location. We include the Poisson model to provide a conservative estimate of the probability on faults for which one suspects that

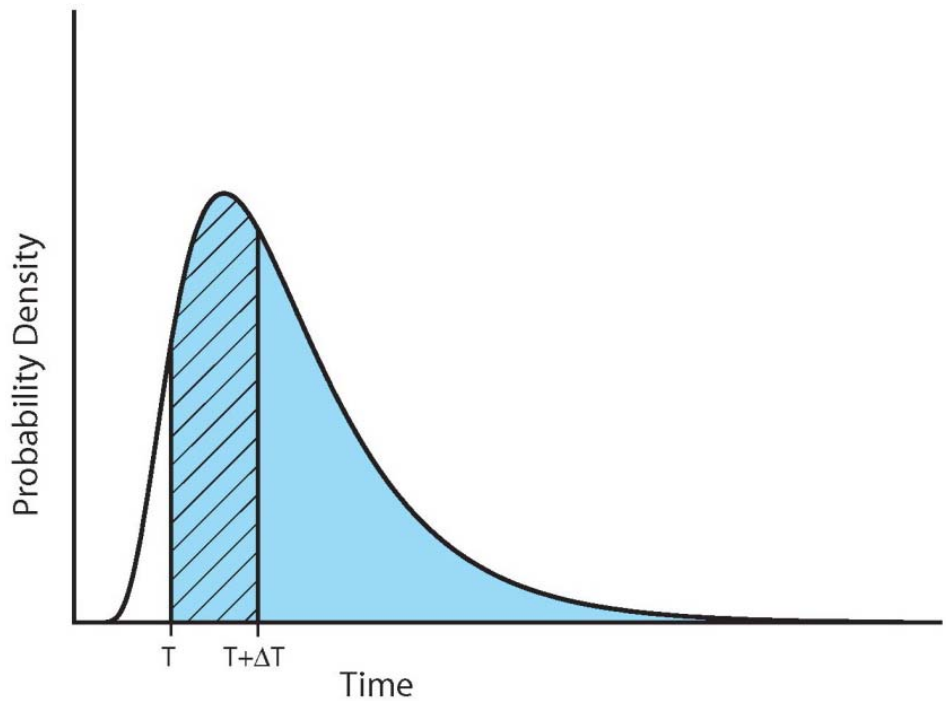

Figure 7.2-1. Illustration of the calculation of conditional probability from a PDF. The time interval of interest (exposure time) is from T (the present time) to T+ΔT (hachured area). The survivor function at time T is equal to the shaded area. The conditional probability is the ratio of these two areas. Source: WGCEP (2003).

the time-dependent models are either too poorly constrained or missing some critical physics of the system (e.g., interactions). The model provides a "baseline" probability calculation that reflects only the long-term rates of earthquakes in the Wasatch Front model.

In the Poisson model, conditional probabilities for a specified time interval depend only on the length of the interval, Δt, and the long-term rate of rupture for each source. The conditional probability for each source is given by

$$1 - e^{-\lambda \Delta t} \qquad (7\text{-}13)$$

where Δt can be a range of years, e.g., 100 years.

Because the expected magnitudes of earthquakes are themselves probabilistic, an additional step is needed to compute probabilities for earthquakes above a given magnitude threshold M_T. For each source, the rate of $\mathbf{M} \geq M_T$ events is determined from the magnitude PDF. The rate at which the rupture source produces earthquakes exceeding M_T is computed from equation (7-6), and assigned to λ in the exponent of equation (7-11).

We modeled the background earthquakes and all rupture sources other than the WFZ central segments and the AI and FI segments of the OGSLFZ (Section 7.2.2) using only the Poisson model.

7.2.2 Time-Dependent – BPT Model

In contrast to the Poisson model, a time-dependent renewal process model embodies the expectation that after one earthquake on a fault segment, another earthquake on that segment is unlikely until sufficient time has elapsed for stress to gradually re-accumulate. Such models require a minimum of two parameters, and typically include knowledge of the time of the most recent rupture. One required parameter is the mean recurrence interval, $\mu = \lambda$, and the other describes the variability of recurrence intervals and can be related to the variance, σ^2, of the distribution (for the Poisson distribution, $\sigma = \mu$). We define this variability of recurrence times as the aperiodicity or COV, $\alpha = \sigma/\mu$.

The BPT model (Matthews *et al*., 2002) is a renewal model that describes the statistical distribution of rupture times. The BPT distribution is also known as the inverse Gaussian distribution. The probability density is defined by

$$f_{BPT}(t) = \sqrt{\frac{\mu}{2\pi a^2 t^3}} \exp\{-\frac{(t-\mu)^2}{2\mu t a^2}\} \qquad (7\text{-}14)$$

and is illustrated on Figure 7.2-2a for a mean rate of 1 and a suite of aperiodicity values. The exponential (Poisson) is shown for comparison. The hazard function (instantaneous failure rate), $h_{BPT}(t)$, is always zero at t = 0. This function increases to achieve a maximum value at a time greater than the mode of $f_{BPT}(t)$, and from there, decreases toward an as-

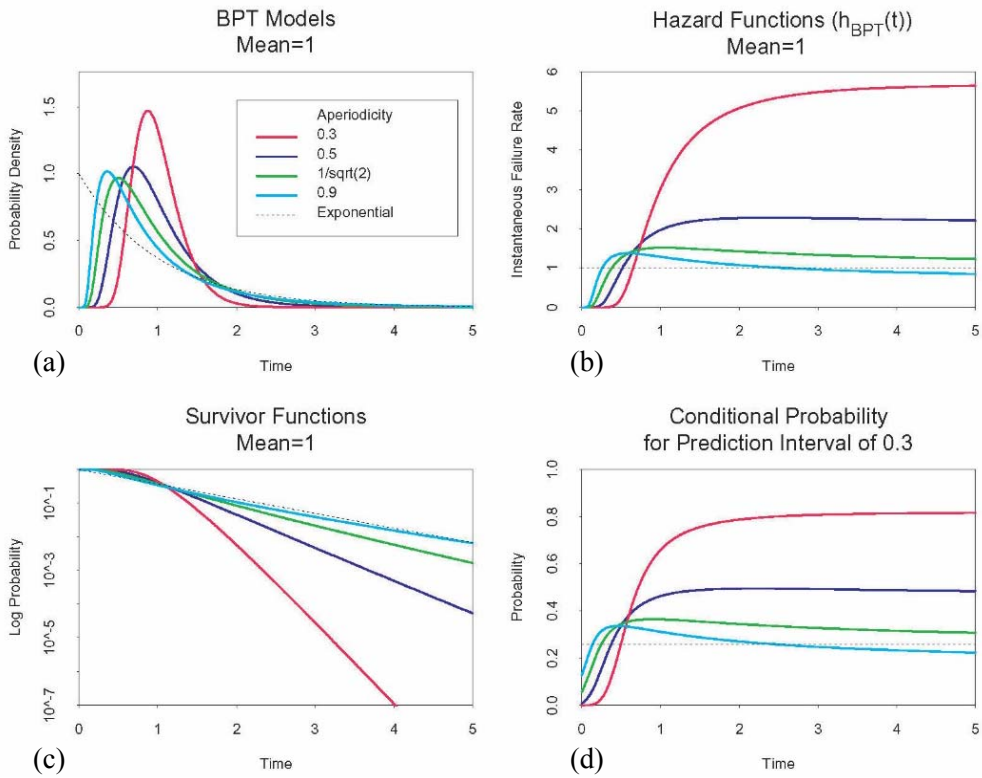

Figure 7.2-2. BPT model for a mean recurrence interval of 1.0: (a) probability density functions for a range of aperiodicity values; exponential probability density function shown for comparison; (b) hazard functions for a range of aperiodicity values; (c) survivor functions for a range of aperiodicity values; (d) conditional probability function for a range of aperiodicity values for a prediction window of 0.3. Source: WGCEP (2003).

ymptotic value of $h_{BPT}(t) = 1/(2\mu\alpha^2)$ (Figure 7.2-2b). Thus, a BPT process always attains a finite quasi-stationary state in which the failure rate is independent of elapsed time. For an aperiodicity of 0.5, this quasi-stationary state is reached by 1.5 times the mean recurrence rate. After that point, conditional probabilities will not continue to increase (Figure 7.2-2d). When the aperiodicity $\alpha = 1/\sqrt{2}$, the asymptotic failure rate is $1/\mu$, which equals the asymptotic failure rate for a Poisson process with the same μ. In practice, the behavior of a BPT model is similar to that of a delayed Poisson process, for which the failure rate is zero up to a finite time following an event and then steps up to an approximately constant failure rate at all succeeding times.

The behavior of a BPT model depends strongly on the value of α. For smaller values of α, $f_{BPT}(t)$ is more strongly peaked and remains close to zero longer. For larger values, the "delay" or "dead time" becomes shorter, $f_{BPT}(t)$ becomes increasingly Poisson-like, and its mode decreases. The hazard function in the quasi-stationary state increases with decreasing values of α and becomes Poisson-like with increasing values (Figure 7.2-2b).

We applied the BPT model to each of the rupture sources with a nonzero time-dependent branch weight (WFZ central segments and the AI and FI segments of the OGSLFZ). We developed recurrence rates for these sources using the approach described in Section 3.5, which includes statistical uncertainty due to the number of samples (events). This approach involves defining a likelihood function that represents the probability of seeing the observed sample of data (observed intervals between past events) given the specified rate parameter, λ. The likelihood function is a function of the PDF describing the distribution of events in time. Thus, the likelihood function for the BPT model is not the same as that for the Poisson model. As a result, the mean rates determined for the BPT model are different than those presented in Section 7.1, and are a function of the aperiodicity value. The rates for all segments with a time-dependent branch are presented in Tables 7.2-1 and 7.2-2. Recurrence intervals (inverse of rate) are provided for ease in comparison with Poisson recurrence intervals. The full distribution of rates provided in Tables 7.2-1 and 7.2-2 were used in the model with the associated weights reflecting the uncertainty in the paleoseismic data and COV. Equivalent Poisson rates can be back calculated from the resulting BPT probabilities by solving for the Poisson rate in Equation (7-13) using the BPT probabilities for a specified time interval. Equivalent Poisson rates can be used in a PSHA to compute time-dependent hazard. As an example, equivalent Poisson rates were computed for a time interval of 50 years, which is the time interval commonly used in U.S. building codes. Tables 7.2-3 and 7.2-4 provide the equivalent Poisson rates for the time-dependent rupture sources in the WFZ and OGSLFZ. Comparison of the mean time-dependent and equivalent Poisson rates in Tables 7.2-1 to 7.2-4 indicate that the time-dependent hazard is significantly larger for the SLCS and BCS. Time-dependent and time-independent results for the central WFZ segments and

Table 7.2-1. Recurrence intervals for time-dependent (BPT) calculations for the WFZ central segments.

Rupture Source	α(COV)	Recurrence Intervals for Characteristic Events Determined from Paleoseismic Data				
		$1/\lambda_{char96.51\%}$ (wt. = 0.101)	$1/\lambda_{char78.83\%}$ (wt. = 0.244)	$1/\lambda_{char50\%}$ (wt. = 0.31)	$1/\lambda_{char21.17\%}$ (wt. = 0.244)	$1/\lambda_{char3.49\%}$ (wt. = 0.101)
BCS	0.3	1891	1633	1453	1293	1115
	0.5	2576	2033	1679	1385	1084
	0.7	3577	2626	2034	1566	1121
WS	0.3	1703	1487	1337	1202	1053
	0.5	2274	1834	1544	1300	1048
	0.7	3108	2346	1866	1479	1100
SLCS	0.3	1866	1601	1418	1257	1079
	0.5	2576	2015	1653	1354	1052
	0.7	3608	2618	2009	1531	1081
PS	0.3	1653	1434	1281	1145	994
	0.5	2177	1735	1447	1206	959
	0.7	2948	2190	1718	1342	981
NS	0.3	1559	1299	1125	975	814
	0.5	2289	1714	1358	1073	799
	0.7	3367	2330	1716	1253	840

Table 7.2-2. Recurrence intervals for time-dependent (BPT) calculations for the OGSLFZ.

Rupture Source	α(COV)	Recurrence Intervals for Characteristic Events Determined from Paleoseismic Data				
		$1/\lambda_{char96.51\%}$ (wt. = 0.101)	$1/\lambda_{char78.83\%}$ (wt. = 0.244)	$1/\lambda_{char50\%}$ (wt. = 0.31)	$1/\lambda_{char21.17\%}$ (wt. = 0.244)	$1/\lambda_{char3.49\%}$ (wt. = 0.101)
AI	0.3	7232	5877	4976	4210	3410
	0.5	10,464	7546	5765	4381	3095
	0.7	15,302	10,083	7062	4868	3028
FI	0.3	5882	4764	4028	3401	2742
	0.5	8521	6197	4793	3696	2659
	0.7	12,395	8318	5984	4274	2784

Table 7.2-3. Equivalent Poisson rupture rates for time-dependent (BPT) rupture sources of the WFZ.

Rupture Source	Equivalent Poisson Rupture Rates		
	$\lambda_{5th\%}$ ($1/\lambda_{5th\%}$)	λ_{mean} ($1/\lambda_{mean}$)	$\lambda_{95th\%}$ ($1/\lambda_{95th\%}$)
BCS	5.79×10^{-4} (1730)	1.63×10^{-3} (610)	3.91×10^{-3} (260)
WS	5.49×10^{-5} (18,200)	3.98×10^{-4} (2510)	8.29×10^{-4} (1210)
SLCS	4.50×10^{-4} (2220)	1.29×10^{-3} (780)	2.78×10^{-3} (360)
PS	9.56×10^{-5} (10,500)	5.75×10^{-4} (1740)	1.50×10^{-3} (670)
NS	2.16×10^{-9} (463,000,000)	1.03×10^{-4} (9710)	5.15×10^{-4} (1940)

Table 7.2-4. Equivalent Poisson rupture rates for time-dependent (BPT) rupture sources of the OGSLFZ.

Rupture Source	Equivalent Poisson Rupture Rates		
	$\lambda_{5th\%}$ ($1/\lambda_{5th\%}$)	λ_{mean} ($1/\lambda_{mean}$)	$\lambda_{95th\%}$ ($1/\lambda_{95th\%}$)
AI	$<1.00 \times 10^{-12}$	4.17×10^{-6} (239,900)	1.02×10^{-5} (98,000)
FI	4.66×10^{-5} (21,500)	3.64×10^{-4} (2450)	8.35×10^{-4} (1200)

the AI and FI segments of the OGSLFZ are discussed further in Section 8.3.2. For fault models that have segments which rupture both as single-segment and as part of a multi-segment rupture, we only modeled those segments that rupture only as a single-segment as time-dependent. Paleoseismic data were insufficient for us to estimate time-dependent recurrence rates for multi-segment ruptures because at most, only two such events have been identified in the paleoseismic record for a given pair or three of the central WFZ segments (Section 4.1.5).

Because we calculated probabilities at the rupture source level, aggregating probabilities for fault segments, faults, and the region is simple. We expect the BPT model to provide accurate estimates of earthquake probability to the extent that (1) the model represents the statistics of recurrence intervals for rupture sources, and (2) the time of the most recent event is known or constrained.

A key input to the BPT model is the time of the most recent rupture—the time at which the renewal model is "reset." Estimates of these times come from several lines of evidence, including paleoseismic observations, dates of historical ruptures, and historical seismicity, as described in Section 4.

As was the case of the WGCEP (2003, 2008), we chose not to model the other faults with a time-dependent model, even though for a few of the faults information exists on the most recent rupture and recurrence intervals. At most, the latter consisted of a single interval which was judged by the WGUEP to be insufficient to include in the forecast.

7.2.3 Time-Independent versus Time-Dependent Weights

A critical judgment in the calculation of probabilities is the choice of weights to be assigned to the time-dependent BPT and time-independent Poisson models. This decision is a major source of epistemic uncertainty. As in the WGCEP (2003, 2008) process, the weights are decided by expert judgment after considerable discussion of the pros, cons, and implications. As described earlier, we considered only the WFZ central segments and the AI and FI segments of the OGSLFZ to have sufficiently robust paleoseismic data to calculate time-dependent probabilities. Unlike the WGCEP process, the paleoseismic data were more plentiful than any of the faults considered in the northern California forecasts, and we did not need to consider stress interaction and shadow because of the length of the paleoseismic record. Hence, the WGUEP considered the weighting of the alternative models for the WFZ central segments and the AI and FI segments to be more straightforward and not plagued to the same extent by the large uncertainties faced by the WGCEP.

The quality and quantity of the paleoseismic data were significant factors in selecting the weights. In the end, the WGUEP gave considerable weight, 0.8, to the BPT model and only 0.2 weight to a Poisson model for individual segment ruptures. This reflects our judgment that the paleoseismic record is robust enough to calculate time-dependent probabilities for future surface-faulting earthquakes on the WFZ central segments and the AI and FI segments of the OGSLFZ in the next 100 years. More importantly, we believe that these faults do not behave in a Poisson matter (i.e., that the elastic rebound model is applicable). One criticism of the high weight given to the BPT model within the WGUEP was that the recurrence intervals were not sufficiently periodic and too variable. However, this criticism is not germane to whether a time-dependent model should be used because the periodicity or lack thereof is addressed through the value of the COV used in the calculations. As stated previously, a wide range of COVs was used in the calculations.

As noted in Section 7.2.2, we did not apply the BPT model to multi-segment ruptures due to a lack of paleoseismic data to constrain recurrence intervals. For fault models with multi-segment ruptures, only segments that rupture as single-segments are modeled as time-dependent. Therefore, the effective weight of the time-dependent model is less than 0.8 and varies by segment. For example, the BCS ruptures as part of multi-segment ruptures in all fault models except the SSR model. The effective weight of the time-dependent model for the BCS is 0.8 x 0.7 = 0.56. Similarly, the effective time-dependent weights for the WS, SLCS, PS, and NS are 0.56, 0.66, 0.62, and 0.066, respectively.

8 EARTHQUAKE PROBABILITIES

In this section, we summarize and discuss the earthquake probabilities making up the WGUEP earthquake forecast for the Wasatch Front region. We estimated multiple probabilities, including probabilities associated with (1) all the characterized earthquake sources in the region, both in aggregate and individually; (2) different future time horizons (30, 50, and 100 years); and (3) different magnitude thresholds. Thus, for a specified time horizon and magnitude threshold, one can view the probability that one or more earthquakes will occur either in the Wasatch Front region as a whole, on an individual fault system or segment, or in the background. For each case examined, we report the mean or best-estimate probability together with its formal uncertainty, specified in terms of the 5th and 95th percentile values of the probability distribution (as described in Section 7).

Section 8.1 describes the earthquake probabilities for the Wasatch Front region for magnitude thresholds of **M** 6.75 and **M** 6.0 and for time horizons of 30, 50, and 100 years (starting from 2014). Probabilities for background earthquakes in the region are also given. In Section 8.2, we give a breakdown of the regional probabilities into the component probabilities for individual faults and fault segments, focusing our discussion on 50-year probabilities for earthquakes of **M** ≥ 6.75. Finally, in Section 8.3, we examine and discuss the sensitivity of the probability calculations: first, to different fault-rupture models; second, to different probability models (time-independent vs. time-dependent); and third, to two selected input parameters—the COV in the time-dependent BPT model, and the choice of the magnitude relation used in calculating the characteristic magnitude for a fault or fault segment.

8.1 Earthquake Probabilities in the Wasatch Front Region

8.1.1 50-Year Probabilities

Figure 8.1-1 and Table 8.1-1 summarize earthquake probabilities for the next 50 years (2014 to 2063). The probability of one or more large (**M** ≥ 6.75) earthquakes somewhere in the Wasatch Front region in the next 50 years is 43%. This regional probability is a combined probability, obtained from aggregating the probabilities of earthquakes on all of the characterized faults. The probability of at least one large surface-faulting earthquake (**M** ≥ 6.75) specifically on the Wasatch fault zone (WFZ) in the next 50 years is 18% (Table 8.1-1). Other fault zones having significant 50-year probabilities of one or more **M** ≥ 6.75 earthquakes are the Oquirrh–Great Salt Lake fault zone (OGSLFZ) (5.9%) and the Eastern Bear Lake fault (6.3%) (Figure 8.1-1). Excluding the WFZ and the OGSLFZ, the combined probability of one or more large earthquakes (**M** ≥ 6.75) on one of the other studied faults in the region is 25%. (We remind the reader that only the WFZ central segments and the Antelope Island and Fremont Island segments of the OGSLFZ were treated in a time-dependent manner; ruptures on the other faults were modeled as time-independent.) The total probability of at least one large (**M** ≥ 6.75) earthquake near the Salt Lake City metropolitan area in the next 50 years from the WFZ and OGSLFZ is 23%.

For each of the earthquake probabilities listed in Table 8.1-1 (and for those in following tables), the 90% confidence limits are given. For example, the table indicates that for at least one earthquake of **M** ≥ 6.75, the mean 50-year probability for the Wasatch Front region as a whole is 43%; the corresponding 5th and 95th percentile probabilities are 33% and 54%, respectively.

Considering that Utah's population is the youngest in the nation with a median age of 29.2 years (2010 U.S. Census data), the 50-year probabilities imply that there is a realistic chance that many current residents of the Wasatch Front region will experience a large (**M** ≥ 6.75) earthquake in their lifetimes—whether that earthquake is on the WFZ (18% probability) or somewhere in the Wasatch Front region (43% probability). For one or more earthquakes of **M** ≥ 6.0, which includes background seismicity, the 50-year probability in the Wasatch Front region as a whole increases to 57% (Table 8.1-1), and for **M** ≥ 5.0 the probability is 93%.

To gain some insight into what the 50-year probability numbers mean, we can consider a simple analogy (admittedly imperfect, because the earthquake probabilities include some time-dependent components). Consider random natural events, for example a storm that occurs on average every 50, 100, or 250 years. During a future 50-year period, the corresponding probabilities for such events happening are 63%, 39%, and 18%, respectively. Thus, a 43% chance of one or more large (**M** ≥ 6.75) earthquakes happening somewhere in the Wasatch Front region in the next 50 years is roughly the same (39%) as for a 100-year storm in the same region. Similarly, an 18% chance of one or more large earthquakes on the WFZ in the next 50 years is the same as the chance (18%) of a 250-year storm somewhere along the length of the fault, and a 57% chance in 50 years of one or more earthquakes of **M** ≥ 6.0 in the Wasatch Front region is nearly the same as the chance (63%) of a 50-year storm in the same region. In all three cases, the earthquake probability numbers are in the range of other real-world hazards against which communities and individuals take sensible defensive actions.

8.1.2 30-Year, 100-Year, and Background Seismicity Probabilities

Earthquake probabilities in the Wasatch Front region for 30-year and 100-year time horizons are summarized in Tables 8.1-2 and 8.1-3, respectively. Compared to the 50-year probabilities, corresponding probabilities for a 30-year time horizon are lower and those for a 100-year time horizon are higher—as one would expect. Over a 30-year time horizon, the probability of one or more large (**M** ≥ 6.75) earthquakes is 11% on the WFZ and 28% somewhere in the Wasatch Front

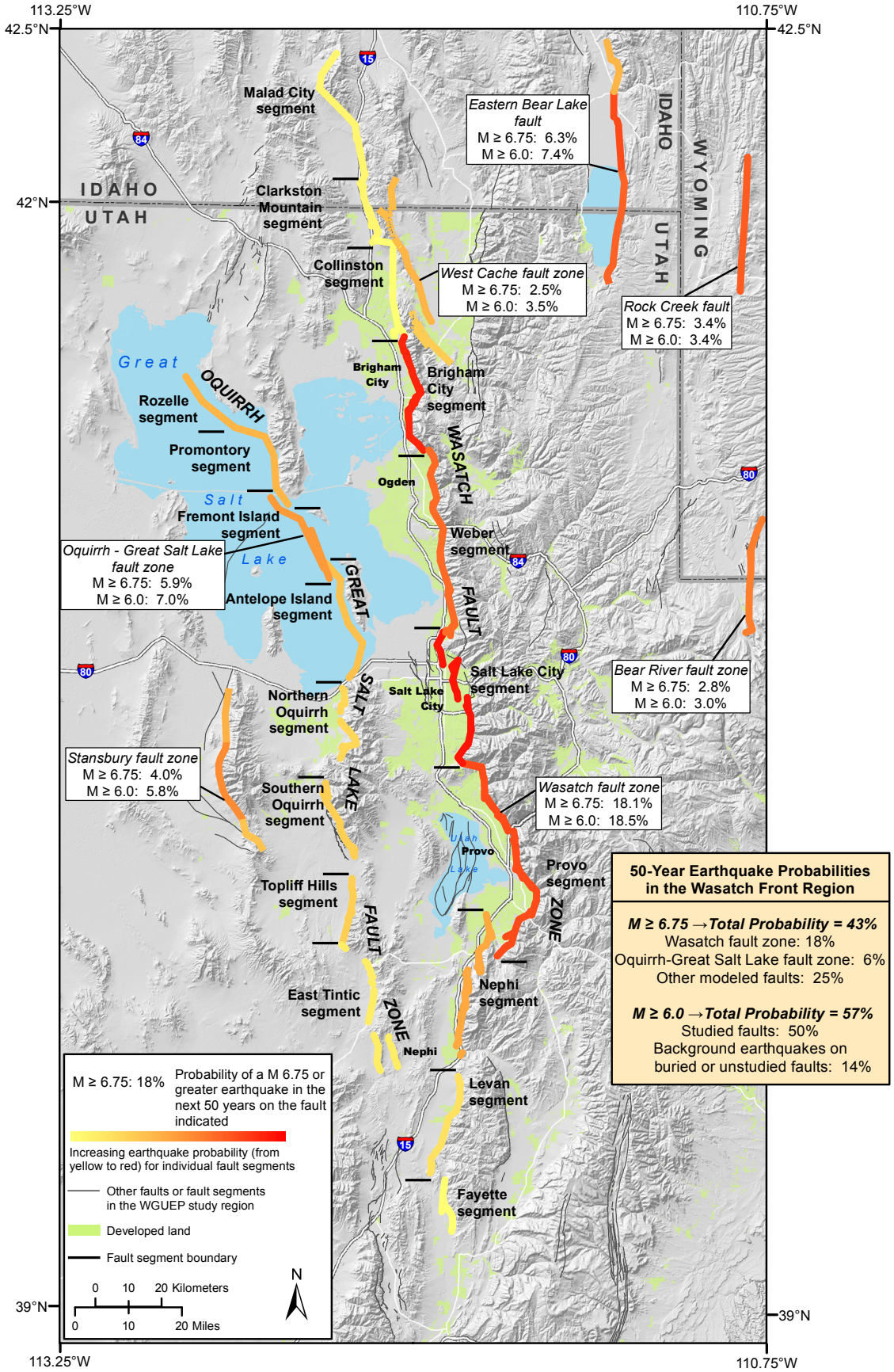

Figure 8.1-1. Probabilities of one or more earthquakes of **M** 6.0 and 6.75 or greater in the next 50 years in the Wasatch Front region. "Other modeled faults" are those faults other than the Wasatch and the Oquirrh–Great Salt Lake fault zones. Shaded topography generated from 90-m digital elevation data (https://eros.usgs.gov/elevation-products).

Table 8.1-1. Wasatch Front region 50-year probabilities.

	M ≥ 6.0			M ≥ 6.75		
	Mean	**5th Percentile**	**95th Percentile**	**Mean**	**5th Percentile**	**95th Percentile**
WFZ	18.5%	10.5%	29.7%	18.1%	10.3%	29.3%
OGSLFZ	7.0%	3.5%	11.6%	5.9%	2.5%	10.9%
Other Faults	34.3%	23.4%	47.5%	25.2%	16.7%	36.0%
Background	14.2%	6.6%	23.1%	NA	NA	NA
Wasatch Front Region	**57.2%**	**46.8%**	**68.6%**	**42.5%**	**32.8%**	**54.0%**

Table 8.1-2. Wasatch Front region 30-year probabilities.

	M ≥ 6.0			M ≥ 6.75		
	Mean	**5th Percentile**	**95th Percentile**	**Mean**	**5th Percentile**	**95th Percentile**
WFZ	11.5%	6.4%	18.9%	11.3%	6.3%	18.6%
OGSLFZ	4.3%	2.2%	7.2%	3.6%	1.5%	6.6%
Other Faults	22.4%	14.8%	32.1%	16.1%	10.4%	23.5%
Background	8.9%	4.0%	14.6%	NA	NA	NA
Wasatch Front Region	**40.1%**	**31.4%**	**50.0%**	**28.3%**	**21.2%**	**37.1%**

Table 8.1-3. Wasatch Front region 100-year probabilities.

	M ≥ 6.0			M ≥ 6.75		
	Mean	**5th Percentile**	**95th Percentile**	**Mean**	**5th Percentile**	**95th Percentile**
WFZ	33.7%	20.1%	51.4%	33.1%	19.7%	50.8%
OGSLFZ	13.5%	7.0%	21.9%	11.4%	4.9%	20.6%
Other Faults	56.3%	41.4%	72.5%	43.7%	30.6%	59.1%
Background	26.2%	12.8%	40.9%	NA	NA	NA
Wasatch Front Region	**81.5%**	**71.8%**	**90.2%**	**66.8%**	**55.0%**	**79.0%**

region. Over a century, there is a 2-out-of-3 chance (67%) that at least one large (**M** ≥ 6.75) earthquake will occur somewhere in the Wasatch Front region, and the chance of at least one occurring on the WFZ, undoubtedly with damaging impact, is roughly 1 in 3 (33%). Also over a century, the probability of at least one potentially damaging earthquake of **M** ≥ 6.0 in the Wasatch Front region is relatively high (82%). One factor that adds to the risk in the coming decades is that Utah's population, with continued concentration in the Wasatch Front urban corridor, is projected to nearly double by 2050 (Utah Foundation, 2014).

Table 8.1-4 summarizes the probabilities for background earthquakes of **M** ≥ 5.0 and **M** ≥ 5.5 in the Wasatch Front region. There is a 69% chance that one or more background earthquakes of **M** ≥ 5.0 will occur in the next 30 years and an 85% chance in the next 50 years. Preparing for earthquakes requires keeping in mind that even earthquakes in the **M** 5 range can cause significant localized damage. Damaging shocks in the Wasatch Front region (discussed in Appendix E) include the **M** 5.8 Cache Valley, Utah, earthquake in August 1962, and even the **M** 4.9 Magna, Utah, earthquake in September 1962.

Table 8.1-4. Background seismicity probabilities.

	M ≥ 5.0	M ≥ 5.5
30 years	69.2%	29.5%
50 years	85.1%	43.7%
100 years	97.1%	67.1%

8.2 Probabilities for Individual Faults and Fault Segments

In this section, we provide the probabilities that were computed for individual segments of the WFZ and OGSLFZ and for other faults and fault segments in the Wasatch Front region that were considered in the WGUEP forecast. Probabilities are given for both **M** ≥ 6.0 and **M** ≥ 6.75. The probabilities for these two magnitude thresholds are roughly the same for the WFZ segments and generally comparable for the OGSLFZ segments and other faults. This is essentially due to the use of the recurrence models, particularly for the WFZ and OGSLFZ, where moderate-sized earthquakes (**M** 6 to 6.75) are not being modeled.

Table 8.2-1 and Figure 8.2-1 show the 50-year probabilities for large (**M** ≥ 6.75) earthquakes on the WFZ. As expected, the probabilities are higher for the central segments. The probabilities of the end segments are small, less than 1%. The two central segments with the highest probabilities, each ~6%, are the Brigham City segment and the Salt Lake City segment (Table 8.2-1). The elapsed time since the most recent event on the Salt Lake City segment is approximately equivalent to its recurrence interval and, as well documented (Section 4), the elapsed time on the Brigham City segment has significantly exceeded its mean recurrence interval. Intuitively, one would expect the probability on the Brigham City segment to be much higher than 6% (Section 8.3). However, the effective time-dependent weight for the Brigham City segment is only 0.56. For the Salt Lake City segment, the time-dependent weight is 0.66 (Section 7.2.3).

The other major segmented fault is the OGSLFZ. Table 8.2-2 shows the 50-year probabilities for the OGSLFZ segments, and indicates that the probability for at least one large (**M** ≥ 6.75) earthquake on each individual segment is small, 2% or less. Table 8.2-3 shows the 50-year probabilities for the other, mostly unsegmented, faults in the Wasatch Front region. Ruptures on all these faults are modeled as time-independent. Five faults in the "other" category have the relatively highest 50-year probabilities for generating at least one large (**M** ≥ 6.75) earthquake (Table 8.2-3, Figure 8.1-1). The segmented Eastern Bear Lake fault, which has a relatively high slip rate centered on 0.6 mm/yr (Appendix D), has a total probability of 6%. The segmented Stansbury fault zone, which has a best-estimate slip rate of 0.4 mm/yr, has a total probability of 4%. The other three faults are the Rock Creek fault (unsegmented, 3.4% probability), the Bear River fault (unsegmented, 2.8% probability), and the segmented West Cache fault (segmented, 2.5% total probability). The probabilities for **M** ≥ 6.0 events are consistently lower if not the same as the **M** ≥ 6.75 events (i.e., the larger the earthquake, the less frequent it is).

Tables 8.2-4 through 8.2-9 summarize the 30-year and 100-year probabilities for the WFZ, OGSLFZ, and the "other modeled faults" in the Wasatch Front region. The same general patterns exhibited in the 50-year probabilities discussed above are reflected in the 30-year and 100- year probabilities.

Table 8.2-1. WFZ segment 50-year probabilities.

Fault Segment	M ≥ 6.0			M ≥ 6.75		
	Mean	5th Percentile	95th Percentile	Mean	5th Percentile	95th Percentile
Malad City	0.3%	<0.1%	0.8%	0.3%	<0.1%	0.8%
Clarkston Mtn	0.3%	<0.1%	0.8%	0.3%	<0.1%	0.7%
Collinston	0.2%	<0.1%	0.6%	0.2%	<0.1%	0.5%
Brigham City	5.8%	1.6%	15.1%	5.6%	1.4%	15.5%
Weber	3.2%	0.3%	8.1%	3.2%	0.3%	8.3%
Salt Lake City	5.9%	1.9%	13.3%	5.8%	1.8%	13.3%
Provo	3.9%	0.5%	8.9%	3.9%	0.5%	9.0%
Nephi	1.8%	<0.1%	6.3%	1.8%	<0.1%	6.3%
Levan	1.0%	<0.1%	2.6%	0.9%	0.1%	2.4%
Fayette	0.5%	<0.1%	1.5%	0.5%	<0.1%	1.3%

Table 8.2-2. OGSLFZ segment 50-year probabilities.

Fault Segment	M ≥ 6.0			M ≥ 6.75		
	Mean	5th Percentile	95th Percentile	Mean	5th Percentile	95th Percentile
Rozelle	1.7%	0.4%	3.4%	1.5%	0.3%	3.4%
Promontory	2.0%	0.4%	5.0%	1.6%	0.1%	5.0%
Fremont Island	2.3%	0.4%	6.3%	2.0%	0.2%	6.1%
Antelope Island	1.2%	<0.1%	4.8%	1.2%	<0.1%	4.8%
Northern Oquirrh	0.7%	0.1%	2.1%	0.6%	0.1%	2.0%
Southern Oquirrh	0.7%	0.1%	2.1%	0.7%	0.1%	1.9%
Topliff Hills	0.9%	0.1%	2.4%	0.7%	0.1%	1.8%
East Tintic	0.4%	0.1%	1.2%	0.4%	0.1%	1.1%

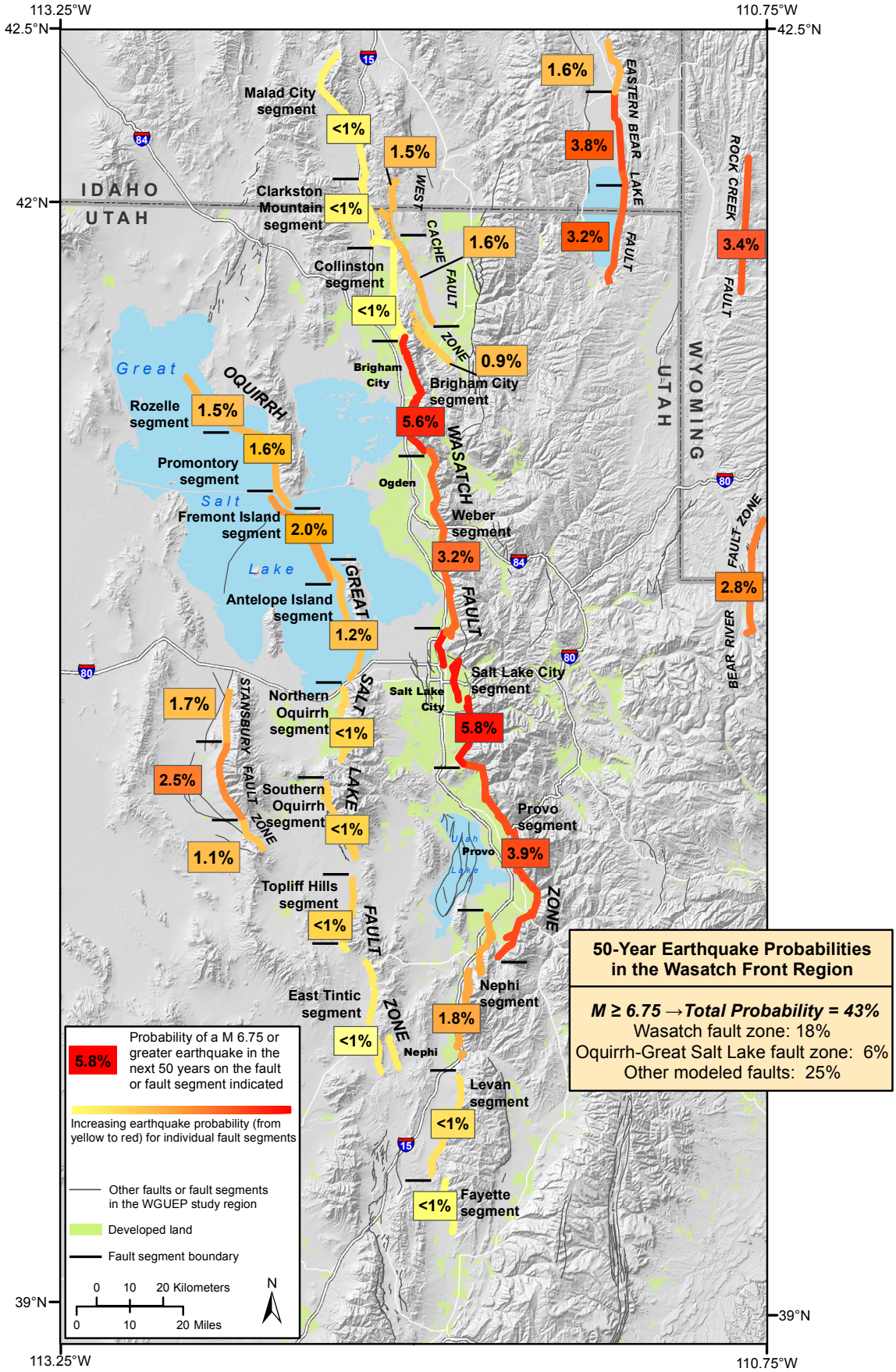

Figure 8.2-1. Probabilities of one or more earthquakes of **M** 6.75 or greater in the next 50 years for selected faults and fault segments. Shaded topography generated from 90-m digital elevation data (https://eros.usgs.gov/elevation-products).

Table 8.2-3. "Other modeled fault" 50-year probabilities.

Fault or Fault Segment	M ≥ 6.0			M ≥ 6.75		
	Mean	5th Percentile	95th Percentile	Mean	5th Percentile	95th Percentile
Bear River	3.0%	1.4%	6.4%	2.8%	1.2%	6.4%
Carrington	1.7%	0.4%	3.6%	1.4%	0.4%	3.6%
Crater Bench and Drum Mountains	0.2%	<0.1%	0.7%	0.2%	<0.1%	0.7%
Crawford Mountains	0.1%	<0.1%	0.4%	0.1%	<0.1%	0.2%
Curlew Valley	2.2%	0.3%	6.4%	0.5%	0.1%	2.0%
East Cache - Total	2.0%	0.4%	5.1%	1.4%	0.2%	3.8%
East Cache - North	0.9%	0.1%	2.7%	0.9%	0.1%	2.7%
East Cache - Central	1.3%	0.2%	3.3%	0.7%	<0.1%	2.6%
East Cache - South	0.4%	<0.1%	1.7%	0.4%	<0.1%	1.7%
East Dayton-Oxford	0.3%	<0.1%	0.7%	0.1%	<0.1%	0.3%
Eastern Bear Lake - Total	7.4%	1.8%	17.7%	6.3%	1.3%	16.1%
Eastern Bear Lake - North	2.3%	0.5%	5.8%	1.6%	0.1%	5.4%
Eastern Bear Lake - Central	4.3%	0.9%	12.5%	3.8%	0.5%	12.1%
Eastern Bear Lake - South	3.3%	0.5%	10.2%	3.2%	0.5%	10.2%
Faults along the edge of Scipio Valley-Pavant Range	0.8%	0.1%	2.9%	0.8%	0.1%	2.9%
Gunnison	0.6%	0.1%	2.3%	0.6%	0.1%	2.3%
Hansel Valley	0.4%	<0.1%	1.5%	0.1%	<0.1%	0.3%
Joes Valley	0.4%	<0.1%	1.0%	0.3%	<0.1%	1.0%
Little Valley	1.0%	0.1%	3.3%	0.2%	<0.1%	0.9%
Main Canyon	0.1%	<0.1%	0.5%	0.1%	<0.1%	0.2%
Morgan	0.2%	<0.1%	0.4%	<0.1%	<0.1%	0.2%
North Promontory	1.6%	0.3%	4.8%	1.0%	0.2%	2.8%
Porcupine Mountain	0.1%	<0.1%	0.4%	0.1%	<0.1%	0.3%
Rock Creek	3.4%	0.5%	8.5%	3.4%	0.5%	8.3%
Skull Valley	1.5%	0.2%	3.6%	1.4%	0.2%	3.6%
Snow Lake Graben	0.3%	<0.1%	1.0%	0.1%	<0.1%	0.5%
Stansbury - Total	5.8%	0.6%	13.7%	4.0%	0.4%	11.4%
Stansbury - North	2.2%	0.3%	5.3%	1.7%	0.2%	4.6%
Stansbury - Central	2.7%	0.3%	8.8%	2.5%	0.2%	8.0%
Stansbury - South	2.3%	0.2%	6.0%	1.1%	<0.1%	4.0%
Stinking Springs	1.3%	0.2%	4.1%	<0.1%	<0.1%	0.2%
Strawberry	0.6%	0.2%	1.8%	0.6%	0.1%	1.5%
Utah Lake	1.0%	<0.1%	4.3%	0.4%	<0.1%	1.7%
West Cache - Total	3.5%	0.8%	8.4%	2.5%	0.4%	7.0%
West Cache - North	2.1%	0.4%	5.0%	1.5%	0.2%	3.7%
West Cache - Central	1.8%	0.2%	6.9%	1.6%	0.1%	6.9%
West Cache - South	1.1%	0.2%	3.5%	0.9%	0.1%	3.5%
West Valley	0.7%	<0.1%	4.6%	<0.1%	<0.1%	0.1%
Western Bear Lake	1.2%	<0.1%	6.7%	0.1%	<0.1%	0.9%

Table 8.2-4. WFZ segment 30-year probabilities.

Fault Segment	M ≥ 6.0			M ≥ 6.75		
	Mean	5th Percentile	95th Percentile	Mean	5th Percentile	95th Percentile
Malad City	0.2%	<0.1%	0.5%	0.2%	<0.1%	0.5%
Clarkston Mtn	0.2%	<0.1%	0.5%	0.2%	<0.1%	0.4%
Collinston	0.1%	<0.1%	0.4%	0.1%	<0.1%	0.3%
Brigham City	3.5%	1.0%	9.6%	3.4%	0.8%	9.6%
Weber	1.9%	0.2%	5.1%	1.9%	0.2%	5.0%
Salt Lake City	3.6%	1.1%	8.1%	3.6%	1.1%	8.1%
Provo	2.3%	0.3%	5.6%	2.3%	0.3%	5.6%
Nephi	1.1%	<0.1%	3.8%	1.1%	<0.1%	3.8%
Levan	0.6%	<0.1%	1.6%	0.5%	<0.1%	1.4%
Fayette	0.3%	<0.1%	0.9%	0.3%	<0.1%	0.8%

Table 8.2-5. OGSLFZ segment 30-year probabilities.

Fault Segment	M ≥ 6.0			M ≥ 6.75		
	Mean	5th Percentile	95th Percentile	Mean	5th Percentile	95th Percentile
Rozelle	1.0%	0.2%	2.0%	0.9%	0.2%	2.0%
Promontory	1.2%	0.2%	3.1%	1.0%	0.1%	3.1%
Fremont Island	1.4%	0.2%	3.9%	1.2%	0.1%	3.7%
Antelope Island	0.7%	<0.1%	2.9%	0.7%	<0.1%	2.9%
Northern Oquirrh	0.4%	0.1%	1.3%	0.4%	<0.1%	1.2%
Southern Oquirrh	0.4%	0.1%	1.2%	0.4%	0.1%	1.2%
Topliff Hills	0.6%	0.1%	1.4%	0.4%	0.1%	1.1%
East Tintic	0.3%	<0.1%	0.7%	0.3%	<0.1%	0.7%

8.3 Sensitivity of Results to Models and Parametric Uncertainty

The probabilities in the WGUEP forecast are a function of many models, relations, and input parameters. In this section we investigate the sensitivity to some of these variables. First, for the WFZ and OGSLFZ, we look at the sensitivity to the various fault rupture models (Section 8.3.1). Then, we explore the sensitivity to the selected probability model and, for those segments modeled as time-dependent, to the COV (Section 8.3.2). Finally, we examine the sensitivity to the choice of magnitude relation used in calculating the characteristic magnitude for a fault or fault segment (Section 8.3.3).

8.3.1 Fault Rupture Models

For the central segments of the WFZ, the sensitivity of the 50-year probabilities of earthquakes of **M** ≥ 6.75 to fault rupture model is shown in Table 8.3-1. The single-segment rupture model, which was given the largest weight, results in the highest probabilities for the Brigham City and Salt Lake City segments. Note that the weight assessed for the time-dependent model is not equal for each of the fault rupture models, as discussed in Section 7.2.3. The Brigham City segment was not modeled as time-dependent in any fault rupture model except the single-segment rupture model. Similarly, the impact of time-dependence can be seen with the Nephi segment. For rupture models of the Nephi segment where a time-dependent branch was included (single-segment rupture, Intermediate A and Intermediate C), the probabilities are much lower than for those rupture models where only the Poisson model was used (Table 8.3-1).

For each of the WFZ central segments, except for the Brigham City segment, the unsegmented model results in a higher probability than the segmented models (Table 8.3-1). Although the segment moment rates for the unsegmented model are similar to those of the other fault models (Figure 7.1-6), the range of magnitudes for the unsegmented model, which uses the DTGR recurrence model, includes many more smaller events; hence, the rate of these events is higher.

Table 8.3-2 shows the sensitivity to fault rupture model for the OGSLFZ. As with the WFZ, the unsegmented fault model (Model 5) results in the highest probabilities due to the use of the DTGR recurrence model. All segmented rupture models (models 1–4) use only the maximum magnitude recurrence model.

Table 8.2-6. "Other modeled fault" 30-year probabilities.

Fault or Fault Segment	M ≥ 6.0			M ≥ 6.75		
	Mean	5th Percentile	95th Percentile	Mean	5th Percentile	95th Percentile
Bear River	1.8%	0.9%	3.9%	1.7%	0.7%	3.9%
Carrington	1.0%	0.2%	2.2%	0.9%	0.2%	2.2%
Crater Bench and Drum Mountains	0.1%	<0.1%	0.4%	0.1%	<0.1%	0.4%
Crawford Mountains	0.1%	<0.1%	0.2%	<0.1%	<0.1%	0.1%
Curlew Valley	1.3%	0.2%	3.9%	0.3%	<0.1%	1.2%
East Cache - Total	1.2%	0.2%	3.1%	0.9%	0.1%	2.3%
East Cache - North	0.5%	0.1%	1.6%	0.5%	0.1%	1.6%
East Cache - Central	0.8%	0.1%	2.0%	0.4%	<0.1%	1.6%
East Cache - South	0.2%	<0.1%	1.0%	0.2%	<0.1%	1.0%
East Dayton-Oxford	0.2%	<0.1%	0.4%	0.1%	<0.1%	0.2%
Eastern Bear Lake - Total	4.6%	1.1%	11.0%	3.9%	0.8%	10.0%
Eastern Bear Lake - North	1.4%	0.3%	3.5%	1.0%	0.1%	3.4%
Eastern Bear Lake - Central	2.7%	0.5%	7.8%	2.3%	0.3%	7.5%
Eastern Bear Lake - South	2.0%	0.3%	6.3%	2.0%	0.3%	6.3%
Faults along the edge of Scipio Valley-Pavant Range	0.5%	<0.1%	1.8%	0.5%	<0.1%	1.8%
Gunnison	0.4%	<0.1%	1.4%	0.4%	<0.1%	1.4%
Hansel Valley	0.2%	<0.1%	0.9%	<0.1%	<0.1%	0.2%
Joes Valley	0.2%	<0.1%	0.6%	0.2%	<0.1%	0.6%
Little Valley	0.6%	<0.1%	2.0%	0.1%	<0.1%	0.5%
Main Canyon	0.1%	<0.1%	0.3%	<0.1%	<0.1%	0.1%
Morgan	0.1%	<0.1%	0.3%	<0.1%	<0.1%	0.1%
North Promontory	0.9%	0.2%	2.9%	0.6%	0.1%	1.7%
Porcupine Mountain	0.1%	<0.1%	0.2%	0.1%	<0.1%	0.2%
Rock Creek	2.1%	0.3%	5.2%	2.1%	0.3%	5.0%
Skull Valley	1.0%	0.1%	2.2%	0.8%	0.1%	2.2%
Snow Lake Graben	0.2%	<0.1%	0.6%	0.1%	<0.1%	0.3%
Stansbury - Total	3.6%	0.4%	8.4%	2.4%	0.2%	7.0%
Stansbury - North	1.3%	0.2%	3.2%	1.0%	0.1%	2.8%
Stansbury - Central	1.6%	0.2%	5.4%	1.5%	0.1%	4.9%
Stansbury - South	1.4%	0.1%	3.7%	0.7%	<0.1%	2.4%
Stinking Springs	0.8%	0.1%	2.5%	<0.1%	<0.1%	0.1%
Strawberry	0.4%	0.1%	1.0%	0.3%	0.1%	0.9%
Utah Lake	0.7%	<0.1%	2.7%	0.3%	<0.1%	1.0%
West Cache - Total	2.1%	0.5%	5.1%	1.5%	0.2%	4.2%
West Cache - North	1.3%	0.2%	3.1%	0.9%	0.1%	2.2%
West Cache - Central	1.1%	0.1%	4.2%	1.0%	0.1%	4.2%
West Cache - South	0.7%	0.1%	2.1%	0.5%	<0.1%	2.1%
West Valley	0.4%	<0.1%	2.5%	<0.1%	<0.1%	0.1%
Western Bear Lake	0.7%	<0.1%	4.2%	0.1%	<0.1%	0.5%

Table 8.2-7. WFZ 100-year probabilities.

Fault Segment	M ≥ 6.0			M ≥ 6.75		
	Mean	5th Percentile	95th Percentile	Mean	5th Percentile	95th Percentile
Malad City	0.5%	<0.1%	1.5%	0.5%	<0.1%	1.5%
Clarkston Mtn	0.6%	0.1%	1.6%	0.5%	<0.1%	1.5%
Collinston	0.5%	0.1%	1.2%	0.4%	0.1%	1.1%
Brigham City	11.0%	3.1%	28.4%	10.7%	2.8%	28.4%
Weber	6.3%	0.8%	15.3%	6.3%	0.8%	15.3%
Salt Lake City	11.2%	3.8%	25.2%	11.2%	3.8%	25.2%
Provo	7.7%	1.4%	16.4%	7.7%	1.4%	16.4%
Nephi	3.6%	<0.1%	12.1%	3.6%	<0.1%	12.1%
Levan	1.9%	0.2%	5.1%	1.7%	0.2%	4.7%
Fayette	1.0%	<0.1%	2.9%	0.9%	<0.1%	2.6%

Table 8.2-8. OGSLFZ segment 100-year probabilities.

Fault Segment	M ≥ 6.0			M ≥ 6.75		
	Mean	5th Percentile	95th Percentile	Mean	5th Percentile	95th Percentile
Rozelle	3.3%	0.7%	6.6%	2.9%	0.7%	6.6%
Promontory	3.9%	0.7%	9.7%	3.2%	0.3%	9.6%
Fremont Island	4.5%	0.7%	12.1%	4.0%	0.5%	11.7%
Antelope Island	2.3%	<0.1%	9.2%	2.3%	<0.1%	9.2%
Northern Oquirrh	1.3%	0.2%	4.1%	1.3%	0.2%	3.8%
Southern Oquirrh	1.4%	0.2%	4.0%	1.3%	0.2%	3.7%
Topliff Hills	1.9%	0.3%	4.6%	1.4%	0.2%	3.5%
East Tintic	0.9%	0.1%	2.3%	0.8%	0.1%	2.3%

8.3.2 Probability Models

We examined sensitivity to probability model for the segments of the WFZ and OGSLFZ that we modeled using both the time-independent (Poisson) and time-dependent (BPT) probability models. Table 8.3-3 reports the nominal time-independent and time-dependent probabilities for the central segments of the WFZ for one or more **M** ≥ 6.75 earthquakes for the next 30, 50, and 100 years. Because these probabilities are the weighted mean from all fault models, the listed "time-dependent" probabilities are not 100% time-dependent, as explained in the footnote in Table 8.3-3. The sensitivity to the time-dependent model is better examined using the probabilities for the single-segment rupture model, where all segments are time-dependent. As seen in Table 8.3-4, the BPT model gives significantly higher probabilities than the Poisson model for the Brigham City and Salt Lake City segments. In contrast, the probabilities using the BPT model are lower than the Poisson model for the other three segments, especially the Nephi segment which has an elapsed time since the most recent event of less than one-third of its mean recurrence interval.

As discussed in Section 7.2.2, the BPT model is very sensitive to the value of COV. A small COV indicates very periodic behavior, while a large COV models less periodic behavior. The BPT model has a delay period where the probability of another event is low immediately following an event. This delay is shorter for larger values of COV. A COV of 0.7 models close-to-Poisson behavior once the elapsed time nears the mean recurrence interval (Figure 7.2-1b).

Table 8.3-5 provides the segment BPT probabilities for each of the three values of COV (0.3, 0.5 and 0.7) compared to the Poisson probabilities. For the Brigham City segment, a COV of 0.3 results in a probability (14.9%) that is 4.6 times larger than the Poisson probability. The ratio of elapsed time to mean recurrence interval is provided to help understand sensitivity to the BPT model. Looking at Figure 7.2-1b, the x-axis labeled time is this ratio, while the y-axis, or instantaneous failure rate can also be thought of as the ratio of the BPT probability to the Poisson probability. For the Salt Lake City segment, which has an elapsed time approximately equal to the mean recurrence interval, the BPT probability for a COV of 0.3 (10.3%) is 2.9 times larger than the Poisson probability (as discussed in Section 7.2.2, the mean recurrence interval for the BPT model is also a function of COV). The other three segments have mean elapsed times less than or equal to one-half their mean recurrence intervals.

The BPT model with a COV of 0.3 implies that the fault segments are still in the delay period of the stress renewal model. The resulting BPT probabilities range from less than 0.1%

Table 8.2-9. "Other modeled fault" 100-year probabilities.

Fault or Fault Segment	M ≥ 6.0			M ≥ 6.75		
	Mean	5th Percentile	95th Percentile	Mean	5th Percentile	95th Percentile
Bear River	5.8%	2.8%	12.3%	5.5%	2.5%	12.3%
Carrington	3.3%	0.7%	7.1%	2.8%	0.7%	7.1%
Crater Bench and Drum Mountains	0.3%	<0.1%	1.5%	0.3%	<0.1%	1.5%
Crawford Mountains	0.3%	0.1%	0.8%	0.1%	<0.1%	0.4%
Curlew Valley	4.2%	0.5%	12.4%	1.1%	0.1%	3.9%
East Cache - Total	4.0%	0.8%	9.9%	2.8%	0.4%	7.4%
East Cache - North	1.8%	0.2%	5.2%	1.8%	0.2%	5.2%
East Cache - Central	2.5%	0.5%	6.5%	1.3%	<0.1%	5.1%
East Cache - South	0.7%	0.1%	3.3%	0.7%	0.1%	3.3%
East Dayton-Oxford	0.6%	0.1%	1.4%	0.2%	<0.1%	0.6%
Eastern Bear Lake - Total	13.9%	3.5%	32.3%	11.4%	2.4%	29.5%
Eastern Bear Lake - North	4.4%	0.9%	11.1%	3.2%	0.3%	10.1%
Eastern Bear Lake - Central	8.3%	1.8%	23.2%	7.3%	1.0%	22.4%
Eastern Bear Lake - South	6.2%	0.9%	18.9%	6.1%	0.9%	18.8%
Faults along the edge of Scipio Valley-Pavant Range	1.5%	0.1%	5.8%	1.5%	0.1%	5.8%
Gunnison	1.2%	0.1%	4.6%	1.2%	0.1%	4.6%
Hansel Valley	0.7%	<0.1%	3.0%	0.1%	<0.1%	0.6%
Joes Valley	0.7%	0.1%	2.0%	0.5%	<0.1%	2.0%
Little Valley	2.0%	0.2%	6.4%	0.5%	<0.1%	1.7%
Main Canyon	0.3%	0.1%	0.9%	0.2%	<0.1%	0.4%
Morgan	0.3%	0.1%	0.9%	0.1%	<0.1%	0.3%
North Promontory	3.1%	0.5%	9.3%	2.1%	0.4%	5.5%
Porcupine Mountain	0.3%	0.1%	0.8%	0.3%	0.1%	0.7%
Rock Creek	6.7%	1.0%	16.3%	6.6%	1.0%	15.8%
Skull Valley	3.1%	0.4%	7.1%	2.6%	0.3%	7.1%
Snow Lake Graben	0.6%	0.1%	2.0%	0.3%	<0.1%	1.0%
Stansbury - Total	11.0%	1.2%	25.4%	7.7%	0.8%	21.5%
Stansbury - North	4.2%	0.5%	10.0%	3.3%	0.3%	8.9%
Stansbury - Central	5.2%	0.5%	16.8%	4.8%	0.4%	15.2%
Stansbury - South	4.5%	0.4%	11.7%	2.1%	<0.1%	7.8%
Stinking Springs	2.6%	0.3%	8.0%	0.1%	<0.1%	0.4%
Strawberry	1.3%	0.3%	3.5%	1.1%	0.3%	3.0%
Utah Lake	2.1%	<0.1%	8.6%	0.8%	<0.1%	3.4%
West Cache - Total	6.8%	1.5%	16.0%	4.9%	0.7%	13.4%
West Cache - North	4.1%	0.8%	9.6%	2.8%	0.4%	7.2%
West Cache - Central	3.4%	0.4%	13.3%	3.2%	0.2%	13.3%
West Cache - South	2.2%	0.4%	6.7%	1.7%	0.1%	6.7%
West Valley	1.2%	<0.1%	8.0%	<0.1%	<0.1%	0.2%
Western Bear Lake	2.3%	<0.1%	13.4%	0.2%	<0.1%	1.7%

Table 8.3-1. Sensitivity of 50-year probabilities for **M** ≥ 6.75 earthquakes to fault rupture models used for the WFZ central segments.

Fault Segment	Single-Segment Rupture Model (wt 0.70)	Intermediate Rupture Model A (wt 0.05)	Intermediate Rupture Model B (wt 0.05)	Intermediate Rupture Model C (wt 0.075)	Minimum Rupture Model (wt 0.025)	Unsegmented (wt 0.1)	Wt. Mean
Brigham City	6.6%	3.0%	3.0%	3.0%	2.9%	3.8%	5.6%
Weber	2.3%	3.4%	3.4%	3.4%	3.4%	9.2%	3.2%
Salt Lake City	5.6%	3.5%	5.6%	5.6%	3.2%	9.3%	5.8%
Provo	3.1%	3.9%	3.9%	3.1%	4.0%	9.9%	3.9%
Nephi	1.3%	1.3%	3.8%	1.3%	3.1%	4.6%	1.8%

Table 8.3-2. Sensitivity of 50-year probabilities for **M** ≥ 6.75 earthquakes to fault rupture models used for the OGSLFZ segments.

Fault Segment	Model 1	Model 2	Model 3	Model 4	Model 5	Wt. Mean
Rozelle	1.3%	1.3%	1.3%	1.3%	2.4%	1.5%
Promontory	1.0%	1.0%	1.0%	1.0%	4.0%	1.6%
Fremont Island	1.4%	1.4%	1.5%	1.4%	4.5%	2.1%
Antelope Island	0.3%	0.3%	1.5%	0.3%	3.7%	1.2%
Northern Oquirrh	0.6%	0.4%	0.4%	0.4%	0.6%	0.6%
Southern Oquirrh	0.6%	0.5%	0.5%	0.6%	1.4%	0.7%
Topliff Hills	0.6%	0.6%	0.6%	0.6%	1.1%	0.7%
East Tintic	0.3%	0.3%	0.3%	0.3%	0.8%	0.4%

Table 8.3-3. WFZ central segments, all fault models, **M** ≥ 6.75 earthquake probabilities.

Fault Segment	30 Years		50 Years		100 Years	
	Poisson	Time-Dependent[1]	Poisson	Time-Dependent[1]	Poisson	Time-Dependent[1]
Brigham City	2.0%	3.8%	3.2%	6.2%	6.2%	11.8%
Weber	2.5%	1.8%	4.0%	3.0%	7.7%	6.0%
Salt Lake City	2.6%	3.8%	4.2%	6.2%	8.0%	11.9%
Provo	2.8%	2.2%	4.6%	3.7%	8.7%	7.4%
Nephi	2.7%	0.7%	4.4%	1.1%	8.4%	2.4%

[1] Note that for fault models with multi-segment ruptures, not all segments are time-dependent. The time-dependent probabilities are not 100% time-dependent. The effective time-dependent weight for the probabilities listed above are: BCS 0.7, WS 0.7, SLCS 0.83, PS 0.78, NS 0.83.

Table 8.3-4. WFZ central segments, single-segment rupture model, **M** ≥ 6.75 earthquake probabilities.

Fault Segment	30 Years		50 Years		100 Years	
	Poisson	BPT	Poisson	BPT	Poisson	BPT
Brigham City	1.9%	4.6%	3.2%	7.5%	6.2%	14.2%
Weber	2.1%	1.2%	3.5%	2.0%	6.8%	4.3%
Salt Lake City	2.2%	3.7%	3.6%	6.1%	7.1%	11.8%
Provo	2.4%	1.7%	4.0%	2.8%	7.7%	6.0%
Nephi	2.7%	0.3%	4.4%	0.5%	8.6%	1.3%

(Nephi segment) to 40% (Provo segment) of the Poisson probabilities. At the other end of the range of COV values (COV = 0.7), the BPT probabilities for the Brigham City and Salt Lake City segments are similar to the Poisson probabilities. The BPT probabilities for the other three segments are less than the Poisson probabilities because the ratio of the mean elapsed time to mean recurrence intervals for those segments (0.2 to 0.4) indicates these segments are still in the delay period for a COV of 0.7.

Table 8.3-6 provides a comparison of the Poisson and BPT segment probabilities for the Fremont Island and Antelope Island segments of the OGSLFZ for fault model 2 (single-segment rupture model). The BPT probabilities are larger for the Fremont Island segment, and lower for the Antelope Island segment. Table 8.3-7 provides the sensitivity to COV for these segments.

8.3.3 Magnitude Relations

The choice of magnitude relation used in calculating the characteristic magnitude for a fault or fault segment does not have a notable impact on probabilities for the WFZ (Table 8.3-8). (One can examine, for example, the ratio of the highest to the lowest probabilities in a given row of Table 8.3-8.) There is some impact for the northern and southern end segments of the WFZ, but little impact for the central segments, where earthquake rates are determined by recurrence intervals. The primary impact of the different magnitude relations is on the characteristic magnitude.

For the OGSLFZ, the impact of the choice of magnitude relation on earthquake probabilities (Table 8.3-9) is more comparable to that for the WFZ end segments than for its central segments. This again appears to reflect how earthquake rates were calculated; the probabilities for segments that have rates calculated using geologic slip rates show more variability than those calculated using recurrence intervals. The extent of the variability was examined for two other modeled faults having high slip rates: the East Cache fault zone and Eastern Bear Lake fault. The results, shown in Table 8.3-10, indicate that the choice of magnitude relation leads to a variability in probability similar to that seen for the end segments of the WFZ and for the segments of the OGSLFZ.

Table 8.3-5. Sensitivity to COV: WFZ central segments, single-segment rupture model, **M** ≥ 6.75 earthquake 50-year probabilities.

Fault Segment	Poisson Probability	BPT, α = 0.3			BPT, α = 0.5			BPT, α = 0.7		
		Probability	Lapse Time / Mean RI	Ratio of BPT to Poisson Probability	Probability	Lapse Time / Mean RI	Ratio of BPT to Poisson Probabiltiy	Probability	Lapse Time / Mean RI	Ratio of BPT to Poisson Probability
Brigham City	3.2%	14.9%	1.7	4.6	6.3%	1.5	2.0	3.7%	1.3	1.2
Weber	3.4%	1.1%	0.5	0.3	2.0%	0.4	0.6	2.6%	0.38	0.8
Salt Lake City	3.6%	10.3%	1.0	2.9	5.5%	0.9	1.5	3.7%	0.74	1.0
Provo	4.0%	1.7%	0.5	0.4	3.1%	0.5	0.8	3.2%	0.39	0.8
Nephi	4.4%	<0.1%	0.3	0.007	0.48%	0.3	0.1	1.0%	0.21	0.2

Table 8.3-6. OGSLFZ, single-segment rupture model, **M** ≥ 6.75 earthquake probabilities.

Fault Segment	30 Years		50 Years		100 Years	
	Poisson	BPT	Poisson	BPT	Poisson	BPT
Fremont Island	0.8%	0.8%	1.2%	1.4%	2.5%	2.8%
Antelope Island	0.9%	0.01%	1.4%	0.02%	2.8%	0.05%

Table 8.3-7. Sensitivity to COV: OGSLFZ, single-segment rupture model, **M** ≥ 6.75 earthquake 50-year probabilities.

Fault Segment	Poisson	BPT, α = 0.3	BPT, α = 0.5	BPT, α = 0.7
Fremont Island	1.2%	2.1%	1.3%	0.9%
Antelope Island	1.4%	<0.01%	< 0.01%	0.07%

Table 8.3-8. Sensitivity to magnitude relations: WFZ central segments, **M** ≥ 6.75 earthquake 50-year probabilities.

Fault Segment	Magnitude-Moment (Hanks and Kanamori, 1979)	Magnitude – SRL (Wesnousky, 2008)	Magnitude – SRL (Wells and Coppersmith, 1994)	Magnitude – SRL (Stirling *et al*., 2002)
Total Fault	18.0%	17.1%	16.8%	17.8%
Malad City	0.22%	0.27%	0.38%	0.24%
Clarkston Mountain	0.22%	0.25%	0.28%	0.24%
Collinston	0.20%	0.22%	0.29%	0.20%
Brigham City	5.7%	4.8%	4.7%	5.8%
Weber	3.2%	3.2%	3.2%	3.2%
Salt Lake City	5.8%	5.6%	5.5%	5.9%
Provo	3.9%	3.9%	3.9%	3.9%
Nephi	1.8%	1.7%	1.7%	1.8%
Levan	0.77%	0.88%	1.32%	0.75%
Fayette	0.39%	0.47%	0.72%	0.42%

Table 8.3-9. Sensitivity to magnitude relations: OGSLFZ, **M** ≥ 6.75 earthquake 50-year probabilities.

Fault Segment	Magnitude-Moment (Hanks and Kanamori, 1979)	Magnitude – SRL (Wesnousky, 2008)	Magnitude – SRL (Wells and Coppersmith, 1994)	Magnitude – SRL (Stirling *et al*., 2002)
Total Fault	5.4%	5.7%	5.1%	6.8%
Rozelle	1.4%	1.3%	1.2%	1.7%
Promontory	1.3%	1.4%	1.3%	2.0%
Fremont Island	1.8%	2.0%	1.8%	2.4%
Antelope Island	1.0%	1.5%	1.4%	1.2%
Northern Oquirrh	0.54%	0.86%	0.79%	0.66%
Southern Oquirrh	0.57%	0.95%	0.88%	0.68%
Topliff Hills	0.64%	0.79%	0.69%	0.70%
East Tintic	0.35%	0.67%	0.65%	0.39%

Table 8.3-10. Sensitivity to magnitude relations: East Cache and Eastern Bear Lake faults, **M** ≥ 6.75 earthquake 50-year probabilities.

Fault	Magnitude-Moment (Hanks and Kanamori, 1979)	Magnitude – SRL (Wesnousky, 2008)	Magnitude – SRL (Wells and Coppersmith, 1994)	Magnitude – SRL (Stirling *et al*., 2002)
East Cache	1.2%	1.8%	1.7%	1.5%
Eastern Bear Lake	5.8%	7.4%	7.2%	5.6%

9 FUTURE DIRECTIONS AND LIMITATIONS

The formal analysis of earthquake probabilities in California extends back almost three decades; however, the Wasatch Front region has not had adequate information for similar analyses until this decade. This study represents the first formal community estimate of earthquake probabilities in the Wasatch Front region as well as the first formal earthquake forecast in the U.S. outside of California. The assessment was carried out by nationally recognized experts with first-hand knowledge of the paleoseismology, seismology, and geodesy of the study region and the surrounding Intermountain West.

In the process of this study, much has been learned. Indeed, the efforts described in this report have notably advanced the earthquake science of the Wasatch Front region. At the same time, we have identified some key issues for which lack-of-knowledge uncertainties should be reduced. The WGUEP hopes and intends that this forecast will be a cornerstone for future forecasts of earthquake probabilities in this region that will inevitably benefit from new data, continually improving methods of analysis, and further research.

The WFZ, the principal focus of this forecast, is now one of the best characterized faults in the world with a well quantified paleoseismic record that extends back to at least the middle Holocene for its central segments, thanks to numerous paleoseismic trench investigations since the late 1960s. Despite this progress, important questions persist regarding the nature of fault segmentation, earthquake rupture extent, and the timing and recurrence of mid- to early Holocene earthquakes.

Additional work is necessary to more rigorously test the WFZ segmentation model. Our analyses focused on the per-segment earthquake histories, which served to refine the earthquake data, but also limited our ability to exhaustively define and evaluate all possible rupture permutations. For example, what is the frequency and rupture extent of earthquakes that have ruptured only part of a segment or crossed a segment boundary? Understanding the segmentation of the fault over the Holocene and the rupture extent of individual earthquakes (e.g., by targeted paleoseismic investigations near segment boundaries) would serve to improve models of multi-segment rupture on the fault. Ultimately, we suggest that an evaluation of possible ruptures across the WFZ segment boundaries using the site earthquake data be conducted to yield a more comprehensive suite of rupture models (e.g., Biasi and Weldon, 2009).

Poorly constrained mid-Holocene to latest Pleistocene earthquakes add uncertainty to the rupture behavior of the WFZ. Thus, additional paleoseismic data for this time period would serve to refine individual rupture extents and improve inter-event and mean recurrence data for the fault. For example, questions remain regarding long (~2 kyr) inter-event periods on the segments that could reflect either variability in strain accumulation and moment release (e.g., aperiodic earthquake behavior) or could be the product of incomplete paleoseismic records. Continuing to improve the paleoseismic data for the central segments would result in more robust mean-recurrence and COV estimates for the WFZ, and ultimately, a more accurate Wasatch Front earthquake forecast. For the WFZ end segments, individual earthquake times and displacements are needed to better constrain mean recurrence intervals and slip rates for these less-active parts of the fault zone. Finally, improving the understanding of the subsurface geometry of the fault (e.g., planar versus listric) is important for comparing geologic slip rates for the WFZ to geodetic extension rates for the region.

Substantial uncertainties also exist in the characterization of the "other modeled faults" in the Wasatch Front region. We have attempted to quantify those uncertainties and include them in our forecast; however, additional paleoseismic data, and the systematic review and synthesis of previous data are necessary to better understand the hazard posed by these faults.

The approach taken in our Wasatch Front region forecast is generally straightforward and has leaned heavily on methodologies developed by the Working Groups on California Earthquake Probabilities (WGCEP). Compared to the California efforts, our task has been easier in one regard, in that we did not have to deal with the complexities of being along a plate boundary.

Our WGUEP forecast depends to a large degree on expert judgment. Compared to the WGCEP exercises, the involvement of scientists outside our immediate working group was limited due to the smaller community of experts on earthquake processes in the Wasatch Front region. However, we did attempt to capture the views of others not taking part in the WGUEP deliberations. Our WGUEP forecast should be viewed as a "consensus" forecast in the sense that our deliberations were extensive and consensus was reached for the vast majority of inputs. The appropriate role of geodetic information in characterizing the rate of fault activity is still controversial, and total agreement was not reached on its use in this forecast. Geodetic information was not used to estimate fault slip rates in our evaluation (see Section 9.3).

A number of the issues recognized by the WGCEP beginning in 1988 also apply to the Wasatch Front region and the BRP as well. In particular, the following issues have been the subject of ongoing study in the Wasatch Front region and we suggest should continue to be targets for future research.

9.1 Characteristic Earthquake Model and Fault Segmentation

Current concepts of a "characteristic earthquake" and fault segmentation had their beginnings in paleoseismic studies of the WFZ (Section 3.1). The WGUEP gave considerable

weight to the maximum magnitude model, a variation on the characteristic earthquake model, because the paleoseismic evidence strongly suggests that it is applicable to the WFZ. Based on limited data, the model also appears to apply to some other faults in the Wasatch Front region. We made the decision to apply the maximum magnitude model to all of the longer faults in the region.

In California, the segmentation model has lost its consensus support. However, that is not the case in Utah and the BRP because the paleoseismic data are, in large part, consistent with fault segmentation. This is not to suggest that multi-segment ruptures are not possible. Some observations of paleoearthquake timing, especially when including associated uncertainties, permit, but do not require multi-segment ruptures. The WGUEP did include some multi-segment ruptures in the forecast. Paleoseismic investigations (e.g., DuRoss and Hylland, 2015) continue to assess the applicability of different rupture models to the central WFZ.

9.2 Fault Interactions

The WGCEP strongly considered fault interactions and stress shadows in their Uniform California Earthquake Rupture Forecasts (UCERF2 and, most recently, UCERF3). Fault-interaction and stress-shadow models have not yet been comprehensively evaluated in the Wasatch Front region. At least one study (Chang and Smith, 2002) suggests that fault interaction may be an operative process along the WFZ central segments. These possible factors influencing the recurrence intervals of the major faults on the Wasatch Front region may need to be considered in future analyses.

9.3 Use of Geodetic Data

Estimating fault slip rates from geodetic data has become increasingly popular. Most recently in UCERF3, the WGCEP used geodetic data to determine slip rates in California. As described in Section 6, the geodetic moment rates for the Wasatch Front region and three of the four defined subregions are consistent with the geological/seismological moment rates for these regions calculated for the WGUEP earthquake rate model. However, the WGUEP judged at an early stage that the use of geodetic data to estimate fault slip rates in the region was still premature. Future studies are required before geodetic data can be used confidently to estimate fault slip rates in the Wasatch Front region. The geodetically-derived rates can be used in a logic tree framework as an alternative to geologic slip rates.

9.4 Estimating Characteristic Magnitudes

Magnitude regressions used in this study characterize the upper and lower bounds of the uncertainty in the estimated characteristic magnitude **M** for the analyzed faults. However, questions remain regarding (1) the source of the discrepancy in estimates of **M** between displacement- and length-based regressions, (2) the best way to address this **M** discrepancy for faults in the region that have length but not displacement data, (3) the use of L_{seg}, L_{sub}, or SRL in the calculation of A and M_0 (see Section 3.6), and (4) the suitability of all-fault-type regressions to BRP normal faults. Certainly, more empirical data would help address these questions. In the meantime, multiple branches are required in a logic tree approach as was employed in this study.

9.5 COV

As described in Section 7.2.2, the coefficient of variation (COV) in the BPT model is a critical parameter. We have adopted a COV range of 0.5 ± 0.2 for the central WFZ segments and the OGSLFZ based on a global COV (Ellsworth *et al*., 1999), as well as a composite COV for the central WFZ segments (Section 4.1.3). Segment-specific COVs range from 0.2 to 0.6, although the datasets are small (Section 4.1.2). The use of actual segment-specific COVs would have resulted in significantly different probabilities (Section 8.3.2). Obtaining complete paleoseismic records beyond 6.0 ka for the WFZ central segments would refine segment-specific COVs and, hence, potentially improve time-dependent probabilities.

9.6 Time-Dependent Model Weights

As described in Section 7.2.3, the WGUEP assigned a weight of 0.8 to the time-dependent BPT model and 0.2 weight to the time-independent Poisson model for the WFZ central segment ruptures. We judged that the elastic rebound model is applicable to both the central WFZ and to the Antelope Island and Fremont Island segments of the OGSLFZ and that available data on the rupture histories of these segments do not favor Poisson behavior. We emphasize, however, that the assigned time-dependent model weight for each of these segments is diluted because multi-segment ruptures required a time-independent model weight of 1.0, due to a lack of paleoseismic data to constrain recurrence intervals. For example, for the Brigham City segment, which is of significant concern because of its long elapsed time, the effective time-dependent weight is only 0.56. The reduced time-dependent model rate for this and the other central WFZ segments has an obvious influence on the probabilities estimated in this study. Ultimately, a longer and more complete paleoseismic record is needed to reduce uncertainties relating to modeling rupture behavior on the WFZ and other major faults such as the OGSLFZ.

10 ACKNOWLEDGMENTS

This research was supported in part by the U.S. Geological Survey (USGS), Department of the Interior, under USGS award numbers G11AP20010 and G13AP00003 to URS Corporation and award numbers G10AC00058, G11AP20004, and G13AP00002 to the Utah Geological Survey (UGS). The WGUEP thanks the many individuals who provided assistance, including Glenn Biasi (University of Nevada, Reno); James Dewey, Charles Mueller, Bruce Presgrave, and Yuehua Zhang (USGS); Gordon Douglass, Tyler Knudsen, Pam Perri, Lori Steadman, and Corey Unger (UGS); Michael Machette (Paleo Seis Surveys LLC); Gabriel Toro (Lettis Consultants International, Inc.); Katherine Whidden (University of Utah Seismograph Stations); and Robert Youngs (AMEC Foster Wheeler). We also thank Melinda Lee (URS Corporation) and John Good (UGS) for their assistance in preparing this report.

Our thanks to Rich Briggs (USGS) for guiding us through the USGS review process, and to the reviewers who included Glenn Biasi and Bill Hammond (UNR); Jim Dewey, Ryan Gold, Chuck Mueller, Morgan Page, Kate Scharer, and Wayne Thatcher (USGS); and Mark Stirling (GNS Science).

11 REFERENCES

Aki, K., 1979, Characterization of barriers on an earthquake fault: Journal of Geophysical Research, v. 84, p. 6140–6148.

Aki, K., 1984, Asperities, barriers, and characteristic earthquakes: Journal of Geophysical Research, v. 89, p. 5867–5872.

Allmendinger, R.W., 1983, Geologic map of the North Hansel Mountains, Idaho and Utah: U.S. Geological Survey Miscellaneous Field Studies Map MF-1643, 1 sheet, scale 1:24,000.

Allmendinger, R.W., and Royce, F., 1995, Is the Sevier Desert reflection of west-central Utah a normal fault?: Comment and reply: Geology, v. 23, p. 669–670.

Allmendinger, R.W., Sharp, J.W., Von Tish, D., Serpa, L., Brown, L., Kaufman, S., and Oliver, J., 1983, Cenozoic and Mesozoic structure of the eastern Basin and Range Province, Utah, from COCORP seismic-reflection data: Geology, v. 11, p. 532–536.

Anders, M.H., and Christie-Blick, N., 1994, Is the Sevier Desert detachment of west-central Utah a normal fault?: Geology, v. 22, p. 771–774.

Anders, M.H., Christie-Blick, N., Wills, S., and Krueger, S.W., 2001, Rock deformation studies in the Mineral Mountains and Sevier Desert of west-central Utah—implications for upper crustal low-angle normal faulting: Geological Society of America Bulletin, v. 113, p. 895–907.

Anderson, J.G., 1979, Estimating the seismicity from geological structure for seismic risk studies: Bulletin of the Seismological Society of America, v. 69, p. 135–158.

Anderson, J.G., Wesnousky, S.G., and Stirling, M.W., 1996, Earthquake size as a function of fault slip rate: Bulletin of the Seismological Society of America, v. 86, p. 683–690.

Anderson, L.W., 2008, Evaluation of the seismogenic potential of the Joes Valley fault zone—Joes Valley Dam, Emery County Project—Utah: U.S. Bureau of Reclamation Technical Memorandum No. 86-68321-2008-10, 12 p., 2 attachments.

Anderson, R.E., and Bucknam, R.C., 1979, Map of fault scarps in unconsolidated sediments, Richfield 1° x 2° quadrangle, Utah: U.S. Geological Survey Open-File Report 79-1236, 15 p. pamphlet, 1 sheet, scale 1:250,000.

Arabasz, W.J., Burlacu, R., and Pankow, K.L., 2007, An overview of historical and contemporary seismicity in central Utah, *in* Willis, G.C., Hylland, M.D., Clark, D.L., and Chidsey, T.C., Jr., editors, Central Utah—diverse geology of a dynamic landscape: Utah Geological Association Publication 36, p. 237–253.

Arabasz, W.J., Pankow, K.L, Pechmann, J.C., and Burlacu, R., 2010, Cooperative regional/urban seismic monitoring—Wasatch Front, Utah, and neighboring Intermountain West area, February 1, 2007–January 31, 2010: Final Technical Report to the U.S. Geological Survey, National Earthquake Hazards Reduction Program, Cooperative Agreement No. 07HQAG0022, 55 p.

Arabasz, W.J., Pechmann, J.C., and Brown, E.D., 1992, Observational seismology and the evaluation of earthquake hazards and risk in the Wasatch Front area, Utah, *in* Gori, P.L., and Hays, W.W., editors, Assessment of regional earthquake hazards and risk along the Wasatch Front, Utah: U.S. Geological Survey Professional Paper 1500-D, 36 p.

Arabasz, W.J., Richins, W.D., and Langer, C.J., 1981, The Pocatello Valley (Idaho-Utah border) earthquake sequence of March to April 1975, Bulletin of the Seismological Society of America, v. 71, p. 803–826.

Atwood, W.W., 1916, The physiographic conditions at Butte, Montana, and Bingham Canyon, Utah, when the copper ores in these districts were enriched: Economic Geology, v. 11, p. 732–740.

Bacon, C. R., 1983, Eruptive history of Mount Mazama and Crater Lake Caldera, Cascade Range, USA: Journal of Volcanology and Geothermal Research, v. 18, p. 57–115.

Barnhard, T.P., and Dodge, R.L., 1988, Map of fault scarps formed on unconsolidated sediments, Tooele 1° x 2° quadrangle, northwestern Utah: U.S. Geological Survey Miscellaneous Field Studies Map MF-1990, 1 sheet, scale 1:250,000.

Barrientos, S.E., Stein, R.S., and Ward, S.N., 1987, Comparison of the 1959 Hebgen Lake, Montana and the 1983

Borah Peak, Idaho, earthquakes from geodetic observations: Bulletin of the Seismological Society of America, v. 77, p. 784–808.

Barrientos, S.E., Ward, S.N., Gonzalez-Ruiz, J.R., and Stein, R.S., 1985, Inversion for moment as a function of depth from geodetic observations and long period body waves of the 1983 Borah Peak, Idaho, earthquake, *in* Stein, R.S., and Bucknam, R.C., editors, Proceedings of Workshop XXVIII on the Borah Peak, Idaho Earthquake, U.S. Geological Survey Open-File Report 85-290, p. 485–518.

Baskin, R.L., and Allen, D.V., 2005, Bathymetric map of the south part of Great Salt Lake, Utah, 2005: U.S. Geological Survey Scientific Investigation Map 2894, 1 sheet, scale 1:100,000.

BC Hydro, 2012, Probabilistic seismic hazard analysis (PSHA) model, volume 2—seismic source characterization (SSC) model: Parts 1 to 4, Engineering Report E658.

Benedetti, L., Manighetti, I., Gaudemer, Y., Finkel, R., Malavieille, J., Pou, K., Arnold, M., Aumaitre, G., Bourles, D., and Keddadouche, K., 2013, Earthquake synchrony and clustering on Fucino faults (central Italy) as revealed from in situ ^{36}Cl exposure dating: Journal of Geophysical Research – Solid Earth, v. 118, p. 4948–4974.

Benson, L.V., Lund, S.P., Smoot, J.P., Rhode, D.E., Spencer, R.J., Verosub, K.L., Louderback, L.A., Johnson, C.A., Rye, R.O., and Negrini, R.M., 2011, The rise and fall of Lake Bonneville between 45 and 10.5 ka: Quaternary International, v. 235, p. 57–69.

Biasi, G.P. and Weldon, R.J., 2006, Estimating surface rupture length and magnitude of paleoearthquakes from point measurements of rupture displacement: Bulletin of the Seismological Society of America, v. 96, p. 1612–1623.

Biasi, G.P. and Weldon, R.J., 2009, San Andreas fault rupture scenarios from multiple paleoseismic records—stringing pearls: Bulletin of the Seismological Society of America, v. 99, p. 471–498.

Biasi, G., and Wesnousky, S., 2015, Fault linkage, complexity, and earthquake displacement, *in* Lund, W.R., editor, Proceedings Volume, Basin and Range Province Seismic Hazards Summit III: Utah Geological Survey Miscellaneous Publication 15-5, technical session 2, variously paginated, CD.

Biek, R.F., Oaks, R.Q., Jr., Janecke, S.U., Solomon, B.J., and Swenson Barry, L.M., 2003, Geologic maps of the Clarkston and Portage quadrangles, Box Elder and Cache Counties, Utah and Franklin and Oneida Counties, Idaho: Utah Geological Survey Map 194, 41 p. pamphlet, 3 plates, scale 1:24,000.

Bird, P., 2014, Appendix C—Estimation of fault slip rates in the conterminous western United States with statistical and kinematic finite-element programs, *in* Petersen, M.D., Zeng, Y., Haller, K.M., McCaffrey, R., Hammond, W.C., Bird, P., Moschetti, M., Shen, Z., Bormann, J., and Thatcher, W., Geodesy- and geology-based slip-rate models for the western United States (excluding California) National Seismic Hazard Maps: U.S. Geological Survey Open-File Report 2013-1293, http://dx.doi.org/10.3133/ofr20131293, p. 48–57.

Black, B.D., Giraud, R.E., and Mayes, B.H., 2000, Paleoseismic investigation of the Clarkston, Junction Hills, and Wellsville faults, West Cache fault zone, Cache County, Utah: Utah Geological Survey Special Study 98, 23 p.

Black, B.D., and Hecker, S., compilers, 1999a, Fault number 2407, Topliff Hill fault zone, *in* Quaternary Fault and Fold Database of the United States: U.S. Geological Survey website, http://earthquakes.usgs.gov/hazards/qfaults.

Black, B.D., and Hecker, S., compilers, 1999b, Fault number 2420, East Tintic Mountains (west side) faults, *in* Quaternary Fault and Fold Database of the United States: U.S. Geological Survey website, http://earthquakes.usgs.gov/hazards/qfaults.

Black, B.D., Hecker, S., Hylland, M.D., Christenson, G.E., and McDonald, G.N., 2003, Quaternary fault and fold database and map of Utah: Utah Geological Survey Map 193DM, scale 1:50,000, CD.

Black, B.D., Hylland, M.D., and Hecker, S., compilers, 1999, Fault number 2439, Clear Lake fault zone, *in* Quaternary fault and fold database of the United States: U.S. Geological Survey website, http://earthquakes.usgs.gov/hazards/qfaults.

Black, B.D., Lund, W.R., Schwartz, D.P., Gill, H.E., and Mayes, B.H., 1996, Paleoseismic investigation of the Salt Lake City segment of the Wasatch fault zone at the South Fork Dry Creek and Dry Gulch sites, Salt Lake County, Utah—Paleoseismology of Utah, Volume 7: Utah Geological Survey Special Study, 92, 22 p., 1 plate.

Bonilla, M.G., Mark, R.K. and Lienkaemper, J.J., 1984, Statistical relations among earthquake magnitude, surface rupture length, and surface fault displacement: Bulletin of the Seismological Society of America, v. 74, p. 2379–2411.

Bortz, L.C., Cook, S.A., and Morrison, O.J., 1985, Great Salt Lake area, Utah, *in* Gries, R.R, and Dyer, R.C., editors, Seismic exploration of the Rocky Mountain region: Rocky Mountain Association of Geologists and the Denver Geophysical Society, p. 275–281.

Bourne, S.J., England, P.C., and Parsons, B., 1998, The motion of crustal blocks driven by flow of the lower lithosphere and implications for slip rates of continental strike-slip faults: Nature, v. 391, p. 655–659.

Bronk Ramsey, C., 2008, Depositional models for chronological records: Quaternary Science Reviews, v. 27, p. 42–60.

Bronk Ramsey, C., and Lee, S., 2013, Recent and planned developments of the program OxCal: Radiocarbon, v. 55, p. 720–730.

Bruhn, R.L., Gibler, P.R., and Parry, W.T., 1987, Rupture characteristics of normal faults—an example from the Wasatch fault zone, Utah, *in* Coward, M.P., Dewey, J.F., Hancock, P.L., editors, Continental extensional tectonics: Geological Society of London, Special Publication no. 28, p. 337–353.

Bruhn, R.L., and Schultz, R.A., 1996, Geometry and slip distribution in normal fault systems—implications for mechanics and fault-related hazards: Journal of Geophysical Research, v. 101, p. 3401–3412.

Bryant, B., 1990, Geologic map of the Salt Lake City 30′ x 60′ quadrangle, north-central Utah, and Uinta County, Wyoming: U.S. Geological Survey Miscellaneous Investigations Series Map I-1944, scale 1:100,000.

Buck, W.R., 1988, Flexural rotation of normal faults: Tectonics, v. 7, p. 959–973.

Bucknam, R.C., 1977, Map of suspected fault scarps in unconsolidated sediments, Tooele 2° sheet, Utah: U.S. Geological Survey Open-File Report 77-495, scale 1:250,000.

Bucknam, R.C., and Anderson, R.E., 1979, Map of fault scarps on unconsolidated sediments, Delta 1° x 2° quadrangle, Utah: U.S. Geological Survey Open-File Report 79-366, 21 p. pamphlet, 1 sheet, scale 1:250,000.

Carney, S.M., Janecke, S.U., Oriel, S.O., Evans, J.C., and Link, P.K., 2002, Geologic map of the Clifton quadrangle, Franklin and Oneida Counties, Idaho: Idaho Geological Survey Technical Report 03-4, scale 1:24,000.

Carpenter, N.S., Payne, S.J, and Schafer, A.L., 2012, Toward reconciling magnitude discrepancies estimated from paleoearthquake data: Seismological Research Letters, v. 83, p. 555–565.

Castellaro, S., and Bormann, P., 2007, Performance of different regression procedures on the magnitude conversion problem: Bulletin of the Seismological Society of America, v. 97, p. 1167–1175.

Castellaro, S., Mulargia, F., and Kagan, Y.Y., 2006, Regression problems for magnitudes: Geophysical Journal International, v. 165, p, 913–930.

Chang, W.-L., 2004, GPS (Global Positioning System) studies of the Wasatch fault zone, Utah, with implications for elastic and viscoelastic fault behavior and earthquake hazard: Salt Lake City, University of Utah, Ph.D. disertation, 201 p.

Chang, W.-L., and Smith, R.B., 2002, Integrated seismic-hazard analysis of the Wasatch Front, Utah: Bulletin of the Seismological Society of America, v. 92, p. 1904–1922.

Chang, W.-L., Smith, R.B., Meertens, C.M., and Harris, R.A., 2006, Contemporary deformation of the Wasatch Front, Utah, from GPS measurements with implications for interseismic fault behavior, earthquake hazard observations and kinematic analysis: Journal of Geophysical Research, v. 111, B11405.

Christie-Blick, N., Anders, M.H., Manatschal, G., and Wernicke, B.P., 2009, Testing the extensional detachment paradigm—a borehole observatory in the Sevier Desert basin: Scientific Drilling, no. 8, p. 57–59.

Cline, E.J., and Bartley, J.M., 2007, Nature of the Cenozoic-Mesozoic contact in Sevier Valley and tectonic implications, *in* Willis, G.C., Hylland, M.D., Clark, D.L., and Chidsey, T.C., Jr., editors, Central Utah—diverse geology of a dynamic landscape: Utah Geological Association Publication 36, p. 31–45.

Cluff, L.S., Brogan, G.E., and Glass, C.E., 1973, Wasatch fault, southern portion—earthquake fault investigation and evaluation—a guide to land use planning: unpublished Woodward-Lundgren and Associates report prepared for the Utah Geological and Mineralogical Survey, 79 p., 23 sheets, approximate scale 1:24,000, also available in Utah Geological Survey Open-File Report 548.

Cluff, L.S., Glass, C.E., and Brogan, G.E., 1974, Investigation and evaluation of the Wasatch fault north of Brigham City and Cache Valley faults, Utah and Idaho—a guide to land-use planning with recommendations for seismic safety: unpublished Woodward-Lundgren and Associates report prepared for the U.S. Geological Survey, 147 p., 1 appendix, 25 sheets, scale 1:24,000, also available in Utah Geological Survey Open-File Report 548.

Collettini, C., and Sibson, R.H., 2001, Normal faults, normal friction?: Geology, v. 29, p. 927–930.

Coogan, J.C., 2008, Stratigraphic, structural, and velocity interpretations of seismic reflection profiles CGG-WAS-202 and CGG-WAS-207 in the vicinity of Joes Valley and Snow Lake grabens of the Wasatch Plateau, Utah, *in* Anderson, L.W., Evaluation of the seismogenic potential of the Joes Valley fault zone—Joes Valley Dam, Emery County Project—Utah: U.S. Bureau of Reclamation Technical Memorandum no. 86-68321-2008-10, 14 p.

Coogan, J.C., and DeCelles, P.G., 1996, Extensional collapse along the Sevier Desert reflection, northern Sevier Desert basin, western United States: Geology, v. 24, p. 933–936.

Coogan, J.C., and DeCelles, P.G., 2007, Regional structure and kinematic history of the Sevier fold-and-thrust belt, central Utah—Reply: Geological Society of America Bulletin, v. 119, p. 508–512.

Coogan, J.C., and King, J.K., 2001, Progress report—geologic map of the Ogden 30′ x 60′ quadrangle, Utah and Wyoming, year 3 of 3: Utah Geological Survey Open-File Report 365, 34 p. pamphlet, scale 1:100,000.

Cook, K.L., Bankey, V. Mabey, D. R., and DePangher, M., 1989, Complete Bouger gravity anomaly map of Utah: Utah Geological and Mineral Survey Map 122, scale 1:500,000.

Cook, K.L. and Berg, J.W., 1961, Regional gravity survey along the central and southern Wasatch Front, Utah: U.S. Geological Survey Professional Paper 316-E, p. 75–89.

Cook, K.L., Gray, E.F., Iverson, R.M., and Strohmeier, M.T., 1980, Bottom gravity meter regional survey of the Great Salt Lake, Utah, *in* J.W. Gwynn, editor, Great Salt Lake—a scientific, historical, and economic overview: Utah Geological and Mineral Survey Bulletin 116, p. 125–143.

Cress, L.D., 1983, Late Quaternary faulting and earthquake hazard in Curlew Valley, southern Oneida County, Idaho, and northern Box Elder County, Utah [abs.]: Geological Society of America Abstracts with Programs, v. 15, p. 376.

Crone, A.J., editor, 1983a, Paleoseismicity along the Wasatch Front and adjacent areas, central Utah, *in* Gurgel, K.D., editor, Geologic excursions in neotectonics and engineering geology in Utah, Guidebook—Part IV: Utah Geological and Mineral Survey Special Studies 62, p. 1–45.

Crone, A.J., 1983b, Amount of displacement and estimated age of a Holocene surface faulting event, eastern Great Basin, Millard County, Utah, *in* Crone, A.J., editor, Paleoseismicity along the Wasatch Front and adjacent areas, central Utah, *in* Gurgel, K.D., editor, Geologic excursions in neotectonics and engineering geology in Utah, Guidebook—Part IV: Utah Geological and Mineral Survey Special Studies 62, p. 49–55.

Crone, A.J. and Haller, K.M., 1991, Segmentation and the coseismic behavior of Basin and Range normal faults—examples from east-central Idaho and southwestern Montana, U.S.A.: Journal of Structural Geology, v. 13, p. 151–164.

Crone, A.J., Machette, M.N., Bonilla, M.G., Lienkaemper, J.J., Pierce, K.L., Scott, W.E., and Bucknam, R.C., 1987, Surface faulting accompanying the Borah Peak earthquake and segmentation of the Lost River fault, central Idaho: Bulletin of the Seismological Society of America, v. 77, p. 739–770.

Crone, A.J., Personius, S.F., DuRoss, C.B., Machette, M.N., and Mahan, S.A., 2014, History of late Holocene earthquakes at Willow Creek site and on the Nephi segment, Wasatch fault zone, Utah—Paleoseismology of Utah, Volume 25: Utah Geological Survey Special Study 151, 55 p., CD.

dePolo, C.M., 1994, The maximum background earthquake for the Basin and Range Province, western North America: Bulletin of the Seismological Society of America, v. 84, p. 466–472.

dePolo, C.M., Clark, D.G., Slemmons, D.B., and Aymard, W.H., 1989, Historical Basin and Range Province surface faulting and fault segmentation, *in* Schwartz, D.P., and Sibson, R.H., editors, Fault Segmentation and Controls of Rupture Initiation and Termination, Proceedings of Workshop XLV: U.S. Geological Survey Open-File Report 89-315, p. 131–162.

Dinter, D.A., and Pechmann, J.C., 1999, Multiple Holocene earthquakes on the East Great Salt Lake fault, Utah—Evidence from high-resolution seismic reflection data: Eos, Transactions of the American Geophysical Union, v. 80, p. F734.

Dinter, D.A., and Pechmann, J.C., 2000, Paleoseismology of the East Great Salt Lake fault: Final Technical Report to the U.S. Geological Survey National Earthquake Hazards Reduction Program, Award No. 98HQGR1013, 6 p.

Dinter, D.A., and Pechmann, J.C., 2005, Segmentation and Holocene displacement history of the Great Salt Lake fault, Utah, *in* Lund, W.R., editor, Basin and Range Province Seismic Hazards Summit II: Utah Geological Survey Miscellaneous Publication 05-2, p. 82–86, CD.

Dinter, D.A., and Pechmann, J.C., 2012, Paleoseismology of active normal faults submerged beneath the Great Salt Lake, Utah: AEG News (Association of Environmental and Engineering Geologists), v. 55, p. 52–53.

Doser, D.I., 1985, Source parameters and faulting processes of the 1959 Hebgen Lake, Montana, earthquake sequence: Journal of Geophysical Research, v. 90, p. 4537–4555.

Doser, D.I., 1989, Extensional tectonics in northern Utah–southern Idaho, U.S.A., and the 1934 Hansel Valley sequence: Physics of the Earth and Planetary Interiors, v. 54, p. 120–134.

Doser, D.I., and Smith, R.B., 1985, Source parameters of the 28 October 1983 Borah Peak, Idaho, earthquake from body wave analysis: Bulletin of the Seismological Society of America, v. 75, p. 1041–1051.

Doser, D.I. and Smith, R.B., 1989, An assessment of source parameters of earthquakes in the Cordillera of the western United States: Bulletin of the Seismological Society of America, v. 79, p. 1383–1409.

DuRoss, C.B., 2008, Holocene vertical displacement on the central segments of the Wasatch fault zone; Utah: Bulletin of the Seismological Society of America, v. 98, p. 2918–2933.

DuRoss, C.B., 2014, Paleoseismic investigation to determine the mid-Holocene chronology of surface-faulting earthquakes on the Nephi segment of the Wasatch fault zone, Utah and Juab Counties, Utah: Final Technical Report to the U.S. Geological Survey, National Earthquake Hazards Reduction Program, award no. G12AP20076, 48 p., 2 plates.

DuRoss, C.B., and Hylland, M.D., 2014, Evaluating surface faulting chronologies of graben-bounding faults in Salt Lake Valley, Utah—new paleoseismic data from the Salt Lake City segment of the Wasatch fault zone and the West Valley fault zone—Paleoseismology of Utah, Volume 24: Utah Geological Survey Special Study 149, 76 p., 14 appendices, 2 plates, CD.

DuRoss, C.B., and Hylland, M.D., 2015, Synchronous ruptures along a major graben-forming fault system—Wasatch and West Valley fault zones, Utah, USA: Bulletin of the Seismological Society of America, v. 105, p. 14–37.

DuRoss, C.B., Hylland, M.D., McDonald, G.N., Crone, A.J., Personius, S.F., Gold, R.D., and Mahan, S.A., 2014, Holocene and latest Pleistocene paleoseismology of the Salt Lake City segment of the Wasatch fault zone, Utah, at the Penrose Drive trench site, *in* DuRoss, C.B., and Hylland, M.D., Evaluating surface faulting chronologies of graben-bounding faults in Salt Lake Valley, Utah—new paleoseismic data from the Salt Lake City segment of the Wasatch fault zone and the West Valley fault zone—Paleoseismology of Utah, Volume 24: Utah Geological Survey Special Study 149, p. 1–39, 6 appendices, 1 plate, CD.

DuRoss, C.B., McDonald, G., and Lund, W.R., 2008, Paleoseismic investigation of the northern strand of the Nephi segment of the Wasatch fault zone at Santaquin, Utah—Paleoseismology of Utah, Volume 17: Utah Geological Survey Special Study 124, 30 p., 1 plate, CD.

DuRoss, C.B., Personius, S.F., Crone, A.J., McDonald, G.N., and Briggs, R., 2012, Late Holocene earthquake history of the Brigham City segment of the Wasatch fault zone at the Hansen Canyon, Kotter Canyon, and Pearsons Canyon trench sites, Box Elder County, Utah—Paleoseismology of Utah, Volume 22: Utah Geological Survey Special Study 142, 28 p., 3 plates, 5 appendices.

DuRoss, C.B., Personius, S.F., Crone, A.J., McDonald, G.N., and Lidke, D.J., 2009, Paleoseismic investigation of the northern Weber segment of the Wasatch fault zone at the Rice Creek trench site, North Ogden, Utah—Paleoseismology of Utah, Volume 18: Utah Geological Survey Special Study 130, 37 p., 2 plates, CD.

DuRoss, C.B., Personius, S.F., Crone, A.J., Olig, S.S., Hylland, M.D., Lund, W.R., and Schwartz, D.P., 2016, Fault segmentation—new concepts from the Wasatch fault zone, Utah, USA: Journal of Geophysical Research – Solid Earth, , v. 121, 27 p., doi: 10.1002/2015JB012519.

DuRoss, C.B., Personius, S.F., Crone, A.J., Olig, S.S., and Lund, W.R., 2011, Integration of paleoseismic data from multiple sites to develop an objective earthquake chronology—application to the Weber segment of the Wasatch fault zone: Bulletin of the Seismological Society of America, v. 101, p. 2765–2781.

Earthquake Engineering Research Institute, 2015, Scenario for a magnitude 7.0 earthquake on the Wasatch fault—Salt Lake City segment: Salt Lake City, Earthquake Engineering Research Institute, Utah Chapter, 53 p.

Electric Power Research Institute (EPRI), U.S. Department of Energy (DOE), and U.S. Nuclear Regulatory Commission (NRC), 2012, Technical report—Central and Eastern United States seismic source characterization for nuclear facilities, v. 1: Palo Alto, California, http://www.ceus-ssc.com/index.htm.

Elliott, A.J., Oskin, M.E., Liu-Zeng, J., and Shao, Y., 2015, Rupture termination at restraining bends—the last great earthquake on the Altyn Tagh fault: Geophysical Research Letters, v. 42, no. 7, p. 2164–2170, doi:10.1002/2015GL063107.

Ellsworth, W.L., Matthews, M.V., Nadeau, R.M., Nishenko, S.P., Reasenberg, P.A., and Simpson, R.W., 1999, A physically-based earthquake recurrence model for estimation of long-term earthquake probabilities: U.S. Geological Survey Open-File Report 99-522, 22 p.

Evans, J.P., 1991, Structural setting of seismicity in northern Utah: Utah Geological Survey Contract Report 91-5, 37 p.

Evans, J.P., and McCalpin, J.P., 2012, Determination of paleoearthquake timing and magnitudes on the southern segment of the East Cache fault, Utah: GEO-HAZ Consulting, Inc., Final Technical Report to the U.S. Geological Survey, National Earthquake Hazards Reduction Program, Award No. 07HQGR0079, 54 p.

Evans, J.P., and Oaks, R.Q., Jr., 1996, Three-dimensional variations in extensional fault shape and basin form—the Cache Valley basin, eastern Basin and Range Province, United States: Geological Society of America Bulletin, v. 108, p. 1580–1593.

Everitt, B.L., 1995, Activity classification of the Saleratus Creek fault: Utah Division of Water Resources memorandum dated January 3, 1995 to Dennis Strong, 5 p. plus figures.

Everitt, B.L., and Kaliser, B.N., 1980, Geology for assessment of seismic risk in the Tooele and Rush Valleys, Tooele County, Utah: Utah Geological and Mineral Survey Special Studies 51, 33 p.

Felzer, K.R., 2007, Calculating California seismicity rates—Appendix I *in* Working Group on California Earthquake Probabilities, The Uniform California Earthquake Rupture Forecast, Version 2 (UCERF2): U.S. Geological Survey Open-File Report 2007-1437I, and California Geological Survey Special Report 203-I.

Field, E.H., Biasi, G.P., Bird, P., Dawson, T.E., Felzer, K.R., Jackson, D.D., Johnson, K.M., Jordan, T.H., Madden, C., Michael, A.J., Milner, K.R., Page, M.T., Parsons, T., Powers, P.M., Shaw, B.E., Thatcher, W.R., Weldon, R.J., II, and Zeng, Y., 2013, Uniform California earthquake rupture forecast, version 3 (UCERF3)—the time-independent model: U.S. Geological Survey Open-File Report 2013–1165, California Geological Survey Special Report 228, and Southern California Earthquake Center Publication 1792, 97 p., http://pubs.usgs.gov/of/2013/1165/.

Field, E.H., Dawson, T.E., Felzer, K.R., Frankel, A.D., Gupta, V., Jordan, T.H., Parsons, T., Petersen, M.D., Stein, R.S., Weldon II, R.J., and Wills, C.J., 2009, Uniform California Earthquake Ruputre Forecast, Version 2 (UCERF2): Bulletin of the Seismological Society of America, v. 99, p. 2053–2107.

Foley, L.L., Martin, R.A., Jr., and Sullivan, J.T., 1986, Seismotectonic study for Joes Valley, Scofield, and Huntington North Dams, Emery County and Scofield Projects,

Utah: U.S. Bureau of Reclamation Seismotectonic Report 86-7, 132 p., 3 plates.

Fong, A.W., 1995, Geologic map of the Fountain Green South quadrangle, Sanpete and Juab Counties, Utah: Utah Geological Survey Miscellaneous Publication MP-95-1, 18 p., 2 plates, scale 1:24,000.

Forman, S.L., Machette, M.N., Jackson, M.E., and Maat, P., 1989, An evaluation of thermoluminescence dating of paleoearthquakes on the American Fork segment, Wasatch fault zone, Utah: Journal of Geophysical Research, v. 94, p. 1622–1630.

Forman, S.L., Nelson, A.R., and McCalpin, J.P., 1991, Thermoluminescence dating of fault-scarp-derived colluvium—deciphering the timing of earthquakes on the Weber segment of the Wasatch fault zone, north-central Utah: Journal of Geophysical Research, v. 96, p. 595–605.

Frankel, A., Peterson, M., Mueller, C., Haller, K., Wheeler, R., Leyendecker, E., Wesson, R., Harmsen, S., Cramer, C., Perkins, D., and Rukstales, K., 2002, Documentation for the 2002 update of the National Seismic Hazard Maps: U.S. Geological Survey Open-File Report 02-420, 33 p.

Friedrich, A.M., Wernicke, B.P., Niemi, N.A., Bennett, R.A., and Davis, J.L., 2003, Comparison of geodetic and geologic data from the Wasatch region, Utah, and implications for the spectral character of Earth deformation at periods of 10 to 10 million years: Journal of Geophysical Research, v. 108, no. B4, 23 p.

Gardner, J.K., and Knopoff, L., 1974, Is the sequence of earthquakes in southern California, with aftershocks removed, Poissonian?: Bulletin of the Seismological Society of America, v. 64, p. 1363–1367.

Geomatrix Consultants, Inc., 1999, Fault evaluation study and seismic-hazard assessment, Private Fuel Storage Facility, Skull Valley, Utah: Unpublished report prepared for Stone & Webster Engineering Corp., three volumes, variously paginated.

Gilbert, G. K., 1890, Lake Bonneville, U. S. Geological Survey Monograph 1, 438 p.

Gilluly, J., 1928, Basin-Range faulting along the Oquirrh Range, Utah: Bulletin of the Geological Society of America, v. 39, p. 1103–1130.

Gilluly, J., 1932, Geology and ore deposits of the Stockton and Fairfield quadrangles, Utah: U.S. Geological Survey Professional Paper 173, 171 p.

Godsey, H.S., Currey, D.R., and Chan, M.A., 2005, New evidence for an extended occupation of the Provo shoreline and implications for regional climate change, Pleistocene Lake Bonneville, Utah, USA: Quaternary Research, v. 63, p. 212–223.

Godsey, H.S., Oviatt, C.G., Miller, D.M., and Chan, M.A., 2011, Stratigraphy and chronology of offshore to nearshore deposits associated with the Provo shoreline, Pleistocene Lake Bonneville, Utah: Palaeogeography, Palaeoclimatology, Palaeoecology, v. 310, p. 442–450.

Goode, H.D., 1959, Surficial deposits, geomorphology, and Cenozoic history of the Eureka quadrangle, Utah: Boulder, University of Colorado, Ph.D. dissertation, 120 p.

Grünthal, G., Mayer-Rosa, D., and Lenhardt, W., 1998, Abschätzung der Erdbebengefährdung für die D-A-CH-Staaten—Deutschland, Österreich, Schweitz [Estimation of seismic hazard for the DA-CH countries—Germany, Austria, Switzerland]: Bautechnik, v. 75, p. 753–767.

Hakimhashemi, A.H., and Grünthal, G., 2012, A statistical method for estimating catalog completeness applicable to long-term nonstationary seismic data: Bulletin of the Seismological Society of America, v. 102, p. 2530–2546.

Haller, K.M., and Harmsen, S.C., 2011, Toward a geologically consistent seismogenic-source model for graben-bounding faults [abs.]: American Geophysical Union, abstract no. S11C-03.

Haller, K.M., and Lewis, R.S., compilers, 2004, Fault number 2351a, Wasatch fault zone, Malad City section, *in* Quaternary Fault and Fold Database of the United States: U.S. Geological Survey website, http://earthquakes.usgs.gov/regional/qfaults.

Haller, K.M., and Wheeler, R.L., 2008, Parameters for faults in the Intermountain West, *in* Petersen, M.D., Frankel, A.D., Harmsen, S.C., Mueller, C.S., Haller, K.M., Wheeler, R.L., Wesson, R.L., Zeng, Y., Boyd, O.S., Perkins, D.M., Luco, N., Field, E.H., Wills, C.J., and Rukstales, K.S., Documentation for the 2008 update of the National Seismic Hazard Maps: U.S. Geological Survey Open-File Report 2008-1128, p. G-1–G-18.

Hammond, W.C., and Thatcher, W., 2004, Contemporary tectonic deformation of the Basin and Range Province, western United States—10 years of observation with the Global Positioning System: Journal of Geophysical Research, v. 109, B08403, 21 p.

Handwerger, D.A., Cerling, T.E., and Bruhn, R.L., 1999, Cosmogenic 14C in carbonate rocks: Geomorphology, v. 27, p. 13–24.

Hanks, T.C., and Kanamori, H., 1979, A moment magnitude scale: Journal of Geophysical Research, v. 84, p. 2348–2350.

Hanson, K.L., Swan, F.H., and Schwartz, D.P., 1981, Study of earthquake recurrence intervals on the Wasatch fault, Utah: San Francisco, California, Woodward-Clyde Consultants, sixth annual technical report prepared for U.S. Geological Survey under contract no. 14-08-0001-19115, 22 p., also available in Utah Geological Survey Miscellaneous Publication 13-3.

Hanson, K.L., Swan, F.H., and Schwartz, D.P., 1982, Study of earthquake recurrence intervals on the Wasatch fault, Utah: San Francisco, California, Woodward-Clyde Consultants, seventh annual technical report prepared for U.S. Geological Survey under contract no. 14-08-0001-

19842, 10 p., also available in Utah Geological Survey Miscellaneous Publication 13-3.

Hecker, S., 1993, Quaternary tectonics of Utah with emphasis on earthquake-hazard characterization: Utah Geological Survey Bulletin 127, 157 p., scale 1:500,000.

Hecker, S., Abrahamson, N.A., and Wooddell, K.E., 2013, Variability of displacement at a point—implications for earthquake-size distribution and rupture hazard on faults: Bulletin of the Seismological Society of America, v. 103, p. 651–674.

Helm, J.M., 1994, Structure and tectonic geomorphology of the Stansbury fault zone, Tooele County, Utah, and the effect of crustal structure on Cenozoic faulting patterns: Salt Lake City, University of Utah, M.S. thesis, 128 p.

Helm, J.M. 1995, Quaternary faulting in the Stansbury fault zone, Tooele County, Utah, *in* Lund, W.R., editor, Environmental and Engineering Geology of the Wasatch Front Region: Utah Geological Association Publication 24, p. 31–44.

Hemphill-Haley, M.A., and Weldon, R.J., 1999, Estimating prehistoric earthquake magnitude from point measurements of surface rupture: Bulletin of the Seismological Society of America, v. 89, p. 1264–1279.

Hintze, L.H., and Davis, F.D., 2003, Geology of Millard County, Utah: Utah Geological Survey Bulletin 133, 303 p.

Hoover, J.D., 1974, Periodic Quaternary volcanism in the Black Rock Desert, Utah: Brigham Young University Geology Studies, v. 21, p. 3–72.

Hylland, M.D., 2007a, Surficial-geologic reconnaissance and scarp profiling on the Collinston and Clarkston Mountain segments of the Wasatch fault zone, Box Elder County, Utah—paleoseismic inferences, implications for adjacent segments, and issues for diffusion-equation scarp-age modeling—Paleoseismology of Utah, Volume 15: Utah Geological Survey Special Study 121, 18 p., CD.

Hylland, M.D., 2007b, Spatial and temporal patterns of surface faulting on the Levan and Fayette segments of the Wasatch fault zone, central Utah, from surficial geologic mapping and scarp profile data, *in* Willis, G.C., Hylland, M.D., Clark, D.L., and Chidsey, T.C., Jr., editors, Central Utah—diverse geology of a dynamic landscape: Utah Geological Association Publication 36, p. 255–271.

Hylland, M.D., DuRoss, C.B., McDonald, G.N., Olig, S.S., Oviatt, C.G., Mahan, S.A., Crone, A.J., and Personius, S.F., 2014, Late Quaternary paleoseismology of the West Valley fault zone—insights from the Baileys Lake trench site, *in* DuRoss, C.B., and Hylland, M.D., Evaluating surface faulting chronologies of graben-bounding faults in Salt Lake Valley, Utah—new paleoseismic data from the Salt Lake City segment of the Wasatch fault zone and the West Valley fault zone—Paleoseismology of Utah, Volume 24: Utah Geological Survey Special Study 149, p. 41–76, 8 appendices, 1 plate, CD.

Hylland, M.D., and Machette, M.N., 2008, Surficial geologic map of the Levan and Fayette segments of the Wasatch fault zone, Juab and Sanpete Counties, Utah: Utah Geological Survey Map 229, 37 p., 1 plate, scale 1:50,000.

Jackson, M., 1991, Number and timing of Holocene paleoseismic events on the Nephi and Levan segments, Wasatch fault zone, Utah—Paleoseismology of Utah, Volume 3: Utah Geological Survey Special Study 78, 23 p.

Jackson, J.A. and White, N.J., 1989, Normal faulting in the upper continental crust—observations from regions of active extension: Journal of Structural Geology, v. 11, p. 15–36.

Janecke, S.U., and Oaks, R.Q., Jr., 2011, Reinterpreted history of latest Pleistocene Lake Bonneville—geologic setting of threshold failure, Bonneville flood, deltas of the Bear River, and outlets for two Provo shorelines, southeastern Idaho, USA, *in* Lee, J., and Evans, J.P., editors, Geologic field trips to the Basin and Range, Rocky Mountains, Snake River Plain, and terranes of the U.S. Cordillera: Geological Society of America Field Guide 21, p. 195–222.

Kagan, Y.Y., 2002, Modern California earthquake catalogs and their comparison: Seismological Research Letters, v. 73, p. 921–929.

Kagan, Y.Y., 2003, Accuracy of modern global earthquake catalogs: Physics of the Earth and Planetary Interiors, v. 135, p. 173–209.

Keaton, J.R., Currey, D.R., and Olig, S.J., 1993, Paleoseismicity and earthquake hazards evaluation of the West Valley fault zone, Salt Lake City urban area: Utah Geological Survey Contract Report 93-8, 55 p.

Keefer, D.L., and Bodily, S.E., 1983, Three-point approximations for continuous random, variables: Management Science, v. 29, no. 5, p. 595–609.

Klinger, Y., Etchebes, M., Tapponnier, P., and Narteau, C., 2011, Characteristic slip for five great earthquakes along the Fuyun fault in China: Nature Geoscience, v. 4, p. 389–392.

Kostrov, V.V., 1974, Seismic moment and energy of earthquakes, and seismic flow of rock: Izvestiya, Earth Physics, v. 1, p. 23–40.

Leonard, M., 2010, Earthquake fault scaling—self-consistent relating of rupture length, width, average displacement and moment release: Bulletin of the Seismological Society of America, v. 100, p. 1971–1988.

Lienkaemper, J.J., and Bronk Ramsey, C., 2009, OxCal—versatile tool for developing paleoearthquake chronologies—a primer: Seismological Research Letters, v. 80, p. 431–434.

Lifton, N., Caffee, M., Finkel, R., Marrero, S., Nishiizumi, K., Phillips, F.M., Goehring, B., Gosse, J., Stone, J., Schaefer, J., Theriault, B., Jull, A.J.T., and Fifield,

K., 2015, *In situ* cosmogenic nuclide production rate calibration for the CRONUS-Earth project from Lake Bonneville, Utah, shoreline features: Quaternary Geochronology, v. 26, p. 56–69.

Lolli, B., and Gasperini, P., 2012, A comparison among general orthogonal regression methods applied to earthquake magnitude conversions: Geophysical Journal International, v. 190, p. 1135–1151.

Long, S.P., Link, P.K., Janecke, S.U., Perkins, M.E., and Fanning, C.M., 2006, Multiple phases of Tertiary extension and synextensional deposition of the Miocene-Pliocene Salt Lake Formation in an evolving supradetachment basin, Malad Range, southeast Idaho, U.S.A.: Rocky Mountain Geology, v. 41, p. 1–27.

Long, S.P., Link, P.K., Janecke, S.U., and Rodgers, D.W., 2004, Geologic map of the Henderson Creek quadrangle, Oneida County, Idaho: Idaho Geological Survey Technical Report 04-3, 1 sheet, scale 1:24,000.

Lowry, A.R., and Perez-Gussinye, M., 2011, The role of crustal quartz in controlling Cordilleran deformation, Nature, v. 471, p. 353–357.

Lund, W.R., 2005, Consensus preferred recurrence interval and vertical slip rate estimates—review of Utah paleoseismic-trenching data by the Utah Quaternary Fault Parameters Working Group: Utah Geological Survey Bulletin 134, 109 p., CD.

Lund, W.R., editor, 2006, Basin and Range Province Earthquake Working Group seismic-hazard recommendations to the U.S. Geological Survey National Seismic Hazard Mapping Program: Utah Geological Survey Open-File Report 477, 23 p.

Lund, W.R., editor, 2012, Basin and Range Province Working Group II—recommendations to the U.S. Geological Survey National Seismic Hazard Mapping Program for the 2014 update of the National Seismic Hazard Maps: Utah Geological Survey Open-File Report 591, 17 p.

Lund, W.R., and Black, B.D., 1998, Paleoseismic investigation at Rock Canyon, Provo segment, Wasatch fault zone, Utah County, Utah—Paleoseismology of Utah, Volume 8: Utah Geological and Mineral Survey Special Study 93, 22 p.

Lund W.R., Schwartz, D.P., Mulvey, W.E., Budding, K.E., and Black, B.D., 1991, Fault behavior and earthquake recurrence on the Provo segment of the Wasatch fault zone at Mapleton, Utah County, Utah—Paleoseismology of Utah, Volume 1: Utah Geological and Mineral Survey Special Study 75, 41 p.

Machette, M.N., Crone, A.J., Personius, S.F., Dart, R.L., Lidke, D.J., Mahan, S.A., and Olig, S.S., 2007, Paleoseismology of the Nephi segment of the Wasatch fault zone, Juab County, Utah—preliminary results from two large exploratory trenches at Willow Creek: U.S. Geological Survey Scientific Investigations Map SI-2966, 2 plates.

Machette, M.N., Personius, S.F., and Nelson, A.R., 1992, Paleoseismology of the Wasatch fault zone—a summary of recent investigations, conclusions, and interpretations, *in* Gori, P.L., and Hays, W.W., editors, Assessment of regional earthquake hazard and risk along the Wasatch Front, Utah: U.S. Geological Survey Professional Paper 1500A, p. A1–A71.

Machette, M.N., Personius, S.F., Nelson, A.R., Schwartz, D.P., and Lund, W.R., 1991, The Wasatch fault zone, Utah—segmentation and history of Holocene earthquakes: Journal of Structural Geology, v. 13, p. 137–149.

Mason, D.B., 1996, Earthquake magnitude potential of the Intermountain Seismic Belt, USA, from surface-parameter scaling of late Quaternary faults: Bulletin of the Seismological Society of America, v. 86, p. 1487–1506.

Matthews, M.V., Ellsworth, W.L., and Reasenberg, P.A., 2002, A Brownian model for recurrent earthquakes: Bulletin of the Seismological Society of America, v. 92, p. 2233–2250.

Mattson, A., and Bruhn, R.L., 2001, Slip-rate estimates for undated fault scarps along the Wasatch fault zone and the west flank of the Oquirrh Mountains: Journal of Geophysical Research, v. 106, p. 13,739–13,750.

McBride, J.H., Nelson, S.T., Heiner, B.D., Tingey, D.G., Morris, T.H., and Rey, K.A., 2015, Neotectonics of the Sevier Desert basin, Utah, as seen through the lens of multi-scale investigations: Tectonophysics, v. 654, p. 131–155.

McBride, J.H., Stephenson, W.J., and McBride, E.I.P., 2010, Reanalysis of the COCORP Utah Line 1 deep seismic reflection profile—toward an improved understanding of the Sevier Desert detachment question: Geosphere, v. 6, p. 840–854.

McCaffrey, R., Bird, P., Bormann, J., Haller, K.M., Hammond, W.H., Thatcher, W., Wells, R.E., and Zeng, Y., 2014, Appendix A—NSHMP block model of western United States active tectonics, *in* Petersen, M.D., Zeng, Y., Haller, K.M., McCaffrey, R., Hammond, W.C., Bird, P., Moschetti, M., Shen, Z., Bormann, J., and Thatcher, W., Geodesy- and geology-based slip-rate models for the western United States (excluding California) National Seismic Hazard Maps: U.S. Geological Survey Open-File Report 2013-1293, p. 26–37, http://dx.doi.org/10.3133/ofr20131293.

McCalpin, J., 1985, Quaternary fault history and earthquake potential of the Hansel Valley area, north-central Utah: Final Technical Report to U.S. Geological Survey, contract no. 14-08-001-21899, 37 p.

McCalpin, J.P., 1989, Surficial geologic map of the East Cache fault zone, Cache County, Utah: U.S. Geological Survey Miscellaneous Field Studies Map MF-2107, 1 sheet, scale 1:50,000.

McCalpin, J.P., 1990, Latest Quaternary faulting in the northern Wasatch to Teton corridor (NWTC): Technical re-

port to U.S. Geological Survey, contract no. 14-08-001-G1396, October 1990, 42 p.

McCalpin, J.P., 1993, Neotectonics of the northeastern Basin and Range margin, western USA: Zeitschrift fur Geomophologie N. Folge, v. 94, p. 137–157.

McCalpin, J.P, 1994, Neotectonic deformation along the East Cache fault zone, Cache County, Utah—Paleoseismology of Utah, Volume 5: Utah Geological Survey Special Study 83, 37 p.

McCalpin, J.P., 2002, Post-Bonneville paleoearthquake chronology of the Salt Lake City segment, Wasatch fault zone, from the 1999 "Megatrench" site—Paleoseismology of Utah, Volume 10: Utah Geological Survey Miscellaneous Publication 02-7, 37 p.

McCalpin, J.P., 2003, Neotectonics of the Bear Lake Valley, Utah and Idaho; A preliminary assessment: Utah Geological Survey Miscellaneous Publication 03-4, 43 p.

McCalpin, J.P. and Evans, J.P., 2012, Determination of paleoearthquake timing and magnitude on the southern segment of the East Cache fault, Utah: Final Technical Report to the U.S. Geological Survey National Earthquake Hazards Reduction Program, contract 07HQGR0079, 54 p.

McCalpin, J.P., and Forman, S.L., 1991, Late Quaternary faulting and thermoluminescence dating of the East Cache fault zone, north-central Utah: Bulletin of the Seismological Society of America, v. 81, p. 139–161.

McCalpin, J.P., and Forman, S.L., 2002, Post-Provo earthquake chronology of the Brigham City segment, Wasatch fault zone, Utah—Paleoseismology of Utah, Volume 11: Utah Geological Survey Miscellaneous Publication 02-9, 46 p.

McCalpin, J.P., Forman, S.L., and Lowe, M., 1994, Reevaluation of Holocene faulting at the Kaysville site, Weber segment of the Wasatch fault zone, Utah: Tectonics, v. 13, p. 1–16.

McCalpin, J.P., and Nishenko, S.P., 1996, Holocene paleoseismicity, temporal clustering, and probabilities of future large (M > 7) earthquakes on the Wasatch fault zone, Utah: Journal of Geophysical Research, v. 101, p. 6233–6253.

McCalpin, J.P., Robison, R.M., and Garr, J.D., 1992, Neotectonics of the Hansel Valley–Pocatello Valley corridor, northern Utah and southern Idaho, *in* Gori, P.L., and Hays, W.W., editors, Assessment of regional earthquake hazards and risk along the Wasatch Front, Utah: U.S. Geological Survey Professional Paper 1500, p. G1–G18.

McCalpin, J.P., and Warren, G.A., 1992, Quaternary faulting on the Rock Creek fault, overthrust belt, Wyoming [abs.]: Geological Society of America Abstracts with Programs, v. 24, p. 51.

McDonald, R.E., 1976, Tertiary tectonics and sedimentary rocks along the transition—Basin and Range Province to plateau and thrust belt province, Utah, *in* Hill, J.G., editor, Geology of the Cordilleran Hingeline: Denver, Colorado, Rocky Mountain Association of Geologists, p. 281–317.

McGuire, R.K., 2004, Seismic hazard and risk analysis: Earthquake Engineering Research Institute, MNO-10, 221 p.

Mikulich, M.J., and Smith, R.B., 1974, Seismic-reflection and aeromagnetic surveys of the Great Salt Lake, Utah, *in* Seismic-reflection and aeromagnetic surveys of the Great Salt Lake, Utah: Geological Society of America Bulletin, p. 991–1002, 1 plate.

Miller, A.C., and Rice, T.R., 1983, Discrete approximations of probability distributions: Management Science, v. 29, p. 352–362.

Miller, D.M., Oviatt, C.G., and McGeehin, J.P., 2013, Stratigraphy and chronology of Provo shoreline deposits and lake-level implications, late Pleistocene Lake Bonneville, eastern Great Basin, USA: Boreas, v. 42, p. 342–361.

Mohapatra, G.K., and Johnson, R.A., 1998, Localization of listric faults at thrust ramps beneath the Great Salt Lake Basin, Utah—evidence from seismic imaging and finite element modeling: Journal of Geophysical Research, v. 103, p. 10,047–10,063.

Molnar, P., 1979, Earthquake recurrence intervals and plate tectonics: Bulletin of the Seismological Society of America, v. 69, p. 115–133.

Moore, W.J., and Sorensen, M.L. 1979, Geologic map of the Tooele 1° x 2° Quadrangle, Utah: U.S. Geological Survey Miscellaneous Investigation Series Map I-1132, scale 1:250,000.

Morris, H.T., 1975, Geologic map and sections of the Tintic Mountain quadrangle and adjacent part of the McIntyre quadrangle, Juab and Utah Counties: U.S. Geological Survey Miscellaneous Investigations Map I-883, scale 1:24,000.

Morris, H.T., 1987, Preliminary geologic map of the Delta 2° quadrangle, Tooele, Juab, Millard, and Utah Counties, Utah: U.S. Geological Survey Open-File Report 87-185, 18 p., scale 1:250,000.

Musson, R.M.W., 2012, The effect of magnitude uncertainty on earthquake activity rates: Bulletin of the Seismological Society of America, v. 102, p. 2771–2775.

National Aeronautics and Space Administration, 2012, Visible Earth—a catalog of NASA images and animations of our home planet—Nevada and Utah: Online, http://visibleearth.nasa.gov/view.php?id=55874.

Nelson, A.R., 1988, The northern part of the Weber segment of the Wasatch fault zone near Ogden, Utah, *in* Machette, M.N., editor, In the footsteps of G.K. Gilbert—Lake Bonneville and neotectonics of the eastern Basin and Range Province, Geological Society of America Guidebook for Field Trip Twelve, the Geological Society of America 100th Annual Meeting: Utah Geological and Mineral Survey Miscellaneous Publication 88-1, p. 33–37.

Nelson, A.R., Lowe, M., Personius, S., Bradley, L., Forman, S.L., Klauk, R., and Garr, J., 2006, Holocene earthquake history of the northern Weber segment of the Wasatch fault zone, Utah—Paleoseismology of Utah, Volume 13: Utah Geological Survey Miscellaneous Publication 05-8, 39 p., 2 plates, CD.

Nelson, A.R., and Martin, R.A., Jr., 1982, Seismotectonic study for Soldier Creek Dam, Central Utah Project: U.S. Bureau of Reclamation Seismotectonic Report 82-1, 115 p.

Nelson, A.R., and Sullivan, J.T., 1992, Late Quaternary history of the James Peak fault, southernmost Cache Valley, north-central Utah, *in* Gori, P.L. and Hays, W.W., editors, Assessment of regional earthquake hazards and risk along the Wasatch Front, Utah: U.S. Geological Survey Professional Paper 1500-J, 13 p.

Nelson, A.R., and Van Arsdale, R.B., 1986, Recurrent late Quaternary movement on the Strawberry normal fault, Basin and Range—Colorado Plateau transition zone, Utah: Neotectonics, v. 1, p. 7–37.

Niemi, N.A., Wernicke, B.P., Friedrich, A.M., Simons, M., Bennett, R.A., and Davis, J.L., 2004, BARGEN continuous GPS data across the eastern Basin and Range Province, and implications for fault system dynamics: Geophysical Journal International, v. 159, p. 842–862.

Nishenko, S.P., and Schwartz, D.P., 1990, Preliminary estimates of large earthquake probabilities along the Wasatch fault zone, Utah [abs.]: Eos American Geophysics Union Transactions, v. 71, p. 1448.

Olig, S.S., Gorton, A.E., Black, B.D., and Forman, S.L., 2001, Paleoseismology of the Mercur fault and segmentation of the Oquirrh-East Great Salt Lake fault zone, Utah: Final Technical Report to the U.S. Geological Survey National Earthquake Hazards Reduction Program, Award No. 98HQGR1036, variously paginated.

Olig, S.S., Gorton, A.E., and Chadwell, L.C., 1999a, Quaternary behavior along the southern Oquirrh fault zone, Utah [abs.]: Association of Engineering Geologists Program with Abstracts, p. 80.

Olig, S.S., Gorton, A.E., and Chadwell, L., 1999b, Mapping and Quaternary fault scarp analysis of the Mercur fault and West Eagle Hill faults, Wasatch Front, Utah: U.S. Geological Survey National Earthquake Hazards Reduction Program Final Technical Report, Reston, Virginia, Award no. 1434-HQ-97-GR-03154, variously paginated.

Olig, S.S., Lund, W.R., Black, B.D., 1994, Large mid-Holocene and late Pleistocene earthquakes on the Oquirrh fault zone: Journal of Geomorphology, v. 10, p. 285–315.

Olig, S.S., Lund, W.R., Black, B.D., and Mayes, B.H., 1996, Paleoseismic investigation of the Oquirrh fault zone, Tooele County, Utah, *in* Lund, W.R., editor, The Oquirrh fault zone, Tooele County, Utah—surficial geology and paleoseismicity—Paleoseismology of Utah, Volume 6: Utah Geological Survey Special Study 88, p. 18–64, 1 plate, scale 1:24,000.

Olig, S., McDonald, G., Black, B., DuRoss, C., and Lund, W., 2006, A longer and more complete paleoseismic record for the Provo segment of the Wasatch fault zone, Utah [abs.]: Seismological Research Letters, v. 77, p. 274.

Olig, S.S., McDonald, G.N., Black, B.D., DuRoss, C.B., Lund, W.R., Hylland, M.D., Simon, D.B., Giraud, R.E., and Christenson, G.E., 2011, Extending the paleoseismic record of the Provo segment of the Wasatch fault zone, Utah: Final Technical Report to the U.S. Geological Survey, National Earthquake Hazards Reduction Program, Award No. 02HQGR0109, variously paginated.

Olig, S., Thomas, P., and Wong, I., 2005, Time-dependent probabilistic seismic hazard analyses along the Wasatch Front, Utah and the need for longer paleoseismic records [abs.], *in* Lund, W.R., editor, Western States Seismic Policy Council, Proceedings Volume, Basin and Range Province Seismic-Hazards Summit: Utah Geological Survey Miscellaneous Publication 05-2, p. 39.

Otton, J.K., 1995, Western frontal fault of the Canyon Range—is it the breakaway zone of the Sevier Desert detachment?: Geology, v. 23, p. 547–550.

Oviatt, C.G., 1989, Quaternary geology of part of the Sevier Desert, Millard County, Utah: Utah Geological and Mineral Survey Special Studies 70, 41 p., 1 plate, scale 1:100,000.

Oviatt, C.G., 1991, Quaternary geology of the Black Rock Desert, Millard County, Utah: Utah Geological and Mineral Survey Special Studies 73, 23 p., 1 plate, scale 1:100,000.

Oviatt, C.G., 1997, Lake Bonneville fluctuations and global climate change: Geology, v. 25, p. 155–158.

Oviatt, C.G., 2015, Chronology of Lake Bonneville, 30,000 to 10,000 yr B.P.: Quaternary Science Reviews, v. 110, p. 166–171.

Oviatt, C.G., and Nash, W.P., 1989, Late Pleistocene basaltic ash and volcanic eruptions in the Bonneville basin, Utah: Geological Society of America Bulletin, v. 101, p. 292–303.

Pankow, K.L., Arabasz, W.J., and Burlacu, R., 2009, Seismicity and seismotectonic issues of western Utah, *in* Tripp, B.T., Krahulec, K., and Jordan, J.L., editors, Geology and geologic resource issues of western Utah: Utah Geological Association Publication 38, p. 1–15.

Payne, S.J., Zollweg, J.E., and Rodgers, D.W., 2004, Stress triggering of conjugate normal faulting—late aftershocks of the 1983 Ms 7.3 Borah Peak, Idaho, earthquake: Bulletin of the Seismological Society of America, v. 94, p. 828–844.

Pechmann, J.C., and Arabasz, W.J., 1995, The problem of the random earthquake in seismic hazard analysis—Wasatch Front region, Utah, *in* Lund, W.R., editor, Environmental and engineering geology of the Wasatch Front region: Utah Geological Association Publication 24, p. 77–93.

Personius, S.F., 1990, Surficial geologic map of the Brigham City segment and adjacent parts of the Weber and Collinston segments, Wasatch fault zone, Box Elder and Weber Counties, Utah: U.S. Geological Survey Miscellaneous Investigations Series Map I-1979, scale 1:50,000.

Personius, S.F., 1991a, Paleoseismic analysis of the Wasatch fault zone at the Brigham City trench site, Brigham City, Utah, *in* Personius, S.F., Paleoseismic analysis of the Wasatch fault zone at the Brigham City trench site, Brigham City and Pole Patch trench site, Pleasant View, Utah—Paleoseismology of Utah, Volume 2: Utah Geological and Mineral Survey Special Study 76, 39 p. 1–17.

Personius, S. F., 1991b, Paleoseismic analysis of the Wasatch fault zone at the Pole Patch trench site, Pleasant View, Utah, *in* Personius, S.F., Paleoseismic analysis of the Wasatch fault zone at the Brigham City trench site, Brigham City and Pole Patch trench site, Pleasant View, Utah—Paleoseismology of Utah, Volume 2: Utah Geological and Mineral Survey Special Study 76, p. 19–39.

Personius, S.F., DuRoss, C.B., and Crone, A.J., 2012, Holocene behavior of the Brigham City segment—implications for forecasting the next large-magnitude earthquake on the Wasatch fault zone, Utah, USA: Bulletin of the Seismological Society of America, v. 102, no. 6, p. 2265–2281.

Petersen, M.D., Cramer, C.H., Reichle, M.S., Frankel, A.D., and Hanks, T.C., 2000, Discrepancy between earthquake rates implied by historic earthquakes and a consensus geologic source model for California: Bulletin of the Seismological Society of America, v. 90, p. 1117–1132.

Petersen, M.D., Frankel, A.D., Harmsen, S.C., Mueller, C.S., Haller, K.M., Wheeler, R.L., Wesson, R.L., Zeng, Y., Boyd, O.S., Perkins, D.M., Luco, N., Field, E.H., Wills, C.J., and Rukstales, K.S., 2008, Documentation for the 2008 update of the United States National Seismic Hazard Maps: U.S. Geological Survey Open-File Report 2008-1128, 61 p.

Petersen, M.D., Zeng, Y., Haller, K.M., McCaffrey, R., Hammond, W.C., Bird, P., Moschetti, M., Shen, Z., Bormann, J., and Thatcher, W., 2014, Geodesy and geology-based slip-rate models for the western United States (excluding California); U.S. Geological Survey Open-File Report 2013-1293, 80 p.

Piety, L.A., Anderson, L.W., and Ostenna, D.A., 2010, Late Quaternary faulting in East Canyon Valley, northern Utah—Paleoseismology of Utah, Volume 19: Utah Geological Survey Miscellaneous Publication 10-5, 40 p., CD.

Planke, S., and Smith, R.B., 1991, Cenozoic extension and evolution of the Sevier Desert basin, Utah, from seismic reflection, gravity, and well log data: Tectonics, v. 10, p. 345–365.

Plate Boundary Observatory (PBO), 2011, Website, http://pbo.unavco.org/data/gps, accessed Aug. 11, 2011.

Pope, A.D., Blair, J.J., and Link, P.K., 2001, Geologic map of the Wakley Peak quadrangle, Bannock and Oneida Counties, Idaho: Idaho Geological Survey Technical Report 01-4, 1 sheet, scale 1:24,000.

Reheis, M.C., Adams, K.D., Oviatt, C.G., and Bacon, S.N., 2014, Pluvial lakes in the Great Basin of the Western United States—a view from the outcrop: Quaternary Science Reviews, v. 97, p. 33–57.

Reimer, P.J., Baillie, M.G.L., Bard, E., Bayliss, A., Beck, J.W., Blackwell, P.G., Ramsey, C.B., Buck, C.E., Burr, G.S., Edwards, R.L., Friedrich, M., Grootes, P.M., Guilderson, T.P., Hajdas, I., Heaton, T.J., Hogg, A.G., Hughen, K.A., Kaiser, K.F., Kromer, B., McCormac, F.G., Manning, S.W., Reimer, R.W., Richards, D.A., Southon, J.R., Talamo, S., Turney, C.S.M., van der Plicht, J., and Weyhenmeyer, C.E., 2009, IntCal09 and Marine09 radiocarbon age calibration curves, 0-50,000 years cal BP: Radiocarbon, v. 51, p. 1111–1150.

Richins, W.D., Pechmann, J.C., Smith, R.B., Langer, C.J., Goter, S.K., Zollweg, J.E., and King, J.J., 1987, The 1983 Borah Peak, Idaho, earthquake and its aftershocks: Bulletin of the Seismological Society of America, v. 77, p. 694–723.

Romney, C., 1957, Seismic waves from the Dixie Valley–Fairview Peak earthquakes: Bulletin of the Seismological Society of America, v. 47, p. 301–319.

Ryall, A., 1962, The Hebgen Lake, Montana, earthquake of August 18, 1959—P waves: Bulletin of the Seismological Society of America: v. 52, p. 235–271.

Scharer, K., Weldon, R., II, Streig, A., and Fumal, T., 2014, Paleoearthquakes at Frazier Mountain, California delimit extent and frequency of past San Andreas Fault ruptures along 1857 trace: Geophysical Research Letters, v. 41, p. 4527–4534.

Schelling, D.D., Strickland, D.K., Johnson, K.R., and Vrona, J.P., 2007, Structural geology of the central Utah thrust belt, *in* Willis, G.C., Hylland, M.D., Clark, D.L., and Chidsey, T.C., Jr., editors, Central Utah—diverse geology of a dynamic landscape: Utah Geological Association Publication 36, p. 1–29.

Schwartz, D.P., 1988, Geologic characterization of seismic sources—moving into the 1990's, *in* Von Thun, L., editor, Earthquake Engineering and Soil Dynamics II—recent advances in ground motion evaluation: American Society of Civil Engineers Special Geotechnical Publication 20, p. 1–42.

Schwartz, D.P., 1989, Paleoseismicity, persistence of segments, and temporal clustering of large earthquakes—examples from the San Andreas, Wasatch, and Lost River fault zones: U.S. Geological Survey Open File Report 89-315, p. 361–375

Schwartz, D.P., and Coppersmith, K.J., 1984, Fault behavior and characteristic earthquakes—examples from the

Wasatch and San Andreas fault zones: Journal of Geophysical Research, v. 89, p. 5681–5698.

Schwartz, D.P., and Coppersmith, K.J., 1986, Seismic hazards—new trends in analysis using geologic data: Washington, D.C., National Academy Press, Studies in Geophysics, Active Tectonics, p. 80–94.

Schwartz, D.P., Haeussler, P.J., Seitz, G.G., and Dawson, T.E., 2012, Why the 2002 Denali fault rupture propagated onto the Totschunda fault—implications for fault branching and seismic hazards: Journal of Geophysical Research, v. 117, B11304, doi:10.1029/2011JB008918.

Schwartz, D.P., and Lund, W.R., 1988, Paleoseismicity and earthquake recurrence at Little Cottonwood Canyon, Wasatch fault zone, Utah, *in* Machette, M.N., editor, In the footsteps of G.K. Gilbert—Lake Bonneville and neotectonics of the eastern Basin and Range Province, Geological Society of America Guidebook for Field Trip Twelve, Geological Society of America 100th Annual Meeting: Utah Geological and Mineral Survey Miscellaneous Publication 88-1, p. 82–85.

Scripps Orbit and Permanent Array Center (SOPAC), 2012, Website, sopac.ucsd.edu, accessed July 6, 2012.

Shen, Z., and Wang, M., 2012, Unified western U.S. crustal motion map [abs.]: Southern California Earthquake Center Annual Meeting 2012, Meeting Program, Sept. 8-12, 2012, p. 137.

Shenon, P.J., 1936, The Utah earthquake of March 12, 1934, *in* Neumann, F., United States earthquakes, 1934: U.S. Department of Commerce, Serial No. 593, p. 43–48.

Skeen, R.C., 1976, A reflection seismic study of the subsurface structure and sediments of Bear Lake, Utah-Idaho: Salt Lake City, University of Utah, senior thesis, 24 p.

Slemmons, D.B., 1957, Geological effects of the Dixie Valley–Fairview Peak, Nevada, earthquakes of December 16, 1954: Bulletin of the Seismological Society of America, v. 47, p. 353–375.

Smith, R.B., and Arabasz, W.J., 1991, Seismicity of the Intermountain Seismic Belt, *in* Slemmons, D.B., Engdahl, E.R., Zoback, M.D., and Blackwell, D.D., editors, Neotectonics of North America: Geological Society of America, Decade Map Volume 1, p. 185–228.

Smith, R.B., and Bruhn, R.L., 1984, Intraplate extensional tectonics of the eastern Basin-Range—inferences on structural style from seismic reflection data, regional tectonics, and thermal-mechanical models of brittle-ductile deformation: Journal of Geophysical Research, v. 89, p. 5733–5762.

Smith, R.B., Nagy, W.C., Julander, K.A., Viveiros, J.J., Barker, C.A., and Gants, D.G., 1989, Geophysical and tectonic framework of the eastern Basin and Range–Colorado Plateau–Rocky Mountain transition, *in* Pakiser, L.C., and Mooney, W.D., editors, Geophysical framework of the Continental United States: Geological Society of America Memoir 172, p. 205–233.

Solomon, B.J., 1996, Surficial geology of the Oquirrh fault zone, Tooele County, Utah, *in* Lund, W.R., editor, The Oquirrh fault zone, Tooele County, Utah—surficial geology and paleoseismicity—Paleoseismology of Utah, Volume 6: Utah Geological Survey Special Study 88, p. 1–17, 1 plate, scale 1:24,000.

Solomon, B.J., 1998, New evidence for the age of faulting on the West Valley fault zone: Utah Geological Survey, Survey Notes, v. 30, p. 8–13.

Solomon, B.J., 1999, Surficial geologic map of the West Cache fault zone and nearby faults, Box Elder and Cache Counties, Utah: Utah Geological Survey Map 172, 20 p., 2 sheets, scale 1:50,000.

Stein, R.S., and Barrientos, S.E., 1985, Planar high-angle faulting in the Basin and Range—geodetic analysis of the 1983 Borah Peak, Idaho, earthquake: Journal of Geophysical Research, v. 90, p. 11,355–11,366.

Stirling, M.W., and Goded, T., 2012, Magnitude scaling relationships—report prepared for the GEM Faulted Earth & Regionalisation Global Components: Lower Hutt, New Zealand, GNS Science Miscellaneous Series 42, 35 p., http://www.nexus.globalquakemodel.org/.

Stirling, M., Rhoades, D., and Berryman, K., 2002, Comparison of earthquake scaling relations derived from data of the instrumental and preinstrumental era: Bulletin of the Seismological Society of America, v. 92, p. 812–830.

Stuiver, M., and Reimer, R.J., 1993, Extended ^{14}C data base and revised CALIB 3.0 ^{14}C age calibration program: Radiocarbon, v. 35, p. 215–230.

Stuiver, M., Reimer, P.J., Bard, E., Beck, J.W., Burr, G.S., Hughen, K.A., Kromer, B., McCormac, G., Van Der Plicht, J., and Spurk, M., 1998, INTCAL98 radiocarbon age calibration, 24,000-0 cal BP: Radiocarbon v. 40, p. 1041–1083.

Sullivan, J.T., and Nelson, A.R., 1992, Late Quaternary displacement on the Morgan fault, a back valley fault in the Wasatch Range of northeastern Utah, *in* Gori, P.L., and Hays, W.W., editors, Assessment of regional earthquake hazards and risk along the Wasatch Front: U.S. Geological Survey Professional Paper 1500-I, 19 p.

Sullivan, J.T., Nelson, A.R., LaForge, R.C., Wood, C.K., and Hansen, R.A., 1988, Central Utah regional seismotectonic study: U.S. Bureau of Reclamation Seismotectonic Report 88 5, 269 p.

Suter, M., 2006, Contemporary studies of the 3 May 1887 MW 7.5 Sonora, Mexico (Basin and Range Province) earthquake: Seismological Research Letters, v. 77, no. 2, p. 134–147.

Suter, M., 2008, Structural configuration of the Otates fault (Southern Basin and Range Province) and its rupture in the 3 May 1887 M 7.5 Sonora, Mexico, earthquake: Bulletin of the Seismological Society of America, v. 98, p. 2879–2893.

Suter, M., 2015, Rupture of the Pitáycachi Fault in the 1887 M_w 7.5 Sonora, Mexico earthquake (southern Basin-and-Range Province)—rupture kinematics and epicenter inferred from rupture branching patterns: Journal of Geophysical Research – Solid Earth, v. 120, p. 617–641.

Swan, F.H. III, Schwartz, D.P., and Cluff, L.S., 1980, Recurrence of moderate to large magnitude earthquakes produced by surface faulting on the Wasatch fault zone, Utah: Bulletin of the Seismological Society of America, v. 70, p. 1431–1562.

Swan, F.H., III, Schwartz, D.P., Hanson, K.L., Knuepfer, P.L., and Cluff, L.S., 1981, Study of earthquake recurrence intervals on the Wasatch fault at the Kaysville site, Utah: U.S. Geological Survey Open-File Report 81-228, 30 p.

Tinti, S., and Mulargia, F., 1985, Effects of magnitude uncertainties on estimating the parameters in the Gutenberg-Richter frequency-magnitude law: Bulletin of the Seismological Society of America, v. 75, p. 1681–1697.

U.S. Geological Survey, 2013, Quaternary Fault and Fold Database of the United States: Online, U.S. Geological Survey Earthquake Hazards Program, http://earthquake.usgs.gov/hazards/qfaults/.

Utah Foundation, 2014, A snapshot of 2050—an analysis of projected population change in Utah: Online, Research Report 720, 16 p., http://www.utahfoundation.org/uploads/rr720.pdf.

Valastro, S., Davis, E.M., and Varela, A.G., 1972, University of Texas at Austin radiocarbon dates IX: Radiocarbon, v. 14, p. 461–485.

van Stiphout, T., Zhuang, J., and Marsan, D., 2012, Seismicity declustering: Community Online Resource for Statistical Seismicity Analysis, doi: 10.5078/corssa-52382934, http//www.corsa.org, accessed January 2014.

Velasco, M.S., Bennett, R.A., Johnson, R.A., and Hreinsdottir, S., 2010, Subsurface fault geometries and crustal extension in the eastern Basin and Range Province, western U.S.: Tectonophysics, v. 488, p. 131–142.

Veneziano, D., and Van Dyck, J., 1985, Analysis of earthquake catalogs for incompleteness and recurrence rates—Appendix A-6, *in* McGuire, R.K., project manager, Seismic hazard methodology for nuclear facilities in the eastern United States, v. 2, Appendix A: Electric Power Research Institute Project No. P101-29, EPRI/Seismicity Owners Group Draft 85-1 (April 30, 1985), p. A-220–297.

Viveiros, J.J., 1986, Cenozoic tectonics of Great Salt Lake from seismic-reflection data: Salt Lake City, University of Utah, unpublished M.S. thesis, 81 p.

Von Tish, D.B., Allmendinger, R.W., and Sharp, J.W., 1985, History of Cenozoic extension in central Sevier Desert, west-central Utah, from COCORP seismic reflection data: American Association of Petroleum Geologists Bulletin, v. 69, p. 1077–1087.

Wallace, R.E., 1984, Fault scarps formed during the earthquakes of October 2, 1915, in Pleasant Valley, Nevada, and some tectonic implications: U.S. Geological Survey Professional Paper 1274-A, 32 p.

Walter, H.G., 1934, Hansel Valley, Utah, earthquake: The Compass of Sigma Gamma Epsilon, v. 14, p. 178–181.

Ward, S.N., 1994, A multidisciplinary approach to seismic hazard in Southern California: Bulletin of the Seismological Society of America, v. 84, p. 1293–1309.

Weichert, D.H., 1980, Estimation of the earthquake recurrence parameters for unequal observation periods for different magnitudes: Bulletin of the Seismological Society of America, v. 70, p. 1337–1346.

Wells, D.L., 2013, Updated empirical relationships among magnitude, rupture area, rupture length, and surface displacement [abs.]: Seismological Research Letters, v. 84, p. 309.

Wells, D.L., 2015, Improved regression relations for earthquake source parameters [abs.]: Seismological Research Letters, v. 86, p. 623.

Wells, D.L., and Coppersmith, K.J., 1994, New empirical relationships among magnitude, rupture length, rupture width, rupture area, and surface displacement: Bulletin of the Seismological Society of America, v. 84, p. 974–1002.

Wernicke, B.P., and Axen, G.J., 1988, On the role of isostasy in the evolution of normal fault systems: Geology, v. 16, p. 848–851.

Wesnousky, S.G., 1986, Earthquakes, Quaternary faults, and seismic hazard in California: Journal of Geophysical Research, v. 91, p. 12,587–12,631.

Wesnousky, S.G., 2008, Displacement and geometrical characteristics of earthquake surface ruptures—issues and implications for seismic-hazard analysis and the process of earthquake rupture: Bulletin of the Seismological Society of America, v. 98, p. 1609–1632.

West, M.W., 1994, Seismotectonics of north-central Utah and southwestern Wyoming—Paleoseismology of Utah, Volume 4: Utah Geological Survey Special Study 82, 93 p.

Wheeler, R.L., and Krystinik, K.B., 1992, Persistent and nonpersistent segmentation of the Wasatch fault zone, Utah—statistical analysis for evaluation of seismic hazard, *in* Gori, P.L., and Hays, W.W., editors, Assessment of regional earthquake hazards and risk along the Wasatch Front, Utah: U.S. Geological Survey Professional Paper 1500, p. B1–B47.

Wills, S., and Anders, M.H., 1999, Tertiary normal faulting in the Canyon Range, eastern Sevier Desert: Journal of Geology, v. 107, p. 659–681.

Wills, S., Anders, M.H., and Christie-Blick, N., 2005, Pattern of Mesozoic thrust surfaces and Tertiary normal faults in the Sevier Desert subsurface, west-central Utah: American Journal of Science, v. 305, p. 42–100.

Witkind, I.J., 1975, Preliminary map showing known and suspected active faults in Idaho: U.S. Geological Survey Open-File Report 75-278, 71 p. pamphlet, 1 sheet, scale 1:500,000.

Wong, I.G., and Olig, S.S., 1998, Seismic hazards in the Basin and Range Province—perspectives from probabilistic analyses, *in* Lund, W.R., editor, Western States Seismic Policy Council, Proceedings Volume, Basin and Range Province Seismic-Hazards Summit: Utah Geological Survey Miscellaneous Publication 98-2, p. 110–127.

Wong, I., Olig, S., Green, R., Moriwaki, Y., Abrahamson, N., Baures, D., Silva, W., Somerville, P., Davidson, D., Pilz, J., and Dunne, B., 1995, Seismic hazard evaluation of the Magna tailings impoundment, *in* Lund, W.R., editor, Environmental and engineering geology of the Wasatch Front region: Utah Geological Association Publication 24, p. 95–110.

Wong, I., Olig, S., and Thomas, P., 2009, Assessing the earthquake ground shaking hazard along the Wasatch Front, Utah—a long and winding road [abs.]: Abstracts With Programs, Geological Society of America, Rocky Mountain Section, v. 41, p. 41.

Wong, I., Silva, W., Olig, S., Thomas, P., Wright, D., Ashland, F., Gregor, N., Pechmann, J., Dober, M., Christenson, G., and Gerth, R., 2002, Earthquake scenario and probabilistic ground shaking maps for the Salt Lake City, Utah, metropolitan area: Utah Geological Survey Miscellaneous Publication MP-02-05, 49 p.

Wong, I., Thomas, P., Olig, S., Dober, M., and Terra, F., 2007, Screening/scoping level probabilistic seismic hazard analysis, Currant Creek Dam, Soldier Creek Dam, Central Utah Project–Bonneville Unit, and Moon Lake Dam, Moon Lake Project, north-central Utah: Oakland, California, URS Corporation, unpublished final report prepared for the U.S. Bureau of Reclamation, 46 p.

Working Group on California Earthquake Probabilities (WGCEP), 1988, Probabilities of large earthquakes occurring in California: U.S. Geological Survey Open-File Report 88-398, 62 p.

Working Group on California Earthquake Probabilities (WGCEP), 1990, Probabilities of large earthquakes in the San Francisco Bay region, California: U.S. Geological Survey Circular 1053, 51 p.

Working Group on California Earthquake Probabilities (WGCEP), 1995, Seismic hazards in southern California—probable earthquakes, 1994 to 2024: Bulletin of the Seismological Society of America, v. 95, p. 379–439.

Working Group on California Earthquake Probabilities (WGCEP), 1999, Earthquake probabilities in the San Francisco Bay region—2000 to 2030—a summary of findings: U.S. Geological Survey Open-File Report 99-517, 55 p.

Working Group on California Earthquake Probabilities (WGCEP), 2003, Earthquake probabilities in the San Francisco Bay region—2002–2031: U.S. Geological Survey Open-File Report 03-214.

Working Group on California Earthquake Probabilities (WGCEP), 2008, The uniform California earthquake rupture forecast, version 2 (UCERF2): U.S. Geological Survey Open-File Report 2007-1437.

Working Group on California Earthquake Probabilities (WGCEP) (Field, E.H., Arrowsmith, R.J., Biasi, G.P., Bird, P., Dawson, T.E., Felzer, K.R., Jackson, D.D., Johnson, K.M., Jordan, T.H., Madden, C., Michael, A.J., Milner, K.R., Page, M.T., Parsons, T., Powers, P.M., Shaw, B.E., Thatcher, W.R., Weldon, R.J., II, and Zeng, Y.), 2014, Uniform California Earthquake Rupture Forcast, Version 3 (UCERF3)—the time-independent model: Bulletin of the Seismological Society of America, v. 104, no. 3, p. 1122–1180, doi: 10.1785/0120130164.

Wu, D., and Bruhn, R. L., 1994, Geometry and kinematics and active normal faults, south Oquirrh Mountains, Utah—implication for fault growth: Journal of Structural Geology, v. 16, p. 1061–1075.

Xiao, H., and Suppe, J., 1992, Origin of rollover: American Association of Petroleum Geologists Bulletin, v. 76, p. 509–529.

Youngs, R.R. and Coppersmith, K.J., 1985, Implications of fault slip rates and earthquake recurrence models to probabilistic seismic hazard estimates: Bulletin of the Seismological Society of America, v. 75, p. 939–964.

Youngs, R.R., Swan, F.H., Power, M.S., Schwartz, D.P., and Green, R.K., 1987, Probabilistic analysis of earthquake ground shaking hazards along the Wasatch Front, Utah, *in* Gori, P.L., and Hays, W.W., editors, Assessment of regional earthquake hazards and risk along the Wasatch Front, Utah, Volume II: U.S. Geological Survey Open-File Report 87-585, p. M-1–110.

Youngs, R.R., Swan, F.H., Power, M.S., Schwartz, D.P., and Green, R.K., 2000, Probabilistic analysis of earthquake ground shaking hazards along the Wasatch Front, Utah, *in* Gori, P.L., and Hays, W.W., editors, Assessment of Regional Earthquake Hazards and Risk Along the Wasatch Front, Utah: U.S. Geological Survey Professional Paper 1500-K-R, p. M1–M74.

Zeng, Y., and Shen, Z., 2014, Appendix D—A fault-based model for crustal deformation in the western United States, *in* Petersen, M.D., Zeng, Y., Haller, K.M., McCaffrey, R., Hammond, W.C., Bird, P., Moschetti, M., Shen, Z., Bormann, J., and Thatcher, W., Geodesy- and geology-based slip-rate models for the western United States (excluding California) National Seismic Hazard Maps: U.S. Geological Survey Open-File Report 2013-1293, p. 57–67, http://dx.doi.org/10.3133/ofr20131293.

Zoback, M.L., 1983, Structure and Cenozoic tectonism along the Wasatch fault zone, Utah, *in* Miller, D.M., Todd, V.R., and Howard, K.A., editors, Tectonic and stratigraphic studies in the eastern Great Basin: Geological Society of America Memoir 157, p. 3–27.

Zoback, M.L., 1992, Superimposed late Cenozoic, Mesozoic, and possible Proterozoic deformation along the Wasatch fault zone in central Utah, *in* Gori, P.L., and Hayes, W.W., editors, Assessment of regional earthquake hazards and risk along the Wasatch Front, Utah: U.S. Geological Survey Professional Paper 1500–E, p. E-1–E-20.

APPENDIX A

MOMENT-MAGNITUDE REGRESSIONS CONSIDERED BY THE WGUEP

By

Christopher DuRoss and Susan Olig

APPENDIX A

Moment-Magnitude Regressions Considered by the WGUEP

Regression	Parameter[a]	Region	Fault Type	Equation	N[b]	R[b]	σ[b]	Notes	GEM rank[c]	BRPEWGII[c]	This study[d]
Hanks and Kanamori (1979)	M_0	California	all	$2/3\log(M_0) - 10.7$	100s	NA	NA	Relation derived from three independent earthquake datasets. D_{ave} in M_0 calculation is average fault-parallel displacement on fault plane; sensitive to fault dip.	-	-	A,B,C
Wells and Coppersmith (1994)	SRL	global	all	$1.16\log(SRL) + 5.08$	77	0.89	0.28	Systematically underestimates moment magnitude (**M**) compared to displacement- and M_0-based regressions	-	X	A,B,C
Wells and Coppersmith (1994)	SRL	global	normal	$1.32\log(SRL) + 4.86$	15	0.81	0.34	Because their dataset was small for normal-slip earthquakes and they found no statistically significant difference between different slip types, they recommend using the more statistically-robust all slip type relations.	-	X	-
Wells and Coppersmith (1994)	A	global	all	$0.98\log(A) + 4.07$	148	0.95	0.24	A based on subsurface rupture length (L_{sub}), not SRL. For segmented faults, L_{sub} likely exceeds SRL if based on L_{seg}.	2	X	AFP
Wells and Coppersmith (1994)	D_{ave}	global	all	$0.82\log(D_{ave}) + 6.93$	56	0.75	0.39	Surface displacement including vertical, horizontal, and net (vector addition of vertical and horizontal) slip	-	-	-
Wells and Coppersmith (1994)	D_{ave}	global	normal	$0.65\log(D_{ave}) + 6.78$	12	0.64	0.33	Because their dataset was small for normal slip earthquakes and they found no statistically significant difference between different slip types, they recommend using the more statistically-robust all slip type relations.	-	-	-
Wells and Coppersmith (1994)	D_{max}	global	all	$0.74\log(D_{max}) + 6.69$	80	0.78	0.40	Surface displacement including vertical, horizontal, and net (vector addition of vertical and horizontal) slip	-	-	-
Wells and Coppersmith (1994)	D_{max}	global	normal	$0.71\log(D_{max}) + 6.61$	16	0.80	0.34	Because their dataset was small for normal slip earthquakes and they found no statistically significant difference between different slip types, they recommend using the more statistically-robust all slip type relations.	-	-	-
Anderson *et al*. (1996)	SRL, SR	global	all	$1.16\log(SRL) - 0.20\log(SR) + 5.12$	43	NR	0.26	Earthquakes limited to regions where seismogenic depth is 15–20 km. Regression requires slip rate, which is generally poorly constrained for many faults in the WGUEP region.	2	X	-
Mason (1996) (Ms)	SRL, D_{max}	global	normal	$0.55\log(SRL*D_{max}) + 5.95$	20	0.79	0.20	Regression for Ms not **M**. SRL is average of both straight-line and along-trace lengths.	-	-	-
Hemphill-Haley and Weldon (1999)	D_{ave}	global	all	$0.82\log(D_{ave}*MVCDS) + 6.93$	14	NA	NA	D_{ave} is observed data (from trench sites) and MVCDS is a mode value statistic based on number of observations (n) and percent of fault length that the n observations cover.	-	-	-
Stirling *et al*. (2002)	SRL	global	all	$0.8\log(SRL) + 5.88$	50	NR	0.30	Using updated Wells and Coppersmith (1994) earthquake database, but censored for SRL <10 km, A < 200 km2, D_{ave} <2 m, and **M** < 6.5 (censored instrumental data).	2	X	A,B,C
Stirling *et al*. (2002)	A	global	all	$0.73\log(A) + 5.09$	47	NR	0.26	Using updated Wells and Coppersmith (1994) earthquake database, but censored for SRL <10 km, A < 200 km2, D_{ave} < 2 m, and **M** < 6.5 (censored instrumental data).	2	-	AFP
Wesnousky (2008)	SRL	global	all	$1.02\log(SRL) + 5.30$	27	0.81	0.28	Global dataset, but many Basin and Range Province earthquakes. SRL > 15 km	1	-	A,B,C
Wesnousky (2008)	SRL	global	normal	$0.47\log(SRL) + 6.12$	6	0.36	0.27	Global dataset, but many Basin and Range Province earthquakes. SRL > 15 km. Relatively low regression coefficient.	1	-	-
Leonard (2010)	SRL	Inter-plate	dip-slip	$1.52\log(SRL) + 4.40$	NR	NA	NA	Developed self-consistent relations based on fault scaling relations and definition of moment. Dip-slip earthquake dataset includes megathrust earthquakes. Dataset not explicitly documented.	1	-	-
Leonard (2010)	A	Inter-plate	dip-slip	$\log(A) + 4.0$	NR	NA	NA	Developed self-consistent relations based on fault scaling relations and definition of moment. Dip-slip earthquake dataset includes megathrust earthquakes. Dataset not explicitly documented.	1	-	-

Regression	Parameter[a]	Region	Fault Type	Equation	N[b]	R[b]	σ[b]	Notes	GEM rank[c]	BRPEWGII[c]	This study[d]
Carpenter *et al*. (2012)	L_{seg}	global	strike-slip, normal	$0.88\log(L_{seg}) + 5.67$	7	0.80	NR	Unweighted least-squares regression. Scaling relation for L_{seg} based on observation that SRL often exceeds L_{seg}; using L_{seg} in place of SRL in SRL-**M** regressions will underestimate **M**. Limited range of L_{seg}.	-	-	-
Carpenter *et al*. (2012)	L_{seg}	global	strike-slip, normal	$0.92\log(L_{seg}) + 5.70$	7	0.60	NR	Weighted (by inverse of L_{seg} uncertainties) least-squares regression.	-	-	-

[a] D_{ave} - average displacement; Lsub - subsurface fault length; Lseg - segment length (straight-line); M_O - seismic moment ($m*Lsub*W*D_{ave}$) where m is crustal rigidity of $3x10^{11}$ dyne/cm^2; D_{max} - maximum displacemen; A - rupture area; SR - fault slip rate; SRL - surface rupture length (straight line); W - down-dip fault width.
[b] N - number of earthquakes; R - regression coefficient; σ - standard deviation in magnitude; NA - not applicable; NR - not reported.
[c] GEM rank: 1 - best available, 2 - good (Stirling and Goded, 2012); no value indicated regression not discussed. Xs indicate regressions that the Basin and Range Province Earthquake Working Group II (BRPEWGII) recommended for consideration in the development of the U.S. Geological Survey National Seismic Hazard Maps (Lund, 2012).
[d] A,B,C indicate regressions used for WGUEP category A, B, and C faults (see text for discussion); AFP indicates regressions used for the secondary fault in antithetic fault pairs where the down-dip width is truncated by the primary (master) fault at a relatively shallow seismogenic depth.

APPENDIX B

HOLOCENE PALEOSEISMOLOGY OF THE CENTRAL SEGMENTS OF THE WASATCH FAULT ZONE, UTAH

By

Christopher B. DuRoss[1,7], Stephen F. Personius[2], Anthony J. Crone[3], Susan S. Olig[4,8], Michael D. Hylland[1], William R. Lund[5], and David P. Schwartz[6]

[1]Utah Geological Survey, Salt Lake City, Utah
[2]U.S. Geological Survey, Golden, Colorado
[3]U.S. Geological Survey, Emeritus
[4]URS Corporation, Oakland, California
[5]Utah Geological Survey, Emeritus
[6]U.S. Geological Survey, Menlo Park, California
[7]Currently U.S Geological Survey, Golden, Colorado
[8]Currently Olig Seismic Geology, Martinez, California

2016

Research supported by the U.S. Geological Survey (USGS), Department of the Interior, under USGS award numbers G11AP20004 and G13AP00002 to the Utah Geological Survey.

Any use of trade, firm, or product names is for descriptive purposes only and does not imply endorsement by the U.S. Government.

Suggested citation:

DuRoss, C.B., Personius, S.F., Crone, A.J., Olig, S.S., Hylland, M.D., Lund, W.R., and Schwartz, D.P., 2016, Holocene paleoseismology of the central segments of the Wasatch fault zone, Utah—Appendix B, *in* Working Group on Utah Earthquake Probabilities (WGUEP), Earthquake probabilities for the Wasatch Front region in Utah, Idaho, and Wyoming: Utah Geological Survey Miscellaneous Publication 16-3, p. B1–B70.

CONTENTS

INTRODUCTION 1
SURFACE-FAULTING EARTHQUAKE HISTORIES 3
Brigham City Segment 4
Paleoseismic Data 4
Earthquake Chronology 6
Weber Segment 6
Paleoseismic Data 6
Earthquake Chronology 7
Salt Lake City Segment 8
Paleoseismic Data 8
Earthquake Chronology 9
Provo Segment 9
Paleoseismic Data 9
Earthquake Chronology 12
Nephi Segment 13
Paleoseismic Data 13
Earthquake Chronology 14
EARTHQUAKE RECURRENCE AND FAULT SLIP RATES 15
Earthquake Recurrence Intervals 15
Mean Recurrence per Segment 15
Composite Recurrence for the Central WFZ 16
Coefficient of Variation on Recurrence 17
Vertical Displacement 18
Vertical Displacement per Earthquake and Rupture Source 18
Vertical Displacement per Source 19
Vertical Slip Rate per Segment 20
RUPTURE MODELS 21
Evaluation of Possible Multi-Segment Ruptures on the Central WFZ 21
Rupture Models for the Central WFZ 23
Single-Segment Rupture Model 24
Intermediate and Multi-Segment Rupture Models 24
Unsegmented Rupture Model 26
Segment Boundary Uncertainties 26
CONCLUSIONS 27
REFERENCES 28

TABLES

Table B-1. Correlation of surface-faulting earthquakes on the Brigham City segment
Table B-2. Correlation of surface-faulting earthquakes on the Weber segment
Table B-3. Correlation of surface-faulting earthquakes on the Salt Lake City segment
Table B-4. Correlation of surface-faulting earthquakes on the Provo segment
Table B-5. Correlation of surface-faulting earthquakes on the Nephi segment
Table B-6. Summary of earthquake timing data for the central WFZ
Table B-7. Mean recurrence intervals
Table B-8. Vertical displacement per site and rupture
Table B-9. Modeled vertical displacement per rupture
Table B-10. Summary of displacement per rupture source
Table B-11. Open and closed mean vertical slip rates
Table B-12. Weighted mean vertical slip rates
Table B-13. Multi-segment ruptures included in the central WFZ rupture models
Table B-14. Rupture models and weights
Table B-15. Timing of multi-segment earthquakes
Table B-16. Segment-boundary uncertainties and rupture lengths
Table B-17. Summary of segment-boundary uncertainties

FIGURES

Figure B-1. Segments of the WFZ
Figure B-2. Central segments of the WFZ
Figure B-3. Correlation of surface-faulting earthquakes
Figure B-4. Timing of surface-faulting earthquakes
Figure B-5. Composite recurrence intervals
Figure B-6. Composite coefficient of variation of earthquake recurrence
Figure B-7. Examples of analytical displacement curves fit to displacement observations
Figure B-8. Analytical displacement curves for single-segment ruptures
Figure B-9. PDF overlap for pairs of earthquakes
Figure B-10. Analytical displacement curves for multi-segment ruptures
Figure B-11. Single-segment rupture model
Figure B-12. Intermediate rupture model
Figure B-13. Multi-segment rupture model
Figure B-14. Segment-boundary uncertainties for single-segment ruptures
Figure B-15. Segment-boundary uncertainties for multi-segment ruptures

INTRODUCTION

The Wasatch fault zone (WFZ) is Utah's longest and most active normal-slip fault, extending about 350 km from southern Idaho to central Utah, and forming the general structural boundary between the Basin and Range Province to the west and the relatively more stable Middle Rocky Mountain and Colorado Plateau provinces to the east. The WFZ has a complex trace that comprises ten structural segments defined on the basis of fault geometry and structure (Schwartz and Coppersmith, 1984; Machette *et al*., 1992; Wheeler and Krystinik, 1992) (Figure B-1). Five central segments (Brigham City to Nephi; figure B-2) have geomorphic (scarp-profile) and paleoseismic (mostly fault-trench) evidence of repeated Holocene surface-faulting earthquakes (Machette *et al*., 1992; Lund, 2005), and are the focus of this appendix. These segments are thought to generally rupture as seismogenically independent parts of the WFZ on the basis of clear differences in earthquake timing—especially for the best constrained most recent earthquakes—that occur across the prominent structural boundaries (DuRoss *et al.*, 2016). Thus, in the absence of well-defined rupture boundaries for prehistoric ruptures of the WFZ, we use the structural boundaries, together with paleoseismic earthquake timing and displacement data, as the basis for defining the fault's surface rupture characteristics and uncertainties. Additional discussion of paleoseismic data in the context of structural complexities along the WFZ is included in DuRoss *et al.* (2016). The end segments—including the Malad City, Clarkston Mountain, and Collinston segments to the north and the Levan and Fayette segments to the south (Figure B-1)—are discussed in Section 4.2 of the main report.

Segmentation models for the WFZ have evolved as additional paleoseismic data have been obtained along the fault. Schwartz and Coppersmith (1984) used the results of five early paleoseismic studies (described by Swan *et al*., 1980, 1981) to formulate a six-segment model between Collinston and Levan. Schwartz and Coppersmith (1984) also used these data to support a characteristic earthquake model, which implies that some faults or segments tend to produce similar-sized earthquakes at the upper end of their possible magnitude ranges, and thus have relatively large and constant displacement at a point in individual earthquakes (see also Hecker *et al*., 2013). Machette *et al*. (1992) developed a ten-segment model following the acquisition of additional paleoseismic data (see also Lund, 2005). This now well-established model is supported by (1) well-defined fault salients that are marked by complex and diffuse faulting and shallow bedrock (indicating decreased fault displacement), which separates adjacent hanging-wall basins; (2) along-strike changes in fault geometry and range-front morphology, and timing of most recent surface faulting; and (3) for each of the five central segments (Figure B-2), unique Holocene surface-faulting earthquake chronologies (Swan *et al*., 1980; Schwartz and Coppersmith, 1984; Machette *et al*., 1992; Wheeler and Krystinik, 1992). Although fault and paleoearthquake data generally support the Machette *et al*. (1992) model for the central segments, remaining uncertainties in paleoearthquake timing and displacement data permit alternative models (Chang and Smith, 2002; DuRoss, 2008; DuRoss *et al*., 2011).

On the central WFZ, prominent fault scarps displace late Holocene to latest Pleistocene geomorphic surfaces as much as several tens of meters and have been the focus of numerous paleoseismic fault-trench investigations. To date, 23 research trench sites (excluding trench projects for pre-development fault-setback and educational purposes) have yielded earthquake timing and/or displacement data. The majority of these sites are on faulted Holocene alluvial-fan surfaces, although scarps on latest Pleistocene surfaces related to phases of pluvial Lake

Bonneville (e.g., Oviatt *et al.*, 1992; Godsey *et al.*, 2005, 2011) have also provided important paleoseismic information (Lund, 2005). Fourteen of these research trench projects span the late 1970s (e.g., Swan *et al.*, 1980) to the late 1990s (e.g., Lund and Black, 1998), which we refer to as legacy data. Studies of the remaining nine sites occurred in the 11 years from the 1999 Little Cottonwood Canyon megatrench work (McCalpin, 2002) to the 2010 trenches on the Salt Lake City segment at Penrose Drive (DuRoss *et al.*, 2014). These more recent investigations capitalized on advances in numerical dating, such as improved soil sampling and sorting methods (e.g., the separation and identification of charcoal fragments; Puseman and Cummings, 2005), accelerator mass spectrometry (AMS) radiocarbon dating of minute charcoal fragments (e.g., Tucker *et al.*, 1983), optically stimulated luminescence (OSL) dating of clastic grains (e.g., Huntley *et al.*, 1985; Aitken, 1994; Duller, 2008), and the quantitative assessment of numerical ages using chronostratigraphic models (OxCal; Bronk Ramsey, 1995, 2001, 2008). For more thorough discussions of the evolution of WFZ paleoseismic data and dating methods see Lund (2005), Nelson *et al.* (2006), DuRoss *et al.* (2011), and Personius *et al.* (2012).

Paleoseismic data indicate that the central WFZ has been very active in Holocene time. Lund (2005) reported mean recurrence times of 1.3 to 2.5 kyr (kilo-year) for late Holocene (post ~6 ka [thousand years ago]) surface-faulting earthquakes on the central WFZ. Results of the more recent (1999–2010) trenching investigations (e.g., Machette *et al.*, 2007; DuRoss *et al.*, 2009; Olig *et al.*, 2011) show that the mean recurrence time for surface-rupturing earthquakes is similar for the five central segments, closer to ~1.3 kyr than ~2.5 kyr. DuRoss (2008) showed that the mean net vertical displacement per surface-rupturing earthquake for the central segments is 2.2 ± 1.0 m ($\pm 1\sigma$), and average vertical slip rates range from about 0.5 to 2.2 mm/yr using paleoseismic and geomorphic data (Machette *et al.*, 1992; Friedrich *et al.*, 2003; Lund, 2005). However, despite all of these paleoseismic data, important questions remained regarding earthquakes on the central five segments of the WFZ at the time of this analysis. For example, should legacy paleoseismic data be superseded by or integrated with the results of more recent paleoseismic studies, which have generally yielded smaller earthquake-timing uncertainties due to improved sampling and dating methods? How complete are the paleoseismic data for each segment, and what methods should be used to calculate earthquake recurrence values and fault slip rates? How robust is the segmentation model for the fault—that is, should alternative (e.g., multi-segment-rupture) models be included to assess the hazard? Finally, which magnitude regression parameters, such as surface rupture length and average displacement (e.g., Wells and Coppersmith, 1994), are most suitable to characterize prehistoric earthquake magnitudes for the central WFZ?

To address these questions, we systematically examined paleoseismic data for the central WFZ segments to rigorously characterize their surface-faulting earthquake histories and rates of activity. For each segment, we (1) reviewed and compiled published paleoseismic data from each trench site (we considered, but generally excluded incomplete and unpublished data); (2) constructed time-stratigraphic OxCal models for each site (using version 4 of Bronk Ramsey [1995, 2001] and the terrestrial calibration curve of Reimer *et al.* [2009]), which yielded earthquake-timing probability density functions (PDFs) for each site; (3) constructed earthquake histories for each segment by correlating and combining the per-site earthquake-timing PDFs along the segment; (4) using the revised earthquake histories per segment, calculated inter-event and mean earthquake recurrence intervals; and (5) calculated vertical slip rates using displacement per rupture and source estimates and the recurrence-interval data. Finally, we evaluated the segmentation of the

central WFZ and constructed several rupture models that address epistemic uncertainties in fault segmentation and earthquake rupture extent.

In this analysis, we compared and combined site-earthquake data (i.e., paleoseismic trench data) for each segment separately. That is, we did not systematically compare site earthquakes along the fault (i.e., on adjacent segments) to exhaustively allow for all possible rupture combinations (e.g., Biasi and Weldon, 2009). The assumption of single-segment ruptures on the central WFZ is consistent with Machette *et al*. (1992), Lund (2005), and DuRoss (2008), but affects the determination of the segment chronologies and recurrence intervals. Ultimately, we considered the potential for rupture beyond the segment boundaries and defined rupture uncertainties to account for more flexibility in the segmentation of the fault, but considered the treatment of the fault in a fully unsegmented manner outside the scope of this work.

SURFACE-FAULTING EARTHQUAKE HISTORIES

We reviewed, compiled, and evaluated paleoseismic data for the central WFZ segments to determine their surface-faulting earthquake histories, including the elapsed time since the most recent surface-faulting earthquakes (MRE) on each segment. For each segment, we used trench stratigraphy and numerical ages to construct time-stratigraphic OxCal models for each site, which allowed us to objectively model earthquake timing (e.g., Bronk Ramsey, 2008; Lienkaemper and Bronk Ramsey, 2009) and to generate earthquake-timing PDFs for each site (site PDFs; Figure B-3; Tables B-1 to B-5). We correlated the site PDFs along the segment using a quantitative measure of the amount of overlap in the site PDFs (after Biasi and Weldon, 2009), as well as inferences and conclusions in the original paleoseismic reports. For each segment, we then combined the site PDFs to construct earthquake histories for each entire segment (segment PDFs; Figures B-3 and B-4) using either the mean or the product methods of DuRoss *et al.* (2011) (Table B-6). Because of the detailed nature of this work, we only include a summary of the paleoseismic data for each segment here. More thorough discussions of original paleoseismic data and segment-wide earthquake chronologies can be found in DuRoss *et al.* (2011) (Weber segment), Personius *et al.* (2012) (Brigham City segment), and Crone *et al.* (2014) (Nephi segment). Paleoseismic site data for the Nephi, Salt Lake City, and Provo segments are also discussed by DuRoss *et al.* (2008), DuRoss *et al.* (2014), and Olig *et al.* (2011), respectively. Legacy paleoseismic data for the central WFZ are summarized by Machette *et al.* (1992) and Lund (2005).

To combine two or more site PDFs into a single-segment PDF, we used both the product and mean methods of DuRoss *et al.* (2011). The product method takes the product of the probabilities for each common time bin in the site PDFs; the mean method takes the average of the individual site PDF probabilities. We relied primarily on the product method, which focuses on the overlap in the site PDFs, giving more weight to the best constrained PDFs from the sites that establish the tightest limits on earthquake timing. In this method, we used all of the site PDF data, rather than excluding or subjectively weighting the less well-constrained data. However, DuRoss *et al.* (2011) caution that the product method is best suited to paleoseismic datasets in which: (1) the OxCal models (and resulting site PDFs) are supported by geologic observations and judgment; and (2) the correlation of site PDFs to form a segment (or fault-rupture) chronology is consistent with earthquake-timing data (i.e., segment earthquakes constrained by overlapping site PDFs) and fault geometry and displacement information (e.g., site PDF correlation supported by mapped segment

boundaries and per-event displacements). Thus, where the site PDFs contributing to a segment-wide earthquake have poor overlap, or the correlation of site PDFs from site to site is uncertain, we used the mean method to combine the site PDFs (Table B-6) because it more accurately represents the uncertainty in the earthquake time. See DuRoss *et al.* (2011) for a detailed description of these methods and their application to the Weber segment, and Personius *et al.* (2012) for their application to the Brigham City segment.

Brigham City Segment

Paleoseismic Data

The Brigham City segment (BCS) is the northernmost segment of the central WFZ that has evidence of Holocene surface rupture. The surface trace extends 35 km (all length measurements in this appendix are straight line, end-to-end) from a range-front reentrant near Coldwater Canyon near Honeyville to the southern terminus of the segment's Holocene faulting at the Pleasant View salient near North Ogden. At the Coldwater Canyon reentrant, scarps on Holocene to late Pleistocene surficial deposits form a zone of complex faulting that overlaps with the southern end of the Collinston segment (Personius 1990; Hylland, 2007). At the Pleasant View salient, complexly faulted late Pleistocene alluvial-fan deposits bury shallow bedrock on the hanging wall of the WFZ (Personius, 1990).

Paleoseismic data for the BCS span several decades and are dominantly from the northern half of the segment. Near Brigham City in the north-central part of the BCS, Personius (1991a) excavated a trench at the Bowden Canyon site. On the southern BCS, Personius (1991b) studied a modified gravel-pit exposure of a subsidiary fault trace on the Pleasant View salient at the Pole Patch site. Later, about 2 km south of Bowden Canyon, McCalpin and Forman (2002) excavated several trenches across a Lake Bonneville delta at the mouth of Box Elder Canyon. And most recently, DuRoss *et al.* (2012) excavated trenches at two sites on the northern BCS—the Hansen Canyon and Kotter Canyon sites—and one site on the southern BCS—the Pearsons Canyon site, which is about 6 km north of the southern end of the Holocene scarps on the segment. We constructed OxCal models for the Box Elder Canyon, Bowden Canyon, Kotter Canyon, and Pearsons Canyon paleoseismic sites. Earthquake times reported for these sites are the mean values and two-sigma (2σ) uncertainties from the OxCal models (Table B-1); see Personius *et al.* (2012) for an expanded discussion of the original paleoseismic data and the OxCal modeling results. We did not develop OxCal models for the Hansen Canyon and Pole Patch sites because the earthquake times are too broadly constrained.

At the Bowden Canyon (BC) site, Personius (1991a) exposed evidence for three Holocene surface-faulting earthquakes in a trench across an 8-m-high scarp. Based on minimum- and maximum-limiting radiocarbon (^{14}C) ages from bulk soil organics, the youngest earthquake (BC2) occurred at about 3.7 ± 0.5 ka and the preceding earthquake (BC3) at about 4.6 ± 0.6 ka. The oldest earthquake (BC4) is only constrained by minimum ages, and thus has a broadly constrained time of 5.8 ± 1.6 ka. Personius (1991a) did not find evidence for an earthquake younger than about 3.6 ka; however, the structure and stratigraphy in the trench was complicated and included multiple fault zones and extensive erosional unconformities. Personius (1991a, p. 6) noted the possible presence of an additional buried soil in the colluvial sequence, which permitted an alternative interpretation of an earthquake younger than about 3.6 ka. Considering this, as well as evidence from the adjacent Kotter Canyon and Box Elder Canyon trench sites (2 km to the north and south,

respectively) where there is evidence of a post-3.6-ka earthquake, our OxCal model for the Bowden Canyon site includes an additional earthquake (BC1) at 2.6 ± 1.0 ka (see Personius *et al.* [2012] for discussion). Earthquakes BC3 and BC4 each produced about 2.5 m of vertical displacement, compared to about 1.0 m in BC2.

The Pole Patch (PP) trench revealed evidence for three surface-faulting earthquakes: two postdating the Bonneville highstand, and an MRE (PP1) that occurred prior to 4.5 ± 0.7 ka based on a ^{14}C age for bulk soil organics. Personius (1991b) estimated a time of 4.6 ± 0.5 ka for PP1. The two older earthquakes were broadly constrained between the age of the MRE and the time of the Bonneville flood at ~18 ka (based on Oviatt [1997]). Each of the older earthquakes produced about 1.5 to 2.5 m of vertical displacement, compared to about 0.7 to 1.3 m in PP1 (Personius, 1991b).

At the Box Elder Canyon (BEC) site, McCalpin and Forman (2002) excavated 14 trenches across a complex fault zone formed on a Lake Bonneville (Provo-phase) delta and used ^{14}C and thermoluminescence (TL) ages to constrain the timing of six surface-faulting earthquakes younger than ~8.5 ka. The youngest and best-constrained earthquakes occurred at 2.2 ± 0.6 ka (BEC1), 3.2 ± 0.5 ka (BEC2), 4.4 ± 1.1 ka (BEC3), and 5.6 ± 0.8 ka (BEC4). Two older, less well-constrained earthquakes occurred at 7.7 ± 1.5 ka (BEC5) and 9.5 ± 2.1 ka (BEC6). BEC1 and BEC2 had minimum vertical displacements of 1.1 m and 0.5 to 1.2 m, respectively (McCalpin and Forman, 2002). They reported only poorly constrained minimum displacements due to the complex fault zone, which complicated the measurement of total throw per event across the entire zone.

At the Hansen Canyon (HC) site, DuRoss *et al.* (2012) excavated two trenches across a 4-m-high scarp and exposed evidence of a single late Holocene surface-faulting earthquake. Four maximum and three minimum ^{14}C ages broadly constrained the time of the youngest earthquake (HC1) to 2.1 to 4.2 ka. DuRoss *et al.* (2012) attributed the broadly constrained time of HC1 to ^{14}C ages affected by both detrital charcoal (inherited ages) and burrowing. Because of the broad time range, which overlaps with BEC1–BEC3, we chose not to include HC1 in our analysis of BCS earthquake-timing data.

DuRoss *et al.* (2012) excavated one trench across an 8-m-high scarp at the Kotter Canyon (KC) site and found evidence of two late Holocene earthquakes. Based on OSL and charcoal ^{14}C ages, the youngest earthquake (KC1) occurred at 2.5 ± 0.3 ka and the penultimate earthquake (KC2) at 3.5 ± 0.3 ka. The timing of KC1 and KC2 corresponds well with Box Elder Canyon earthquakes BEC1 (~2.5 ka) and BEC2 (~3.2 ka) and Bowden Canyon earthquake BC2 (~3.7 ka). DuRoss *et al.* (2012) measured an average displacement of 2.1 ± 0.2 m for KC1 and KC2.

At the Pearsons Canyon (PC) site, DuRoss *et al.* (2012) excavated two trenches across a 2-m-high main scarp and a 0.2-m-high antithetic scarp north of Pearsons Canyon on the southern BCS. The trenches exposed evidence for a single earthquake, the timing of which is tightly constrained to 1.2 ± 0.05 ka (PC1) by multiple ^{14}C ages on charcoal from alluvial-fan deposits, scarp colluvium, and a post-earthquake debris flow. PC1 is much younger than the youngest earthquake on the northern part of the BCS at ~2.2 to 2.6 ka and likely represents a partial rupture of the southernmost BCS during an earthquake that ruptured the adjacent Weber segment (WS) to the south (discussed below and in DuRoss *et al.* [2012] and Personius *et al.* [2012]). About 0.5 m of vertical displacement (0.1–0.9 m range, which accounts for antithetic faulting) occurred in PC1 (DuRoss *et al.*, 2012).

Earthquake Chronology

The Kaysville, East Ogden, Garner Canyon, and Rice Creek trench investigations each yielded evidence for at least three large-displacement, surface-faulting earthquakes during the Holocene. DuRoss *et al.* (2011) correlated and combined these data into a record of five earthquakes at about 0.6 ka (W1), 1.1 ka (W2), 3.1 ka (W3), 4.5 ka (W4), and 5.9 ka (W5) (Table B-2). Based on their analysis, DuRoss *et al.* (2011) concluded that (1) W3, W2, and W1 likely ruptured the entire segment, although questions remain whether W2 ruptured the Kaysville site; (2) W4 was not exposed (or possibly not identified) at Kaysville; and (3) W5 was likely exposed at both Rice Creek and Kaysville, but predated the stratigraphic record exposed at East Ogden, supporting the inference of McCalpin *et al.* (1994) that Kaysville earthquake K4 (~5.7 ka) is a separate, older earthquake than East Ogden earthquake EO4 (~4.0 ka) (Table B-2). Although Nelson *et al.* (2006) had previously considered W1 a possible partial rupture confined to the northern WS, DuRoss *et al.* (2011) concluded that this earthquake ruptured at least from Rice Creek in the north to Kaysville on the south. Thus, consistent with DuRoss *et al.* (2011), we include W1 as a full rupture of the WS.

Weber Segment

Paleoseismic Data

The 56-km-long Weber segment (WS) is the second longest WFZ segment and extends from the Pleasant View salient to the Salt Lake salient near North Salt Lake. At the Pleasant View salient, a 1.5-km-wide left step separates the WS from the Holocene trace of the BCS (Personius, 1990; Nelson and Personius, 1993). At the Salt Lake salient, the WS terminates in Tertiary bedrock, close to an about 2-km-wide zone of en-echelon, right-stepping faults between the WS and the Warm Springs fault of the Salt Lake City segment (Nelson and Personius, 1993).

Paleoseismic data for the WS are from trench investigations at the Kaysville site on the southern WS (Swan *et al.*, 1980, 1981; later reoccupied by McCalpin *et al.*, 1994), the East Ogden site on the north-central part of the segment (Nelson, 1988; Nelson *et al.*, 2006), and the Rice Creek site on the northern WS (DuRoss *et al.*, 2009). Study of a cut-slope excavation 5 km north of East Ogden at the Garner Canyon site provided additional data on earthquake-times and displacements for the northern WS (Nelson, 1988; Forman *et al.*, 1991; Nelson *et al.*, 2006). We constructed OxCal models for all four WS sites, which yielded the mean and 2σ earthquake times discussed in Table B-2. See DuRoss *et al.* (2011) for an expanded discussion of the original paleoseismic data and OxCal modeling results.

At the Kaysville (K) site about 20 km north of the southern end of the WS, a 22-m-high fault scarp has been the subject of two trench investigations. In one of the first paleoseismic studies on the WFZ, Swan *et al.* (1980, 1981) excavated several trenches across the scarp and exposed evidence of at least three surface-faulting earthquakes. However, the two youngest earthquakes were only constrained by a maximum ^{14}C age of ~1.6 ka. In 1988, McCalpin *et al.* (1994) reexcavated the Kaysville site and used ^{14}C and TL ages to constrain the timing of three mid-Holocene earthquakes. However, based on the analysis of paleoseismic data discussed in DuRoss *et al.* (2011), we modeled four earthquakes at the site: 0.6 ± 0.2 ka (K1), 0.9 ± 0.5 ka (K2), 2.8 ± 1.7 ka (K3), and 5.7 ± 1.3 ka (K4). The addition of earthquake K2 stems from DuRoss *et al.*' (2011) review and synthesis of stratigraphic and structural data from both Kaysville investigations and the

chronological constraints from McCalpin *et al*. (1994). Stratigraphic and structural evidence of K2 includes prominent fissures and likely scarp colluvium that predates K1 and postdates K3; furthermore, the incremental rotation of colluvial-wedge sediments into the fault zone, fault terminations, differential offset of stratigraphic horizons, and a possible buried fault scarp support the interpretation of an additional earthquake. Vertical displacement per event ranges from about 1.4 to 1.8 m (K1 and K4) to 3.9 m (K3) (McCalpin *et al.*, 1994).

At the East Ogden site (EO), Nelson (1988) excavated a total of five trenches across two main (west-facing) scarps having 5 and 8 m of vertical offset, and an antithetic scarp that has 2 m of vertical offset. He used ^{14}C ages on bulk-soil sediment and charcoal and TL ages on quartz-bearing sediment to limit the timing of four late-Holocene earthquakes. Based on limiting ages in Nelson *et al.* (2006), the earthquakes occurred at 0.5 ± 0.2 ka (EO1), 0.9 ± 0.4 ka (EO2), 3.0 ± 0.4 ka (EO3), and 4.0 ± 0.5 ka (EO4). Per-event vertical displacements are generally large, including 2.6 m in EO2 and 4.2 m in both EO3 and EO4 (Nelson *et al.*, 2006). Nelson *et al.* (2006) suggested that EO1—which only had about 0.5 m of displacement—may be a separate, younger earthquake than the youngest Kaysville (K1) and Garner Canyon (GC1) events, and thus, possible evidence of a partial segment rupture on the northern WS.

At the Garner Canyon (GC) site, Nelson *et al.* (2006) mapped the exposure excavated into a 4-m-high fault scarp and reported stratigraphic and structural evidence of four earthquakes. Based on the OxCal model of DuRoss *et al.* (2011), these earthquakes occurred at 0.6 ± 0.4 ka (GC1), 1.5 ± 0.5 ka (GC2), 3.2 ± 0.6 ka (GC3), and 4.4 ± 0.6 ka (GC4). Earthquakes GC4 and GC3 have no maximum age constraints; and thus, the timing of GC4 and GC3 is based on a plausible correlation of these events with earthquakes EO4 and EO3 at East Ogden (Nelson *et al.*, 2006). This correlation is supported by geologic mapping that shows similar amounts of vertical displacement on late Holocene alluvial fans at both Garner Canyon and East Ogden (Nelson and Personius, 1993). Per-event vertical displacements for GC1–GC3 range from about 1.0 m to 1.5 m (Nelson *et al.*, 2006).

DuRoss *et al.* (2009) excavated two trenches across 4-m- and 8-m-high main (west-facing) scarps and a 1-m-high antithetic scarp at the Rice Creek (RC) site, near the northern end of the WS. Based on ^{14}C ages on charcoal, OSL ages, and the OxCal model in DuRoss *et al.* (2011), the trenches exposed evidence for five earthquakes that occurred at 0.6 ± 0.08 ka (RC1), 1.2 ± 0.3 ka (RC2), 3.4 ± 0.7 ka (RC3), 4.6 ± 0.5 ka (RC4), and 6.0 ± 1.0 ka (RC5). DuRoss *et al.* (2011) concluded that earthquake RC1 at ~0.6 ka likely corresponds with events at ~0.6 ka at Kaysville (KC1), ~0.5 ka at East Ogden (EO1), and ~0.6 ka at Garner Canyon (GC1). DuRoss *et al.* (2009) included an additional earthquake (RC6, which occurred before 7.8–9.9 ka); however, the time of this event is poorly constrained by a single minimum-limiting age. Vertical displacements for individual earthquakes at Rice Creek ranged from about 1.1 m in RC3 to 3.2 m in RC2; RC1, RC4, and RC5 each had about 2.0 m of displacement.

Earthquake Chronology

The Kaysville, East Ogden, Garner Canyon, and Rice Creek trench investigations each yielded evidence for at least three large-displacement, surface-faulting earthquakes during the Holocene. DuRoss *et al.* (2011) correlated and combined these data into a record of five earthquakes at about 0.6 ka (W1), 1.1 ka (W2), 3.1 ka (W3), 4.5 ka (W4), and 5.9 ka (W5) (Table B-2). Based on their analysis, DuRoss *et al.* (2011) concluded that (1) W3, W2, and W1 likely ruptured the entire

segment, although questions remain whether W2 ruptured the Kaysville site; (2) W4 was not exposed (or possibly not identified) at Kaysville; and (3) W5 was likely exposed at both Rice Creek and Kaysville, but predated the stratigraphic record exposed at East Ogden, supporting the inference of McCalpin *et al.* (1994) that Kaysville earthquake K4 (~5.7 ka) is a separate, older earthquake than East Ogden earthquake EO4 (~4.0 ka) (Table B-2). Prior to the Rice Creek study, Nelson *et al.* (2006) had interpreted W1 as a possible partial rupture that was confined to the northern WS, but we favor the interpretation that this earthquake ruptured at least from Rice Creek in the north to Kaysville on the south. See DuRoss *et al.* (2011) for further discussion.

Salt Lake City Segment

Paleoseismic Data

The Salt Lake City segment (SLCS) comprises three subsections (separate fault strands) that are separated by prominent left steps: the Warm Springs, East Bench, and Cottonwood faults (Scott and Shroba, 1985; Personius and Scott, 1992, 2009). The SLCS extends 40 km from the northern end of the Warm Springs fault, which bounds the western edge of the Salt Lake salient, to the southern end of the Cottonwood fault, where the Traverse Mountains and east-west oriented Fort Canyon fault separate the SLCS from the Provo segment (Bruhn *et al.*, 1992). The individual faults have end-to-end trace lengths of 7.5 to 10.5 km (Warm Springs fault), 12 km (East Bench fault), and 20 km (Cottonwood fault), and the step-over zones between them are 2–3 km (Cottonwood–East Bench faults) to 3–4 km (East Bench–Warm Springs faults) wide.

Paleoseismic data for the SLCS are from fault-trench investigations at the Little Cottonwood Canyon (LCC; Swan *et al.*, 1981; later reoccupied by McCalpin, 2002) and South Fork Dry Creek (SFDC) sites (Schwartz and Lund, 1988; Black *et al.*, 1996), both on the Cottonwood fault, and the Penrose Drive (PD) site on the East Bench fault (DuRoss *et al*., 2014; DuRoss and Hylland, 2015). Earthquake-timing data are not available for the Warm Springs fault because extensive surface disturbance and development along the fault trace has apparently eliminated all suitable study sites (DuRoss and Hylland, 2015). We constructed OxCal models for the LCC and SFDC sites; mean and 2σ earthquake times from these models are reported in Table B-3. OxCal models for the PD site are included in DuRoss and Hylland (2015); because the PD data were not available at the time of our SLCS analysis, our segment-wide earthquake times only reflect data from LCC and SFDC. However, the youngest PD earthquake times overlap well with older events at the LCC and SFDC sites, and if we had included them, this addition would have had only a minor (30–50-yr) effect on segment-wide earthquake times (Table B-3). See DuRoss *et al.* (2014) and DuRoss and Hylland (2015) for expanded discussions of the OxCal models for the SLCS. Paleoseismic data for the SLCS are also available from exploratory trenches across the East Bench fault (Dresden Place site; Machette *et al.*, 1992) and geotechnical studies of the Warm Springs fault (Robison and Burr, 1991; Simon-Bymaster, 1999); however, these studies did not yield information on the times of earthquakes, and are not included in our analysis.

Both Swan *et al.* (1981) and McCalpin (2002) trenched the LCC site. Swan *et al.* (1981) reported evidence for two or three Holocene earthquakes, but could only constrain the minimum time of the penultimate earthquake to the early Holocene. McCalpin (2002) reoccupied the LCC site and interpreted seven post-Bonneville age (<18 ka) earthquakes. Using paleoseismic data from McCalpin (2002) in an OxCal model, the four youngest earthquakes occurred at 1.3 ± 0.04 ka (LCC1), 2.1 ± 0.3 ka (LCC2), 4.4 ± 0.5 ka (LCC3), 5.5 ± 0.8 ka (LCC4). Two older earthquakes

occurred at 7.8 ± 0.7 ka (LCC5) and 9.5 ± 0.2 ka (LCC6); however, McCalpin (2002) interpreted a period of seismic quiescence on the SLCS between about 9 and 17 ka. Using the total displacement (~7.5 m) across the lower of two fault zones, McCalpin (2002) estimated an average displacement of 1.8 m per event for the youngest four earthquakes. However, this average displacement estimate does not account for possible displacement on the upper (eastern) fault and thus could be a minimum value.

At the SFDC site, about 5 km south of LCC, Schwartz and Lund (1988) and Black *et al.* (1996) excavated trenches across six scarps and constrained the timing of four events. Based on the SFDC data, as well as the results of a geotechnical trench excavation at Dry Gulch (Black *et al.*, 1996), the four earthquakes occurred at 1.3 ± 0.2 ka (SFDC1), 2.2 ± 0.4 ka (SFDC2), 3.8 ± 0.6 ka (SFDC3), and 5.0 ± 0.5 ka (SFDC4). Average per-event displacement for SFDC is 1.5 to 2.5 m based on a debris-flow levee that was vertically offset by two and possibly three earthquakes (Black *et al.*, 1996; DuRoss, 2008).

Earthquake Chronology

LCC and SFDC paleoseismic data indicate that the four youngest surface-rupturing earthquakes on the segment occurred at about 1.3 ka (S1), 2.2 ka (S2), 4.1 ka (S3), and 5.3 ka (S4) (Table B-3). Our correlation of earthquakes between LCC and SFDC corresponds with that of McCalpin (2002) and DuRoss and Hylland (2015), and is also consistent with results from the PD site. The youngest PD earthquakes occurred at 4.0 ± 0.5 ka (2σ) (PD1) and 5.9 ± 0.7 ka (PD2), consistent with earthquakes at ~3.8 to 4.4 ka and ~5.0 to 5.5 ka at LCC and SFDC. McCalpin (2002) reported three earthquakes between about 6 ka and ~18 ka (timing of the highstand of Lake Bonneville), and discussed the possibility of a period of seismic quiescence on the SLCS between about 9 and 17 ka. Although our analysis of the SLCS is limited to the youngest four, late Holocene earthquakes, which corresponds with the time period over which the paleoseismic record for the central WFZ is likely complete, questions regarding the completeness of the early Holocene–latest Pleistocene earthquake record, and McCalpin's inference of an 8-kyr quiescent period are important. However, we note that data from the PD site show that two earthquakes occurred during this time period (PD4 at 10.9 ± 0.2 ka and PD5 at 12.1 ± 1.6 ka), which suggests that the apparent lack of earthquakes at LCC between 9 and 17 ka is likely related to an incomplete paleoseismic record rather than a quiescent interval. DuRoss and Hylland (2015) suggested that PD4 and PD5 could have ruptured the Cottonwood fault, but may have been difficult to recognize at LCC because of the fault zone's complexity and/or because of abundant soil carbonate in the deposits, which complicated the interpretation of depositional environments at LCC (McCalpin, 2002).

Provo Segment

Paleoseismic Data

The Provo segment (PS) bounds the eastern margin of Utah Valley and is the longest segment on the WFZ, consisting of three distinct subsections that have a total end-to-end length of 59 km. The segment extends from the Traverse Mountains salient and the Fort Canyon fault east of the Traverse Mountains on the north to an en-echelon, 5- to 9-km-wide, right-step with the Nephi segment near Santaquin on the south. Machette *et al.* (1992) informally subdivided the segment into three 17- to 24-km-long subsections: the American Fork at the northern end, the Central or Provo-restricted, and the Spanish Fork at the southern end. However, paleoseismic data strongly

suggest that the entire segment typically ruptures during surface-faulting earthquakes (Lund *et al.*, 1991; Machette *et al.*, 1992) as originally proposed by Schwartz and Coppersmith (1984) and is consistent with our findings. However, given the length and complexity of fault trace geometry, the three subsections remain a convenient way to discuss the PS segment paleoseismic data and is used here.

A total of seven paleoseismic trench sites have been investigated along the Provo segment (Figure B-1), but only four of these sites had sufficient timing data available to explicitly be included in this analysis. Importantly, we do have paleoseismic data analyzed for each of the three PS subsections and these are discussed in more detail below. On the northern part of the PS, Forman *et al.* (1989) and Machette *et al.* (1992) excavated several trenches at the American Fork (AF) site about 10 km from the segment's northern end and immediately south of the mouth of American Fork Canyon. Near the center of the segment, Lund and Black (1998) excavated a trench at the Rock Canyon (ROC) site and studied a natural exposure of the fault along Rock Creek. Lund *et al.* (1991) excavated trenches across faulted late Holocene fans on the southern PS at two sites approximately one kilometer apart: two trenches at the Mapleton South (MS) site and two trenches at the Mapleton North (MN) site just east of the city of Mapleton. Olig *et al.* (2011) later reoccupied the MN site in a single, large (megatrench) excavation, which was excavated just north of the original MN trenches. We constructed OxCal models for the AF, ROC, MN (the original and megatrench combined) and MS sites using paleoseismic data from Machette *et al.* (1992), Lund and Black (1998), and Olig *et al.* (2011), and mean and 2σ earthquake times from those models are discussed here (Table B-4).

The three paleoseismic trench sites on the PS that are not included in this OxCal/Matlab analysis are Hobble Creek, Woodland Hills, and Water Canyon (Figure B-1), and the reasons are briefly explained here. At the Hobble Creek site, a few kilometers north of the MN site, Swan *et al.* (1980) and Schwartz *et al.* (1983) found evidence for six to seven surface-faulting earthquakes that produced 11.5 to 13.5 m of cumulative net vertical displacement since a Provo delta formed between 14,500 and 12,000 ^{14}C yr B.P. (revised Provo phase ages from Godsey *et al*., 2005). These data were calendar calibrated and used in this study to estimate slip rates, but unfortunately absolute age constraints for individual events were lacking, precluding construction of OxCal models for the Hobble Creek site.

At the Woodland Hills site, two trenches were excavated across a west-northwest-dipping splay fault above the highest Bonneville shoreline, termed the Woodland Hills fault by Machette (1992), which is about 6 km from the southern end of the PS. Machette (1992) reported evidence for three or four late Quaternary events on the Woodland Hills fault that produced about 3 m of vertical displacement, including a late Holocene event that he correlated to the MRE at MN, but given the large uncertainties in the legacy dates, it may actually correlate to the penultimate event observed at the MN site (discussed further below). Machette (1992) reported AMRT dates of 1190 ± 50 and 1380 ± 60 ^{14}C yr B.P. from a block of soil that had fallen off the free face and he interpreted these dates to provide a minimum estimate of 1.0 ± 0.3 ka since faulting (including calendar calibration and subtracting 200 years for soil formation). However, because trench logs and other age data were not available, and because of the issues with interpreting legacy bulk soil dates, we did not construct an OxCal model for this site.

The Water Canyon site is on the southern PS near the junction with the Woodland Hills fault. Here, the U.S. Bureau of Reclamation (USBR) excavated three trenches near a pipeline crossing for the Central Utah Project. They exposed evidence for at least four or possibly five surface-faulting events since 4,600 ± 75 ^{14}C yr B.P., including two events in one trench that were younger than 890 ± 75 ^{14}C yr B.P. based on a bulk sample ^{14}C date from an A horizon underlying the penultimate event colluvial wedge (D. Ostenaa, USBR, personal communication, cited in Olig *et al.*, 2011). Unfortunately, the investigation remains unpublished except for an abstract (Ostenaa, 1990). We reviewed copies of field logs made by Michael Machette that were available from UGS files, but the limited documentation made constructing detailed OxCal models for the Water Canyon site beyond the scope of this study, although additional time and resources might make this a worthwhile future endeavor.

At the AF site, Forman *et al.* (1989) and Machette *et al.* (1992) excavated three trenches (AF-1 through AF-3) across most, but not all, of the complex distribution of overlapping post-Bonneville fault scarps at this site. They found evidence for at least four surface-faulting earthquakes that occurred since 8 ka, but we emphasize that this paleoseismic record is a minimum for this site because the ages of the youngest colluvial wedges exposed on two different west-dipping late Holocene fault scarps (the eastern fault splay in Trench AF1 and the main fault in Trench AF-3) were not constrained. In addition, the easternmost, west-dipping fault scarp at the site was not trenched due to landowner restrictions (see Figure 3 of Machette *et al.*, 1992). Our OxCal model for the AF site is based on the published paleoseismic data (Machette *et al.*, 1992) and review of original field logs from USGS file archives (including previously unpublished logs for Trenches AF-2, AF-3, and the eastern part of Trench AF-1), as well as discussions of these data with M.N. Machette (U.S. Geological Survey [retired], written communication, 2011). Based on our OxCal analysis, the four earthquakes occurred at 0.4 ± 0.2 ka (AF1), 2.0 ± 0.8 ka (AF2), 4.3 ± 1.5 ka (AF3), and 6.2 ± 1.0 ka (AF4). During review of field logs, we considered but ultimately discounted suggestive stratigraphic evidence for a possible younger event in trench AF-2 that would have occurred at 0.3 ± 0.1 ka, but only apparently on an antithetic fault. The average per-event vertical displacement for AF1–AF3 is 2.5 ± 0.3 m, based on the total displacement at the site divided by the number of events (Machette *et al.*, 1992).

At the ROC site, Lund and Black (1998) excavated a trench and studied a natural exposure of the fault and found evidence of a single surface-faulting earthquake since about 2 ka. Several ^{14}C ages on bulk soil and charcoal constrain the earthquake time (ROC1) to 0.6 ± 0.06 ka from our OxCal analysis of the data. Based on the stratigraphic separation measured across the entire deformation zone, Lund and Black (1998) measured about 3.3 m of net vertical displacement for ROC1. Finally, we emphasize that not all fault scarps on unconsolidated deposits were trenched at this site, including scarps on various Lake Bonneville deposits (see Figure 3 of Lund and Black, 1998).

Near Mapleton, both Lund *et al.* (1991) and Olig *et al.* (2011) excavated trenches across a 19- to 23-m-high scarp. At the MN site, Lund *et al.* (1991) excavated two trenches across the lower one-third of the scarp and found evidence of two surface-faulting earthquakes, but were only able to date the youngest event at 0.6 ± 0.2 ka. Olig *et al.* (2011) reoccupied the site and excavated a single, large trench across the entire 50-m-wide deformation zone, which revealed evidence of at least seven, probably ten, surface-faulting earthquakes that occurred since 13 ka. We combined the paleoseismic data from these two studies to construct a single OxCal model for the MN site. Based on our analyses, earthquakes occurred at 0.6 ± 0.08 ka (MN1), 1.5 ± 0.4 ka (MN2), 3.2 ±

1.3 ka (MN3) 4.7 ± 0.3 ka (MN4), and 5.6 ± 0.5 ka (MN5). Estimates of per event vertical displacement from the MN site used in this analysis are: 4.7 ± 0.5 m for MN1, and a minimum of 0.5 to 2.2 m for MN2 (Olig *et al.*, 2011).

About 0.8 km south of the MN site, Lund *et al.* (1991) excavated three trenches across two west-facing scarps at the MS site, but they only logged one trench in detail because suitable material for dating was not found in the other two trenches. They found evidence for two events since about 3 ka, but the time of the youngest event was poorly constrained. Based on our OxCal analysis of their data, surface-faulting earthquakes occurred at 0.7 ± 0.7 ka (MS1) and 2.2 ± 0.8 ka (MS2). Reliable estimates of per event displacement could not be made at MS because of incomplete exposure of the deformation zone (Lund *et al.*, 1991).

Based on these earthquake times, MS1 likely correlates with MN1 (and AF1), whereas MS2 likely correlates with MN3 and AF2, with MN2 only identified at the MN site, because it was not exposed or dated at other sites, or because it did not rupture elsewhere, which seems less likely given the relatively large displacements for this event (Olig *et al.*, 2011). However, given the timing uncertainties of events, we also considered correlations among AF2, MN2, and MS2, with paleoearthquake MN3 as the additional event not identified at the other sites. However, we ultimately preferred the former correlation (AF2, MN3, and MS2) because it has a better overlap between PDFs of event times, although we acknowledge that additional paleoseismic investigations of the PS are needed to better determine the extent of the MN2 rupture and verify the AF2, MN3, and MS2 correlation of events.

Earthquake Chronology

At least five post-mid-Holocene earthquakes have caused surface-rupture on the PS: 0.6 ka (P1), 1.5 ka (P2), 2.2 ka (P3), 4.7 ka (P4), and 5.9 ka (P5) (Table B-4). These earthquake times are based on our review of PS paleoseismic data from all of the study sites and our preferred correlation of earthquakes along the segment. Based on our analysis, we consider the post-mid-Holocene earthquake record complete for the MN site because it includes earthquake P2 (MN2) that occurred at ~1.5 ka. In our analysis, we have assumed events A2, MN3, and MS2 correlated in the P3 rupture, and P2 either did not rupture the full extent of the PS or evidence of it was not exposed at the AF, ROC, and MS sites. The relatively large displacement of 0.5 to 2.2 m for MN2 supports the latter. Additionally, for AF and MS, the latter explanation is more plausible because ages of at least two colluvial wedges exposed in the AF trenches were poorly constrained and could correlate to MN2, as well as the AF trenches did not span all of the fault traces (the easternmost down-to-the west fault trace in a complex zone was not trenched), and at the MS site, only the lower part of a large, complexly faulted scarp was exposed in the trench that was logged. At ROC, P2 postdates the oldest buried soil at the site (dated to about 2.4 ka; Lund and Black, 1998), but considering the limited exposure of the soil (not exposed in the fault zone) and additional fault traces (on older unconsolidated sediments, but showing evidence of complex surface faulting) both east and west of the ROC site that were not trenched, we consider it possible that P2 ruptured the ROC site, but was not exposed.

Nephi Segment

Paleoseismic Data

The Nephi segment (NS) is the southernmost segment of the central WFZ that has evidence of multiple Holocene surface-faulting earthquakes. The NS extends 43 km and comprises two subsections—a 17-km-long northern strand and a 25-km-long southern strand—which are separated by a 4- to 5-km-wide right step in bedrock. The northern strand extends along a steep range front from near Santaquin Canyon northward into southern Utah Valley where it overlaps the southern PS by 12 km (Machette, 1992). The southern strand bounds a steep range front in eastern Juab Valley and terminates to the south at a 7-km-wide gap in faulting between the Nephi and Levan segments (Harty *et al.*, 1997).

Paleoseismic data for the NS are from three trench sites on the southern strand and one site on the northern strand. At North Creek (NC) on the northern part of the southern strand, Hanson *et al.* (1981, 1982a) excavated several trenches, and at Red Canyon (REC) on the southern part, Jackson (1991) excavated one trench near the southern terminus of the NS (12 km south of North Creek). Both investigations found evidence for three surface-faulting earthquakes. Machette *et al.* (2007) excavated trenches at the Willow Creek (WC) site midway between the NC and REC sites). At the Santaquin (SQ) site on the northern strand, DuRoss *et al.* (2008) excavated trenches across a single-event scarp near the center of the strand. We constructed OxCal models for all NS sites (included in DuRoss, 2014), which yielded the mean and 2σ earthquake times discussed here (Table B-5). Horns *et al.* (2009) excavated trenches on the northern strand for geology field courses; however, these limited data are only published in an abstract, and thus, we do not include them in our analysis. In 2012, the UGS and USGS reoccupied the NC site and excavated a trench on the northern strand near Spring Lake to help resolve the timing of large earthquakes on the NS; however, results were not available at the time of this analysis.

At the NC site, Hanson *et al.* (1981) excavated three trenches, and exposed stratigraphic evidence for two surface-faulting earthquakes. They used six maximum and two minimum ^{14}C ages on bulk soil and charcoal fragments to constrain the timing of NC1 to 0.4 ± 0.5 ka. The young age of this earthquake is consistent with the steep scarp angles and the presence of a stream-channel nickpoint in North Creek just above the scarp (Hanson *et al.*, 1982b). The timing of older earthquakes is complicated by ^{14}C ages that cluster in two groups (~1.3–1.4 ka and 3.7–4.1 ka). Based on the discussion of these data in DuRoss *et al.* (2008), and considering radiocarbon-dating limitations and uncertainties discussed by Nelson *et al.* (2006) and DuRoss *et al.* (2011), we used the younger limiting ages to model earthquake times at 1.4 ± 0.3 ka (NC2) and 1.9 ± 0.5 ka (NC3). This differs from the interpretation of Hanson *et al.* (1982a, 1982b), who preferred the older ages, concluding that the younger ages "may represent younger material incorporated into the soil prior to burial." NC1 and NC2 both had about 2.1 to 2.3 m of per-event vertical displacement (Hanson *et al.*, 1981).

At the REC site on the southern strand, Jackson (1991) excavated one trench and found evidence for three Holocene surface-faulting earthquakes. The OxCal model for the REC site is based largely on the discussion and analysis of REC data included in DuRoss *et al.* (2008), and includes ^{14}C ages on bulk soil and TL ages that constrain the timing of these earthquakes to 0.5 ± 0.5 ka (REC1), 1.2 ± 0.3 ka (REC2), and 4.7 ± 2.5 ka (REC3). The large (2.5-kyr) uncertainty for REC3 stems from the lack of a numerical maximum constraining age for that event. Jackson (1991)

inferred that REC3 occurred after deposition of the REC alluvial fan at approximately 7 to 15 ka. Per-event vertical displacements range from about 1.4 m (REC1) to 1.7 m (REC3) (Jackson, 1991).

A trench investigation on the southern strand at the WC site by Machette *et al.* (2007) improved the late-Holocene (younger than about 2.5 ka) earthquake chronology for the southern strand. They used ^{14}C and OSL ages to constrain the timing of three surface-faulting earthquakes to 0.2 ± 0.09 ka (WC1), 1.2 ± 0.1 ka (WC2), and 2.0 ± 0.5 ka (WC3). Machette *et al.* (2007) also found indirect evidence for at least one earlier earthquake (WC4) based on the 6.2 ka age and minimum offset of footwall alluvial-fan sediments exposed in the trenches. However, they did not expose stratigraphic (*e.g.*, colluvial-wedge) evidence of the additional earthquake(s) in their trenches. Based on the time range for earthquake WC3 and 6.2 ka OSL ages for sediments exposed in the footwall of the fault, WC4 is poorly constrained to 4.7 ± 1.8 ka. Machette *et al.* (2007) did not calculate per-event vertical displacements for WC1–WC3.

On the northern strand, DuRoss *et al.* (2008) excavated trenches across a scarp having 3 m of vertical surface offset at the SQ site and found evidence of one surface-faulting earthquake. DuRoss *et al.* (2008) modeled a time for the Santaquin earthquake (SQ1) of 0.5 ± 0.2 ka based on two ~0.5-ka charcoal ages for a pre-faulting soil that provide a maximum constraint and a charcoal age of ~0.4 ka for scarp colluvium that provides a minimum constraint. However, considering the similarity in the maximum and minimum ages, it is possible that the 0.4-ka charcoal was recycled from the pre-faulting soil exposed in the footwall. Thus, we modeled an SQ1 time of 0.3 ± 0.2 ka (this study) by excluding the 0.4-ka minimum age. Considering both possibilities, the broadest possible time range for SQ1 is ~0.1–0.7 ka, which overlaps with both the youngest earthquake on the southern strand of the NS (~0.2 ka at WC) and the youngest earthquake on the PS (~0.6 ka). DuRoss *et al.* (2008) did not find evidence of a penultimate earthquake at the SQ site; however, this earthquake likely occurred prior to 1.5 ka based on soil charcoal, or possibly prior to 6.9 ka based on detrital charcoal from alluvial-fan sediments. About 3.0 m of vertical displacement occurred in SQ1 (DuRoss *et al.*, 2008).

Earthquake Chronology

Based on our analyses of these paleoseismic data (see expanded discussion in Crone *et al.*, 2014) and the discussion of these data in DuRoss *et al.* (2008), we model four late to middle Holocene earthquakes on the NS that occurred at 0.2 ka (N1), 1.2 ka (N2), 2.0 ka (N3), and 4.7 ka (N4) (Table B-5). These earthquake times rely heavily on the WC study, which found good evidence of three earthquakes younger than ~2.5 ka, and indirect evidence for an additional earthquake N4 (WC4) (Table B-5). We used the WC4 time (4.7 ± 1.8 ka) to define the N4 time, excluding REC earthquake REC3 (4.7 ± 2.5 ka) due to its larger 2σ uncertainty. Given their very broadly constrained (uniformly distributed) earthquake-timing PDFs, and the 6-km distance between the WC and REC trench sites, we did not correlate WC4 and REC3. In addition, we considered, but did not use the youngest earthquake on the northern strand from the SQ site (SQ1, 0.3 ± 0.2 ka, this study) to define the N1 time due to the uncertainty in the timing and rupture extent of the SQ1 earthquake. Given this uncertainty in earthquake timing, SQ1 could correlate with either the youngest earthquake on the southern strand (best constrained by WC1 at ~0.2 ka) or the youngest earthquake on the PS (P1 ~0.6 ka) (Crone *et al.*, 2014). While we consider it more likely that SQ1 corresponds with WC1, including SQ1 does not affect the N1 time because of the broad SQ1 uncertainty or N1 rupture extent because the Santaquin site is within the rupture-extent uncertainty

we defined for northern NS (see Section 4.1.6). Finally, excluding SQ1 is consistent with DuRoss *et al.* (2008), who considered multiple SQ1 correlation possibilities, but ultimately had insufficient data to draw conclusions regarding the behavior of the northern strand.

EARTHQUAKE RECURRENCE AND FAULT SLIP RATES

Earthquake Recurrence Intervals

Earthquake recurrence intervals, which describe the time between large earthquakes on a fault or segment, and the elapsed time since the MRE (a minimum recurrence interval) are critical for modeling time-dependent earthquake probabilities. For each central WFZ segment, we calculated individual (inter-event) and mean recurrence intervals using our revised earthquake times (Table B-6). Because the segments have limited earthquake records (yielding only three to four inter-event intervals), we also grouped the individual recurrence intervals for the central segments and calculated a composite mean recurrence interval for the central WFZ. Although grouping the intervals does not serve to increase the length of the record, it does increase the number of inter-event observations and allow for calculation of a more robust late Holocene mean recurrence interval. Recurrence intervals discussed here do not account for sample-size uncertainties.

Mean Recurrence per Segment

We calculated earthquake recurrence intervals for each central WFZ segment using a Monte Carlo model (with 10,000 simulations) to randomly sample the segment PDFs. In each segment-specific simulation, we used earthquake times sampled from the original segment PDFs (e.g., for B1 to B4; Figure B-3) to define time intervals over which the earthquakes and closed seismic intervals occurred. We calculated inter-event recurrence (e.g., the B4–B3 time; Table B-6) and closed mean recurrence, which is the total elapsed time between the oldest and youngest earthquakes divided by the number of closed intervals between them (e.g., the total time between earthquakes B4 and B1 divided by 3; Table B-7). We also calculated open mean recurrence intervals using the total elapsed time from the maximum age constraint on the oldest event (e.g., 5.9 ± 0.4 ka for B4; Table B-7) to the present (time of analysis, 2011) divided by the number of earthquakes that occurred in that period (open mean recurrence; B4 maximum age to the present divided by 4). This calculation yields an approximate maximum likelihood value for open recurrence, or the number of events per unit time (*N*-in-*T*).

The resulting recurrence estimates were filtered to eliminate values less than 195 ± 165 yr (2σ), which DuRoss *et al.* (2011) used as an estimated minimum time required to degrade a fault-scarp free face and begin to deposit scarp-derived colluvium along the rupture in a semiarid environment. The minimum time likely ranges from approximately a few tens to a few hundred years based on the elapsed times since the Borah Peak, Idaho, earthquake rupture (~30 yr) (which is now forming colluvial wedges; Crone and Haller, 2004) and the most recent earthquake on the NS (less than ~360 yr). The filtered inter-event recurrence intervals are similar (less than 10-yr difference) to those determined without a minimum time, with the exception of estimates for B4-B3, W2-W1, P3-P2, and N4-N3, where the filtered recurrence estimates are about 20 to 70 yr longer than the unfiltered results because of overlapping segment PDFs (Figure B-3). The filtered recurrence intervals do not significantly affect mean recurrence estimates for the segments (less than 10-yr

difference compared to unfiltered mean recurrence). We converted the recurrence values from all simulations into probability plots (PDFs) and calculated the mean and 2σ values reported in Table B-7.

Inter-event intervals for the central WFZ segments show moderate variability (Table B-6). For example, the youngest four earthquakes (B4 to B1) on the BCS yield consistent inter-event intervals of 1.0 to 1.1 kyr; however, about 2.5 kyr have elapsed since the most recent BCS earthquake, B1. Inter-event intervals for the WS, SLCS, PS, and NS are also irregular, ranging from about 0.7 kyr to 2.7 kyr, and varying by a factor of 2.4–3.5 per segment. For example, although two inter-event intervals for the WS are ~1.4 kyr (W5–W4 and W4–W3), the longest interval of 1.9 kyr for W3–W2 is 2.9 times greater than the 0.7-kyr interval for W2–W1. These inter-event intervals are useful for understanding and comparing the variability in earthquake recurrence on the central WFZ, but they do not necessarily represent the longer-term mean recurrence for the segments.

Closed mean recurrence intervals per segment (Table B-7) are based on the number of closed seismic intervals in the time between the oldest (generally mid-Holocene and youngest earthquakes (Table B-6). With the exception of the NS, the mean recurrence intervals are similar, ranging from 1.1 kyr on the BCS to 1.3 kyr on the WS, SLCS, and PS. These similar mean recurrence intervals reflect the most current earthquake data per segment and form the basis for our composite (grouped) central WFZ recurrence estimate (discussed below). The NS has a shorter mean recurrence interval of 0.9 kyr; this value is based on only two intervals between N3 and N1. The closed mean recurrence for the NS is 1.5 kyr if calculated using the N4–N1 time. However, we are not confident in this recurrence value because of the large uncertainty in the timing of N4 and concerns about the completeness of the earthquake record between N3 and N4 (*i.e.*, we do not correlate WC4 [4.7 ± 1.8 ka] with REC3 [4.7 ± 2.5 ka], which could be evidence of two separate NS earthquakes).

Open mean (*N*-in-*T*) recurrence intervals (Table B-7) are very similar to the closed mean recurrence intervals, with differences related to the elapsed time since the MRE or the time between the oldest earthquake and its maximum age constraint. The open mean recurrence values for the WS, SLCS, and PS are within about 0.1 kyr of the closed mean values. The BCS has the largest difference between the two values (~1.1 kyr–mean, ~1.5 kyr–open) because of the long elapsed time since its MRE (2.5 kyr). The NS has an intermediate (~0.2-kyr) difference in the recurrence values (~0.9 kyr–mean, ~1.1 kyr–open), which stems from the 1.2-kyr elapsed time between N3 (~2.0 kyr) and its maximum limiting age (~3.2 kyr).

Composite Recurrence for the Central WFZ

We calculated a composite mean recurrence interval for the central WFZ (Figure B-5) based on the observation that the central five segments essentially behave in a similar manner—that is, they have similar long-term (post-Provo) slip rates and recurrence of surface rupture. The advantage of a composite recurrence interval is that the sample size for closed intervals increases from 2–4 per segment to 16 for the central WFZ, which yields a more statistically robust mean recurrence estimate for the region.

We calculated the composite closed (inter-event) recurrence interval by grouping and then sampling each of the 16 inter-event recurrence distributions (PDFs) in 10,000 simulations. In each

simulation we (1) sampled each of the inter-event PDFs, yielding a subset of 16 recurrence values (one for each of the inter-event pairs, such as W5–W4), (2) calculated the mean recurrence of this composite subset, and (3) compiled these composite mean recurrence values (n = 10,000). The mean and 2σ range of the composite mean dataset, or distribution of means calculated in the simulations, is 1.2 ± 0.1 kyr (5th–50th–95th values of 1.1–1.2–1.3 kyr) (Figure B-5). For comparison, we also calculated a composite mean by grouping all of the inter-event values (n = 160,000), rather than taking the mean in each simulation. This method conveys the full distribution of possible recurrence estimates given the initial recurrence distributions (e.g., W5–W4). As expected, the calculation results in a greatly increased width of the recurrence distribution because all of the individual recurrence values are included and treated equally, rather than grouped in individual simulations to generate mean values. This alternate composite recurrence interval (for all recurrence records) is 1.2 ± 1.1 kyr (2σ). Ultimately, the composite mean calculated using the mean per simulation better reflects the average recurrence behavior of the central WFZ as it limits the effect of the end-member recurrence values at the tails of the recurrence distributions (e.g., 82 yr between W2 and W1 or 2966 yr between P4 and P3 at 2σ). However, we caution that the uncertainty represents the distribution of the mean values, rather than the complete dataset, and does not include sample-size uncertainties.

Coefficient of Variation on Recurrence

The coefficient of variation (COV) on recurrence, the standard deviation of inter-event recurrence intervals divided by their mean, is a measure of the periodicity of earthquakes on a fault. The smaller the COV, the more periodic is the recurrence. A large COV value indicates a more variable time interval between earthquakes. For example, a COV of 0.1 reflects very periodic recurrence behavior, whereas a COV of 1.0 indicates that recurrence is essentially random. The WGCEP (2003, 2008) used a COV of 0.5 ± 0.2 based on a global dataset of repeating earthquake sequences (Ellsworth *et al.*, 1999).

To test the suitability of the global COV to the central WFZ, we calculated a composite COV for the central WFZ using inter-event recurrence times between earthquakes on each of the five segments (e.g., those for BCS earthquakes B4–B3 and WS earthquakes W5–W4) (Figure B-6). We did not use recurrence times between earthquakes on different segments (e.g., the time between W4 and B4), which would yield significantly shorter recurrence times (mean of ~300 yr). We only calculated a single (composite) COV for the central WFZ because inter-event recurrence data per segment are limited (2–4 intervals per segment). The basis for the composite COV is similar mean recurrence parameters for the individual segments. Grouping the inter-event recurrence data allowed us to calculate a more statistically robust COV; however, the estimate does account for sample-size uncertainties

To compute the composite COV for the central WFZ, we compiled 16 inter-event-recurrence PDFs and sampled them in a Monte Carlo model. We used the recurrence PDFs filtered for the minimum recurrence value of ~195 ± 165 yr (described above) in our calculations; however, we achieved similar results (COV within 0.01) using the inter-event recurrence estimates not filtered for a minimum time. We did not include open intervals (e.g., the elapsed time since the most recent earthquake per segment) in our COV calculation. We sampled the group of inter-event recurrence PDFs through 10,000 simulations; each simulation randomly selected a single recurrence value from each inter-event recurrence PDF and added it to a group of recurrence values. That is, in each

simulation, one recurrence value was selected for B4–B3, one for W4–W3, etc., thus forming a set of 16 recurrence intervals from which we calculated the COV (standard deviation divided by the mean of the 16 recurrence intervals). This process was repeated in each simulation, yielding a dataset of COV values, from which we determined the mean and 2σ standard deviation. Although sampling the inter-event distributions yield combinations of inter-event times that violate the paleoseismic records per segment (e.g., summed inter-event times exceeding the total record length), these combinations occur infrequently, for example, when the large-recurrence tails of several inter-event distributions are sampled concurrently. Thus, their contribution to the model results, while adding slight variance, is considered insignificant.

For comparison, we again followed this method but segregated the sampled recurrence PDFs by segment and computed segment-specific COVs, which we then summed to form a composite COV (Figure B-6). In this method, poorly constrained data (e.g., the NS COV based on only two recurrence intervals) receive equal weight as better constrained data (e.g., the WS COV based on four recurrence intervals). Both contributed about 20% (1/5) to the composite COV value. However, we have greater confidence in the composite method rather than the segment-specific method because individual recurrence records are combined and thus have less impact on the final COV value. For example, the four WS recurrence intervals contribute 25% (4/16) to the composite COV whereas the two NS intervals only contribute 12.5% (2/16).

The composite COV for the central WFZ is 0.5 ± 0.1 (2σ), with a minimum–maximum range of about 0.3 to 0.7 (Figure B-6). Although the composite approach yields the most robust mean COV for the region, COV estimates for the individual segments show more variability. The per-segment COVs range from 0.3 ± 0.4 (NS) to 0.6 ± 0.3 (PS); however, each is based on a small dataset (two to three inter-event periods). Summing the per-segment COV PDFs yields a per-segment composite COV with a mean and 2σ uncertainty of 0.4 ± 0.4. As discussed above, the composite COV is a more robust estimate for the central WFZ as a whole as it is based on a larger (grouped) sample set. The composite COV for the WFZ is similar to the value of 0.5 ± 0.2 used by the WGCEP (2003, 2008). The consensus of the WGUEP is to use a central WFZ COV of 0.5 ± 0.2 based on the global COV (Ellsworth *et al.*, 1999) and calculated composite COV mean (0.5) and possible range of uncertainty (± ~0.2).

Vertical Displacement

Vertical Displacement per Earthquake and Rupture Source

We compiled data to estimate the vertical displacement per site and for each surface rupture (Table B-8) for the central WFZ. These data are derived from the original paleoseismic-data sources discussed above (summarized and discussed in DuRoss [2008]), and also include recently obtained data from the HC, KC, and PC sites (DuRoss *et al.*, 2012), RC site (DuRoss *et al.*, 2009), and PD site (DuRoss *et al.*, 2014; DuRoss and Hylland, 2015). Using our correlation of site events along the segments (Tables B-1 to B-5), we combined individual vertical displacements per site into mean and minimum–maximum range displacements per rupture (e.g., for events B1 through B4; Tables B-8 and B-9), and ultimately, mean displacement per rupture source (e.g., for the BCS; Table B-10). We discuss these methods and results for single-segment ruptures; mean displacements for combinations of rupture sources (multi-segment ruptures) are discussed in the Rupture Models for the Central WFZ section.

To estimate the displacement per single-segment earthquake, we plotted the location of the site displacements along a rupture and modeled the average displacement for that rupture based on the well-documented observation that displacement tapers toward the ends of a surface rupture (Hemphill-Haley and Weldon, 1999; Biasi and Weldon, 2006; Wesnousky, 2008; Biasi and Weldon, 2009) (Figure B-7). Our approach is similar to that of Chang and Smith (2002), who fit analytical (ellipse-shaped) displacement profiles to central WFZ site displacements by varying the maximum height (displacement) of the ellipse. However, rather than fixing the shape of the displacement curve, we also allowed its shape to change by using the function $([\sin(\pi x/L)]^n)h$ (after Biasi and Weldon, 2009), where x/L is the normalized distance along the rupture (in 0.1-km increments), h controls the maximum height of the displacement curve, and n controls its shape. To achieve this, we (1) compiled displacement observations (and uncertainties) along each earthquake rupture that we modeled (Table B-8); (2) computed a suite of analytical displacement curves for each rupture having a large (several meter) range of maximum heights (h) and shapes (exponent n) varying from mostly flat or uniform (n=0.1) to peaked (n=0.9); and (3) used a least-squares regression to determine a best-fit analytical displacement curve that minimized the error between the modeled and observed displacements (sum of squared deviation from the displacement observations). For ruptures having two or more displacement observations, we took the least-squares, best-fit displacement curve, which most closely matched the observations, sampled it every 0.1 km, and calculated a modeled mean displacement (Figure B-7). For ruptures having only one displacement observation or two closely spaced observations, we arbitrarily fit three displacement curves to the data with flat, half-ellipse, and peaked shapes (exponent n values of 0.2, 0.5, and 0.8, respectively, while allowing h to vary), then sampled and computed the means for these profiles, and computed the mean displacement for the rupture by averaging these three means. To account for uncertainty in rupture displacement, we followed these methods using the mean, minimum, and maximum site displacements in separate models (Table B-9). Thus, the minimum and maximum displacements for a rupture are based on a best-fit displacement curve that fits the minimum and maximum site displacements, respectively. The modeled mean displacements per rupture are summarized as displacement per rupture source in Table B-10.

An important question is whether our best-fit displacement curve method reasonably models average displacement for historical normal-faulting earthquakes. We tested our method using along-strike displacement observations from historical normal-faulting earthquakes compiled by Wesnousky (2008). We were able to closely approximate the mean rupture displacement, even if the rupture had an asymmetric shape. Our least-squares mean displacements varied by 0 to 13% from mean displacements based on field observations and mean displacements from rupture profiles with points interpolated between observations (Wesnousky, 2008). For example, our best-fit displacement curve for displacement observations from the 1983 Borah Peak earthquake rupture indicates an average displacement of 0.8 m (Figure B-7), which is the same value for the average displacement based on interpolation of Wesnousky's (2008) displacement profiles.

Vertical Displacement per Source

We determined mean displacement per rupture source (i.e., per segment; Table B-10) by taking the mean of the modeled per-rupture displacements (based on displacement curves calculated using the mean observed displacements). Minimum and maximum displacements per source are based on the smallest and largest modeled displacements per rupture (based on displacement curves calculated using the minimum and maximum observed displacements, respectively). The

modeled mean displacements per source range from 1.7 m for the BCS and SLCS to 2.6 m for the PS (Figure B-8). These yield a mean displacement for the central WFZ of 2.1 m, which is similar to the unmodeled mean of 2.0 m, and a mean of 2.2 m reported by DuRoss (2008), but based on a subset of the data used in this analysis. Limitations of these data include assumptions regarding the position of the displacement observation along the rupture and several individual rupture displacements that are based on only one to two displacement observations (e.g., B1; Table B-8). However, despite the sparse data (not all sites yielded displacement observations for each rupture), per-rupture displacements are similar for each rupture source (Table B-9).

Vertical Slip Rate per Segment

We used the mean displacements per earthquake rupture and per single-segment rupture source, the individual earthquake times, and the open and closed mean recurrence intervals to calculate vertical slip rates for the central WFZ segments (Table B-11) and for the central WFZ as a whole (composite slip rates). For each segment, we determined (1) a closed-interval slip rate using the modeled mean displacement for the segment (Table B-10) divided by the segment's closed mean recurrence interval (Table B-7), (2) an open-interval slip rate for which we used the total displacement in the time period defined by the maximum limiting age for the oldest earthquake to the present (Tables B-7 and B-11), and (3) long-term rates based on the vertical offset of geomorphic surfaces related to the latest Pleistocene-age Provo phase (14.0–17.6 ka; Godsey *et al.*, 2005, 2011) and highstand (about 17.6 ± 0.3 ka; based on Oviatt, 1997) of Lake Bonneville (Table B-11). We calculated composite slip rates comprising (1) a composite, long-term slip rate based on eight long-term (latest Pleistocene) slip rates (Table B-11), and (2) a composite, closed-interval, mean slip rate for which we used the mean of the average displacements per segment divided by the closed-interval mean composite recurrence interval for the central WFZ. We report a weighted mean slip rate per segment that uses these slip rates and a weighting scheme described below and in Table B-12.

We calculated weighted-mean slip rates for the central WFZ segments using two weighting schemes (Table B-12) that stem from expert opinion. For the WS, SLCS, and PS, the weighted mean slip rate is based on the closed mean slip rate per segment (0.35 weight), the composite closed mean slip rate for the central WFZ (0.35 weight), and the composite long-term (latest Pleistocene) slip rate for the central WFZ (0.3 weight). The closed mean slip rates received the greatest weight (0.35 each) as the earthquake records and mean recurrence intervals for these segments are well constrained. We did not use the open-interval slip rates for these segments because of the robust closed recurrence data. The long-term rate received slightly less weight (0.3) on account of the spatial distribution of geologic units and surfaces used to make the displacement measurements, which are generally limited in horizontal extent and clustered nonuniformly along the fault (generally at the segment boundaries). For the BCS and NS, we used the composite long-term slip rate (0.3 weight), but gave slightly less weight to the closed mean slip rate per segment (0.2 weight) and the composite closed mean slip rate (0.3 weight). Reduced weight for the closed mean slip rates allowed for the inclusion of open-mean slip rate per segment (0.2 weight). We included the open mean rate for the BCS because it accounts for the long elapsed time since the BCS MRE (which is excluded in the closed mean rate). For the NS, we chose to use the open mean rate because the closed mean rate is based on only two closed recurrence intervals.

WS, SLCS, and PS	Weight
Closed mean slip rate per segment	0.35
Composite closed mean slip rate	0.35
Composite long-term slip rate	0.3

BCS and NS	Weight
Closed mean slip rate per segment	0.2
Open mean slip rate per segment	0.2
Composite closed mean slip rate	0.3
Composite long-term slip rate	0.3

The weighted mean slip rates are very similar for each segment ranging from 1.3 mm/yr for the BCS and SLCS (the shortest segments), to 1.5 and 1.6 mm/yr for the WS and PS, respectively (the longest segments) (Table B-12). The similarity in these rates reflects the fairly consistent closed-interval slip rates (1.3–2.0 mm/yr) and open-interval slip rates (1.2–2.1 mm/yr), as well as the composite rates, which are included in the weighted-mean calculation for each segment. The composite long-term slip rate is 1.0 mm/yr (0.6–1.4 mm/yr range) based on both measured displacements across Provo-phase and Bonneville highstand surfaces of the Bonneville lake cycle. The composite closed-interval slip rate is 1.7 mm/yr (0.9–2.7 mm/yr range) using the mean of the mean displacements per segment (~2.1 m) divided by the composite mean recurrence interval (1.2 ± 0.1 kyr).

RUPTURE MODELS

Evaluation of Possible Multi-Segment Ruptures on the Central WFZ

Prominent structural segment boundaries along the central WFZ represent persistent (long-term) features that may act as barriers to lateral propagation of surface faulting (Machette *et al.*, 1992). Support for the seismogenic independence of the segments stems from their unique late Holocene earthquake histories as well as significant differences in most recent earthquake timing across these complex structural boundaries (Schwartz and Coppersmith, 1985; Machette *et al*., 1992; Lund, 2005; DuRoss, 2008). However, similar to Machette *et al*., (1992), we cannot rule out the simultaneous rupture of adjacent segments (e.g., Chang and Smith, 2002) considering moderate to large uncertainties in earthquake timing and limited mid-Holocene earthquake records for the segments. Thus, we used the refined earthquake chronologies and displacement estimates per segment to identify possible and probable multi-segment ruptures on the central WFZ. These ruptures are included in rupture models that capture the range of possible earthquake rupture behavior on the central WFZ.

We evaluated possible multi-segment ruptures using: (1) the degree of overlap in the segment PDFs (PDF overlap; Figure B-9); (2) the number and location of sites where a specific rupture was identified, which defines the percentage of the rupture's length that has been studied and identifies along-strike gaps in paleoseismic data; and (3) the mean and along-strike displacements per rupture (from individual paleoseismic sites) (Table B-8). The PDF overlap is the sum of the minimum probabilities for time bins common to two PDFs (e.g., earthquake-timing PDFs for earthquakes on adjacent segments) and ranges from 0 (no overlap) to 1 (complete overlap of two identical PDFs) (after Biasi and Weldon, 2009; see also DuRoss *et al.*, 2011). Our evaluation relied mostly on the amount of PDF overlap (giving preference to PDFs with overlap values greater than an arbitrary amount of 0.5, which visually represents a moderate amount of overlap) and the displacement data rather than solely focusing on the locations of the paleoseismic sites along the ruptures because these are also a function of many other factors unrelated to the paleoseismology such as access, urbanization, or landowner restrictions. We considered ruptures at least as long as the largest known historic normal slip earthquake in the Basin and Range Province, the **M** 7.5 ± 0.3 1887 Sonora, Mexico earthquake that ruptured 102 km along three sections (Pitaycachi, Teras, and Otates sections) of a 300-km-long range-bounding normal fault in northern Mexico (Bakun, 2006; Suter, 2006) as plausible. On the central WFZ, two-segment ruptures yield rupture lengths of about 90 to 100 km (table B-13), consistent with the 1887 Sonora earthquake. However, we also considered ruptures as long as three adjacent segments if the paleoseismic data warranted it. Finally, we also made a qualitative assessment of the strength or persistence of a segment boundary based on its fault complexity and geometry (e.g., the horizontal distance between fault traces in a step-over zone), timing of most recent surface faulting, and the amount and quality of the paleoseismic data available at or adjacent to the boundary.

Based on our evaluation of earthquake timing data for the central WFZ, we found multi-segment ruptures between the BCS and WS, SLCS and PS, and PS and NS to be most probable. In particular, possible multi-segment ruptures B4+W5, S2+P3, and P3+N3 have significant overlap (~0.6) in their segment-PDF pairs, a large percentage (56–80%) of their total rupture lengths studied (having paleoseismic data), and minimal gaps between paleoseismic sites along the rupture (gaps less than 50% of the total rupture length) (Table B-13). Multi-segment rupture B3+W4 also has significant PDF overlap (0.7), but only 35% of the rupture length studied because no evidence is reported for W4 on the southern part of the WS (Kaysville site). However, because the Kaysville site may not have exposed evidence of all mid-Holocene earthquakes on the WS (DuRoss *et al.*, 2011), we consider B3+W4 a probable multi-segment rupture. Using these criteria, we consider multi-segment ruptures W2+S1, P2+N2, B2+W3, S3+P4, and S2+P3+N3 (the only three-segment rupture considered, which is based on similar PDF overlap values of 0.59 for S2–P3 and P3–N3) to be less likely. These ruptures have less overlap in their respective segment-PDF pairs (less than 0.4), more significant paleoseismic data gaps, and/or remaining questions regarding earthquake timing and rupture extent from the site data. In addition, we dismissed multi-segment ruptures involving poorly constrained earthquakes on a segment, such as N4 or P5.

We also evaluated possible multi-segment ruptures using estimates of mean displacement. To determine mean displacements for the multi-segment ruptures, we used analytical displacement curves fit to the per-site displacement data (discussed above in the Vertical Displacement per Rupture and Earthquake Source section), but using rupture lengths shown in Table B-13 and Figure B-10. On the BCS and WS, displacements are moderately large (~1.5–2.5 m) along the segments, and have large-displacement (4.2 m) peaks near the segment boundary, supporting multi-segment

ruptures between the two segments (e.g., B2+W3 and B3+W4). Ruptures having moderately large displacements along two segments, but lacking a clear displacement peak near the possible rupture center (segment boundary) (e.g., 1.4–2.5 m along B4+W5, 1.5–3.2 m along W2+S1, and 1.4–2.5 m along S3+P4) provide less compelling evidence of multi-segment ruptures. Several segment pairs have more limited displacement data (~3 observations), but still show a half-ellipse-shaped displacement profile along the possible rupture length (*e.g.*, S2+P3 and S3+P4), providing a small degree of confidence in our possible multi-segment ruptures.

Mean displacement per multi-segment rupture (e.g., B2+W3), using our analytical displacement curves, is mostly about 2 m, but ranges from about 1.7 m (S2+P3+N3) to 3.8 m (P3+N3) (Figure B-10). These displacements are similar to those for single-segment ruptures (Table B-9) because we chose to honor the per-earthquake site displacements rather than model the displacement using a surface rupture length (SRL)–displacement scaling relation (e.g., Wells and Coppersmith, 1994; c.f., Biasi and Weldon, 2009). Doing so would result in larger displacements (e.g., 4–8 m for a 100-km-long rupture using the all- and normal-fault type maximum displacement–SRL regressions of Wells and Coppersmith, 1994) than generally observed (most per-earthquake displacements are < 3 m). Although our moderate multi-segment rupture displacements (similar to those for single-segment ruptures) may stem from sparse data along the rupture, it is also plausible that displacement values reach a maximum value once a certain rupture length (or possibly down-dip rupture width) is achieved (e.g., see Wesnousky, 2008).

Rupture Models for the Central WFZ

We developed rupture models for the central WFZ (Table B-14; Figures B-11 to B-13) using methods somewhat similar to those of the Working Group on California Earthquake Probabilities (WGCEP, 2003; Earthquake Probabilities in the San Francisco Bay Area) and WGCEP (2008; The Uniform California Earthquake Rupture Forecast [UCERF2]). WGCEP (2003) constructed rupture scenarios, which they defined as combinations of rupture sources that describe possible differing modes of failure of an entire fault (e.g., single- or multi-segment ruptures) in one earthquake cycle. These scenarios were combined into various fault-rupture models—ideally representing the long-term behavior of the fault—and the various scenarios were assigned weights based on the opinion of experts. A significant difference with our rupture models is that they are based on paleoseismic data that span the middle to late Holocene, and thus encompass the behavior of the central WFZ over multiple earthquake cycles. We only apply a single set of weights for these rupture models rather than various weights for the multiple fault-rupture models described in WGCEP (2003). Our rupture models yield different rupture-source combinations, similar to WGCEP (2003). For the UCERF2, WGCEP (2008) constructed B-priori models of fault rupture using paleoseismic data to determine single- and multi-segment earthquake rates and magnitudes (e.g., appendix F in WGCEP, 2008). Our rupture models are similar to WGCEP (2008) a-priori maximum, geologic-insight (preferred models that correspond with observations such as slip rate and paleoseismic event records), and minimum rupture models.

Rupture models address epistemic uncertainties in the segmentation of the central WFZ. Five models include: (1) a model in which each rupture is confined to a single-segment (single-segment rupture model; Figure B-11), (2) three intermediate models consisting primarily of single-segment ruptures, but including three combinations of multi-segment ruptures (intermediate models A, B, and C; Figure B-12), and (3) a model in which we include as many multi-segment ruptures as possible, which results in the fewest number of ruptures (multi-segment rupture model; Figure B-

13). These models were developed using the per-segment earthquake chronologies, rather than the individual trench-site data. We also included an unsegmented model, which accounts for potential multi-segment and/or partial-segment ruptures that we did not identify in these models (i.e., ruptures are allowed to "float" along the fault and are not constrained by segment boundaries).

Single-Segment Rupture Model

The single-segment rupture model includes 22 individual earthquakes on the central WFZ segments (Table B-6 and B-14; Figure B-11). Preference (model weight of 0.7) for the single-segment rupture model over those including multi-segment ruptures is based on (1) prominent along-strike variations in fault geometry (e.g., fault step-overs, gaps, and changes in strike), complexity (e.g., areas of diffuse faulting), and structure (e.g., range-front morphology and relief) that define prominent fault salients, hanging-wall basins, and fault segments; (2) differences in the timing of the youngest surface-faulting earthquakes at sites along the WFZ (e.g., compare the timing of the youngest events along the BCS, WS, SLCS, and PS; Figure B-3); (3) unique late Holocene surface-faulting earthquake histories per segment (Figure 4.1-2); (4) differences in per-event vertical displacement across the segment boundaries (e.g., compare DuRoss *et al*., 2011 to Personius *et al*., 2012, see also DuRoss, 2008); (5) long-term (latest Pleistocene) slip deficits at the segment boundaries (Machette *et al*., 1992); and (6) paleoseismic evidence for at least one spillover rupture from the WS to the BCS (DuRoss *et al*., 2012; Personius *et al*., 2012), rather than the simultaneous rupture of both segments. Per-earthquake displacements do not unequivocally support single-segment ruptures; however, we note that our single-segment analytical displacement curves better fit the displacement observations than the multi-segment curves (average error of 0.6 vs. 2.0 m, respectively). Single-segment earthquakes have median SRLs of 35 to 59 km and moment magnitudes of 6.9 to 7.3 based on SRL and 7.1 to 7.4 based on seismic moment (M_O) (see discussion in Calculating Magnitudes section).

We incorporated uncertainty into the location of each segment boundary (following WGCEP 2003; see discussion in Segment Boundary Uncertainties section) to allow for variability in single-segment rupture lengths. Although we cannot discount the occurrence of multi-segment ruptures, spillover rupture across segment boundaries (i.e., coseismic rupture across a "leaky" segment boundary; Crone and Haller, 1991) is more consistent with the WFZ paleoseismic data. For example, spillover rupture across the WS-BCS boundary in earthquake W2 shows that the segment boundary has failed in the late Holocene. However, the rupture only continued onto the southern ~8 km of the BCS (DuRoss *et al.*, 2012), despite the relatively large amount of accumulated seismic moment on the northern part of the BCS at the time of the event (Personius *et al.*, 2012). The 1983 Borah Peak earthquake demonstrated similar behavior, where surface faulting at the north end of the Thousand Springs segment crossed the segment boundary and ruptured about 8 km of the adjacent Warm Spring segment (Crone *et al.*, 1987). This treatment of the WFZ is consistent with the hybrid characteristic slip model of DuRoss (2008) in which "large-displacement single-segment ruptures dominate the fault history but are interrupted by anomalously small- and large-displacement events (i.e., possible partial- and multi-segment ruptures, respectively)."

Intermediate and Multi-Segment Rupture Models

The intermediate and multi-segment rupture models include combinations of both single-segment and multi-segment ruptures consistent with the central WFZ paleoseismic data (Tables B-14 and

B-15; Figures B-12 and B-13). In cases where several single-segment earthquakes could potentially combine to yield more than one multi-segment rupture, we relied on the PDF overlap value (as well as displacement data, if available) to guide our choice of a preferred rupture, or we included those combinations of ruptures in multiple models. For example, we preferred a rupture of S1+P2 (PDF overlap of 0.46) over S1+W2 (PDF overlap of 0.39). Likewise, we preferred B3+W4 over W4+S3 on the basis of the PDF overlap, but also because of the lack of evidence that W4 produced rupture on the southern part of the WS. Because of the similar PDF overlap values for the earthquake pairs of S2+P3 and P3+N3, we included both of these ruptures in separate models.

The intermediate rupture models each contain 19 to 20 earthquakes, most of which are single-segment ruptures, but two to three of which are the most probable multi-segment ruptures (Figure B-12). We have greater confidence in the intermediate models over the multi-segment rupture model because they include three multi-segment ruptures supported by similar earthquake times on adjacent segments (PDF overlap greater than 0.5), and for the BCS+WS, large (4.2-m) vertical displacements on the northern part of the WS (close to the BCS–WS segment boundary). We recognize that our three intermediate models represent only a few of all the possible models given the most probable ruptures shown in Table B-13.

We limited our intermediate models to three variations of the multi-segment ruptures we consider most probable: B4+W5, B3+W4, S2+P3, and P3+N3. Each of the intermediate models includes B4+W5 and B3+W4, which have very similar earthquake times (PDF overlap of about 0.6–0.7), large (4.2 m) displacements close to the BCS–WS segment boundary (at the northern end of the WS; Figure B-10), and a segment boundary that has failed in at least one spillover earthquake (continuation of WS earthquake W2 rupture about 8 km onto the southernmost BCS; DuRoss *et al.*, 2012; Personius *et al.*, 2012). Intermediate model C includes multi-segment ruptures B4+W5 and B3+W4; all of the remaining earthquakes are single-segment ruptures. Intermediate models A and B are identical to intermediate model C, but also include S2+P3 (model A) and P3+N3 (model B), which are supported by significant overlap (PDF overlap of 0.59) in their respective segment earthquake times (Table B-13). We prefer modeling S2, P3, and N3 as separate earthquakes and therefore prefer intermediate model C over models A and B, which include 85- to 99-km-long ruptures in S2+P3 and P3+N3. Given the broad timing uncertainties (± 0.5–0.7 kyr) for the individual earthquakes forming multi-segment ruptures in these models, we assign a total weight of 0.175 to the intermediate rupture models, with individual weights of 0.05, 0.05, and 0.075 to models A, B, and C, respectively.

The multi-segment rupture model includes 14 earthquakes—seven multi-segment and seven single-segment ruptures (Figure B-13), which is the fewest number of ruptures based on earthquake timing (PDF overlap). The model includes six two-segment ruptures and one three-segment rupture (S2+P3+N3) that we cannot fully dismiss given the earthquake-timing and displacement data. These multi-segment earthquakes have median SRLs of 88 to 128 km and moment magnitudes of 7.3 to 7.6 based on SRL and 7.4 to 7.5 based on M_O (see discussion in Calculating Magnitudes section).

Consistent with Machette *et al*. (1992), Lund (2005), and DuRoss (2008), we found no observational basis to conclude that earthquakes on the central WFZ regularly rupture multiple segments. That is, the most recent and best-constrained earthquakes per segment support individual-segment ruptures (figure B-3), at least one spillover rupture on the central WFZ has

been documented with paleoseismic data (Personius *et al*., 2012), and large numbers of multi-segment ruptures are inconsistent with the presence of prominent segment boundaries along the fault. Thus, we assigned relatively low weight to the multi-segment and intermediate rupture models (total weight of 0.2) compared to the single-segment rupture model (weight of 0.7). We gave more weight to the intermediate models (combined weight of 0.175) compared to the multi-segment rupture model (weight of 0.025) because they include the most probable multi-segment ruptures. Although some of the two (and three-) segment ruptures included in the multi-segment model may have occurred, we find it highly unlikely that all them occurred given the earthquake timing, segment-boundary, and spillover rupture arguments discussed above.

Together, the single-segment, intermediate, and multi-segment rupture models highlight possible modes of rupture along the central WFZ. However, our analyses are limited by modeling assumptions and poorly constrained mid-Holocene earthquake data. For example, although our analysis of the site PDF data by segment is consistent with the body of work indicating a segmented fault (e.g., Schwartz and Coppersmith, 1984; Machette *et al.*, 1992; Lund, 2005; DuRoss, 2008; Personius *et al.*, 2012) and serves to help limit the per-segment earthquake chronologies (e.g., DuRoss *et al.*, 2011), our ability to define and evaluate all possible rupture permutations is limited. We have addressed this limitation by constructing multi-segment and unsegmented rupture scenarios and by defining segment-boundary uncertainties, which allow for both partial-segment and spillover ruptures not specifically accounted for in the rupture models. However, we suggest that an evaluation of possible ruptures across the WFZ segment boundaries using the site earthquake data be conducted to yield a more comprehensive suite of rupture models (e.g., Biasi and Weldon, 2009). Finally, although the youngest earthquakes along the WFZ are consistent with a segmented fault, poorly constrained mid-Holocene earthquakes allow for longer rupture lengths. Additional mid- to early Holocene paleoseismic data for the central WFZ would aid in evaluating which of these multi-segment ruptures are most plausible.

Unsegmented Rupture Model

An unsegmented rupture model is implemented in the WGUEP forecast to account for ruptures on the central WFZ and the WFZ as a whole, irrespective of fault segmentation model and defined rupture boundaries. This model uses a distribution of magnitudes (as opposed to rupture lengths) ranging from **M** 6.75 to 7.6 (Section 3.4). To some degree, this model accounts for a level of partial-segment rupture and rupture across a segment boundary (spillover rupture) greater than that allowed by the segment boundary uncertainties. We assigned a relatively low weight (0.1) to the unsegmented model because the central WFZ is characterized by prominent segment boundaries and because the paleoseismic data suggests that ruptures on the central WFZ are not spatially random (e.g., the youngest earthquakes on the BCS are significantly older than those on the adjacent WS). Furthermore, we account for many multi-segment ruptures in our multi-segment and intermediate models, where those ruptures honor available paleoseismic earthquake timing and displacement data. Rates for the unsegmented model are based on the central WFZ closed-mean slip rate (~1.7 mm/yr; 0.2 weight), long-term slip rate (~1.0 mm/yr; 0.3 weight), as well as the broad range in slip rates for the northernmost end segments (Section 4.2.2).

Segment Boundary Uncertainties

To define segment-boundary uncertainties for the central WFZ (table B-16), we considered the geometry and extent of Holocene faulting near the ends of the segments, and, if available,

paleoseismic data from sites close to the segment boundaries (Figures B-14 and B-15; Table B-17). Most segment boundaries are moderately well constrained (3–8 km); however, we include large uncertainties (13–17 km) for the complex overlapping fault step-over between the PS and NS. The best-constrained boundary is the BCS–Collinston segment (CS) boundary (± 3 km) based on the extent of Holocene surface faulting on the BCS, the apparent lack of Holocene rupture on the CS, and 3 km of spillover rupture from the BCS onto the southern CS (Personius, 1990; Personius *et al.*, 2012). We applied asymmetric uncertainties for several segment boundaries. The uncertainty for the BCS and WS is 3 to 8 km (depending on the segment; Figure B-14), which accounts for the spillover rupture that occurred during earthquake W2 (DuRoss *et al.*, 2012; Personius *et al.*, 2012). An asymmetric uncertainty for the PS and NS (+4, –13 km for the southern PS and +5, –17 km for the northern NS) is based on overlap between the two segment traces, the total length of the northern strand of the Nephi segment. Additional descriptions of geologic data used to constrain the segment-boundary uncertainties are included in Table B-17.

We used these uncertainties to define a range of rupture-lengths for both single- and multi-segment ruptures (Table B-16). For single-segment earthquake sources, rupture lengths range from a minimum of about 20 to 46 km to a maximum of 41 to 71 km. Ruptures equal to the minimum lengths would represent the partial rupture of each segment, or rupture of 47 to 82% of the median rupture lengths (e.g., 35 km for the BCS; Table B-16), defined using the traditional segmentation model (Machette *et al.*, 1992). Ruptures equal to the maximum lengths would entail rupture of about 117 to 133% of the median rupture lengths, and thus, spillover rupture of about 3 to 8 km at each end of the rupture. For the multi-segment ruptures, we used the same segment-boundary uncertainties, and defined minimum and maximum rupture lengths of 76–115 km and 100–141 km, respectively. These values result in the rupture percentages varying from 80–91% (using minimum lengths) to 110–114% (using maximum lengths) of the median multi-segment rupture lengths.

CONCLUSIONS

At least 22 surface-faulting earthquakes have ruptured the central segments of the WFZ since about 6.0 ka. These data stem from our systematic analysis of previous paleoseismic data, OxCal model development, and integration of site earthquake data along each segment. Using our revised surface-faulting earthquake histories for each segment, we calculated inter-event, open mean, and closed mean recurrence intervals. These data indicate moderately periodic earthquake recurrence on the central WFZ as a whole: inter-event recurrence intervals range from 0.7 to 2.7 kyr and yield a composite COV of ~0.5, and open and closed mean recurrence intervals for the segments (0.9–1.3 kyr and 1.1–1.5 kyr, respectively) are similar to a composite closed mean recurrence calculated for the central WFZ (~1.2 kyr). Using these recurrence data and modeled mean vertical displacements per rupture and segment, we calculated weighted mean vertical slip rates for the segments of ~1.3 to 1.6 mm/yr, based on closed-seismic-interval slip rates of ~1.3 to 2.0 mm/yr, open-interval rates of ~1.2 to 2.1 mm/yr, and composite rates for the central WFZ. A composite closed-interval slip rate, based on the mean central WFZ displacement of ~2.1 m divided by the 1.2-kyr composite recurrence, is ~1.7 mm/yr; a mean long-term slip rate for the central WFZ based on offset latest Pleistocene geomorphic surfaces is ~1.0 mm/yr.

Although single-segment ruptures may be the dominant earthquake process on the central WFZ, earthquake-timing uncertainties allow for alternative (e.g., multi-segment) scenarios. To address epistemic uncertainties in the WFZ segmentation, we constructed rupture models from the per-segment earthquake histories and also defined segment-boundary uncertainties. Five rupture models include both single- and multi-segment ruptures; an unsegmented model accounts for potential multi-segment and/or partial-segment (i.e., floating) ruptures not identified in our rupture models. Ultimately, prominent segment boundaries and significant differences in the timing of the most recent and best-constrained earthquakes per segment support the seismogenic independence of the segments. As we have no observational basis to conclude that earthquakes on the central WFZ regularly rupture multiple segments, we gave the greatest weight to rupture models dominated by single-segment earthquakes. Further, our segment-boundary uncertainties allow for more complex (e.g., partial and spillover) ruptures, and are consistent with paleoseismic observations. Our treatment of the central WFZ addresses uncertainties in fault segmentation and rupture extent, but is limited by our initial per-segment analysis. Thus, we suggest future work focused on the development of a comprehensive suite of possible ruptures from the individual per-site earthquake data.

REFERENCES

Aitken, M.J., 1994, Optical dating—a non-specialist review: Quaternary Geochronology (Quaternary Science Reviews), v. 13, p. 503–508.

Bakun, W.H., 2006, MMI attenuation and historical earthquakes in the Basin and Range Province of western North America: Bulletin of the Seismological Society of America, v. 96, no. 6, p. 2206–2220, doi: 10.1785/0120060045.

Biasi, G.P., and Weldon, R.J., 2006, Estimating surface rupture length and magnitude of paleoearthquakes from point measurements of rupture displacement: Bulletin of the Seismological Society of America, v. 96, no. 5, p. 1612–1623.

Biasi, G.P., and Weldon, R.J., 2009, San Andreas fault rupture scenarios from multiple paleoseismic records–stringing pearls: Bulletin of the Seismological Society of America, v. 99, no. 2A, p. 471–498, doi: 10.1785/0120080287.

Black, B.D., Hecker, S., Hylland, M.D., Christenson, G.E., and McDonald, G.N., 2003, Quaternary fault and fold database and map of Utah: Utah Geological Survey Map 193DM, scale 1:50,000, CD.

Black, B.D., Lund, W.R., Schwartz, D.P., Gill, H.E., and Mayes, B.H., 1996, Paleoseismic investigation on the Salt Lake City segment of the Wasatch fault zone at the South Fork Dry Creek and Dry Gulch sites, Salt Lake County, Utah – Paleoseismology of Utah, Volume 7: Utah Geological Survey Special Study 92, 22 p., 1 plate.

Bronk Ramsey, C., 1995, Radiocarbon calibration and analysis of stratigraphy—the OxCal program: Radiocarbon, v. 37, no. 2, p. 425–430.

Bronk Ramsey, C., 2001, Development of the radiocarbon program OxCal: Radiocarbon, v. 43, no. 2a, p. 355–363.

Bronk Ramsey, C., 2008, Depositional models for chronological records: Quaternary Science Reviews, v. 27, no. 1-2, p. 42–60.

Bruhn, R., Gibler, P., Houghton, W., and Parry, W., 1992, Structure of the Salt Lake segment, Wasatch normal fault zone—Implications for rupture propagation during normal faulting, *in* Gori, P.L., and Hays, W.W., editors, Assessment of regional earthquake hazards and risk along the Wasatch Front, Utah: U. S. Geological Survey Professional Paper 1500-B-J, p. H1–H25.

Chang, W.L., and Smith, R.B., 2002, Integrated seismic-hazard analysis of the Wasatch Front, Utah: Bulletin of the Seismological Society of America, v. 92, no. 5, p. 1904–1922.

Crone, A.J., and Haller, K.M., 1991, Segmentation and the coseismic behavior of Basin and Range normal faults—Examples from east-central Idaho and southwestern Montana, U.S.A.: Journal of Structural Geology, v. 13, no. 2, p. 151–164.

Crone, A.J., and Haller, K.M., 2004, Twenty years after the Borah Peak earthquake–Field guide to surface-faulting earthquakes along the Lost River fault, Idaho, *in* Haller, K.M., and Wood, S.H., editors, Geological field trips in southern Idaho, eastern Oregon, and northern Nevada: Department of Geosciences, Boise State University, Boise, Idaho, p. 116–133.

Crone, A.J., Machette, M.N, Bonilla, M.G., Lienkaemper, J.J., Pierce, K.L., Scott, W.E., and Bucknam, R.C., 1987, Surface faulting accompanying the Borah Peak earthquake and segmentation of the Lost River fault, central Idaho: Bulletin of the Seismological Society of America, v. 77, no. 3, p. 739–770.

Crone, A.J., Personius, S.F., DuRoss, C.B., Machette, M.N., and Mahan, S.A., 2014, History of late Holocene earthquakes at the Willow Creek site and on the Nephi segment, Wasatch fault zone, Utah—Paleoseismology of Utah, Volume 25: Utah Geological Survey Special Study 151, 43 p., CD.

Duller, G.A.T., 2008, Luminescence dating—Guidelines on using luminescence dating in archaeology: Swindon, United Kingdom, English Heritage Publishing, 45 p., online at http://www.aber.ac.uk/en/media/english_heritage_luminescence_dating.pdf, accessed March 2012.

DuRoss, C.B., 2008, Holocene vertical displacement on the central segments of the Wasatch fault zone, Utah: Bulletin of the Seismological Society of America, v. 98, no. 6, p. 2918–2933, doi: 10.1785/0120080119.

DuRoss, C.B., 2014, Paleoseismic investigation to determine the mid-Holocene chronology of surface-faulting earthquakes on the Nephi segment of the Wasatch fault zone, Utah and Juab Counties, Utah: Final Technical Report to the U.S. Geological Survey, National Earthquake Hazards Reduction Program, award no. G12AP20076, 48 p., 2 plates.

DuRoss, C.B., and Hylland, M.D., 2015, Synchronous ruptures along a major graben-forming fault system—Wasatch and West Valley fault zones, Utah, USA: Bulletin of the Seismological Society of America, v. 105, p. 14–37.

DuRoss, C.B., Hylland, M.D., McDonald, G.N., Crone, A.J., Personius, S.F., Gold, R.D., and Mahan, S.A., 2014, Holocene and latest Pleistocene paleoseismology of the Salt Lake City segment of the Wasatch fault zone at the Penrose Drive trench site, *in* DuRoss, C.B., and

Hylland, M.D., Evaluating surface faulting chronologies of graben-bounding faults in Salt Lake Valley, Utah—New paleoseismic data from the Salt Lake City segment of the Wasatch fault zone and the West Valley fault zone—Paleoseismology of Utah, Volume 24: Utah Geological Survey Special Study 149, 76 p., 12 appendices, CD.

DuRoss, C.B., McDonald, G.N., and Lund, W.R., 2008, Paleoseismic investigation of the northern strand of the Nephi segment of the Wasatch fault zone at Santaquin, Utah—Paleoseismology of Utah, Volume 17: Utah Geological Survey Special Study 124, 33 p., 1 plate, CD.

DuRoss, C.B., Personius, S.F., Crone, A.J., McDonald, G.N., and Briggs, R., 2012, Late Holocene earthquake history of the Brigham City segment of the Wasatch fault zone at the Hansen Canyon, Kotter Canyon, and Pearsons Canyon trench sites, Box Elder County, Utah—Paleoseismology of Utah, Volume 22: Utah Geological Survey Special Study 142, 28 p., 3 plates, 5 appendices.

DuRoss, C.B., Personius, S.F., Crone, A.J., McDonald, G.N., and Lidke, D.J., 2009, Paleoseismic investigation of the northern Weber segment of the Wasatch fault zone at the Rice Creek trench site, North Ogden, Utah—Paleoseismology of Utah, Volume 18: Utah Geological Survey Special Study 130, 37 p., 2 plates, CD.

DuRoss, C.B., Personius, S.F., Crone, A.J., Olig, S.S., Hylland, M.D., Lund, W.R., and Schwartz, D.P., 2016, Fault segmentation—New concepts from the Wasatch fault zone, Utah, USA: Journal of Geophysical Research – Solid Earth, v. 121, 27 p., doi: 10.1002/2015JB012519.

DuRoss, C.B., Personius, S.F., Crone, A.J., Olig, S.S., and Lund, W.R., 2011, Integration of paleoseismic data from multiple sites to develop an objective earthquake chronology—Application to the Weber segment of the Wasatch fault zone: Bulletin of the Seismological Society of America, v. 101, no. 6, p. 2765–2781, doi: 10.1785/0120110102.

Ellsworth, W.L., Matthews, M.V., Nadeau, R.M., Nishenko, S.P., Reasenberg, P.A., and Simpson, R.W., 1999, A physically-based earthquake recurrence model for estimation of long-term earthquake probabilities: U.S. Geological Survey Open-File Report 99-522, 22 p.

Friedrich, A.M., Wernicke, B.P., Niemi, N.A., Bennett, R.A., and Davis, J.L., 2003, Comparison of geodetic and geologic data from the Wasatch region, Utah, and implications for the spectral character of Earth deformation at periods of 10 to 10 million years: Journal of Geophysical Research, v. 108, no. B4, p. 2199, doi:10.1029/2001JB000682.

Forman, S.L., Machette, M.N., Jackson, M.E., and Maat, P., 1989, An evaluation of thermoluminescence dating of paleoearthquakes on the American Fork segment, Wasatch fault zone, Utah: Journal of Geophysical Research, v. 94, no. B2, p. 1622–1630.

Forman, S.L., Nelson, A.R., and McCalpin, J.P., 1991, Thermoluminescence dating of fault-scarp-derived colluvium—Deciphering the timing of earthquakes on the Weber segment of the Wasatch fault zone, north-central Utah: Journal of Geophysical Research, v. 96, no. B1, p. 595–605.

Godsey, H.S., Currey, D.R., and Chan, M.A., 2005, New evidence for an extended occupation of the Provo shoreline and implications for regional climate change, Pleistocene Lake

Bonneville, Utah, USA: Quaternary Research, v. 63, no. 2, p. 212–223, doi:10.1016/j.yqres.2005.01.002.

Godsey, H.S., Oviatt, C.G., Miller, D.M., and Chan, M.A., 2011, Stratigraphy and chronology of offshore to nearshore deposits associated with the Provo shoreline, Pleistocene Lake Bonneville, Utah: Palaeogeography, Palaeoclimatology, Palaeoecology, v. 310, no. 3–4, p. 442–450, doi: 10.1016/j.palaeo.2011.08.005.

Hanson, K.L., Swan, F.H., and Schwartz, D.P., 1981, Study of earthquake recurrence intervals on the Wasatch fault, Utah: San Francisco, California, Woodward-Clyde Consultants, sixth annual technical report prepared for U.S. Geological Survey under contract no. 14-08-0001-19115, 22 p., also available in Utah Geological Survey Miscellaneous Publication 13-3.

Hanson, K.L., Swan, F.H., and Schwartz, D.P., 1982a, Study of earthquake recurrence intervals on the Wasatch fault, Utah: San Francisco, California, Woodward-Clyde Consultants, seventh annual technical report prepared for U.S. Geological Survey under contract no. 14-08-0001-19842, 10 p., also available in Utah Geological Survey Miscellaneous Publication 13-3.

Hanson, K.L., Swan, F.H., and Schwartz, D.P., 1982b, Guidebook to late Pleistocene and Holocene faulting along the Wasatch Front and vicinity—Little Cottonwood Canyon to Scipio, Utah, *in* Hanson, K.L., and Schwartz, D.P., editors, Proceedings of the American Geophysical Union Chapman Conference on Fault Behavior and the Earthquake Generation Process, Snowbird, Utah, 40 p.

Harty, K.M., Mulvey, W.E., and Machette, M.N., 1997, Surficial geologic map of the Nephi segment of the WFZ, eastern Juab County, Utah: Utah Geological Survey Map 170, 14 p., 1 plate, scale 1:50,000.

Hemphill-Haley, M.A., and Weldon, R.J., 1999, Estimating prehistoric earthquake magnitude from point measurements of surface rupture: Bulletin of the Seismological Society of America, v. 89, no. 5, p. 1264–1279.

Horns, D.M., Rey, K.A., Barnes, C.S., Mcshinsky, R.D., and Palmer, M., 2009, New constraints on the timing of prehistoric earthquakes on the northernmost part of the Nephi segment of the Wasatch fault zone, Utah [abs.]: Geological Society of America Abstracts with Programs, v. 41, no. 6, p. 42.

Huntley, D.J., Godfrey-Smith, D.I., and Thewalt, M.L.W., 1985, Optical dating of sediments: Nature, v. 313, p. 105–107.

Hylland, M.D., 2007, Surficial-geologic reconnaissance and scarp profiling on the Collinston and Clarkston Mountain segments of the Wasatch fault zone, Box Elder County, Utah – Paleoseismic inferences, implications for adjacent segments, and issues for diffusion-equation scarp-age modeling—Paleoseismology of Utah, Volume 15: Utah Geological Survey Special Study 121, 18 p., CD.

Jackson, M., 1991, Number and timing of Holocene paleoseismic events on the Nephi and Levan segments, Wasatch fault zone, Utah—Paleoseismology of Utah, Volume 3: Utah Geological Survey Special Study 78, 23 p.

Lienkaemper, J.J., and Bronk Ramsey, C., 2009, OxCal – versatile tool for developing paleoearthquake chronologies—A primer: Seismological Research Letters, v. 80, no. 3, p. 431–434.

Lund, W.R., 2005, Consensus preferred recurrence-interval and vertical slip-rate estimates—Review of Utah paleoseismic-trenching data by the Utah Quaternary Fault Parameters Working Group: Utah Geological Survey Bulletin 134, 109 p., CD.

Lund, W.R., 2007, Summary—Utah Quaternary Fault Parameters Working Group Annual Meeting—Wednesday, February 28, 2007, Unpublished minutes of the Utah Quaternary Fault Parameters Working Group, 13 p., available online at http://geology.utah.gov/ghp/workgroups/pdf/uqfpwg/UQFPWG-2007_Summary.pdf.

Lund, W.R., and Black, B.D., 1998, Paleoseismic investigation at Rock Canyon, Provo segment, Wasatch fault zone, Utah County, Utah – Paleoseismology of Utah, Volume 8: Utah Geological Survey Special Study 93, 21 p.

Lund, W.R., Schwartz, D.P., Mulvey, W.E., Budding, K.E., and Black, B.D., 1991, Fault behavior and earthquake recurrence on the Provo segment of the Wasatch fault zone at Mapleton, Utah County, Utah – Paleoseismology of Utah, Volume 1: Utah Geological and Mineral Survey Special Study 75, 41 p.

Machette, M.N., 1992, Surficial geologic map of the Wasatch fault zone, eastern part of Utah Valley, Utah County and parts of Salt Lake and Juab Counties, Utah: U.S. Geological Survey Miscellaneous Investigations Series Map I-2095, scale 1:50,000, 30 p. pamphlet.

Machette, M.N., Crone, A.J., Personius, S.F., Mahan, S.A., Dart, R.L., Lidke, D.J., and Olig, S.S., 2007, Paleoseismology of the Nephi segment of the Wasatch fault zone, Juab County, Utah – Preliminary results from two large exploratory trenches at Willow Creek: U.S. Geological Survey Scientific Investigations Map SI-2966, 2 plates.

Machette, M.N., Personius, S.F., and Nelson, A.R., 1992, Paleoseismology of the Wasatch fault zone—A summary of recent investigations, interpretations, and conclusions, *in* Gori, P.L., and Hays, W.W., editors, Assessment of regional earthquake hazards and risk along the Wasatch Front, Utah: U.S. Geological Survey Professional Paper 1500-A, p. A1–A71.

McCalpin, J.P., 2002, Post-Bonneville paleoearthquake chronology of the Salt Lake City segment, Wasatch fault zone, from the 1999 "megatrench" site – Paleoseismology of Utah, Volume 10: Utah Geological Survey Miscellaneous Publication 02-7, 37 p.

McCalpin, J.P., and Forman, S.L., 2002, Post-Provo earthquake chronology of the Brigham City segment, Wasatch fault zone, Utah – Paleoseismology of Utah, Volume 11: Utah Geological Survey Miscellaneous Publication 02-9, 46 p.

McCalpin, J.P., Forman, S.L., and Lowe, M., 1994, Reevaluation of Holocene faulting at the Kaysville site, Weber segment of the Wasatch fault zone, Utah: Tectonics, v. 13, no. 1, p. 1-16.

Nelson, A.R., 1988, The northern part of the Weber segment of the Wasatch fault zone near Ogden, Utah, *in* Machette, M.N., editor, In the footsteps of G.K. Gilbert—Lake Bonneville and neotectonics of the eastern Basin and Range Province, Geological Society of America Guidebook for Field Trip Twelve, the Geological Society of America 100th Annual Meeting: Utah Geological and Mineral Survey Miscellaneous Publication 88-1, p. 33–37.

Nelson, A.R., Lowe, M., Personius, S., Bradley, L.A., Forman, S.L., Klauk, R., and Garr, J., 2006, Holocene earthquake history of the northern Weber segment of the Wasatch fault zone, Utah—Paleoseismology of Utah, Volume 13: Utah Geological Survey Miscellaneous Publication 05-8, 39 p., 2 plates.

Nelson, A.R., and Personius, S.F., 1993, Surficial geologic map of the Weber segment, Wasatch fault zone, Weber and Davis Counties, Utah: U.S. Geological Survey Miscellaneous Investigations Series Map I-2199, 22 p. pamphlet, scale 1:50,000.

Olig, S.S., McDonald, G.N., Black, B.D., DuRoss, C.B., Lund, W.R., Hylland, M.D., Simon, D.B., Giraud, R.E., and Christenson, G.E., 2011, Extending the paleoseismic record of the Provo segment of the Wasatch fault zone, Utah: URS Corporation, Final Technical Report to the U.S. Geological Survey, National Earthquake Hazards Reduction Program, Award No. 02HQGR0109, variously paginated.

Ostenaa, D., 1990, Late Holocene displacement history, Water Canyon site, Wasatch fault zone [abs.]: Geological Society of America Abstracts with Programs, v. 22, no. 6, p. 42.

Oviatt, C.G., 1997, Lake Bonneville fluctuations and global climate change: Geology, v. 25, p. 155–158.

Oviatt, C.G., Currey, D.R., and Sack, D., 1992, Radiocarbon chronology of Lake Bonneville, eastern Great Basin, USA: Paleogeography, Paleoclimatology, Paleoecology, v. 99, p. 225–241.

Personius, S.F., 1990, Surficial geologic map of the Brigham City segment and adjacent parts of the Weber and Collinston segments, Wasatch fault zone, Box Elder and Weber Counties, Utah: U.S. Geological Survey Miscellaneous Investigations Series Map I-1979, scale 1:50,000.

Personius, S.F., 1991a, Paleoseismic analysis of the Wasatch fault zone at the Brigham City trench site, Brigham City, Utah, *in* Personius, S.F., Paleoseismic analysis of the Wasatch fault zone at the Brigham City trench site, Brigham City and Pole Patch trench site, Pleasant View, Utah—Paleoseismology of Utah, Volume 2: Utah Geological and Mineral Survey Special Study 76, 39 p. 1–17.

Personius, S.F., 1991b, Paleoseismic analysis of the Wasatch fault zone at the Pole Patch trench site, Pleasant View, Utah, *in* Personius, S.F., Paleoseismic analysis of the Wasatch fault zone at the Brigham City trench site, Brigham City and Pole Patch trench site, Pleasant View, Utah—Paleoseismology of Utah, Volume 2: Utah Geological and Mineral Survey Special Study 76, p. 19–39.

Personius, S.F., DuRoss, C.B., and Crone, A.J., 2012, Holocene behavior of the Brigham City segment—Implications for forecasting the next large-magnitude earthquake on the Wasatch fault zone, Utah, USA: Bulletin of the Seismological Society of America, v. 102, no. 6, p. 2265–2281, doi: 10.1785/0120110214.

Personius, S.F., and Scott, W.E., 1992, Surficial geologic map of the Salt Lake City segment and parts of adjacent segments of the Wasatch fault zone, Davis, Salt Lake, and Utah Counties, Utah: U.S. Geological Survey Miscellaneous Investigations Series Map I-2106, scale 1:50,000.

Personius, S.F., and Scott, W.E., 2009 (digital release), Surficial geologic map of the Salt Lake City segment and parts of adjacent segments of the Wasatch fault zone, Davis, Salt Lake, and Utah Counties, Utah (digitized from U.S. Geological Survey Miscellaneous Investigations Series Map I-2106 [1992]): Utah Geological Survey Map 243DM, GIS data, scale 1:50,000.

Puseman, K., and Cummings, L.S., 2005, Separation and identification of charcoal and organics from bulk sediment samples for improved radiocarbon dating and stratigraphic correlations, *in* Lund, W.R., editor, Western States Seismic Policy Council Proceedings Volume of the Basin and Range Province Seismic Hazards Summit II: Utah Geological Survey Miscellaneous Publication 05-2, 10 p., CD.

Robison, R.M., and Burr, T.N., 1991, Fault-rupture hazard analysis using trenching and borings—Warm Springs fault, Salt Lake City, Utah, *in* McCalpin, J.P., editor, Proceedings of the 27th Symposium on Engineering Geology and Geotechnical Engineering: Boise, Idaho Department of Transportation, p. 26-1–26-13.

Schwartz, D.P., and Coppersmith, K.J., 1984, Fault behavior and characteristic earthquakes—Examples from the Wasatch and San Andreas fault zones: Journal of Geophysical Research, v. 89, p. 5681–5698.

Schwartz, D.P., Hanson, K.L., and Swan, F.H., III, 1983, Paleoseismic investigations along the Wasatch fault zone – An update, *in* Gurgel, D.K., editor, Geologic Excursions in Neotectonics and Engineering Geology in Utah, Geological Society of America Rocky Mountain and Cordilleran Sections Meeting, Salt Lake City, Utah, Field Trip Guidebook – Part IV: Utah Geological and Mineral Survey Special Studies 62, p. 45–48.

Schwartz, D.P., and Lund, W.R., 1988, Paleoseismicity and earthquake recurrence at Little Cottonwood Canyon, WFZ, Utah, *in* Machette, M.N., editor, In the footsteps of G.K. Gilbert—Lake Bonneville and neotectonics of the eastern Basin and Range Province: Utah Geological and Mineral Survey Miscellaneous Publication 88-1, p. 82–85.

Simon-Bymaster, Inc., 1999, Report of geologic investigation; Salt Palace Convention Center Expansion Project; 100 South West Temple Street, Salt Lake City: Unpublished consultant report prepared for Salt Lake County, 27 p.

Scott, W.E., and Shroba, R.R., 1985, Surficial geologic map of an area along the Wasatch fault zone in the Salt Lake Valley, Utah: U.S. Geological Survey Open-File Report 85-448, 18 p, 2 plates, scale 1:24,000.

Suter, M., 2006, Contemporary studies of the 3 May 1887 M_W 7.5 Sonora, Mexico (Basin and Range Province) earthquake: Seismological Research Letters, v. 77, no. 2, p. 134–147.

Swan, F.H., III, Schwartz, D.P., and Cluff, L.S., 1980, Recurrence of moderate to large magnitude earthquakes produced by surface faulting on the Wasatch fault zone, Utah: Bulletin of the Seismological Society of America, v. 70, p. 1431–1462.

Swan, F.H., III, Schwartz, D.P., Hanson, K.L., Knuepfer, P.L., and Cluff, L.S., 1981, Study of earthquake recurrence intervals on the Wasatch fault at the Kaysville site, Utah: U.S. Geological Survey Open-File Report 81-228, 30 p.

Tucker, A.B., Woefti, W., Bonani, G., Suter, M., 1983, Earthquake dating—An application of carbon-14 atom counting: Science, v. 219, p. 1320–1321.

Wells, D.L., and Coppersmith, K.J., 1994, New empirical relationships among magnitude, rupture length, rupture width, rupture area, and surface displacement: Bulletin of the Seismological Society of America, v. 84, no. 4, p. 974–1002.

Wesnousky, S.G., 2008, Displacement and geometrical characteristics of earthquake surface ruptures—Issues and implications for seismic-hazard analysis and the process of earthquake rupture: Bulletin of the Seismological Society of America, v. 98, no. 4, p. 1609–1632, doi: 10.1785/0120070111.

Wheeler, R.L., and Krystinik, K.B., 1992, Persistent and nonpersistent segmentation of the Wasatch fault zone, Utah—Statistical analysis for evaluation of seismic hazard, *in* Gori, P.L., and Hays, W.W., editors, Assessment of regional earthquake hazards and risk along the Wasatch front, Utah: U.S. Geological Survey Professional Paper 1500, p. B1–B47.

Working Group on California Earthquake Probabilities, 2003, Earthquake probabilities in the San Francisco Bay region 2002–2031: U.S. Geological Survey Open-File Report 03-214, variously paginated.

Working Group on California Earthquake Probabilities, 2008, The Uniform California Earthquake Rupture Forecast: U.S. Geological Survey Open File Report 2007-1437, 96 p., 16 appendices.

Table B-1. Correlation of surface-faulting earthquakes on the Brigham City segment.

Brigham City Segment	**Kotter Canyon**	**Bowden Canyon**	**Box Elder Canyon**	**Pearsons Canyon**
no evidence	*no evidence*	*no evidence*	*no evidence*	PC1 1.2 ± 0.05
B1 2.4 ± 0.3	KC1 2.5 ± 0.3	BC1 2.6 ± 1.0	BEC1 2.2 ± 0.6	*not exposed*
B2 3.5 ± 0.2	KC2 3.5 ± 0.3	BC2 3.7 ± 0.5	BEC2 3.2 ± 0.5	-
B3 4.5 ± 0.5	*not exposed*	BC3 4.6 ± 0.6	BEC3 4.4 ± 1.1	-
B4 5.6 ± 0.7	-	BC4 5.8 ± 1.6	BEC4 5.6 ± 0.8	-

Earthquake times are mean ± two sigma (2σ) in thousands of calendar years B.P. (1950) (ka) based on OxCal modeling. BCS earthquakes B1–B4 are based on the correlation of site data; for example, KC1, BC1, and BEC1 correlate and are used to define earthquake B1 (see DuRoss *et al.*, 2011 for methodology). PC1, which is likely the northern continuation of WS earthquake W2, did not rupture the northern BCS.

Table B-2. Correlation of surface-faulting earthquakes on the Weber segment.

Weber Segment	**Rice Creek**	**Garner Canyon**	**East Ogden**	**Kaysville**
W1 0.6 ± 0.07	RC1 0.6 ± 0.08	GC1 0.6 ± 0.07	EO1 0.5 ± 0.2	K1 0.6 ± 0.2
W2 1.1 ± 0.6	RC2 1.2 ± 0.3	GC2 1.5 ± 0.5	EO2 0.9 ± 0.4	K2 0.9 ± 0.5
W3 3.1 ± 0.3	RC3 3.4 ± 0.7	GC3 3.2 ± 0.6	EO3 3.0 ± 0.4	K3 2.8 ± 1.7
W4 4.5 ± 0.3	RC4 4.6 ± 0.5	GC4 4.4 ± 0.6	EO4 4.0 ± 0.9	*no evidence*
W5 5.9 ± 0.5	RC5 6.0 ± 1.0	*not exposed*	*not exposed*	K4 5.7 ± 1.3

Earthquake times are mean ± two sigma (2σ) in thousands of calendar years B.P. (1950) (ka) based on OxCal modeling. WS earthquakes W1–W5 are based on the correlation of site data; for example, RC1, GC1, EO1, and K1 correlate and are used to define earthquake W1 (see DuRoss *et al.*, 2011 for methodology).

Table B-3. Correlation of surface-faulting earthquakes on the Salt Lake City segment**.**

Salt Lake City Segment		***Penrose Drive***		**Little Cottonwood Canyon**		**South Fork Dry Creek**	
S1	1.3 ± 0.2	*no evidence*		LCC1	1.3 ± 0.04	SFDC1	1.3 ± 0.2
S2	2.2 ± 0.2	*no evidence*		LCC2	2.1 ± 0.3	SFDC2	2.2 ± 0.4
S3	4.2 ± 0.3	*PD1*	*4.0 ± 0.5*	LCC3	4.4 ± 0.5	SFDC3	3.8 ± 0.6
S4	5.3 ± 0.2	*PD2*	*5.9 ± 0.7*	LCC4	5.5 ± 0.8	SFDC4	5.0 ± 0.5

Earthquake times are mean ± two sigma (2σ) in thousands of calendar years B.P. (1950) (ka) based on OxCal modeling. SLCS earthquakes S1–S4 are based on the correlation of site data; for example, LCC1 and SFDC1 correlate and are used to define earthquake S1 (see DuRoss *et al.*, 2011 for methodology). Penrose Drive data, shown in *italics* (DuRoss *et al.*, 2014; DuRoss and Hylland, 2015), were not used to define the times of earthquakes S3 and S4, but are shown for comparative purposes. Including PD1 would result in an S3 time of 4.2 ± 0.2 ka; including PD2 would have an insignificant (<50-yr) effect on the S4 time.

Table B-4. Correlation of surface-faulting earthquakes on the Provo segment.

Provo Segment		**American Fork**		**Rock Canyon**		**Mapleton North**		**Mapleton South**	
P1	0.6 ± 0.05	AF1	0.4 ± 0.2	ROC1	0.6 ± 0.07	MN1	0.6 ± 0.07	MS1	0.7 ± 0.7
P2	1.5 ± 0.4	*not dated or exposed?*		*not exposed?*		MN2	1.5 ± 0.4	*not exposed?*	
P3	2.2 ± 0.4	AF2	2.0 ± 0.8	*not exposed*		MN3	3.2 ± 1.6	MS2	2.2 ± 0.8
P4	4.7 ± 0.3	AF3	4.3 ± 1.5	-		MN4	4.7 ± 0.3	*not exposed*	
P5	5.9 ± 1.0	AF4	6.2 ± 1.0	-		MN5	5.6 ± 0.5	-	

Earthquake times are mean ± two sigma (2σ) in thousands of calendar years B.P. (1950) (ka) based on OxCal modeling. PS earthquakes P1–P5 are based on the correlation of site data; for example, AF1, ROC1, MN1, and MS1 correlate and are used to define earthquake P1 (see DuRoss *et al.*, 2011 for methodology). Possible reasons as to why MN2 was not identified at other sites are discussed in the text, as well as uncertainties in correlating AF2 with MN3 and MS2 (versus the alternative of correlating AF2 with MN2 and MS2).

Table B-5. Correlation of surface-faulting earthquakes on the Nephi segment.

Nephi Segment		**Santaquin Canyon**		**North Creek**		**Willow Creek**		**Red Canyon**	
N1	0.2 ± 0.09	SQ1	0.3 ± 0.2*	NC1	0.4 ± 0.5	WC1	0.2 ± 0.09	REC1	0.5 ± 0.5
N2	1.2 ± 0.1	*no evidence*		NC2	1.4 ± 0.3	WC2	1.2 ± 0.1	REC2	1.2 ± 0.3
N3	2.0 ± 0.4	*no evidence/not exposed?*		NC3	1.9 ± 0.5	WC3	2.0 ± 0.5	*no evidence*	
N4	4.7 ± 1.8	*no evidence/not exposed?*		*not exposed?*		WC4	4.7 ± 1.8	REC3	4.7 ± 2.5*

Earthquake times are mean ± two sigma (2σ) in thousands of calendar years B.P. (1950) (ka) based on OxCal modeling. NS earthquakes N1–N4 are based on the correlation of site-data; for example, NC1, WC1, and REC1 correlate and are used to define earthquake N1 (see DuRoss *et al.*, 2011 for methodology). * Indicates earthquakes that are not used to define a segment earthquake on account of uncertainty in the site correlation (SQ1) or a very broadly defined earthquake time (REC3).

Table B-6. Summary of earthquake timing data for the central WFZ.

Rupture[1]	**PDFs combined**[2]		**Earthquake Timing**[3] (ka)		**Inter-event recurrence**[4] (kyr)
	Site PDFs	Integration method	Mean ± 2σ	5th–50th–95th [mode]	
B1	BEC1, BC1, KC1	product	2.4 ± 0.3	2.2–2.4–2.6 [2.4]	-
B2	BEC2, BC2, KC2	product	3.5 ± 0.2	3.4–3.5–3.7 [3.4]	1.1 ± 0.3 (B2–B1)
B3	BEC3, BC3	product	4.5 ± 0.5	4.1–4.5–5.0 [4.5]	1.0 ± 0.6 (B3–B2)
B4	BEC4, BC4	product	5.6 ± 0.6	5.0–5.6–6.1 [5.6]	1.1 ± 0.8 (B4–B3)
W1	RC1, K1, EO1, GC1	product	0.6 ± 0.1	0.5–0.6–0.6 [0.5]	-
W2	RC2, K2, EO2, GC2	mean	1.1 ± 0.6	0.7–1.2–1.7 [1.3]	0.7 ± 0.6 (W2–W1)
W3	RC3, K3, EO3, GC3	product	3.1 ± 0.3	2.9–3.1–3.3 [3.1]	1.9 ± 0.7 (W3–W2)
W4	RC4, EO4, GC4	product	4.5 ± 0.3	4.2–4.5–4.7 [4.5]	1.4 ± 0.4 (W4–W3)
W5	RC5, K4	product	5.9 ± 0.5	5.6–5.9–6.4 [5.6]	1.4 ± 0.6 (W5–W4)
S1	LCC1, SFDC1	mean	1.3 ± 0.2	1.2–1.3–1.5 [1.3]	-
S2	LCC2, SFDC2	product	2.2 ± 0.2	2.0–2.2–2.3 [2.2]	0.8 ± 0.3 (S2–S1)
S3	LCC3, SFDC3	product	4.1 ± 0.3	3.9–4.1–4.4 [4.1]	2.0 ± 0.4 (S3–S2)
S4	LCC4, SFDC4	product	5.3 ± 0.2	5.1–5.2–5.5 [5.2]	1.1 ± 0.4 (S4–S3)
P1	MN1, AF1, ROC1, MS1	product	0.6 ± 0.05	0.5–0.6–0.6 [0.6]	-
P2	MN2	-	1.5 ± 0.4	1.2–1.5–1.8 [1.7]	0.9 ± 0.4 (P2–P1)
P3	MN3, AF2, MS2	product	2.2 ± 0.4	1.9–2.3–2.6 [2.3]	0.8 ± 0.5 (P3–P2)
P4	MN4, AF3	product	4.7 ± 0.3	4.5–4.7–4.9 [4.7]	2.5 ± 0.5 (P4–P3)
P5	MN5, AF4	mean	5.9 ± 1.0	5.2–5.8–6.9 [5.6]	1.2 ± 1.0 (P5–P4)
N1	NC1, WC1, REC1	product	0.2 ± 0.1	0.1–0.2–0.3 [0.2]	-
N2	NC2, WC2, REC2	product	1.2 ± 0.1	1.2–1.2–1.3 [1.2]	1.0 ± 0.1 (N2–N1)
N3	NC3, WC3	product	2.0 ± 0.4	1.7–2.0–2.3 [2.0]	0.8 ± 0.4 (N3–N2)
N4	WC4	-	4.7 ± 1.8	3.3–4.7–6.1 [5.8]	2.7 ± 1.8 (N4–N3)

[1] Rupture abbreviations: B – Brigham City segment, W – Weber segment, S – Salt Lake City segment, P – Provo segment, N – Nephi segment. Numerical values indicate youngest (e.g., B1) and progressively older earthquakes (e.g., B2–B4) (Tables B-1 to B-5).

[2] Site PDFs contributing to the segment-wide rupture times; e.g., BEC1, BC1, and KC1 were combined to determine the time of rupture B1. Integration method is the product or mean of the site PDF probabilities (over common time bins); see text and DuRoss *et al.* (2011) for discussion.

[3] Summary statistics based on integration of per-site earthquake-timing PDFs (derived from OxCal models) following the method of DuRoss *et al.* (2011). Earthquake times are in thousands of years before 1950.

[4] Individual recurrence interval (RI) is mean recurrence time between earthquakes (e.g., B4–B3 time).

Table B-7. Mean recurrence intervals for the central WFZ.

Segment	**Closed mean RI**[1] (kyr)	**Open mean RI (*N*-in-*T*)**[2] (kyr)	**Time since MRE**[3] (kyr)
BCS	1.1 ± 0.2 (B4–B1)	1.5 ± 0.1; 4 events <5.9 ± 0.4 ka [BEC4]	2.5 ± 0.3
WS	1.3 ± 0.1 (W5–W1)	1.4 ± 0.3; 5 events <7.1 ± 1.4 ka [RC5]	0.6 ± 0.07
SLCS	1.3 ± 0.1 (S4–S1)	1.3 ± 0.09; 4 events <5.2 ± 0.4 ka [SFDC4]	1.4 ± 0.2
PS	1.3 ± 0.2 (P5–P1)	1.2 ± 0.03; 5 events <6.1 ± 0.2 ka [MN5]	0.6 ± 0.05
NS	0.9 ± 0.2 (N3–N1)	1.1 ± 0.04; 3 events <3.2 ± 0.1 ka [WC3]	0.3 ± 0.09

[1] Closed mean recurrence per segment is elapsed time between oldest and youngest earthquakes per segment (e.g., B4–B1; Tables B-1 to B-5) divided by the number of closed intervals.

[2] Open mean recurrence per segment is the time from the maximum constraining age on the oldest event (e.g., 5.9 ± 0.4 ka for B4) to the present (2011) divided by number of events.

[3] Time (to the present; 2011) since the most recent earthquake (MRE).

Table B-8. Vertical displacement per site and rupture for the central WFZ.

Rupture[1]	**Site earthquake**[1] [**distance along rupture** (km)][2]	**Site Displacement**[3] (m)			**Rupture Displacement**[5] (m)			
		Mean	Range	Type[4]	Mean	Min	Max	n
Single-segment ruptures								
B1	BE1[a] [17.1]	>0.9	0.4	TD				
B1	KC1 [13.4]	2.1	0.2	TD				
B1					**2.1**	**1.9**	**2.3**	1
B2	BEC2[a] [17.1]	>1.0	0.0	TD				
B2	BC2 [14.9]	1.0	0.0	TD				
B2	KC2 [13.4]	2.1	0.2	TD				
B2					**1.6**	**1.5**	**1.7**	2
B3	BC3 [14.9]	2.5	0.0	TD				
B3	PP1 [34.6]	1.0	0.3	TD				
B3					**1.8**	**1.6**	**1.9**	2
B4	BEC4[a] [17.1]	>1.1	0.2	TD				
B4	BC4 [14.9]	2.5	0.0	TD				
B4					**2.5**	**-**	**-**	1
W1	RC1 [2.7]	2.0	0.7	SD				
W1	K1 [36.1]	1.8	0.1	TD				
W1	EO1 [11.8]	0.7	0.2	TD				
W1	GC1 [6.5]	1.2	0.2	TD				
W1					**1.4**	**1.1**	**1.7**	4
W2	PC1[b] [3.7]	0.5	0.4	TD				
W2	RC2 [11.8]	3.2	0.5	TD				
W2	EO2 [20.8]	2.6	0.0	TD				
W2	GC2 [15.5]	1.5	0.7	TD				
W2					**2.0**	**1.6**	**2.4**	4
W3	RC3 [2.7]	1.1	0.3	TD				
W3	K3 [36.1]	2.9	0.6	TD				
W3	EO3 [11.8]	4.2	0.0	TD				
W3	GC3 [6.5]	1.0	0.1	TD				
W3					**2.3**	**2.1**	**2.6**	4
W4	RC4 [2.7]	2.0	0.4	TD				
W4	EO4 [11.8]	4.2	0.0	TD				
W4					**3.1**	**2.9**	**3.3**	2
W5	RC5 [2.7]	2.0	0.4	CWT				
W5	K4 [36.1]	1.4	0.0	TD				
W5					**1.7**	**1.5**	**1.9**	2
S1	LLC1 [30.8]	1.8	0.0	TR				
S1	SFDC1 [34.1]	2.0	0.5	TD				
S1					**1.9**	**1.7**	**2.2**	2
S2	LCC2 [30.8]	1.8	0.0	TR				
S2	SFDC2 [34.1]	2.0	0.5	TD				

S2					**1.9**	**1.7**	**2.2**	2
S3	LCC3 [30.8]	1.8	0.0	TR				
S3	PD1 [9.4]	1.4	0.4	CWT, TD				
S3					**1.6**	**1.4**	**1.8**	2
S4	LCC4 [30.8]	1.8	0.0	TR				
S4	PD2 [9.4]	1.0	0.3	CWT, TD				
S4					**1.4**	**1.3**	**1.6**	2
P1	MN1 [46.0]	4.7	0.5	TD				
P1	AF1 [8.7]	2.5	0.3	TD				
P1	ROC1 [28.1]	3.3	0.0	SD				
P1					**3.5**	**3.2**	**3.8**	3
P2	MN2 [46.0]	1.4	0.9	TD[a]	**1.4**	**0.5**	**2.3**	1
P3	AF2 [8.7]	2.5	0.3	TD	**2.5**	**2.2**	**2.8**	1
P4	AF3 [8.7]	2.5	0.3	TD	**2.5**	**2.2**	**2.8**	1
P5	no data							
N1	NC1 [26.1]	2.1	0.1	CWT				
N1	REC1 [39.0]	1.4	0.3	CWT				
N1					**1.8**	**1.6**	**2.4**	2-3
N2	NC2 [26.1]	2.3	0.3	TD				
N2	REC2 [39.0]	1.5	0.2	CWT				
N2					**1.9**	**1.7**	**2.2**	2
N3	no data							
N4	REC3 [39.0]	1.7	0.4	CWT	**1.7**	**1.4**	**2.0**	1
-	SQ1[c]	3.0	0.2	SD				

Multi-segment ruptures

Rupture[1]	**Site earthquakes**[1] [**distance along rupture** (km)][2]	**Rupture displacement**[5] (m)			
		Mean	Min	Max	n
B2+W3	KC2 [13.3], BC2 [14.9], RC3 [37.7], GC3 [41.4], EO3 [46.7], K3 [71.0]	**2.1**	**1.9**	**2.3**	6
B3+W4	BC3 [14.9], PP1 [34.8], RC4 [37.7], EO4 [46.7]	**2.4**	**2.3**	**2.6**	4
B4+W5	BC4 [14.9], RC5 [37.7], K4 [71.0]	**2.0**	**1.8**	**2.1**	3
W2+S1	PC1 [3.7], RC2 [11.5], GC2 [15.3], EO2 [20.6], LLC1 [94.6], SFDC1 [97.9]	**1.9**	**1.6**	**2.3**	6
S2+P3+N3	LLC2 [30.2], SFDC2 [33.6], AF2 [47.7]	**2.1**	**1.9**	**2.3**	3
S3+P4	PD1 [9.4], LLC3 [30.1], AF3 [48.6]	**1.9**	**1.7**	**2.1**	3
P2+N2	MN2 [42.8], NC2 [71.0], REC2 [83.8]	**1.7**	**1.3**	**2.2**	3
P3+N3	AF2 [7.7]	**2.5**	**2.2**	**2.8**	1
S2+P3	LLC2 [30.1], SFDC2 [34.2], AF2 [48.6]	**2.1**	**1.8**	**2.4**	3

[1] Individual site earthquakes (e.g., KC1) that correspond to single or multi-segment ruptures.

[2] Distance along rupture is site location along linear rupture length (end-to-end), measured from the northern end. For example, the displacement in site earthquake KC1 occurred 13.4 km south of the northern end of the BCS B1 rupture. Distance measurements are used to construct along-strike displacement profiles for analytical displacement modeling (Figure B-8; Table B-9); see text for discussion.

[3] Displacement per site earthquake (e.g., KC1) based on individual trench data (see text for discussion of site paleoseismic data; also DuRoss [2008]). [a] Displacement not used (minimum estimate); [b] PC1 displacement is likely for W2 (DuRoss *et al.*, 2012; Personius *et al.*, 2012)–displacement not used; [c] displacement for SQ1 is not used to constrain N1 due to uncertainty in whether SQ1 corresponds with southern-NS N1 or PS P1.

[4] Displacement-measurement types include TD - total displacement (or surface offset) at site apportioned to individual events, either equally or based on colluvial wedge thickness (CWT) or a trench reconstruction. CWT indicates per-event displacement based on maximum thickness of scarp colluvium, min-max range is generally maximum thickness to two-times that thickness. SD is stratigraphic displacement. [a] Displacement for P2 (MN2) is based on an eroded buried free-face height minus back tilting and antithetic faulting.

[5] Rupture displacement based on simple mean of site displacements corresponding to the rupture (e.g., mean of BC2 and KC2 displacements for rupture B2). n is number of site displacement observations.

Table B-9. Modeled vertical displacement per rupture for the central WFZ.

Rupture	Modeled Displacement Profiles (ellipses)[1]									
	Mean[2]	Error	n, h	Min[2]	Error	n, h	Max[2]	Error	n, h	Notes
B1	**1.7**	1.0E-03	0.5, 2.2	**1.5**	7.0E-04	0.5, 2.0	**1.8**	1.0E-03	0.5, 2.4	fixed-shape
B2	**1.2**	6.0E-01	0.5, 1.6	**1.2**	4.0E-01	0.5, 1.5	**1.3**	9.0E-01	0.5, 1.7	fixed-shape
B3	**2.0**	7.0E-03	0.4, 2.5	**1.8**	3.0E-03	0.6, 2.5	**2.1**	2.0E-03	0.3, 2.5	best-fit
B4	**2.0**	1.0E-03	0.5, 2.5	**1.5**	*(average of B1-B3)*[a]		**2.1**	*(max of B1-B3)*[a]		fixed-shape (mean)
W1	**1.4**	1.2E+00	0.1, 1.5	**1.1**	8.0E-01	0.1, 1.2	**1.7**	2.2E+00	0.1, 1.8	best-fit
W2	**2.1**	2.4E+00	0.7, 3.0	**1.8**	2.9E+00	0.9, 2.7	**2.5**	2.3E+00	0.5, 3.3	best-fit
W3	**2.7**	3.4E+00	0.7, 3.9	**2.4**	4.5E+00	0.6, 3.3	**3.0**	2.6E+00	0.7, 4.3	best-fit
W4[b]	**4.0**	4.0E-01	0.5, 5.3	**3.8**	6.0E-01	0.5, 5.1	**4.1**	5.0E-01	0.5, 5.5	best-fit/fixed-shape
W5	**1.7**	4.0E-01	0.1, 1.8	**1.5**	1.0E-01	0.1, 1.6	**1.9**	9.0E-01	0.1, 2.0	best-fit
S1[c]	**1.9**	2.0E-01	0.5, 2.5	**1.7**	1.0E-02	0.5, 2.2	**2.2**	6.0E-01	0.5, 2.8	fixed-shape
S2	**1.9**	2.0E-01	0.5, 2.5	**1.7**	1.0E-02	0.5, 2.2	**2.2**	6.0E-01	0.5, 2.8	fixed-shape
S3[c]	**1.5**	8.0E-02	0.3, 1.8	**1.3**	3.0E-01	0.2, 1.5	**1.7**	1.0E-04	0.5, 2.2	best-fit
S4	**1.3**	3.0E-01	0.2, 1.5	**1.2**	6.0E-01	0.1, 1.3	**1.5**	1.0E-01	0.1, 1.6	best-fit
P1	**3.3**	2.2E+00	0.2, 3.8	**3.1**	1.6E+00	0.3, 3.7	**3.6**	3.2E+00	0.1, 3.9	best-fit
P2[d]	**1.3**	7.0E-04	0.5, 1.7	**1.3**	7.0E-04	0.5, 1.7	**1.3**	7.0E-04	0.5, 1.7	fixed-shape
P3	**2.9**	7.0E-04	0.5, 3.8	**2.6**	5.0E-05	0.5, 3.4	**3.3**	2.0E-04	0.5, 4.3	fixed-shape
P4	**2.9**	7.0E-04	0.5, 3.8	**2.6**	5.0E-05	0.5, 3.4	**3.3**	2.0E-04	0.5, 4.3	fixed-shape
P5	**2.6**	*(average of P1-P4)*[a]		**2.4**	*(average of P1-P4)*[a]		**2.9**	*(average of P1-P4)*[a]		average
N1[e]	**1.8**	4.0E-03	0.4, 2.2	**1.5**	3.0E-03	0.5, 2.0	**2.3**	8.0E-01	0.3, 2.7	best-fit
N2	**1.9**	3.0E-03	0.4, 2.4	**1.7**	3.0E-03	0.4, 2.1	**2.1**	2.0E-03	0.4, 2.7	best-fit
N3	**2.0**	*(average of N1,N2,N4)*[a]		**1.7**	*(average of N1,N2,N4)*[a]		**2.4**	*(average of N1,N2,N4)*[a]		average
N4	**2.4**	6.0E-04	0.5, 3.2	**2.0**	2.0E-04	0.5, 3.6	**2.7**	2.0E-02	0.5, 3.4	fixed-shape
B2+W3	**1.9**	8.3E+00	0.2, 2.2	**1.7**	8.2E+00	0.3, 2.0	**2.1**	8.2E+00	0.2, 2.4	best-fit
B3+W4	**2.3**	5.4E+00	0.1, 2.5	**2.2**	6.7E+00	0.1, 2.3	**2.4**	4.2E+00	0.2, 2.7	best-fit
B4+W5	**1.9**	7.0E-01	0.1, 2.0	**1.8**	8.0E-01	0.1, 1.9	**2.1**	7.0E-01	0.1, 2.2	best-fit
W2+S1[b]	**2.7**	2.8E+00	0.5, 3.5	**2.4**	3.3E+00	0.6, 3.3	**2.9**	3.0E+00	0.4, 3.7	best fit

S2+P3+N3	**1.7**	9.0E-03	0.9, 2.6	**1.6**	2.0E-01	0.9, 2.4	**1.9**	2.0E-01	0.7, 2.7	best fit
S3+P4	**1.7**	1.0E-01	.5, 2.3	**1.5**	1.0E-02	0.6, 2.1	**2.0**	4.0E-01	0.3, 2.4	best fit
P2+N2	**1.8**	5.0E-01	0.1, 1.9	**1.2**	1.3E+00	0.1, 1.3	**2.2**	2.0E-01	0.2, 2.5	best fit
P3+N3	**3.8**	5.0E-04	0.5, 5.0	**3.3**	5.0E-04	0.5, 4.5	**4.2**	3.0E-04	0.5, 5.7	fixed-shape
S2+P3	**1.5**	6.0E-02	0.9, 2.3	**1.3**	1.0E-01	0.9, 2.0	**1.7**	2.0E-01	0.9, 2.6	best fit

[1] Modeled displacement profiles, using least-squares best fit of ellipses modeled using the function $([\sin(x/L)]^n)h$ (after Biasi and Weldon, 2009), where x/L is the normalized distance along the rupture (in 0.1-km increments), h controls the maximum height of the displacement curve, and n controls its shape (mostly uniform [0.1] to peaked [0.9]); see text for discussion. Error is the sum of the squared deviations of the modeled and observed displacements.

[2] Mean, minimum (min), and maximum (max) displacements per rupture are modeled mean displacements for analytical curves fit to the mean, min, and max site displacements, respectively. For ruptures having only one or two closely spaced displacement observations (Table B-8), the mean is the mean displacement from three ellipses with fixed shapes, using n = 0.2, 0.5, and 0.8. [a] The modeled mean, min, or max displacement reported for these ruptures is the average of modeled mean values for other ruptures on the source. However, for B4, the max displacement is the max of B1–B3 to yield a value greater than the B4 mean (2.0 m). [b] For W4 and W2+S1, the least-squares best-fit ellipse is used for the mean, whereas fixed-shape ellipses (n = 0.2 and 0.8) are used for the range, which yields more reasonable results. [c] For S1 and S3, the best-fit ellipses are used; however, fixed-shape ellipses yield similar results. [d] Because of significant uncertainties in the P2 displacement measurement (0.5–2.3 m; Table B-8), only a mean value is used; the small 0.5 m minimum displacement is not considered suitable for defining the PS minimum displacement. [e] For N1, observed and modeled mean and min displacement values exclude displacement from Santaquin site; the max displacement for N1 includes the Santaquin site displacement.

Table B-10. Summary of displacement per rupture source on the central WFZ.

Rupture Source[1]	**Obs. D**[2] (m)	**Modeled D (displacement curves)**[3] (m)			**EQs obs.**[4]	**Disp. obs.**[4]
	μ	μ	min	max		
BCS	2.0	1.7	1.2	2.1	4	6
WS	2.1	2.4	1.1	4.1	5	16
SLCS	1.7	1.7	1.2	2.2	4	8
PS	2.5	2.6	1.3	3.6	4	6
NS	1.8	2.0	1.5	2.7	3	5-6
BCS+WS	2.2	2.0	1.7	2.4	3	13
WS+SLCS	1.9	2.7	2.4	2.9	1	6
SLCS+PS+NS	2.1	1.7	1.6	1.9	1	3
SLCS+PS	2.0	1.6	1.3	2.0	2	6
PS+NS	2.1	2.8	1.2	4.2	2	4

[1] Vertical displacement (D) for single-segment rupture sources. See "Evaluation of Possible Multi-Segment Ruptures on the Central WFZ" section for discussion of multi-segment ruptures.

[2] Mean (μ) of observed displacement per earthquake on the source (Figure B-8; Table B-8). For example, mean observed displacement for BCS is mean of displacement estimates for B1, B2, B3, and B4 (Table B-8).

[3] Mean (μ) and min-max range of modeled displacement per earthquake on the source, using analytical displacement curves (Figure B-8; Table B-9).

[4] EQs. obs. is total number of earthquakes on the source. Disp. obs. is the total number of site observations of displacement for the source.

Table B-11. Open and closed mean vertical slip rates for the central segments of the WFZ.

Closed-interval vertical slip rate (average displacement and recurrence)[1]										
Source	**Average displacement** (m)			**Average recurrence interval** (yr)				**Vertical slip rate** (mm/yr)		
	Mean	Min	Max	Mean	2σ	Min	Max	Mean	Min	Max
BCS	1.7	1.2	2.1	1062	235	827	1297	1.6	0.9	2.5
WS	2.4	1.1	4.1	1332	124	1208	1456	1.8	0.8	3.4
SLCS	1.7	1.2	2.2	1303	90	1213	1393	1.3	0.9	1.8
PS	2.6	1.3	3.6	1327	249	1078	1576	2.0	0.8	3.3
NS(N3)[a]	2.0	1.5	2.7	901	199	702	1100	2.3	1.4	3.8
NS(N4)[a]	2.0	1.5	2.7	1499	586	913	2085	1.4	0.7	3.0

Closed-interval vertical slip rate (total displacement and elapsed time)[2]										
Source	**Elapsed time** (yr)			**Total displacement** (m)				**Vertical slip rate** (mm/yr)		
	Mean	Min	Max	Mean	Min	Max	Events	Mean	Min	Max
BCS (B4-B1)	3183	2280	4086	4.9	4.5	5.2	B3-B1	1.5	1.1	2.3
WS (W5-W1)	5330	4759	5901	10.2	9.1	11.2	W4-W1	1.9	1.5	2.4
SLCS (S4-S1)	3907	3523	4291	5.3	4.7	6.1	S3-S1	1.4	1.1	1.7
PS (P5-P1)	5312	4262	6362	10.4	9.6	11.5	P4-P1	2.0	1.5	2.7
NS (N3-N1)[a]	1798	1324	2272	3.7	3.2	4.4	N2-N1	2.1	1.4	3.3
NS (N4-N1)[a,b]	4493	2639	6347	5.7	4.9	6.8	N3-N1	1.3	0.8	2.6

Open-interval vertical slip rate[3]										
Source	**Limiting age constraint** (ka)			**Total displacement** (m)				**Vertical slip rate** (mm/yr)		
	Event	Time	2σ	Mean	Min	Max	Events	Mean	Min	Max
BCS	B4 (BEC4) max	5.9	0.4	6.9	6.0	7.3	B4-B1	1.2	0.9	1.3
WS	W5 (RC5) max	7.1	1.4	11.9	10.6	13.1	W5-W1	1.7	1.2	2.3
SLCS	S4 (SFDC4) max	5.2	0.4	6.6	5.9	7.6	S4-S1	1.3	1.0	1.6
PS	P5 (MN5) max	6.1	0.2	13.0	12.0	14.4	P5-P1	2.1	1.9	2.4
NS(N3)	N3 (WC3) max	3.2	0.1	5.7	4.9	6.8	N3-N1	1.7	1.5	2.2
NS(N4)[a]	N4 (WC4) max	6.2	0.1	8.1	6.9	9.5	N4-N1	1.3	1.1	1.5

Long-term vertical slip rates[4]										
Source	**Surface Age** (ka)			**Displacement/offset** (m)				**Vertical slip rate** (mm/yr)		
	Surface	Midpt.	Range	Midpt.	Min	Max	Source	Midpt.	Min	Max
BCS	P	15.8	1.8	15.5	10.0	21.0	a	1.0 [j]	0.6	1.5
BCS	B	17.6	0.3	21.5	16.0	27.0	a, b	1.2 [k]	0.9	1.6
WS	B/P	15.8	1.8	17.6	7.0	28.3	c	1.1 [l]	0.4	2.0
WS	P	15.8	1.8	14.2	4.6	23.7	b, c	0.9 [m]	0.3	1.7
SLCS	~B	15.9	0.7	14.5	11.5	24.5	e, f	0.9 [n]	0.7	1.6
PS	P	15.8	1.8	12.5	11.5	13.5	b, g, h	0.8 [o]	0.7	1.0
PS	B	17.6	0.3	21.5	15.0	28.0	b, h	1.2 [p]	0.8	1.6
NS	B	17.6	0.3	9.0	8.1	9.9	i	0.5 [q]	0.5	0.6
							Mean long-term SR for central WFZ:	**1.0**	**0.6**	**1.4**

[1] Closed interval slip rate per segment based on the modeled mean displacement (Table B-10) divided by the closed mean recurrence interval (Table B-7). [a] NS closed interval slip rates based on NS mean recurrence intervals determined using N3 or N4.

[2] Closed interval slip rate based on the total displacement (sum individual rupture displacements on the segment; for example, for B1 to B3; table B-9) following the elapsed time between earthquakes (e.g., B4 and B1), using the mean and two-sigma ranges for events (in parentheses) included in table B-6. [a] NS closed interval slip rates are based on the elapsed time between N4 and N1 and N3 and N1. [b] For the NS slip rate since N4, a displacement range of 2.0 (1.7-2.4) m is used for N3 based on N1, N2, and N4 (Table B-9).

[3] Open-interval slip rate per segment is based on the total displacement (sum of individual rupture displacements; Table B-9) divided by the elapsed time since the maximum limiting age on the oldest earthquake (e.g., B4 max for site earthquake BEC4) to the present (2011). [a] A displacement range of 2.0 (1.7-2.4) m is used for N3 based on N1, N2, and N4 (Table B-9).

[4] Long term slip rates based on displacements postdating the Bonneville (B) and Provo (P) shorelines. Sources: [a] Personius (1990), [b] Lund (2005), [c] Nelson and Personius (1993), [d] Nelson *et al.* (2006), [e] Personius and Scott (1992), [f] Lund (2007), [g] Machette *et al.* (1992), [h] Machette (1992), [i] DuRoss *et al.* (2008). Slip rate per source notes: [j] 10 m—P gravel south of Box Elder Cyn. 21 m—P delta at Box Elder Cyn, P gravel south of Pearsons Canyon. Personius *et al.* (2012) calculated a maximum rate of 1.3 ± 0.2 mm/yr using 21.2 ± 2.1 m (at Box Elder Canyon) and a P occupation time of 16.0 ± 1.0 ka (after Benson *et al.*, 2011), which is consistent with our min (0.6 mm/yr) and max (1.5 mm/yr) results for the BCS. [k] 16 m—undifferentiated gravel and B gravel north of Cook Cyn. 27 m—B delta north of Willard Canyon. [l] 17.6 m—mean of least-squares best-fit ellipse (shape: sin(L)^0.6, height: 24 m) using 22 displacements digitized from Nelson *et al.* (2006; their Figure 6). [m] 4.6 m—P shoreline north of Davis Cr. 19 m—P gravel S of Coldwater Canyon. 23.7 m—estimate from East Ogden trench site (Lund, 2005). [n] 14.5 m—mean displacement from Bells Canyon moraine (Swan et al., 1981). Age from Lips (Lund, 2007); Undifferentiated B displacement of 11.7–15.8 m from Warm Springs fault fits within min-max range. [o] 11.5-13.5 m—post P displacement at Hobble Creek. [p] 15 m—post B displacement at American Fork Canyon. 28 m—B Sand displaced north of Spanish Fork. We excluded a displacement of 40-45 m at Hobble Creek because of question of lower surface measured across large graben. [q] 9 m—offset of B shoreline at Santaquin Canyon (with 10% uncertainty added).

Table B-12. Weighted mean vertical slip rates for the central WFZ.

Slip Rate (SR):	**BCS** mm/yr [wt.]	**WS** mm/yr [wt.]	**SLCS** mm/yr [wt.]	**PS** mm/yr [wt.]	**NS** mm/yr [wt.]
Closed mean SR per segment[1]	1.6 (1.0–2.4) [0.2]	1.9 (1.1–2.9) [0.35]	1.3 (1.0–1.8) [0.35]	2.0 (1.2–3.0) [0.35]	1.7 (1.1–3.2) [0.2]
Open mean SR per segment[2]	1.2 (0.9–1.3) [0.2]	1.7 (1.2–2.3) [0]	1.3 (1.0–1.6) [0]	2.1 (1.9–2.4) [0]	1.5 (1.3–1.8) [0.2]
Composite closed mean SR[3]	1.7 (0.9–2.7) [0.3]	1.7 (0.9–2.7) [0.35]	1.7 (0.9–2.7) [0.35]	1.7 (0.9–2.7) [0.35]	1.7 (0.9–2.7) [0.3]
Composite long-term SR[4]	1.0 (0.6–1.4) [0.3]	1.0 (0.6–1.4) [0.3]	1.0 (0.6–1.4) [0.3]	1.0 (0.6–1.4) [0.3]	1.0 (0.6–1.4) [0.3]
Weighted mean SR[5]	**1.3 (0.8–2.0)**	**1.5 (0.9–2.4)**	**1.3 (0.8–2.0)**	**1.6 (0.9–2.4)**	**1.4 (0.9–2.2)**

[1] Closed-interval slip rate (SRs) are the average of mean, minimum, and maximum SRs based on (1) average displacement and recurrence and (2) elapsed time and total displacement (Table B-11). For the NS, the closed mean slip rate is the mean of SRs calculated using the N4–N1 and N3–N1 mean recurrence.

[2] Open-interval SRs are based on the total displacement since the maximum limiting age for the oldest earthquake on the segment (Tables B-7 and B-11). For the NS, the open mean slip rate is the mean of SRs calculated using the total displacement postdating N3 and N4.

[3] The composite closed mean SR is based on the mean of the per-source modeled mean displacements (Table B-10) and the composite closed recurrence interval for the central WFZ; see text for discussion.

[4] The composite long-term SR is the mean of the long-term SRs per segment based on the total net vertical displacement of latest Pleistocene-age geomorphic surfaces related to the Provo phase and highstand of Lake Bonneville (Table B-11).

[5] Weighted mean SRs per segment are based on weighting scheme for per-segment and composite SRs (weights shown in brackets).

Table B-13. Multi-segment ruptures included in central WFZ rupture models.

Multi-segment rupture[1]	**L**[2] (km)	**PDF over-lap**[3]	**Length of rupture studied**[4]			**Gap in paleoseismic data**[5]		**Displacement per rupture**[6] (m)			
								Observed		Modeled	
			(km)	(%)	n	(km)	(%)	range	n	mean	min-max
B3+W4	91	0.73	32	35%	5	45	49%	1.0–4.2	3	2.3	2.2–2.4
B4+W5	91	0.64	56	62%	4	33	36%	1.4–2.5	4	1.9	1.8–2.1
S2+P3	99	0.59	55	56%	5	37	37%	1.8–2.5	3	1.5	1.3–1.7
P3+N3	88	0.59	70	80%	5	35	40%	2.5	1	3.8	3.3–4.2
W2+S1	104	0.39	94	90%	6	50	48%	0.5–3.2	6	2.7	2.4–2.9
P2+N2	88	0.25	41	47%	4	43	49%	1.4–2.3	3	1.8	1.2–2.2
B2+W3	91	0.07	58	64%	7	24	26%	1.0–4.2	6	1.9	1.7–2.1
S3+P4	99	0.07	55	56%	4	38	38%	1.4–2.5	3	1.7	1.5–2.0
S2+P3+N3	128	NA	88	69%	7	36	28%	1.8–2.5	3	1.7	1.6–1.9

[1] Multi-segment ruptures included in the intermediate and multi-segment rupture models; see text for discussion.

[2] L – end to end rupture length.

[3] Overlap in segment PDFs (after Biasi and Weldon, 2009; see also DuRoss *et al.* (2011) (e.g., between PDFs for B4 and W5), which we consider good if greater than 0.5; see text for discussion.

[4] Straight-line distance between northernmost and southernmost paleoseismic sites where the earthquake has been identified (km) divided by L (%). We consider ruptures having paleoseismic data for greater than 50% of L to be well constrained. n is number of paleoseismic sites where data defines the earthquake-timing PDFs (site PDFs) that contribute to the rupture.

[5] Largest straight-line distance between paleoseismic sites or between a site and the end of the rupture (km) divided by L (%). We consider ruptures have paleoseismic data gaps of less than about 50% of L to be moderately well constrained.

[6] Observed displacement is range in site displacements along the rupture (Figure B-10); modeled displacement is mean and min-max range based on analytical displacement curves fit to the displacement observations (see text for discussion; Figure B-10; Table B-9).

Table B-14. Rupture models and weights for the central WFZ.

Rupture Model[1]	**Rupture Sources**[2]	**WGUEP Weight**[3]	**Earthquakes**[4]	**Notes**
SSR	B, W, S, P, N	0.7	22 SSR	Only SSRs occur
Int. C	B, W, S, P, N, B+W	0.075	18 SSR, 2 MSR	SSRs, including B+W MSR
-	B, W, S, P, N, W+S	-	-	W+S accounted for in MSR model
-	B, W, S, P, N, S+P	-	-	S+P ruptures separately
-	B, W, S, P, N, P+N	-	-	P+N ruptures separately
Int. A	B, W, S, P, N, B+W, S+P	0.05	16 SSR, 3 MSR	SSRs, including most-probable MSRs
Int. B	B, W, S, P, N, B+W, P+N	0.05	16 SSR, 3 MSR	SSRs, including most-probable MSRs
-	B, W, S, P, N, B+W, W+S…†	-	-	Accounted for in MSR model
MSR	B, W, S, P, N, B+W, W+S, S+P, P+N, S+P+N	0.025	7 SSR, 7 MSR	All possible MSRs occur
-	Unsegmented‡	0.1	-	-

[1] Rupture models include (1) all single-segment ruptures (SSRs) (SSR model; Figure B-11), (2) combinations of SSRs and multi-segment ruptures (MSRs) we consider most probable (Intermediate [Int.] A, B, and C; Figure B-12), and (3) all possible MSRs (MSR model; Figure B-13). See text for discussion of model development.

[2] Rupture sources: B – BCS, W – WS, S – SLCS, P – PS, N – NS; combinations of these indicate multi-segment-rupture sources (e.g., B+W). † Model representing SSRs plus one of many possible combinations of MSRs (e.g., B+W, W+S; or B+W, S+P). ‡The unsegmented model accounts for possible multi-segment and/or partial-segment ruptures not included in these models.

[3] Consensus weight of the WGUEP. No assigned weight indicates that rupture model not included.

[4] Number of earthquakes included in each rupture model; see Table B-15 for timing information for individual earthquakes.

Table B-15. Timing of multi-segment earthquakes on the central WFZ.

Rupture[1]	**Rupture model**[2]	**Earthquake Timing**[3] (ka)					
		Mean	Two sigma	5th	50th	95th	Mode
B2+W3	MSR	3.3	0.5	2.9	3.4	3.6	3.4
B3+W4	Int. A, B, C	4.5	0.4	4.1	4.5	4.9	4.5
B4+W5	Int. A, B, C	5.8	0.6	5.2	5.8	6.3	5.6
W2+S1	MSR	1.2	0.5	0.7	1.3	1.6	1.3
S3+P4	MSR	4.4	0.6	4.0	4.4	4.9	4.7
S2+P3	Int. A	2.2	0.3	1.9	2.2	2.5	2.2
S2+P3+N3	MSR	2.1	0.4	1.8	2.2	2.5	2.2
P2+N2	MSR	1.4	0.4	1.2	1.3	1.7	1.2
P3+N3	Int. B	2.1	0.5	1.7	2.1	2.5	2.1
B2+W3	MSR	3.3	0.5	2.9	3.4	3.6	3.4

[1] Rupture abbreviations: B – Brigham City segment (BCS), W – Weber segment (WS), S – Salt Lake City segment, P – Provo segment, N – Nephi segment. B2+W3 indicates a multi-segment rupture of BCS earthquake B2 and WS earthquake W3.

[2] Rupture model: MSR – multi-segment rupture model, Int. – Intermediate (A, B, C) models.

[3] Summary statistics based on integration of per-segment earthquake-timing PDFs.

Table B-16. Segment boundary uncertainties and rupture lengths for the central WFZ.

Rupture	**Median SRL**[1] (km)	**SRL uncert.**[2] (km) North end	South end	**Min SRL**[3] (km)	**Max SRL**[3] (km)
Brigham City segment (BCS)	35	± 3	+ 3, -8	24	41
Weber segment (WS)	56	+8, -3	± 7	46	71
Salt Lake City (SLCS)	40	± 7	± 6	27	53
Provo segment (PS)	59	± 6	+4, -13	40	69
Nephi segment (NS)	43	+5, -17	± 6	20	54
BCS+WS	91	± 3	± 7	81	101
WS+SLCS	104	+8, -3	± 6	95	118
SLCS+PS	99	± 7	+4, -13	79	110
PS+NS	88	± 6	± 6	76	100
SLCS+PS+NS	128	± 7	± 6	115	141

[1] Median surface rupture length (SRL) per rupture source based on the linear distance between segment ends.

[2] SRL uncertainties at the northern and southern rupture ends based on segment-boundary uncertainties (Figures B-14 and B-15). Two values indicate asymmetric uncertainties about median value.

[3] Minimum and maximum possible SRL per rupture source based on segment-boundary uncertainties.

Table B-17. Summary of segment-boundary uncertainties for the central WFZ.

Rupture	SRL[1] (km)	Segment Boundary Uncertainty[2]			
		North end		South end	
		km	Description	km	Description
Brigham City segment (BCS)	35	± 3	Based on 3 km of Holocene spillover rupture from the BCS onto the southernmost Collinston segment (CS) mapped by Personius (1990) (see also Personius *et al.*, 2012). A larger uncertainty was not considered because the CS does not have evidence of Holocene surface faulting.	+ 3, -8	3-km uncertainty based on the geometry of the fault step-over between the BCS and WS, and the distance from the south end of the BCS to the Rice Creek trench site on the WS. Rupture beyond 3 km likely consisted of multi-segment ruptures (e.g., B4+W5) accounted for the paleoseismic rupture models. The 8-km uncertainty is based on the spillover rupture of WS earthquake W2 onto the southern BCS (DuRoss *et al.*, 2012; Personius *et al.*, 2012).
Weber segment (WS)	56	+8, -3	See description for south end of BCS.	± 7	Uncertainty based on the geometry of the Salt Lake salient (WS–SLCS segment boundary), the length of the Warm Springs fault (~7–10 km), and the distance from the south end of the WS to the Penrose Drive trench site on the SLCS.
Salt Lake City (SLCS)	40	± 7	See description for south end of WS.	± 6	Uncertainty based on the geometry of the SLCS–PS segment boundary and the distance from the boundary to the Little Cottonwood Canyon and South Fork Dry Creek trench sites on the SLCS.
Provo segment (PS)	59	± 6	See description for south end of SLCS.	+4, -13	4-km uncertainty based on the distance from the southern end of the PS to the southern end of the northern strand of the NS. Larger uncertainty not included because we do not consider it likely that spillover rupture would extend from the PS to the southern strand of the NS (this scenario included in paleoseismic rupture models). 13-km uncertainty based on the distance from the southern end of the PS to the north end of the northern strand of the NS. This distance also corresponds with the distance from the south end of the PS to the Mapleton trench site.

Nephi segment (NS)	43	+5, -17	5-km uncertainty based on the distance from the north end of the northern strand of the NS to the Mapleton trench site on the PS. 17-km uncertainty based on the length of the northern strand of the NS.	± 6	Uncertainty based on the distance from the south end of the NS to the north end of the Levan segment (the gap in the rupture trace).
BCS+WS	91	± 3	See description for north end of the BCS.	± 7	See description for south end of the WS.
WS+SLCS	104	+8, -3	See description for north end of the WS.	± 6	See description for south end of the SLCS.
SLCS+PS	99	± 7	See description for north end of the SLCS.	+4, -13	See description for south end of the PS.
PS+NS	88	± 6	See description for north end of the PS.	± 6	See description for south end of the NS.
SLCS+PS+NS	128	± 7	See description for north end of the SLCS.	± 6	See description for south end of the NS.

[1] Median surface rupture length (SRL) per rupture source based on the linear distance between segment ends.

[2] SRL uncertainties at the northern and southern rupture ends based on segment-boundary uncertainties (Figures B-14 and B-15). Two values indicate asymmetric uncertainties about median value.

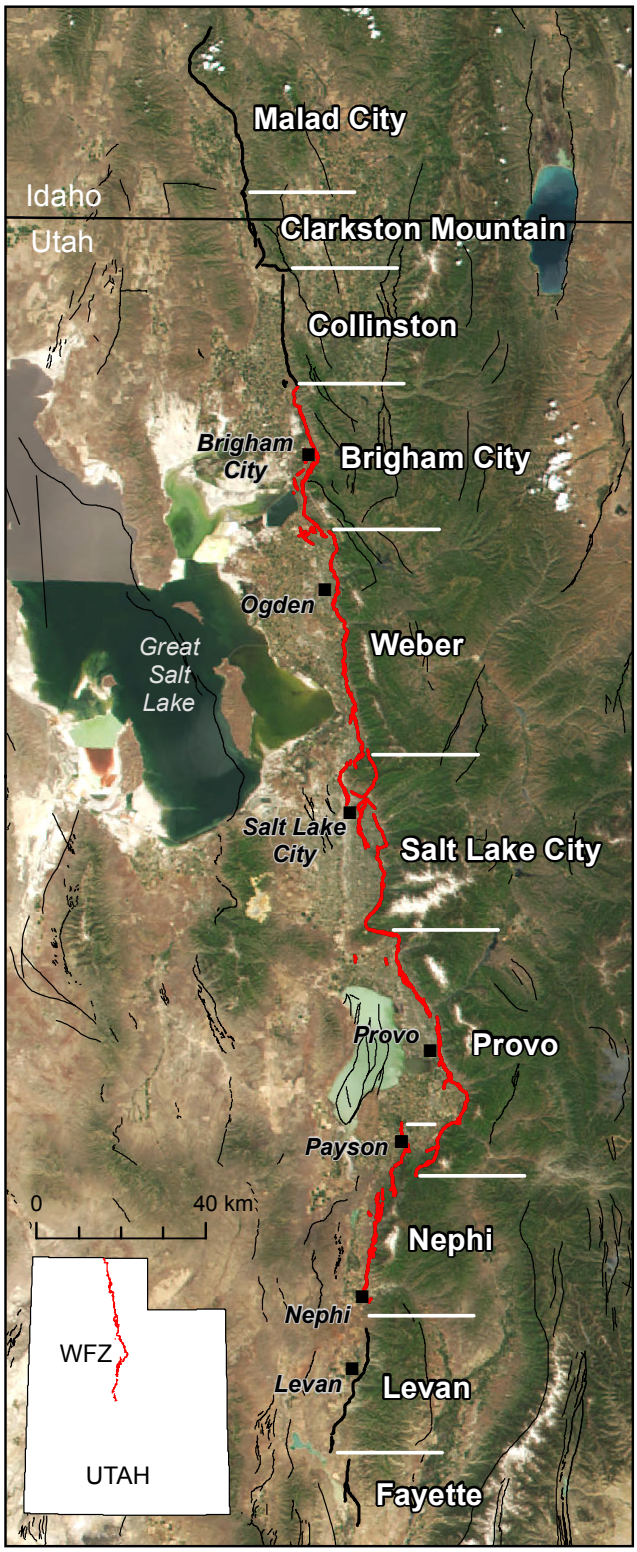

Figure B-1. Segments of the Wasatch fault zone (WFZ) in southern Idaho and northern Utah. The central WFZ, which has evidence of repeated Holocene surface-faulting earthquakes, is shown in red; end segments of the WFZ are shown in black. Other Quaternary faults in northern Utah are shown in dark gray. Fault traces are from Black *et al*. (2003); base map is true-color satellite image from the National Aeronautics & Space Administration (NASA; http://visibleearth.nasa.gov/view.php?id=55874).

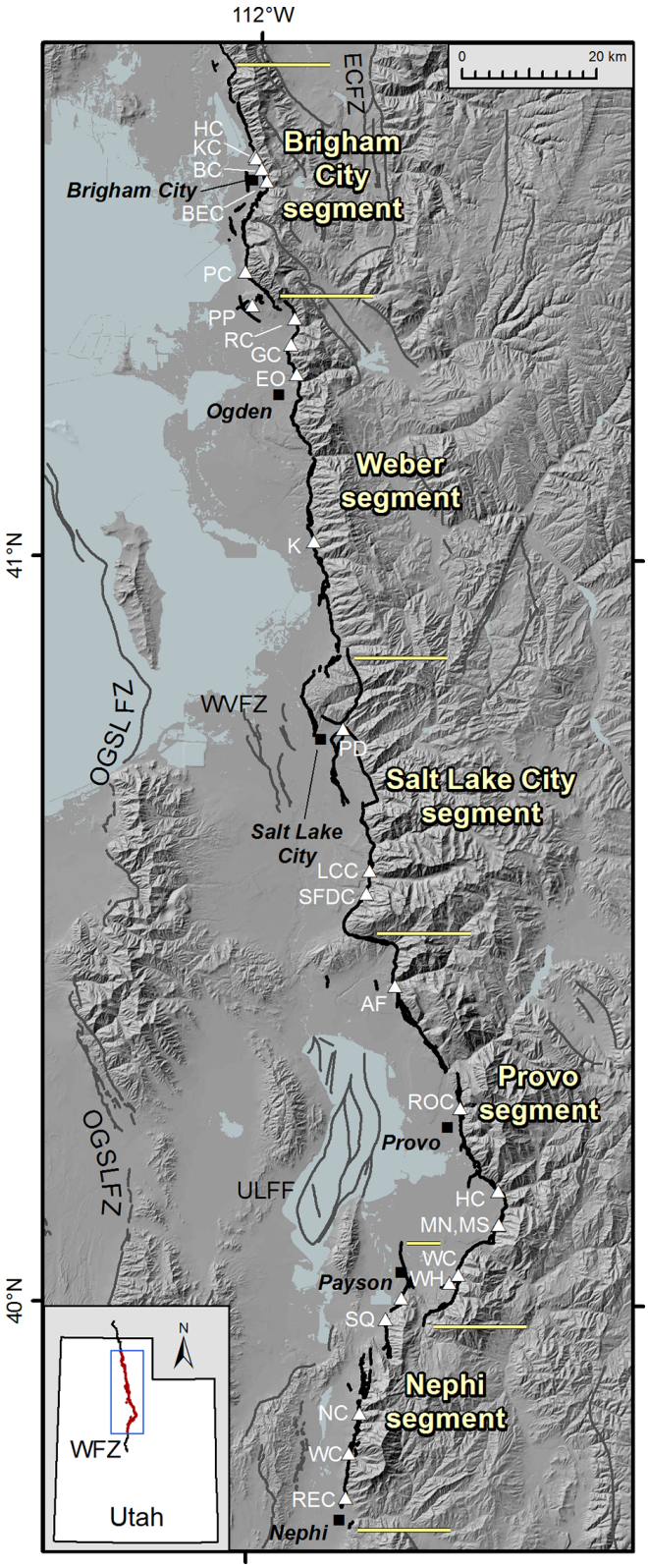

Figure B-2. Central segments of the WFZ (from Black *et al*., 2003) showing paleoseismic research sites (yellow triangles; see appendix A for site abbreviations). ECFZ – East Cache fault zone, ETMF – East Tintic Mountains fault, GSLFZ – Great Salt Lake fault zone, OFZ – Oquirrh fault zone, SOMFZ – Southern Oquirrh Mountains fault zone, THFZ – Topliff Hills fault zone, ULFF – Utah Lake faults and folds, WVFZ – West Valley fault zone. Shaded topography generated from 10-m digital elevation data (https://lta.cr.usgs.gov/NED).

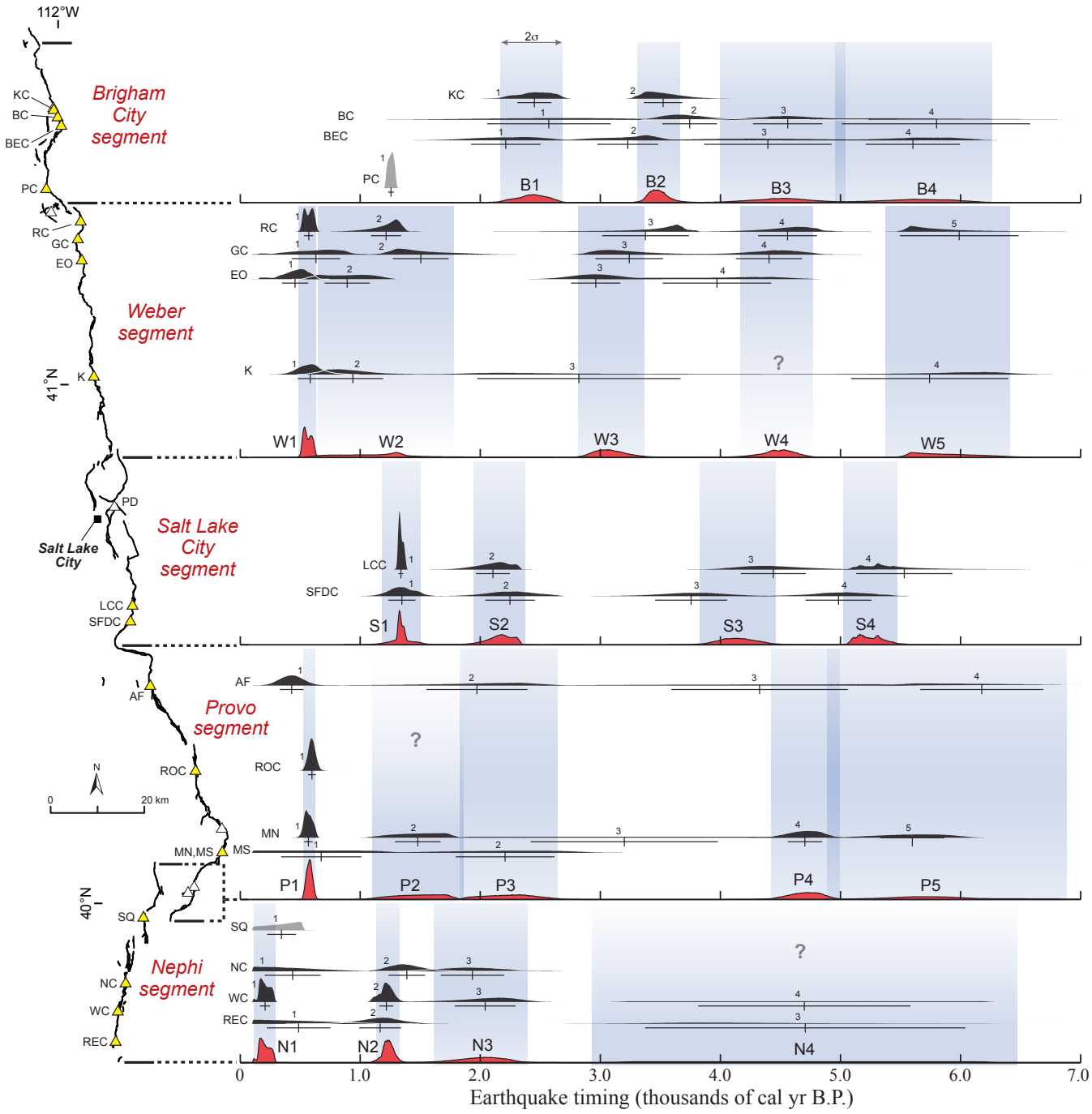

Figure B-3. Correlation of surface-faulting earthquakes identified at paleoseismic sites (yellow triangles) on the central WFZ. For each segment, black earthquake-timing distributions are site probability density functions (site PDFs) derived from OxCal (appendix A); abbreviations and event numbers correspond to Tables B-1 to B-5. Vertical blue bands show correlation of site PDFs along segment to form segment PDFs (red-filled time distributions; e.g., B1; Table B-6). Site earthquake PDFs not included in segment-PDF calculation (e.g., PC1 and SQ1) are shaded gray. See text for additional discussion.

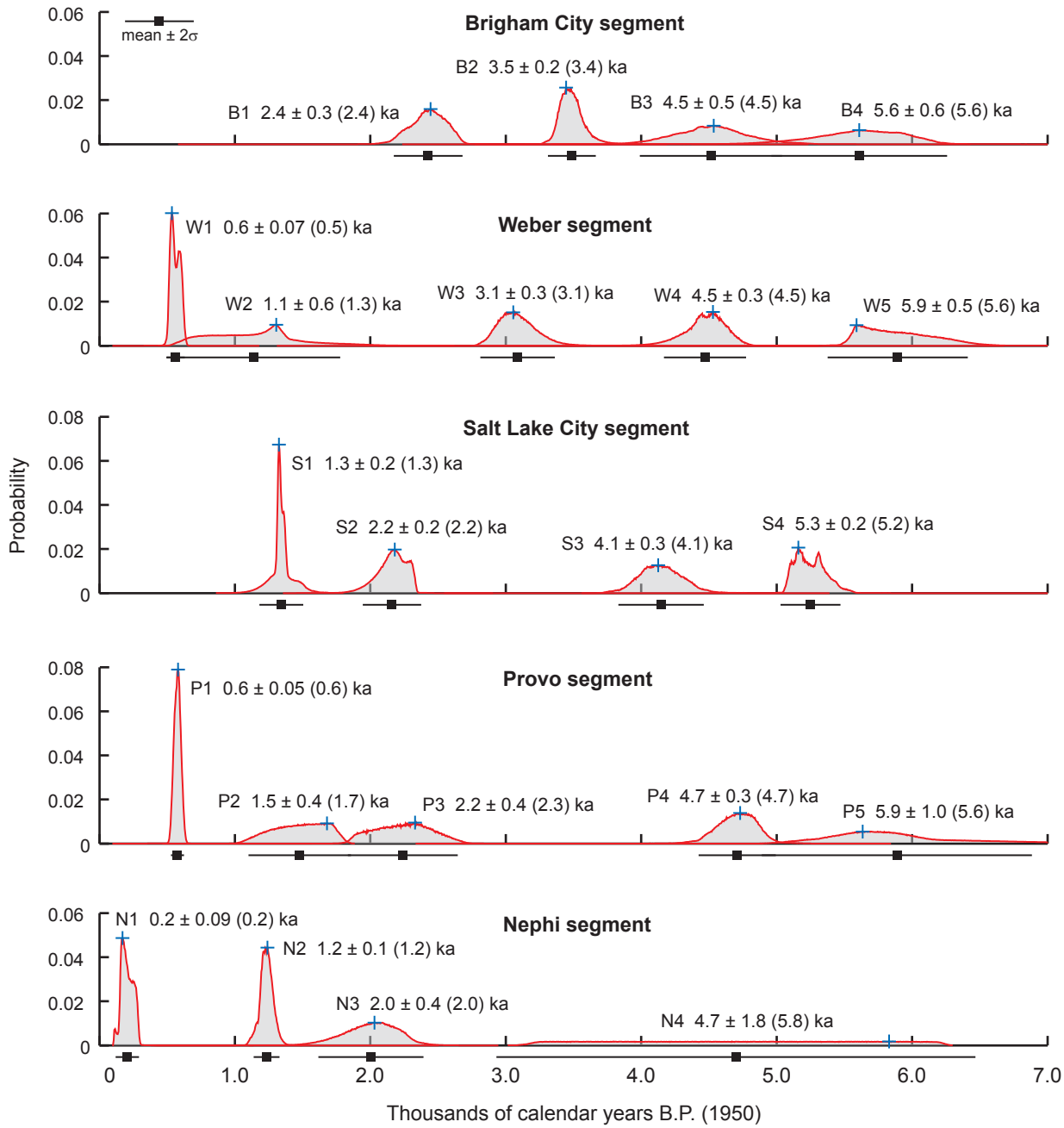

Figure B-4. Timing of surface-faulting earthquakes on the central segments of the WFZ. Red lines are earthquake-timing probability density functions (PDFs) derived from our integration of site paleoseismic data (Figure B-3; appendix C; see text for discussion). Earthquake times are reported as mean ± 2σ, and modal times (corresponding to the peak probabilities) are shown by blue crosses with modal value in parentheses.

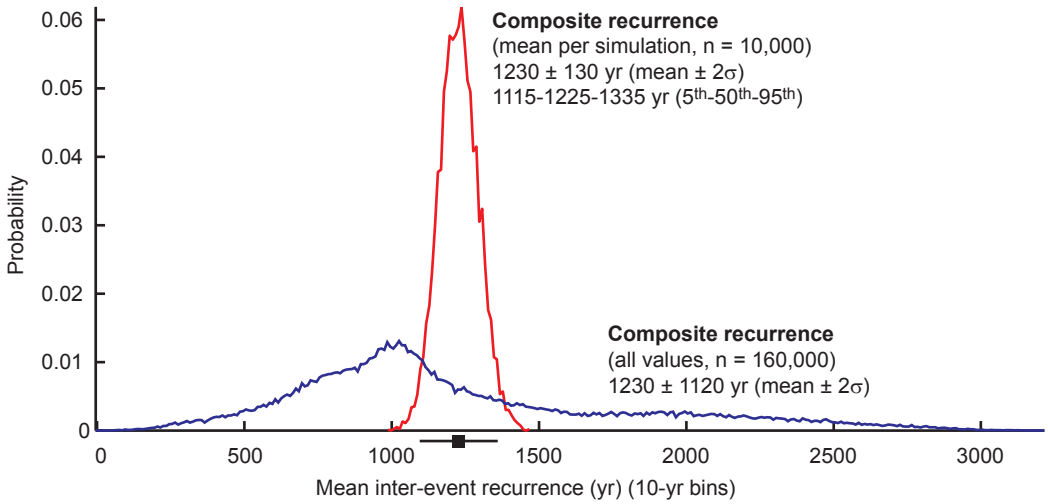

Figure B-5. Composite recurrence intervals for the central WFZ determined by (1) sampling and averaging 16 inter-event recurrence intervals (per segment; e.g., W5–W4, but not W5–B4) in numerous simulations (red shaded PDF—see text for discussion) and (2) taking all possible inter-event recurrence intervals in numerous simulations (blue line). The composite recurrence, or distribution of means, is narrower than the recurrence distribution for the complete (grouped) dataset, where each inter-event recurrence value is included and treated equally.

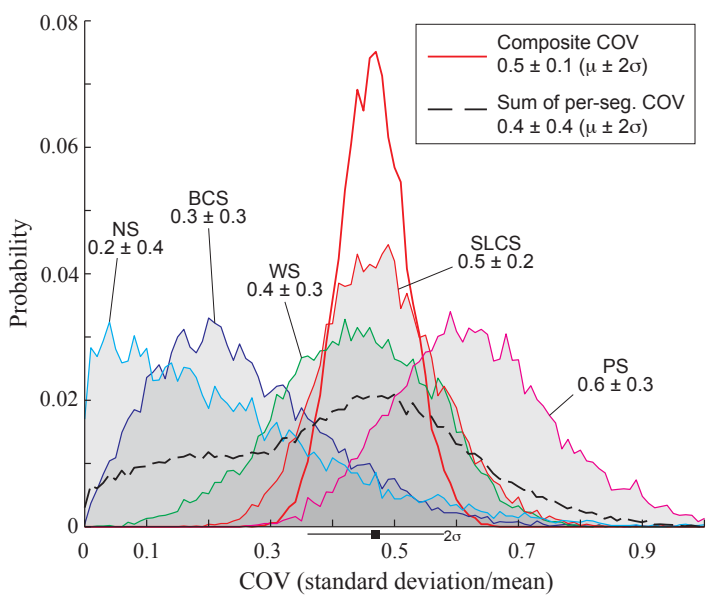

Figure B-6. Composite coefficient of variation (COV) of earthquake recurrence for the central WFZ (solid black line), calculated by compiling 16 inter-event-recurrence PDFs (per segment; e.g., W5–W4, but not W5–B4) and sampling them in a Monte Carlo model. Each simulation produced a group of 16 randomly sampled inter-event recurrence times from which we calculated the COV (standard deviation divided by the mean of the 16 recurrence intervals). The COV calculation thus uses the full inter-event recurrence distributions, but does not account for sample-size uncertainties. The composite COV distribution (and mean and 2σ values) is based on the COVs calculated in numerous simulations. The 5th–95th percentile range for the NS is shown in parentheses because of the asymmetric shape of the COV distribution. We also segregated the sampled recurrence PDFs by segment and computed segment-specific COVs (dashed and colored COV distributions; segment abbreviations correspond with Figure B-3), which we then summed to form a composite COV (dashed black line). Ultimately, the composite approach yields the most robust mean COV for the region; however, the COV estimates for the individual segments, although based on limited data, show more variability.

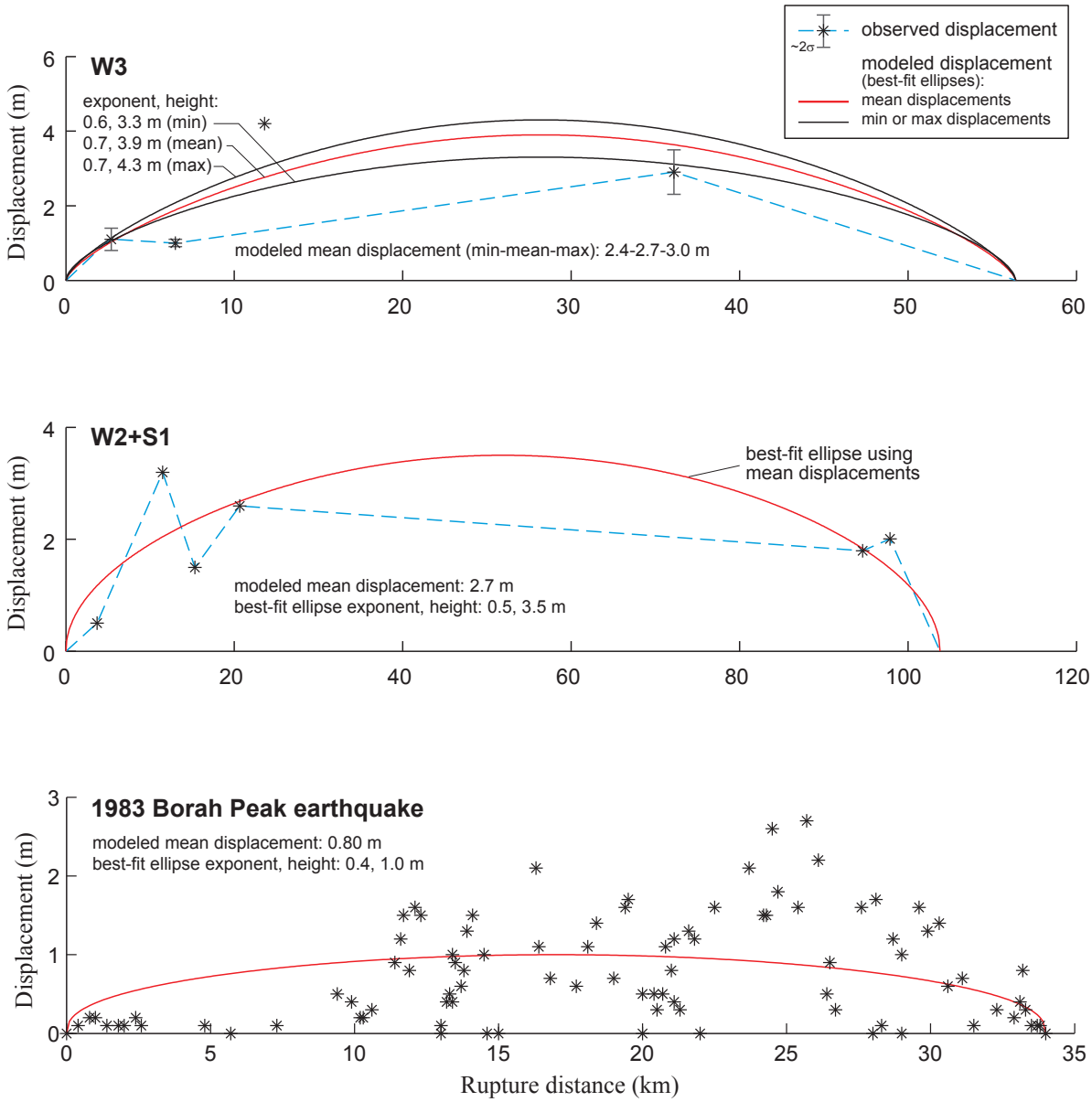

Figure B-7. Examples of analytical displacement curves fit to displacement observations for single and multiple segment ruptures on the central WFZ (upper two panels) and the 1983 Borah Peak earthquake (lower panel). In upper panel, the three curves are fit to the mean (red), and minimum and maximum (black) displacement observations using a least-squares, best fit method (see text for discussion). For the lower two panels, only displacement curves fit to the mean displacement values are shown. Per-site displacement observations are shown as black asterisks (Borah Peak observations are from Wesnousky [2008]); blue dashed lines are simple displacement profiles (between displacement observations); not shown for the Borah Peak displacements. Modeled mean displacements are determined by sampling the analytical displacement curves in 0.1 km increments.

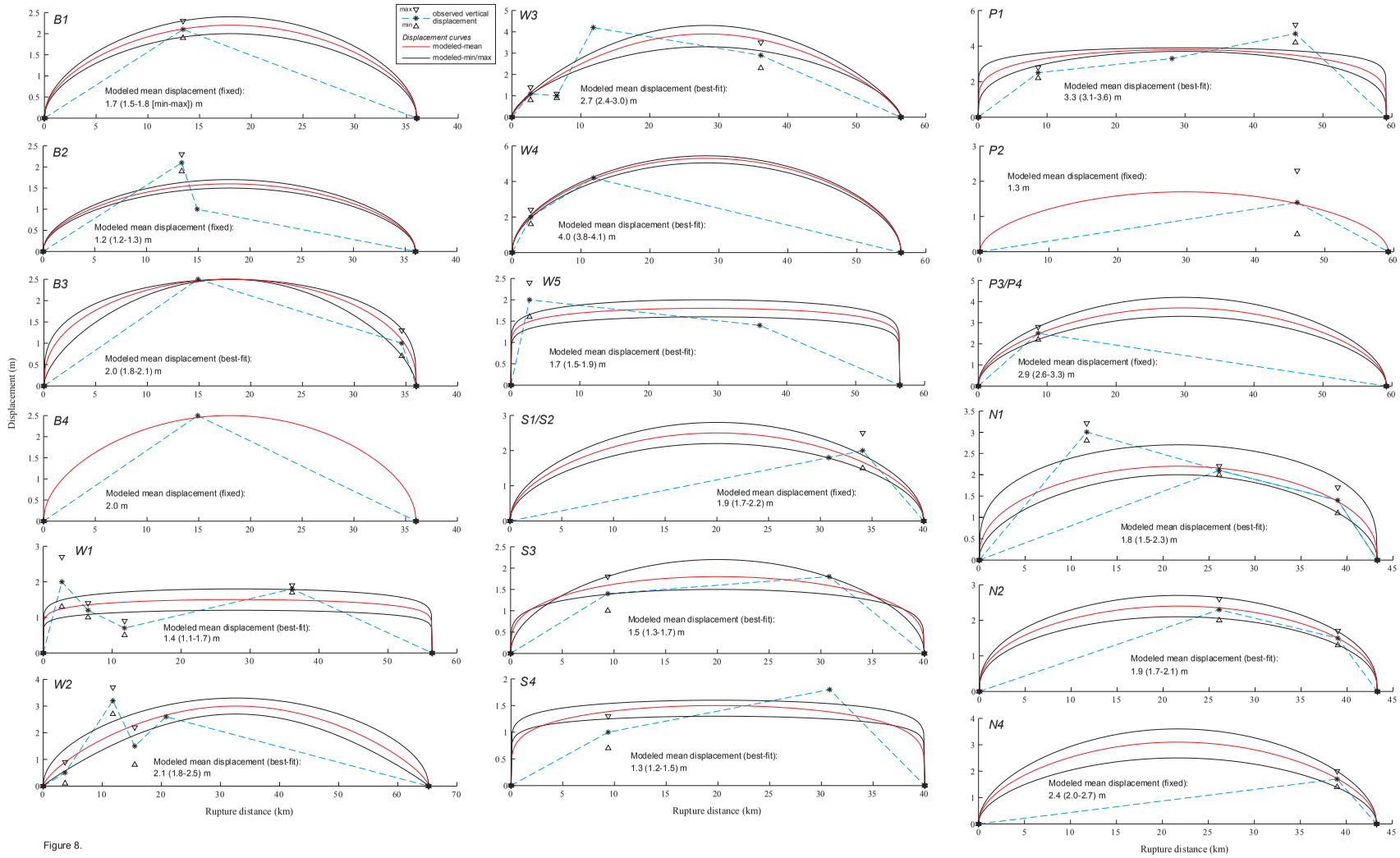

Figure B-8. Analytical displacement curves for single-segment ruptures on the central WFZ. Single displacement curves indicate those fit to the mean displacement observations (using a least-squares method with the curve shape and maximum height allowed to vary); multiple curves (e.g., for B1) are analytical displacement curves with fixed shapes (flat, half-ellipse, and peaked) are fit to the displacement observations (see text for discussion of both methods). Site displacements (black asterisks) correspond to table B-8; blue dashed lines are simple displacement profiles (between displacement observations). Modeled displacements, calculated by sampling the analytical displacement curves in 0.1 km increments, correspond to table B-9.

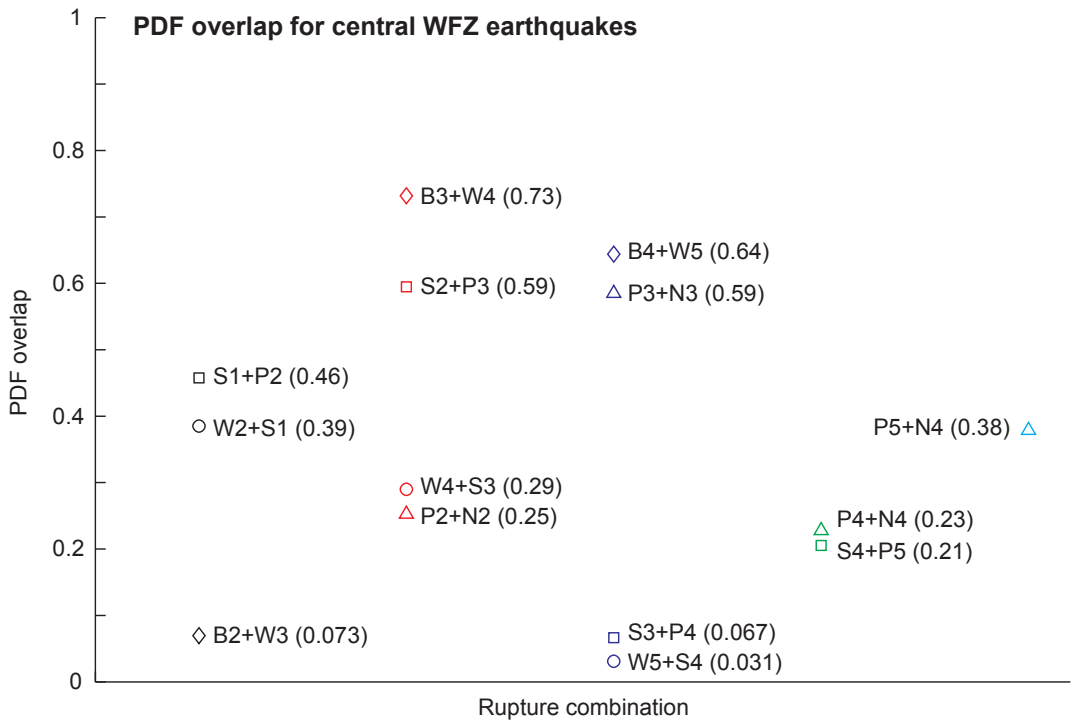

Figure B-9. PDF overlap for pairs of earthquakes on the central WFZ (adjacent segments only). PDF overlap ranges from 0 (no overlap) to 1 (two identical PDFs) and is found by summing the minimum probabilities for common time bins in two overlapping PDFs (Biasi and Weldon, 2009; see also DuRoss *et al*., 2011). The letter-number pairs refer to individual earthquakes on specific segments; B–Brigham City, W–Weber, S–Salt Lake City, P–Provo, and N–Nephi (tables B-1 to B-5).

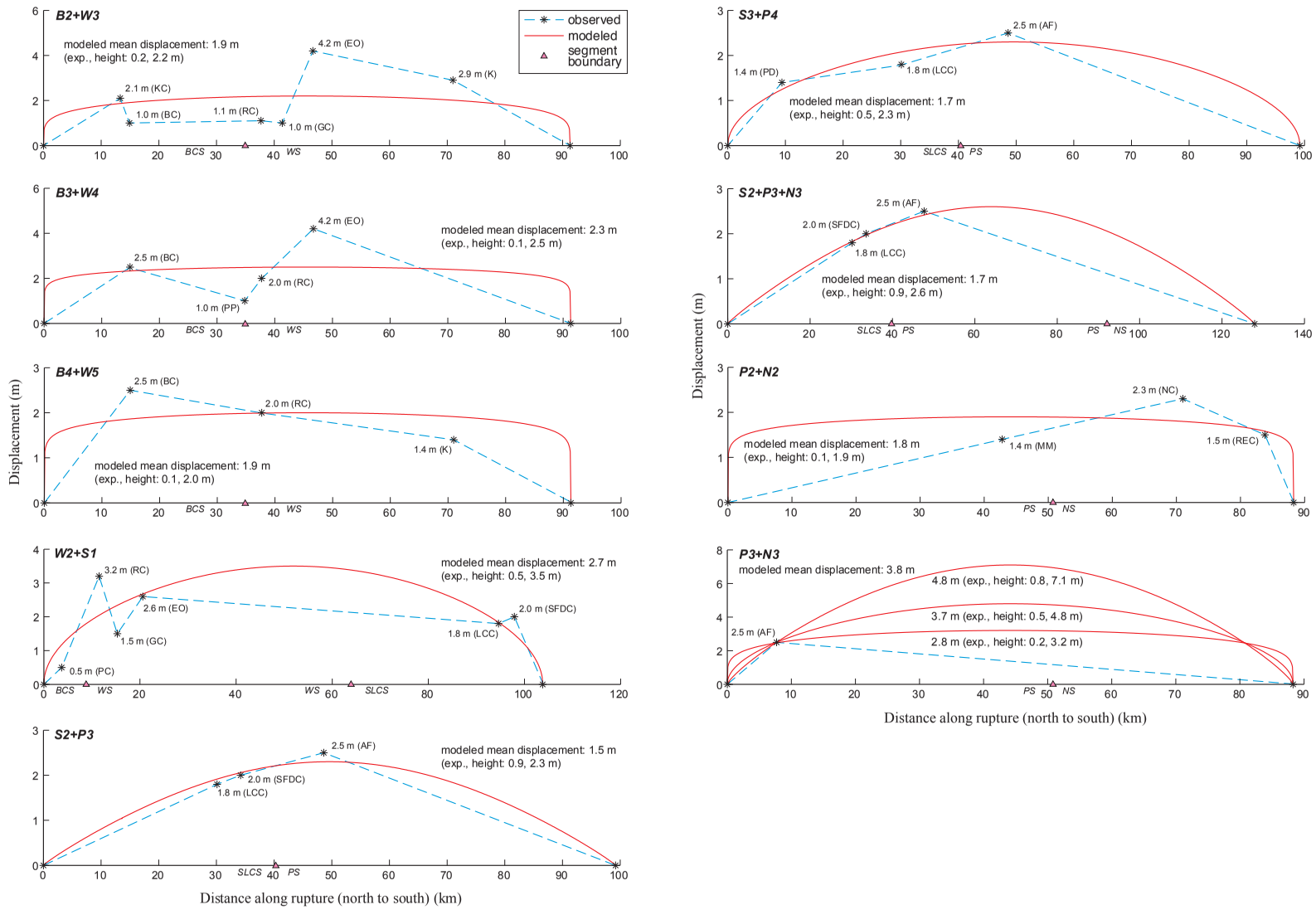

Figure B-10. Analytical displacement curves for multi-segment ruptures on the central WFZ. All curves are fit to the mean displacement observations (using a least-squares method with the curve shape and maximum height allowed to vary), with the exception of P3+N3, where three analytical displacement curves with fixed shapes (flat, half-ellipse, and peaked) are fit to the displacement observation (see text for discussion of both methods). Site displacements (black asterisks) correspond to table B-8; blue dashed lines are simple displacement profiles (between displacement observations). Modeled displacements, calculated by sampling the analytical displacement curves in 0.1 km increments, correspond to table B-9.

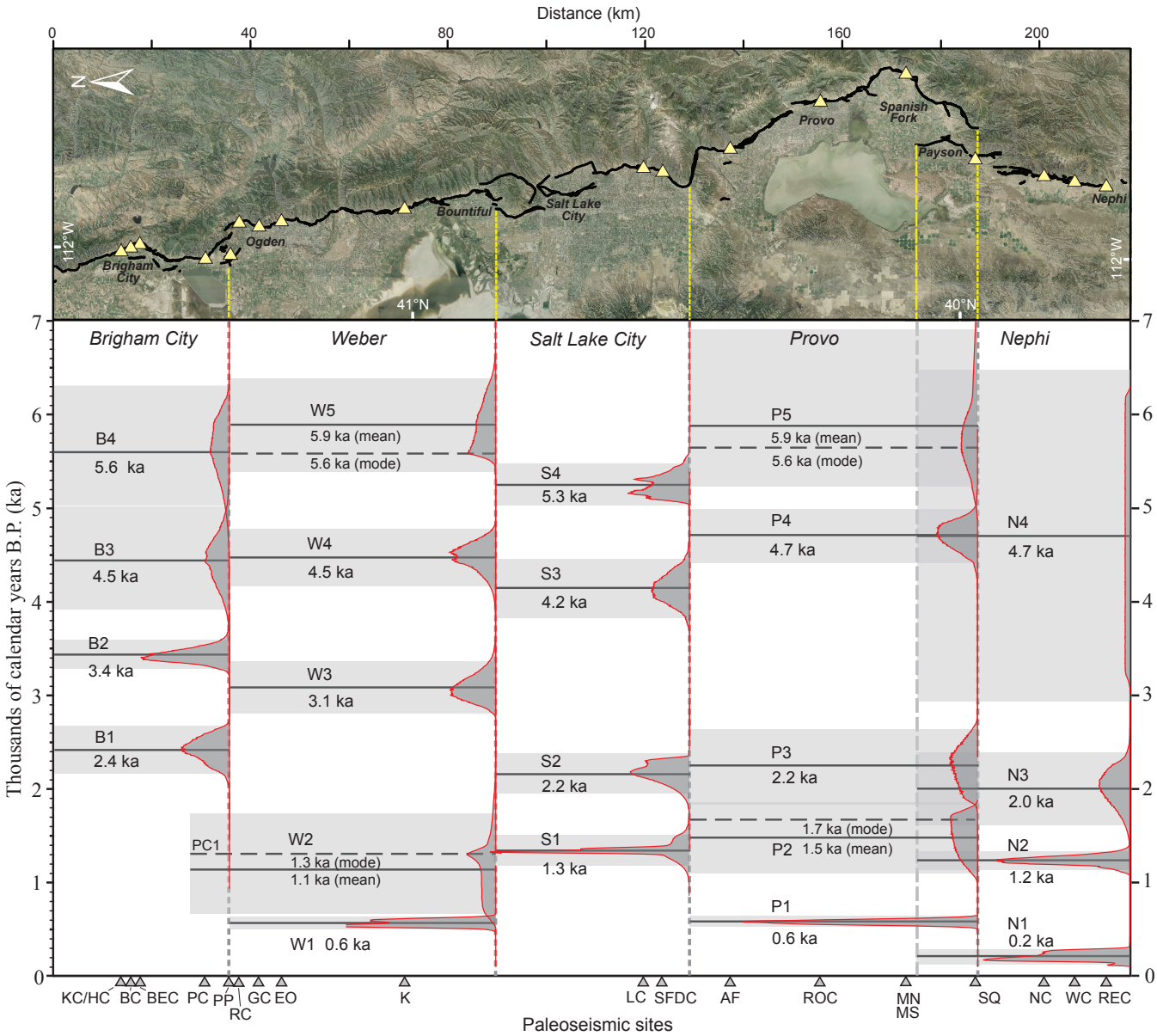

Figure B-11. Single-segment rupture model for the central WFZ. Upper panel shows map of the central segments; yellow triangles show locations of paleoseismic study sites. Lower panel shows times of earthquakes on each segment. Solid horizontal lines indicate mean earthquake times (dashed lines indicate modal times for select earthquakes); gray boxes show 2σ time ranges. Red lines with gray-shaded fill are segment PDFs from Figure B-3; see text for discussion and table B-6 for correlation of site-PDFs and site abbreviations. Base map is aerial imagery (https://gdg.sc.egov.usda.gov/) overlain on shaded topography generated from 10-m digital elevation data (https://lta.cr.usgs.gov/NED).

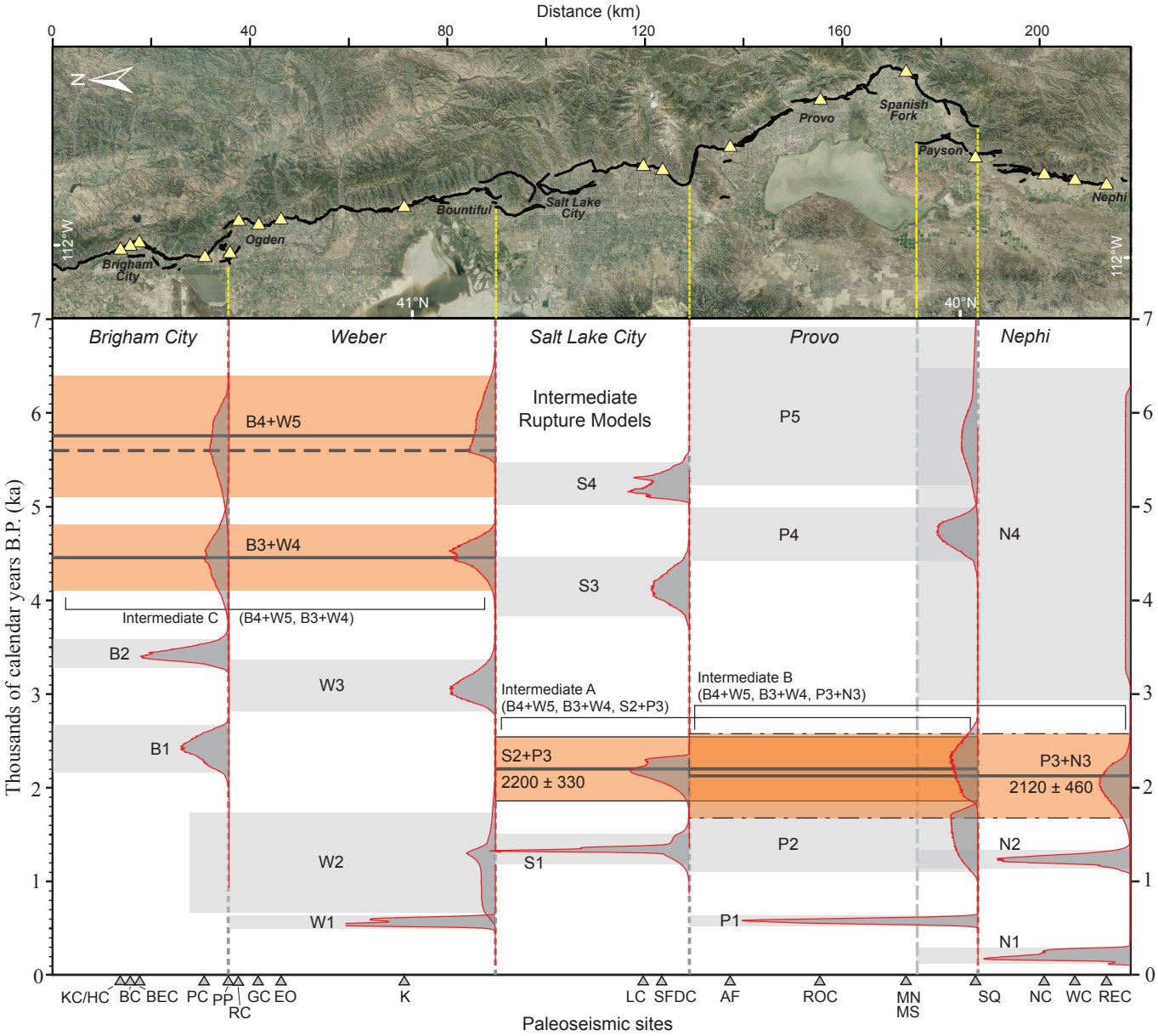

Figure B-12. Intermediate rupture models for the central WFZ. Upper panel is the same as in Figure B-8. Intermediate model A consists of single-segment ruptures (gray boxes showing 2σ ranges) and multi-segment ruptures B4+W5, B3+W4, and S2+P3 (orange boxes showing 2σ ranges). Intermediate model B includes P3+N3 in place of S2+P3. Intermediate model C has single-segment ruptures as well as multi-segment ruptures B4+W5 and B3+W4. Solid horizontal lines indicate mean earthquake times (dashed lines indicate modal times for select earthquakes). Red lines with gray-shaded fill are segment PDFs from Figure B-3; see text for discussion and tables B-6 and B-8 for correlation of site-PDFs and site abbreviations. Base map is aerial imagery (https://gdg.sc.egov.usda.gov/) overlain on shaded topography generated from 10-m digital elevation data (https://lta.cr.usgs.gov/NED).

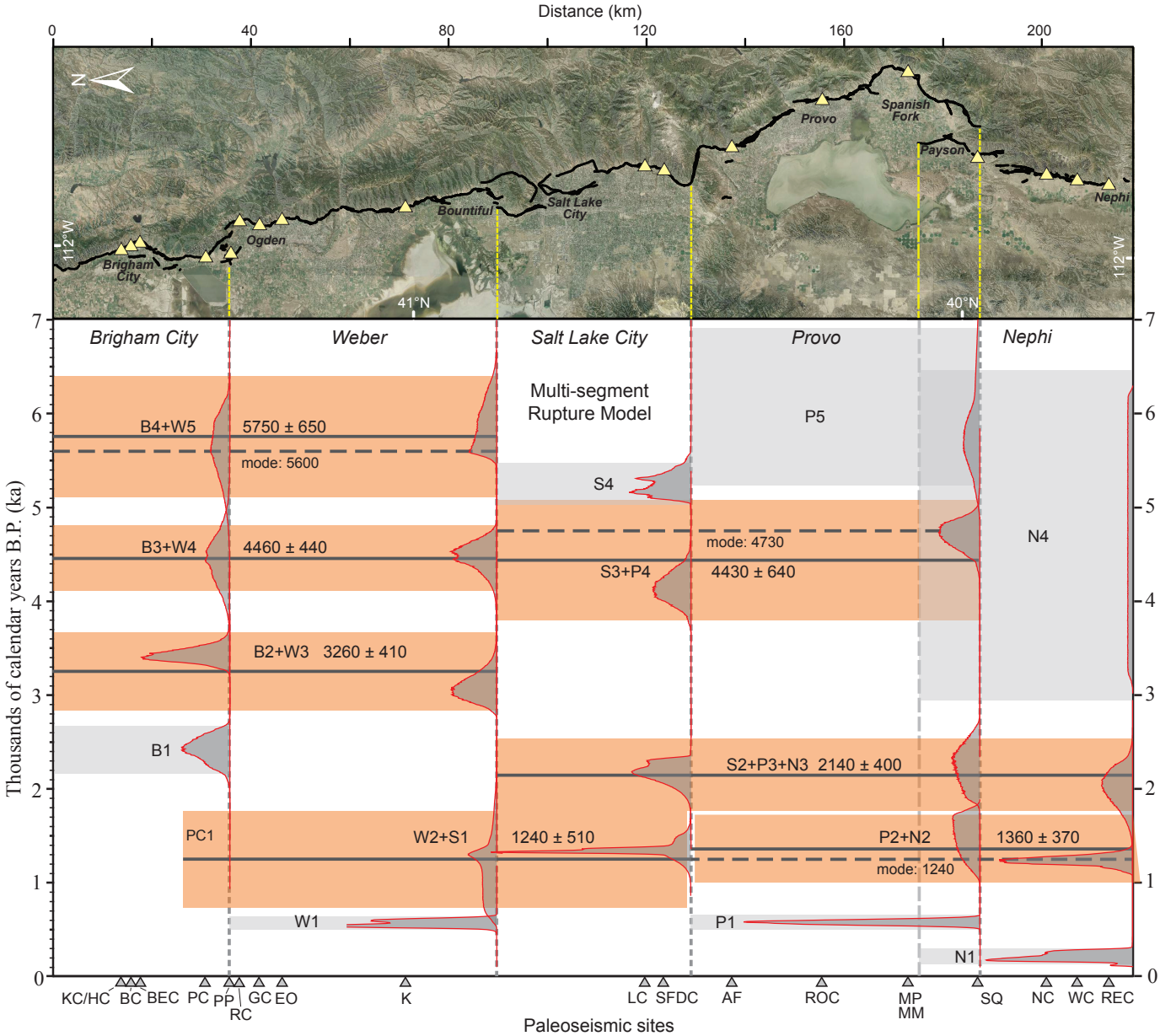

Figure B-13. Multi-segment rupture model for the central WFZ consisting of single-segment ruptures (gray boxes showing 2σ ranges) and multi-segment ruptures (orange boxes showing 2σ ranges). Solid horizontal lines indicate mean earthquake times (dashed lines indicate modal times for select earthquakes). Red lines with gray-shaded fill are segment PDFs from Figure B-3; see text for discussion and tables B-6 and B-8 for correlation of site-PDFs and site abbreviations. Base map is aerial imagery (https://gdg.sc.egov.usda.gov/) overlain on shaded topography generated from 10-m digital elevation data (https://lta.cr.usgs.gov/NED).

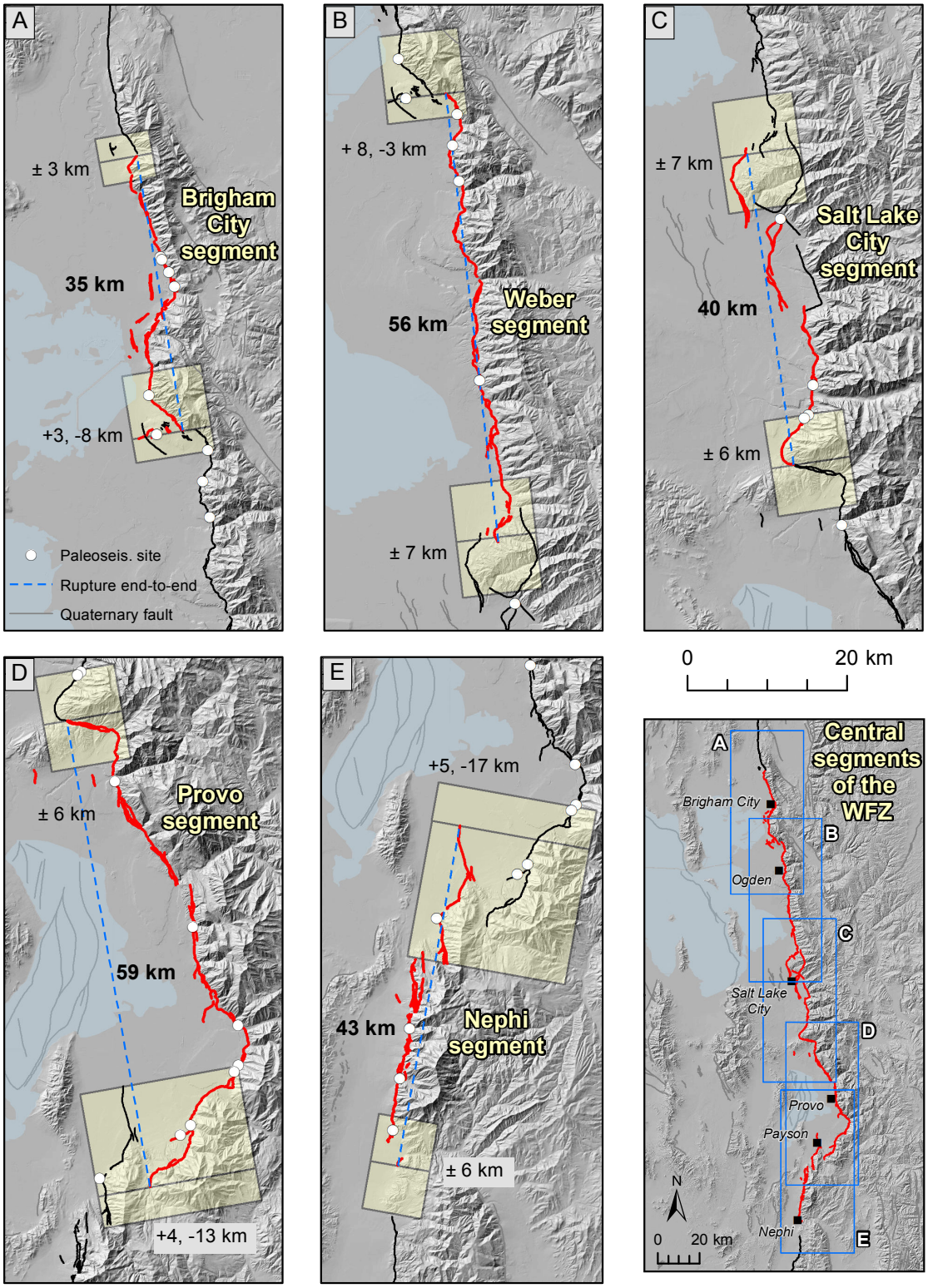

Figure B-14. Segment-boundary uncertainties for single-segment ruptures on the central WFZ. Yellow boxes correspond to segment-boundary uncertainties defined using the geometry and timing of faulting close to the segment boundaries, and paleoseismic data, if available. White dots show paleoseismic sites, and blue dashed lines are straight-line length measurements (between rupture ends), with median rupture lengths (e.g., 35 km for the BCS) shown. See text and table B-17 for discussion of individual segment-boundary uncertainties. Shaded topography generated from 10-m digital elevation data (https://lta.cr.usgs.gov/NED).

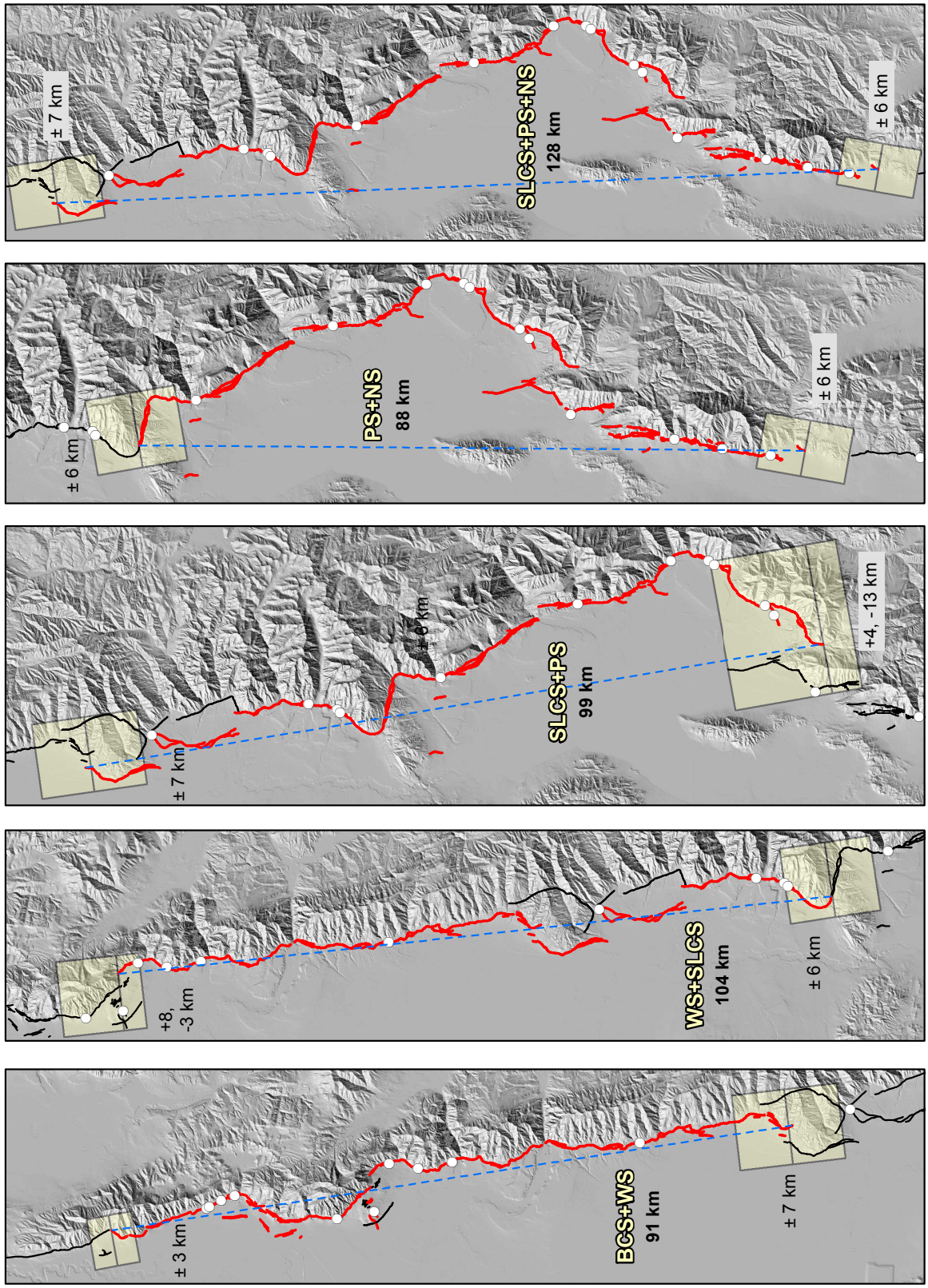

Figure B-15. Segment-boundary uncertainties for multi-segment ruptures on the central WFZ. Yellow boxes correspond to segment-boundary uncertainties defined using the geometry and timing of faulting and paleoseismic data, and are the same as those defined for single-segment ruptures (Figure B-14). White dots show paleoseismic sites, and blue dashed lines are straight-line length measurements (between rupture ends), with median rupture lengths (e.g., 91 km for the BCS+WS multi-segment rupture source) shown. See text and table B-17 for discussion of individual segment-boundary uncertainties. Shaded topography generated from 10-m digital elevation data (https://lta.cr.usgs.gov/NED).

APPENDIX C

OQUIRRH–GREAT SALT LAKE FAULT ZONE

By

Susan Olig and Christopher DuRoss

C-1. OxCal Input Models

C-2. OxCal Model Results

C-3. Displacement Inputs

C-4. Modeled Vertical Displacements

Appendix C-1. OxCal Input Models

NO Segment Input File: NOFZ_bc_pc_comb3

```
Plot()
 {
  Sequence("Big Canyon and Pole Canyon Sites Combined-Rev3")
  {
   Boundary("Sequence start");
   Comment("Data from Olig et al. 1994; 1996");
   Comment("Event P3 excluded");
   Phase("Unit B2-faulted stream alluvium")
   {
    R_Date("OFPC-RC5", 33950, 1160);
    R_Date("OFPC-RC3", 26200, 120);
   };
   Date("P2")
   {
    color="Red";
   };
   R_Date("OFPC-RC2 Unit D1a-LB trans. marsh", 20370, 120);
   Phase("Unit 12-faulted debris flow");
   {
    R_Date("BCST-12-1 ", 7650, 90);
    R_Date("BCST-12-RC2", 6840,100);
   };
   Date("P1")
   {
    color="Red";
   };
   Comment("BCST-13f-4 from Unit 13f excluded-probably contains older detrital carbon");
   #R_Date("BCST-13f-4", 8230,120);
   R_Date("BCNN-19-1 Unit 19-unfaulted stream alluvium",4340,60);
Boundary("Sequence end",1847);
   C_Date("2010",2010,0);
  };
```

SO Segment OxCal Input File: MercurCynrev3

```
Plot()
 {
  //Three trenches (West, Central and East) all combined into one model
  //Ages are AMS 14C dates from Beta and Infrared Stimulated Luminescence (IRSL)
  //by S. L. Forman (U of IL) using Multiple aliquot additive dose method
  //Data from Olig et al. (2001) and
  //written comm. from SLF (5/15/01) for pending age of MCET2-L5T
  Sequence("Mercur_Canyon_Rev3")
  {
   Boundary("Sequence start");
   Comment("C_date is IRSL sample collection date[2000] rounded to decade minus lab date");
   Combine("E Trench Unit 2a-loess")
   {
    C_Date("MCET2-L5Z", -90000,7000);
    C_Date("MCET2-L5Y", -83600,6100);
   };
   Date("Event Ve and Vc")
   {
    color="Red";
   };
   Combine("W Trench Unit 2-loess")
   {
    C_Date("MCWT2-L2", -78700,6300);
    C_Date("MCWT2-L1", -66700,5200);
   };
   Date("Event We and Ww")
   {
    color="Red";
   };
   Phase("W Trench Unit 4-loess")
   {
    C_Date("MCWT2-L4", -44700,3800);
    C_Date("MCWT2-L3", -35000,3000);
   };
   Date("Event Xw")
   {
    color="Red";
   };
   Date("Event Yw")
   {
    color="Red";
   };
   Delta_R("Charcoal-no MRT correction",0,0);
   R_Date("MCWT6-1RC Unit 6a", 4110,60);
   Date("Event Zw")
   {
    color="Red";
   };
   R_Date("MCWT7-1RC Unit 7a", 1510,60);
  };
  Boundary("Sequence end",1847);
  C_Date("2010",2010,0);
 };
```

Appendix C-2. OxCal Model Results

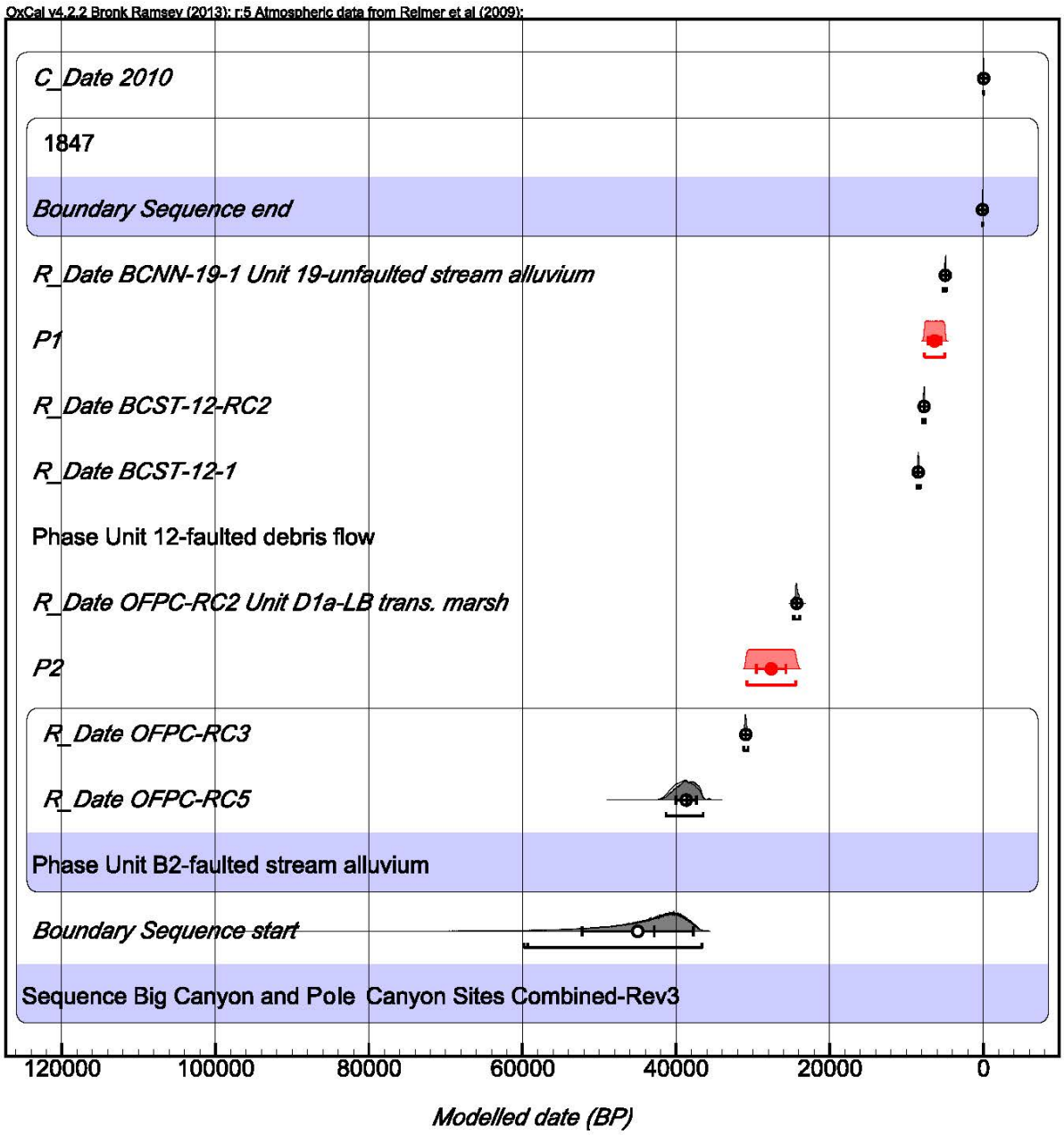

Figure C-1. Plot of OxCal model results for NO segment paleoearthquake chronology (see Table C-1 for details). Horizontal axis in calendar-calibrated years before 1950.

Table C-1. Oxcal results for NO segment (NOFZ_bc_pc_comb3out)*

Name	Unmodelled (BP)						Modelled (BP)						Indices Amodel 100.2 Aoverall 100.2	
	from	to	%	mu	sigma	median	from	to	%	mu	sigma	median	A	C
C_Date 2010 1847	-50	-60	95.4	-60	0	-60	-50	-60	95.4	-60	0	-60	100	100
Boundary Sequence end	110	100	95.4	100	0	100	110	100	95.4	100	0	100	100	100
R_Date BCNN-19-1 Unit 19-unfaulted stream alluvium	5270	4820	95.3	4940	90	4930	5270	4820	95.3	4940	90	4930	100.8	100
P1							7640	4970	95.4	6320	800	6320		99.9
R_Date BCST-12-RC2	7930	7510	95.4	7700	90	7690	7930	7510	95.5	7700	90	7690	99.6	100
R_Date BCST-12-1	8630	8210	95.4	8460	90	8460	8630	8210	95.4	8460	90	8460	99.9	100
Phase Unit 12-faulted debris flow														
R_Date OFPC-RC2 Unit D1a-LB trans. marsh	24750	23880	95.4	24290	200	24300	24750	23880	95.4	24290	200	24290	99.9	99.9
P2							30800	24430	95.4	27600	1920	27600		99.8
R_Date OFPC-RC3	31160	30610	95.4	30910	140	30930	31160	30620	95.4	30910	140	30930	100.4	100
R_Date OFPC-RC5	41490	36570	95.4	38990	1330	38960	41310	36470	95.4	38680	1310	38620	99.9	99.7
Phase Unit B2-faulted stream alluvium														
Boundary Sequence start							59780	36630	95.4	45000	7240	42830		95.8
Sequence Big Canyon and Pole Canyon Sites Combined-Rev3														

*Modelled using OxCal v.4.2.2 (Bronk Ramsey, 2013) with IntCal09 (Reimer et al., 2013). Input data from Olig et al. (1994;1996). This model combines age data for Event P1 from the Big Canon Trench site and for Event P2 from the Pole Canyon trench site because Event P2 was not exposed at Big Canyon and Event P1 was only constrained as post-Lake Bonneville at Pole Canyon (and so assumed to correlate with the event at Big Canyon). Modelled ages for Events P1, P2 and Sample OFPC-RC3 used in Approach 2 rate calculations.

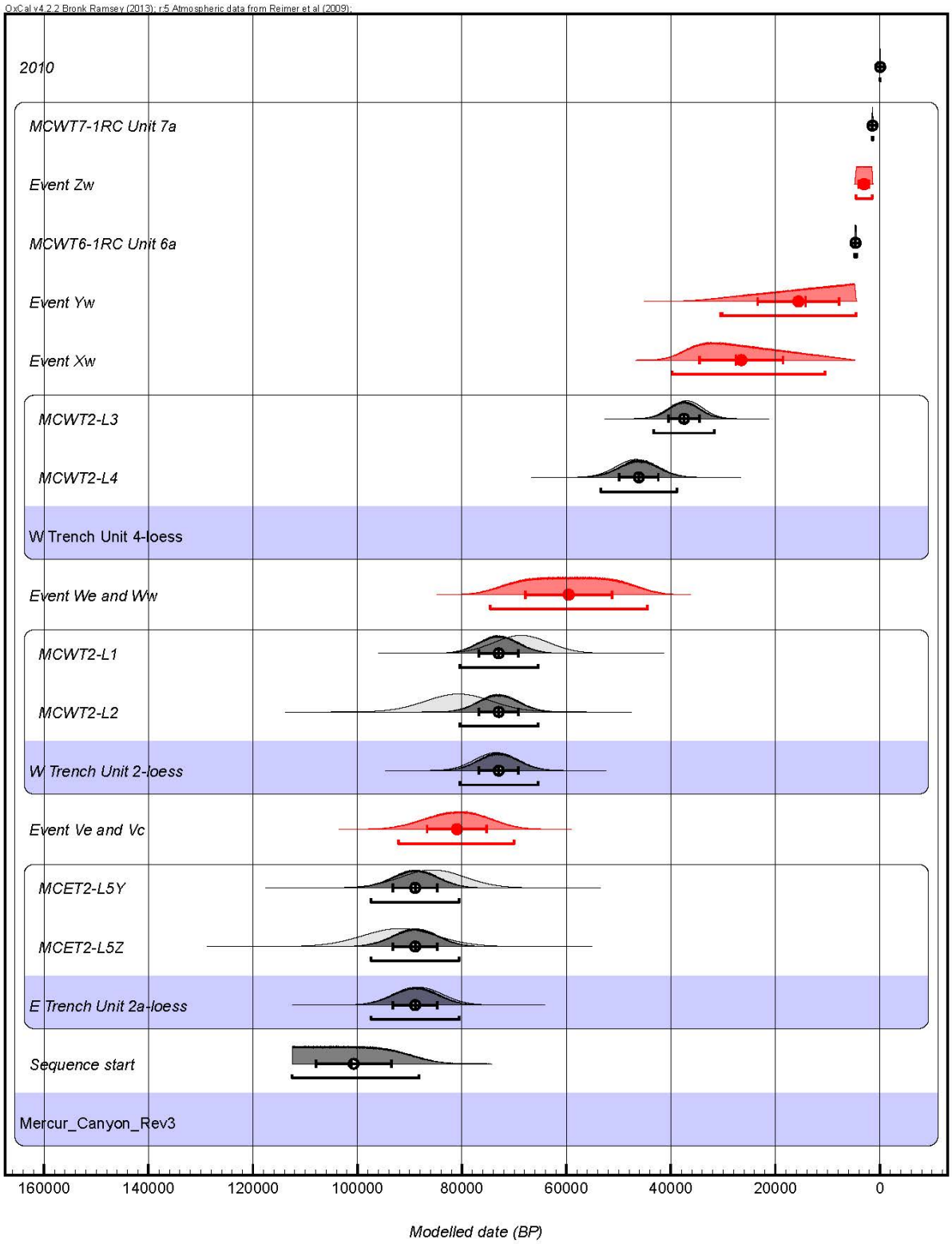

Figure C-2. Plot of OxCal model results for SO segment paleoearthquake chronology (see Table C-2 for details). Horizontal axis in calendar-calibrated years before 1950.

Table C-2. OxCal results for SO segment (MecurCynrev3out)*

Name	Unmodelled (BP)						Modelled (BP)						Indices Amodel 84.2 Aoverall 92	
	from	to	%	mu	sigma	median	from	to	%	mu	sigma	median	A	C
C_Date 2010	-59	-60	95.4	-59	0	-59	-59	-60	95.4	-59	0	-59	100	100
1847 Boundary Sequence end	1846.5	1847.5	95.4	1847	0	1847	1846.5	1847.5	95.4	1847	0	1847	100	100
R_Date MCWT7-1RC Unit 7a	1524	1305	95.4	1412	64	1402	1524	1305	95.4	1411	63	1401	100.1	99.9
Event Zw							4573	1464	95.4	3031	938	3030		99.8
R_Date MCWT6-1RC Unit 6a	4827	4445	95.4	4648	103	4642	4828	4445	95.4	4651	103	4646	100	99.9
Delta_R Charcoal-no MRT correction	-0.5	0.5	95.4	0	0	2.64E-16	-0.5	0.5	95.4	0	0	1.37E-15	100	100
Event Yw							30508	4558	95.4	15578	7814	14196		98.8
Event Xw							39780	10462	95.4	26502	7992	27552		98.6
C_Date MCWT2-L3	42936	30965	95.4	36951	3000	36951	43335	31656	95.4	37478	2958	37482	99.9	98
C_Date MCWT2-L4	54234	39068	95.4	46651	3800	46651	53404	38793	95.4	46130	3723	46122	100.4	97.3
Phase W Trench Unit 4-loess														
Event We and Ww							74597	44423	95.4	59566	8310	59541		98.4
C_Date MCWT2-L1	79026	58275	95.4	68651	5200	68651	80420	65379	95.4	72956	3797	72977	91.2	98.1
C_Date MCWT2-L2	93221	68081	95.4	80651	6300	80651	80420	65379	95.4	72956	3797	72977	70.2	98.1
Combine W Trench Unit 2-loess	81516	65511	95.4	73513	4010	73513	80420	65379	95.4	72956	3797	72977		98.1
Event Ve and Vc							92192	69975	95.4	80952	5720	80846		99
C_Date MCET2-L5Y	97723	73379	95.4	85551	6100	85551	97369	80544	95.4	88947	4265	88918	104.6	98.2
C_Date MCET2-L5Z	105919	77982	95.4	91951	7000	91951	97369	80544	95.4	88947	4265	88918	112.8	98.2
Combine E Trench Unit 2a-loess	97491	79136	95.4	88313	4599	88313	97369	80544	95.4	88947	4265	88918		98.2
Sequence start Mercur_Canyon_Rev3							112503	88245	95.4	100718	7229	101127		98.7

*Modelled using OxCal v.4.2.2 (Bronk Ramsey, 2013) with IntCal09 (Reimer et al., 2013). Input data from Olig et al. (2001) and previously unpublished IRSL age of sample MCET2-L5Y from Unit 2a (Section 4.3.1.3). This model assumes 5 events and that Event We (youngest earthquake on eastern fault) occurred coseismically with Event Ww (oldest event on western fault), and that Event Ve (oldest event on eastern fault) occurred coseismically with Event Vc (event on central fault)(see Olig et al., 2001 for further discussion). Combined age for Unit 2a loess in E Trench used for Approach 1 rate calculations of 5 to 7 events.

Appendix C-3. Displacement Inputs

Table C-3. Net Vertical Displacement Per site and Rupture for Sources of the OGSLFZ*

Source: SO segment

Data from Olig et al. (2001)

Event	Pref D*	Min D	Max D	Total Length (km)	Along Strike Distance (km)	Normalized site location
Mercur Canyon Site						
P1	1	0.75	1.25	31.2	19.5	0.63
P2	2	2	2.25			
P3	1.75	1	2			
P4	2.05	1.45	2.9			
P5	2.95	1.6	3.3			

Source: NO segment

Data from Olig et al. (1994; 1996)

Event	Pref D*	Min D	Max D	Total Length (km)	Along Strike Distance (km)	Normalized site location
Pole Canyon Site						
P1	2.7	2.2	3.3	29.75	8.96	0.30
P2	2.3	1.9	2.9			
Big Canyon Site						
P1	2.2	2	2.7	29.75	6.26	0.21

Source: NO+SO segments

Data from Olig et al. (1994; 1996;2001)

Event	Pref D*	Min D	Max D	Total Length (km)	Along Strike Distance (km)	Normalized site location
Pole Canyon Site						
P1	2.7	2.2	3.3	60.95	8.96	0.15
P2	2.3	1.9	2.9			
Big Canyon Site						
P1	2.2	2	2.7	60.95	6.26	0.10
Mercur Canyon Site						
P1	1	0.75	1.25	60.95	49.27	0.81
P2	2	2	2.25			

*All backtilting and antithetic faulting removed

Appendix C-4. Modeled Vertical Displacements

Table C-4. Modeled Vertical Displacements Per Rupture for the OGSLFZ

		D - fixed ellipse shapes			D - least-sq. best-fit ellipses		
Rupture	**Obs.**	**Mean D**	**Min D**	**Max D**	**Mean D**	**Min D**	**Max D**
SO P1	1	0.79	0.62	1.00	*insufficient data to calculate best-fit ellipse*		
SO P2	1	1.59	1.59	1.80	"		
SO P3	1	1.41	0.79	1.59	"		
SO P4	1	1.64	1.16	2.31	"		
SO P5	1	2.36	1.28	2.65	"		
NO P1	2	2.22	1.92	2.73	2.18	1.91	2.67
NO P2	1	1.97	1.61	2.46	*insufficient data to calculate best-fit ellipse*		
SO+NO P1	3	2.20	1.82	2.68	1.96	1.68	2.43
SO+NO P2	2	2.31	2.08	2.74	2.15	2.01	2.62
SO+NO P1 (SL)	3	2.18	1.82	2.68	1.96	1.68	2.43
SO+NO P2 (SL)	2	2.31	2.08	2.74	2.15	2.06	2.52

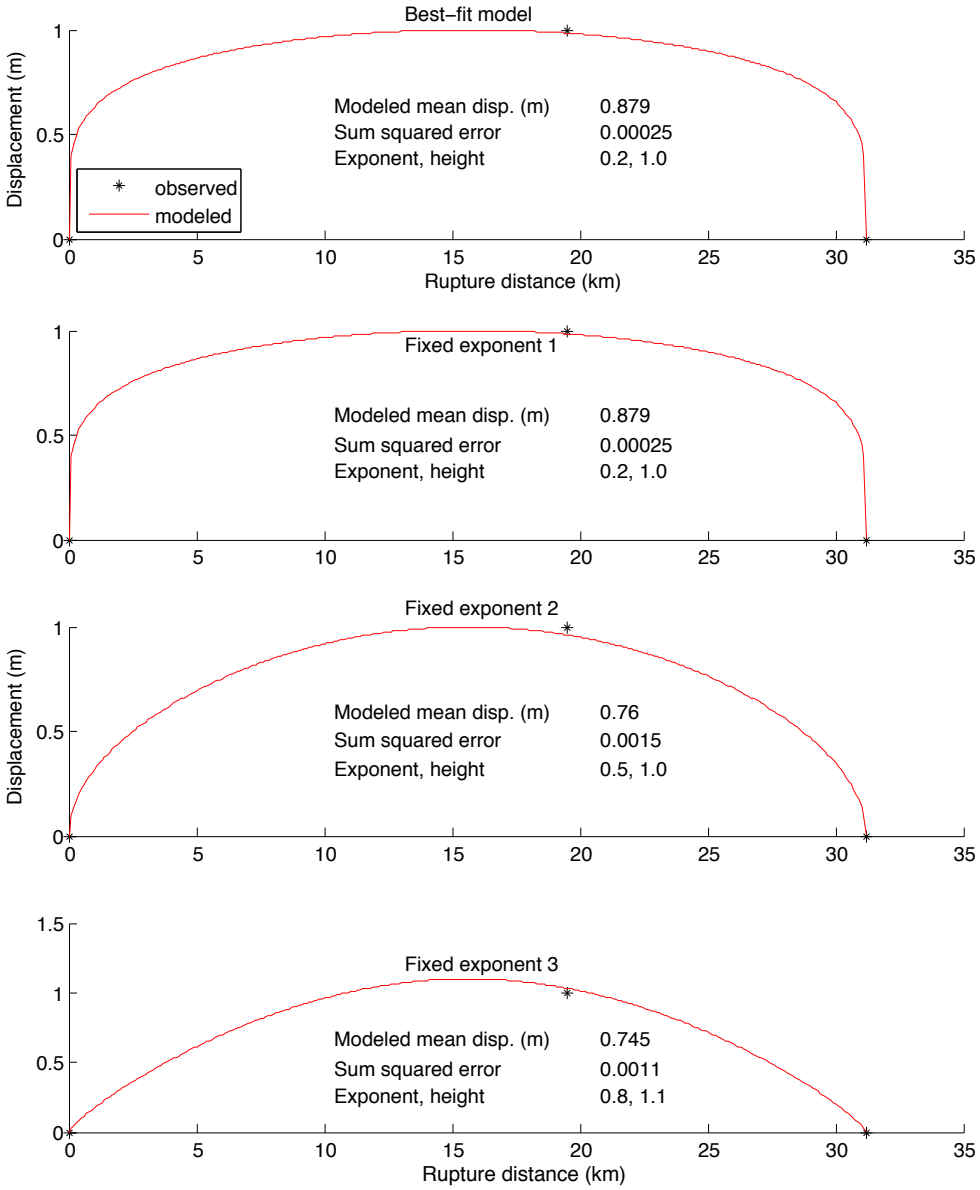

Figure C-3. Analytical displacement curves for the SO segment P1 rupture.

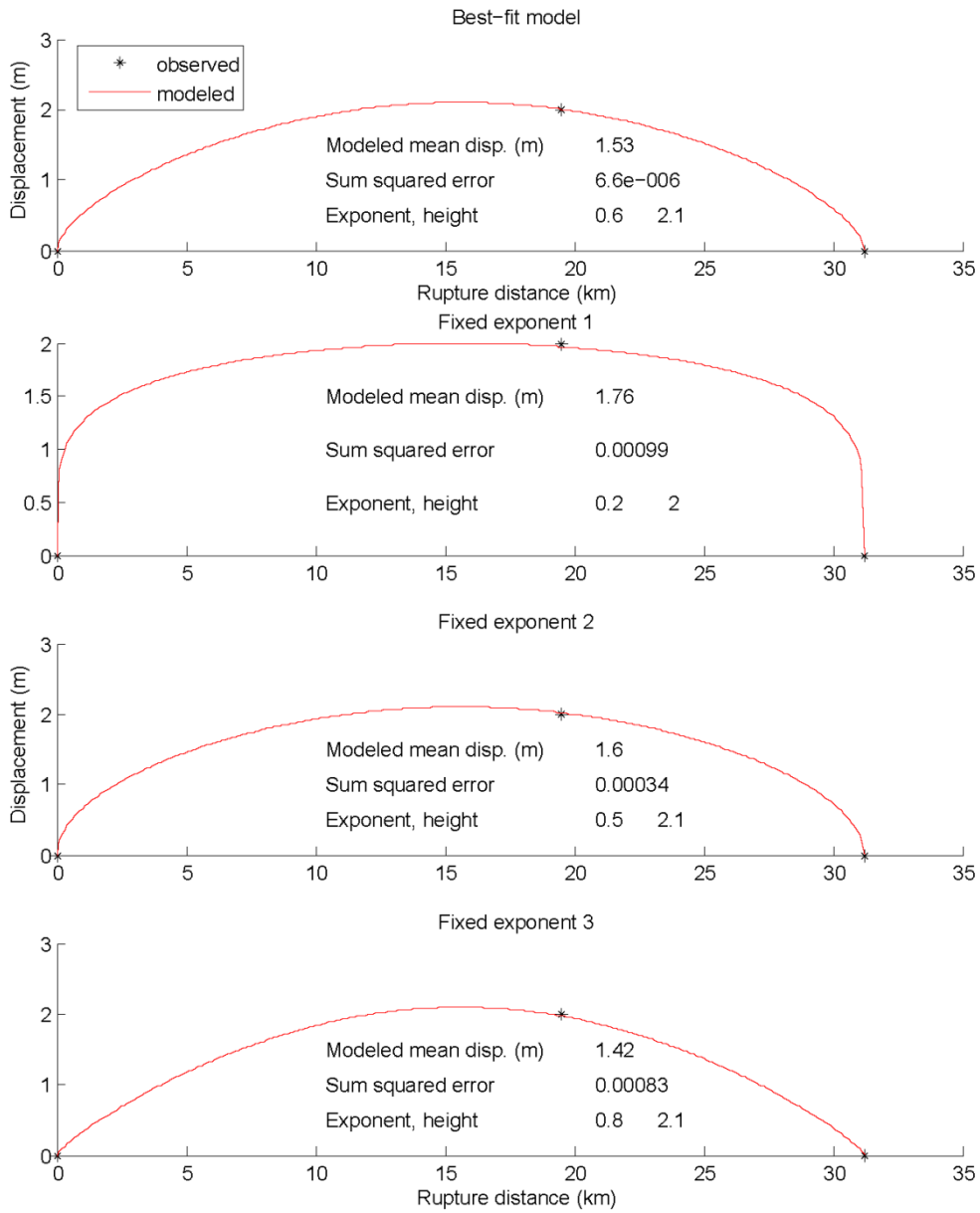

Figure C-4. Analytical displacement curves for the SO segment P2 rupture.

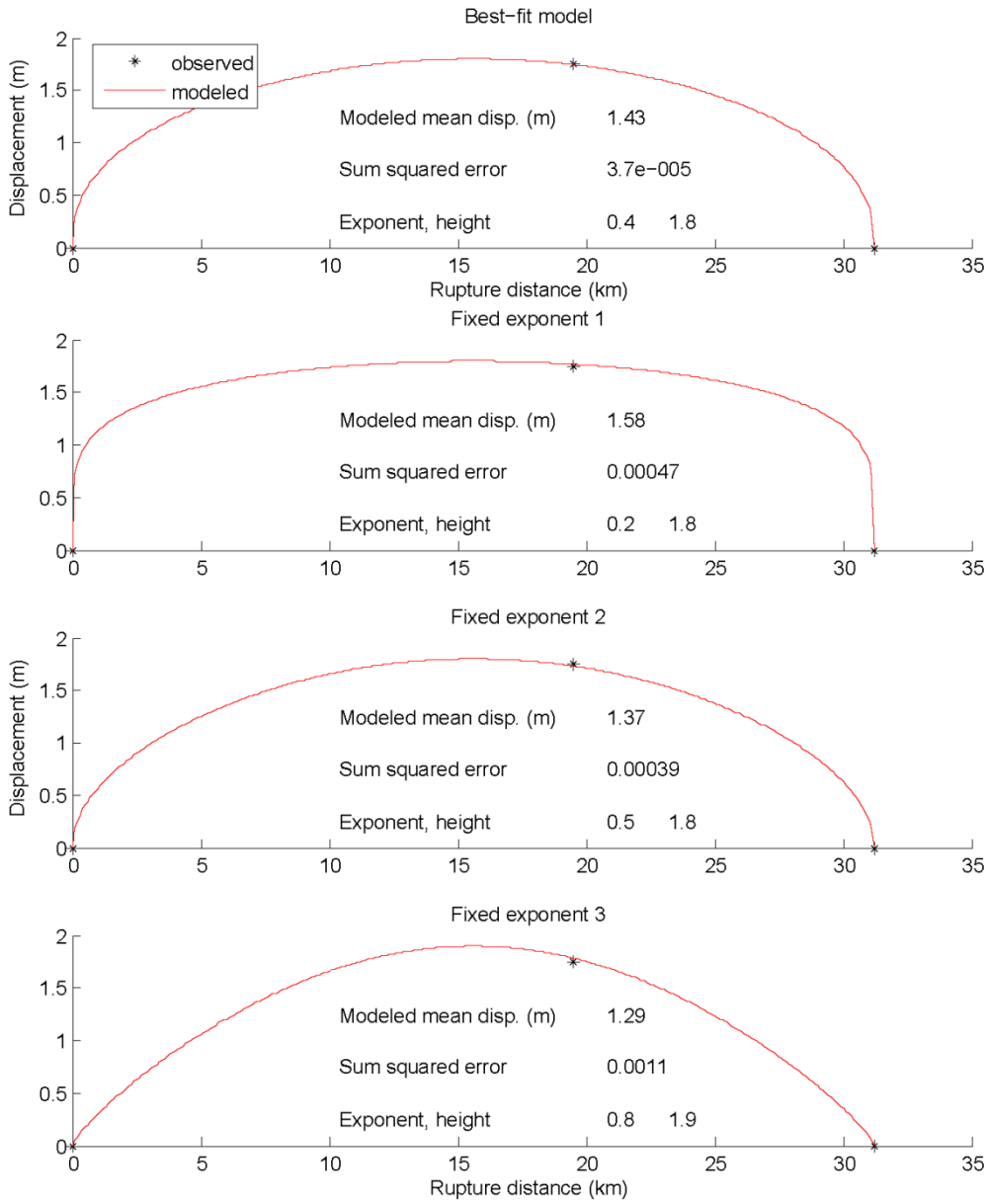

Figure C-5. Analytical displacement curves for the SO segment P3 rupture.

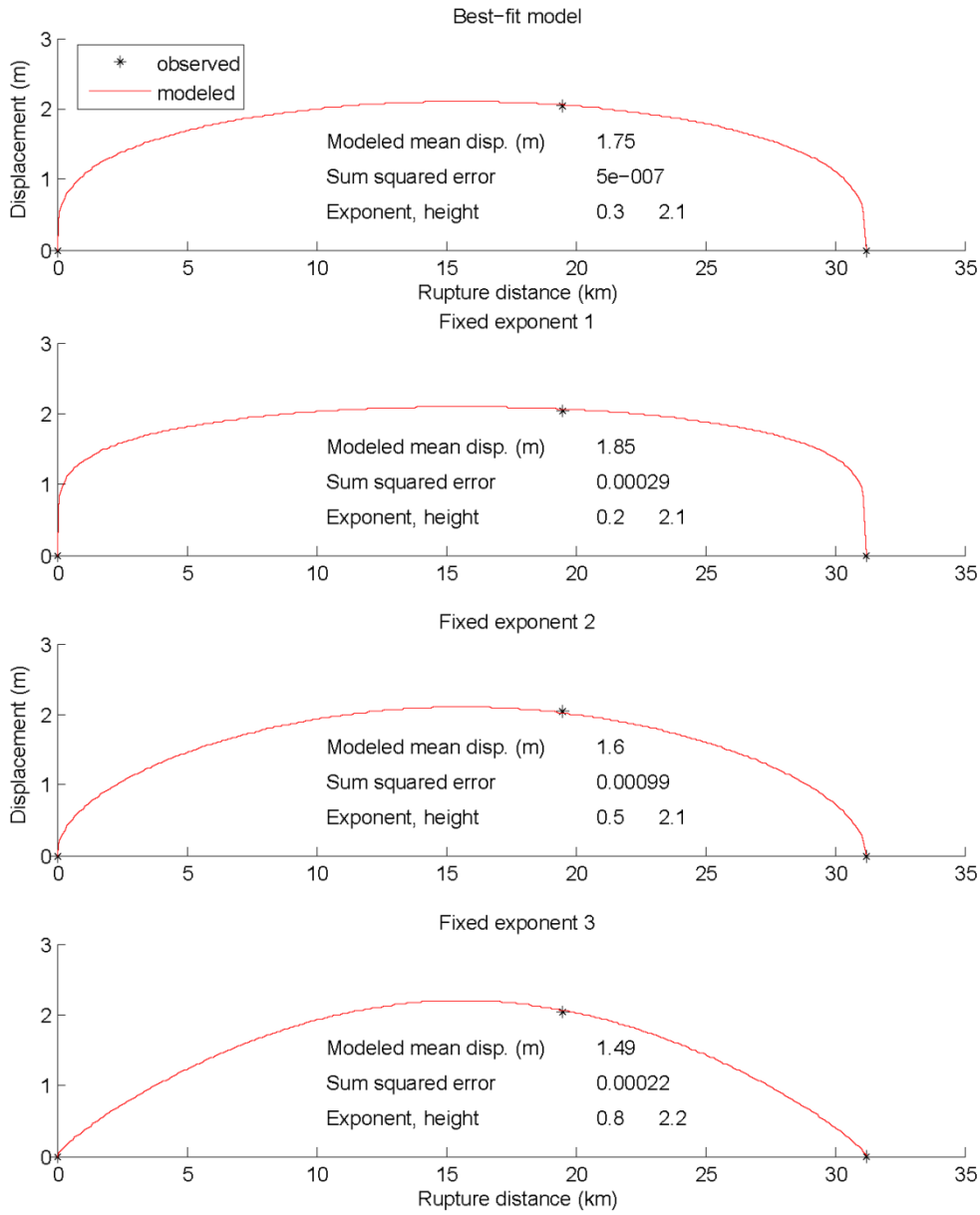

Figure C-6. Analytical displacement curves for the SO segment P4 rupture.

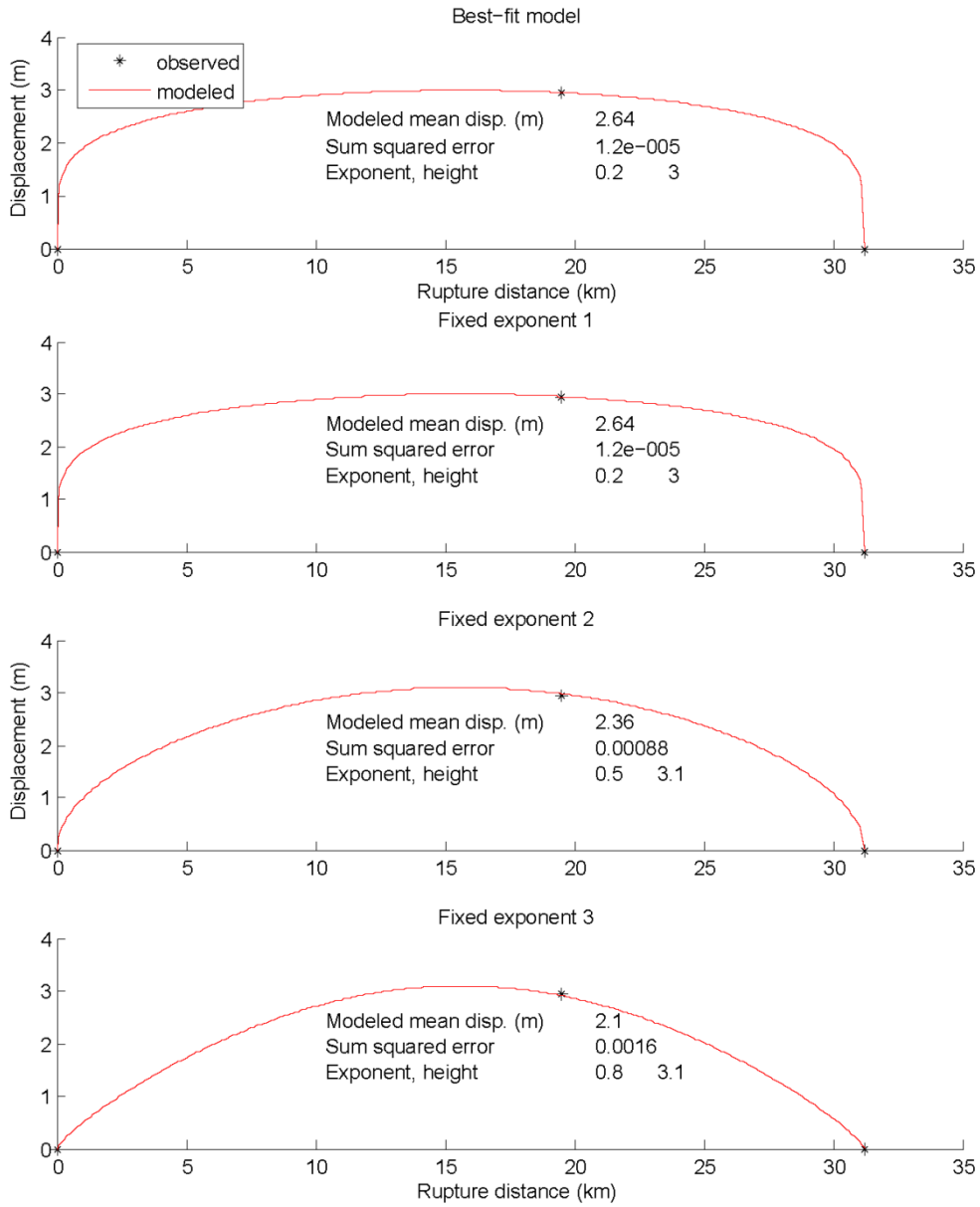

Figure C-7. Analytical displacement curves for the SO segment P5 rupture.

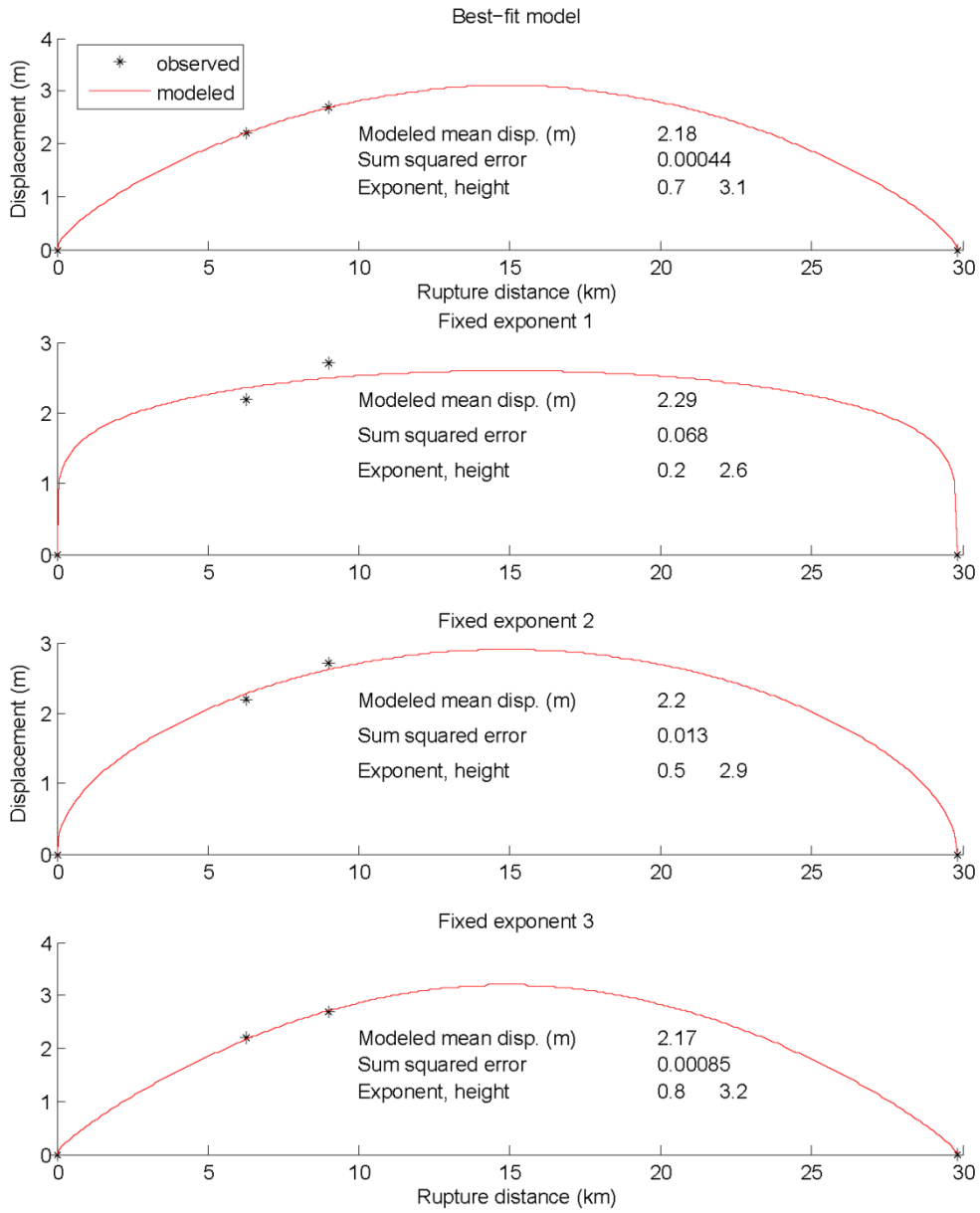

Figure C-8. Analytical displacement curves for the NO segment P1 rupture.

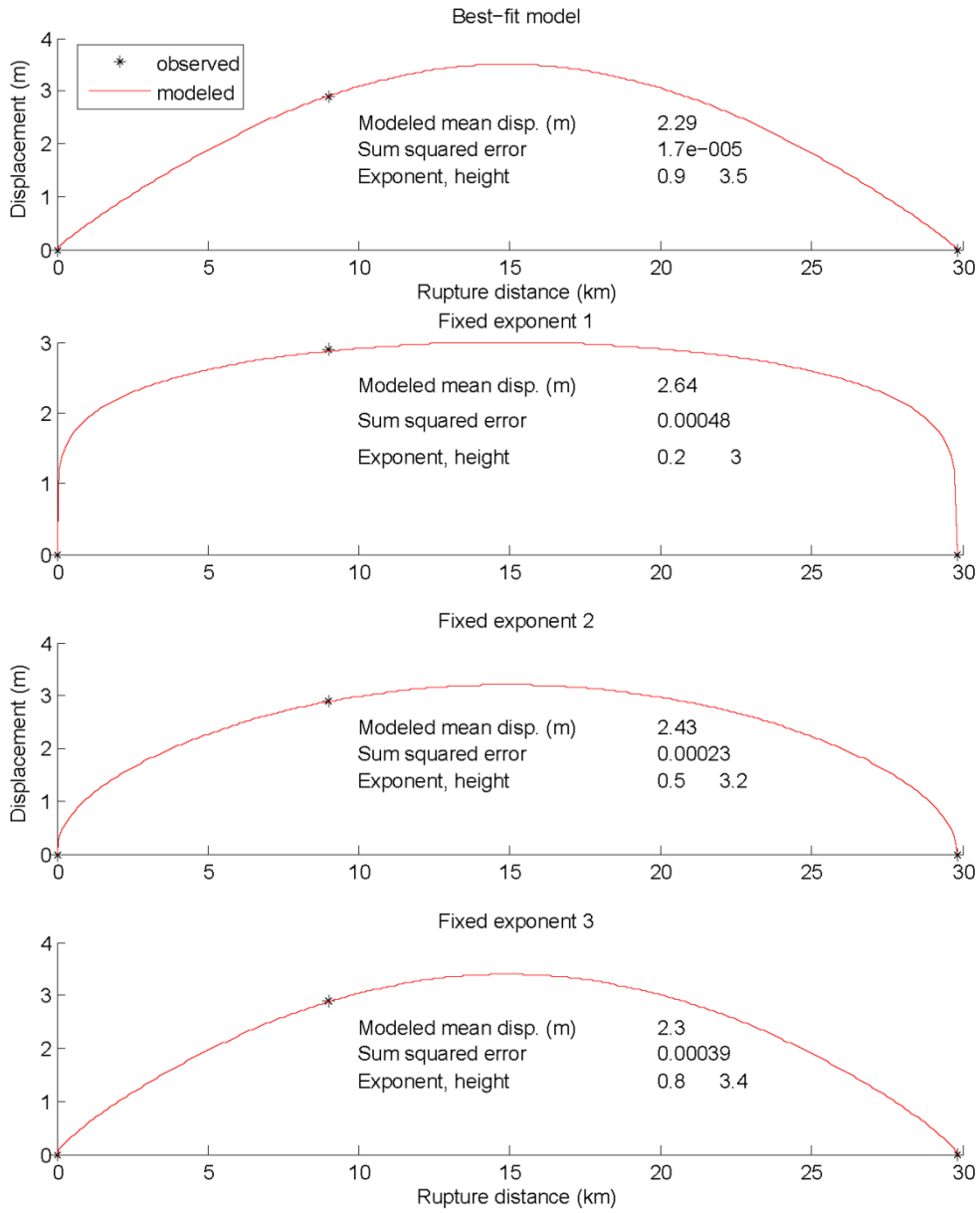

Figure C-9. Analytical displacement curves for the NO segment P2 rupture.

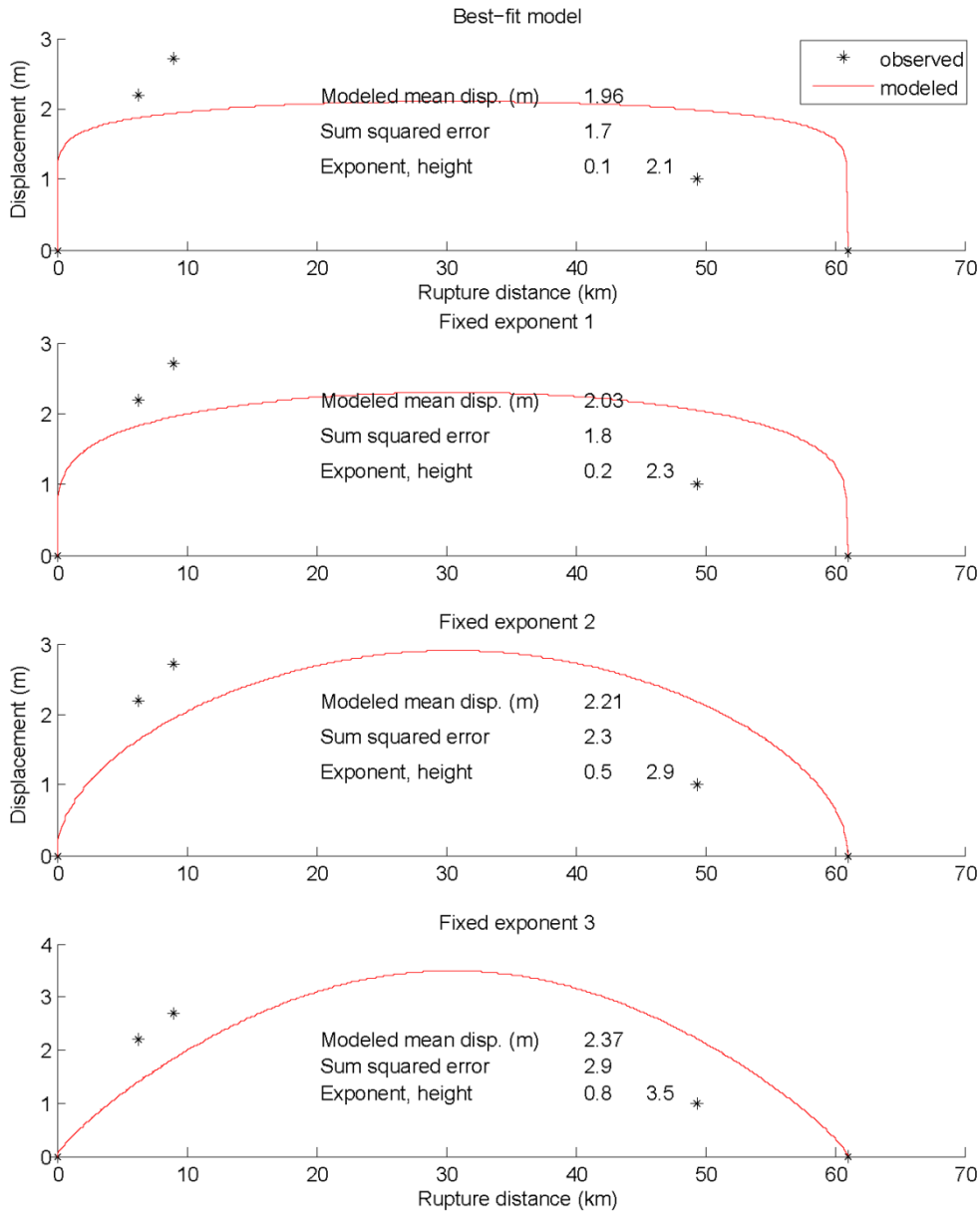

Figure C-10. Analytical displacement curves for the SO+NO segments P1 rupture.

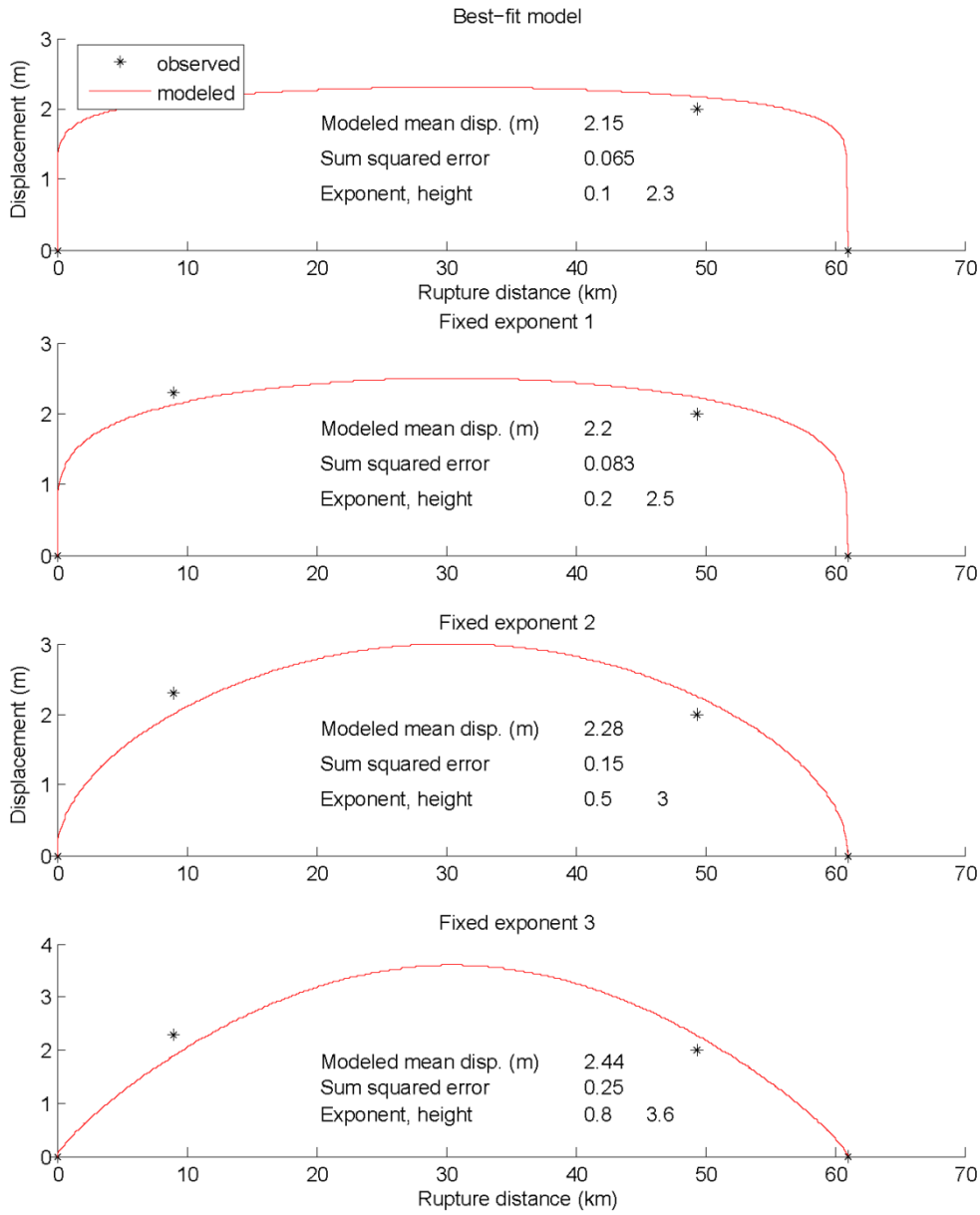

Figure C11. Analytical displacement curves for the SO+NO segment P2 rupture.

APPENDIX D

OTHER FAULT PARAMETER DATABASE

By

William R. Lund and Susan Olig

Table D-1. Parameters for Other Wasatch Front Faults

Fault Name	Rupture Model[1]	Probability of Activity[2]	Fault Category[3]	SRL (km)[4]	Dip Degrees)[5]	Seismogenic Depth (km)[6]	M_{char}[7]	Vertical Slip Rate (mm/yr)	Recurrence Interval (yr)	Comments
Bear River fault zone (Holocene)	Independent (1.0)	1.0	C	35	50±15	15±3 (E)	6.96	—	1000 (0.2) 2300 (0.6)[8] 3500 (0.2)	Detailed trenching and mapping by West (1994) revealed evidence for two large, late Holocene surface-faulting earthquakes on this apparently geologically young normal fault with no associated range front. This west-dipping fault may merge into a ramp of the Laramide-age Darby-Hogsback thrust fault at a depth of about 5-7 km (West, 1994). There is no evidence, at this time, that the fault zone has discrete rupture segments.
Carrington fault (Latest Quaternary)	Independent (1.0)	1.0	C	~30[9]	50 ± 15	15 ± 3 (W)	6.89	—	1800 (0.2)[10] 4200 (0.6) 6600 (0.2)	Dinter and Pechmann (2005) first identified the Carrington fault based on displacements observed in high-resolution seismic reflection profiles in the Great Salt Lake. The northeast-striking, ~30-km-long, down-to-the-northwest normal fault, which is northwest of Carrington Island, is clearly visible on a recent bathymetry map of Great Salt Lake (Baskin and Allen, 2005). This scarp is as high as 1.5 m, and likely has experienced multiple Holocene surface-faulting events, similar to the Antelope and Fremont Island segments of the Great Salt Lake fault zone. However, earthquake times remain unconstrained (D. Dinter, University of Utah, written communication, 2010). Based on the apparent similarities of the lakebed scarps, we assigned a recurrence interval distribution similar to the Antelope Island segment of the Great Salt Lake fault zone.
Crater Bench faults and Drum Mountains fault zone (Latest Quaternary and Holocene)	Linked (1.0)	0.5	C	Drum Mountains fault zone - 52 Crater Bench faults - 16 The two fault zones completely overlap	50 ± 15	15 ± 3 (W)	7.13	0.01 (0.2) 0.04 (0.6) 0.2 (0.02)	—	Comments from Tony Crone (U.S. Geological Survey [USGS]): "In the absence of better data, I'd favor leaving the linked Drum Mountains/Crater Bench fault zone in their current low slip rate category (<0.2 mm/yr) for two reasons. First our knowledge of the actual net slip across the entire complex zone is imperfect. The net slip could actually be very small. With current Global Positioning System technology we have an opportunity to efficiently and

Fault Name	Rupture Model[1]	Probability of Activity[2]	Fault Category[3]	SRL (km)[4]	Dip Degrees)[5]	Seismogenic Depth (km)[6]	M_{char}[7]	Vertical Slip Rate (mm/yr)	Recurrence Interval (yr)	Comments
										accurately measure profiles several kilometers long; so we could obtain the net slip. However, this work hasn't been done yet, so we don't have a basis for saying the slip rate across the entire zone should be higher. Second, I'm not totally convinced about the seismogenic potential of the Drum Mountains/Crater Bench faults. The complex, widely distributed zone of scarps is unusual for tectonic faults, and the scarps are spread out a fair distance east of the Drum Mountains range front, which lacks the morphology of a classic active range front. A possible issue is the role of subsurface evaporite deposits in forming the Drum Mountain/Crater Bench scarps. Deep wells in the region report [thick accumulations of] subsurface salt and gypsum. Considering the complex pattern of the scarps and the possible presence of significant amounts of subsurface evaporites, the possibility that the Drum Mountain/Crater Bench scarps could be halokinetic features related to salt/evaporite movement cannot be ruled out. If this is the case, then they would not be seismogenic, and would not be a factor in a seismic-hazard assessment. I think that this possibility needs to be considered carefully when assigning some level of seismic hazard to these faults." There is also a possible connection of these two fault zones with the Sevier detachment fault at shallow depth (3-5 km).
Crawford Mountains (west side) fault (Late Quaternary)	Independent (1.0)	1.0	C	25	50 ± 15	15 ± 3 (W)	6.81	0.01 (0.3) 0.02 (0.4) 0.04 (0.3)	—	Although Everitt (1995) included scarps on alluvium south of the Bear River, Black and others (2003) included those with the Saleratus Creek fault (not included in this database) to the south, and we follow that convention here. Further study is required to resolve the relation between the Crawford Mountains (west side) and Saleratus Creek faults. Due to a lack of data, a slip-rate distribution similar to the Morgan fault (Lund [2005] see below) was assigned to the Crawford Mountains fault.
Curlew Valley faults (Latest Quaternary)	Independent (1.0)	1.0	C	20	50 ± 15	15 ± 3 (W)	6.71	0.1 (0.4)[11] 0.3 (0.4) 0.8 (0.2)	—	These post-Bonneville northeast-trending en echelon faults mapped along the eastern margin of Curlew Valley by Allmendinger (1983) are

Fault Name	Rupture Model[1]	Probability of Activity[2]	Fault Category[3]	SRL (km)[4]	Dip Degrees)[5]	Seismogenic Depth (km)[6]	M_{char}[7]	Vertical Slip Rate (mm/yr)	Recurrence Interval (yr)	Comments
										the southern portion of the much longer East Side of Arbon Valley fault of Witkind (1975), which included faults with pre-Quaternary movement to the north. Cress (1983) observed fault scarps as high as 24 m on undifferentiated lacustrine sediments, which may be associated with the Little Valley lake cycle (> 130 ka) or the Bonneville lake cycle (12 to 30 ka). The maximum slip rate assumes 24 m of vertical displacement since 30 ka, whereas the other rates assume 20 m since 60 and 150 ka (20 m accounts for some likely antithetic faulting and backtilting).
East Cache fault zone (Southern segment includes the James Peak and Broadmouth Canyon faults)	Unsegmented (0.2) Segmented (0.8)	1.0	B	Unsegmented – 86[12] (floating rupture length = 43.5)	50 ± 15	15 ± 3 (E)	7.15	0.04 (0.2)[13] 0.2 (0.6) 0.4 (0.2)	—	Paleoseismic trench data are only available for the Central segment (McCalpin, 1994) and the James Peak fault (Nelson and Sullivan, 1992), which at the recommendation of the Utah Quaternary Fault Parameters Working Group (UQFPWG; Lund, 2005) is included as part of the Southern segment along with the Broadmouth Canyon fault.
				Northern segment - 41 (Quaternary)			7.12	0.04 (0.3)[14] 0.1 (0.4) 0.2 (0.3)	—	
				Central segment - 17 (Holocene)			6.71	**0.8** 0.04 (0.2)[15] 0.2 (0.6) 0.4 (0.2)	**0.2** 4000 (0.3)[15] 10,000 (0.4) 15,000 (0.3)	
				Southern segment - 29 (Late Quaternary)			6.96	**0.8** 0.01 (0.3)[16] 0.03 (0.4) 0.07 (0.3)	**0.2** 10,000 (0.3)[16] 50,000 (0.4) 100,000 (0.3)	
East Dayton - Oxford faults (Late Quaternary)	Independent (1.0)	1.0	C	23	50 ± 15	15 ± 3 (E)	6.77	0.01 (0.3)[17] 0.05 (0.6) 0.1 (0.1)	—	This north-trending, down-to-east, normal fault bounds the eastern margin of the Bannock Range, and is considered by some to be a northward extension of the West Cache fault zone, which is known to displace Quaternary-age Lake Bonneville sediments farther south in Utah. There is no documented evidence of late Quaternary fault scarps. Mapping by Carney *et al*. (2002) shows the trace of the fault as entirely covered, but adjacent to the abrupt mountain front termination of various Quaternary deposits suggests, but does not prove, Quaternary deformation.
Eastern Bear Lake fault	Segmented (0.7)	1.0	B	Unsegmented - 78 (floating	50 ± 15	15 ± 3 (E)	7.10	0.2 (0.2) 0.6 (0.6)	—	Central segment and unsegmented scenario assigned the same slip-rate distribution as the

Fault Name	Rupture Model[1]	Probability of Activity[2]	Fault Category[3]	SRL (km)[4]	Dip Degrees)[5]	Seismogenic Depth (km)[6]	M_{char}[7]	Vertical Slip Rate (mm/yr)	Recurrence Interval (yr)	Comments
Eastern Bear Lake fault	Unsegmented (0.3)	1.0	B	rupture length = 39)	50 ± 15	15 ± 3 (E)	7.10	1.6 (0.2)	—	Southern segment (Lund, 2005) due to the presence of large scarps on likely Holocene and latest Pleistocene deposits. The Northern segment lacks compelling evidence for latest Quaternary movement and consequently is assigned a lower slip rate (one half the UQFPWG's Southern segment consensus value).
				Northern segment - 19 (Middle - Late Quaternary)			6.76	0.1 (0.2) 0.3 (0.6) 0.8 (0.2)	—	
				Central segment - 24 (Latest Quaternary)			6.87	0.2 (0.2) 0.6 (0.6) 1.6 (0.2)	—	
				Southern segment - 35 (Holocene)			7.05	**0.8** 0.2 (0.2)[15] 0.6 (0.6) 1.6 (0.2)	**0.2** 3000 (0.2)[15] 8000 (0.6) 15,000 (0.2)	
Faults along the western edge of Scipio Valley and eastern base of the Pavant Range (from south to north includes the Red Canyon fault scarps, Maple Grove faults, Pavant Range fault, Scipio fault zone, and Scipio Valley faults). (Latest Quaternary to Late Quaternary)	Linked (1.0)	1.0	C	Total length - 45	50 ± 15	15 ± 3 (W)	7.06	0.02 (0.2)[18] 0.1 (0.6) 0.4 (0.2)	—	Several north-striking, individually short faults along the north side of the Pavant Range and the western side of Scipio Valley that are in close alignment and show evidence for late Quaternary surface faulting (Anderson and Bucknam, 1979; Bucknam and Anderson, 1979). Therefore, we link these faults to form a single unsegmented fault zone. Scarps vary from 2 to 11 m on unconsolidated deposits, but ages are not well constrained. The preferred slip rate assumes 3 to 4 m of slip since 30 ka, whereas the minimum slip rate assumes 2 m of slip since 130 ka, and the maximum rate assumes 11 m of slip since 30 ka.
Gunnison fault (Latest Quaternary)	Independent (1.0)	0.8	C	42	50 ± 15	15 ± 3 (W)	7.04	0.02 (0.2) 0.1 (0.6) 0.4 (0.2)	—	Little is known about rates of activity, but scarps and location are similar to the faults along the north side of the Pavant Range and the western side of Scipio Valley. Therefore a slip-rate distribution similar to the Scipio Valley faults was assigned to this fault. This structure may be related to salt tectonics and therefore was given a reduced probability of activity.
Hansel Valley fault (includes Hansel Mountains [east side] faults and Hansel Valley [valley floor] faults) (Historic - Mid- to	Linked (1.0) Independent (0.6) Coseismic (0.4)	1.0	AFP	30	50 ± 15	Antithetic fault truncated against the North Promontory fault.	6.49	0.06 (0.2)[15] 0.1 (0.6) 0.2 (0.2)	—	Both the number and timing of surface-faulting earthquakes on the Hansel Valley fault(s) are unknown. The fault exhibits an irregular pattern of surface faulting with inter-event intervals ranging from possibly as little as 1-2 kyr to more than 30 kyr, indicating that earthquake recurrence has been highly variable through

Fault Name	Rupture Model[1]	Probability of Activity[2]	Fault Category[3]	SRL (km)[4]	Dip Degrees)[5]	Seismogenic Depth (km)[6]	M_{char}[7]	Vertical Slip Rate (mm/yr)	Recurrence Interval (yr)	Comments
Late Quaternary)										time (McCalpin and others, 1992). The 1934 historical surface-faulting earthquake may have been a strike-slip event on a different, unrecognized fault, which implies that the historical scarps and lineaments are not primary tectonic features
Joes Valley fault zone (Latest Quaternary) (combined East, West, and Intragraben faults)	Linked (1.0) Shallow (4 km) (0.6) Deeply penetrating (0.4)	Shallow (0.4) Deep (1.0)	AFP (shallow) C (deep)	37 (Length restricted to that part of fault that shows Latest Quaternary < 15 ka displacement - overall length 84 km)	70 ± 15[19]	Available geologic and geophysical evidence is inconclusive regarding whether the Joes Valley faults penetrate to seismogenic depth (15±3 km; deep) or become listric and sole into a detachment fault at a depth of about 4 km (shallow).	6.67	—	5000 (0.2)[15] 10,000 (0.6) 50,000 (0.2)	As per the UQFPWG (Lund, 2005), this zone of faults is linked into a single source due to the geometry of the individual faults and their proximity to each other. A low probability of activity was assigned to the shallow-fault scenario based on arguments that these faults may not be seismogenic structures as summarized in the "Discussion" section of p. 61 in Lund (2005). These arguments include the lack of significant net displacement across the entire Joes Valley graben (Foley *et al*., 1986), and the fault zone's spatial association with the crest of the Wasatch Plateau monocline, suggesting that the faults may be a keystone graben that is not seismogenic. Additionally, recent interpretation of seismic lines suggests that offsets do not extend below a few kilometers depth (Coogan, 2008).
Little Valley faults (Latest Quaternary)	Independent (1.0)	1.0	C	20	50 ± 15	15 ± 3 (W)	6.72	0.02 (0.2) 0.1 (0.6) 0.4 (0.2)	—	Little is known about rates of activity, but scarps and location are similar to the faults along the western side of Scipio Valley. Therefore a slip-rate distribution similar to the Scipio Valley faults was assigned to the Little Valley faults.
Main Canyon fault (formerly East of East Canyon fault) (Holocene)	Independent (1.0)	1.0	C	26	50 ± 15	15 ± 3 (E)	6.83	0.01(0.3)[20] 0.02 (0.4) 0.04 (0.3)	—	Although identified and mapped by Bryant (1990) and Coogan and King (2001), this fault is not included in Black and others (2003), and was only recently included in the *Quaternary Fault and Fold Database of the United States* (USGS, 2013). The Main Canyon fault bounds the east side of East Canyon Valley and the East Canyon fault bounds the west side. A previous study (Sullivan *et al*., 1988) considered the East Canyon fault to be the more active and dominant fault primarily based on thicker late Cenozoic deposits along the west side of the

Fault Name	Rupture Model[1]	Probability of Activity[2]	Fault Category[3]	SRL (km)[4]	Dip Degrees)[5]	Seismogenic Depth (km)[6]	M_{char}[7]	Vertical Slip Rate (mm/yr)	Recurrence Interval (yr)	Comments
										basin, and the geomorphic expression of the bedrock scarp. However, stratigraphic and structural relations, and radiocarbon and luminescence ages provide evidence for two surface-faulting earthquakes during the past 30 to 38 kyr on the Main Canyon fault (Piety *et al*., 2010). The most recent event likely occurred shortly before 5 to 6 ka, but could be as old as 12 to 15 ka. There was also limited evidence for an unknown number of surface-faulting earthquakes older than 38 ka. Differences in stratigraphic units on opposite sides of the fault in the trench prevented the determination of either the amount of offset or slip rate of the fault.
Morgan fault (includes linked northern, central, and southern sections) (Holocene - Late Quaternary)	Linked (1.0)	1.0	C	17	50 ± 15	15 ± 3 (E)	6.64	**0.8** 0.01(0.3)[15] 0.02 (0.4) 0.04 (0.3)	**0.2** 25,000 (0.5)[15] 100,000 (0.5)	The northern, central, and southern sections as defined by Sullivan and Nelson (1992) are grouped together based on: (1) short section lengths; (2) along-strike patterns of topographic profiles; and (3) similar geomorphic expression (Sullivan and others, 1988).
North Promontory fault (Holocene - Latest Pleistocene)	Independent (1.0)	1.0	C	26	50±15	15±3 (W)	6.83	0.1 (0.3)[15] 0.2 (0.4) 0.5 (0.3)	—	Range-front fault bounding eastern Hansel Valley showing evidence for Holocene movement and multiple late Pleistocene events (McCalpin, 1985; McCalpin and others, 1992).
Porcupine Mountain faults (Late Quaternary - Quaternary)	Independent (1.0)	1.0	C	35	50 ± 15	15 ± 3 (E)	6.96	0.01 (0.3)[20] 0.02 (0.4) 0.04 (0.3)	—	This fault offsets apparently young (Holocene-latest Pleistocene?) alluvial fans (Jon King, Utah Geological Survey, written communication, 2000). Due to a lack of data, a slip-rate distribution similar to the Morgan fault is assigned to this fault.
Rock Creek fault (Holocene)	Independent (1.0)	1.0	C	41	50 ± 15	15 ± 3 (E)	7.02	**0.8** 0.2 (0.1) 0.6 (0.6) 1.0 (0.3)	**0.2** 600 [21] (0.1) 4000 (0.6) 10,000 (0.3)	The Rock Creek fault is a high-angle, down-to-west normal fault within the Tunp Range; it may sole into the Laramide-age Tunp thrust fault. Most of the fault's length is characterized by scarps on steep colluvial slopes. McCalpin (1993) stated that some scarps are as much as 25 m high. He excavated one trench across the fault. The most recent event is bracketed by radiocarbon ages of 3280 ± 70 and 3880 ± 60 ^{14}C yr BP (McCalpin and Warren, 1992), or roughly 3.6 ± 0.3 ka, whereas the penultimate (older) event is about 4.6 ± 0.2 ka. This equates to a permissible recurrence interval of about 0.6-1.5 kyr. However, the late Quaternary

Fault Name	Rupture Model[1]	Probability of Activity[2]	Fault Category[3]	SRL (km)[4]	Dip Degrees)[5]	Seismogenic Depth (km)[6]	M_{char}[7]	Vertical Slip Rate (mm/yr)	Recurrence Interval (yr)	Comments
										recurrence interval must be quite variable: elapsed time since the last surface-faulting earthquake has been about 3.6 ± 0.3 kyr, and at least 10 kyr before the penultimate event (15 ka is the inferred time of deposition of older faulted deposits at the trench site).
Skull Valley (mid valley) faults (Latest Quaternary)	Independent (1.0)	0.9	C	34	50 ± 15	15 ± 3 (W)	6.91	0.05 (0.2) 0.3 (0.6) 0.5 (0.2)	—	Includes only that portion of the Skull Valley fault referred to in the Quaternary Fault and Fold Database as "northwest-trending normal faults in southern Skull Valley," and identified as Holocene-latest Pleistocene in age. A northeast-trending normal fault in northern Skull Valley of questionable Quaternary age is now identified in the Quaternary Fault and Fold Database as part of the Skull Valley fault system, but was formerly referred to as the "Springline fault." Because of its age and general lack of surface expression, that portion of the Skull Valley fault is not considered here. The activity of these faults may be dependent on the Stansbury fault; therefore, a lower probability of activity was assigned, although Geomatrix Consultants (1999) found definite evidence for repeated late Pleistocene offsets. Slip-rate distribution is based on late Pleistocene vertical slip rates of 0.3 (± 0.1) and 0.05 (± 0.01) mm/yr for the East and West faults, respectively (Geomatrix Consultants, 1999).

Fault Name	Rupture Model[1]	Probability of Activity[2]	Fault Category[3]	SRL (km)[4]	Dip Degrees)[5]	Seismogenic Depth (km)[6]	M_{char}[7]	Vertical Slip Rate (mm/yr)	Recurrence Interval (yr)	Comments
Snow Lake Graben[21] (Latest Quaternary)	Linked (1.0) Deeply penetrating (0.4) Shallow (4 km) (0.6)	0.4 (shallow) 1.0 (deep)	AFP (shallow) C (deep)	26	70 ± 15	Available geologic and geophysical evidence is inconclusive regarding whether the Snow Lake graben faults penetrates to seismogenic depth (15 ± 3 km; deep) or become listric and sole into a detachment fault at a depth of about 4 km (shallow).	6.83	—	5000 yrs (0.2) 10,000 yrs (0.4) 50,000 yrs (0.4)	These prominent north-south striking fault scarps in bedrock trend along the crest of the Wasatch Plateau and form a narrow graben similar to the Joes Valley fault zone. However, far less is known about these poorly studied faults, so we assumed rates of activity similar to the Joes Valley fault zone, but give heavier weight to longer recurrence intervals based on less extension and less prominent scarps. A low probability of activity was assigned to the shallow-fault scenario based on the argument that like the Joes Valley fault zone, these faults may not be seismogenic structures. Evidence for a nonseismogenic origin includes the lack of significant net displacement across the graben, and the fault zone's spatial association with the crest of the Wasatch Plateau monocline, suggesting that the faults may form a keystone graben that is not seismogenic.
Stansbury fault	Unsegmented (0.3)	1.0	B	70 (Straight line distance from the north end Geomatrix Section A to the south end of Section D) (floating rupture length = 35)	50±15	15±3 (W)	7.05	0.07 (0.2)[18] 0.4 (0.6) 1.0 (0.2)	—	Segmentation model modified from Helm (1995) and Geomatrix Consultants (1999). Maximum rupture lengths measured on plate 6 of Geomatrix Consultants (1999). Slip-rate distribution based on long-term (Miocene) vertical slip rates of 0.07 (0.02) mm/yr (Helm, 1995), late Pleistocene vertical slip rates of 0.4 (0.1) mm/yr (Geomatrix Consultants, 1999), and comparison with the Oquirrh and Great Salt Lake fault zones for the maximum slip value. The surface trace of the Stansbury fault is simple south of Pass Canyon, but complex to the north, suggesting the fault may consist of two independent sections. A down-to-the-south cross-fault at Pass Canyon forms the boundary between the sections (Helm, 1994). In the south, a single fault strand consisting of a main fault and a subsidiary antithetic fault cuts Quaternary alluvial fans and forms a narrow (about 20-m-wide) graben along most of the fault trace (Helm, 1994). North of Pass Canyon, the trace is a complex fault zone consisting of multiple synthetic and antithetic fault traces showing evidence of Quaternary movement. Based on
	Segmented (0.7) Northern Segment (Section A of Geomatrix Consultants, 1999) (Latest Quaternary)			24			6.87	0.07 (0.2)[18] 0.4 (0.6) 1.0 (0.2)		
	Central Segment (Sections B and C of Geomatrix			33			6.96	0.07 (0.2)[18] 0.4 (0.6) 1.0 (0.2)		

Fault Name	Rupture Model[1]	Probability of Activity[2]	Fault Category[3]	SRL (km)[4]	Dip Degrees)[5]	Seismogenic Depth (km)[6]	M_{char}[7]	Vertical Slip Rate (mm/yr)	Recurrence Interval (yr)	Comments
	Consultants, 1999) (Latest Quaternary)			33			6.96	0.07 (0.2)[18] 0.4 (0.6) 1.0 (0.2)		scarp morphology and observation of stream knickpoints a short distance from the fault trace, Everitt and Kaliser (1980) concluded that the most recent movement was during the Holocene. Helm (1994) reports maximum scarp angle versus scarp height plots suggest the Stansbury fault is generally older than the highstand of Lake Bonneville. However, Geomatrix Consultants, Inc. (1999) states that the southern section of the fault is inferred to have moved in a single event during the early to middle Holocene.
	Southern Segment (Section D of Geomatrix Consultants, 1999) (Quaternary)			17			6.71	0.07 (0.2)[18] 0.4 (0.6) 1.0 (0.2)		
Stinking Springs fault (Late Quaternary)	Independent (1.0)	1.0	C	10	50±15	15±3 (E)	6.41	0.03 (0.2)[23] 0.1 (0.6) 0.3 (0.2)	—	Slip-rate data are lacking for this poorly understood fault as much of the central portion lies underwater, so we assumed a slip-rate distribution similar to the Strawberry fault (Lund, 2005) based on a similar geomorphic expression.
Strawberry fault (Holocene)	Independent (1.0)	1.0	C	32	50±15	15±3 (E)	6.92	**0.5** 0.03 (0.2)[15] 0.1 (0.6) 0.3 (0.2)	**0.5** 5000 (0.2)[15] 15,000 (0.6) 25,000 (0.2)	Maximum rupture length includes the southernmost suspected Quaternary fault trace of Hecker (1993). Trenches across a subsidiary fault exposed evidence for two to three earthquakes displacing alluvial-fan deposits estimated to be 15 to 30 ka based on soil development (Nelson and Martin, 1982; Nelson and Van Arsdale, 1986). Note that URS Corporation (unpublished data) assigned slip-rate values of 0.04 (0.2), 0.2 (0.6), 0.5 (0.2) based on data in Nelson and Van Arsdale (1986) because they considered the UQFPWG's distribution to underestimate the large uncertainties of the limited paleoseismic data obtained from a subsidiary fault (i.e., earthquake timing constraints and estimates of total slip are lacking for the main fault).
Utah Lake faults[23] (Latest Quaternary)	Independent (0.5) Coseismic (0.5)	1.0	AFP	31	50±15	Antithetic fault zone truncated against the Provo segment of the WFZ.	6.79	0.1 (0.2) 0.4 (0.6) 0.6 (0.2)	—	The Utah Lake faults are a complex system of east and west dipping normal faults beneath Utah Lake. There are no known subaerial exposures of this fault zone. Recent (2010) high-quality seismic reflection profiles suggest that as many as eight surface-rupturing, north-striking faults displace very young lake sediments 1 to 3 meters (David Dinter, University of Utah, written communication, 2011). Because these faults occupy a similar

Fault Name	Rupture Model[1]	Probability of Activity[2]	Fault Category[3]	SRL (km)[4]	Dip Degrees)[5]	Seismogenic Depth (km)[6]	M_{char}[7]	Vertical Slip Rate (mm/yr)	Recurrence Interval (yr)	Comments
										position in relation to the Provo segment of the WFZ as does the West Valley fault zone (WVFZ) to the Salt Lake City segment of the WFZ, and because the Utah Geological Survey is in the process of developing new paleoseismic data for the WVFZ, we use the current best available information for the WVFZ as an analog for the Utah Lake faults. This assumption may change as more data become available for the Utah Lake faults. Dinter (written communication, 2011) estimates that there have been one or two surface-faulting earthquakes on the Utah Lake faults in the past 1 kyr, but he lacks the data necessary to estimate a slip rate
West Cache fault zone (Holocene)	Unsegmented (0.3) Segmented (0.7)	1.0	B	Unsegmented - 59 (floating rupture length = 32.5)	50±15	15±3 (E)	7.01	0.1 (0.2)[25] 0.4 (0.6) 0.7 (0.2)	—	Seismic reflection data indicate that the West Cache fault zone has significantly less cumulative displacement than the East Cache fault zone (Evans, 1991; Evans and Oaks, 1996), suggesting that the former is antithetic to the latter (Sullivan and others, 1988). However, subsequent detailed mapping and trenching studies have shown that the latest Quaternary behavior of the two faults is different, implying generally independent behavior (Black and others, 2000). Therefore, a probability of activity of 1.0 is assigned to the West Cache fault zone. Fault trace geometry, lengths, and segmentation model are after Black and others. (2003).
				Clarkston segment - 21			6.81	0.1 (0.2)[15] 0.4 (0.6) 0.7 (0.2)	—	
				Junction Hills segment - 24			6.87	0.05 (0.2)[15] 0.1(0.6) 0.2 (0.2)	—	
				Wellsville segment - 20			6.79	0.05 (0.2)[15] 0.1 (0.6) 0.2 (0.2)	—	
West Valley fault zone (Holocene)	Independent (0.25) Coseismic (0.75)	1.0	AFP	Granger fault - 16 Taylorsville fault - 15	50±15	Antithetic fault truncated against the Salt Lake City segment of the WFZ.	6.34	0.1 (0.2)[15] 0.4 (0.6) 0.6 (0.2)	—	Due to their proximity and similar dip, we assume that the Granger and Taylorsville faults of the WVFZ merge at a shallow depth, and that the primary moment release occurs on the Granger fault as it appears to have the greatest cumulative displacement (Keaton *et al*., 1993). The WVFZ is antithetic to, and 3 to 13 km west of the Salt Lake City segment of the WFZ. We allowed for both independent and coseismic rupture of the WVFZ with the Salt Lake City segment based on trenching results by the UGS of the Granger fault. Current slip-rate distribution is based on data in Keaton *et al.* (1993) and Hylland *et al.* (2014) for a variety of time periods. A comprehensive trenching

Fault Name	Rupture Model[1]	Probability of Activity[2]	Fault Category[3]	SRL (km)[4]	Dip Degrees)[5]	Seismogenic Depth (km)[6]	M_{char}[7]	Vertical Slip Rate (mm/yr)	Recurrence Interval (yr)	Comments
										investigation has not been performed for the Taylorsville fault, although Solomon (1998) reported limited timing and displacement information for one earthquake identified in a consultant's trench.
Western Bear Lake fault (Holocene)	Independent (0.5)[26] Coseismic (0.5)	1.0	AFP	26	50±15	Antithetic fault truncated against the East Bear Lake fault.	6.51	0.1 (0.2) 0.5 (0.6) 0.8 (0.2)	—	Maximum rupture length based on total extent of scarps on unconsolidated sediments (McCalpin, 2003). Based on kinematic and geometric relations (Skeen, 1976; McCalpin, 1990; Evans, 1991) the rupture model for this fault includes the possibility that the Western Bear Lake fault ruptures coseismically with the Eastern Bear Lake fault and is not an independent seismic source. Untrenched antithetic faults make the 1.75 m maximum displacement (McCalpin, 2003) a poorly constrained estimate. Slip rates based on McCalpin (2003); however, slip on the Western Bear Lake fault is poorly constrained.

[1] Rupture models include independent, linked, segmented, coseismic (antithetic fault pairs), and deep or shallow penetrating for the Joes Valley fault zone and Snow Lake graben.

[2] Probability of activity is the likelihood that the fault is a seismogenic source capable of generating earthquakes within the modern stress field.

[3] Fault categories are: *A* - WFZ and Oquirrh-Great Salt Lake fault zone (not included in this table); *B* - segmented faults thought to behave in a manner similar to the Wasatch fault zone; *C* - unsegmented faults and short linked faults; *AFP* - antithetic fault pairs where the secondary fault is truncated by the primary (master) fault at relatively shallow depth.

[4] Measured straight line end-to-end as reported in the *Quaternary Fault and Fold Database of the United States* (USGS, 2013) unless noted otherwise. Discrepancies between unsegmented fault length and the sum of individual segment lengths is chiefly the result of overlapping segment boundaries or gaps and stepovers at segment boundaries.

[5] Range of crustal fault dips (50 ± 15 degrees) recommended by the Basin and Range Province Earthquake Working Group II (Lund, 2012) to the USGS, and adopted by the WGUEP for most normal faults in the Wasatch Front Region and weighted 35 (0.3), 50 (0.4), 65 (0.3). The exceptions are the Joes Valley fault zone and Snow Lake graben, which are assigned a dip of 70 ± 15 degrees and weighted 55 (0.3), 70 (0.4), 85 (0.3).

[6] Range of seismogenic depths (15 ± 3 km) adopted by the WGUEP for normal faults in the WGUEP study; weighted 12 (0.2), 15 (0.7), 18 (0.1) west of the WFZ and 12 km (0.1), 15 km (0.7), 18 (0.2) east of the WFZ.

[7] M_{char} is the characteristic magnitude for a rupture source, which assumes full rupture of the source and is computed from magnitude relations relating length, area, or average displacement to magnitude. The "Other" faults in the WGUEP model for the Wasatch Front region (Table 4.5-1) are either category *B*, *C*, or *AFP* faults (see section 3.5.2), the magnitude relations and weights used to determine M_{CHAR} for the "Other" faults are presented in Table 3.5-2.

[8] West (1994) identified two earthquakes on the Bear River fault zone at 4620 ± 690 and 2370 ± 1050 yr. BP with resulting single closed-seismic-cycle recurrence interval of 2250 ± 1260 (rounded to nearest decade). West calendar calibrated the earthquake ages, but did not correct for the mean resident time of the carbon in the bulk soil samples from which the ages were obtained, and therefore feels the ages may be too old by several hundred years.

[9] Jim Pechmann, University of Utah Seismograph Stations, written communication, 2011 (see WGUEP Meeting #4 summary at http://geology.utah.gov/ghp/workgroups/pdf/wguep/WGUEP-2011A_Presentations.pdf).

[10] Assigned the same slip rate as the Fremont Island and Antelope Island segments of the Great Salt Lake fault zone.

[11] Modified from URS Corporation (unpublished data). USGS (2013) *Quaternary Fault and Fold Database of the United States* reports a value of < 0.2 mm/yr, higher slip rates acknowledge the presence of large scarps (24 m) on possible late Pleistocene lacustrine deposits.

[12] End-to-end straight line length of the East Cache fault zone includes the James Peak and Broadmouth Canyon faults at the so the end of the Southern segment; therefore, the unsegmented length is longer than the length reported in the *Quaternary Fault and Fold Database of the United Sta*tes (USGS, 2013)

[13] UQFPWG consensus values (Lund, 2005) for the Central segment also applied to the unsegmented model.

[14] Modified from McCalpin (1987; 1989) and URS Corporation (unpublished data).

[15] Utah Quaternary Fault Parameter Working Group (UQFPWG) consensus values (Lund, 2005)
[16] Slip-rate and recurrence-interval distributions assigned to the Southern segment are from Lund (2005) for the James Peak fault. The James Peak and Broadmouth Canyon faults are combined with the Southern segment of the East Cache fault zone to form a composite Southern segment.
[17] Assigned same slip-rate distribution as the northern segments of the WFZ.
[18] Modified from URS Corporation (unpublished data).
[19] Based on surface expression (narrow "keystone" graben with minimal displacement across it) and seismic evidence, the WGUEP assigned a steeper dip (70 ± 15) to the Joes Valley fault(s) than the dip adopted for the other normal-slip faults in the WGUEP study area; weighted 55 (0.3), 70 (0.4), 85 (0.3).
[20] Because scarps and location are similar to the Morgan fault, a similar slip-rate distribution (Lund, 2005) was assigned to this fault.
[21] McCalpin and Warren (1992); McCalpin (1993)
[22] Assigned same rupture model, fault-dip distribution, seismogenic depth, and recurrence distribution as the Joes Valley fault zone.
[23] Assigned same rupture model, fault-dip distribution, and slip-rate distribution as the Strawberry fault.
[24] Assigned the same fault rupture model and slip-rate distribution as the West Valley fault zone
[25] Unsegmented model assigned same slip rate as the Clarkston fault

Appendix E

A Uniform Moment Magnitude Earthquake Catalog and Background Seismicity Rates for the Wasatch Front and Surrounding Utah Region

By

Walter J. Arabasz, James C. Pechmann, and Relu Burlacu

University of Utah Seismograph Stations
Salt Lake City, Utah 84112

2016

Research supported by the State of Utah through a line-item appropriation to the University of Utah Seismograph Stations and by the U.S. Geological Survey (USGS), Department of the Interior, under USGS Cooperative Agreement Nos. G10AC00085 and G15AC00028. The views and conclusions contained in this document are those of the authors and should not be interpreted as necessarily representing the official policies, either expressed or implied, of the U.S. Government.

Suggested citation:

Arabasz, W.J., Pechmann, J.C., and Burlacu, R., 2016, A uniform moment magnitude earthquake catalog and background seismicity rates for the Wasatch Front and surrounding Utah region—Appendix E, *in* Working Group on Utah Earthquake Probabilities (WGUEP), 2016, Earthquake probabilities for the Wasatch Front region in Utah, Idaho, and Wyoming: Utah Geological Survey Miscellaneous Publication 16-3, p. E1–E126.

CONTENTS

SUMMARY 1
INTRODUCTION 5
Spatial Extent of the Earthquake Catalog 5
Background Earthquake Models 6
Key Products 7
Organization of the Appendix 7
STEPS IN DEVELOPING A UNIFIED EARTHQUAKE CATALOG 8
Data Sources for the Unified Catalog 8
NON-TECTONIC SEISMIC EVENTS AND HUMAN-TRIGGERED EARTHQUAKES 9
Seismicity Associated with Underground Mining 10
Areas of Coal-Mining Seismicity in East-Central Utah 10
Trona-Mining Seismicity in Southwestern Wyoming 11
Injection-Induced Earthquakes 11
Paradox Valley 12
Rangely Oil Field 12
Red Wash Oil Field 13
UNIFORM MOMENT MAGNITUDE AND MAGNITUDE UNCERTAINTY 13
Uniform Moment Magnitude 14
Different Approaches to "Uniform Moment Magnitude" 14
Magnitude Uncertainty 15
Uncertainties in $\mathbf{M}_{obs}$ and Other Size Measures 15
σ as the average standard error 16
σ from statistics of two different catalogs 16
Nominal values of σ for $\mathbf{M}_{obs}$ 17
Propagation of Uncertainties in Regressing $\mathbf{M}_{obs}$ vs. a Single Size Measure 17
Propagation of Uncertainties in Two-Step Regressions 17
Propagation of Uncertainties in Inverse-Variance Weighting 18
METHODOLOGY FOR ESTIMATION OF UNBIASED RECURRENCE PARAMETERS 19
Correcting for Magnitude Uncertainty 19
Equivalence of Best-Estimate Moment Magnitudes to $\mathbf{M}_{obs}$ 20
Effect of Magnitude Rounding 21
MAGNITUDE CONVERSION RELATIONSHIPS 21
Moment Magnitude Data 22
General Orthogonal Regression vs. Least Squares Regression 23
Presentation of Magnitude Conversion Results 23
Overview of Reported Magnitudes 23
Overview of Magnitude Conversion Relationships 24

M$_{pred}$ from UUSS M_L Magnitudes 25
CR-1, 1a 25
CR-2, 2a 26
M$_{pred}$ from UUSS M_C Magnitudes 26
CR-3, 3a 26
CR-4, 4a 26
CR-5, 5a 26
M$_{pred}$ from USGS M_L Magnitudes 26
CR-6, 6a 27
CR-7, 7a 27
M$_{pred}$ from m_b PDE Magnitudes 28
CR-8, 8a 28
CR-9, 9a 29
CR-10, 10a 29
M$_{pred}$ from ISC m_b Magnitudes 29
CR-11, 11a 30
M$_{pred}$ from Maximum Modified Mercalli Intensity, I_0 30
CR-13, 13a 31
CR-14, 14a 31
M$_{pred}$ from the Logarithm of the Total Felt Area 32
CR-12, 12a 32
M$_{pred}$ from the Logarithm of the Area Shaken at or Greater than MMI IV–VII 33
M$^{\sim}$, Magnitude Types Assumed to be Equivalent to **M** 34
M_S Magnitudes 35
RESULTS OF CATALOG COMPILATION 35
Earthquake Catalog Database (Electronic Supplements) 36
Electronic Supplement E-1 (BEM Earthquake Catalog) 36
Electronic Supplement E-2 (Moment Magnitude Data) 37
Electronic Supplements E-3 to E-5 (Merged Subcatalogs A, B, and C) 38
Electronic Supplement E-6 (Worksheets for **M**$_{obs}$, **M**$^{\sim}$, **M**$_{pred}$|I_0) 38
Electronic Supplements E-7 to E-9 (Worksheets for **M**$_{pred}$|Xnon, Xmix, Xvar, Xi) 38
Errata Relating to Electronic Supplements E-8 and E-9 39
Electronic Supplement E-10 (*N** Counts for the WGUEP and Utah Regions) 39
Overview of Best-Estimate Moment Magnitude (BEM) Catalog 40
Largest Mainshocks (**M** $\geq$ 4.85) in the Utah and WGUEP Regions 40
1. 1884, Nov. 10. Near Paris, Idaho (**M** 5.58) 40
2. 1901, Nov. 14. Tushar Mountains, Utah (**M** 6.63) 41
3. 1902, Nov. 17. Pine Valley, Utah (**M** 6.34) 41

4. 1909, Oct. 6. Hansel Valley (**M** 5.58) 41
5. 1910, May 22. Salt Lake City, Utah (**M** 5.28) 41
6. 1921, Sept. 29. Elsinore, Utah (**M** 5.45) 41
7. 1934, Mar. 12. Hansel Valley, Utah (**M** 6.59) 42
8. 1937, Nov. 19. Nevada-Utah-Idaho tri-state area (**M** 5.40) 43
9. 1950, Jan. 18. Northwestern Uinta Basin (**M** 5.30) 43
10. 1959, July 21. Arizona-Utah border (**M** 5.55) 44
11. 1962, Aug. 30. Cache Valley, Utah (**M** 5.75) 44
12. 1962, Sept. 5. Magna, Utah (**M** 4.87) 44
13. 1963, July 7. Juab Valley, Utah (**M** 5.06) 45
14. 1966, Aug. 16. Nevada-Utah border (**M** 5.22) 45
15. 1967, Oct. 4. Marysvale, Utah (**M** 5.08) 45
16. 1975, Mar. 28. Pocatello Valley, Idaho (**M** 6.02) 46
17. 1988, Aug. 14. San Rafael Swell, Utah (**M** 5.02) 46
18. 1989, Jan. 30. Southern Wasatch Plateau, Utah (**M** 5.20) 46
19. 1992, Sept. 2. St. George, Utah (**M** 5.50) 46

IDENTIFICATION AND REMOVAL OF DEPENDENT EVENTS (DECLUSTERING) 47
Declustering Algorithm Used 47
Checks on Effectiveness of Declustering 48
Space-Time Plots 48
Kolmogorov-Smirnov (K-S) Tests 49
PERIODS OF COMPLETENESS 49
Seismographic Monitoring 50
Early Historical Earthquake Record 50
Population Distribution and Growth in the UTR 51
Population Distribution in 1850 51
Population Distribution in 1860 51
Population Distribution in 1880 52
Population Distribution and Sampling of Earthquake Ground Shaking 52
Data and Basis for Completeness Periods 53
t_0 from CRCs (1963–1986) 53
t_0 from CRCs and Other Arguments (1908, 1880) 53
1908 53
1880 54
t_0 from Other Arguments (1850, 1860, 1880) 54
N^* VALUES AND SEISMICITY RATE PARAMETERS 55
N^* Values 55
Seismicity Rate Parameters 55

Background Earthquake Model for the WGUEP (Wasatch Front) Region 55
Background Earthquake Model for the Utah Region 57
ACKNOWLEDGMENTS 58
REFERENCES (including citations in the Electronic Supplements) 58

TABLES

Table E-1. Coordinates defining catalog domains and areas of non-tectonic and human-triggered seismicity shown on figure E-1
Table E-2. Overview of merged source catalogs by time period
Table E-3. Seismic events in the trona-mining district of southwestern Wyoming
Table E-4. Suspected injection-induced earthquakes in the Paradox Valley, Rangely, and Red Wash areas
Table E-5. Directly-determined magnitude uncertainties using the average-standard-error approach
Table E-6. Indirectly-determined magnitude uncertainties from the magnitude difference in two catalogs
Table E-6a. Addendum—Summary of uncertainties assessed for original catalog magnitudes
Table E-7. Sources of $\mathbf{M}_{obs}$ used in this study
Table E-8. Conversion relationships based on general orthogonal regression
Table E-9. Conversion relationships based on least squares regression
Table E-10. Regression statistics for general orthogonal regressions
Table E-11. Regression statistics for least squares regressions
Table E-12. Measurements of A_{MMI} used in either developing or applying magnitude conversion relationships for A_{IV} to A_{VII}
Table E-13. Magnitude types termed $\mathbf{M}^{\sim}$ assumed to be equivalent to **M**
Table E-14. Largest mainshocks in the Utah Region, $\mathbf{M} \geq 4.85$, 1850–September 2012
Table E-15. Summary of declustering results by catalog domain
Table E-16. Completeness periods for the WGUEP and Utah regions (BEM catalog, declustered)
Table E-17. Area of shaking of MMI IV or greater and approximate total felt area expected to be associated with earthquakes of **M** 4.95–6.45
Table E-18. Data for seismicity rate calculations, WGUEP Region (BEM catalog, declustered)
Table E-19. Data for seismicity rate calculations, Utah Region (BEM catalog, declustered)
Table E-20. Cumulative rates of independent background earthquakes, WGUEP Region
Table E-21. Cumulative rates of independent background earthquakes, Utah Region

FIGURES

Figure E-1. Location map

Figure E-2. Equivalent approaches to determining unbiased recurrence rates

Figure E-3. Map showing the locations of 114 earthquakes for which reliable moment magnitudes were compiled for this study

Figure E-4. Overview of magnitude types reported in the merged source catalogs for the UTREXT

Figure E-5. Data for conversion relationship CR-1 (CR-1a): regression of $\mathbf{M}_{obs}$ on M_L UU1

Figure E-6. Data for conversion relationship CR-3 (CR-3a): regression of $\mathbf{M}_{obs}$ on M_C UU1

Figure E-7. Data for the first step of conversion relationship CR-6 (CR-6a): regression of M_L UU on M_L GS in the UTR, 1974–2012

Figure E-8. Data for the first step of conversion relationship CR-7 (CR-7a): regression of M_L UU on M_L GS in the Extended Border Region (EBR), 1981–2012

Figure E-9. Data for conversion relationship CR-8 (CR-8a): regression of $\mathbf{M}_{obs}$ on m_b PDE1 > 3.5 in the Extended Utah Region (UTREXT), 1991–2012

Figure E-10. Data for the first step of conversion relationship CR-9 (CR-9a): regression of M_L UU or M_C UU on m_b PDE2 ≥ 3.5 in the Utah Region, 1978–1990

Figure E-11. Data for the first step of conversion relationship CR-10 (CR-10a): regression of M_L UU or M_C UU on m_b PDE3 (3.3–5.0) in the Utah Region, 1963–1977

Figure E-12. Data for conversion relationship CR-11 (CR-11a): regression of $\mathbf{M}_{obs}$ on m_b ISC (Nsta ≥ 5)

Figure E-13. Data for conversion relationship CR-13 (CR-13a): regression of $\mathbf{M}_{obs}$ on maximum Modified Mercalli Intensity (I_0) ≥ V

Figure E-14. Data for provisional conversion relationship CR-14 (CR-14a) of maximum Modified Mercalli Intensity (I_0) < V to **M**

Figure E-15. Data for conversion relationship CR-12 (CR-12a): regression of $\mathbf{M}_{obs}$ on the natural logarithm of the total felt area (FA), in km^2

Figure E-16. Data for conversion relationships CR-15 (CR-15a) to CR-18 (CR-18a): regression of $\mathbf{M}_{obs}$ on the logarithm of the extent of area shaken, in km^2, at or greater than MMI IV (A_{IV}) to MMI VII (A_{VII})

Figure E-17. Epicenter map of all earthquakes (clustered) in the BEM catalog, 1850 through September 2012

Figure E-18. Epicenter map of independent mainshocks in the Utah Region, 1850 through September 2012 (BEM catalog, declustered)

Figure E-19. Epicenter map of independent mainshocks in the WGUEP Region, 1850 through September 2012 (BEM catalog, declustered)

Figure E-20. Space-time diagram (latitude vs. time since 1960) of earthquakes in the WGUEP Region (**M** ≥ 2.9, clustered)

Figure E-21. Space-time diagram (latitude vs. time since 1960) of mainshocks in the WGUEP Region (**M** ≥ 2.9, declustered)

Figure E-22. Space-time diagram (latitude vs. time since 1960) of earthquakes in the Utah Region (**M** ≥ 2.9, clustered)

Figure E-23. Space-time diagram (latitude vs. time since 1960) of mainshocks in the Utah Region (**M** ≥ 2.9, declustered)

Figure E-24. Cumulative distribution functions of interval times for earthquakes in selected magnitude bins in the WGUEP and Utah regions, including comparisons with a Poisson model

Figure E-25. Population density map of the Utah Region and the expected area shaken at or greater than MMI IV (A_{IV}) for earthquakes of various magnitudes

Fiigure E-26. Cumulative recurrence curves (CRCs) for declustered earthquakes in the WGUEP Region for incremental magnitude thresholds listed in table E-16 from **M** 2.85 to **M** 5.65

Figure E-27. Cumulative recurrence curves (CRCs) for declustered earthquakes in the Utah Region for incremental magnitude thresholds listed in table E-16 from **M** 2.85 to **M** 5.65

Figure E-28. Background earthquake model for the WGUEP Region. Frequency-magnitude distribution of independent earthquakes (**M** ≥ 2.85), corrected for magnitude uncertainty and calculated using the maximum-likelihood algorithm of Weichert (1980).

Figure E-29. Background earthquake model for the Utah Region. Frequency-magnitude distribution of independent earthquakes (**M** ≥ 2.85), corrected for magnitude uncertainty and calculated using the maximum-likelihood algorithm of Weichert (1980).

ELECTRONIC SUPPLEMENTS

Electronic Supplement E-1. Best-Estimate Moment Magnitude (BEM) Earthquake Catalog

Electronic Supplement E-2. Moment Magnitude Data

Electronic Supplement E-3. Merged Subcatalog A, Jan. 1850–June 1962

Electronic Supplement E-4. Merged Subcatalog B, July 1962–Dec. 1986

Electronic Supplement E-5. Merged Subcatalog C, Jan. 1987–Sept. 2012

Electronic Supplement E-6. Worksheets for $\mathbf{M}_{obs}$, $\mathbf{M}^{\sim}$, $\mathbf{M}_{pred}$ (I_0)

Electronic Supplement E-7. Worksheets for X_{non}, X_{mix} (Subcatalogs A, B)

Electronic Supplement E-8. Worksheets for X_{var}, X_i (Subcatalog B)

Electronic Supplement E-9. Worksheets for X_{var}, X_i (Subcatalog C)

Electronic Supplement E-10. *N** Counts for the WGUEP and Utah Regions

SUMMARY

This appendix describes full details of the construction and analysis of a refined earthquake catalog and the calculation of seismicity rates for the Wasatch Front and surrounding Utah region. A distillation of this appendix, with primary focus on a background earthquake model for the Wasatch Front region, appears as section 5 of the report of the Working Group on Utah Earthquake Probabilities (WGUEP, 2016). Anticipating other applications, the scope of this appendix, both in terms of the earthquake catalog and the calculation of seismicity rates, extends beyond the WGUEP study region to the larger "Utah Region" (lat. 36.75° to 42.50° N, long. 108.75° to 114.25° W).

The earthquake catalog we constructed for our target Utah Region unifies existing catalogs compiled or produced directly by the two primary agents of seismic monitoring of the region: the University of Utah Seismograph Stations (UUSS) and the U.S. Geological Survey (USGS). The catalog covers the time period from 1850 through September 2012. To avoid possible edge effects from "declustering" (i.e., the identification and removal of dependent events) along the periphery of our target region, we expanded the bounds of our catalog compilation to a larger rectangular area termed the Extended Utah Region (UTREXT, lat. 36.0º to 43.5º N, long. 108.0º to 115.0º W). The UTREXT thus encompasses the Utah Region (UTR), within which the WGUEP Region is embedded. The outer frame of the UTREXT surrounding the UTR is termed the Extended Border Region (EBR).

The following key products are presented in this appendix, which includes ten electronic supplements:

- A unified earthquake catalog for the Extended Utah Region, both clustered and declustered, with uniform moment magnitude, **M**, and quantified magnitude uncertainty, covering the time period from 1850 through September 2012
- A compilation of reliable moment magnitude data for 114 earthquakes ($3.17 \leq \mathbf{M} \leq 7.35$) within or near the UTREXT catalog region
- Eighteen region-specific conversion relationships to moment magnitude (16 new, two revised) for an assortment of instrumental magnitudes and shaking-intensity size measures reported for earthquakes in the catalog
- Electronic spreadsheets that allow examination of the stepwise construction of the earthquake catalog, including listings of available size measures for each earthquake in the final catalog and the basis of its measured or estimated moment magnitude and corresponding uncertainty
- Background earthquake models represented by unbiased, maximum-likelihood seismicity rate parameters for both the Wasatch Front (WGUEP) and Utah regions

Background earthquakes are those not associated with known faults and of a size generally below the threshold of surface faulting. The background earthquake model for the Wasatch Front region depicts the frequency-magnitude distribution of future mainshocks expected to occur on seismic sources other than the faults included in the WGUEP fault model. For the WGUEP study, the parameter of primary interest is the rate of future mainshocks of **M** 5.0 or

greater up to a maximum of **M** 6.75 ± 0.25. In addition to the background earthquake model for the WGUEP region, we also developed a similar model for the Utah Region.

To develop the desired background earthquake models, we first constructed an up-to-date earthquake catalog that meets the needs of state-of-practice seismic hazard analysis, namely, a catalog that: (1) is complete in terms of accounting for all known earthquakes in the magnitude range of interest; (2) assigns a uniform moment magnitude to each event; (3) identifies "dependent" events (foreshocks, aftershocks, and the smaller events of earthquake swarms) forming parts of earthquake clusters that can be removed for statistical analysis of mainshock recurrence parameters; (4) excludes non-tectonic seismic events such as blasts and mining-induced seismicity; (5) identifies human-triggered earthquakes for optional removal; and (6) quantifies the uncertainty and rounding error associated with the assigned magnitude of each earthquake.

We restricted attention to the UTR for the identification and removal of non-tectonic seismic events and human-triggered earthquakes from the earthquake catalog. Retaining any such events in the EBR has no practical effect on the resulting catalog of independent mainshocks in the UTR after declustering—but it means the catalog *outside* the UTR must be used with caution. Non-tectonic seismic events in the UTR consist primarily of surface blasts and mining-induced seismicity associated with underground coal mining in east-central Utah and underground mining of trona (a sodium evaporate mineral) in southwestern Wyoming. Human-triggered earthquakes are associated with deep fluid injection in three areas of the eastern UTR (outside the WGUEP Region) in the Utah-Colorado border region. These injection-induced earthquakes were retained in our catalog but not used in the calculations for earthquake rates in the UTR.

In order to get unbiased estimates of seismicity rate parameters for the background earthquake models, we used as a *general* guide the methodology framework outlined in the final report of a project co-sponsored by the Electric Power Research Institute (EPRI), the U.S. Department of Energy (DOE), and the U.S. Nuclear Regulatory Commission (NRC) (EPRI/DOE/NRC (2012). Key elements are the assignment of a uniform moment magnitude to each earthquake in the catalog, assessment of magnitude uncertainties, and the application of bias corrections based on those uncertainties to estimate unbiased recurrence parameters. Throughout, our definition of moment magnitude, **M**, follows Hanks and Kanamori (1979): $\mathbf{M} = 2/3 \log M_0 - 10.7$, where M_0 is the earthquake's scalar seismic moment in dyne-cm, generally determined from inversions of either long-period waveforms or surface-wave spectra.

Our unified catalog for the UTREXT contains more than 5300 earthquakes larger than about magnitude 2.5, but direct instrumental measurements of **M** are available for only 107 of them (excluding known and suspected mining-related seismic events). Using these observed values of **M** plus values for seven supplementary events, we developed eighteen conversion relationships to moment magnitude (16 new, two revised) for an assortment of shaking-intensity size measures (maximum Modified Mercalli intensity, MMI; total felt area; extent of area shaken at or greater than various levels of MMI) and instrumental magnitudes (including Richter local magnitude, coda or duration magnitude, and body-wave magnitude) that varied with time and reporting agency. Where multiple size measures were available for an individual earthquake without a measured **M**, we computed an inverse-variance-weighted mean of **M** values computed from conversion relations to get a best estimate of **M**.

Different approaches can be utilized to transform an earthquake catalog with a minor fraction of direct instrumental measurements of **M** into one with "uniform moment magnitude." In the methodology of EPRI/DOE/NRC (2012), the uniform estimate of moment magnitude is E[**M**], the "expected value of moment magnitude," given uncertainty in either the observed value of **M** or in the value of **M** estimated from one or more other size measures. It is important to note that E[**M**] is a statistical construct with the specific underlying purpose of estimating unbiased earthquake recurrence parameters. Further, the equations for E[**M**] in EPRI/DOE/NRC (2012) implicitly assume the consistent use of least-squares regression (LSR) in magnitude conversions.

We decided not to use the "E[**M**]" approach for three reasons. First, we wanted an earthquake catalog with uniform moment magnitude that could serve other general purposes. Because E[**M**] is a statistical construct, it does not serve the same purposes as **M** outside the context of estimating unbiased earthquake recurrence parameters. Second, the use of general orthogonal regression (GOR) is favored by many experts over LSR for magnitude conversions. Consequently, the use of LSR for consistency with the E[**M**] approach as applied in EPRI/DOE/NRC (2012) will not generally provide the best estimate of **M**. Third, by consistently using GOR instead of LSR for magnitude conversions, many of the complexities of the E[**M**] methodology in EPRI/DOE/NRC (2012) can be eliminated.

We call the alternative uniform moment magnitude used to construct our catalog a "best-estimate" moment magnitude. Our Best-Estimate Moment Magnitude (BEM) catalog assigns a value of moment magnitude to each earthquake that either is directly observed as **M** ($\mathbf{M}_{obs}$), is a conversion of one or more other size measures to **M** using empirical predictive equations based on GOR (which yield predicted values, $\mathbf{M}_{pred}$), or is a reported value of magnitude which we assume to be equivalent to **M** (termed $\mathbf{M}^{\sim}$). Where $\mathbf{M}_{obs}$ was reported for an earthquake, it was given precedence over other size measures in the catalog. Our focus in producing the unified earthquake catalog was on the uniformity and quality of magnitude, not on epicentral quality. Therefore the resulting catalog should not necessarily be considered the "best" available for purposes relating to the accuracy of earthquake locations.

Our approach to estimating earthquake recurrence parameters involves a standard procedure used in Probabilistic Seismic Hazard Analysis—namely, the use of the Weichert (1980) maximum-likelihood approach to fit a truncated exponential distribution to earthquake counts in magnitude bins. Two known potential sources of bias that can affect the seismicity-rate calculations are magnitude uncertainty and the discretization or rounding of magnitude values to some specified nearest decimal value. In this study, the effect of rounded magnitude values is shown to be insignificant and is ignored.

Quantifying magnitude uncertainty is necessary for three aspects of our analysis of background seismicity: (1) correcting for bias in earthquake recurrence rates; (2) specifying the error-variance ratio between dependent and independent variables when using GOR for magnitude conversions; and (3) using inverse-variance weighting when combining different size measures to get a robust estimate of moment magnitude for an individual earthquake. The magnitude of an earthquake is generally taken as the mean value of magnitude determinations of the same type made at multiple recording stations. In the absence of systematic and rounding errors, the mean value of the event magnitude can be viewed as having random errors that are normally distributed with zero mean and standard deviation, σ (Tinti and Mulargia, 1985; Veneziano and

Van Dyke, 1985b). Following these cited authors, we define the latter statistic σ as the *magnitude uncertainty*.

For each earthquake in the master catalog, we provide a value of uniform moment magnitude and its corresponding uncertainty σ. To determine σ, uncertainties were first assessed for observed values of **M** and for reported values of other size measures that were converted to **M** through regressions. For most of the entries in the master catalog, σ comes from the propagation of uncertainties involved in regressions or from inverse-variance weighting of multiple estimates of **M** from various size measures.

For conformity with procedures used by the USGS in earthquake catalog processing for the U.S. National Seismic Hazard Maps, we used the computer program *cat3w* developed by Dr. Charles Mueller of the USGS for declustering. The program implements the method of Gardner and Knopoff (1974), in which smaller earthquakes within fixed time and distance time windows of larger shocks are identified as dependent events. We verified the effectiveness of using *cat3w* to decluster our BEM catalog by (1) comparing space-time plots of the original and declustered versions of the catalog and (2) using the Kolmogorov-Smirnov (K-S) test to analyze data in critical magnitude bins.

A critical element for constructing the background earthquake models is the completeness period, T_C, for which the reporting of earthquakes at or above a given magnitude threshold in the earthquake catalog is complete. To determine T_C for different magnitude thresholds in the declustered catalog, we used cumulative recurrence curves (plots of the cumulative number of earthquakes above a given magnitude threshold versus time) together with general information on the space-time evolution of seismographic control, population, and newspapers.

Our BEM earthquake catalog for the UTREXT contains 5388 earthquakes ($\mathbf{M} \leq 6.63$). The declustered version contains 1554 independent mainshocks ($2.50 \leq \mathbf{M} \leq 6.63$) in the UTR and 660 independent mainshocks ($2.50 \leq \mathbf{M} \leq 6.59$) in the WGUEP Region. We provide descriptions, including the basis of their estimated moment magnitudes, for the 19 independent mainshocks of **M** 4.85 or larger in the UTR, nine of which are within the WGUEP Region.

The earthquake catalog database is presented in ten electronic supplements, each in the form of a Microsoft Excel workbook with multiple worksheets. Each workbook contains an explanatory "README" file to guide the reader. The electronic supplements allow examination not only of the final unified catalog but also its building blocks. These include merged, chronologically sorted, and edited individual line entries from the diverse USGS and UUSS source catalogs; tabulated available size measures for each event in the master catalog; and calculations behind the assigned value of uniform moment magnitude and corresponding uncertainty for each earthquake.

The culmination of the appendix is the calculation of seismicity rate parameters to represent background earthquake models for the WGUEP and Utah regions. We use the N^* approach originally proposed by Tinti and Mulargia (1985) to achieve unbiased earthquake recurrence parameters. N^* is a count of earthquakes in a specified magnitude interval, adjusted for magnitude uncertainty. We followed the EPRI/DOE/NRC (2012) steps of (1) calculating N^* from σ on an earthquake-by-earthquake basis (using $N^* = \exp\{-(b \ln(10))^2\sigma^2/2\}$), (2) summing N^* for earthquakes within specified magnitude intervals, (3) dividing each N^* sum by the period

of completeness for its respective magnitude interval, and (4) using the maximum-likelihood algorithm of Weichert (1980) to compute seismicity rate parameters from the equivalent N^* counts. For the N^* calculations, we used a b-value of 1.05 assessed from preliminary processing of the BEM catalog.

Expressed in terms of a truncated exponential distribution with a minimum magnitude, m_0, of 2.85 and an upper-bound magnitude, m_u, of 7.00, the cumulative annual rate of independent mainshocks in the WGEUP Region greater than or equal to $m_0 = 2.85$ is 7.70 with a standard error of 0.52. The b-value determined for the model is 1.06 with a standard error of 0.06. For the Utah Region, the cumulative annual rate greater than or equal to $m_0 = 2.85$ is 18.0 with a standard error of 0.81. The b-value determined for the model is 1.07 with a standard error of 0.04. These models predict average recurrence intervals for $\mathbf{M} \geq 5.0$ earthquakes of 25 yrs (90% conf. limits: 17 to 44 yrs) for the WGUEP Region and 11 yrs (90% conf. limits: 8 to 16 yrs) for the Utah Region.

INTRODUCTION

This appendix describes full details of the construction and analysis of a refined earthquake catalog and the calculation of seismicity rates for the Wasatch Front and surrounding Utah region (figure E-1). A distillation of this appendix, with primary focus on a background earthquake model for the Wasatch Front region, appears as section 5 of the report of the Working Group on Utah Earthquake Probabilities (WGUEP, 2016). This appendix is intended to serve as a stand-alone document. It repeats some of the content of section 5 of the WGUEP report but its scope extends to a significantly larger area than the Wasatch Front region defined for the WGUEP probabilistic forecast (herein termed “the WGUEP Region”).

Spatial Extent of the Earthquake Catalog

The standard region for which the University of Utah Seismograph Stations (UUSS) has the responsibility for seismic monitoring and catalog reporting as part of the U.S. Advanced National Seismic System is termed the “Utah Region” (lat. 36.75° to 42.50° N, long. 108.75° to 114.25° W). Anticipating other applications beyond the WGUEP study, we undertook to develop an improved historical and instrumental earthquake record for the whole Utah Region that unifies existing catalogs compiled or produced directly by the two primary agents of seismic monitoring of the region: the UUSS and the U.S. Geological Survey (USGS).

The unified UUSS-USGS earthquake catalog that we constructed for our target Utah Region covers the time period from 1850 through September 2012. To avoid possible edge effects from “declustering” (i.e., the identification and removal of dependent events) along the periphery of our target region, we expanded the bounds of our catalog compilation to a larger rectangular area termed the Extended Utah Region (UTREXT, lat. 36.0º to 43.5º N, long. 108.0º to 115.0º W). The UTREXT thus encompasses the Utah Region (UTR), within which the WGUEP Region is embedded. The outer frame of the UTREXT surrounding the UTR is termed the Extended Border Region (EBR). The geographic boundaries of these regions are specified in table E-1 and their spatial relations are shown on figure E-1.

Background Earthquake Models

Background earthquakes are those not associated with known faults and of a size generally below the threshold of surface faulting. The background earthquake model for the Wasatch Front study region depicts the frequency-magnitude distribution of future mainshocks expected to occur on seismic sources other than the faults included in the WGUEP fault model. In terms of earthquake size, the WGUEP background earthquake model provides rates of future mainshocks of moment magnitude, **M**, 5.0 or greater up to a maximum of **M** 6.75 ± 0.25. We similarly construct a background earthquake model for the Utah Region as a whole. Our analyses of background seismicity involve more thorough and rigorous treatments of the earthquake record, magnitude estimates, and magnitude uncertainties than previously attempted, for example by Youngs and others (1987, 2000) and by Pechmann and Arabasz (1995).

In the WGUEP seismic source model (see WGUEP, 2016, section 2.1), background seismicity logically should exclude earthquakes that can be associated with faults included in the WGUEP model and also are above the minimum magnitude of earthquakes modeled on those faults. Based on figure 7.1-4 of WGUEP (2016), this minimum magnitude effectively is **M** ~5.9 (for rates $\geq 10^{-4}$ per year). In the case of the Wasatch Front Region—and, indeed, throughout the Intermountain seismic belt in Utah—few historical or instrumentally located earthquakes can confidently be associated with mapped surface faults (e.g., Arabasz *et al*., 1992, 2007). The only surface-rupturing earthquake in the Utah Region during the time period of the 1850–2012 catalog was the 1934 **M** 6.6 Hansel Valley, Utah, earthquake, and the surface fracturing associated with it may not have been primary tectonic surface faulting (Doser, 1989). The vast majority of the earthquakes in our catalog within the Utah Region appear to be background earthquakes on buried or unmapped secondary faults. For this reason we used our refined earthquake catalog, without removing any mainshocks near modeled faults, to calculate rates of background earthquakes for the WGUEP and Utah regions.

The desired background earthquake models for the Wasatch Front and Utah regions require an up-to-date earthquake catalog that meets the needs of state-of-practice seismic hazard analysis, namely, a catalog that: (1) is complete in terms of accounting for all known earthquakes in the magnitude range of interest; (2) assigns a moment magnitude to each event ; (3) identifies "dependent" earthquakes (foreshocks, aftershocks, and the smaller events of earthquake swarms) forming parts of earthquake clusters that can be removed for statistical analysis of mainshock recurrence parameters; (4) excludes non-tectonic seismic events such as blasts and mining-induced seismicity; (5) identifies human-triggered earthquakes for optional removal; and (6) quantifies the uncertainty and rounding error associated with the assigned magnitude of each earthquake.

Two U.S. studies exemplify the rigorous development and treatment of earthquake catalogs for calculating background seismicity rates: EPRI/DOE/NRC (2012), for the central and eastern United States, and Felzer (2007), for California. We have used the former study, first, as a *general* guide in developing an earthquake catalog with uniform moment magnitude for the Wasatch Front and Utah regions and, second, for methodology guidance in handling magnitude uncertainties for calculating unbiased seismicity rate parameters. In a later section, we describe how we depart from the EPRI/DOE/NRC (2012) methodology.

Key Products

The following key products are presented in this appendix, which includes ten electronic supplements:

- A unified earthquake catalog for the Extended Utah Region, both clustered and declustered, with uniform moment magnitude and quantified magnitude uncertainty, covering the time period 1850 through September 2012

  [Note: The Extended Utah Region was designed to facilitate declustering along the periphery of the Utah Region. Because we did not systematically identify and remove non-tectonic seismic events and human-triggered earthquakes in the Extended Border Region, the catalog outside the Utah Region must be used with caution.]

- A compilation of reliable moment magnitude data for 114 earthquakes ($3.17 \leq \mathbf{M} \leq 7.35$) within or near the UTREXT catalog region
- Eighteen region-specific conversion relationships to moment magnitude (16 new, two revised) for an assortment of instrumental magnitudes and shaking-intensity size measures reported for earthquakes in the catalog
- Electronic spreadsheets that allow examination of the stepwise construction of the earthquake catalog, including listings of available size measures for each earthquake in the final catalog and the basis of its measured or estimated moment magnitude and corresponding uncertainty
- Background earthquake models, in terms of unbiased, maximum-likelihood seismicity rate parameters, for both the Wasatch Front (WGUEP) Region and the Utah Region

Organization of the Appendix

We begin by outlining the steps taken to develop a unified earthquake catalog, after which we elaborate on our treatment of non-tectonic seismic events and human-triggered earthquakes. In subsequent major sections, we explain key issues of uniform moment magnitude and magnitude uncertainty, methodology for estimating unbiased earthquake recurrence parameters, and the handling of various size measures in the earthquake record together with magnitude conversions to moment magnitude. We then describe the resulting earthquake catalog, followed by descriptions of how dependent events were removed to achieve a “declustered” catalog of independent mainshocks and how we assessed periods of completeness for different magnitude ranges. Finally, we summarize the calculation of unbiased seismicity rate parameters that characterize background earthquake models for the Wasatch Front and Utah regions.

STEPS IN DEVELOPING A UNIFIED EARTHQUAKE CATALOG

To develop a unified earthquake catalog with uniform moment magnitude, the following basic steps were followed:

- Selection of a catalog region large enough for effective declustering around the edges of the region of interest
- Merging, chronological sorting, and editing of individual line entries from diverse USGS and UUSS source catalogs—accounting for all reported earthquakes, removing duplicates and non-tectonic events, and selecting the line entry with the preferred time and location for each unique earthquake event
- Compilation and evaluation of available size measures for each event in the master catalog
- Assessment of magnitude uncertainties and rounding errors for individual magnitudes
- Tabulation of available instrumental measurements of moment magnitude, **M**, for earthquakes in the catalog region
- Determination of conversion relationships between **M** and other available size measures using general orthogonal regression (for comparison, corresponding ordinary least-squares regressions were also done)
- Assignment of a uniform moment magnitude and corresponding uncertainty to each earthquake in the master catalog, based on either direct measurement or conversion from other size measures (duly accounting for the propagation of uncertainties)

Data Sources for the Unified Catalog

In aiming for a unified UUSS-USGS catalog, focus was placed on authoritative source catalogs compiled or produced directly by the UUSS and the USGS. For historical earthquakes, these catalogs are compilations based on various primary and secondary sources and documented by USGS and UUSS researchers. For instrumentally recorded earthquakes, the source catalogs consist of tabulations directly resulting from regional seismic monitoring by the UUSS since mid-1962 and from national-scale seismic monitoring by the USGS since 1973 (or in earlier decades by the U.S. Coast and Geodetic Survey).

The following source catalogs were assembled for sorting, merging, and editing: (1) the UUSS historical earthquake catalog (downloaded from UUSS files on March 21, 2013); (2) the UUSS instrumental earthquake catalog (downloaded from UUSS files on June 12 and 14, 2013); (3) a version of the USGS catalog used in the 2008 national seismic hazard maps, termed the "Western Moment Magnitude" (WMM) catalog, updated through 2010 and provided by C.S. Mueller of the USGS on June 6, 2011; (4) a USGS in-house catalog termed the "SRA" catalog (after Stover, Reagor, and Algermissen,1986) for the western U.S., downloaded from the USGS Earthquake Hazards Program website on February 1, 2012; (5) the USGS PDE online catalog, sorted for the UTREXT and downloaded on March 9, 2013; and (6) Stover and Coffman's (1993) tabulations of significant earthquakes in the U.S. The catalog of Pancha and others (2006), which was adopted extensively into the USGS WMM catalog that was provided to us, was not directly merged into the raw master catalog but was checked to ensure that all reported earthquakes were accounted for.

As outlined in table E-2, the master catalog comprises three subcatalogs, A, B, and C, corresponding to three different time periods. Break points correspond to the start of the UUSS instrumental catalog on July 1, 1962, and the end of the SRA catalog on December 31, 1986. The table indicates which source catalogs were merged and synthesized to form each subcatalog. The master catalog begins in 1850, the date of the earliest reported historical earthquake in the UTREXT, and ends on September 30, 2012. Minimum magnitudes vary with each source catalog. One of our aims was to try to achieve as long a record as possible in the UTR down to **M** 3.0 or smaller. To this end, all events in the UUSS instrumental earthquake catalog of magnitude 2.45 or larger (on whatever scale) were imported into the master catalog.

NON-TECTONIC SEISMIC EVENTS AND HUMAN-TRIGGERED EARTHQUAKES

We restricted attention to the UTR for the identification and removal of non-tectonic seismic events from the earthquake catalog. Retaining any such events in the EBR has no practical effect on the resulting catalog of independent mainshocks in the UTR after declustering—but it means the catalog *outside* the UTR must be used with caution. One notable non-tectonic event in the EBR that was removed from the master catalog was the Project Rio Blanco underground nuclear test (m_b USGS 5.4), 58 km northwest of Rifle, Colorado, on May 17, 1973.

Non-tectonic seismic events in the UTR primarily consist of seismicity associated with underground mining and surface blasts associated with quarrying and surface mining. We are not aware of any documented cases of reservoir-triggered seismicity in the UTR (see Smith and Arabasz, 1991, for an earlier review of induced seismicity in the Intermountain region). There is, however, uncertain evidence for *decreases* in seismicity within 40 km following the impounding of Glen Canyon (Lake Powell) and Flaming Gorge reservoirs (Simpson, 1976 and references therein).

Injection-induced earthquakes are another type of human-triggered seismicity in the UTR, but we treated these differently from mining-induced seismicity (MIS). MIS was considered to release predominantly non-tectonic stress and was removed at early stages of compiling the master catalog. Earthquakes induced by the injection of fluids into underground formations, on the other hand, more commonly release stored tectonic stress on preexisting faults and can contribute to seismic hazard (see Ellsworth, 2013). To give future hazard analysts the option of how to deal with earthquakes potentially induced by fluid injection, we retained them in the catalog. But as we explain presently, we removed such events from the declustered version of the catalog before calculating seismicity rate parameters for the UTR. The WGUEP Region is unaffected (see locations of circular areas on figure E-1).

Surface blasts are systematically identified and excluded from the UUSS source catalogs we used. Blast identification is accomplished by contacting individual blasting operators and/or by correlation with known blasting areas and the time of day of frequent blasting. In editing the merged UUSS-USGS catalogs, all unique events in the UTR that derived from one or more USGS sources and without a corresponding UUSS event line were carefully scrutinized for their validity. For the instrumental period (subcatalogs B and C), this scrutiny included cross-checking UUSS files of “manmade” seismic events to ensure that a solitary USGS-derived event in the merged catalog was not one which the UUSS had identified and removed as a blast.

To be clear, although we made diligent efforts to exclude surface blasts from the BEM earthquake catalog for the UTR, we relied on UUSS observatory practices for eliminating such events from the UUSS source catalogs that we used. We did not undertake an additional screening process and admit the possibility that our final earthquake catalog may still contain a few blasts near some known quarry and mine sites in the UTR. We judge that the total number of such events is small and inconsequential for the earthquake rate calculations in this study.

Seismicity Associated with Underground Mining

Known areas of prominent MIS in the UTR are identified on figure E-1 and their boundaries are specified in table E-1. These include two areas of extensive underground coal mining in east-central Utah labeled WP-BC, for the Wasatch Plateau-Book Cliffs coal-mining region, and SUFCO, for the Southern Fuel Company coal-mining area. Another area of prominent MIS labeled TRONA is for an area of underground trona mining in southwestern Wyoming.

Areas of Coal-Mining Seismicity in East-Central Utah

MIS caused by underground mining in the arcuate crescent of the Wasatch Plateau and Book Cliffs coalfields in east-central Utah (WP-BC and SUFCO areas on figure E-1) is a well-recognized phenomenon that has been studied since the 1960s (see reviews by Wong, 1993; Arabasz and others, 1997, 2007; and Arabasz and Pechmann, 2001). The region's largest mining seismic event to date ($\mathbf{M}_{obs}$ 4.16, Whidden and Pankow, 2012) was the August 6, 2007, Crandall Canyon mine collapse (Pechmann and others, 2008).

The boundaries of the WP-BC and SUFCO areas specified in table E-1 are standard ones used by the UUSS to encompass areas of abundant MIS in Utah's coal-mining region. A sort of the UUSS instrumental catalog for the period July 1, 1962–September 30, 2012, yielded 20,416 events in the WP-BC area; of these, 522 had M_L or $M_C \geq 2.45$. For the SUFCO area, the number of sorted events was 2680 of which 97 had M_L or $M_C \geq 2.45$. Because of the large numbers involved, all of the events within the WP-BC and SUFCO areas were removed prior to merging the UUSS and USGS instrumental catalogs in subcatalogs B and C (with three exceptions discussed below). For the historical earthquake period of subcatalog A, which chiefly predates the occurrence of significant MIS in Utah, events with epicenters within the MIS areas were examined individually. We removed three events as probable mining-related events (see the README file in the electronic supplement for merged subcatalog A).

A recurring question when MIS is removed from the WP-BC and SUFCO areas is whether these areas contain tectonic earthquakes as well as MIS. We have scrutinized the MIS data set in the UUSS instrumental catalog a number of times to address this issue (Arabasz and Pechmann, 2001; Arabasz and others, 2005; Arabasz and others, 2007). Three known tectonic events, identified on the basis of their focal depths and source mechanisms, have occurred within the WP-BC area and are retained in the BEM catalog: (1) June 2, 1996, 08:09 UTC, **M** 3.18 (Arabasz and Pechmann, 2001, p. 4-8); (2) July 14, 2008, 23:50 UTC, **M** 3.17 (Whidden and Pankow, 2012); and (3) November 10, 2011, 04:27 UTC, **M** 3.96 (UUSS unpublished data).

As a further check for this study, we sorted the UUSS catalog for the WP-BC and SUFCO areas (July 1, 1962–September 30, 2012; $M \geq 2.45$) and then searched for events with well-constrained focal depths that would confidently place them below shallow mining activity. We searched for

event solutions meeting the following quality criteria: (1) epicentral distance to the nearest station less than or equal to the focal depth or 5 km, whichever is larger, and (2) standard vertical hypocentral error (ERZ) of 2 km or less, as calculated by the location program. This search yielded only three events with a well-constrained depth greater than 2 km—two of the already known tectonic earthquakes and an event in 1970 that had been located with a restricted focal depth of 7.0 km. Thus, we believe that removing events in the WP-BC and SUFCO areas from the instrumental earthquake catalog—except for the three identified tectonic earthquakes—is adequately justified for this project, particularly for the magnitude threshold of **M** 2.85 that we ultimately use for our seismicity rate calculations. For seismic hazard or risk analyses involving lower magnitudes, a different approach may be advisable.

Trona-Mining Seismicity in Southwestern Wyoming

The association of seismicity with the underground mining of trona (a sodium evaporate mineral) in southwestern Wyoming was highlighted by the occurrence of a magnitude 5.2 (M_L UU, revised) seismic event on February 3, 1995. A collapse of part of the Solvay Mine was the dominant source of seismic radiation (Pechmann and others, 1995). Ground truth for associating an event of magnitude 4.3 (M_L UU) on January 30, 2000, with a roof fall in the Solvay Mine, was documented by McCarter (2001).

In order to identify suspected mine seismicity associated with trona mining in this region, we used information on the website of the Wyoming Mining Association (www.wma-minelife.com). Specifically, we used a "Known Sodium Leasing Area (KSLA) Map" (Anadarko Petroleum Corporation, 2005) showing the location of the principal areas of trona mining to demarcate a rectangular area specified in table E-1 that encompasses what we believe is predominantly, if not exclusively, trona-mining seismicity. Sixteen seismic events ($2.5 \leq M_L$ UU ≤ 5.2) within the "TRONA" rectangle were sorted from the master catalog and are listed in table E-3. All were deleted from our merged subcatalogs B and C as non-tectonic events.

Some local seismic monitoring was initiated by operators of the Solvay Mine after the 1995 mine collapse, but these data are not integrated into the regional seismic monitoring from which our source catalogs were produced. As a result, both epicentral and focal-depth resolution in our source catalogs are relatively poor for the TRONA area, and we have little basis for discriminating tectonic events from mining events in the area less than about **M** 3.5.

Injection-Induced Earthquakes

There are two known areas in the UTR where injection-induced earthquakes are of significant number and size to be of concern for our purposes. These are as shown on figure E-1 as circular areas along the Colorado-Utah border, labeled PV for Paradox Valley and R for the Rangely oil field. A third area, labeled RW for the Red Wash oil field in northeastern Utah, adjoins the Rangely area and has a handful of events in the earthquake catalog that we suspect may also be injection-induced. For each of these areas, we chose a radial distance of 25 km, with center points given in table E-1, to sort out suspected injection-induced earthquakes in the catalog. The selected radius was intended to allow for epicentral location errors and is in reasonable agreement with available earthquake information for the Paradox Valley and Rangely source areas; it is somewhat arbitrary, however, for the Red Wash source area.

Table E-4 lists the mainshocks in each of the three areas of suspected injection-induced seismicity that we decided to remove from the declustered catalog before calculating seismicity rates for a background earthquake model for the UTR. Earthquakes in the Paradox Valley and Rangely areas that were earlier removed as dependent events are identified in footnotes in table E-4.

Paradox Valley

The U.S. Bureau of Reclamation (USBR) has thoroughly monitored, studied, and documented injection-induced seismicity in the Paradox Valley (PV) area (figure E-1) associated with its Colorado River Basin Salinity Control Project (e.g., Ake and others, 2005; Block and others, 2012). To divert the seepage and flow of salt brine into the Dolores River, a tributary of the Colorado River, the USBR extracts aquifer brine from nine shallow wells along the river in western Colorado and injects the brine under high pressure at a depth of 4.3 to 4.8 km below surface in a deep disposal well (Ake and others, 2005). According to these authors, injection testing occurred between July 1991 and March 1995, and continuous injection began in May 1996. Up-to-date summaries of the ongoing induced seismicity resulting from this injection are provided by Ellsworth (2013) and in Appendix K of a report by the Committee on Induced Seismicity Potential in Energy Technologies (2013).

Table E-4 lists 19 mainshocks with epicenters within the Paradox Valley (PV) source area, all later than 1996, identified for removal from the declustered catalog; two dependent events are noted in footnote 3 of the table. The three largest events occurred in June and July 1999 (**M** 3.66 and **M** 3.69, respectively) and in May 2000 (**M** 3.80). Since 2002, injection-induced earthquakes have occurred out to 16 km from the disposal well (figure K.1 in Committee on Induced Seismicity Potential in Energy Technologies, 2013).

We emphasize that the data for the earthquakes in table E-4 originate primarily from the UUSS source catalog; data for two come from the USGS PDE catalog. The USBR has continuously operated the Paradox Valley Seismic Network (PVSN) in the PV area since 1985 (Ake and others, 2005). Data from a few stations of the PVSN have been telemetered to the UUSS since 1989 to enhance seismographic control in the eastern part of the UTR, but operation of these stations was occasionally interrupted. Most (13 of 19) of the earthquake locations in table E-4 have hypocentral control from at least one PVSN station. Higher resolution earthquake locations from the PVSN are documented internally by the USBR but are not contained in national earthquake catalogs.

Rangely Oil Field

The Rangely oil field in northwestern Colorado is described by the Energy and Minerals Field Institute (EMFI, 2005) as “one of the oldest and largest oil fields in the Rocky Mountain region.” Reservoir rocks are part of a northwest-southeast anticline about 12 miles (19 km) long and 5 miles (8 km) wide (Gibbs and others, 1973). The case for induced seismicity associated with the injection of fluid in the Rangely oil field is well documented (Gibbs and others, 1973; Raleigh and others, 1976; Ellsworth, 2013). Secondary oil recovery using “water-flooding” in water-injection wells began in late 1957 and continued until 1986, when a tertiary recovery program using carbon dioxide (CO_2) injection was started (EMFI, 2005; Clark, 2012). The latter involves pumping CO_2 and water into the subsurface in alternating cycles (EMFI, 2005). Moran (2007)

reviews the occurrence of earthquakes in the Rangely area and includes a figure showing epicentral scatter within about 25 km of the center of the oil field.

The full catalog contains 17 earthquakes in the Rangely circular source area. Seven of these are independent mainshocks ($2.97 \leq \mathbf{M} \leq 4.26$) that we removed as suspected injection-induced earthquakes (table E-4). Another nine were identified as dependent events by the declustering algorithm (footnote 4, table E-4) and removed earlier. The remaining earthquake, which occurred on February 21, 1954 (20:20 UTC, **M** 3.67), predates fluid injection in the oil field and was retained in the catalog. All seven mainshocks marked for removal occurred during known periods of fluid injection in the Rangely field, either for secondary or tertiary oil recovery.

Red Wash Oil Field

Sparse information is available for correlating earthquake activity with fluid injection in the Red Wash oil field, and our decision to remove earthquakes in this source area from the declustered catalog as injection-induced is arguable. Their removal or inclusion has little effect on calculated seismicity rates for the UTR.

Fluid injection has been used at the Red Wash field as part of secondary and tertiary oil recovery (Schuh, 1993; Chidsey and others, 2003). The field's geocode coordinates (table E-1) place it about 30 km to the west of the northwestern end of the Rangely field. Given its proximity to the Rangely field, the Red Wash area plausibly may share a susceptibility to triggered earthquakes, perhaps on the same buried Pennsylvanian fault system identified at Rangely (Raleigh and others, 1976).

Table E-4 identifies five earthquakes in the Red Wash source area as suspected injection-induced events. (The source area also includes the smaller Wonsits Valley oil field; for convenience, we simply use "Red Wash" as the general identifier.) An earthquake of **M** 4.02 in 1967 also lies within the Rangely circular area. This earthquake is the most distal from the Red Wash center point and more likely is associated with fluid-injection activities at Rangely in the 1960s. The other four shocks ($\mathbf{M} \leq 3.92$) occurred between 1990 and 2000. In the process of routinely issuing UUSS press releases following shocks of magnitude 3.5 and larger in the Utah Region, we became familiar with these earthquakes at the times of their occurrence and also with their apparent spatial association with the Red Wash oil field.

UNIFORM MOMENT MAGNITUDE AND MAGNITUDE UNCERTAINTY

The primary purpose for compiling the earthquake catalog is to develop unbiased estimates of seismicity rate parameters for the background earthquake models. To achieve that goal, we used as a *general* guide the methodology framework outlined in the final report of a project co-sponsored by the Electric Power Research Institute (EPRI), the U.S. Department of Energy (DOE), and the U.S. Nuclear Regulatory Commission (NRC) (EPRI/DOE/NRC (2012). Key elements are the assignment of a uniform moment magnitude to each earthquake in the catalog, assessment of magnitude uncertainties, and the application of bias corrections based on those uncertainties to estimate unbiased recurrence parameters.

Uniform Moment Magnitude

We require an earthquake catalog with a uniform size measure for each event specified in terms of moment magnitude, **M**, defined by Hanks and Kanamori (1979):

$$\mathbf{M} = 2/3 \log M_0 - 10.7 \qquad \text{(E-1)}$$

where M_0 is the earthquake's scalar seismic moment in dyne-cm, generally determined from inversions of either long-period waveforms or surface-wave spectra. Moment magnitude is used in state-of-practice seismic hazard analyses for consistency with modern ground-motion prediction equations. Moreover, moment magnitude has become the size measure preferred by seismologists because it is the best indicator of an earthquake's true relative size and can be directly tied to physical properties of the earthquake source.

Our culled master catalog for the Extended Utah Region contains more than 5300 earthquakes larger than about magnitude 2.5, but direct instrumental measurements of **M** are available for only 107 of them (excluding known and suspected mining-related seismic events). Using these observed values of **M** plus values for seven supplementary events (see Electronic Supplement E-2), eighteen conversion relationships to moment magnitude were developed for this project (16 new, two revised) for an assortment of shaking-intensity size measures and instrumental magnitudes that varied with time and reporting agency. The principal instrumental magnitudes in the source catalogs are Richter local magnitude (M_L), coda or duration magnitude (M_C, M_D), and body-wave magnitude (m_b). The non-instrumental size measures that were converted to **M** are: the maximum value of Modified Mercalli Intensity, MMI (I_0); total felt area (FA); and the extent of area shaken at or greater than MMI IV, V, VI, and VII (A_{IV}, A_V, $A_{VI,}$ and A_{VII}). Where multiple size measures were available for an individual earthquake, we computed a weighted mean of these measures using inverse-variance weighting to get a best estimate of **M**.

Different Approaches to "Uniform Moment Magnitude"

Different approaches can be utilized to transform an earthquake catalog with a minor fraction of direct instrumental measurements of **M** into one with "uniform moment magnitude." In the methodology of EPRI/DOE/NRC (2012), the uniform estimate of moment magnitude is E[**M**], the "expected value of moment magnitude," given uncertainty in either the observed value of **M** or in the value of **M** estimated from one or more other size measures. It is important to note that E[**M**] is a statistical construct with a specific underlying purpose, namely: "to estimate [unbiased] earthquake recurrence parameters using standard techniques, such as the Weichert (1980) maximum likelihood approach using earthquake counts in magnitude bins" (EPRI/DOE/NRC, 2012, p. 3-12). Further, the equations for E[**M**] in EPRI/DOE/NRC (2012) implicitly assume the consistent use of ordinary least-squares regression in magnitude conversions (Robert R. Youngs, AMEC Foster Wheeler, verbal communication, September 5, 2013).

We decided not to use the "E[**M**]" approach for three reasons. First, we wanted an earthquake catalog with uniform moment magnitude that could serve other general purposes. Because E[**M**] is a statistical construct, it does not serve the same purposes as **M** outside the context of estimating unbiased earthquake recurrence parameters. Second, the use of general orthogonal regression (GOR) is favored by many experts over least-squares regression (LSR) for magnitude

conversions (e.g., Castellaro and others, 2006, Castellaro and Bormann, 2007, Lolli and Gasperini, 2012; see also Gasperini and Lolli, 2014). Consequently, the use of LSR for consistency with the E[**M**] approach as applied in EPRI/DOE/NRC (2012) will not generally provide the best estimate of **M**. Third, by consistently using GOR instead of LSR for magnitude conversions, many of the complexities of the E[**M**] methodology in EPRI/DOE/NRC (2012) can be eliminated.

We call the alternative uniform moment magnitude used to construct our catalog a "best-estimate" moment magnitude. Our Best-Estimate Moment Magnitude (BEM) catalog assigns a value of moment magnitude to each earthquake that is either (a) directly observed as **M** ($\mathbf{M}_{obs}$); (b) a conversion of one or more other size measures to **M** using empirical predictive equations based on GOR (which yield predicted values, $\mathbf{M}_{pred}$); or (c) a reported value of magnitude which we assume to be equivalent to **M** (termed $\mathbf{M}^{\sim}$). Details for constructing the BEM catalog and differences in treating this catalog versus an E[**M**] catalog for estimating earthquake recurrence parameters are explained in a later section, *Methodology for Estimation of Unbiased Recurrence Parameters*.

Magnitude Uncertainty

Quantifying magnitude uncertainty (defined presently) is necessary for three aspects of our analysis of background seismicity: (1) correcting for bias in earthquake recurrence rates (see Musson, 2012, and references therein); (2) specifying the error-variance ratio between dependent and independent variables when using GOR for magnitude conversions; and (3) using inverse-variance weighting when combining different size measures to get a robust estimate of moment magnitude for an individual earthquake.

The magnitude of an earthquake is generally taken as the mean value of magnitude determinations of the same type made at multiple recording stations. In the absence of systematic and discretization (rounding) errors, the mean value of the event magnitude can be viewed as having random errors that are normally distributed with zero mean and standard deviation, σ (Tinti and Mulargia, 1985; Veneziano and Van Dyke, 1985b). Following these cited authors, we define the latter statistic σ (interchangeably using the notation "sigM" in the electronic supplements) as the *magnitude uncertainty*. This term is equivalent to "magnitude accuracy" used by Kagan (2002, 2003).

For each earthquake in the master catalog, we provide a value of uniform moment magnitude and its corresponding uncertainty σ. As noted above, values of σ were also required for other purposes. To determine σ, uncertainties were first assessed for observed values of **M** and for reported values of other size measures that were converted to **M** through regressions. For most of the entries in the master catalog, σ comes from the propagation of uncertainties involved in regressions or from inverse-variance weighting of multiple estimates of **M** from various size measures.

Uncertainties in $\mathbf{M}_{obs}$ and Other Size Measures

Estimating uncertainties in original catalog magnitudes can be a challenging exercise. Example approaches include (1) making "an estimate of the global standard deviation σ (computed for earthquakes with at least three station estimates)" (Castellaro and others, 2006); (2) comparing

statistically independent magnitude estimates from two different catalogs (Kagan 2002, 2003); (3) bootstrapping of station magnitudes to estimate the magnitude error for individual earthquakes in a catalog (Felzer and Cao, 2007); and, when needed data are not available, (4) relying on nominal values of σ for a particular type of magnitude during different time periods (e.g., EPRI/DOE/NRC, 2012, p. 3-21). In this study, approaches (1), (2), and (4) were variously used. For clarity we explain how they were applied to estimate the values of σ specified in several tables.

σ as the average standard error: For some original magnitude types, a data set was assembled for earthquakes with at least three station measures. The sample standard deviation, *STDEV* (with denominator $N - 1$ for a sample size of N), was computed for each earthquake and then corrected for sample bias ($STDEV_{\text{corrected}}$). This correction was made, assuming a normal distribution, by using the bias corrections of Gurland and Trapathi (1971), as tabulated in Rohlf and Sokal (1981), as a function of sample size—in this case, the number of station measures (*Nsta*). For each individual earthquake, the standard error of the *event* magnitude, SE_{em}, was then calculated as the standard deviation of the mean, *SDOM*:

$$SE_{em} = SDOM = \frac{STDEV_{\text{corrected}}}{\sqrt{Nsta}} \tag{E-2}$$

The average standard error of event magnitudes, $\overline{\boldsymbol{SE_{em}}}$, i.e., the average *SDOM* for as large a number of earthquakes as feasible, was adopted as an estimate of the population standard error or magnitude uncertainty, σ, for the specified magnitude type.

Regarding the uncertainty in a *single-station measurement* of a magnitude type, it is useful to note that the average of sample $STDEV_{\text{corrected}}$ of station magnitudes for a sizeable number of earthquakes represents an estimate of the population standard deviation for a single-station magnitude. Dividing the latter by the square root of *Nsta* gives an estimate of σ for an event magnitude having *Nsta* as the number of station measures. We used this approach for some event magnitudes with *Nsta* < 3. Estimates of σ for some original magnitude types using the average-standard-error approach are given in table E-5 (see also table E-6a, added to help give the reader an overview of estimated uncertainties in original catalog magnitudes).

σ from statistics of two different catalogs: Indirect approaches are commonly used to assess magnitude uncertainty for some magnitude types, particularly for observed values of moment magnitude, $\mathbf{M}_{\text{obs}}$. Kagan (2002, 2003) uses error analysis to determine the magnitude uncertainty associated with some magnitude types by comparing reported values in two different catalogs. If the magnitude estimates are statistically independent, the uncertainty in the magnitude difference between the two catalogs is a linear combination of the squared magnitude uncertainties in the first catalog, σ_{M1}, and the second catalog, σ_{M2}, respectively:

$$\sigma_{\Delta M}^2 = \sigma_{M1}^2 + \sigma_{M2}^2 \tag{E-3}$$

where $\sigma_{\Delta M}$ is the standard deviation of the magnitude difference for matched earthquakes in the two catalogs. If one assumes that both catalogs have the same magnitude uncertainty, then $\sigma_{M1} = \sigma_{M2}$ can simply be computed by dividing the observed $\sigma_{\Delta M}$ by the square root of 2. Equation (E-3) can also be used to solve for σ_{M1} or σ_{M2} in cases where one or the other and $\sigma_{\Delta M}$ are

known. Estimates of σ for some original magnitude types using the two-catalog approach are given in table E-6 (see also table E-6a).

Nominal values of σ for $\mathbf{M}_{obs}$: When data were unavailable to assess σ for the instrumental moment magnitudes of specific earthquakes in this study, nominal values of σ for $\mathbf{M}_{obs}$ were adopted from the following tabulation in EPRI/DOE/NRC (2012, p. 3-21), which was constructed for a similar purpose: nominal $\sigma[\mathbf{M}|\mathbf{M}_{obs}] = 0.30$ for 1920–1959; 0.15 for 1960–1975; 0.125 for 1976–1984; and 0.10 for 1985–2008. Where these nominal uncertainty values were adopted for these time periods, they were assumed for both single **M** determinations and (in three cases) for the mean values of two **M** determinations.

Propagation of Uncertainties in Regressing $\mathbf{M}_{obs}$ vs. a Single Size Measure

A noteworthy methodology step in EPRI/DOE/NRC (2012) is shown in their equation (3.3.1-8), which with adapted notation is reproduced here as

$$\sigma^2[\mathbf{M}|\mathrm{X}] = \sigma^2[\mathbf{M}_{obs}|\mathrm{X}] - \sigma^2[\mathbf{M}|\mathbf{M}_{obs}] \qquad \text{(E-4)}$$

In words, when one regresses observed values of moment magnitude, $\mathbf{M}_{obs}$, against another size measure X, the resulting uncertainty $\sigma^2[\mathbf{M}|\mathrm{X}]$ (expressed as a variance) in <u>true</u> **M** given X equals $\sigma^2[\mathbf{M}_{obs}|\mathrm{X}]$, the square of the standard error in the predicted value of **M** from the regression, minus or reduced by $\sigma^2[\mathbf{M}|\mathbf{M}_{obs}]$, the variance in the observed values $\mathbf{M}_{obs}$ used in the regression of $\mathbf{M}_{obs}$ versus X. From basic propagation of errors, this rule applies whether LSR or GOR is used.

Note: For all of our linear regressions, the statistic used to express the standard error in the predicted value of y is the standard error of estimate of y on x, $S_{y,x}$, given by

$$S_{y,x} = \sqrt{\frac{\sum_i^N (y_i - y_i')^2}{DOF}} \qquad \text{(E-5)}$$

where y_i and y_i' are the observed and predicted values of y, respectively, for the ith data point and DOF is the number of degrees of freedom. Given N paired values of x and y, DOF is $N - 2$ for the linear regressions and $N - 3$ for the non-linear regressions (which have three constants).

Propagation of Uncertainties in Two-Step Regressions

For many earthquakes in the catalog, **M** was estimated using two sequential regression steps, for which the propagation of uncertainties had to be analyzed. Because direct measurements of **M** make up a small fraction of the earthquake catalog, we encountered secondary size measures, X_2, for which direct regression of $\mathbf{M}_{obs}$ versus X_2 was not feasible. However, in most cases we had a regression for $\mathbf{M}_{obs}$ versus a primary size measure X_1 (let us call it Regression A), and we were able to develop a regression for X_1 versus X_2 (let us call it Regression B). If values of X_1 are estimated from X_2 using Regression B and then substituted in Regression A to estimate **M**, the resulting uncertainty in **M**, $\sigma[\mathbf{M}|X_2]$ must be determined.

Our approach to this problem was to estimate the additional uncertainty resulting from the use of $X_1 = \mathrm{f}(X_2)$ in Regression A, assuming that X_1 and X_2 are independent random variables and using

basic theorems for the linear combination of variances (e.g., Chapman and Schaufele, 1970, p. 131). Letting $\mathbf{M}_{obs} = a_1 X_1 + a_2$ for Regression A and letting $X_1 = b_1 X_2 + b_2$ for Regression B, where a_i and b_i are constants, the following equation was derived for the uncertainty in **M** calculated from Regression A with the substitution of $X_1 = f(X_2)$:

$$\sigma^2[\mathbf{M}|X_2] = \sigma^2[\mathbf{M}|X_1] + a_1^2\,(\sigma^2[X_1|X_2] - \sigma^2\,[X_1]) \qquad \text{(E-6)}$$

where $\sigma^2[X_1|X_2]$ is the square of the standard error of estimate, $S_{y,x}$, from Regression B; $\sigma^2\,[X_1]$ is the variance of values of X_1 used to develop Regression A; and $\sigma^2[\mathbf{M}|X_1]$ is the variance in true **M**, given X_1. The latter, as specified by equation (E-4), is

$$\sigma^2[\mathbf{M}|X_1] = \sigma^2[\mathbf{M}_{obs}|X_1] - \sigma^2[\mathbf{M}|\mathbf{M}_{obs}] \qquad \text{(E-7)}$$

To give a concrete example, consider the case of $X_1 = M_L$ UU1 determined by the University of Utah and $X_2 = m_b$ PDE2 determined by the USGS. The conversion relationships based on general orthogonal regressions are given in tables E-8 and E-10. To estimate **M**, given m_b PDE2, we first use conversion relationship CR-9 to estimate M_L UU1 and then use conversion relationship CR-1. For this circumstance, $\sigma[\mathbf{M}|\,M_L\text{ UU1}] = 0.139$, $a_1 = 0.791$, $\sigma[M_L\text{ UU1}|\,m_b\text{ PDE2}] = 0.429$, and $\sigma[M_L\text{ UU1}] = 0.07$ (table E-10). The desired uncertainty, $\sigma[\mathbf{M}|m_b\text{ PDE2}]$, is thus given by

$$\sigma[\mathbf{M}|m_b\text{ PDE2}] = \sqrt{0.139^2 + 0.791^2(0.429^2 - 0.07^2)} = 0.362 \qquad \text{(E-8)}$$

Propagation of Uncertainties in Inverse-Variance Weighting

The procedure for finding the best estimate of a quantity x from several measured (or estimated) values, each with a corresponding uncertainty σ, is straightforward using a weighted average (see, for example, Taylor, 1982, p. 148–150). For the ith value, its weight w_i is the inverse of the variance associated with that value ($1/\sigma_i^{\,2}$); hence, inverse-variance weighting. Formulas from Taylor (1982) provide an instructive starting point:

$$x_{best} = \frac{\sum_i w_i x_i}{\sum_i w_i} \qquad \text{(E-9)}$$

for which the uncertainty in x_{best} is given by

$$\sigma_{x_{best}} = \frac{1}{\sqrt{\sum_i w_i}} \qquad \text{(E-10)}$$

Referring to equation (3.3.1-10) in EPRI/DOE/NRC (2012) and following notation in that report, if we seek a best estimate of uniform moment magnitude from a vector **X** of R observed size measures, for which X_i is a single measure of the vector **X**, then the combined variance, CV, for the complete inverse-variance weighted estimate is

$$\sigma^2[\mathbf{M}|\mathbf{X}] = \frac{1}{\sum_i \frac{1}{\sigma^2\,[\mathbf{M}|X_i]}} \qquad \text{(E-11)}$$

which is readily seen to be an alternative expression of equation (E-10).

As explained earlier, we depart from the EPRI/DOE/NRC (2012) methodology by not using E[**M**] as our uniform estimate of moment magnitude. Equation (3.3.1-9) in that report specifies how to calculate the inverse-variance-weighted estimate of E[**M**]. In similar form, the equation we use to calculate a best estimate of **M** from multiple size measures using inverse-variance weighting is

$$\mathbf{M}_{best} = \sum_{i}^{N} \frac{\mathrm{CV}}{\sigma^2[\mathbf{M}|X_i]} \cdot \mathbf{M}|X_i \qquad \text{(E-12)}$$

where CV = $\sigma^2[\mathbf{M}|\mathbf{X}]$ is the combined variance from equation (E-1), $\mathbf{M}|X_i$ is the estimate of **M** (i.e., $\mathbf{M}_{\text{pred}}$ or $\mathbf{M}^{\sim}$), given X_i, and $\sigma^2[\mathbf{M}|X_i]$ is the variance from the latter estimate (we introduce "CV" to simplify notation and to help guide calculations in the electronic supplements).

Equation (3.3.1-9) of EPRI/DOE/NRC (2012) differs from equation (E-12) in that it includes a correction term, $+(R-1)\beta \cdot \mathrm{CV}$, where $\beta = b \ln\{10\}$. This correction term is obviated when the conversion of the X_i size measures to **M** is based on orthogonal regressions instead of least squares regressions.

METHODOLOGY FOR ESTIMATION OF UNBIASED RECURRENCE PARAMETERS

Our approach to estimating earthquake recurrence parameters involves a standard procedure used in Probabilistic Seismic Hazard Analysis—namely, the use of the Weichert (1980) maximum-likelihood approach to fit a truncated exponential distribution to earthquake counts in magnitude bins (see, for example, EPRI/DOE/NRC, 2012). In mathematical form, the truncated exponential distribution can be expressed (see Youngs and Coppersmith, 1985) as

$$N(m) = N(m_0)\,\frac{10^{-b(m-m_0)} - 10^{-b(m_u-m_0)}}{1 - 10^{-b(m_u-m_0)}} \qquad \text{(E-13)}$$

where $N(m)$ is the number of earthquakes per year of magnitude m or larger, m_0 is the minimum magnitude, m_u is the upper bound magnitude, and b is the slope constant in the frequency-magnitude relation. Two known potential sources of bias that can affect the seismicity-rate calculations are magnitude uncertainty and the discretization or rounding of magnitude values to some specified nearest decimal value.

Correcting for Magnitude Uncertainty

The effect of magnitude uncertainty on calculations of earthquake rate parameters is described by Musson (2012), who reviews different approaches to correct for bias in frequency-magnitude relations. He also underscores the complexity of the issue. Basically, because of the exponential distribution of magnitude, observed magnitudes (measured with normally distributed errors) together with their counts in discrete bins can have "apparent" values that differ from their "true" values—typically shown using simulated earthquake catalogs.

As a conceptual guide, figure E-2 illustrates the equivalence of approaches proposed independently by Tinti and Mulargia (1985) and Veneziano and Van Dyke (1985b) to correct for magnitude uncertainty σ in calculating unbiased ("true") seismicity rates. [Note: The draft report

by Veneziano and Van Dyke (1985b) is difficult to access. Veneziano and Van Dyke's methodology was implemented and is described in EPRI (1988).]

Without dwelling on the mathematical equations (see Tinti and Mulargia, 1985; EPRI/DOE/NRC, 2012), the following key points can be grasped from figure E-2. First, in a frequency-magnitude plot, bias caused by magnitude uncertainty can equivalently be corrected either in the *x*-direction using an adjusted magnitude called **M*** ("M-star") or in the *y*-direction using an adjusted rate called *N** ("N-star"). Second, the sign of the necessary corrections depends on whether the starting data lie along the line based on values of $\mathbf{M}_{obs}$ or its equivalent, as is the case for the BEM catalog, or along the line based on values of E[**M**], as is the case for an E[**M**] catalog developed following the equations and steps of the EPRI/DOE/NRC (2012) methodology. EPRI/DOE/NRC (2012) showed that for catalogs with variable levels of magnitude completeness, the *N** approach performs better than the **M*** approach. Accordingly, we used the *N** approach in this study. The specific steps we followed are described in a later section, *N* Values and Seismicity Rate Parameters.*

Equivalence of Best-Estimate Moment Magnitudes to $\mathbf{M}_{obs}$

Our assertion that our best-estimate moment magnitudes are equivalent to $\mathbf{M}_{obs}$, in terms of where they lie in the frequency-magnitude space of figure E-2, is essential to establish because it is fundamental to how we apply correction terms for magnitude uncertainty vis-à-vis figure E-2. To begin, magnitudes in our BEM catalog determined as $\mathbf{M}_{obs}$ are straightforward and need no further comment.

Our second type of best-estimate moment magnitudes are estimates of **M** using the results of orthogonal regressions of $\mathbf{M}_{obs}$ vs. other size measures. In the E[**M**] methodology, a key element is that all least squares regressions of $\mathbf{M}_{obs}$ vs. other size measures yield estimates of **M** that lie along the E[**M**] line in figure E-2. This situation changes, however, if orthogonal regression is used. Based on guidance and numerical simulations from Gabriel Toro of Lettis Consultants International, Inc., one of the principal experts on the EPRI/DOE/NRC (2012) methodology team: if orthogonal regression is used, then the results should be treated as equivalent to $\mathbf{M}_{obs}$ and *N** should be calculated as if no regression was performed. This guidance was first provided to us during a WebEx online meeting convened by the USGS on September 5, 2013, to address methodology issues relating to the treatment of magnitude uncertainty for U.S. National Seismic Hazard Maps. As part of the teleconference, G. Toro distributed and discussed a PowerPoint presentation titled, "Uncertainty in magnitude: Numerical experiment with M_L [to] M_w using orthogonal regression." Confirmation of how to correctly handle results of orthogonal regressions was also provided to us by G. Toro in follow-up written communications during September 2013.

The third type of best-estimate moment magnitudes in our BEM catalog are those identified as **M**˜. In this case, we followed guidance provided to us by Robert ("Bob") Youngs (AMEC Foster Wheeler, written communication, Aug. 8, 2013), another of the principal experts on the EPRI/DOE/NRC (2012) methodology team. According to his guidance, if one assumes that a magnitude scale is equivalent to **M**, then the measured magnitude values should be treated as "noisy **M** values." They thus lie along the $\mathbf{M}_{obs}$ line in figure E-2, above the line of "true" recurrence rates, and are corrected accordingly. This guidance from Bob Youngs was confirmed during the above-mentioned USGS teleconference on September 5, 2013.

Effect of Magnitude Rounding

The potential overestimation of seismicity rates due to the rounding of reported magnitudes in an earthquake catalog was examined by Felzer (2007). Note that the object of her study, an earthquake catalog for California, involved a substantial proportion of events in the early to middle 1900s whose assigned magnitudes (M_L) were rounded to the nearest 0.5. Further, because of an assumed equivalence between M_L and **M**, rounded values of M_L (except where a measured value of **M** was also available) translated directly into similarly rounded values of **M** in her moment-magnitude catalog, thus motivating the need for correction. In the EPRI/DOE/NRC (2012) study, the potential impact of rounding of data to the nearest 0.1 magnitude unit was examined using simulated data sets, and statistical tests showed that the effect of the rounding could be ignored.

In this study, all values of **M** are uniformly rounded to the nearest 0.01 magnitude unit as the result of calculating **M** either from a measured value of scalar seismic moment or from magnitude-conversion relationships, in which case the effects of rounding in original size measures are subsumed in the regressions. The only exceptions to rounding **M** to the nearest 0.01 magnitude unit in our BEM catalog are those associated with values of $\mathbf{M}^{\sim}$, which were reported to the nearest 0.1 magnitude. For the WGUEP region, none of the independent mainshocks has an $\mathbf{M}^{\sim}$ value within a completeness period that enters into our final seismicity-rate calculations; for the UTR, two such events enter into the seismicity-rate calculations. The effect of rounded magnitude values was judged to be insignificant in our calculations and was ignored. Felzer's (2007) correction for magnitude rounding, given a *b*-value of 1.05 (determined in our initial processing of the BEM catalog) and rounding to the nearest 0.01, would involve multiplying the number of earthquakes above the completeness threshold by 0.988.

MAGNITUDE CONVERSION RELATIONSHIPS

A major part of constructing our BEM catalog was the conversion of other size measures to a best estimate of **M**. Key steps involved (1) compiling reliable measurements of observed moment magnitude $\mathbf{M}_{obs}$ to form the basis for developing conversion relationships of other size measures to **M**; (2) using general orthogonal regression (GOR) to regress $\mathbf{M}_{obs}$ on other size measures, yielding $\mathbf{M}_{pred}$; and (3) inverse-variance weighting of multiple estimates of **M**, including $\mathbf{M}_{pred}$ from different size measures and occasionally $\mathbf{M}^{\sim}$. Where $\mathbf{M}_{obs}$ was reported for an earthquake, it was given precedence over other size measures in the catalog, following rules described below.

The magnitude conversion relationships developed in this study should be considered region-specific. Our primary goal was achieving uniform moment magnitude estimates in the UTR, so we focused our data selection on the UTR, expanding the use of data from the EBR only where necessary. In some cases we supplemented a particular data set with size measures from a few large earthquakes outside the UTREXT (see figure E-3). The region of applicability of individual conversion relationships is indicated in the tables.

Moment Magnitude Data

Observed moment magnitudes were compiled for 114 earthquakes ($3.17 \leq \mathbf{M} \leq 7.35$) in or near the UTREXT (figure E-3), including 107 in the master catalog and seven supplementary events. The latter include three mainshocks outside the UTREXT (Hebgen Lake, Montana, 1959; Borah Peak, Idaho, 1983; and Kelly, Wyoming, 2010) together with four earthquakes in the UTREXT in late 2012 and early 2013. Documentation of the moment magnitude data is provided in Electronic Supplement E-2. For each earthquake, the documentation includes hypocentral information, the source of the seismic moment from which $\mathbf{M}_{obs}$ was calculated using the definition of Hanks and Kanamori (1979), and an assessment of magnitude uncertainty. A breakdown by source of the 114 values of $\mathbf{M}_{obs}$ used in this study, or more precisely the reported values of M_0 from which $\mathbf{M}_{obs}$ was calculated, is given in table E-7. Reported seismic moments for known and suspected mining-related seismic events are excluded from the list and were not used in developing magnitude conversion relationships.

For earthquakes in 1989 and later, all values of $\mathbf{M}_{obs}$ were calculated from a *single* seismic moment. In cases where more than one reported value of M_0 was available, the selected value followed the hierarchy shown in the upper part of table E-7. Thus, if a seismic moment was reported by more than one source, the Global CMT (GCMT) catalog was given precedence, followed by Whidden and Pankow (2012) and so forth, down to the Oregon State University moment-tensor catalog. Most of the UUSS moment tensors (MTs) we used are for earthquakes within the UTR and are given priority above corresponding SLU MTs, chiefly because the UUSS MTs are more numerous in our region of interest and because we have a better understanding of their quality control.

As part of their study, Pechmann and Whidden (2013) found that values of $\mathbf{M}_{obs}$ (as we define it) from UUSS seismic moments (Whidden and Pankow, 2012; Whidden, unpublished) agree closely with those calculated from seismic moments reported by St. Louis University (Herrmann and others, 2011; SLU moment-tensor website), with mean $\Delta\mathbf{M} = 0.001$ and $\sigma_{\Delta M} = 0.071$ for 36 events (table E-6). In contrast, Pechmann and Whidden (2013) found a systematic difference between GCMT $\mathbf{M}_{obs}$ values and UUSS/SLU $\mathbf{M}_{obs}$ values. To compensate, we reduced all GCMT $\mathbf{M}_{obs}$ values in our catalog by 0.14, based on the average difference between GCMT and SLU $\mathbf{M}_{obs}$ values for 24 shallow earthquakes that occurred in the western U.S. between 1998 and 2013 ($\sigma_{\Delta M} = 0.076$; table E-6).

In our compilation of moment magnitude data, we excluded seismic moments published by Doser and Smith (1982) that were determined from long-period spectral levels of body waves for 19 earthquakes in the UTR prior to 1977. Shemeta (1989) discusses problems with the data used by Doser and Smith (1982), particularly single-station data at regional distances, which may account for the unusually high seismic moments relative to M_L determined by them for earthquakes of $M_L < 5.0$. For five of the excluded seismic moments, including those for the three largest shocks, we used available values of M_0 that were determined from inversions of either long-period waveforms or surface-wave spectra. Based on values of $\mathbf{M}_{obs}$ from these other data, together with additional values of $\mathbf{M}_{pred}$, we infer that Doser and Smith (1982) systematically overestimated M_0 for shocks less than about $\mathbf{M}$ 5.75.

We examined values of $\mathbf{M}_{obs}$ that were calculated from seismic moments reported by Oregon State University (OSU) for earthquakes in the UTR during 1995–1998 and judged them to be

reliable. In three cases, a corresponding $\mathbf{M}_{obs}$ was available from Whidden and Pankow (2012), and the paired values were virtually identical. In seven other cases, $\mathbf{M}_{obs}$ from the OSU data agreed closely with $\mathbf{M}_{pred}$ from M_L determined by the UUSS. OSU moment tensors elsewhere in the Intermountain Seismic Belt, north of the UTR, appeared to yield $\mathbf{M}_{obs}$ systematically lower than $\mathbf{M}_{pred}$ from UUSS M_L data and were not used.

General Orthogonal Regression vs. Least Squares Regression

Castellaro and others (2006) discuss the underlying assumptions for least squares regression (LSR), most notably that the uncertainty in the independent (predictor) variable is at least an order of magnitude smaller than that in the dependent (response) variable. They point out that this assumption is seldom satisfied in magnitude conversions. For unbiased regression parameters, Castellaro and others (2006) show that general orthogonal regression (GOR) is superior to LSR for magnitude conversions when both dependent and independent variables are affected by uncertainty. GOR requires that the ratio η of the dependent variable variance (σ_y^2) to the independent variable variance (σ_x^2) be known. If η is unknown, assuming a value of 1 and using simple orthogonal regression still generally performs better than LSR (Castellaro and Bormann, 2007).

In this study, we were able to measure or reasonably estimate the uncertainties in both dependent and independent variables involved in our magnitude conversions, allowing us to apply GOR. GOR calculations for the linear conversion relations were performed in Excel spreadsheets using equations from Castellaro and others (2006), corrected for typographic errors that we confirmed by comparison with the original equations in Fuller (1987) that Castellero and others (2006) referenced. For the one non-linear conversion relation that we determined, CR-12, we carried out the GOR using a generalization of the method of Cheng and Van Ness (1999, p. 10) for two predictor variables (described in Pechmann and others, 2010).

Presentation of Magnitude Conversion Results

Up to this point, we have laid the methodology groundwork for presenting and discussing our magnitude conversion relationships (CRs), which entail considerable detail. We summarize much of this detail in tables. We begin with overviews of available magnitude data and the CRs we developed and then proceed to discuss the individual CRs, some under grouped headings.

Overview of Reported Magnitudes

Figure E-4 gives a schematic overview of the magnitude types reported in the source catalogs for the UTREXT. These data shaped our efforts to pursue conversion relationships to a uniform moment magnitude. For the historical period prior to July 1962 (subcatalog A), instrumentally-determined magnitudes are relatively sparse. Seismic moments are available for the 1934 Hansel Valley, Utah, earthquake and its largest aftershock, and an assortment of instrumental magnitudes is available for 68 earthquakes between 1917 and 1962. Most of these are M_L magnitudes determined at Pasadena for earthquakes in the southwestern part of the UTREXT between 1936 and 1962. An early 1917 magnitude comes from Wiechert seismographs operating at Reno, Nevada (Jones, 1975). Thus, size estimates for historical earthquakes prior to July 1962 rely greatly upon non-instrumental information. Size measures that we converted to **M** were: the maximum value of Modified Mercalli Intensity, MMI (I_0); total felt area (FA); and

the extent of area shaken at or greater than MMI IV, V, VI, and VII (A_{IV}, A_V, A_{VI}, and A_{VII}, respectively).

For the instrumental period from July 1962 through September 2012 (subcatalogs B and C), figure E-4 shows a gradually increasing availability of **M** with time. But most of the available data require reliance upon other instrumental magnitudes that varied with time and reporting agency. The instrumental magnitudes in the source catalogs that we converted to **M** come primarily from the UUSS and the USGS, and secondarily from the International Seismological Centre, ISC. They are Richter local magnitudes (M_L), coda or duration magnitudes (M_C, M_D), or body-wave magnitudes (m_b). There are ten values of M_S reported by the USGS for earthquakes in the UTREXT between 1984 and 2008, which we discuss but did not attempt to convert to **M**. The remainder of the magnitude data consists of more than a dozen other miscellaneous magnitude types for which data were inadequate for conversion to **M**. These magnitude types appear as the sole instrumental magnitude available for 188 earthquakes in the master catalog. We discuss them under the label **M**~.

Overview of Magnitude Conversion Relationships

Using the available data represented on figure E-4, we developed 16 new CRs and refined two CRs earlier developed by Pechmann and Whidden (2013). For each of these 18 magnitude conversions, we performed both GOR and LSR, with results shown for comparison on each regression plot that we present. Table E-8 summarizes the GOR results, which provide the basis for estimates of **M** that enter into our BEM catalog. For the convenience of others who may wish to pursue the alternative E[**M**] approach using our data and the correction terms in EPRI/DOE/NRC (2012), we summarize our LSR results in table E-9.

Throughout, counterpart CRs in the tables and figures for GOR and LSR are given the same ID, but the letter "a" is appended to the CR-ID for the LSR results (e.g., CR-1a). Our discussion of the CRs focuses on the GOR results.

Based on our discussions with Gabriel Toro and Bob Youngs, practitioners are advised to <u>consistently</u> use either GOR or LSR in developing magnitude conversion relations. Otherwise, neither the BEM nor E[**M**] approaches to correcting event counts for magnitude uncertainty, as we have described them, can be used correctly without other complicated adjustments.

Regression statistics related to the CRs are presented in table E-10 for each GOR and in table E-11 for each LSR. Terms specific to GOR in table E-10 include σ_y and σ_x, the uncertainties in the dependent and independent variables, respectively, and η, the ratio of ${\sigma_y}^2$ to ${\sigma_x}^2$. In both tables E-10 and E-11, ID is the CR-ID in table E-8 or E-9; $S_{y,x}$ is the standard error of estimate of y on x; σ[**M**|X] is the uncertainty in true **M**, given the size measure X; and R^2 is the coefficient of determination for the regression. The minimum and maximum values of the independent variable x for each LSR, given in table E-11, are the same as for its counterpart GOR in table E-10.

Plots for each of the 13 regressions in tables E-10 and E-11 and for two model fits relating M_L magnitudes determined by the USGS to M_L magnitudes of the UUSS are shown in figures E-5 through E-15. A summary of the miscellaneous magnitudes encountered in the merged source catalogs for which data were insufficient to develop conversion relationships to **M** is presented in

table E-13. The table also gives the value of σ that we assessed for each of these magnitude types and its basis.

Except for CR-12 (and 12a), which has a non-linear form that follows EPRI/DOE/NRC (2012), all the conversion relationships to **M** that we developed are linear, as justified by the resulting correlation coefficients for our linear regressions and, for some relationships, by antecedent studies. M_L, M_C (or M_D), and m_b are commonly shown to be linearly correlated with **M**, at least over limited ranges of **M** up to 3.0 to 3.5 magnitude units (e.g., Braunmiller and others, 2005; EPRI/DOE/NRC, 2012). The same is true for the logarithm of the area shaken at or greater than a specified MMI in the western U.S. (Hanks and Johnston, 1992; Toppozada and Branum, 2002). In developing some of the CRs we chose to limit the size range of the data points used (CRs 8, 8a, 9, 9a, 10, 10a) or to use segmented linear regression (CRs 13 and 14 , along with their LSR counterparts). For CRs 8, 9, and 10 (and their LSR counterparts), which involve values of m_b PDE during specified time periods, the extrapolation of the CRs outside the defined segments of the independent variable is risky—as evident from inspection of figures E-9, E-10, and E-11.

For the linear regressions, the square root of R^2 listed in tables E-10 and E-11 yields the linear correlation coefficient R, which provides one basis for justifying the linear models. Using a standard table for the probabilities of correlation coefficients (e.g., Appendix C in Taylor, 1982) one can quantitatively assess the linear correlation of two variables. Such a table gives the probability $P_N(|R| \geq |R_o|)$ that N measurements of two uncorrelated variables would result in a coefficient R as large as observed, R_o. Small P_N indicates a likely correlation. If $P_N(|R| \geq |R_o|) \leq 0.05$, the correlation is deemed *significant*; if ≤ 0.01, then *highly significant* (Taylor, 1982, p. 248). Based on the N and R^2 statistics in tables E-10 and E-11, the evidence for linear correlation is highly significant for every one of the linear regressions.

$\mathbf{M_{pred}}$ from UUSS $\mathbf{M_L}$ Magnitudes

Richter local magnitude, M_L, measured on paper (and later synthetic) Wood-Anderson (W-A) seismograms, has been reported by the UUSS since mid-1962. Figure E-4 indicates two periods of M_L UU. M_L UU1 designates revised M_L values in the UUSS catalog since 1981 described by Pechmann and others (2007). M_L UU2 designates M_L values predating 1981 and based exclusively on paper seismograms from up to four W-A stations in Utah, as described by Griscom and Arabasz (1979). Empirical M_L station corrections determined by Pechmann and others (2007) minimize differences between M_Ls calculated from paper and synthetic W-A records and were designed to ensure uniformity of UUSS M_L values since 1962. The reason for distinguishing M_L UU1 from M_L UU2 is a change in magnitude uncertainty.

CR-1, 1a: Pechmann and Whidden (2013) used 65 data pairs for earthquakes predominantly in the UTR to regress $\mathbf{M}_{obs}$ (as defined herein) on M_L UU. The data consist of 64 paired values from 1983–2013 and one from 1967, and are plotted on figure E-5. The regression results reported here are a refinement of those given by Pechmann and Whidden (2013). In the refined regressions, GCMT $\mathbf{M}_{obs}$ values were reduced by 0.14, for reasons explained earlier in the section *Moment Magnitude Data*. For CR-1, the value of 0.139 for $\sigma[\mathbf{M}|M_L \text{ UU1}]$ comes from $S_{y,x} = 0.1473$ from the GOR reduced by the average uncertainty of 0.05 for the values of $\mathbf{M}_{obs}$ used in the GOR [see equation (E-4) and table E-10].

CR-2, 2a: A conversion relationship from M_L UU2 to **M** is based on the uniformity of M_L UU1 and M_L UU2 except for their differing magnitude uncertainty. Accordingly, we developed a two-step conversion, using CR-1, in which a larger σ of 0.24 for M_L UU2 (see footnote 3 in table E-5) is accounted for. Equation (E-6) yields a value of 0.229 for the uncertainty σ[**M**|M_L UU2] (table E-8). The calculation follows the example of equation (E-8), using the value of 0.24 for σ[M_L UU1|M_L UU2].

M_{pred} from UUSS M_C Magnitudes

Coda or duration magnitudes reported by the UUSS have changed with time, as indicated on figure E-4. This change is chiefly due to changes in recording methods—from paper seismograms used from July 1962 through September 1974 (M_C UU3) to 16-mm film recorders used from October 1974 through December 1980 (M_C UU2) to digital recording starting in January 1981 (M_C UU1). UUSS coda-magnitude scales for all three periods have been calibrated to the UUSS M_L scale (Griscom and Arabasz, 1979; Pechmann and others, 2010).

CR-3, 3a: The M_C scale calibrated by Pechmann and others (2010), which we designate M_C UU1, is the result of major efforts to automate and homogenize coda magnitudes determined by the UUSS from digital recordings since 1981. Pechmann and Whidden (2013) used 63 data pairs for earthquakes predominantly in the UTR from 1983 to 2013 to regress $\mathbf{M}_{obs}$ on M_C UU1 (figure E-6). Just as for CR-1, the regression results reported here are a refinement of those given by Pechmann and Whidden (2013). For CR-3, the value of 0.225 for σ[**M**|M_C UU1] comes from $S_{y,x}$ = 0.2310 from the GOR reduced by the average uncertainty of 0.05 for the values of $\mathbf{M}_{obs}$ used in the GOR [see equation (E-4) and table E-10].

CR-4, 4a: A conversion relationship from M_C UU2 (measured on 16-mm Develocorder film) to **M** is based on the calibration of M_C UU2 to M_L UU with a standard error of estimate of 0.27 (Griscom and Arabasz, 1979). A two-step conversion was developed, using CR-1, in which the larger σ of 0.27 for M_C UU2 is accounted for. Equation (E-6) yields a value of 0.249 for the uncertainty σ[**M**|M_C UU2] (table E-8). The calculation follows the example of equation (E-8), using the value of 0.27 for σ[M_L UU1|M_C UU2].

CR-5, 5a: A conversion relationship from M_C UU3 (measured on short-period, vertical-component Benioff seismograms) to **M** is based on the calibration of M_C UU3 to M_L UU with a standard error of estimate of 0.28 (Griscom and Arabasz, 1979). A two-step conversion was developed, using CR-1, in which the larger σ of 0.28 for M_C UU3 is accounted for. Equation (E-6) yields a value of 0.256 for the uncertainty σ[**M**|M_C UU3] (table E-8). The calculation follows the example of equation (E-8), using the value of 0.28 for σ[M_L UU1|M_C UU3].

M_{pred} from USGS M_L Magnitudes

M_L magnitudes designated "ML GS" appear in the USGS SRA catalog for earthquakes as early as 1969. Because this start time predates 1973, when the National Earthquake Information Center (NEIC) was transferred from the National Oceanic and Atmospheric Administration to the USGS, the designation "ML GS" for the pre-1973 earthquakes is confusing—but, more importantly, we are uncertain how those magnitudes were actually calculated.

Information from Bruce Presgrave (USGS, written communication, Nov. 29, 2012) is central to our understanding of M_L GS as it was reported by the USGS beginning in 1974 until sometime in

2011, when the USGS/NEIC began to compute M_L from synthetic horizontal W-A seismograms using its *Hydra* earthquake processing system. The following is an excerpt from Bruce Presgrave's written communication:

> Our magnitude we call ML (GS) has been the same from [1974] until we started using Hydra routinely for nearly all local events about 1 year ago. 'Our' (GS) ML was computed from the largest amplitude on the vertical short-period seismogram, with the amplitude adjusted to what it would have been on a Wood-Anderson instrument (i.e., nominal 2800 magnification). This was a two-stage process, either manually or by computer. First, we'd use the instrument calibration to convert from trace to ground amplitude, then convert that ground amplitude back to an amplitude at 2800 magnification. If the event were in or close to an area where a regional network (such as yours) was using ML off a true W-A instrument, we would often adjust the magnitude so that our values agreed more closely to what you or Caltech or Berkeley (etc.) might get. This usually involved adding 0.3 to 0.5 to the ML we computed off the vertical instrument.

Other relevant information in the written communication includes: (1) an evolution from the brief initial use of paper records to data from 16-mm film recorders to digital data, beginning about 1981; and (2) the routine calculation of M_L as an average, using data from any calibrated station available at NEIC that was within 5.4 degrees of the hypocenter. By Presgrave's account, the USGS/NEIC procedures used to determine M_L from 1974 to 2012 were basically pragmatic. Nevertheless, we found a good empirical correlation of M_L GS values to M_L UU values in the UTR (figure E-7) and in the EBR (figure E-8) that enabled conversion relationships to **M**.

CR-6, 6a: A conversion relationship from M_L GS to **M** applicable to the UTR for 1974−2012 is based on a comparison of M_L GS to M_L UU. Figure E-7 shows data for 69 data pairs for this time period. Because of the basic equivalence of both magnitude scales (Richter's amplitude-distance corrections are used for both), and given the apparent linear correlation between them, we adopted a simple offset model for which M_L UU = M_L GS − 0.11 ± 0.245 (1 std. deviation). An examination of a subset of the data (12 paired values) for the 1974−1980 period indicated a slightly larger offset of – 0.16 ± 0.34, but given the sparse data, we chose to use the grouped data for the entire 1974−2012 period.

A two-step conversion to **M** was then developed using CR-1 for the second step, as indicated in table E-8. Equation (E-6) yields a value of 0.232 for the uncertainty σ[**M**|M_L GS] (table E-8). The calculation follows the example of equation (E-8), using the value of 0.245 for σ[M_L UU1|M_L GS].

In completing the BEM catalog, we encountered four earthquakes in the UTR during 1970−1973 for which M_L GS (2.6−3.2) was the only instrumental magnitude available; we applied CR-6 to estimate **M** for these earthquakes.

CR-7, 7a: Similar to our approach for CR-6, we developed a conversion relationship from M_L GS to **M** applicable to the EBR for 1981−2012. Figure E-8 shows 280 data pairs for this region and time period. There were no data pairs for earthquakes prior to 1981, and the data set is heavily dominated by numerous aftershocks of the Draney Peak, Idaho, earthquake of February 3, 1994 ($\mathbf{M}_{obs}$ = 5.66), and of the Wells, Nevada, earthquake of February 21, 2008 ($\mathbf{M}_{obs}$ = 5.91).

For the 280 data pairs, we adopted a simple offset model, for which M_L UU = M_L GS + 0.09 ± 0.242 (1 std. deviation).

A two-step conversion to **M** was then developed using CR-1 for the second step, as indicated in table E-8. Equation (E-6) yields a value of 0.230 for the uncertainty σ[**M**|M_L GS] (table E-8). The calculation follows the example of equation (E-8), using the value of 0.242 for σ[M_L UU1|M_L GS].

In completing the BEM catalog, we encountered nine earthquakes in the EBR during 1969−1973 for which M_L GS (2.7−4.0) was the sole available size measure; we applied CR-7 to estimate **M** for these earthquakes.

$\mathbf{M_{pred}}$ from $\mathbf{m_b}$ PDE Magnitudes

The magnitude m_b PDE (also designated m_b GS after 1973) refers to teleseismic short-period body-wave magnitudes reported in the Preliminary Determination of Epicenters (PDE) bulletins published by the USGS/NEIC and its predecessors. Dewey and others (2003, 2004, 2011, including pdf copies of the corresponding poster presentations provided to us by J. Dewey, USGS) describe time-varying changes in m_b PDE, which they associate with temporal changes in procedures and data used at the NEIC in calculating this magnitude. We used their observations for earthquakes less than magnitude 6 to help us distinguish three periods for which m_b PDE in the UTREXT appears to differ. The periods are illustrated on figure E-4 and designated in table E-8 as m_b PDE1 (1991–2012), m_b PDE2 (1978–1990), and m_b PDE3 (1963–1977).

We chose 1991 as the start for m_b PDE1. This is the year in which the USGS inaugurated the U.S. National Seismograph Network, providing broadband digital data to the NEIC from a rapidly growing number of stations from which m_b began to be increasingly calculated from filtered data simulating the output of a short-period seismometer (Dewey and others, 2003). At about 1990, Dewey and others (2004) saw evidence of a decrease in m_b PDE values of about 0.2 magnitude unit when comparing m_b PDE with m_b predicted from local magnitudes such as M_L at Pasadena and Berkeley.

The change from m_b PDE3 to m_b PDE2 in 1978 marks when the USGS/NEIC sharply reduced the use of amplitudes and periods measured at regional distances between 5° and 15° (these tend to increase event m_b) to calculate m_b PDE for shallow-focus U.S. earthquakes (Dewey and others, 2003, 2004). During the period prior to 1978, other factors contributing to the heterogeneity of m_b PDE3 for smaller earthquakes include: computations from a relatively small number of stations; changes in the distribution of contributing stations, such as the closing of VELA arrays in the early 1970s (including UBO in Utah); and the measurement of amplitudes and periods from the first three cycles of the initial P-wave rather than from a larger time window (Dewey and others, 2003, 2004).

CR-8, 8a: The magnitude conversion from m_b PDE1 to **M** for the period 1991–2012 is the most straightforward of the three m_b PDE conversions. The availability of a sufficient number of data pairs allows a direct regression of $\mathbf{M}_{obs}$ on m_b PDE1 (figure E-9). Figure E-9 shows a divergence of data points for the smallest earthquakes, which is understandable for measurements of m_b made at teleseismic distances. We truncated the data set and limited the regressions to $m_b > 3.5$.

Of the 23 data pairs included in the regressions, 14 are for earthquakes in the UTR; nine, in the EBR.

For CR-8, the value of 0.207 for σ[**M**|m_b PDE1] comes from $S_{y,x}$ = 0.2154 from the GOR reduced by the average uncertainty of 0.06 for the values of $\mathbf{M}_{obs}$ used in the GOR[see equation (E-4) and table E-10].

CR-9, 9a: A conversion relationship from m_b PDE2 to **M** for the UTR for 1978−1990 is based on a regression of M_L UU or M_C UU (when M_L UU was not available) against m_b PDE2. Figure E-10 shows data for 23 data pairs for this time period. Just as for m_b PDE1, we truncated the data set, here limiting the regressions to 21 data pairs for $m_b \geq 3.5$. (The dependent variable is M_L UU for 16 of the 21 data pairs and M_C UU for five.) For the GOR, $S_{y,x}$ = 0.4292 (table E-10).

A two-step conversion to **M** was then developed using CR-1 for the second step (with the simplifying assumption that M_C UU = M_L UU), as indicated in table E-8. Equation (E-6) yields a value of 0.362 for the uncertainty σ[**M**|m_b PDE2] (table E-8). The calculation follows the example of equation (E-8), using the value of 0.429 for σ[M_L UU1|m_b PDE2].

CR-10, 10a: A conversion relationship from m_b PDE3 to **M** for the UTR for 1963−1977 is based on a regression of M_L UU or M_C UU (when M_L UU was not available) against m_b PDE3. Figure E-11 shows data for 110 data pairs for this time period. The scattered data reflect heterogeneity in m_b PDE during the 1960s and 1970s, attributable to factors discussed earlier. The data suggest a non-linear relationship with m_b, which is systematically larger than UUSS local magnitude below m_b 5.0 (see also Griscom and Arabasz, 1979). The data shown on figure E-11 were the most problematic m_b PDE data to deal with, but pursuing a magnitude conversion relationship was important because m_b PDE was the only instrumental magnitude available in the master catalog during 1963−1977 for 50 earthquakes in the EBR and 13 shocks in the UTR. All had magnitudes in the 3 and 4 range. We trimmed the data set as shown on figure E-11 ($3.3 \leq m_b$ PDE ≤ 5.0) and performed linear regressions on the 103 remaining data pairs. (The dependent variable is M_L UU for 59 of the 103 data pairs and M_C UU for 44.) For the GOR, $S_{y,x}$ = 0.5369 (table E-10).

A two-step conversion to **M** was then developed using CR-1 for the second step (with the simplifying assumption that M_C UU = M_L UU), as indicated in table E-8. Equation (E-6) yields a value of 0.443 for the uncertainty σ[**M**|m_b PDE3] (table E-8). The calculation follows the example of equation (E-8), using the value of 0.537 for σ[M_L UU1|m_b PDE3]. Because of this relatively large σ, we applied CR-10 only when m_b PDE3 was the sole instrumental magnitude available.

$\mathbf{M_{pred}}$ from ISC $\mathbf{m_b}$ Magnitudes

Teleseismic short-period body-wave magnitudes, m_b, have been reported by the ISC since 1964. In July 2012 when we extracted data from the ISC catalog (International Seismological Centre, 2010), the catalog was current to April 2010. Compared to m_b PDE, m_b ISC provides a more stable reference, affected by fewer procedural changes with time. In exploring the ISC data set it became apparent that m_b ISC was an attractive additional size measure for earthquakes in the UTR, independent of those in the source catalogs we had merged, particularly for shocks in the

magnitude 4 and 5 range. For data quality, we used only values of m_b ISC based on five or more stations (Nsta ≥ 5).

CR-11, 11a: A conversion relationship from m_b ISC (Nsta ≥ 5) to **M** is based on 13 data pairs shown on figure E-12 for earthquakes between 1967 and 2010. All of the earthquakes are in the UTR except for one: the Wells, Nevada, earthquake of February 21, 2008 ($\mathbf{M}_{obs}$ 5.91). For CR-11, the value of 0.295 for $\sigma[\mathbf{M}|m_b \text{ ISC}]$ in table E-8 comes from $S_{y,x}$ = 0.3053 from the GOR reduced by the average uncertainty of 0.08 for the values of $\mathbf{M}_{obs}$ used in the GOR [see equation (E-4) and table E-10].

$\mathbf{M}_{pred}$ from Maximum Modified Meralli Intensity, $\mathbf{I_0}$

The historical source catalogs for the UTREXT (subcatalog A) rely heavily on observations of Modified Mercalli Intensity (MMI) for estimates of earthquake size. (We use Roman and Arabic numerals interchangeably for MMI.) The maximum observed intensity is not necessarily identical to epicentral intensity, I_0, but is commonly assumed to be equivalent (e.g., Rogers and others, 1976). The maximum intensity reported by Stover and Coffman (1993) is the value closest to the epicenter. As noted in EPRI/DOE/NRC (2012), one can argue from the isoseismal maps in Stover and Coffman (1993) that the maximum intensity is typically very close to the epicenter.

In this study, we assume an approximate equivalence between maximum observed MMI and I_0. For the I_0-$\mathbf{M}_{obs}$ pairs that we used in our regressions, associated with earthquakes between 1934 and 2012, we scrutinized the epicentral distance associated with the maximum reported intensity for each earthquake. For older earthquakes, two useful resources were the annual publications of *U.S. Earthquakes* for 1934–1985 and the National Geophysical Data Center's *U.S. Earthquake Intensity Database* for 1683 to 1985 (www.ngdc.noaa.gov/hazard/int_srch.shtml). For earthquakes in the UTREXT since 2001, our primary resource was the USGS "Did You Feel It?" (DYFI) website (http://earthquake.usgs.gov/earthquakes/dyfi/, see also Atkinson and Wald, 2007).

For all but two of the I_0-$\mathbf{M}_{obs}$ pairs, the maximum intensity was observed within 20 km epicentral distance. One of the exceptions was an I_0-$\mathbf{M}_{obs}$ pair (5, 4.00) for an earthquake on July 14, 2006, near Georgetown, Idaho, for which I_0 = 5 was observed at Grace, Idaho, 25 km distant. The other presumed exception was an I_0-$\mathbf{M}_{obs}$ pair (6, 5.20) for the Southern Wasatch Plateau, Utah, earthquake of January 30, 1989; in this case, it was unclear whether I_0 = 6 was observed at the nearby town of Salina (population ~2400), 26 km distant, or at a closer site. Where I_0 (maximum MMI) came from DYFI data, we only used values of I_0 based on five or more responses within 20 km epicentral distance. We were able to evaluate proximity based on our familiarity with the location of population centers, without relying on the DYFI distances which are calculated relative to the centers of zip code areas.

For historical shocks in Utah of MMI V or greater, Rogers and others (1976) showed that estimated magnitude (M) plotted vs. I_0 reasonably followed Gutenberg and Richter's (1956) relation $M = 1 + 2/3\ I_0$. This same relation was used by Arabasz and McKee (1979) in compiling the UUSS historical earthquake catalog for the UTR. Gutenberg and Richter (1956) based their relation chiefly on data for $I_0 \geq$ V, with a single data point for I_0 = IV (see their figure 6). With

more modern data, the empirical scaling of I_0 with M is observed to be non-linear with a change in slope below I_0 = V (e.g., EPRI/DOE/NRC, 2012, chapter 3, and references therein).

Mindful that I_0 was the only available size measure for most of the events in the pre-instrumental time period, we took care when merging the source catalogs to indicate a preferred value of I_0. USGS sources were given precedence, and the following order of priority was adopted: (1) Stover and Coffman (1993), two experienced compilers who had examined and revised maximum MM intensities in the process of producing multiple reports and publications on U.S. earthquakes, (2) the USGS-SRA catalog, and (3) the UUSS historical earthquake catalog.

For developing a conversion relationship from I_0 to **M**, we started with our compilation of $\mathbf{M}_{obs}$ and sought corresponding values of I_0 observed at small epicentral distance. In this exercise our assigned values of I_0 came exclusively from USGS (or predecessor) sources. Throughout, priority was given to Stover and Coffman (1993). For 1934–1985, supplementary values of I_0 came from annual editions of *U.S. Earthquakes*. Supplementary values of I_0 for 1986–2012 came from the USGS/NEIC PDE catalog and (for earthquakes in the UTREXT since 2001) the USGS DYFI website. If I_0 reported in the PDE catalog differed from DYFI data, we used the latter if well-founded.

CR-13, 13a: Data for converting $I_0 \geq$ V to **M** are plotted on figure E-13, showing the expected change in slope below I_0 =5. For $I_0 \geq$ V, the 24 data pairs are fit with a linear model. Our aim was to develop a region-specific relationship for the UTR, and 20 of the data pairs are for earthquakes within the UTR between 1934 and 2012. To provide control at the upper end of the regression, we added I_0-$\mathbf{M}_{obs}$ pairs for four shocks outside the UTR with the following (I_0, $\mathbf{M}_{obs}$) values: (1) 1959 Hebgen Lake, Montana (10, 7.35); (2) 1983 Borah Peak, Idaho (9, 6.82); (3) 1994 Draney Peak, Idaho (7, 5.66); and (4) Wells, Nevada (8, 5.93).

For the GOR (CR-13) we treated the independent variable I_0 as quasi-continuous, measured as discrete integers but with an uncertainty of 0.5. As shown in table E-10, values of 0.4474 and 0.429 were computed for $S_{y,x}$ and $\sigma[\mathbf{M}|I_0 \geq V]$, respectively. For our final CR-13 (table E-8), we adopted 0.5 as a nominal value for $\sigma[\mathbf{M}|\ I_0 \geq V]$, corresponding to what EPRI/DOE/NRC (2012) determined applying LSR to a much larger data set.

Conversion relationships for magnitude versus I_0 can differ regionally. Relationships in California (e.g., Toppozada, 1975; Gutenberg and Richter, 1956) differ significantly from that determined by EPRI/DOE/NRC (2012) for the central and eastern United States (CEUS). Comparisons must be made with care, taking into account the regression method, the type of magnitude being regressed, and the data available to control the regression, particularly at higher intensities. Keeping these issues in mind, the predicted magnitude for a given I_0 in the CEUS appears to be about a half to one magnitude unit lower than what would be predicted in California for the same I_0 in the range of V to VIII. For the Utah Region, figure E-13 shows that our conversion relationships CR-13 and CR-13a are close to Gutenberg and Richter's (1956) relation for California—rather than suggesting something transitional between California and the CEUS.

CR-14, 14a: Our conversion of I_0 < V to **M** must be viewed as provisional and approximate. We wanted a relationship to estimate **M** for numerous earthquakes in the master catalog whose only reported size measure was MMI 2, 3, or 4. The earthquakes in question occurred before the

start of periods of complete reporting for these smaller shocks, so our seismicity-rate calculations are unaffected. Our approach is shown on figure E-14. To enlarge the data set for $I_0 < V$ shown on figure E-13, we added data pairs for earthquakes in the UTR in which the magnitude is $\mathbf{M}_{pred}$ from M_L UU ≥ 2.75 and I_0 is from DYFI data (black open circles in figure E-14). We then performed GOR on the expanded data set using data for $I_0 = 3$ or larger and including $I_0 = 5$ data for control. Just as for CR-13, we treated the independent variable I_0 as quasi-continuous, measured as discrete integers but with an uncertainty of 0.5. Our preferred GOR relationship (CR-14, table E-8) is labeled "GOR constrained" on figure E-14. This regression line is constrained to pass through the (x,y) value (5,4.05) predicted from CR-13 for $I_0 \geq 5$, thus tying conversions for I_0 above and below 5. For the constrained GOR, $\sigma[\mathbf{M}|\ I_0 < V]$ is 0.308, but we adopt the nominal value of 0.5 (see table E-8), just as for CR-13.

To explore whether CR-14 could reasonably be extrapolated to $I_0 = 2$, we further added data pairs for earthquakes in the UTR in which the magnitude is $\mathbf{M}_{pred}$ from M_L UU < 2.75 and I_0 is from DYFI data (red open circles in figure E-14). Note that this magnitude range is below the limit of data for CR-1 (figure E-5). These added data were not used in any of the regressions but are shown on figure E-14 for illustration. Overall, the data on figure E-14 indicate it is reasonable to use CR-14 (GOR constrained) to estimate **M** for $I_0 < 5$ in the UTR. It also appears reasonable to extrapolate CR-14 to $I_0 = 2$. Again, we emphasize that our use of CR-14 is provisional and approximate.

$\mathbf{M}_{pred}$ from the Logarithm of the Total Felt Area

Regressions of magnitude M on the logarithm of the macroseismic felt area, whether total felt area (FA) or the area shaken at or greater than a specified level of MMI (A_{MMI}, e.g., A_{VI}) generally provide more robust estimates of M than regressions of M on I_0 (Toppozada, 1975; Toppozada and Branum, 2002; see also Hanks and others, 1975). We first describe a conversion relationship for FA (CR-12) and then describe relationships for A_{VII}, A_{VI}, A_V, and A_{IV} (CR-15 to CR-18). All areas are measured in km^2.

CR-12, 12a: There are theoretical reasons why the scaling of log(FA) or ln(FA) with **M** is expected to be non-linear (Frankel, 1994). An updated data set of **M** versus ln(FA) for the central and eastern United States (EPRI/DOE/NRC, 2012, Fig. 3.3-44) clearly displays this non-linearity. To develop a conversion relationship from FA to **M**, we followed the model used by EPRI/DOE/NRC (2012): $\mathbf{M} = c_0 + c_1 \times \ln(FA) + c_2 \sqrt{FA}$, where c_0, c_1, and c_2 are constants.

Figure E-15 shows a plot of ln(FA)-$\mathbf{M}_{obs}$ data pairs, truncated at ln(FA) = 8 (i.e., FA ~3000 km^2), that we regressed to fit the above model. Above the truncation point, there are 26 data pairs, predominantly for shocks in the UTR. For additional control on the regression we included data for four shocks outside the UTR with the following (ln(FA), $\mathbf{M}_{obs}$) values: (1) 1959 Hebgen Lake, Montana (13.98, 7.35); (2) 1983 Borah Peak, Idaho (13.66, 6.82); (3) 1994 Draney Peak, Idaho (12.14, 5.66); and (4) a 2001 earthquake near Soda Springs, Idaho (10.76, 5.17).

The FA values for 12 of the 26 earthquakes come from isoseismal maps—as measured and reported by Stover and Coffman (1993) for ten and as measured by ourselves for two. For the remainder, the FA values come from measurements we made on Community Internet Intensity Maps (CIIMs) from the DYFI website. We systematically searched the DYFI archives for CIIMs associated with earthquakes in the UTR that were based on at least 50 responses (the

resulting median was ~160) and had sufficient zip-code "granularity" such that the interior of the felt area encompassed several or more zip codes. For the selected CIIMs, we outlined the felt area with an elliptical or curvilinear boundary, taking into account the known distribution of towns in rural areas and using judgment to transect zip codes at the periphery of the felt area with only one or a few responses.

In order to determine an uncertainty in ln(FA) for our measured felt areas, we converted all 26 FA values into equivalent circular areas, each with an effective radius. Examining both the historical and DYFI data, we assessed an uncertainty of ± 20 percent in the effective radius for an individual earthquake. Taking the geometric mean of the asymmetric error in the plus and minus directions gave us an uncertainty of 0.4 in ln(FA) for use in the GOR. The corresponding mean uncertainty for $\sqrt{\mathrm{FA}}$ is 55 km for our data set of 26 earthquakes.

The GOR and LSR fits to our adopted non-linear model for $\mathbf{M}_{obs}$ vs. ln(FA), shown on figure E-15, are nearly identical and are well constrained by the data. To explore the implied trend of the regressions below ln(FA) = 8, we added data pairs for five small earthquakes (open circles, figure E-15) for which **M** is $\mathbf{M}_{pred}$ from M_L UU and FA was measured from DYFI data. These data are consistent with the trend of CR-12 at its lower end.

For CR-12, the value of 0.339 for $\sigma[\mathbf{M}|\ln(\mathrm{FA})]$ in table E-8 comes from $S_{y,x}$ = 0.3535 from the GOR reduced by the average uncertainty of 0.10 for the values of $\mathbf{M}_{obs}$ used in the GOR [see equation (E-4) and table E-10].

In applying CR-12, it became apparent that FA values reported for early historical shocks were underestimated and unreliable. Toppozada (1975) noted the difficulty of determining FA for pre-1932 events because of sparse population and because weakly felt ground shaking may not have been considered noteworthy. Stover and Coffman (1993) report FA to the nearest 1000 km^2; their values of FA for older smaller earthquakes are low compared to modern DYFI data. For these reasons, we did not use any measurement of FA for historical earthquakes earlier than 1930, and our truncation of CR-12 at ln(FA) = 8 excludes FA values less than ~3000 km^2.

$\mathbf{M}_{pred}$ from the Logarithm of the Area Shaken at or Greater than MMI IV–VII

We turn now to A_{MMI}, the area shaken at or greater than a specified MMI, as a further means of estimating **M** from observations of macroseismic felt area. Table E-12 summarizes a region-specific data set that we compiled for A_{MMI} using available isoseismal maps for 22 earthquakes. The table is divided into three parts, indicating: (1) A_{MMI} used to develop CRs for A_{VII}, A_{VI}, $A_{V,}$ and A_{IV} that are displayed on figure E-16; (2) A_{MMI} used in applying the resulting CRs, contributing to the best-estimate moment magnitudes; and (3) A_{MMI} that was measured but not used for earthquakes after 1962. The data are predominantly from the UTR; however, the $\mathbf{M}_{obs}$-A_{MMI} pairs for the regressions include data from two earthquakes in the UTREXT (Draney Peak, Idaho, and Wells, Nevada) and two earthquakes outside the UTREXT (Hebgen Lake, Montana, and Borah Peak, Idaho).

Using the isoseismal maps indicated in table E-12, contours were digitized for the desired MMI isoseismals. These contours were not available for some earthquakes because of grouped intensities; in some other cases, the desired isoseismal was incomplete. Areas within the

digitized contours were then measured using a spatial mapping tool in *ArcGIS*, a geographic information system (GIS). Measured areas in table E-3 are rounded to the nearest 10 km^2.

Using data from the ten earthquakes for which $\mathbf{M}_{obs}$ was available, we developed direct magnitude conversion relationships by regressing $\mathbf{M}_{obs}$ on $\log(A_{MMI})$, following Toppozada (1975) and Toppozada and Branum (2002). For the ranges of magnitude and $\log(A_{MMI})$ considered, the $\mathbf{M}_{obs}$-A_{MMI} pairs for each of the MMI thresholds display a linear relationship, and the regressions are well constrained (figure E-16). Parameters for the four CRs based on GOR, CR-15 to CR-18, are given in table E-8, and regression statistics are given in table E-10. For the GORs, we estimated an uncertainty of 0.18 in $\log(A_{MII})$ in a way equivalent to how we estimated uncertainty in ln(FA). We used 0.18 as the nominal value for σ_x in all four GORs (table E-10).

We adopted a generic value of 0.35 for $\sigma[\mathbf{M}|\log(A_{MMI})]$ for CR-15 through CR-18 (table E-8) based on evaluating the regression statistics in table E-10. Actual values of $\sigma[\mathbf{M}|\log(A_{MMI})]$ in table E-10 include 0.339 for CR-16, 0.357 for CR-17, and much smaller equivalent values for CR-15 and CR-18. There is also a value of 0.339 for $\sigma[\mathbf{M}|\ln(FA)]$, reflecting scatter associated with a larger sample of areas of shaking. The generic value of 0.35 seems reasonable and was intended, in part, to allow for more scatter likely to be seen in larger samples of A_{VII} through A_{IV}. If multiple estimates of **M** from A_{MMI} were available, we computed the mean of those estimates and treated it as a single estimate with $\sigma = 0.35$.

M˜, Magnitude Types Assumed to be Equivalent to M

In earlier sections we introduced **M˜**, a magnitude type assumed to be equivalent to **M** and one of our three kinds of best-estimate moment magnitudes. Here we address the magnitude types that fall into the category of **M˜** and briefly discuss their relative significance. On the one hand, they are essential for achieving an estimate of **M** for every earthquake in the master catalog. On the other hand, they have an insignificant influence on our seismicity-rate calculations.

In merging diverse source catalogs, a practical problem arose with miscellaneous magnitudes that are the sole instrumental magnitude available for a number of earthquakes and for which there were inadequate data to develop magnitude conversions to **M**. Such magnitudes are among the earliest appearing in the master catalog (figure E-4). Table E-13 lists and describes these magnitudes and gives a breakdown in terms of their number, magnitude range, time period, region, and event type. Perhaps the most relevant information appears at the end of the table where one sees that of the 188 earthquakes having **M˜** as their sole magnitude, 129 are in the EBR and only 13 are mainshocks in the UTR. Of those 13 mainshocks, only two have **M˜** values within periods of completeness that enter into our seismicity-rate calculations for the UTR; no **M˜** values enter into the rate calculations for the WGUEP Region.

To be clear, the magnitude types listed in Table E-13 were used to estimate **M** for a particular earthquake only if no other instrumental magnitude was reported for which we had developed a CR. In such cases, for practicality, the sole available magnitude type was assumed to be equivalent to **M** and its reported value was treated as a "noisy" **M** value (see earlier section, *Equivalence of Best-Estimate Moment Magnitudes to* $\boldsymbol{M}_{obs}$). The assumption of equivalence to **M** can be reasonably justified for magnitude scales such as M_SGR, MLPAS, MLBRK, and the Wiechert magnitude at Reno, MxJON, which Jones (1975) calibrated against magnitude values published by Gutenberg and Richter (1949).

For each of the magnitude types in table E-13, we assign an uncertainty σ and give the basis for the assessment. We note that none of the 19 magnitude types in table E-13 is calculated directly from other earthquake size estimates using a magnitude conversion equation determined by least-squares regression. Consequently, for the purpose of magnitude corrections, we judged it more appropriate within the methodology framework outlined on figure E-2 to treat these 19 magnitude types as noisy **M** values rather than as E[**M**] values.

We caution the reader that our $\mathbf{M}^{\sim}$ approach may not always be appropriate for every problematic magnitude type. In our study, as noted above, only two $\mathbf{M}^{\sim}$ values in our catalog enter into our seismicity-rate calculations for the UTR and none for the WGUEP Region. In other studies where a substantial number of assigned $\mathbf{M}^{\sim}$ values influence such calculations, the hazard analyst will have to determine whether and how to correct those $\mathbf{M}^{\sim}$ values for magnitude uncertainty, according to the magnitude type (see Musson, 2012).

$\mathbf{M_S}$ Magnitudes

The instrumental earthquake catalog (merged subcatalogs B and C) contains only ten reported values of M_S (4.0 to 6.1) for earthquakes in the UTREXT, all determined by the USGS between 1984 and 2008. An earlier value of 3.4 in 1963 reported as "M_S GS" is of uncertain origin and accuracy. For the ten events with USGS determinations of M_S GS, corresponding values of $\mathbf{M_{obs}}$ are available for the six largest, and other magnitudes are available for the remainder, so there was no compelling need in this study for a conversion relationship from M_S to **M**. For researchers interested in this issue, the available data suggest approximate equivalence between M_S GS and **M** above approximately magnitude 5.5 (up to the saturation point of the M_S scale) but a nonlinear relationship over the range of magnitude 4 to 5.5, such as the quadratic equation determined by EPRI/DOE/NRC (2012) for a larger M_S-**M** dataset in the central and eastern United States.

RESULTS OF CATALOG COMPILATION

This section is the culmination of steps outlined at the outset under *Steps in Developing a Unified Earthquake Catalog*. The earthquake catalog database, comprising the full final catalog and its building blocks, is contained in ten electronic supplements. We first give the reader an explanatory guide to those supplements and then give a narrative overview of the final catalog, including descriptions of the largest mainshocks ($\mathbf{M} \geq 4.85$) in the UTR.

It should be emphasized that our focus in producing the unified earthquake catalog was on the uniformity and quality of magnitude, not on epicentral quality. Therefore the resulting catalog should not necessarily be considered the "best" available for purposes relating to the accuracy of earthquake locations. In selecting a preferred epicenter from duplicate entries in the merged catalogs, we made qualitative judgments but did not undertake any formal comparison of solution qualities for the reported epicenters.

For non-instrumentally located earthquakes in subcatalog A (pre-July 1962), we generally selected the location given in the UUSS source catalog, which coincides with the site of the maximum reported MMI. For subcatalogs B and C (post-June 1962), the UUSS location was preferred for epicenters within the UTR. For epicenters in the EBR, a USGS location was

generally preferred. However, for some events in the EBR immediately bordering the Utah Region and for most of the 1994 Draney Peak aftershock sequence, for which the UUSS installed local seismographs, the UUS location was selected. In our compilation of earthquakes in the UTR with an observed moment magnitude (see Electronic Supplement E-2), we adopted and annotated locations based on special study, when available. Most of the assigned focal depths are the centroid depth from an indicated moment-tensor inversion. When available, the depth from a specified well-constrained hypocentral solution was substituted.

We remind the reader that we did not systematically identify and remove non-tectonic seismic events and human-triggered earthquakes in the EBR. For this reason, the catalog outside the Utah Region must be used with caution.

Earthquake Catalog Database (Electronic Supplements)

The earthquake catalog database is presented in ten electronic supplements (E-1 to E-10), each in the form of a Microsoft Excel workbook with multiple worksheets. Each workbook contains an explanatory "README" file to guide the reader. The electronic supplements allow examination not only of the final unified catalog but also its building blocks. The building blocks include merged, chronologically sorted, and edited individual line entries from the diverse USGS and UUSS source catalogs; tabulated available size measures for each event in the master catalog; and calculations behind the assigned value of uniform moment magnitude and corresponding uncertainty for each earthquake.

In brief, electronic supplement E-1 contains the final catalog. E-2 summarizes the moment-magnitude data that were used to determine $\mathbf{M}_{obs}$ and as the basis for magnitude conversions from other size measures. E-3, E-4, and E-5 document how we merged and edited subcatalogs A, B, and C, respectively, as part of compiling a master catalog of unique earthquake events. E-6 to E-9 contain worksheets keyed to the seven general kinds of best-estimate moment magnitude explained below under "Mag Type" in the summary for E-1. For each magnitude type listed, a building-block file was created within E-6 to E-9. Exports from these building-block files in a uniform format were ultimately combined and chronologically sorted to create the final BEM catalog. Electronic supplement E-10 documents counts both of the actual and equivalent number (N^*) of earthquakes, binned by magnitude, for independent mainshocks in the WGUEP and Utah regions.

Electronic Supplement E-1 (BEM Earthquake Catalog)

This workbook contains the Best-Estimate Moment Magnitude (BEM) earthquake catalog for the entire UTREXT, both in its clustered and declustered versions (explained and described in the next major section). For each earthquake line, the following information is given in successive columns (fields), following the structure of the USGS western moment magnitude (WMM) catalog:

BEM	Best-estimate moment magnitude
Long W, Lat N	Longitude and latitude (in degrees) of earthquake location
Depth	Earthquake focal depth (km)

Year, Mo, Day, Hr, Min, Sec	Earthquake origin date and time expressed in Coordinated Universal Time (UTC), or equivalently in Greenwich Mean Time (GMT) prior to 1960. In converting local standard time to UTC (or GMT), we accounted for advances in standard time that took place prior to the institution of Daylight Saving Time in 1967. These occurred during World War I (between March 31 and October 27, 1918, and between March 30 and October 26, 1919) and during World War II (between February 9, 1942, and September 30, 1945). These adjustments explain time differences of 1 hour with some event lines in USGS source catalogs.
sigM	Standard deviation of normally distributed errors in the best-estimate moment magnitude, used to compute N^*.
Round	Rounding error in the listed best-estimate moment magnitude
Mag Type	Descriptor indicating the basis for the best-estimate moment magnitude: Mobs = $\mathbf{M}_{obs}$, observed moment magnitude from a direct instrumental measurement of seismic moment M˜|[source] = **M˜**, a magnitude type assumed to be equivalent to **M** (source indicates the origin of the reported magnitude) Mpred|I_0 = Predicted moment magnitude, $\mathbf{M}_{pred}$, from converting maximum MMI, I_0, to **M** Mpred|Xi = $\mathbf{M}_{pred}$ from converting a single instrumental size measure, X_i, to **M** Mpred|Xvar = $\mathbf{M}_{pred}$ from inverse-variance weighting of $\mathbf{M}_{pred}$ values from two or more instrumental size measures Mpred|Xnon = $\mathbf{M}_{pred}$ from inverse-variance weighting of $\mathbf{M}_{pred}$ values from two or more non-instrumental size measures Mpred|Xmix = $\mathbf{M}_{pred}$ from inverse-variance weighting of $\mathbf{M}_{pred}$ values from a mix of instrumental and non-instrumental size measures
N^*	Equivalent earthquake count assigned to an individual earthquake that accounts for the effects of magnitude uncertainty in computing unbiased earthquake recurrence parameters. $N^* = \exp\{-\beta^2 \mathrm{sigM}^2/2\}$, where $\beta = b \ln(10)$. A b-value of 1.05, assessed from preliminary processing of the BEM catalog, is used for all the N^* calculations.

Electronic Supplement E-2 (Moment Magnitude Data)

This workbook was introduced earlier in the section *Moment Magnitude Data*. For each of the 114 values of $\mathbf{M}_{obs}$ used in this study, documentation is provided for the source of the seismic moment from which we calculated $\mathbf{M}_{obs}$, using the definition of Hanks and Kanamori (1979). Hypocentral information and an assessment of magnitude uncertainty are also provided. Data for $\mathbf{M}_{obs}$ associated with earthquakes in the UTR and the EBR, respectively, and with seven supplementary events are presented in separate worksheets. Another worksheet presents data for $\mathbf{M}_{obs}$ associated with four known or suspected mining-related events in the UTR. These seismic events are excluded from the BEM catalog and their $\mathbf{M}_{obs}$ values were not used in this study.

Electronic Supplements E-3 to E-5 (Merged Subcatalogs A, B, and C)

In these three workbooks the reader can track separately for subcatalogs A, B, and C, respectively, the merging, chronological sorting, culling, and editing of individual line entries from the diverse USGS and UUSS source catalogs. For each subcatalog, multiple worksheets guide the reader through three successive compilations: (1) a merged and filtered raw compilation with the source of each event line identified ("filtered" means that mining-induced seismicity in the UUSS source catalog was removed prior to merging); (2) an expanded version of (1) in which duplicate line entries are identified, a preferred epicenter selected, and comments added; and (3) a culled version that contains event lines representing unique earthquake events, each with a preferred epicenter and a listing of all reported size measures.

Electronic Supplement E-6 (Worksheets for Mobs, M˜, Mpred|I_0)

This workbook contains three relatively straightforward worksheets in the format of the final catalog. The first is a tabulation of 107 earthquakes in the UTREXT for which values of $\mathbf{M}_{obs}$ are available, along with data distilled from electronic supplement E-2. The second worksheet lists all event lines in subcatalogs A, B, and C for which **M˜** is the only available *instrumental* size measure (for historical shocks, an **M˜** measurement was given priority over I_0); the Mag Type descriptor (e.g., M˜|MLPAS) indicates the source of the reported magnitude (see table E-13). The third worksheet lists all event lines (1850–1966, plus one event in 1974) for which I_0 is the only available size measure. An extra column gives the preferred value of I_0 that was identified when editing the merged subcatalogs. With this added information, one can examine the calculation of $\mathbf{M}_{pred}|I_0$ in the spreadsheet's first column that uses either conversion relationship CR-1, for $I_0 \geq V$, or CR-14, for $I_0 < V$ (see table E-8).

Electronic Supplements E-7 to E-9 (Worksheets for Mpred|Xnon, Xmix, Xvar, or Xi)

The workbooks for electronic supplements E-7, E-8, and E-9 deal with all earthquakes in the master catalog whose size information does not belong to one of the three categories of E-6 (i.e., $\mathbf{M}_{obs}$, **M˜**, or solitary I_0). The workbooks show all available size measures for the individual earthquakes, propagated forward from the merged subcatalogs. Added information documents how we used these size measures to determine **M** and σ for each earthquake utilizing the conversion relationships of table E-8. Editing comments and annotations are included.

In these workbooks, our general approach was to use all available size measures to achieve a best estimate of **M** with the following exceptions: (1) We ignored measurements of total felt area for historical earthquakes earlier than 1930 for reasons discussed earlier (see *M_{pred} from the Logarithm of the Felt Area*). (2) For earthquakes after 1963, only instrumental magnitudes were used in inverse-variance weighting. (3) Because of the relatively large uncertainty associated with converting m_b PDE3 to **M** (see figure E-11), we used m_b PDE3 only when it was the sole magnitude available.

Electronic supplement E-7 includes calculations for $\mathbf{M}_{pred}|X_{non}$ (inverse-variance weighting of $\mathbf{M}_{pred}$ values from non-instrumental size measures) and $\mathbf{M}_{pred}|X_{mix}$ (inverse-variance weighting of $\mathbf{M}_{pred}$ values from a mix of non-instrumental and instrumental size measures). The calculations

apply to 16 earthquakes between 1900 and 1962. $\mathbf{M}_{pred}|X_{non}$ was used for 14 earthquakes between 1900 and 1961, and $\mathbf{M}_{pred}|X_{mix}$ was used for the 1959 Arizona-Utah border earthquake and for the 1962 Magna earthquake (both discussed presently as part of a description of the largest mainshocks in the UTR).

Electronic supplements E-8 and E-9 pertain to subcatalogs B and C, respectively. They document the calculation of $\mathbf{M}_{pred}$ for the majority (70%) of individual earthquakes in the BEM catalog based either on $\mathbf{M}_{pred}|X_i$ (the conversion of a single instrumental size measure, X_i, to **M**) or $\mathbf{M}_{pred}|X_{var}$ (inverse-variance weighting of $\mathbf{M}_{pred}$ values from two or more instrumental size measures).

Errata Relating to Electronic Supplements E-8 and E-9

After completing the final BEM catalog and rate calculations, we discovered that some of the values of σ used in the conversions of m_b PDE (labeled "sigM mb PDE") in the workbooks of electronic supplements E-8 and E-9 were not the final correct values listed in table E-8. Specifically, instead of 0.362 for the two-step σ for CR-9, our calculations used 0.346; and instead of 0.443 for the two-step σ for CR-10, our calculations used 0.401. We examined what effect these small errors might have on earthquake data for the UTR, the area of interest for this study, and we found the effect to be negligible.

The discrepancy between 0.346 and 0.0362 for CR-9 (for m_b PDE2, 1978–1990) affected calculations for seven mainshocks in the UTR. Of these, the best-estimate moment magnitude remained the same for six and changed by 0.01 magnitude unit for one; N^* remained the same for five and decreased by 0.002 for two. These two tiny changes in N^* entered into the rate calculations for the WGUEP Region but not the UTR (because of the date of the earthquakes vis-à-vis periods of completeness).

The discrepancy between 0.401 and 0.443 for CR-10 (for m_b PDE3, 1963–1977) affected calculations for three mainshocks in the UTR. For all three, the best-estimate moment magnitudes remained the same but N^* decreased by 0.061. These N^* values did not enter into the rate calculations for either the WGUEP Region or the UTR because the shocks were not within periods of completeness.

Electronic Supplement E-10 (N^* Counts for the WGUEP and Utah Regions)

This workbook contains worksheets that allow the reader to track counts of N^* listed in tables E-18 and E-19 for the WGUEP and Utah regions, respectively. For each region, there are two worksheets. The first contains the appropriate geographic sort of the declustered version of the BEM catalog. The second has a color-coded display of the sorted earthquakes showing their grouping into magnitude bins 0.7 unit wide (beginning with $\mathbf{M} \geq 2.85$ up to **M** 7.00) along with counts both of the actual and equivalent number (N^*) of earthquakes in each magnitude bin. Within each color-coded magnitude bin, event lines are chronologically sorted and the period of completeness is demarcated. For the Utah Region, injection-induced earthquakes are excluded, as indicated in table E-4.

Overview of Best-Estimate Moment Magnitude (BEM) Catalog

Our unified and uniform earthquake catalog for the Utah Extended Region, i.e., the BEM catalog, contains 5388 earthquakes ($2.06 \leq \mathbf{M} \leq 6.63$) covering the period from 1850 through September 30, 2012. Only six of the shocks are smaller than **M** 2.50. Figure E-17 shows an epicenter map for all events in the total master catalog. The complete BEM catalog includes mainshocks, foreshocks, aftershocks, and earthquake swarms. Non-tectonic seismic events such as blasts and mining-induced seismicity are excluded.

After the removal of dependent events from the earthquake catalog resulting in a declustered version, the BEM catalog contains 1554 independent mainshocks ($2.50 \leq \mathbf{M} \leq 6.63$) in the UTR and 660 independent mainshocks ($2.50 \leq \mathbf{M} \leq 6.59$) in the WGUEP Region. (The count of 1554 mainshocks includes the 30 injection-induced earthquakes in table E-4). Corresponding epicenter maps are shown on figures E-18 and E-19, respectively.

Largest Mainshocks (M ≥ 4.85) in the Utah and WGUEP Regions

The declustered version of the BEM catalog, 1850 through September 2012, contains 19 independent mainshocks of **M** 4.85 or larger in the UTR, nine of which are within the WGUEP Region. Numbering of these earthquakes, keyed to table E-14, is shown on figures E-18 and E-19. Table E-14 summarizes basic information for each of these earthquakes, including the date and origin time, location, best-estimate moment magnitude and corresponding uncertainty σ, and the type of BEM on which **M** is based. Some description of these significant earthquakes is warranted, particularly regarding the basis of the estimated moment magnitudes.

Our UUSS archives include historical information for many of these earthquakes, including newspaper articles, photographs, individual accounts, and excerpts from publications. (Online access to these materials is expected by mid-2016 as part of an update of our UUSS website, www.quake.utah.edu.)

In the following descriptions of individual earthquakes where epicenters and focal depths are referred to, see table E-14. Estimates of moment magnitude from other size measures, $\mathbf{M}_{pred}$, are from the conversion relationships in table E-8. For convenience here, we simply refer to these values as **M**.

1. 1884, Nov. 10. Near Paris, Idaho (M 5.58): Historical accounts of this earthquake in the Idaho-Utah-Wyoming tri-state area, one of the earliest damaging shocks in the UTR and WGUEP regions, have been studied and analyzed by Evans and others (2003), whose preferred epicenter we adopt. The distribution of felt reports described by Evans and others (2003) suffers from incompleteness and irregularity typical for this early time period. These authors report a failed attempt, due in part to anomalous ground shaking at large epicentral distances, to use Bakun and Wentworth's (1997) inversion method to estimate magnitude from the available felt observations. Our best-estimate moment magnitude, **M** 5.58 ± 0.50, is based on I_0 = VII assessed by Stover and Coffman (1993). Our attempts to use the felt observations reported by Evans and others (2003) proved problematical. The felt area of 70,000 km^2 reported by Evans and others (2003) gives **M** 5.03; their suggestion of a felt area possibly as large as 210,000 km^2, based on the addition of a single felt report, gives **M** 5.77. Figure 3 of Evans and others (2003) indicates A_V of about 1650 km^2, implying **M** 3.84.

2. 1901, Nov. 14. Tushar Mountains, Utah (M 6.63): This damaging earthquake in central Utah rivals the 1934 Hansel Valley earthquake as the largest historical earthquakes in the UTR since pioneer settlement. Williams and Tapper (1953) summarize macroseismic effects, including extensive rockslides and rock falls in the Tushar Mountains betweeen Beaver and Marysvale. No surface faulting was observed. We adopt an epicenter that lies at the mid-point of the area shaken at MMI VIII or greater on Hopper's (2000) isoseismal map. Our best-estimate moment magnitude, **M** 6.63 ± 0.29, is based on inverse-variance weighting of **M** values from I_0 = VIII assessed by Stover and Coffman (1993) and from measures of A_{VI} and A_{VII} in table E-12. The assigned magnitude of this earthquake is just slightly larger than that of the 1934 Hansel Valley mainshock (**M** 6.59 ± 0.30). Comparison of the measures of A_{VI} and A_{VII} for the 1901 and 1934 earthquakes (table E-12) supports the assessment that the 1901 central Utah earthquake was comparable in size or slightly larger than the 1934 Hansel Valley earthquake.

3. 1902, Nov. 17. Pine Valley, Utah (M 6.34): Williams and Tapper (1953) summarize damage reports and felt effects for this earthquake centered in Pine Valley, north of St. George in southwest Utah. Our best-estimate moment magnitude, **M** 6.34 ± 0.50, is based on I_0 = VIII assessed by Stover and Coffman (1993). The asssigned epicenter is from the UUSS catalog, corresponding to coordinates for Pine Valley, based in turn on MMI effects described by Williams and Tapper (1953). Their FA of 10,000 square miles (25,900 km^2) is undoubtedly underestimated, and the lack of an isoseismal map leaves I_0 as the sole size measure.

4. 1909, Oct. 6. Hansel Valley, Utah (M 5.58): Williams and Tapper (1953) note that this earthquake in northern Utah generated waves in Great Salt Lake (GSL) that passed over the Lucin cut-off (a 19-km-long railroad trestle that crosses GSL in an east-west direction) and rolled over a bath house pier at Saltair at the southern end of GSL. Based on the distribution of towns reporting the mainshock, these authors expressed a high degree of confidence that the earthquake originated in Hansel Valley, located at the northern end of GSL. Our assigned epicenter, from the USGS SRA catalog, is on the western side of Hansel Valley on the Hansel Valley fault and ~15 km north of Great Salt Lake. Our best-estimate moment magnitude, **M** 5.58 ± 0.50, is based on I_0 = VII assessed by Stover and Coffman (1993). A felt area of 78,000 km^2 reported by Stover and Coffman (1993), likely an underestimate because of the time period, gives **M** 5.09. Felt reports are inadequate to estimate A_{MMI}. If our assigned location and estimated magnitude are correct, then the large water waves generated in Great Salt Lake could plausibly be explained by an earthquake-induced landslide underneath or into the lake.

5. 1910, May 22. Salt Lake City, Utah (M 5.28): Williams and Tapper (1953) describe effects of this local earthquake in the Salt Lake Valley, which damaged several buildings and toppled many chimneys in Salt Lake City. For consistency with the isoseismal map of Hopper (2000, figure 4), our selected epicenter is from the USGS SRA catalog. Our best-estimate moment magnitude, **M** 5.28 ± 0.29, is based on inverse-variance weighting of two **M** values: an **M** value calculated from I_0 = VII assessed by Stover and Coffman (1993) and a mean **M** value calculated from A_V and A_{VI} (table E-12). A_{VII} gives **M** significantly lower than the other size measures and was judged to be poorly constrained and imprecise.

6. 1921, Sept. 29. Elsinore, Utah (M 5.45): This earthquake was the first and largest of three strong earthquakes that occurred between September 29 and October 1, 1921, causing considerable damage in the small town of Elsinore in the Sevier Valley in central Utah (Pack,

1921; Williams and Tapper, 1953; Stover and Coffman, 1993). Our adopted epicenter for the mainshock is from the UUSS catalog and corresponds to the location of Elsinore.

Estimating the sizes of the three earthquakes poses a challenge. Hopper (2000) noted the contrast between their relatively high maximum intensities (MMI = VIII, VII, VIII, as assessed by Stover and Coffman, 1993) and their very rapid intensity attenuation, concluding that they were probably extremely shallow events. (See Arabasz and Julander, 1986, regarding a discontinuity in seismicity and geological structure at about 6 km depth beneath the Elsinore area.) Isoseismal maps published by Hopper (2000) for the three events are at a small scale, but contours for MMI ≥ VII for the first shock and MMI ≥ VI for the second and third shocks appear to be reasonably constrained by the distribution of towns surrounding Elsinore. Given the early date, FA may be underestimated.

For the first and largest event, our best-estimate moment magnitude, **M** 5.45 ± 0.29, is based on inverse variance weighting of **M** values from A_{VII} (estimated at 400 km^2, **M** 5.01, from the isoseismal map of Hopper, 2000) and from I_0 = VIII (**M** 6.34). Stover and Coffman (1993) and the SRA catalog list a magnitude of "5.20Ukn PAS" for this earthquake. We were unable to find the source of this magnitude and decided not to use it; the earthquake predates the start of seismographic reporting from Caltech in October 1926 (Hileman and others, 1973). (Note: Pasadena is ~750 km from Elsinore.)

The second and third shocks in the sequence were smaller than the first. Stover and Coffman (1993) list maximum MMI = VIII for the third shock, but information in Pack (1921) and Hopper (2000) indicates a size smaller than for the first shock. Based on estimating A_{VI} at 300 km^2 from isoseismal maps of Hopper (2000) for both the second and third shocks, together with Stover and Coffman's (1993) maximum MMI values, our best-estimate moment magnitudes from inverse-variance weighting for the second and third shocks are 4.42 ± 0.29 and 4.67 ± 0.29, respectively. Our magnitudes for all three earthquakes are significantly lower than earlier estimates based on MMI alone.

7. 1934, Mar. 12. Hansel Valley, Utah (M 6.59): This well-known earthquake, which occurred in a sparsely populated area north of Great Salt Lake in northern Utah, is distinguished as the only historical shock to date in the UTR known to have produced surface faulting (see Smith and Arabasz, 1991, for a general review; Neumann, 1936, for a summary of macroseismic effects; and Shenon, 1936, for documentation of geologic effects of the earthquake). MMI was assessed at VIII by Stover and Coffman (1993).

Our best-estimate moment magnitude, **M** 6.59 ± 0.30, is based on $\mathbf{M}_{obs}$ from the geometric mean of two values of M_0 (8.5 x 10^{25} dyne-cm and 8.8 x 10^{25} dyne-cm) reported by Doser (1989) from the inversion of *P* and *S* waveforms recorded at teleseismic and regional distances. This **M** is basically identical to Gutenberg and Richter's surface-wave magnitude (M_S GR) of 6.6 commonly cited for this earthquake (e.g., Stover and Coffman, 1993). A_{MMI} values given in table E-12 yield an average **M** of 6.39. Our adopted epicenter is from Doser (1989), based on a relocation attributed to J.W. Dewey (USGS, written communication to D. Doser, 1986). A focal depth of 9 km indicated in table E-14 is the average of two values (9.7 ± 1.4 km and 8.5 ± 2.0 km) determined by Doser (1989) from her waveform inversions.

8. 1937, Nov. 19. Nevada-Utah-Idaho tri-state area (M 5.40): Reports from varied sources point to the occurrence of a significant earthquake on this date at approximately 00:50 (GMT) in the general vicinity of the Nevada-Utah-Idaho tri-state border, but with an uncertain epicenter. Neumann (1940a) reports this as an earthquake near Wells, Nevada, based on felt reports there, and as a "rather widespread shock" felt as far away as Salt Lake City. The summary of instrumental epicenters located by the U.S.Coast and Geodetic Survey for 1937 (Neumann, 1940b) does not have any entry for a local earthquake in the U.S. on November 18 or 19, 1937.

Jones (1975) gives an instrumental epicenter (unclear whether determined at Reno or at Berkeley) at 42.1º N, 113.9º W, which we adopt. Stover and Coffman (1993) and Slemmons and others (1965, table B) give the same epicenter. Our best-estimate moment magnitude, **M** 5.40 ± 0.37, is an **M**˜ value based on a Wiechert magnitude determined at Reno, Nevada (Jones, 1975).

Epicentral distances estimated by Jones (1975) from Fresno and Reno, presumably based on $S - P$ intervals, are more consistent with the assigned epicenter than for a location closer to Wells, Nevada. However, this epicenter is inconsistent with felt observations reported by Neumann (1940a) and Williams and Tapper (1953). The epicenter is: 142 km from Wells (MMI not specified), where the felt effects apparently were strongest (but not indicative of immediate proximity to a magnitude 5 earthquake); 85 km from Lucin, Utah (MMI = IV); 44 km from Grouse Creek, Utah (MMI = III); and 152 km from Wendover, Utah (MMI not specified). From the felt observations, the earthquake appears to have originated in the general vicinity of the Nevada-Utah-Idaho tri-state border, likely in northeasternmost Nevada (to the southwest of our adopted epicenter) in the area surrounded by Wells, Lucin, Grouse Creek, and Wendover.

9. 1950, Jan. 18. Northwestern Uinta Basin (M 5.30): Information on this earthquake comes primarily from *United States Earthquakes 1950* (Murphy and Ulrich, 1952) and USGS sources. Both the location and size of this earthquake are uncertain. The shock was instumentally located by the U.S. Coast and Geodetic Survey (USCGS) at 40.5° N, 110.5° W, east of the Wasatch Front along the south flank of the Uinta Mountains. Stover and Coffman (1993) and the USGS SRA catalog list the USCGS epicenter. Our best-estimate moment magnitude, **M** 5.30 ± 0.20, is based on **M**˜ (Ukn PAS) reported both by Stover and Coffman (1993) and the USGS SRA catalog.

Murphy and Ulrich (1952) describe the location of the shock as "near Soldier Summit, Utah" (39.929° N, 111.083° W), which is 80 km southwest of the instrumental location and seemingly inconsistent with the description of weak shaking (MMI I to III) in Price, 40 km southeast of Soldier Summit. In aggregate, the irregularity of felt intensities (V at Grand Junction, Colo., 235 km distant; IV at Duchesne, Utah, 38 km distant; IV at Sego, Utah, 177 km distant; IV at Fruita, Colo., 214 km distant; and IV at Moab, Utah, 229 km distant) invites comparison with a shock of **M** 4.68 that occurred on September 30, 1977, almost at the same location (40.458° N, 110.484° W) as the USCGS epicenter for the 1950 earthquake. The 1977 earthquake similarly resulted in irregular felt effects in the Colorado Plateau (see *United States Earthquakes 1977*: Coffman and Stover, 1979). If the two earthquakes indeed occurred in the same area, stronger felt effects reported for the 1977 shock suggest that the 1950 earthquake may have been smaller than **M** 5.30.

10. 1959, July 21. Arizona-Utah border (M 5.55): This slightly damaging earthquake within the Colorado Plateau is well established in the historical earthquake record of the UTR. Felt effects on both sides of the Arizona-Utah border are described in *United States Earthquakes 1959* (Eppley and Cloud, 1961). Our assigned epicenter is from Stover and Coffman (1993). No instrumental M_0 is available for this earthquake, but it is one of three in the UTR for which Bakun (2006) estimated moment magnitude based on an MMI intensity attenuation model for the Basin and Range Province. Instrumental values of $\mathbf{M}_{obs}$ are available for the other two earthquakes: the Cache Valley earthquake of August 1962 and the Pocatello Valley earthquake of March 1975. Our best-estimate moment magnitude, **M** 5.55 ± 0.14, is based on inverse-variance weighting of a value of **M**~ (5.60 MLPAS), reported by Stover and Coffman (1993) and in the USGS SRA catalog, and Bakun's (2006) estimated moment magnitude of 5.5 using the USGS epicenter. We treated Bakun's estimate as a noisy estimate of **M**, using his stated uncertainties.

11. 1962, Aug. 30. Cache Valley, Utah (M 5.75): This damaging earthquake in northern Utah was one of the first to occur in the UTR after the start of regional seismographic monitoring by the University of Utah in July 1962. Damage and felt effects are described in *United States Earthquakes 1962* (Lander and Cloud, 1964). Westaway and Smith (1989) undertook a special study of this earthquake, including a revision of the mainshock's hypocenter and a determination of a moment tensor from inversion of long-period teleseismic body waveforms. Our assigned epicenter and focal depth are from their study. Our best-estimate moment magnitude, **M** 5.75 ± 0.15, is based on $\mathbf{M}_{obs}$, where M_0 is the geometric mean of two measurements: 7.1×10^{24} dyne-cm made by Wallace and others (1981) and $3.1 \pm 0.2 \times 10^{24}$ dyne-cm made by Westaway and Smith (1989).

12. 1962, Sept. 5. Magna, Utah (M 4.87): Six days after the **M** 5.75 shock in Cache Valley, this damaging earthquake occurred 140 km to the south in the Salt Lake Valley. Damage and felt effects are described in *United States Earthquakes 1962* (Lander and Cloud, 1964). Our assigned epicenter and focal depth are from the UUSS catalog. For reasons described earlier (see *Moment Magnitude Data*), a seismic moment determined by Doser and Smith (1982), corresponding to **M** 5.02, was judged to be unreliable (likely an overestimate). In the absence of a reliable seismic moment and because of the occurrence of this earthquake soon after the mid-1962 start of regional seismic monitoring in Utah, we decided to use all available size measures, including non-instrumental ones, to estimate **M**. Available instrumental size measures consist of a single-station M_L UU value of 5.0 (revised), an M_L PAS value of 5.0 (Earthquake Notes, Bulletin of the Seismological Society of America, v. 53, no. 1, p. 215), and an m_b GS value of 5.1. We did not use the latter measurement because our m_b GS regression for this period is poorly constrained (see figure E-11) and the reported value of 5.1 is just outside the bounds of our regression (if used, the conversion relationship would yield **M** 4.88) .

Our best-estimate moment magnitude, **M** 4.87 ± 0.13, is based on inverse-variance weighting that combines $\mathbf{M}_{pred}$ values from M_L UU (**M** 4.81), M_L PAS (**M**~ 5.0), FA (**M** 4.81), I_0 = VI (Stover and Coffman, 1993, **M** 4.81), and A_{MMI} (using the mean of **M** 4.56 and **M** 4.99, calculated from A_V and A_{VI}, respectively). The weighted and individual estimates of **M** are fairly consistent and indicate a size slightly smaller than **M** 5.0 for the 1962 Magna earthquake.

13. 1963, July 7. Juab Valley, Utah (M 5.06): This earthquake in Juab Valley in central Utah reached MMI VI (Stover and Coffman, 1993) and produced slight damage. Damage and felt effects are described in *United States Earthquakes 1963* (von Hake and Cloud, 1965). Our adopted epicenter for this earthquake is from the UUSS catalog. Our best-estimate moment magnitude, **M** 5.06 ± 0.15, is from Patton and Zandt's (1991) moment-tensor solution for this earthquake, determined from the inversion of regional surface-wave data. The focal depth we list for this shock is also from Patton and Zandt (1991).

14. 1966, Aug. 16. Nevada-Utah border (M 5.22): A vigorous earthquake sequence with characteristics of an earthquake swarm occurred from August 1966 into early 1967 in the sparsely populated, southern Nevada-southwestern Utah border area. The largest event, which occurred at the start of the sequence on August 16, 1966, at 18:02 (UTC), is described by Rogers and others (1991) and referred to as the Caliente/Clover Mountains earthquake. Our assigned epicenter is from the UUSS catalog. A joint-hypocenter-determination location at 37.395° N, 114.206° W by Rogers and others (1991), 9 km south-southwest of the UUSS epicenter, still lies within the UTR. Felt effects are described by von Hake and Cloud (1968). Stover and Coffman (1993) assess a shaking intensity of MMI V at Caliente, the closest town (population ~1100) at a distance 28 km from the epicenter of Rogers and others (1991) and 36 km from our UUSS epicenter.

The only available measurement of seismic moment for this earthquake is one by Doser and Smith (1982), corresponding to **M** 5.33. However, for reasons described earlier (see *Moment Magnitude Data*), their M_0 was judged to be unreliable (likely an overestimate). Our best-estimate moment magnitude, **M** 5.22 ± 0.20, is from inverse-variance weighting of $\mathbf{M}_{pred}$ values from two available instrumental size measures: a revised, single-station M_L UU of 5.2 (**M** 4.96) and an m_b ISC of 5.4 from 19 stations (**M** 5.53). The data we have reviewed do not support a magnitude as high as 5.7 to 6.1 reported by Rogers and others (1991) and attributed to the University of California at Berkeley. In addition to the instrumental size measures described above, the area shaken is also indicative of a smaller size. Our measurement of A_V (table E-12) gives **M** 5.25, and the total felt area of 66,000 km^2 estimated by Stover and Coffman (1993) gives **M** 4.99.

In the declustered version of the BEM catalog, the **M** 5.22 earthquake on August 16 at 18:02 (UTC) was originally flagged as a foreshock to a following event on August 17 at 23:07 (UTC) that had a magnitude of $\mathbf{M}^{\sim}$ 5.5, based on an M_L determined at Berkeley. Knowing that the August 16 shock was the largest in the sequence (Rogers and others, 1991, and UUSS data), we re-assigned it to be the mainshock and eliminated the August 17 event as an aftershock. Our best estimate of the mainshock's size suggests that values of $\mathbf{M}^{\sim}$ from MLBRK in the BEM catalog may overestimate **M** by a half magnitude unit or more. Except for two earthquakes in the EBR in 1972 and 1984, all $\mathbf{M}^{\sim}$ entries in the BEM catalog from MLBRK are for aftershocks of the August 16, 1966, earthquake. (It is unclear which stations of the Berkeley array were used to determine the M_L values we used as $\mathbf{M}^{\sim}$; we estimate that the Berkeley stations would be roughly in the 500–700 km distance range from the 1966–1967 Nevada-Utah border earthquakes.)

15. 1967, Oct. 4. Marysvale, Utah (M 5.08): This earthquake caused minor damage within and near the southern Sevier Valley in central Utah and was widely felt. Felt and damage effects are described by von Hake and Cloud (1969). Our best-estimate moment magnitude, **M** 5.08 ± 0.15, is based on Patton and Zandt's (1991) moment tensor for this earthquake, determined from

the inversion of regional surface-wave data. The focal depth we list for this shock is also from Patton and Zandt (1991); our assigned epicenter is from the UUSS catalog. For comparison with other size measures, a three-station M_L UU of 5.4 (revised) yields **M** 5.12. A_{MMI} measures (table E-12) indicate a slightly larger size: the average **M** from A_V, A_{VI}, and A_{VII} is 5.36.

16. 1975, Mar. 28. Pocatello Valley, Idaho (M 6.02): This earthquake, which occurred in a rural valley on the Idaho-Utah border, is the largest to date in the UTR since the beginning of regional seismographic monitoring by the UUSS in July 1962. Details of the foreshock-mainshock-aftershock sequence are described by Arabasz and others (1981). Damage and felt effects are described by Coffman and Stover (1977) and by Cook and Nye (1979). Our assigned epicenter is from the UUSS catalog; the focal depth, from Arabasz and others (1981). Our best-estimate moment magnitude, **M** 6.02 ± 0.06, is based on the geometric mean of four measurements of M_0 from Battis and Hill (1977), Williams (1979), Bache and others (1980), and Wallace and others (1981). The value of $\sigma = 0.06$ is the standard error of the mean calculated from the four values of $\mathbf{M}_{obs}$, after correcting their standard deviation for sample size. A_{MMI} measures (table E-12) are consistent with $\mathbf{M}_{obs}$: the average **M** from A_{IV}, A_{VI}, and A_{VII} is 6.03.

17. 1988, Aug. 14. San Rafael Swell, Utah (M 5.02): This earthquake occurred within the Colorado Plateau of east-central Utah, triggering numerous rockfalls within 40 km of the epicenter. Case (1988) describes geologic and felt effects, and Pechmann and others (1991) describe details of the foreshock-mainshock-aftershock sequence. Our assigned epicenter for the mainshock is from the UUSS catalog; the focal depth of 17 km is from Pechmann and others (1991). Despite its size and date, no instrumental measurements of M_0 are available for this earthquake. Our best-estimate moment magnitude, **M** 5.02 ± 0.13, is based on inverse-variance weighting of $\mathbf{M}_{pred}$ values from four instrumental size measures: M_L UU = 5.17 (**M** 4.94); M_C UU = 4.92 (**M** 4.80); m_b GS = 5.5 (**M** 5.07); and m_b ISC = 5.4 (**M** 5.53).

18. 1989, Jan. 30. Southern Wasatch Plateau, Utah (M 5.20): This shock is often paired with the San Rafael Swell earthquake. It occurred just five months later and 70 km to the southwest within the Basin and Range-Colorado Plateau transition in central Utah. Both shocks had mid-crustal focal depths and occurred on buried Precambrian basement faults, perhaps reflecting regional left-lateral shear (Pechmann and others, 1991). Stover and Coffman (1993) briefly describe felt effects of the1989 mainshock, referencing unpublished USGS intensity data for 1989. Pechmann and others (1991) present and discuss seismological data for the foreshock-mainshock-aftershock sequence; our assigned epicenter and a focal depth of 25 km are from that study.

Our best-estimate moment magnitude, **M** 5.20 ± 0.10, is based on a seismic moment from the Global CMT Catalog (Ekström and Nettles, undated; Dziewonski and others, 1990). As noted earlier (see *Moment Magnitude Data*), we reduce $\mathbf{M}_{obs}$ from Global CMT seismic moments by 0.14.

19. 1992, Sept. 2. St. George, Utah (M 5.50): As of this writing, this earthquake in southwestern Utah was the most recent of **M** ≥ 5.0 in the UTR. The shock damaged buildings within and near the epicentral area and triggered a destructive landslide 44 km away near the town of Springdale (Jibson and Harp, 1995). Geologic effects of the earthquake are described by Black and others (1995), ground shaking and felt effects by Olig (1995), and seismological data by Pechmann and others (1994).

Our best-estimate moment magnitude, **M** 5.50 ± 0.10, is based on a seismic moment from the Global CMT Catalog (Ekström and Nettles, undated; Dziewonski and others, 1993). As noted earlier (see *Moment Magnitude Data*), we reduce $\mathbf{M_{obs}}$ from Global CMT seismic moments by 0.14. Pechmann and others (2007) determined a mean $\mathbf{M}_{obs}$ of 5.54 from seven reported measurements of M_0. Our measurements of A_{MMI} (table E-12) from Olig's (1995) isoseismal map give an average **M** 5.99 from A_V and A_{VI}. Our assigned epicenter for the earthquake is from the UUSS catalog; the focal depth is from the Global CMT solution.

IDENTIFICATION AND REMOVAL OF DEPENDENT EVENTS (DECLUSTERING)

Spatial and temporal clustering is common in natural seismicity. Statistical techniques are required to decompose or "decluster" an earthquake catalog into "main" events that are random and independent in a statistical sense and "dependent" events that relate non-randomly to the main events. Declustering algorithms variously use magnitude-dependent space-time windows, specific cluster models, or stochastic approaches to remove dependent events from an earthquake catalog (e.g., van Stiphout and others, 2012).

The terminology we adopt warrants comment. We define foreshocks, aftershocks, and the smaller events of earthquake swarms to be "dependent" events, following common usage in the published literature relating to declustering and without implying the nature of the dependency. (Veneziano and Van Dyck, 1985a, prefer the adjective "secondary" as a less specific qualifier for such events.) We use the companion term "main" events or "mainshocks" for isolated events and the largest events of earthquake clusters. For specificity, we alternatively refer to the set of main events identified by our selected declustering algorithm as "independent mainshocks," assuming they occur as part of a Poisson process.

Declustering Algorithm Used

For conformity with procedures used by the USGS for earthquake catalog processing associated with the U.S. National Seismic Hazard Maps (see Petersen and others, 2008), we used the computer program *cat3w* developed by C.S. Mueller of the USGS. This program implements the declustering method of Gardner and Knopoff (1974), in which smaller earthquakes within fixed time and distance windows of larger shocks are identified as dependent events (using our terminology). The program *cat3w* uses the window values published by Gardner and Knopoff (1974). Although the Gardner and Knopoff (1974) declustering technique is a relatively simply one, its recent application to seismicity throughout the central and eastern U.S. produced results very similar to those from a stochastic declustering method (EPRI/DOE/NRC, 2012).

For our purposes, we made three modifications to *cat3w* that are hard-coded in the computer program. First, we reduced the minimum magnitude from 4.0 to 2.5. Second, we modified the eastern limit of a geographic sorting boundary so that the entire extended Utah region would be included. Third, we slightly changed the boundaries of sort areas that *cat3w* uses to exclude coal-mining related seismicity in Utah to correspond exactly to the standard boundaries used by the UUSS. We did this so that *cat3w* would not remove events, judged by us to be tectonic, *outside* our defined MIS areas.

Table E-15 summarizes declustering results for each of the spatial domains of the BEM catalog. The relative proportion of independent mainshocks to dependent events in each of the domains should be viewed with caution because it varies significantly with time, particularly before and after the start of regional instrumental monitoring in the early 1960s. The larger proportion of dependent events in the EBR chiefly results from an intense aftershock sequence following the **M** 5.66 Draney Peak, Idaho, earthquake of February 3, 1994; other major contributors are aftershocks of the **M** 5.91 Wells, Nevada, earthquake of February 21, 2008, and events of a swarm sequence near the Nevada-Utah border whose largest event was a shock of **M** 5.22 on August 16, 1966.

Checks on Effectiveness of Declustering

Space-Time Plots

To check the effectiveness of using *cat3w* to decluster our BEM catalog, we first compared space-time plots of the clustered and declustered versions of the catalog to satisfy ourselves that the declustering results were reasonable. Comparative plots are shown in figures E-20 and E-21 for the WGUEP Region and in figures E-22 and E-23 for the Utah Region. In each of the space-time plots, times of earthquake occurrence from 1960 through September 2012 are plotted as a function of latitude and distinguished by earthquake size. We chose 1960 as the starting point of the time range because dependent events are more systematically recorded and amenable to study during the instrumental part of the earthquake catalog. The magnitude bins used in the plots correspond to those analyzed later with respect to completeness and earthquake rates (the only shocks of **M** ≥ 6.5 in the catalog occurred before 1960). The start dates of periods of complete reporting for the three lower magnitude bins are plotted as vertical dashed lines on the declustered versions of the space-time plots.

For the WGUEP Region plots, the declustered version (figure E-21), compared with the clustered version (figure E-20), indicates a favorable outcome: clustered earthquakes have been thinned out in the space-time vicinity of larger shocks, and earthquakes identified as mainshocks have the appearance of being randomly scattered (using the periods of completeness as a visual guide). This observation is qualitatively consistent with a temporal Poisson process. Spatially, rates of occurrence are inhomogeneous and can be seen to be relatively higher in the northern part of the WGUEP Region, north of about latitude 41.5°N. The latitude-vs.-time plots suffer from being two-dimensional, but they serve the purpose of enabling a visual assessment of whether there is a reasonable balance between leaving too many grouped shocks and unduly decimating the catalog.

Comments similar to the above apply to the Utah Region plots (figures E-22 and E-23) in terms of the declustering outcome. In this larger region, spatial inhomogeneity of earthquake occurrence is more evident. Background earthquake activity is relatively higher in the northern and southern parts of the Utah Region and discernibly lower between about latitude 41.5°N and about latitude 39.5°N—the part of Utah's northerly-trending seismic belt that roughly coincides with the five central active segments of the Wasatch fault. This feature of Utah's seismicity is well known (see, for example, Smith and Arabasz, 1991).

Kolmogorov-Smirnov (K-S) Tests

As a quantitative check on whether the declustered catalog for the WGUEP region was Poissonian, we used the Kolmogorov-Smirnov (K-S) test to analyze data in the three lowest magnitude bins plotted on figure E-21, comparing the observed cumulative distribution function (CDF) of inter-event times to that expected for a Poisson distribution (see analogous example of traffic-gap data in Benjamin and Cornell, 1970, p. 470–472). The reason for analyzing the three lowest magnitude bins is that they have sufficient data and are the most sensitive to choices of space-time windows used in the declustering. The data analyzed were restricted to the periods of completeness indicated on figure E-21.

To illustrate the K-S test, figures E-24a and E-24b graphically display data for the two lowest magnitude bins. The K-S statistic**,** *D*, indicated on the plots is the largest absolute difference between the CDF for the observed declustered data and the expected CDF for a Poisson distribution, given the mean inter-event time from the observed sample. The test statistic *D* is 0.042 for $2.85 \leq \mathbf{M} \leq 3.54$ (182 inter-event times), 0.133 for $3.55 \leq \mathbf{M} \leq 4.24$ (38 inter-event times), and for the third magnitude bin (not shown), 0.466 for $4.25 \leq \mathbf{M} \leq 4.94$ (8 inter-event times). Following Benjamin and Cornell (1970), *D* in each case was found to be less than the critical value at the 5 percent significance level, α, for *rejecting* the null hypothesis that the observed CDF is Poissonian (we interpolated some of the values of the critical statistic in table A7 of Benjamin and Cornell, 1970). As expected, *D* values for the clustered CDFs in each of the three magnitude bins exceeded their critical values for $\alpha = 0.05$, indicating that these distributions were not Poissonian.

We similarly used K-S tests to analyze declustered data for the Utah Region shown on figure E-23, again analyzing the three lowest magnitude bins and restricting data to the periods of completeness shown on the figure. Graphical results are displayed on figures E-24c and E-24d. The test statistic *D* is 0.033 for $2.85 \leq \mathbf{M} \leq 3.54$ (427 inter-event times), 0.064 for $3.55 \leq \mathbf{M} \leq 4.24$ (76 inter-event times), and for the third magnitude bin (not shown), 0.181 for $4.25 \leq \mathbf{M} \leq 4.94$ (17 inter-event times). Here too, *D* in each case was found to be less than the critical value at the 5 percent significance level for rejecting the null hypothesis that the observed CDF is Poissonian. Just as for the WGUEP Region, *D* values indicated that all the Utah Region's clustered CDFs were non-Poissonian distributions.

In sum, our testing gives us confidence that the declustered BEM earthquake catalog can be used to develop reliable background earthquake models for the WGUEP and Utah regions. Despite its relative simplicity, the declustering approach of Gardner and Knopoff (1974) that we implemented using the computer program *cat3w* yielded satisfactory results.

PERIODS OF COMPLETENESS

A critical element for constructing the background earthquake models is the completeness period, T_C, for which the reporting of earthquakes at or above a given magnitude threshold in the earthquake catalog is complete. For the WGUEP study, the parameter of the model ultimately of primary concern to the Working Group is the annual rate of occurrence of independent mainshocks of $\mathbf{M} \geq 5.0$ within the *entire* WGUEP Region. Accordingly, this region was treated

as a single domain for assessing periods of completeness. We similarly treated the UTR as a single domain for assessing the periods of completeness for its background earthquake model.

To determine T_C for different magnitude thresholds in the declustered catalog, we used cumulative recurrence curves (CRCs) together with general information on the space-time evolution of seismographic control, population, and newspapers. A CRC is a plot of the cumulative number of earthquakes above a given magnitude threshold versus time. The use of a probabilistic approach, which allows the analysis and use of variable completeness throughout an entire earthquake record (see, for example, EPRI/DOE/NRC, 2012, or Felzer, 2007) was beyond the scope of this study. According to Grünthal and others (1998, as quoted in and cited by Hakimhashemi and Grünthal, 2012), the CRC method is "very simple but rather robust."

Seismographic Monitoring

Seismographic monitoring of the Utah Region by the University of Utah has progressively evolved since June 29, 1907, when a pair of Bosch-Omori horizontal-pendulum seismographs were installed on the university campus in Salt Lake City (Arabasz, 1979). Significant milestones in the UUSS instrumental coverage of the region include the beginning of a skeletal statewide network in Utah of onsite-recording seismographs in July 1962, the start of a regional telemetered seismic network in October 1974, and the start of digital network recording in January 1981 (see Arabasz et al, 1992, and Smith and Arabasz, 1991, for representative maps of seismographic coverage and historical background). Major expansion and modernization of the University of Utah's regional seismic network during the last two decades have enhanced the quality and precision of earthquake locations and magnitudes, but they have not materially affected the completeness of the earthquake record above the lowest threshold of interest here ($\mathbf{M} \geq 2.85$).

Early Historical Earthquake Record

The historical earthquake record for the Utah Region effectively begins with the arrival of Mormon pioneers in the Salt Lake Valley in July 1847, under the leadership of Brigham Young, and the establishment soon thereafter of the first newspaper in Utah in 1850. Other explorers and fur trappers reached the present Utah Region before 1847, but their written records contain no mention of local earthquakes, and there is no known oral history of specific earthquakes felt by Native Americans in the region before the coming of white settlers. The first documented earthquake in the Utah Region occurred on February 22, 1850 (Arabasz and McKee, 1979).

The completeness of Utah's historical earthquake record is influenced by the pattern of settlement after 1847. After reaching the Salt Lake Valley, Brigham Young promptly initiated and directed an extensive program of exploring and colonizing. Between July 1847 and May 1869, when the First Transcontinental Railroad was completed at Promontory Summit north of Great Salt Lake, more than 60,000 Mormon pioneers crossed the plains to settle in Utah (Wahlquist, 1981). For convenience, we use the areas and boundaries of present-day states in describing historical geography.

By the time of Brigham Young's death in 1877, Mormon settlements extended throughout the Intermountain Seismic Belt in the UTR (figure E-1) as well as into outlying parts of Utah and other parts of the UTR in southeastern Idaho, southwestern Wyoming, and northern Arizona (see

Wahlquist, 1981, and Arrington, 1994). Settlements in the region were also founded by railroads, mining companies and non-Mormons (Wahlquist, 1981; Arrington, 1994).

There are useful summaries, figures, and tabulations pertaining to the timing and geographical extent of permanent settlements in the UTR in Wahlquist (1981). The website Utah Digital Newspapers (http://digitalnewspapers.org/about/county_map/) provides the names, dates, and locations of newspapers in the region. We use these sources of information to support arguments for assessing T_C for the magnitude bins of larger earthquakes in the WGUEP and Utah regions, extending backward into historical time.

Population Distribution and Growth in the UTR

To help the reader understand some of our later arguments, we elaborate on the distribution and historical growth of population in the UTR. The variability of modern population density in the UTR is illustrated in the map on figure E-25. Referring to the numbered localities on the map, salient features include: concentrated population in a northerly-trending belt in Utah's Wasatch Front area (1) extending into southeastern Idaho (2); a southwesterly-trending band of population centers extending from the Sanpete Valley (3) in central Utah through the Sevier Valley (4) and Beaver Basin (5) to population centers in the vicinities of Cedar City (6) and St. George (7) in southwestern Utah; a roughly elliptical populated area in the Uintah Basin of northeastern Utah (8); diffusely scattered population centers in southwestern Wyoming (9); and relatively sparse population in Utah's southeast quadrant, where the interior of the Colorado Plateau (10) is bordered by a roughly circular ring of scattered population centers in central and southern Utah (11, 12), northern Arizona (13), northwestern New Mexico (14), and western Colorado (15). Using this modern population map for reference, together with information in Wahlquist (1981), we can characterize the distribution of population in the UTR at earlier stages in 1850, 1860, and 1880—particularly in relation to the Intermountain Seismic Belt (compare figures E-18 and E-25).

Population Distribution in 1850

In 1850, there were at least 37 permanent settlements in Utah, concentrated along the Wasatch Front between Brigham City and Payson and extending west of the Salt Lake Valley into neighboring Tooele Valley (see localities a–d on figure E-25). Again referring to the numbered localities on figure E-25, there also were outlying settlements in Manti (3) in central Utah and near Cedar City (6) in southwestern Utah. These early settlements, combined with the presence of Fort Bridger (16) in southwestern Wyoming established in 1842, and Fort Hall (17) in southeastern Idaho, established in 1834, provided a significant capability for detecting and reporting strong earthquake ground shaking in the WGUEP Region in 1850.

Population Distribution in 1860

A tabulation of more than 400 settlements in Utah with a Mormon ward or branch, including their date of settlement, is given in Wahlquist (1981, page 91). Of the 397 permanent settlements listed, one-third were established by the end of 1860. Utah settlements in 1860 are shown on a map on page 114 of Wahlquist (1981). Importantly, Utah's population during the 1850s expanded from the Wasatch Front area into central and southwestern Utah (along the trend of localities 3, 4, 5, 6, and 7 on figure E-25). Fillmore (locality 18, figure E-25) was also

established in the 1850s as the first capital of the Utah Territory. By 1860, the continuity of population centers along Utah's main seismic belt—in southwestern, central, and northern Utah—was effectively complete.

Population Distribution in 1880

The distribution of communities in Utah in 1880 is illustrated by a map on page 114 in Wahlquist (1981). The map in question is a plot for 1890, but companion data on page 91 of the same publication indicate that 277 (93%) of the 297 communities whose locations are plotted had actually been settled by 1880. These same data indicate that 70% of Utah's permanent communities had been established by 1880. Except for the Uintah Basin and southeasternmost Utah, the general distribution of population in Utah by that time does not differ greatly from that in 1950 or 1970 (compare maps for 1890, 1950, and 1970 on pages 114 and 115 in Wahlquist, 1981).

During the 1860s and 1870s, Mormon expansion beyond Utah had also led to population coverage of the border regions of the UTR in southern and southeastern Idaho, southwestern Wyoming, eastern Nevada, northern Arizona, and northwestern New Mexico (see Wahlquist, 1981, p. 92–93). This additional population coverage, partly reflected in the location of population centers on figure E-25, is germane to capabilities for the detection and reporting of earthquake ground shaking in the UTR in 1880.

Population Distribution and Sampling of Earthquake Ground Shaking

For our use in later arguments, figure E-25 also provides information for visually comparing population distribution and the expected extent of ground shaking of MMI IV or greater, depicted by circular areas equal to A_{IV} predicted for shocks of **M** 4.95 to **M** 6.45. Our purpose in using A_{IV} is to convey the likelihood not only of detecting earthquake ground shaking but also of having sufficient geographic sampling to estimate **M**.

For reference, ground shaking associated with a level of IV on the MM intensity scale is described by Stover and Coffman (1993, p. 3) as follows: "Felt by many to all. Trees and bushes were shaken slightly. Buildings shook moderately to strongly. Walls creaked loudly. Observer described the shaking as 'strong.'" This characterization of effects, which these USGS authors use as a guide for assigning intensity level IV, represents a slight modification of the MM intensity scale outlined by Wood and Neumann (1931).

Table E-17 gives the radii of the equivalent circular areas for A_{IV}. The table also gives the equivalent radii for an approximation of *total* felt area, FA. As noted in the table, the values of A_{IV} were calculated using the results of a general orthogonal regression of $\log(A_{IV})$ on $\mathbf{M}_{obs}$, but FA was approximated by simply inverting the non-linear conversion relationship CR-12 in table E-8. Note that for each magnitude, the equivalent radius of the expected total felt area is roughly double (1.7–2.3 times) the radius for A_{IV}, which greatly increases the chance that an earthquake of a particular magnitude would be reported at multiple localities.

Data and Basis for Completeness Periods

Table E-16 summarizes the completeness periods (T_C) we assessed for the WGUEP and Utah regions. In our rate calculations, we use magnitude bins with a range of 0.7 magnitude unit. The table also provides T_C for magnitude bins with a range of 0.5 magnitude unit for those wishing to use alternative bins in other applications. For each specified magnitude threshold, $T_C = t_e - t_0$, where t_e and t_0 are the end and start dates, respectively, of the completeness period. In this study, t_e uniformly is the end of our earthquake catalog on September 30, 2012.

In the remainder of this section, we explain how we chose t_0 for the various magnitude thresholds we analyzed—based either on a pick from a CRC, on joint consideration of a CRC and other arguments, or solely on other arguments (for **M** ≥ 5.95). CRCs for the WGUEP and Utah regions are presented in figures E-26 and E-27, respectively. To help the reader navigate table E-16 in conjunction with the figures, we will use the same font-type notation for dates as used in table E-16 when discussing our selection of t_0 for the various magnitude bins (e.g., **1986**, ***1908***, *1850*). Also, for convenient shorthand, we will refer to the magnitude bins by the lower end of their range and use "W" for the WGUEP Region and "U" for the UTR (e.g., 2.85W, 3.55U, etc.).

t_0 from CRCs (1963–1986)

For our picks of t_0 from a CRC (indicated by a date in regular bold type in table E-16), we estimated t_0 by inspecting the CRC, superposing a trend line for the most recent time period (assuming stationarity of earthquake rate), and visually picking the point on the CRC backward in time at which the linear trend deviates significantly. The deviation is typically, but not always, a decrease in rate. Our primary objective in selecting each t_0 was to bracket a completeness period whose earthquake rate was convincingly uniform and reliable, particularly for magnitude thresholds below 4.95. For the latter data, the completeness periods we picked from the CRCs should be considered conservative minimum values of T_C. In other words, our selected t_0 does not necessarily mark when network sensitivity changed to enable uniform reporting above that magnitude threshold. For some CRCs, statistical tests of rate information allow T_C to be lengthened, but a t_0 earlier than the one we adopted is not as visually compelling on the CRC.

To check our picks of t_0 from CRCs, the reader can simply examine table E-16 and then refer to the corresponding CRC. For example, for 2.85W, t_0 = **1986**, which can be seen as the labeled pick on figure E-26a. Our direct picks range from **1963** (3.95W, 4.25U) to **1986** (2.85W, 2.85U). The selected dates are internally consistent, and they are consistent with maps of the evolution of seismographic coverage in the UTR. (Besides referring to the maps cited earlier, we also examined annual station maps in UUSS reports.) Our assessments of T_C indicate completeness since 1963 for **M** ≥ 3.95 in the WGUEP Region and for **M** ≥ 4.25 in the UTR.

t_0 from CRCs and Other Arguments (1908, 1880)

1908: In table E-16, two values of t_0 (indicated in italicized bold type: ***1908, 1880***) are based on joint consideration of CRCs and other arguments. For the earthquake record before 1963, the CRC for 18 shocks of **M** ≥ 4.95 in the UTR (4.95U, figure E-27h) suggests completeness and a fairly uniform rate of occurrence extending back to the first decade of the 1900s. The CRC for

the smaller WGUEP Region (4.95W, figure E-26h) is consistent with this conclusion. The installation of seismographs on the University of Utah campus in June 1907 is significant. We believe that any shock of **M** ≥ 4.95 in the UTR after the start of local seismographic recording on that date would not have escaped reporting. Based on this argument and the CRCs, we assign ***1908*** as the t_0 for both 4.95U and 4.95W.

The distribution of population and newspapers in Utah by 1908 and the expected extent of ground shaking of MMI IV or greater (figure E-25) support the expectation that any shock in the UTR of **M** ≥ 4.95 after 1908 would be reported and its size reasonably estimated. These supporting arguments are strongest for Utah's main seismic belt but are admittedly weaker for southeastern Utah. By 1908, local newspapers were being continuously published in 24 of Utah's 29 counties. Three of the exceptions are in southeastern Utah. In Garfield County, publishing began in 1913; in San Juan County, in 1919; and in Kane County, in 1929. Regarding the two other exceptions, local newspaper publishing began in 1909 in Duchesne County in the Uintah Basin and in 1910 in Morgan County in north-central Utah.

1880: The second t_0 value based on joint consideration of CRCs and other arguments is ***1880***. The CRC for 11 shocks of **M** ≥ 5.45 in the UTR (5.45U, figure E-27i) suggests completeness and a fairly uniform rate of occurrence extending back to about 1880 (the first shock in the sample occurred in 1884). The CRC for for the smaller WGUEP Region (5.45W, figure E-26i) also supports this conclusion. Data for the slightly higher threshold of **M** ≥ 5.65 are more sparse (5.65U, figure E-27j, and 5.65W, figure E-26j); however, by extension, completeness for **M** ≥ 5.45 must also apply to **M** ≥ 5.65.

We use figure E-27i as the starting point to argue for ***1880*** as the t_0 for **M** ≥ 5.45 in the UTR, which would logically lead to the same t_0 for 5.45W, 5.65U, and 5.65W. Supporting arguments can be made from the distribution of population in 1880, discussed earlier, and (to a lesser extent) of newspapers. In 1880 newspapers were being continuously published only in the Wasatch Front area. The extent of observed ground shaking caused by the **M** 5.58 earthquake near Paris, Idaho, at the northern end of the UTR in November 1884 (Evans and others, 2003) and the predicted extent of A_{IV} from a shock of **M** 5.45 (figure E-25) also support the expectation that earthquakes of this size in the UTR would be completely reported after 1880—with high confidence if the shock occurred along Utah's main seismic belt. Looking at figure E-25, where in the UTR could one arguably "hide" a shock of **M** 5.45 in 1880? At that time, besides the population distribution we described earlier, there were at least six established communities in the Uintah Basin (locality 8), at least 11 established communities in the coal-mining areas of east-central Utah (locality 11), and a few small communities in southeastern Utah. Conceivably, a shock of **M** 5.45 in the interior of the Colorado Plateau (locality 10) might have had ground shaking of MMI IV or larger insufficiently sampled to estimate the shock's true size, but such an earthquake likely would have been reported felt (because of a predicted felt radius of 207 km).

t_0 from Other Arguments (1850, 1860, 1880)

The BEM catalog contains only four mainshocks of **M** ≥ 5.95 in the UTR, too few to produce informative CRCs, leaving us to make assessments of t_0 solely on the basis of other arguments. For the WGUEP Region, we have confidence in choosing 1850 as t_0 for **M** ≥ 5.95. This choice is based on the population distribution that we described earlier, the 1850 start date for Utah's first newspaper, and the size of A_{IV} compared to the geography of the WGUEP Region (figure E-25).

Isoseismal maps for the 1962 **M** 5.75 Cache Valley, Utah, earthquake and the 1975 **M** 6.02 Pocatello Valley, Idaho, earthquake (Hopper, 2000) strongly argue against the possibility that any shock of **M** ≥ 5.95 in the WGUEP Region in 1850 or later could escape reporting or not have its size reasonably estimated from felt reports.

For the Utah Region as a whole, we are not confident that the population distribution before 1880 was adequate to ensure reasonable sampling of A_{IV} for any shock of **M** ≥ 5.95 (figure E-25). We judge that population distribution was sufficient in 1880, however, and we assign that date as t_0 for the **M** 5.95 threshold in the UTR. For higher magnitude thresholds (**M** 6.35 and **M** 6.45), the expected sizes of A_{IV} and FA are so large (figure E-25, table E-17) that we believe the distribution of Mormon settlements in 1860 justifies assigning that date as t_0 for those size thresholds in the UTR.

*N** VALUES AND SEISMICITY RATE PARAMETERS

The culmination of all the described preceding steps is the calculation of seismicity rate parameters for background earthquake models for the WGUEP and Utah regions. Recall that our goal is to achieve unbiased estimates of seismicity rate parameters. We do this by using the N^* approach developed by Tinti and Mulargia (1985) that was outlined in figure E-2.

*N** Values

N^* is a count of earthquakes in a specified magnitude interval, adjusted for magnitude uncertainty bias, that is used to compute unbiased earthquake recurrence parameters. We followed the EPRI/DOE/NRC (2012) steps of (1) calculating N^* from σ on an earthquake-by-earthquake basis (using $N^* = \exp\{-(b \ln(10))^2\sigma^2/2\}$), (2) summing N^* for earthquakes within specified magnitude intervals, (3) dividing each N^* sum by the period of completeness for its respective magnitude interval, and (4) using a maximum-likelihood approach to compute seismicity rate parameters from the equivalent N^* counts. For the N^* calculations, we used a *b*-value of 1.05 assessed from preliminary processing of the BEM catalog. For our six magnitude intervals of complete reporting, the observed number of independent mainshocks along with equivalent N^* counts are given in tables E-18 and E-19 for the WGUEP Region and the Utah Region, respectively.

Seismicity Rate Parameters

Background Earthquake Model for the WGUEP (Wasatch Front) Region

The data in table E-18 were used as input to the maximum-likelihood algorithm of Weichert (1980) to solve for unbiased recurrence parameters for the WGUEP Region. The Weichert algorithm has the capability to handle binned magnitude data with variable periods of completeness as well as truncation of the exponential magnitude distribution at an upper limit, m_u. Figure E-28 shows the fit of the WGUEP data to a truncated exponential distribution [equation (E-13)]. The fit is for an m_u of 7.00 corresponding to the upper limit of the largest magnitude bin in table E-18 and consistent with a maximum magnitude of **M** 6.75 ± 0.25. We tested alternative values of m_u from 6.75 to 8.00 and determined that both the seismicity rates and *b*-value were insensitive to the change. For the WGUEP Region background earthquake

model, based on N^*, the cumulative annual rate of independent mainshocks greater than or equal to $m_0 = 2.85$ is 7.70 with a standard error of $\sigma(N(m_0)) = 0.52$. The b-value determined for the model is 1.06 with a standard error of $\sigma(b) = 0.06$. Table E-20 provides rate information for **M** ≥ 5.0 and other magnitude ranges, calculated using these parameters and equation (E-13). This table indicates that potentially damaging background earthquakes of **M** ≥ 5.0 occur in the WGUEP Region on the average of once every 25 years, with 90% confidence limits of once every 17 to 44 years.

The confidence limits on the seismicity rates in table E-20 are based on a 25-point discrete probability distribution for paired $N(m_0)$ and b-values that Robert R. Youngs (AMEC Foster Wheeler, written communication, March 16, 2014) determined for us using equation (E-13) with $m_0 = 2.85$ and $m_u = 7.00$, the data in table E-18, and the same likelihood model used to calculate the best-fit $N(m_0)$ and b-values (Weichert, 1980; Veneziano and Van Dyck, 1985b). The likelihood function is

$$L = \prod_i \frac{(\lambda_i T_i)^{n_i} e^{-\lambda_i T_i}}{n_i!} \qquad \text{(E-14)}$$

where n_i is the observed number of earthquakes in the magnitude range $m_i \leq m < m_{i+1}$, T_i is the time period of completeness for this magnitude range, and λ_i is the predicted rate of earthquakes in this magnitude range for a truncated exponential distribution. In terms of equation (E-13), λ_i can be written as:

$$\lambda_i = N(m_0)\,\frac{10^{-b(m_i - m_0)} - 10^{-b(m_{i+1} - m_0)}}{1 - 10^{-b(m_u - m_0)}} \qquad \text{(E-15)}$$

The following text from Robert Youngs (written communication, May 7, 2014) describes how he used this likelihood function to develop a discrete joint probability distribution for $N(m_0)$ and b:

> The process involves setting up a grid of pairs of $N(m_0)$ and b, computing the likelihood that the observed seismicity in a zone is produced by each pair, and then normalizing these likelihoods to form a discrete joint distribution for $N(m_0)$ and b. This process captures the correlation between $N(m_0)$ and b. The grid of b-values is initially set at values spaced at 0.1 [$\sigma(b)$] over the range of ±2.5 [$\sigma(b)$]. The grid of $N(m_0)$ values consists of 51 points over the range of 0.5% to 99.5% of a chi^2 distribution. The grid of 51x51 pairs is then aggregated at 25 points representing the centers of grid sections dividing the range of $N(m_0)$ and b-values into five sections. The weight assigned to each of the 25 points is the sum of the relative likelihoods in each grid partition.

We used the resulting discrete probability distribution for $N(m_0)$ and b to calculate 90% confidence limits on the cumulative seismicity rates for each of the minimum magnitude values m in table E-20. These calculations involved the following steps: (1) for each pair of $N(m_0)$ and b values, calculate the number of earthquakes per year of magnitude m and greater using equation (E-13); (2) sort the resulting table of earthquake rates, and the associated values of $N(m_0)$, b, and branch weight, in order of increasing rate of **M** ≥ m earthquakes $N(m)$; (3) calculate the cumulative weight for each rate value, which is the sum of its weight and the weights for all of the lower rates; and (4) interpolate to find the earthquake rate values $N(m)$

corresponding to cumulative weights of 0.05 and 0.95, which constitute the 90% confidence limits on the rates.

After carrying out this four-step procedure for the WGUEP data set, we found that for all m values of 5.0 and larger tested the cumulative weight associated with each $N(m_0)$-b pair in the 25-point discrete probability distribution was the same. We interpolated to find the $N(m_0)$-b pairs corresponding to the 5th and 95th percentile $N(m)$ values for $m \geq 5.0$. For the 5th percentile rates, $N(m_0) = 7.89$ events/yr and $b = 1.18$ and for the 95th percentile rates, $N(m_0) = 8.61$ events/yr and $b = 1.00$. These interpolated values can be used with equation (E-13) to estimate the 90% confidence limits on $N(m)$ for other magnitude ranges above $\mathbf{M} \geq 5.0$ (e.g., $\mathbf{M} \geq 5.25$). This alternative procedure for estimating confidence limits for magnitude ranges above $\mathbf{M} \geq 5.0$ is an empirical result for our specific WGUEP region data set.

Note that the cumulative rates in table E-20 are for independent *background* earthquakes in the WGUEP Region. In order to reliably estimate cumulative rates of all future mainshocks above **M** 5.0 in this region, one must also account for earthquakes expected to occur on identified faults (see, for example, WGUEP, 2016, figures 7.1-2 and 7.1-5).

Background Earthquake Model for the Utah Region

Following the same steps described above, the data in table E-19 were used as input to the maximum-likelihood algorithm of Weichert (1980) to solve for unbiased recurrence parameters for the Utah Region. Figure E-29 shows the fit to the data for an m_u of 7.00. For the background earthquake model, based on N^*, the cumulative annual rate of independent mainshocks greater than or equal to $m_0 = 2.85$ is 18.1 with a standard error of 0.81. The b-value determined for the model is 1.07 with a standard error of 0.04. Table E-21 provides rate information for $\mathbf{M} \geq 5.0$ and other magnitude ranges, calculated using these parameters and equation (E-13). This table indicates that potentially damaging background earthquakes of $\mathbf{M} \geq 5.0$ occur in the Utah region on the average of once every 11 years, with 90% confidence limits of once every 8 to 16 years. Just as for table E-20, we emphasize that the cumulative rates in table E-21 are for independent *background* earthquakes in the Utah Region and do not account for earthquakes expected to occur on identified faults.

The confidence limits on the Utah region seismicity rates in table E-21 were determined using the procedures described above for the WGUEP Region. The 25-point discrete probability distribution for paired $N(m_0)$ and b-values was provided to us by Robert R. Youngs (written communication, November 18, 2014). As was the case with the WGUEP Region, we found that the $N(m)$ percentile associated with each $N(m_0)$-b pair in the 25-point discrete probability distribution was the same for $m \geq 5.0$. Consequently, one can estimate the 90% confidence limits on $N(m)$ for any magnitude range above $\mathbf{M} \geq 5.0$ by using the following interpolated values for $N(m_0)$ and b in equation (E-13): $N(m_0) = 18.4$ events/yr with $b = 1.15$ for the 5th percentile rate and $N(m_0) = 18.7$ events/yr with $b = 1.01$ for the 95th percentile rate. Although we have found empirically that this alternative procedure for estimating confidence limits for magnitude ranges over **M** 5.0 is applicable to both our Utah and WGUEP region data sets, it may not be applicable to other data sets.

Some caution is warranted regarding use of the UTR background earthquake model. The Working Group on Utah Earthquake Probabilities made the decision to treat the WGUEP Region

as a single domain for constructing a background earthquake model. For this appendix we similarly treated the UTR as a single domain for modeling earthquake rates. The background earthquake model provides a good first-order representation of earthquake occurrence in the UTR, but it primarily reflects earthquake activity within the region's main seismic belt. For site-specific seismic hazard and risk analyses in the UTR, model components such as earthquake counts and periods of completeness should be re-assessed on a finer scale to account for the spatial inhomogeneity of seismicity in the UTR.

ACKNOWLEDGMENTS

We are indebted to colleagues at the U.S. Geological Survey's National Earthquake Information Center (USGS/NEIC) in Golden, Colorado, for data, information, and helpful discussions that enabled us to develop the unified earthquake catalog for the Extended Utah Region. In particular, we thank C.S. Mueller for providing key USGS earthquake catalogs and for sharing his *cat3w* declustering algorithm; J.W. Dewey, for information relating to m_b PDE and m_b ISC; and B.W. Presgrave, for information relating to M_L GS. We are also indebted to R.R. Youngs of AMEC Foster Wheeler, and G.R. Toro of Lettis Consultants International, Inc., for invaluable discussions and helpful guidance relating to methodology for achieving unbiased estimates of seismicity rate parameters. We accept full responsibility for any errors we may have made. R.R. Youngs also kindly generated probability distributions to aid our evaluation of confidence intervals on predicted seismicity rates. We thank the staff of the University of Utah Seismograph Stations for their supportive involvement, particularly P.M. Roberson for major help with the illustrations, S.N. Whittaker for help with ArcGIS analyses of isoseismal maps, and K.M. Whidden for providing her moment-tensor data. C.S. Mueller and J.W. Dewey of the USGS provided valuable review comments that helped improve this appendix.

REFERENCES

(including citations in the Electronic Supplements)

Ake, J., Mahrer, K., O'Connell, D., and Block, L., 2005, Deep-injection and closely monitored induced seismicity at Paradox Valley, Colorado: Bulletin of the Seismological Society of America, v. 95, no. 2, p. 664–683, doi: 10.1785/0120040072.

Anadarko Petroleum Corporation, 2005, Known sodium leasing area (KSLA) map: Online, http://www.wma-minelife.com/trona/tronmine/graphics/KSLA2005.pdf, accessed Feb. 14, 2014.

Arabasz, W.J., 1979, Historical review of earthquake-related studies and seismographic recording in Utah, *in* Arabasz, W.J., Smith, R.B., and Richins, W.D., editors, Earthquake studies in Utah 1850 to 1978: Salt Lake City, University of Utah Seismograph Stations, Department of Geology and Geophysics, p. 33–56.

Arabasz, W.J., Burlacu, R., and Pankow, K.L., 2007, An overview of historical and contemporary seismicity in central Utah, *in* Willis, G.C., Hylland, M.D., Clark, D.L., and Chidsey, T.C., Jr., editors, Central Utah—Diverse Geology of a Dynamic Landscape: Utah Geological Association Publication 36, p. 237–25.

Arabasz. W.J., and Julander, D.R., 1986, Geometry of seismically active faults and crustal deformation within the Basin and Range-Colorado Plateau transition in Utah, *in* Mayer, L., editor, Extensional tectonics of the southwestern United States—a perspective on processes and kinematics: Geological Society of America Special Paper 208, p. 43–74.

Arabasz, W.J., and McKee, M.E., 1979, Utah earthquake catalog, 1850–June 1962, *in* Arabasz, W.J., Smith, R.B., and Richins, W.D., editors, Earthquake studies in Utah 1850 to 1978: Salt Lake City, University of Utah Seismograph Stations, Department of Geology and Geophysics, p. 119–121, 131–143.

Arabasz, W.J., Nava, S.J., McCarter, M.K., Pankow, K.L., Pechmann, J.C., Ake, J., and McGarr, A.M., 2005, Coal-mining seismicity and ground-shaking hazard—a case study in the Trail Mountain area, Emery County, Utah: Bulletin of the Seismological Society of America, v. 95, no. 2, p. 18–30, doi: 10.1785/0120040045.

Arabasz, W.J., Nava, S.J., and Phelps, W.T., 1997, Mining seismicity in the Wasatch Plateau and Book Cliffs coal mining districts, Utah, USA, *in* Gibowicz, S.J., and Lasocki, S., editors, Rockbursts and seismicity in mines, Proceedings of the 4th International Symposium on Rockbursts and Seismicity in Mines, Krakow, Poland: Rotterdam, A.A. Balkema, p. 111–116.

Arabasz, W.J., and Pechmann, J.C., 2001, Seismic characterization of coal-mining seismicity in Utah for CTBT monitoring: Technical Report to Lawrence Livermore National Laboratory, LLNL Research Agreement No. B344836, variously paginated: Online, http://www.quake.utah.edu/wp-content/uploads/LLNLRept.pdf, accessed April 26, 2016.

Arabasz, W.J., Pechmann, J.C., and Brown, E.D., 1992, Observational seismology and the evaluation of earthquake hazards and risk in the Wasatch front area, Utah, *in* Gori, P.L., and Hays, W.W., editors, Assessment of regional earthquake hazards and risk along the Wasatch Front, Utah: U. S. Geological Survey Professional Paper 1500-A-J, p. D-1–36.

Arabasz, W.J., Richins, W.D., and Langer, C.J., 1981, The Pocatello Valley (Idaho-Utah border) earthquake sequence of March to April, 1975: Bulletin of the Seismological Society of America, v. 71, no. 3, p. 803–826.

Arabasz, W.J., Smith, R.B., and Richins, W.D., editors, 1979, Earthquake studies in Utah 1850 to 1978: Salt Lake City, University of Utah Seismograph Stations, Department of Geology and Geophysics, 552 p.

Arrington, L.J., 1994, Colonization of Utah, *in* Powell, A.K., editor, Utah History Encyclopedia: Salt Lake City, Utah, University of Utah Press: Online, http://www.onlineutah.com/colonizationhistory.shtml, accessed April 11, 2014.

Atkinson, G.M., and Wald, D.J., 2007, “Did you feel it?” intensity data: A surprisingly good measure of earthquake ground motion: Seismological Research Letters, v. 78, no. 3, p. 362–368, doi: 10.1785/gssrl.78.3.362.

Bache, T.C., Lambert, D.G., and Barker, T.G., 1980, A source model for the March 28, 1975, Pocatello Valley earthquake from time-domain modeling of teleseismic P waves: Bulletin of the Seismological Society of America, v. 70, no. 2, p. 405–418.

Bakun, W.H., 2006, MMI attenuation and historical earthquakes in the Basin and Range Province: Bulletin of the Seismological Society of America, v. 96, no. 6, p. 2206–2220, doi: 10.1785/0120060045.

Bakun, W.H., and Wentworth, C.M., 1997, Estimating earthquake location and magnitude from seismic intensity data: Bulletin of the Seismological Society of America, v. 87, no. 6, p. 1502–1521.

Barrientos, S.E, Ward, S.N., Gonzalez-Ruiz, J.R., and Stein, R.S., 1985, Inversion for moment as a function of depth from geodetic observations and long period body waves of the 1983 Borah Peak, Idaho earthquake: U. S. Geological Survey Open-File Report OF 85-0290-A, p. 485–518.

Battis, T.C., and Hill, K., 1977, Analysis of seismicity and tectonics of the central and western United States: Interim Scientific Report #1, AFSOR Contract # F44620-76-0063, Texas Instruments, Inc., Dallas, Texas, 109 p.

Benjamin, J.R., and Cornell, C.A., 1970, Probability, statistics, and decision for civil engineers: New York, McGraw Hill Book Company, 684 p.

Black, B.D., Hecker, S., Hylland, M.D., Christenson, G.E., and McDonald, G.N., 2003, Quaternary fault and fold database and map of Utah: Utah Geological Survey Map 193DM, scale 1:500,000, CD-ROM.

Black, B.D, Mulvey, W.E., Lowe, M., and Solomon, B.J., 1995, Geologic effects, *in* Christenson, G.E., editor, The September 2, 1992 M_L 5.8 St. George earthquake, Washington County, Utah: Utah Geological Survey Circular 88, p. 2–11.

Block, L., Yeck, W., King, V., Derouin, S., and Wood, C., 2012, Review of geologic investigations and injection well site selection, Paradox Valley Unit, Colorado: U.S. Bureau of Reclamation Technical Memorandum No. 86-68330-2012-27, 71 p.

Bodle, R.R., 1941, United States earthquakes 1939: U.S. Coast and Geodetic Survey, Serial 637, 69 p.

Bodle, R.R., 1944, United States earthquakes 1942: U.S. Coast and Geodetic Survey, Serial 662, 38 p.

Bodle, R.R., and Murphy, L.M., 1947, United States earthquakes 1945: U.S. Coast and Geodetic Survey, Serial 699, 38 p.

Braunmiller, J., Deichmann, N., Giardini, D., Wiemer, S., and the SED Magnitude Working Group, 2005, Homogeneous moment-magnitude calibration in Switzerland: Bulletin of the Seismological Society of America, v. 95, no. 1, p. 58–74, doi: 10.1785/0120030245.

Brazee, R.J., and Cloud, W.K., 1958, United States earthquakes 1956: U.S. Coast and Geodetic Survey, 78 p.

Brazee, R.J., and Cloud, W.K., 1959, United States earthquakes 1957: U.S. Coast and Geodetic Survey, 108 p.

Brazee, R.J., and Cloud, W.K., 1960, United States earthquakes 1958: U.S. Coast and Geodetic Survey, 76 p.

Brumbaugh, D.A., 2001, The 1994 Draney Peak, Idaho, earthquake sequence: Focal mechanisms and stress field inversion: M.S. thesis, University of Utah, 157 p.

Carver, D., Richins, W.D., and Langer, C.J., 1983, Details of the aftershock process following the 30 September 1977 Uinta Basin, Utah, earthquake: Bulletin of the Seismological Society of America, v. 73, no. 2, p. 435–448.

Case, W.F., 1988, Geologic effects of the 14 and 18 August, 1988 earthquakes in Emery County, Utah: Survey Notes, Utah Geological Survey, v. 22, no. 1, 2, p. 8–15: Online, http://files.geology.utah.gov/surveynotes/archives/snt22-1-2.pdf, accessed April 26, 2016.

Castellaro, S., and Bormann, P., 2007, Performance of different regression procedures on the magnitude conversion problem: Bulletin of the Seismological Society of America, v. 97, no. 4, p. 1167–1175, doi: 10.1785/0120060102.

Castellaro, S., Mulargia, F., and Kagan, Y.Y., 2006, Regression problems for magnitudes: Geophysical Journal International, v. 165, p, 913–930.

Chapman, D.G., and Schaufele, R.A., 1970, Elementary probability models and statistical inference: Waltham, Massachusetts, Xerox College Publishing Company, 358 p.

Cheng, C-L, and Van Ness, J., 1999, Statistical regression with measurement error: London, Edward Arnold Publishers Ltd, 262 p.

Chidsey, T.C., Jr., Morgan, C.D., and Bon, R., 2003, Major oil plays in Utah and vicinity: Utah Geological Survey Quarterly Technical Progress Report, Contract No. DE-FC26-02NT15133, 14 p.

Clark, R., 2012, Rangely Weber sand unit case history (RWSU): Online, http://www.uwyo.edu/eori/_files/co2conference12/rory_rangelycasehistory.pdf, accessed Feb. 11, 2014.

Coffman, J.L., and Stover, C.W., 1977, United States earthquakes 1975: U.S. National and Atmospheric Administration and U.S. Geological Survey, 136 p.

Coffman, J.L., and Stover, C.W., 1979, United States earthquakes 1977: U.S. National and Atmospheric Administration and U.S. Geological Survey, 81 p.

Coffman, J.L., and von Hake, C.A., 1972, United States earthquakes 1970: U.S. National and Atmospheric Administration, 81 p.

Committee on Induced Seismicity Potential in Energy Technologies, 2013, Induced seismicity potential in energy technologies: National Research Council, Washington, DC: Online, https://dels.nas.edu/Report/Induced-Seismicity-Potential-Energy-Technologies/13355, accessed Feb. 14, 2014.

Cook, K.L., and Nye, R.K., 1979, Effects of the Pocatello Valley (Idaho-Utah border) earthquake of March 28, 1975 (UTC), *in* Arabasz, W.J., Smith, R.B., and Richins, W.D., editors, Earthquake studies in Utah 1850 to 1978: Salt Lake City, University of Utah Seismograph Stations, Department of Geology and Geophysics, p. 445–457.

Cook, K.L., and Smith, R.B., 1967, Seismicity in Utah, 1850 through June 1965: Bulletin of the Seismological Society of America, v. 57, no. 4, p. 689–718.

dePolo, C., and Pecoraro, B., 2011, Modified Mercalli Intensity Maps for the February 21, 2008 Wells, Nevada earthquake: *in* dePolo, C. M,, and LaPointe, D. D., editors, The 21 February 2008 M_w 6.0 Wells, Nevada, earthquake—a compendium of earthquake-related investigations prepared by the University of Nevada, Reno (online version): Nevada Bureau of Mines and Geology Special Publication36: Online, http://www.nbmg.unr.edu/Pubs/sp/sp36/, accessed Feb. 14, 2014.

Dewey, J.W., Earle, P.S., and Presgrave, B.W, 2003, Four decades of PDE mb [abs]: Seismological Research Letters, v. 74, no. 2, p. 249.

Dewey, J.W., Earle, P.S., and Presgrave, B.W, 2004, Quantifying year-to-year drifts in PDE mb and explaining their causes [abs.]: Seismological Research Letters, v. 75, no. 2, p. 275.

Dewey, J.W., Presgrave, B.W., and Earle, P.S., 2011, Variations of mb(PDE): 1976–2010 [abs.]: Seismological Research Letters, v. 82, no. 2, p. 295.

Doser, D.I., 1985, Source parameters and faulting processes of the 1959 Hebgen Lake, Montana, earthquake sequence: Journal of Geophysical Research, v. 90, no. B6, p. 4537–4555.

Doser, D.I., 1989, Extensional tectonics in northern Utah-southern Idaho, U.S.A., and the 1934 Hansel Valley sequence: Physics of the Earth and Planetary Interiors, v. 54, p. 120–134.

Doser, D. I., and Kanamori, H., 1987, Long-period surface waves of four western United States earthquakes recorded by the Pasadena strainmeter: Bulletin of the Seismological Society of America, v. 77, no. 1, p. 236–243.

Doser, D.I., and Smith, R.B., 1982, Seismic moment rates in the Utah region: Bulletin of the Seismological Society of America, v. 72, no. 2, p. 525–551.

Doser, D.I., and Smith, R.B., 1985, Source parameters of the 28 October 1983 Borah Peak, Idaho, earthquake from body wave analysis: Bulletin of the Seismological Society of America, v. 75, no. 4, p. 1041–1051.

Dziewonski, A.M., Ekström, G., and Salganik, M.P., 1993, Centroid-moment-tensor solutions for October–December 1992: Physics of the Earth and Planetary Interiors, v. 80, no. 3-4, p. 89–103.

Dziewonski, A.M., Ekström, G., Woodhouse, J.H., and Zwart, G., 1990, Centroid-moment-tensor solutions for January–March 1989, Physics of the Earth and Planetary Interiors, v. 59, no. 4, p. 233–242.

Ekström, G., and Dziewonski, A.M., 1985, Centroid-moment-tensor solutions for 35 earthquakes in western North America (1977–1983): Bulletin of the Seismological Society of America, v. 75, no. 1, p. 23–39.

Ekström, G., and Nettles, M., undated, Global CMT web page: Online, http://www.globalcmt.org/, accessed March 21, 2014.

Electric Power Research Institute (EPRI), 1988, Seismic hazard methodology for the central and eastern United States: 10 volumes, EPRI-NP-4726, Palo Alto, California.

Electric Power Research Institute (EPRI), U.S. Department of Energy (DOE), and U.S. Nuclear Regulatory Commission (NRC), 2012, Technical Report: Central and Eastern United States

Seismic Source Characterization for Nuclear Facilities, v. 1, EPRI, Palo Alto, California: Online: www.ceus-ssc.com/index.htm, accessed Feb. 14, 2014.

Ellsworth, W.L., 2013, Injection-induced earthquakes: Science, v. 341, 1225942, doi: 10.1126/science.1225942.

Energy and Minerals Field Institute (EMFI), 2005, ChevronTexaco's Rangely Oil Field Operations: Online, emfi.mines.edu/emfi2005/ChevronTexaco.pdf, accessed Feb. 11, 2014.

Eppley, R.A., and Cloud, W.K., 1961, United States earthquakes 1959: U.S. Coast and Geodetic Survey, 115 p.

Evans, J.P., Martindale, D.C., and Kendrick, R.D., Jr., 2003, Geologic setting of the 1884 Bear Lake, Idaho, earthquake: Rupture in the hanging wall of a Basin and Range normal fault revealed by historical and geological analyses: Bulletin of the Seismological Society of America, v. 93, no. 4, p. 1621–1632.

Felzer, K.R., 2007, Calculating California seismicity rates: Appendix I *in* Working Group on California Earthquake Probabilities, The Uniform California Earthquake Rupture Forecast, Version 2 (UCERF 2): U.S. Geological Survey Open-File Report 2007-1437I, and California Geological Survey Special Report 203-I.

Felzer, K.R., and Cao, T., 2007, WGCEP historical California earthquake catalog: Appendix H *in* Working Group on California Earthquake Probabilities, The Uniform California Earthquake Rupture Forecast, Version 2 (UCERF 2): U.S. Geological Survey Open-File Report 2007-1437H, and California Geological Survey Special Report 203-H.

Fuller, W.A., 1987, Measurement error models: New York, John Wiley & Sons, 440 p.

Frankel, A., 1994, Implications of felt area-magnitude relations for earthquake scaling and the average frequency of perceptible ground motion: Bulletin of the Seismological Society of America, v. 84, no. 2, p. 462–465.

Gardner, J.K., and Knopoff, L., 1974, Is the sequence of earthquakes in southern California, with aftershocks removed, Poissonian?: Bulletin of the Seismological Society of America, v. 64, no. 5, p. 1363–1367.

Gasperini, P., and Lolli, B., 2014, Comment on "General Orthogonal Regression Relations between Body-Wave and Moment Magnitudes" by Ranjit Das, H.R. Wason, and M.L. Sharma: Seismological Research Letters, v. 85, no. 2, p. 351, doi: 10.1785/0220130096.

Gibbs, J.F., Healy, J.H., Raleigh, C.B., and Coakley, J., 1973, Seismicity in the Rangely, Colorado, area: 1962–1970: Bulletin of the Seismological Society of America, v. 63, no. 5, p. 1557–1570.

Griscom, M., and Arabasz, W.J., 1979, Local magnitude (M_L) in the Wasatch Front and Utah region: Wood-Anderson calibration, coda-duration estimates of M_L, and M_L versus m_b, *in* Arabasz, W.J., Smith, R.B., and Richins, W.D., editors, Earthquake studies in Utah 1850 to 1978: Salt Lake City, University of Utah Seismograph Stations, Department of Geology and Geophysics, p. 433–443.

Grünthal, G., Mayer-Rosa, D., and Lenhardt, W., 1998, Abschätzung der Erdbebengefährdung für die D-A-CH-Staaten—Deutschland, Österreich, Schweitz: Bautechnik, v.75 no. 10, p. 753–767.

Gurland, J., and Tripathi, R.C., 1971, A simple approximation for unbiased estimation of the standard deviation: American Statistician, v. 25, p. 30–32.

Gutenberg, B., and Richter, C.F., 1942, Earthquake magnitude, intensity, energy, and acceleration: Bulletin of the Seismological Society of America, v. 32, no. 3, p. 163–191.

Gutenberg, B., and Richter, C.F., 1949, Seismicity of the Earth and associated phenomena: Princeton, New Jersey, Princeton University Press, 273 p.

Gutenberg, B., and Richter, C.F., 1956, Earthquake magnitude, intensity, energy, and acceleration (Second Paper): Bulletin of the Seismological Society of America, v. 46, no. 2, p. 105–145.

Hakimhashemi, A.H., and Grünthal, G., 2012, A statistical method for estimating catalog completeness applicable to long-term nonstationary seismic data: Bulletin of the Seismological Society of America, v. 102, no. 6, p. 2530–2546, doi: 10.1785/0120110309.

Hanks, T.C., Hileman, J.A., and Thatcher, W., 1975, Seismic moments of the larger earthquakes of the southern California region: Geological Society of America Bulletin, v. 86, p. 1131–1139.

Hanks, T.C., and Johnston, A.C., 1992, Common features of the excitation and propagation of strong ground motion for North American earthquakes: Bulletin of the Seismological Society of America, v. 82, no. 1, p. 1–23.

Hanks, T.C., and Kanamori, H., 1979, A moment magnitude scale: Journal of Geophysical Research, v. 84, no. B5, p. 2348–2350.

Herrmann, R.B., Benz, H., and Ammon, C.J., 2011, Monitoring the earthquake source process in North America: Bulletin of the Seismological Society of America, v. 101, no. 6, p. 2609–2625, doi: 10.1785/0120110095.

Hileman, J.A., Allen, C.R., and Nordquist, J.M., 1973, Seismicity of the southern California region, 1 January 1932 to 31 December, 1972: Pasadena, Seismological Laboratory, California Institute of Technology, variously paginated.

Hopper, M.G., 2000, Isoseismals of some historical earthquakes affecting the Wasatch Front area, Utah, *in* Gori, P.L., and Hays, W.W., editors, Assessment of regional earthquake hazards and risk along the Wasatch Front, Utah: U.S. Geological Survey Professional Paper 1500-K-R, p. Q-1–25.

International Seismological Centre, 2010, On-line Bulletin: www.isc.ac.uk, accessed July 11, 2012.

Jibson, R.W., and Harp, E.L., 1995, The Springdale landslide, *in* Christenson, G., editor, The September 2, 1992 M_L 5.8 St. George earthquake, Washington County, Utah: Utah Geological Survey Circular 88, p. 21–30.

Jones, A.E., 1975, Recording of earthquakes at Reno, 1916–1951: University of Nevada Reno, Bulletin of the Seismological Laboratory, 199 p.

Kagan, Y.Y., 2002, Modern California earthquake catalogs and their comparison: Seismological Research Letters, v. 73, no. 6, p. 921–929.

Kagan, Y.Y., 2003, Accuracy of modern global earthquake catalogs: Physics of the Earth and Planetary Interiors, v. 135, p. 173–209, doi: 10.1016/S0031-9201(02)00214-5.

Lander, J.F., and Cloud, W.K., 1962, United States earthquakes 1960: U.S. Coast and Geodetic Survey, 90 p.

Lander, J.F., and Cloud, W.K., 1963, United States earthquakes 1961: U.S. Coast and Geodetic Survey, 106 p.

Lander, J.F., and Cloud, W.K., 1963, United States earthquakes 1961: U.S. Coast and Geodetic Survey, 106 p.

Lander, J.F., and Cloud, W.K., 1964, United States earthquakes 1962: U.S. Coast and Geodetic Survey, 114 p.

Lolli, B., and P. Gasperini, 2012, A comparison among general orthogonal regression methods applied to earthquake magnitude conversions: Geophysical Journal International, v. 190, p. 1135–1151, doi: 10.1111/j.1365-246X.2012.05530.x.

McCarter, M.K., 2001, Documentation of ground truth for significant seismic events related to underground mining in Utah and Wyoming, *in* Arabasz, W.J., and Pechmann, J.C., 2001, Seismic characterization of coal-mining seismicity in Utah for CTBT monitoring: Technical Report to Lawrence Livermore National Laboratory, LLNL Research Agreement No. B344836, Appendix C: Online, http://www.quake.utah.edu/wp-content/uploads/LLNLRept.pdf, accessed April 26, 2016.

Mendoza, C., and Hartzell, S.H., 1988, Inversion for slip distribution using teleseismic P waveforms; North Palm Springs, Borah Peak, and Michoacan earthquakes: Bulletin of the Seismological Society of America, v. 78, no.3, p. 1092–1111.

Moran, R., 2007, Earthquakes at Rangely, Colorado: Online, http://academic.emporia.edu/aberjame/student/moran4/index.htm, accessed Feb. 11, 2014.

Murphy, L.M., and Cloud, W.K., 1953, United States earthquakes 1951: U.S. Coast and Geodetic Survey, Serial 762, 49 p.

Murphy, L.M., and Cloud, W.K., 1957, United States earthquakes 1955: U.S. Coast and Geodetic Survey, 83 p.

Murphy, L.M., and Ulrich, F.P., 1951, United States earthquakes 1949: U.S. Coast and Geodetic Survey, Serial 748, 63 p.

Murphy, L.M., and Ulrich, F.P., 1952, United States earthquakes 1950: U.S. Coast and Geodetic Survey, Serial 755, 47 p.

Musson, R.M.W., 2012, The effect of magnitude uncertainty on earthquake activity rates: Bulletin of the Seismological Society of America, v. 102, no. 6, p. 2771–2775, doi: 10.1785/0120110224.

Nabelek, J., Eyidogan, H, and Toksoz, M.N., 1985, Source parameters of the Borah Peak, Idaho, earthquake of October 28, 1983 from body-wave inversion: Eos, Transactions, American Geophysical Union, v..66, no. 18, p. 308.

Neumann, F., 1936, United States earthquakes 1934: U.S. Coast and Geodetic Survey, Serial 593, 101 p.

Neumann, F., 1940a, United States earthquakes 1937: U.S. Coast and Geodetic Survey, Serial 619, 55 p.

Neumann, F., 1940b, United States earthquakes 1938: U.S. Coast and Geodetic Survey, Serial 629, 59 p.

Olig, S.S., 1995, Ground shaking and Modified Mercalli intensities, *in* Christenson, G., editor, The September 2, 1992 M_L 5.8 St. George earthquake, Washington County, Utah: Utah Geological Survey Circular 88, p. 12–20.

Oregon State University (OSU), 1998, Moment tensors: online catalog at http://quakes.oce.orst.edu/moment-tensor/, accessed May 10, 2012.

Pack, F.J., 1921, The Elsinore earthquakes in central Utah, September 29 and October 1, 1921: Bulletin of the Seismological Society of America, v. 11, nos. 3 and 4, p. 157–165.

Pancha, A., Anderson, J.G., and Kreemer, C., 2006, Comparison of seismic and geodetic scalar moment rates across the Basin and Range Province: Bulletin of the Seismological Society of America, v. 96, no. 1, p. 11–32, doi: 10.1785/0120040166.

Patton, H.J., and Zandt, G., 1991, Seismic moment tensors of Western U.S. earthquakes and implications for the tectonic stress field: Journal of Geophysical Research, v. 96, no. B11, p. 18,245–18,259.

Pechmann, J.C., and Arabasz, W.J., 1995, The problem of the random earthquake in seismic hazard analysis—Wasatch Front region, Utah, *in* Lund, W.R., editor, Environmental and engineering geology of the Wasatch Front region: Utah Geological Association Publication 24, p. 77–93.

Pechmann, J.C., Arabasz, W.J., and Nava, S.J., 1994, Refined analysis of the 1992 M_L 5.8 St. George, Utah, earthquake and its aftershocks [abs.]: Seismological Research Letters, v. 65, no. 2, p. 32.

Pechmann, J.C., Arabasz, W.J., Pankow, K.L., Burlacu, R., and McCarter, M.K., 2008, Seismological report on the 6 August 2007 Crandall Canyon mine collapse in Utah: Seismological Research Letters, v. 79, no. 5, p.620–636, doi: 10.1785gssrl.79.5.620.

Pechmann, J.C., Bernier, J.C., Nava, S.J., and Terra, F.M., 2010, Correction of systematic time-dependent coda magnitude errors in the Utah and Yellowstone National Park region earthquake catalogs, 1981–2001: Online, http://www.quake.utah.edu/wp-content/uploads/mcpaper.BSSA2010sub-1.pdf, accessed April 26, 2016.

Pechmann, J.C., Brumbaugh, D.A., Nava, S.J., Skelton T.G., Fivas, G.P., and Arabasz, W.J., 1997, The 1994 Draney Peak, ID, earthquake and its aftershocks [abs.]: Eos (Transactions American Geophysical Union), v. 78, no. 46 (Supplement), p. F480.

Pechmann, J.C., Nava, S.J., and Arabasz, W.J., 1991, Seismological analysis of four recent moderate (M_L 4.8 to 5.4) earthquakes in Utah: Technical report to the Utah Geological Survey, Contract No. 89-3659, 107 p.

Pechmann, J.C., Nava, S.J., Terra, F.M., and Bernier, J., 2007, Local magnitude determinations for Intermountain Seismic Belt earthquakes from broadband digital data: Bulletin of the Seismological Society of America, v. 97, no. 2, p. 557–574, doi: 10.1785/0120060114.

Pechmann, J.C., Walter, W.R., Nava, S.J., and Arabasz, W.J., 1995, The February 3, 1995, M_L 5.1 seismic event in the trona mining district of southwestern Wyoming: Seismological Research Letters, v. 66, no. 3, p. 25–34.

Pechmann, J.C., and Whidden, K.M., 2013, The relation of University of Utah local and coda magnitudes to moment magnitudes: The sequel [abs.]: Seismological Research Letters, v. 84, no. 2, p. 299.

Petersen, M.D., Frankel, A.D., Harmsen, S.C., Mueller, C.S., Haller, K.M., Wheeler, R.L., Wesson, R.L., Zeng, Y., Boyd, O.S., Perkins, D.M., Luco, N., Field, E.H., Wills, C.J., and Rukstales, K.S., 2008, Documentation for the 2008 update of the United States National Seismic Hazard Maps: U.S. Geological Survey Open-File Report 2008-1128, 61 p.

Raleigh, C.B., Healy, J.H., and Bredehoeft, J.D., 1976, An experiment in earthquake control at Rangely, Colorado: Science, v. 191, p. 1230–1237.

Richins, W.D., Pechmann, J.C., Smith, R.B., Langer, C.J., Goter, S.K., Zollweg, J.E., and King, J.J., 1987, The 1983 Borah Peak, Idaho, earthquake and its aftershocks: Bulletin of the Seismological Society of America, v. 77, p. 694-723.

Richter, C.F., 1958, Elementary seismology: San Francisco, W.H. Freeman and Company, 768 p.

Rohlf, F.J., and Sokal, R.R., 1981, Statistical Tables: W. H. Freeman and Company, New York, 219 p.

Rogers, A.M., Algermissen, S.T., Hays, W.W., and Perkins, D.M., 1976, A study of earthquake losses in the Salt Lake City, Utah, area: U.S. Geological Survey Open-File Report 76-89, 357 p.

Rogers, A.M., Harmsen, S.C., Corbett, E.J., Priestley, K., and dePolo, D., 1991, The seismicity of Nevada and some adjacent parts of the Great Basin, *in* Slemmons, D.B., Engdahl, E.R., Zoback, M.D., and Blackwell, D.D., editors, Neotectonics of North America: Geological Society of America, Decade Map Volume 1, p. 153–184.

Schuh, M.L., 1993, Red Wash, *in* Hill, B.G., and Bereskin, S.R., editors, Oil and gas fields of Utah: Utah Geological Association Publication 22, non-paginated.

Shemeta, J.E., 1989, New analyses of three-component digital data for aftershocks of the 1983 Borah Peak, Idaho, earthquake source parameters and refined hypocenters: Salt Lake City, Utah, University of Utah, M.S. thesis, 126 p.

Shenon, P.J., 1936, The Utah earthquake of March 12, 1934 (extracts from unpublished report), *in* Neumann, F., United States earthquakes 1934: U.S. Coast and Geodetic Survey, Serial 593, p. 43–48.

Simpson, D.W., 1976, Seismicity changes associated with reservoir loading: Engineering Geology, v. 10, p. 123–150.

Sipkin, S.A, 1986, Estimation of earthquake source parameters by the inversion of waveform data; global seismicity, 1981–1983: Bulletin of the Seismological Society of America, v. 76, no. 6, p. 1515–1541.

Slemmons, D.B., Jones, A.E., and Gimlett, J.I., 1965, Catalog of Nevada earthquakes, 1852–1960: Bulletin of the Seismological Society of America, v. 55, no. 2, p. 519–565.

Smith, R.B., and Arabasz, W.J., 1991, Seismicity of the Intermountain seismic belt, *in* Slemmons, D.B., Engdahl, E.R., Zoback, M.D., and Blackwell, D.D., editors, Neotectonics of North America: Geological Society of America, Decade Map Volume 1, p. 185–228.

Smith, K., Pechmann, J., Meremonte, M., and Pankow, K., 2011, Preliminary analysis of the M_w 6.0 Wells, Nevada, earthquake sequence: *in* dePolo, C.M,, and LaPointe, D.D., editors., The 21 February 2008 M_w 6.0 Wells, Nevada, earthquake—a compendium of earthquake-related investigations prepared by the University of Nevada, Reno (online version): Nevada Bureau of Mines and Geology Special Publication36: Online www.nbmg.unr.edu/Pubs/sp/sp36/, accessed Feb. 14, 2014.

Stover, C.W., 1985, United States earthquakes, 1982: U.S. Geological Survey Bulletin 1655, 141 p.

Stover, C.W., editor, 1987, United States earthquakes, 1983: U.S. Geological Survey Bulletin 1698, 196 p.

Stover, C.W., and Coffman, J.L., 1993, Seismicity of the United States, 1568–1989 (Revised): U.S. Geological Survey Professional Paper 1527, 418 p.

Stover, C.W., Reagor, B.G., and Algermissen, S.T., 1986, Seismicity map of the state of Utah: U.S. Geological Survey Miscellaneous Field Studies Map MF-1856, including data compilation.

Stover, C.W., and von Hake, C.A., editors, 1982, United States earthquakes, 1980: U.S. Geological Survey and U.S. National Oceanic and Atmospheric Administration, 182 p.

Talley, H.C., Jr., and Cloud, W.K., 1962, United States earthquakes 1960: U.S. Coast and Geodetic Survey, 90 p.

Taylor, J.R., 1982, An introduction to error analysis: Mill Valley, California, University Science Books, 270 p.

Tinti, S., and Mulargia, F., 1985, Effects of magnitude uncertainties on estimating the parameters in the Gutenberg-Richter frequency-magnitude law: Bulletin of the Seismological Society of America, v. 75, no. 6, p. 1681–1697.

Toppozada, T.R., 1975, Earthquake magnitude as a function of intensity data in California and western Nevada: Bulletin of the Seismological Society of America, v. 65, no. 5, p. 1223–1238.

Toppozada, T.R., and Branum, D., 2002, California $M \geq 5.5$ earthquakes: Their history and the areas damaged, *in* Lee, W. H., Kanamori, H., and Jennings, P., editors, International Handbook of Earthquake and Engineering Seismology, International Association of Seismology and Physics of the Earth's Interior, Academic Press, New York (full paper on CD-ROM).

U.S. Geological Survey/National Earthquake Information Center (USGS/NEIC), 2012, USGS/NEIC PDE catalog: Online, earthquake.usgs.gov/earthquakes/eqarchives/epic/, accessed May 18, 2012.

van Stiphout, T., Zhuang, J., and Marsan, D., 2012, Seismicity declustering: Community Online Resource for Statistical Seismicity Analysis, doi: 10.5078/corssa-52382934: Online, www.corsa.org, accessed Feb. 14, 2014.

Veneziano, D., and Van Dyck, J., 1985a, Statistical discrimination of “aftershocks” and their contribution to seismic hazard: Appendix A-4 *in* McGuire, R.K., project manager, Seismic hazard methodology for nuclear facilities in the eastern United States, v. 2, Appendix A: Electric Power Research Institute Project No. P101-29, EPRI/Seismicity Owners Group Draft 85-1 (April 30, 1985), p. A-120–186.

Veneziano, D., and Van Dyck, J., 1985b, Analysis of earthquake catalogs for incompleteness and recurrence rates: Appendix A-6 *in* McGuire, R.K., project manager, Seismic hazard methodology for nuclear facilities in the eastern United States, v. 2, Appendix A: Electric Power Research Institute Project No. P101-29, EPRI/Seismicity Owners Group Draft 85-1 (April 30, 1985), p. A-220–297.

von Hake, C.A., and Cloud, W.K., 1965, United States earthquakes 1963, U.S. Coast and Geodetic Survey, 69 p.

von Hake, C.A., and Cloud, W.K., 1968, United States earthquakes 1966, U.S. Coast and Geodetic Survey, 110 p.

von Hake, C.A., and Cloud, W.K., 1969, United States earthquakes 1967, U.S. Coast and Geodetic Survey, 90 p.

Wahlquist, W.L., editor, 1981, Atlas of Utah: Provo, Utah, Brigham Young University Press and Weber State College, 300 p.

Wald, D.J., Quitoriano, V., Dengler, L.A., and Dewey J.W., 1999, Utilization of the Internet for rapid Community Intensity Maps, Seismological Research Letters, v. 70, no. 6, p. 680-697.

Wallace, T.C., Helmberger, D.V., and Mellman, G.R., 1981, A technique for the inversion of regional data in source parameter studies: Journal of Geophysical Research, v. 86, no. B3, p. 1679–1685.

Weichert, D.H., 1980, Estimation of the earthquake recurrence parameters for unequal observation periods for different magnitudes: Bulletin of the Seismological Society of America, v. 70, no. 4, p. 1337–1346.

Westaway, R., and Smith, R.B., 1989, Source parameters of the Cache Valley (Logan), Utah, earthquake of 30 August 1962: Bulletin of the Seismological Society of America, v. 79, no. 5, p. 1410–1425.

Whidden, K.M., and Pankow, K.L., 2012, A catalog of regional moment tensors in Utah from 1998 to 2011: Seismological Research Letters, v. 83, no. 5, p. 775–783, doi: 10.1785/0220120046.

Williams, B.R., 1979, M_0 calculations from a generalized AR parameter method for WWSSN instruments: Bulletin of the Seismological Society of America, v. 69, no.2, p. 329–351.

Williams, J.S., and Tapper, M.L., 1953, Earthquake history of Utah, 1850–1949: Bulletin of the Seismological Society of America, v. 43, no. 3, p. 191–218.

Wong, I.G., 1993, Tectonic stresses in mine seismicity—are they significant?, *in* Youngs, R.P., editor, Rockbursts and seismicity in mines 93—Proceedings of the 3rd International Symposium on Rockbursts and Seismicity in Mines, Ontario, Canada: Rotterdam, A.A. Balkema, p. 273–278.

Wood, H.O., 1947, Earthquakes in southern California with geologic relations, Part Two: Bulletin of the Seismological Society of America, v. 37, no. 3, p. 217–258.

Wood, H.O., and Neumann, F., 1931, Modified Mercalli intensity scale of 1931: Bulletin of the Seismological Society of America, v. 21, no. 4, p. 277–283.

Working Group on Utah Earthquake Probabilities (WGUEP), 2016, Earthquake probabilities for the Wasatch Front region in Utah, Idaho, and Wyoming: Utah Geological Survey Miscellaneous Publication 16-3, 164 p., 5 appendices.

Youngs, R.R., and Coppersmith, K.J., 1985, Implications of fault slip rates and earthquake recurrence models to probabilistic seismic hazard estimates: Bulletin of the Seismological Society of America, v. 75, no. 4, p. 939–964.

Youngs, R.R., Swan, F.H., Power, M.S., Schwartz, D.P., and Green, R.K., 1987, Probabilistic analysis of earthquake ground shaking hazards along the Wasatch Front, Utah, *in* Gori, P.L., and Hays, W.W., editors, Assessment of regional earthquake hazards and risk along the Wasatch Front, Utah, Volume II: U.S. Geological Survey Open-file Report 87-585, p. M-1–110.

Youngs, R.R., Swan, F.H., Power, M.S., Schwartz, D.P., and Green, R.K., 2000, Probabilistic analysis of earthquake ground shaking hazards along the Wasatch Front, Utah, *in* Gori, P.L., and Hays, W.W., editors, Assessment of regional earthquake hazards and risk along the Wasatch Front, Utah: U.S. Geological Survey Professional Paper 1500-K-R, p. M-1–74.

Table E-1. *Coordinates (in degrees of latitude N and longitude W) defining catalog domains and areas of non-tectonic and human-triggered seismicity shown on figure E-1.*

Catalog Domain/Area	Boundary				Center Point[1]		Radius (km)	WP-BC Polygon[2]	
	North	South	West	East	North	West		North	West
Extended Utah Region (UTREXT)[3]	43.500	36.000	115.000	108.000	------	------	------	39.1667	111.3000
Utah Region (UTR)[4]	42.500	36.750	114.250	108.750	------	------	------	39.5833	111.3000
WGUEP Study Region (WGUEP)[5]	42.500	39.000	113.250	110.750	------	------	------	39.6333	111.3667
Southern Fuel Co. MIS area (SUFCO)	39.033	38.903	111.483	111.267	------	------	------	39.7500	111.3667
SW Wyoming trona mining (TRONA)	41.800	41.300	110.000	109.550	------	------	------	39.8333	111.2333
Paradox Valley (PV)	------	------	------	------	38.297	108.895	25.0	39.8333	110.5000
Rangely oil field (R)	------	------	------	------	40.113	108.861	25.0	39.6333	110.2333
Red Wash oil field (RW)	------	------	------	------	40.189	109.313	25.0	39.3667	110.1667
								39.3667	110.5167
								39.5167	110.5500
								39.5833	110.6500
								39.5833	110.9500
								39.1667	110.9500
								39.1667	111.3000

[1] For PV, the location of the U.S. Bureau of Reclamation's deep disposal well operated as part of the Paradox Valley Unit saltwater injection project; for R, the center of the Rangely oil field taken from Gibbs and others (1973); for RW, the Red Wash field's geocode coordinates.

[2] Polygon outlining the Wasatch Plateau (WP)-Book Cliffs (BC) coal-mining region

[3] Area = 498,360 km^2

[4] Area = 300,850 km^2

[5] Area = 82,060 km

Table E-2. *Overview of merged source catalogs by time period.*

Subcatalog	**UUSS Historical** ALL	**USGS SRA** ALL	**USGS WMM** ALL	**Stover and Coffman (1993)** $I_0 \geq 6$, $M \geq 4.5$	**UUSS Instrumental** $M \geq 2.45$	**USGS PDE** ALL
A. Jan 1850–June 1962	X	X	X	X		
B. July 1962–Dec 1986		X	X	X	X	X[3]
C. Jan 1987–Sept 2012			X[1]	X[2]	X	X

[1] The USGS (WMM) catalog received from C.S. Mueller, USGS, extended only through 2010; according to C.S. Mueller (USGS, oral communication, 2013) the USGS PDE catalog provides the basis for extending the WMM catalog beyond 2010.
[2] The compilation of Stover and Coffman (1993) ends in 1989.
[3] The USGS PDE catalog begins on January 1, 1973.

Table E.3. *Seismic events in the trona-mining district of southwestern Wyoming (M ≥ 2.45, July 1962–September2012) that were removed from the merged earthquake catalog as non-tectonic events.*

Year	**MoDay**	**Hr:Min Sec** (UTC)	**Long. W**	**Lat. N**	**Depth**[1] (km)	**Magnitude and Type**[2]		**Note**
1985	0320	01:37 10.53	109.653	41.611	8	3.20	Mc UU	
1986	0605	19:34 02.49	109.667	41.384	7	3.00	Mc UU	
1994	0625	10:07 28.77	109.698	41.609	5	3.58	Mc UU	3
1995	0203	15:26 13.25	109.815	41.526	4	5.18	ML UU	4
1998	0113	05:41 48.21	109.958	41.718	5	2.47	ML UU	
1998	1110	10:14 15.60	109.897	41.672	5	2.90	ML GS	
2000	0130	02:05 32.34	109.776	41.521	7	4.25	ML UU	5
2000	0716	02:05 32.34	109.878	41.621	1	3.06	ML UU	
2000	0817	23:02 30.21	109.700	41.554	7	3.08	ML UU	
2007	0605	03:28 42.45	109.973	41.693	1	3.10	ML UU	
2007	0605	03:29 06.92	109.908	41.588	5	3.42	ML UU	
2007	1122	02:29 36.46	109.736	41.633	5	3.42	ML UU	
2007	1222	05:59 46.45	109.918	41.627	7	2.59	ML UU	
2008	0209	17:41 49.85	109.889	41.668	2	3.32	ML UU	
2009	0307	02:45 10.18	109.923	41.670	5	3.61	ML UU	
2012	0225	06:15 16.00	109.884	41.647	2	2.51	ML UU	

[1] Focal-depth control for this region in the source catalogs is very poor.
[2] Magnitudes and types here are from the original source catalogs.
[3] Suspected mining-related event (Pechmann and others, 1995).
[4] Documented mining-related event (Pechmann and others, 1995).
[5] Documented mining-related event (McCarter, 2001).

Table E-4. *Suspected injection-induced earthquakes in the circular areas demarcated on figure E-1 for Paradox Valley and the Rangely and Red Wash oil fields that were removed from the declustered catalog of independent mainshocks before calculating seismicity rates for the Utah Region.*

Year	MoDay	Hr:Min Sec (UTC)	Long. W	Lat. N	Depth[1] (km)	Magnitude and Type[2]		Note
Paradox Valley[3]								
1997	1215	09:18 47.00	109.080	38.319	0	3.22	BEM	
1998	0410	06:52 16.40	108.827	38.268	5	3.14	BEM	
1998	0508	19:45 00.60	109.102	38.317	3	3.04	BEM	
1999	0204	13:38 55.20	108.920	38.286	3	3.00	BEM	
1999	0321	06:14 24.90	109.050	38.311	0	2.76	BEM	
1999	0603	15:35 34.20	108.940	38.261	1	3.66	BEM	
1999	0706	22:05 45.00	108.879	38.276	1	3.69	BEM	
1999	0916	00:35 03.00	108.907	38.310	5	3.02	BEM	
1999	1011	21:43 05.00	108.888	38.273	1	2.74	BEM	
1999	1104	11:00 19.00	108.814	38.242	5	2.71	BEM	
2000	0315	12:14 27.60	108.911	38.277	2	3.23	BEM	
2000	0527	21:58 19.00	108.881	38.301	3	3.80	BEM	
2002	0606	12:29 11.00	108.941	38.326	2	3.20	BEM	
2004	1107	06:54 59.70	108.911	38.245	1	3.68	BEM	
2005	0807	22:12 13.30	108.914	38.259	1	3.05	BEM	
2007	0801	07:46 08.20	108.985	38.378	4	3.00	BEM	
2009	0419	13:34 52.90	108.918	38.273	2	2.89	BEM	
2009	0430	08:50 34.20	108.914	38.258	0	2.79	BEM	
2009	1117	19:44 38.00	108.870	38.360	5	3.21	BEM	
Rangely Oil Field[4]								
1966	0706	05:47 08.40	108.948	40.090	7	3.78	BEM	
1967	0215	03:28 03.50	109.054	40.113	7	4.02	BEM	5
1970	0421	08:53 53.10	109.008	40.055	7	3.93	BEM	
1979	0319	14:59 30.20	108.859	40.044	7	3.66	BEM	
1993	0513	16:13 24.50	108.884	40.111	0	3.31	BEM	
1995	0320	12:46 16.30	108.820	40.125	3	4.26	BEM	
2007	0907	13:51 26.40	108.904	40.160	0	2.97	BEM	
Red Wash Oil Field								
1967	0215	03:28 03.50	109.054	40.113	7	4.02	BEM	5
1990	0407	15:37 54.50	109.474	40.116	2	3.92	BEM	
1991	0302	08:41 36.60	109.427	40.127	1	3.66	BEM	
1991	1108	13:15 04.70	109.242	40.127	1	3.46	BEM	
2000	1111	21:17 52.70	109.194	40.246	1	3.66	BEM	

[1] Focal-depth control in the source catalogs is fair to good for most of the events in the Paradox Valley area but poor for the areas of the Rangely and Red Wash oil fields.

[2] All magnitudes are best-estimate moment magnitudes from the BEM declustered catalog, into which original source catalogs contributed seismic events of ~M 2.5 and larger.

[3] The following dependent events removed by declustering are not included:
1998 0516 04:30 (**M** 2.50); 1999 0320 15:12 (**M** 2.59).

[4] The following dependent events removed by declustering are not included:
1966 0705 18:26 (**M** 3.38); 1966 0705 20:02 (**M** 3.46); 1967 0215 04:33 (**M** 2.99); 1970 0421 15:05 (**M** 3.55); 1979 0329 22:07 (**M** 2.82); 1995 0320 13:16 (**M** 2.97); 1995 0320 14:33 (**M** 2.77); 1995 0323 03:31 (**M** 3.14); 1995 0401 05:22 (**M** 3.25).

[5] This same event appears in the 25-km radial sorts for both the Rangely and Red Wash oil fields.

Table E-5. *Directly-determined magnitude uncertainties, from sets of earthquakes with three or more station measures for the given magnitude type, using the average-standard-error approach.*

Catalog	**Mag. Type,** ***M***	**No. of Earthquakes**	**Time Period**	**Region**	$\sigma[M]$[1] (± 1 s.d.)	**Single-Station Mag. Uncertainty**[2] (± 1 s.d.)
UUSS	M_L	2517	1996-2012	UTR	0.10 (± 0.06)	0.21 (± 0.10)
UUSS	M_L	41	1962-1980	UTR	0.16 (± 0.10)[3]	0.29 (± 0.17)
UUSS	M_C	873	1986-2000	UTR	0.10 (± 0.04)	0.31 (± 0.10)
ISC	m_b[4]	34	1966-2008	UTREXT	0.12 (± 0.06)	0.38 (± 0.10)

[1] Based on the average standard error of event magnitudes, $\overline{SE_{em}}$, for the total sample of earthquakes.

[2] Population standard deviation estimated from the average of sample standard deviations for event magnitudes (corrected for sample size), $STDEV_{\text{corrected}}$, for all the earthquakes in the sample.

[3] Many values of M_L in the UUSS catalog for this period are based on less than three station measures; for the 299 M_L event magnitudes during 1962-1980, an average value of $\sigma[M_L\,UU]$ of 0.24 was calculated using the single-station magnitude uncertainty of 0.29 and the number of station measures entering into each event M_L value.

[4] Based on five or more station measures.

Table E-6. *Indirectly-determined magnitude uncertainties from the standard deviation of the magnitude difference, $\sigma_{\Delta M}$, in two catalogs.*[1]

Catalogs	Mag. Type	No. of Earthquakes	Time Period	Region	$\sigma_{\Delta M}$	σ_{M1}	σ_{M2}
UUSS, SLU[2]	**M**	36	1998–2013	Intermountain Seismic Belt	0.071	0.05 UUSS	0.05 SLU
SLU, GCMT[2]	**M**	24	2001–2013	Western U.S.[3] (shallow)	0.076	0.05 SLU	0.06 GCMT[4]
UUSS, USGS/PDE	M_L	44	1996–2012	UTR	0.187	0.10 UUSS	0.16 USGS
UUSS, USGS/PDE	M_L	334	1994–2012	UTREXT	0.248	0.10 UUSS	0.23 USGS
USGS/PDE, ISC[5]	m_b	15	1978–2008	UTREXT	0.177	0.13 USGS	0.13 ISC

[1] Where $\sigma_{M1} = \sigma_{M2}$ in the table, the two values were assumed to be equal *a priori*.
[2] Data in this row are revised from Pechmann and Whidden (2013).
[3] 31°–49° N. latitude, 105°–125° W. longitude, depth < 33 km.
[4] From magnitude-difference data in Kagan (2003, Table 5) and the linear combination of squared uncertainties, we derived the following time-varying values of σ_M for reported values of **M** in the GCMT catalog prior to 2001:
$\sigma_M = 0.10$ for global earthquakes 0–70 km depth during 1980–1994,
$\sigma_M = 0.06$ for global earthquakes 0–70 km depth during 1995–2000.
[5] Based on five or more station measures.

Table E-6a. *Addendum—Summary of uncertainties assessed for original catalog magnitudes.*

Local Magnitude, Coda Magnitude, and Body-Wave Magnitude

Catalog	Mag. Type	CR ID[1]	Time Period[2]	Region[3]	$\sigma[M]$[4]	Reference
UUSS	M_L	2	1962-1980	UTR	**0.24**	table E-5, footnote 3
UUSS	M_L	1#	1981-1995	UTR	**0.21**	table E-8, footnote 2 and addendum
UUSS	M_L	1	1996-2012	UTR	0.10	table E-5 (see also table E-8, addendum)
UUSS	M_L	1#	1981-1993	EBR	**0.21**	table E-8, footnote 2 and addendum (same $\boldsymbol{\sigma}[M]$ for UTR assumed for EBR)
UUSS	M_L	1	1994-2012	EBR	0.10	table E-5 (see also table E-8, addendum; same $\boldsymbol{\sigma}[M]$ for UTR assumed for EBR)
UUSS	M_C[5]	3	1981-2012	UTR	0.10	table E-5
USGS	M_L	6	1974-2012	UTR	0.16	table E-6
USGS	M_L	7	1981-2012	EBR	0.23	table E-6 ($\boldsymbol{\sigma}[M]$ determined from UTREXT applied only to EBR)
USGS	m_b	10	1963-1977	UTR	*0.19*	table E-10, footnote 4
USGS	m_b	9	1978-1990	UTREXT	*0.14*	table E-10, footnote 3
USGS	m_b	8	1991-2012	UTREXT	*0.14*	table E-10, footnote 3
ISC	m_b	11	1964-2012	UTREXT	0.12	table E-5 (see also table E-6)

[1] ID number for conversion relationship (CR) listed in table E-8.

[2] The listed time periods cover the ranges indicated for the corresponding conversion relationships in table E-8; the time periods of data contributing to $\sigma[M]$ may differ, as indicated in the references.

[3] Unless otherwise indicated, the source domain of data used for the listed $\sigma[M]$.

[4] Bolded values are used in propagating uncertainties in two-step regressions; italicized values are used as estimates of $\boldsymbol{\sigma}_x$ in general orthogonal regressions (see table E-10).

[5] UUSS coda magnitudes prior to 1981 were based on "network" formulas rather than single-stations formulas (Griscom and Arabasz, 1979); $\sigma[M]$ was not assessed for M_C UU2 and M_C UU3, only $\sigma[M_L \text{ UU1} | M_C \text{ UU2}]$ and $\sigma[M_L \text{ UU1} | M_C \text{ UU3}]$ (see table E-8).

Moment Magnitude **(M_{obs})[6]**

Catalog	Mag. Type	CR ID	Time Period[7]	Region[8]	$\sigma[\mathbf{M}]$	Reference
UUSS	**M**	n/a	1998–2013	ISB	0.05	table E-6
SLU	**M**	n/a	1998–2013	ISB	0.05	table E-6
GCMT	**M**	n/a	1980–1994	global	0.10	table E-6, footnote 4; Kagan (2003)
GCMT	**M**	n/a	1995–2000	global	0.06	table E-6, footnote 4; Kagan (2003)
GCMT	**M**	n/a	2001-2013	WUS	0.06	table E-6

[6] See the "Explanation of Columns" sheet in Electronic Supplement E-2 for $\boldsymbol{\sigma}[\mathbf{M}]$ associated with other values of $\mathbf{M}_{obs}$ not listed here.

[7] Time period of data contributing to $\sigma[\mathbf{M}]$.

[8] Source domain of data used for the listed $\sigma[\mathbf{M}]$: ISB = Intermountain Seismic Belt; global = global earthquakes 0–70 km depth; WUS = Western U.S. (shallow).

Table E-7. *Sources of* M_{obs} *used in this study.*

Source of Reported Seismic Moment, M_0	Number of M_{obs} Values
1989 and Later	
Global Centroid Moment Tensor (GCMT) catalog	7
Whidden and Pankow (2012)	43
Whidden (University of Utah, unpublished data)	13
St. Louis University (SLU): Herrmann and others (2011), SLU online moment tensor catalog	30
Oregon State University (OSU) online moment tensor catalog	7
Pre-1989	
Battis and Hill (1977)	1
Doser (1989)	2
Patton and Zandt (1991)	8
Other (geometric mean of multiple M_0's)	3

TOTAL	114

Table E-8. *Conversion relationships to a predicted "best-estimate" uniform moment magnitude,* $\mathbf{M}_{pred}$*, based on general orthogonal regression. (Unless otherwise noted, relationships were developed for the Utah Region; use in the Extended Utah Region is provisional.)*

Size Measure		Conversion Relationship (CR)		$\sigma[\mathbf{M}\|X]$[1]
Notation	**Description and Applicable Period**	**ID**	**Relationship**	
M_L UU1	M_L Univ. of Utah (1981–2012) [see addendum on following page]	1	$\mathbf{M}_{pred}$ = 0.791 (M_L UU1) + 0.851	0.139[2]
M_L UU2	M_L Univ. of Utah (July 1962–Dec 1980)	2	***Two-step:*** M_L UU1 = M_L UU2 ± 0.24 (see footnote 3, table E-5), where 0.24 = $\sigma_{MLUU1\|MLUU2}$, and use CR-1	0.229
M_C UU1	M_C Univ. of Utah (1981–2012)	3	$\mathbf{M}_{pred}$ = 0.929 (M_C UU1) + 0.227	0.225
M_C UU2	M_C Univ. of Utah (Oct 1974–Dec 1980)	4	***Two-step:*** M_L UU1 = M_C UU2 ± 0.27 (see Griscom and Arabasz, 1979), where 0.27 = $\sigma_{MLUU1\|McUU2}$, and use CR-1	0.249
M_C UU3	M_C Univ. of Utah (July 1962–Sept 1974)	5	***Two-step:*** M_L UU1 = M_C UU3 ± 0.28 (see Griscom and Arabasz, 1979), where 0.28 = $\sigma_{MLUU1\|McUU3}$, and use CR-1	0.256
M_L GS	M_L USGS (1974–2012), <u>Utah Region (UTR)</u>	6	***Two-step:*** M_L UU1 = M_L GS – 0.11 and use CR-1	0.232
M_L GS	M_L USGS (1981–2012), <u>Extended Border Region (EBR)</u>	7	***Two-step:*** M_L UU1 = M_L GS + 0.09 and use CR-1	0.230
m_b PDE1 > 3.5	m_b USGS/PDE (1991–2012), <u>Extended Utah Region (UTREXT)</u>	8	$\mathbf{M}_{pred}$ = 1.078 (m_b PDE1) – 0.427	0.207
m_b PDE2 ≥ 3.5	m_b USGS/PDE (1978–1990)	9	***Two-step:*** $M_{L,C}$ UU = 1.088 m_b PDE2 – 0.652 and use CR-1	0.362
m_b PDE3 3.3–5.0	m_b CGS/USGS/PDE (1963–1977)	10	***Two-step:*** $M_{L,C}$ UU = 1.697 m_b PDE3 – 3.557 and use CR-1	0.443
m_b ISC	m_b ISC, Nsta ≥ 5 (1964–2012)	11	$\mathbf{M}_{pred}$ = 1.162 m_b ISC –0.740	0.295
ln(FA)	ln(FA), in km^2, where FA is the total felt area (1850–2012)	12	$\mathbf{M}_{pred}$ = 0.00 + 0.415 x ln(FA) + 0.0015 $(FA)^{1/2}$	0.339
$I_0 \geq V$	Epicentral value of Modified Mercalli Intensity, MMI ≥ V (1850–2012)	13	$\mathbf{M}_{pred}$ = 0.764 I_0 + 0.229	0.5[3]
$I_0 < V$	Epicentral value of MMI < V (1850–2012)	14	$\mathbf{M}_{pred}$ = 0.386 I_0 + 2.126	0.5[3]

(continued on next page)

Size Measure		Conversion Relationship (CR)		$\sigma[\mathbf{M}\|X]$[1]
Notation	**Description and Applicable Period**	**ID**	**Relationship**	
A_{VII}	Extent of area shaken, in km^2, at or greater than MMI VII (1850–2012)	15	$\mathbf{M}_{pred} = 1.619 \log_{10}(A_{VII}) + 0.802$	0.35[4]
A_{VI}	Extent of area shaken, in km^2, at or greater than MMI VI (1850–2012)	16	$\mathbf{M}_{pred} = 1.341 \log_{10}(A_{VI}) + 0.535$	0.35[4]
A_V	Extent of area shaken, in km^2, at or greater than MMI V (1850–2012)	17	$\mathbf{M}_{pred} = 1.445 \log_{10}(A_V) - 0.809$	0.35[4]
A_{IV}	Extent of area shaken, in km^2, at or greater than MMI IV (1850–2012)	18	$\mathbf{M}_{pred} = 1.306 \log_{10}(A_{IV}) - 0.345$	0.35[4]

[1] Standard deviation of the normally distributed error in **M** when estimated from size measure X. Uncertainties in $\mathbf{M}_{pred}$ are adjusted for the variance in the observed values of **M**, $\mathbf{M}_{obs}$, used in the regression of $\mathbf{M}_{obs}$ versus X; uncertainties for two-step regressions account for the propagation of uncertainties.

[2] The 1981 start date for M_L UU1 is based on Pechmann et al. (2007), but the value of 0.139 for $\sigma[\mathbf{M}|M_L\ UU1]$ is based mostly on M_L observations from multi-station digital data after 1996. Because M_L values in the University of Utah catalog from 1981 until the early 1990s are based on two stations (with an average standard error of 0.21 vs. 0.10 for later M_L UU1), a larger two-step uncertainty of 0.209 for $\sigma[\mathbf{M}|M_L\ UU1]$ is applied to the UTR for 1981–1995 and to the EBR for 1981–1993.

[3] Adopted nominal value.

[4] Adopted generic value.

Addendum to CR-1

For clarity, the instructions below make explicit how CR-1 for M_L Univ. of Utah was applied to the BEM catalog by time period and by region, based on the information provided in footnote 2 above.

Size Measure		Conversion Relationship (CR)		$\sigma[\mathbf{M}\|X]$[1]
Notation	**Description and Applicable Period**	**ID**	**Relationship**	
M_L UU1	M_L Univ. of Utah (1996–2012), UTR	1	$\mathbf{M}_{pred} = 0.791\ (M_L\ UU1) + 0.851$	0.139
M_L UU1$^{\#}$	M_L Univ. of Utah (1981–1995), UTR	1$^{\#}$	***Two-step:*** $M_L\ UU1 = M_L\ UU1^{\#} \pm 0.21$, where $0.21 = \sigma_{MLUU1\|MLUU1\#}$, and use CR-1	0.209
M_L UU1	M_L Univ. of Utah (1994–2012), EBR	1	$\mathbf{M}_{pred} = 0.791\ (M_L\ UU1) + 0.851$	0.139
M_L UU1$^{\#}$	M_L Univ. of Utah (1981–1993), EBR	1$^{\#}$	***Two-step:*** $M_L\ UU1 = M_L\ UU1^{\#} \pm 0.21$, where $0.21 = \sigma_{MLUU1\|MLUU1\#}$, and use CR-1	0.209

Table E-9. *Conversion relationships to a uniform estimate of moment magnitude, E[**M**], based on least squares regression. (Unless otherwise noted, relationships were developed for the Utah Region; use in the Extended Utah Region is provisional.)*

Size Measure		Conversion Relationship (CR)		σ[**M**|**X**][1]
Notation	**Description and Applicable Period**	**ID**	**Relationship**	
M_L UU1	M_L Univ. of Utah (1981–2012) [see addendum on following page]	1a	E[**M**] = 0.769 (M_L UU1) + 0.941	0.137[2]
M_L UU2	M_L Univ. of Utah (July 1962–Dec 1980)	2a	***Two-step:*** M_L UU1 = M_L UU2 ± 0.24 (see footnote 3, table E-5), where 0.24 = $\sigma_{MLUU1\|MLUU2}$, and use CR-1	0.223
M_C UU1	M_C Univ. of Utah (1981–2012)	3a	E[**M**] = 0.838 (M_C UU1) + 0.603	0.216
M_C UU2	M_C Univ. of Utah (Oct 1974–Dec 1980)	4a	***Two-step:*** M_L UU1 = M_C UU2 ± 0.27 (see Griscom and Arabasz, 1979), where 0.27 = $\sigma_{MLUU1\|McUU2}$, and use CR-1	0.243
M_C UU3	M_C Univ. of Utah (July 1962–Sept 1974)	5a	***Two-step:*** M_L UU1 = M_C UU3 ± 0.28 (see Griscom and Arabasz, 1979), where 0.28 = $\sigma_{MLUU1\|McUU3}$, and use CR-1	0.249
M_L GS	M_L USGS (1974–2012), <u>Utah Region (UTR)</u>	6a	***Two-step:*** M_L UU1 = M_L GS – 0.11 and use CR-1	0.227
M_L GS	M_L USGS (1981–2012), <u>Extended Border Region (EBR)</u>	7a	***Two-step:*** M_L UU1 = M_L GS + 0.09 and use CR-1	0.224
m_b PDE1 > 3.5	m_b USGS/PDE (1991–2012), <u>Extended Utah Region (UTREXT)</u>	8a	E[**M**] = 0.974 (m_b PDE1) + 0.036	0.197
m_b PDE2 ≥ 3.5	m_b USGS/PDE (1978–1990)	9a	***Two-step:*** $M_{L,C}$ UU = 0.668 m_b PDE2 + 1.231 and use CR-1	0.320
m_b PDE3 3.3–5.0	m_b CGS/USGS/PDE (1963–1977)	10a	***Two-step:*** $M_{L,C}$ UU = 1.020 m_b PDE3 – 0.804 and use CR-1	0.378
m_b ISC	m_b ISC, Nsta ≥ 5 (1964–2012)	11a	E[**M**] = 1.037 m_b ISC –0.148	0.283
ln(FA)	ln(FA), in km^2, where FA is the total felt area (1850–2012)	12a	E[**M**] = 0.647 + 0.345 x ln(FA) + 0.0018 $(FA)^{1/2}$	0.334
$I_0 \geq V$	Epicentral value of Modified Mercalli Intensity, MMI ≥ V (1850–2012)	13a	E[**M**] = 0.654 I_0 + 0.922	0.5[3]
$I_0 < V$	Epicentral value of MMI < V (1850–2012)	14a	E[**M**] = 0.349 I_0 + 2.393	0.5[3]

(continued on next page)

Size Measure		Conversion Relationship (CR)		σ[**M**|**X**][1]
Notation	**Description and Applicable Period**	**ID**	**Relationship**	
A_{VII}	Extent of area shaken, in km^2, at or greater than MMI VII (1850–2012)	15a	E[**M**] = 1.591 $\log_{10}(A_{VII})$ + 0.896	0.35
A_{VI}	Extent of area shaken, in km^2, at or greater than MMI VI (1850–2012)	16a	E[**M**] = 1.230 $\log_{10}(A_{VI})$ + 0.983	0.35[4]
A_V	Extent of area shaken, in km^2, at or greater than MMI V (1850–2012)	17a	E[**M**] = 1.290 $\log_{10}(A_V)$ – 0.088	0.35[4]
A_{IV}	Extent of area shaken, in km^2, at or greater than MMI IV (1850–2012)	18a	E[**M**] = 1.295$\log_{10}(A_{IV})$ – 0.288	0.35[4]

[1] Standard deviation of the normally distributed error in **M** when estimated from size measure X. Uncertainties in E[**M**] are adjusted for the variance in the observed values of **M**, $\mathbf{M}_{obs}$, used in the regression of $\mathbf{M}_{obs}$ versus X; uncertainties for two-step regressions account for propagation of uncertainties.

[2] The 1981 start date for M_L UU1 is based on Pechmann et al. (2007), but the value of 0.137 for σ[**M**|M_L UU1] is based mostly on M_L observations from multi-station digital data after 1996. Because M_L values in the University of Utah catalog from 1981 until the early 1990s are based on two stations (with an average standard error of 0.21 vs. 0.10 for later M_L UU1), a larger two-step uncertainty of 0.205 for σ[**M**|M_L UU1] should be applied to the UTR for 1981–1995 and to the EBR for 1981–1993.

[3] Adopted nominal value.

[4] Adopted generic value.

Addendum to CR-1a

For clarity, the instructions below make explicit how CR-1a for M_L Univ. of Utah would be applied by time period and by region, based on the information provided in footnote 2 above.

Size Measure		Conversion Relationship (CR)		σ[**M**|**X**][1]
Notation	**Description and Applicable Period**	**ID**	**Relationship**	
M_L UU1	M_L Univ. of Utah (1996–2012), UTR	1a	E**[M]** = 0.769 (M_L UU1) + 0.941	0.137
M_L UU1$^{\#}$	M_L Univ. of Utah (1981–1995), UTR	1$^{\#}$a	***Two-step:*** M_L UU1 = M_L UU1$^{\#}$ ± 0.21, where 0.21 = $\sigma_{MLUU1\|MLUU1\#}$, and use CR-1	0.205
M_L UU1	M_L Univ. of Utah (1994–2012), EBR	1a	E**[M]** = 0.769 (M_L UU1) + 0.941	0.137
M_L UU1$^{\#}$	M_L Univ. of Utah (1981–1993), EBR	1$^{\#}$a	***Two-step:*** M_L UU1 = M_L UU1$^{\#}$ ± 0.21, where 0.21 = $\sigma_{MLUU1\|MLUU1\#}$, and use CR-1	0.205

Table E-10. *Regression statistics for general orthogonal regressions.*

ID	Y	X[1]	Slope (± 1 std. error)	Intercept (± 1 std. error)	N	Uncertainty[2] σ_y	Uncertainty[2] σ_x	η	$S_{y,x}$	σ [M|X][7]	R^2
1	**M**obs	ML UU1	0.791 ± 0.023	0.851 ± 0.096	65	0.05	0.07	0.51	0.1473	0.139	0.950
3	**M**obs	Mc UU1	0.929 ± 0.045	0.227 ± 0.188	63	0.05	0.10	0.25	0.2310	0.225	0.874
8	**M**obs	mb PDE1	1.078 ± 0.083	-0.427 ± 0.375	23	0.06	0.14[3]	0.18	0.2154	0.207	0.889
9	M_L, Mc UU	mb PDE2	1.088 ± 0.307	-0.652 ± 1.380	21	0.14	0.14[3]	1.00	0.4292	n/a	0.402
10	M_L, Mc UU	mb PDE3	1.697 ± 0.191	-3.557 ± 0.779	103	0.24	0.19[4]	1.60	0.5369	n/a	0.440
11	**M**obs	mb ISC	1.162 ± 0.151	-0.740 ± 0.720	13	0.08	0.10	0.64	0.3053	0.295	0.844
13	**M**obs	$I_0 \geq V$	0.764 ± 0.071	0.229 ± 0.459	24	0.13	0.50[5]	0.07	0.4474	*0.429*	0.841
14	**M**obs	$I_0 < V$	0.386 ± 0.009	2.126 ± 0.044	39	0.10	0.50[5]	0.04	0.3236	*0.308*	0.527[9]
15	**M**obs	$\log(A_{VII})$	1.619 ± 0.126	0.802 ± 0.429	6	0.18	0.18[6]	0.97	0.1406	*(0.141)*[8]	0.976
16	**M**obs	$\log(A_{VI})$	1.341 ± 0.203	0.535 ± 0.828	8	0.16	0.18[6]	0.83	0.3767	*0.339*	0.880
17	**M**obs	$\log(A_V)$	1.445 ± 0.226	-0.809 ± 1.057	9	0.16	0.18[6]	0.76	0.3896	*0.357*	0.855
18	**M**obs	$\log(A_{IV})$	1.306 ± 0.076	-0.345 ± 0.369	6	0.16	0.18[6]	0.81	0.1290	*(0.129)*[8]	0.987
12	**M**obs	ln(FA)	Model: $\mathbf{M} = c_0 + c_1 \ln(FA) + c_2 \sqrt{FA}$		26	0.10	-----	-----	0.3535	0.339	
			c_0 = 0.00 (constrained to be non-negative) c_1 = 0.415 c_2 = 0.0015								

[1] X_{min} and X_{max} used in each regression are the same as for the counterpart least squares regression (with "a" appended to the ID) shown in table E-11.

[2] Unless noted otherwise, σ_y and σ_x are the average σ for the individual event magnitudes used in the regression.

[3] Estimated from uncertainties for tabulated event magnitudes of m_b ISC for events of comparable size during the same period; the estimate is supported by an independent one of 0.13 made for m_b PDE, 1978–2008, using a different approach (table E-6).

[4] Estimated by using the single-station σ of 0.38 for m_b ISC in the UTREXT (table E-5) divided by $\sqrt{4}$, where 4 is the average number of station measures reported for m_b PDE3 in the UTR during 1963–1977.

[5] Nominal value for the uncertainty in I_0.

[6] Nominal value for the uncertainty in $\log(A_{IV–VII})$.

[7] Calculated as $\sqrt{S_{y,x}{}^2 - \sigma_y{}^2}$; the italicized values are replaced in table E-8 by either a nominal value, in the case of I_0, or by a generic value, in the case of $\log(A_{IV–VII})$.

[8] Where $\sigma_y{}^2 \geq S_{y,x}{}^2$, the value of $S_{y,x}{}^2$ is shown in parentheses; as indicated above, the value is replaced by a generic value in table E-8.

[9] Constrained case.

Table E-11. *Regression statistics for least squares regressions.*

ID	Y	X	**Slope** (± 1 std. error)	**Intercept** (± 1 std. error)	N	X min, max	$S_{y,x}$	σ [M|X][1]	R^2
1a	**M**obs	ML UU1	0.769 ± 0.022	0.941 ± 0.093	65	2.87, 6.05	0.1462	0.137	0.950
3a	**M**obs	Mc UU1	0.838 ± 0.041	0.603 ± 0.170	63	2.91, 6.06	0.2220	0.216	0.874
8a	**M**obs	mb PDE1	0.974 ± 0.075	0.036 ± 0.339	23	3.6, 5.7	0.2063	0.197	0.889
9a	M_L, Mc UU	mb PDE2	0.668 ± 0.187	1.231 ± 0.845	21	3.5, 5.5	0.3817	n/a	0.402
10a	M_L, Mc UU	mb PDE3	1.020 ± 0.115	-0.804 ± 0.469	103	3.3, 5.0	0.4630	n/a	0.440
11a	**M**obs	mb ISC	1.037 ± 0.134	-0.148 ± 0.641	13	4.00, 5.82	0.2939	0.283	0.844
13a	**M**obs	$I_0 \geq V$	0.654 ± 0.061	0.922 ± 0.394	24	5, 10	0.4175	*0.397*	0.841
14a	**M**obs	$I_0 < V$	0.349 ± 0.054	2.393 ± 0.203	39	3, 5	0.2923	*0.275*	0.527
15a	**M**obs	$\log(A_{VII})$	1.591 ± 0.124	0.896 ± 0.421	6	$\log(A_{VII})$: 2.68, 4.01	0.1397	*(0.140)*[2]	0.976
16a	**M**obs	$\log(A_{VI})$	1.230 ± 0.185	0.983 ± 0.757	8	$\log(A_{VI})$: 2.49, 4.90	0.3658	*0.327*	0.880
17a	**M**obs	$\log(A_V)$	1.290 ± 0.201	-0.088 ± 0.939	9	$\log(A_V)$: 3.32, 5.40	0.3740	*0.339*	0.855
18a	**M**obs	$\log(A_{IV})$	1.295 ± 0.075	-0.288 ± 0.366	6	$\log(A_{IV})$: 3.54, 5.91	0.1286	*(0.129)*[2]	0.987
12a	**Mobs**	ln(FA)	Model: **M** = $c_0 + c_1 \ln(FA) + c_2 \sqrt{FA}$ c_0 = 0.647 ± 0.956 (± 1 std. error) c_1 = 0.345 ± 0.107 (± 1 std. error) c_2 = 0.0018 ± 0.0007 (± 1 std. error)		26	ln(FA): 8.24, 13.98	0.3484	0.334	

[1] Calculated as $\sqrt{S_{y,x}{}^2 - \sigma_y{}^2}$, where $\sigma_y{}^2$ is the uncertainty in the Y values used in the regression, which is the same as that tabulated in table E-10 for the counterpart general orthogonal regression (whose ID is without an appended "a"); the italicized values are replaced in table E-9 by either a nominal value, in the case of I_0, or by a generic value, in the case of $\log(A_{IV\text{-}VII})$.

[2] Where $\sigma_y{}^2 \geq S_{y,x}{}^2$, the value of $S_{y,x}{}^2$ is shown in parentheses; as indicated above, the value is replaced by a generic value in table E-9.

Table E-12. *Measurements of A_{MMI} made with a GIS spatial analysis tool and used in either developing or applying magnitude conversion relationships for A_{IV} to A_{VII} (data for A_{MMI} not used for earthquakes after 1962).*

Date (UTC/GMT)	M[1]	Region	Area (km²) A_{IV}	A_V	A_{VI}	A_{VII}	Source of Isoseismal Map
A_{MMI} used for developing CRs							
Mar. 12, 1934	**6.59**	Hansel Valley, Utah	144,360	66,500	24,060	4240	Hopper (2000)
Aug. 18, 1959	**7.35**	Hebgen Lake, Mont.	816,490	341,170	80,040	10,300	Stover and Coffman (1993)
Aug. 30, 1962	**5.75**	Cache Valley, Utah	----	80,820	6980	830	Hopper (2000)
Oct. 4, 1967	**5.08**	Marysvale, Utah	----	21,660	4900	480	Von Hake and Cloud (1969)
Oct. 1, 1972	**4.35**	Heber City, Utah	3500	2110	310	----	Hopper (2000)
Mar. 28, 1975	**6.02**	Pocatello Valley, Ida.	76,170	----	10,140	2020	Hopper (2000)
Oct. 28, 1983	**6.82**	Borah Peak, Ida.	----	252,000	52,370	5160	Stover and Coffman (1993)
Sept. 2, 1992	**5.50**	St. George, Utah	----	41,630	14,240	----	Olig (1995)
Feb. 3, 1994	**5.66**	Draney Peak, Ida.	48,740	18,350	1080[3]	----	M. Hopper, USGS[5]
Feb. 21, 2008	**5.91**	Wells, Nev.	72,630	31,980	----	----	dePolo and Pecoraro (2011)
A_{MMI} used in applying CRs, contributing to best-estimate moment magnitudes							
Aug. 1, 1900	*4.36*	Eureka, Utah	----	800	500	----	Hopper (2000)
Nov. 1, 1901	*6.63*	Sevier Valley, Utah	----	----	27,260	7250	Hopper (2000)
May 22, 1910	*5.28*	Salt Lake City, Utah	----	9780[2]	3560	240[4]	Hopper (2000)
May 13, 1914	*4.81*	Ogden, Utah	----	4580	820	160	Hopper (2000)
July 15, 1915	*4.34*	Provo, Utah	3,050	1590	660	----	Hopper (2000)
Sept. 29, 1921	*5.45*	Elsinore, Utah	----	----	----	400[6]	Hopper (2000)
Sept. 30, 1921	*4.42*	Elsinore, Utah	----	----	300[6]	----	Hopper (2000)
Oct. 1, 1921	*4.67*	Elsinore, Utah	----	----	300[6]	----	Hopper (2000)
Feb. 22, 1943	*4.24*	Salt Lake City, Utah	5,590	1870	580	----	Hopper (2000)
Feb. 13, 1958	*4.06*	Wallsburg, Utah	3,100	1240	690	----	Hopper (2000)
Sept. 5, 1962	*4.87*	Magna, Utah	----	5190	2090	----	Hopper (2000)
A_{MMI} measured but not used							
Aug. 16, 1966	*5.22*	Nevada-Utah border	----	15,700	----	----	Von Hake and Cloud (1968)
Mar. 9, 1978	*3.38*	Magna, Utah	2200	1140	230	----	Hopper (2000)
Feb. 20, 1981	*3.97*	Orem, Utah	2630	240	----	----	Hopper (2000)
Oct. 8, 1983	*3.92*	West Valley, Utah	5080	920	110	----	Hopper (2000)

[1] Bold values are $\mathbf{M}_{obs}$; italicized values, best-estimate moment magnitudes.

[2] Isoseismal contour completed by extrapolation.

[3] Area smaller than expected: outlier excluded in A_{VI} regression.

[4] Area imprecise.

[5] Isoseismal map for "Modified Mercalli Intensities for Earthquake near Afton, Wyoming, printed April 13, 2000" (M. Hopper, U.S. Geological Survey, written communication, June 2012).

[6] Estimated–but not measured with the GIS spatial analysis tool—using data on isoseismal maps of Hopper (2000).

Table E-13. *Magnitude types termed* ***M˜*** *assumed to be equivalent to* ***M****. These are miscellaneous magnitudes in the merged master catalog that are the sole magnitude available for the indicated number of earthquakes and for which there were inadequate data to develop conversion relationships to* ***M****.*

Mag. Code	Description	a.k.a. (or assumed equivalent)	No.	Mag. Range	Year of Events	Region (No. of Events)	σ	Basis for σ
MsGR	Gutenberg-Richter surface-wave magnitude	------	2	5.25, 5.5	1934	UTR (2)	0.30	Richter (1958) describes uncertainty of at least 0.25 mag. unit for original surface-wave magnitudes
MxJON	Wiechert magnitude at Reno (Jones, 1975)	MxSJG, MLREN	10	4.3–5.5	1917, 1934–1937, 1950	UTR (7), EBR (3)	0.37	Std. error determined by Jones (1975)
MLPAS	ML determined at Pasadena (before 1973)	Ukn PAS (2 events)	65	2.7–5.3,	1936–1967	UTR (19), EBR (46)	0.20	Std. error based on information in Felzer and Cao (2007)
MLBRK	ML determined at Berkeley (before 1973)	------	34	3.6–5.5	1966–1972	UTR (29), EBR (5)	0.20	Std. error based on information in Felzer and Cao (2007)
MLERD	ML determined by Dept. of Energy in Idaho Falls, Idaho	MLAEC, MLERL	4	2.8–3.7	1975–1977	UTR (1), EBR (3)	0.30	Typical single-station std. error for this time period
Ukn UU	Unknown magnitude attributed to Univ. of Utah	------	1	3.5	1962	UTR (1)	0.50	Large std. error assigned because of time period and unknown magnitude type
Miscellaneous Magnitudes Applicable to EBR Only								
MLREN	ML attributed to Nevada Seismological Lab in Reno, Nevada	MDREN (2 events)	39	2.3–4.5	1972–2012	EBR	0.15	Typical std. error for ML (outside California) for this time period
MLBUT	ML attributed to Montana Tech in Butte, Montana	MLMMT	8	2.6–3.6	1988–2011	EBR	0.15	Typical std. error for ML (outside California) for this time period
MDUSBR	MD attributed to U.S. Bureau of Reclamation	------	7	2.3–3.1	1999–2002	EBR	0.15	Typical std. error for this time period
MLPAS	ML determined at Pasadena (after 1972)	------	5	2.5–3.6	1973–2011	EBR	0.10	Std. error based on information in Felzer and Cao (2007)
MLTFO	ML attributed to TFO array in Arizona	------	3	3.8–3.9	1967	EBR	0.30	Typical single-station std. error for this time period
MfaWOO	Magnitude based on felt area estimated by Wood (1947)	------	2	5.0, 5.0	1934, 1940	EBR	0.50	Correlation of M with felt area is approximate and imprecise (see: Wood, 1947; Gutenberg and Richter, 1942)
UKN	Unknown magnitude	UKUKN	2	4.0, 4.0	1934	EBR	0.50	Large std. error assigned because of time period and unknown magnitude type
MLUBO	ML attributed to UBO array in Utah	------	1	4.2	1967	EBR	0.30	Typical single-station std. error for this time period
MLBRK	ML determined at Berkeley (after 1972)	------	1	4.1	1984	EBR	0.10	Std. error based on information in Felzer and Cao (2007)
UK UU	Unknown magnitude attributed to Univ. of Utah	------	1	4.3	1942	EBR	0.50	Large std. error assigned because of time period and unknown magnitude type

(continued on next page)

Mag. Code	Description	a.k.a. (or assumed equivalent)	No.	Mag. Range	Year (No.) of Events	Region (No.) of Events	σ	Basis for σ
UKXXX	Unknown magnitude	------	1	2.7	1966	EBR	0.50	Large std. error assigned because of time period and unknown magnitude type
UNR 1852	Magnitude attributed to Nevada Seismological Lab (abbreviation from Pancha and others, 2006)	------	1	4.9	1952	EBR	0.37	Std. error comparable to that for Wiechert magnitude at UNR for this early time period
ml DNA	Magnitude originating from DNAG catalog	------	1	4.0	1970	EBR	0.50	Large std. error assigned because of time period and unknown magnitude type

Breakdown of M˜ by Region and Event Type

	UTR	WGUEP	EBR
Mainshocks	13	2	76
Dependent Events	46	8	53
Total Number of Events	59	10	129

Table E-14. *Largest mainshocks in the Utah Region, **M** ≥ 4.85, 1850–September 2012.*

ID	Year	MoDay	Hr:Min (UTC/GMT)	Region[1]	M[2]	σ	Long W	Lat N	Depth[3] (km)	BEM Type[4]
1	1884	1110	08:50	*Paris, Idaho*	5.58	0.50	111.400	42.300	-----	Mpred|Io
2	1901	1114	04:39	Tushar Mountains	6.63	0.29	112.400	38.500	-----	Mpred|Xnon
3	1902	1117	19:50	Pine Valley	6.34	0.50	113.520	37.393	-----	Mpred|Io
4	1909	1006	02:41	*Hansel Valley*	5.58	0.50	112.700	41.800	-----	Mpred|Io
5	1910	0522	14:28	*Salt Lake City*	5.28	0.29	111.800	40.700	-----	Mpred|Xnon
6	1921	0929	14:12	Elsinore	5.45	0.29	112.150	38.683	-----	Mpred|Xnon
7	1934	0312	15:05	*Hansel Valley*	**6.59**	0.30	112.795	41.658	9	Mobs
8	1937	1119	00:50	*Idaho-Nevada-Utah tri-state area*	5.40	0.37	113.900	42.100	-----	M~|MxSJG
9	1950	0118	01:55	NW Uinta Basin	5.30	0.20	110.500	40.500	-----	M~|UknPAS
10	1959	0721	17:39	Arizona-Utah border	5.55	0.14	112.370	36.800	-----	Mpred|Xmix
11	1962	0830	13:35	*Cache Valley*	**5.75**	0.15	111.733	41.917	10	Mobs
12	1962	0905	16:04	*Magna*	4.87	0.12	112.089	40.715	7*	Mpred|Xmix
13	1963	0707	19:20	*Juab Valley*	**5.06**	0.15	111.909	39.533	4	Mobs
14	1966	0816	18:02	Nevada-Utah border	5.22	0.20	114.151	37.464	7*	Mpred|Xvar
15	1967	1004	10:20	Marysvale	**5.08**	0.15	112.157	38.543	14	Mobs
16	1975	0328	02:31	*Pocatello Valley, Idaho*	**6.02**	0.06	112.525	42.063	5	Mobs
17	1988	0814	20:03	*San Rafael Swell*	5.02	0.13	110.890	39.133	17	Mpred|Xvar
18	1989	0130	04:06	So. Wasatch Plateau	**5.20**	0.10	111.614	38.823	25	Mobs
19	1992	0902	10:26	St. George	**5.50**	0.10	113.506	37.105	15	Mobs

[1] Unless indicated otherwise, all epicenters are within Utah; italics indicate epicenters within the WGUEP Region.

[2] Bold values are observed moment magnitude, $\mathbf{M}_{obs}$; other values, best-estimate moment magnitudes.

[3] Listed only where there is instrumental focal-depth control; asterisk indicates restricted focal-depth.

[4] Best-estimate moment magnitudes, based either on $\mathbf{M}_{obs}$, **M~** (a magnitude type assumed to be equivalent to **M**), or $\mathbf{M}_{pred}$ from magnitude conversion relationships. Xnon indicates best estimate from inverse-variance weighting of non-instrumental size measures; Xmix, from non-instrumental and instrumental size measures; Xvar, from instrumental size measures. See text for explanation of other details.

Table E-15. *Summary of declustering results by catalog domain.*

Number	UTREXT	UTR	WGUEP	EBR[1]
Total number of earthquakes	5388	2622	1157	2766
Number of mainshocks	2425	1554	660	871
Number of dependent events	2963	1068	497	1895
Number of mainshocks ≥ **M** 5.0	28	18	8	10

[1] Number in EBR = number in UTREXT – number in UTR

Table E-16. *Completeness periods for the WGUEP and Utah regions (BEM catalog, declustered).*

Magnitude Range	Range for Counts	Completeness Period, T_C *Year (Start)*[1]	*Year (End)*	t (years)
WGUEP Region, Magnitude 0.7 Bins				
2.9 ≤ M < 3.6	2.85–3.54	**1986**	2012.75	26.75
3.6 ≤ M < 4.3	3.55–4.24	**1979**	2012.75	33.75
4.3 ≤ M < 5.0	4.25–4.94	**1963**	2012.75	49.75
5.0 ≤ M < 5.7	4.95–5.64	***1908***	2012.75	104.75
5.7 ≤ M < 6.4	5.65–6.34	***1880***	2012.75	132.75
6.4 ≤ M < 7.0	6.35–7.04	*1850*	2012.75	162.75
WGUEP Region, Magnitude 0.5 Bins				
3.0 ≤ M < 3.5	2.95–3.44	**1986**	2012.75	26.75
3.5 ≤ M < 4.0	3.45–3.94	**1979**	2012.75	33.75
4.0 ≤ M < 4.5	3.95–4.44	**1963**	2012.75	49.75
4.5 ≤ M < 5.0	4.45–4.94	**1963**	2012.75	49.75
5.0 ≤ M < 5.5	4.95–5.44	***1908***	2012.75	104.75
5.5 ≤ M < 6.0	5.45–5.94	***1880***	2012.75	132.75
6.0 ≤ M < 6.5	5.95–6.44	*1850*	2012.75	162.75
6.5 ≤ M < 7.0	6.45–6.94	*1850*	2012.75	162.75
Utah Region (UTR), Magnitude 0.7 Bins				
2.9 ≤ M < 3.6	2.85–3.54	**1986**	2012.75	26.75
3.6 ≤ M < 4.3	3.55–4.24	**1986**	2012.75	26.75
4.3 ≤ M < 5.0	4.25–4.94	**1963**	2012.75	49.75
5.0 ≤ M < 5.7	4.95–5.64	***1908***	2012.75	104.75
5.7 ≤ M < 6.4	5.65–6.34	***1880***	2012.75	132.75
6.4 ≤ M < 7.0	6.35–7.04	*1860*	2012.75	152.75
Utah Region (UTR), Magnitude 0.5 Bins				
3.0 ≤ M < 3.5	2.95–3.44	**1986**	2012.75	26.75
3.5 ≤ M < 4.0	3.45–3.94	**1986**	2012.75	26.75
4.0 ≤ M < 4.5	3.95–4.44	**1967**	2012.75	45.75
4.5 ≤ M < 5.0	4.45–4.94	**1963**	2012.75	49.75
5.0 ≤ M < 5.5	4.95–5.44	***1908***	2012.75	104.75
5.5 ≤ M < 6.0	5.45–5.94	***1880***	2012.75	132.75
6.0 ≤ M < 6.5	5.95–6.44	*1880*	2012.75	132.75
6.5 ≤ M < 7.0	6.45–6.94	*1860*	2012.75	152.75

[1] For start dates of completeness periods, bold date was picked from a cumulative recurrence curve (CRC) for the WGUEP and/or the Utah regions; italicized date, based on other arguments; bold italicized date, based on CRC plus other arguments.

Table E-17. *Area of shaking of MMI IV or greater (A_{IV}) and approximate total felt area (FA) expected to be associated with earthquakes of **M** 4.95–6.45 (see figure E-25). Radii of equivalent circular areas are also listed.*

M	$\mathbf{A_{IV}}$[1] (km^2)	**Equivalent Radius** (km)	**FA**[2] (km^2)	**Equivalent Radius** (km)
4.95	11,310	60	61,700	140
5.45	27,320	93	134,320	207
5.65	38,860	111	177,900	238
5.95	65,950	145	263,550	290
6.35	133,490	206	422,100	367
6.45	159,230	225	470,710	387

[1] Predicted from a general orthogonal regression of $\log(A_{IV})$ on $\mathbf{M}_{obs}$ using the data shown in figure E-16d for CR-18.

[2] Approximated by inverting conversion relationship CR-12 (table E-8).

Table E-18. *Data for seismicity rate calculations, WGUEP Region (BEM catalog, declustered).*

Magnitude Range	**Year (Start)**[1]	**Year (End)**	***t*** (years)	**No. of Earthquakes**	**Sum *N**** [2]
2.85 ≤ **M** < 3.55	**1986**	2012.75	26.75	183	170.721
3.55 ≤ **M** < 4.25	**1979**	2012.75	33.75	39	37.553
4.25 ≤ **M** < 4.95	**1963**	2012.75	49.75	9	8.532
4.95 ≤ **M** < 5.65	***1908***	2012.75	104.75	4	3.158
5.65 ≤ **M** < 6.35	***1880***	2012.75	132.75	2	1.926
6.35 ≤ **M** < 7.00	*1850*	2012.75	162.75	1	0.769

[1] Bold date indicates pick from a cumulative recurrence curve (CRC); italicized date, based on other arguments; bold italicized date, based on CRC plus other arguments.

[2] Sum *N** is the sum of the equivalent number of earthquakes in the specified magnitude interval, corrected for magnitude uncertainty on an earthquake-by-earthquake basis.

Table E-19. *Data for seismicity rate calculations, Utah Region (BEM catalog, declustered, injection-induced earthquakes excluded).*

Magnitude Range	**Year (Start)**[1]	**Year (End)**	***t*** (years)	**No. of Earthquakes**	**Sum *N**** [2]
2.85 ≤ **M** < 3.55	**1986**	2012.75	26.75	428	397.518
3.55 ≤ **M** < 4.25	**1986**	2012.75	26.75	77	74.011
4.25 ≤ **M** < 4.95	**1963**	2012.75	49.75	18	16.942
4.95 ≤ **M** < 5.65	***1908***	2012.75	104.75	12	10.218
5.65 ≤ **M** < 6.35	***1880***	2012.75	132.75	3	2.407
6.35 ≤ **M** < 7.00	*1860*	2012.75	152.75	2	1.555

[1] Bold date indicates the start of the completeness period, T_C, based on a pick from a cumulative recurrence curve (CRC); italicized date, based on other arguments; bold italicized date, based on CRC plus other arguments.

[2] Sum N^* is the sum of the equivalent number of earthquakes in the specified magnitude interval, corrected for magnitude uncertainty on an earthquake-by-earthquake basis.

Table E-20. Cumulative rates of independent background earthquakes, WGUEP Region.

Magnitude Range	**Rate** (events/yr)	**90% Confidence Limits on Rate**	
		Lower (events/yr)	**Upper** (events/yr)
M ≥ 3.00	5.34	4.72	5.92
M ≥ 3.50	1.58	1.30	1.83
M ≥ 4.00	0.465	0.344	0.586
M ≥ 4.50	0.137	0.089	0.192
M ≥ 5.00	0.0402	0.0228	0.0606
M ≥ 5.50	0.0116	0.0058	0.0188
M ≥ 6.00	0.00322	0.00141	0.00552
M ≥ 6.50	0.000734	0.000289	0.001328

Table E-21. Cumulative rates of independent background earthquakes, Utah Region.

Magnitude Range	**Rate** (events/yr)	**90% Confidence Limits on Rate**	
		Lower (events/yr)	**Upper** (events/yr)
M ≥ 3.00	12.5	11.5	13.4
M ≥ 3.50	3.65	3.23	4.05
M ≥ 4.00	1.06	0.88	1.26
M ≥ 4.50	0.310	0.236	0.396
M ≥ 5.00	0.0900	0.0628	0.1227
M ≥ 5.50	0.0258	0.0166	0.0374
M ≥ 6.00	0.00706	0.00419	0.01086
M ≥ 6.50	0.00159	0.00088	0.00258

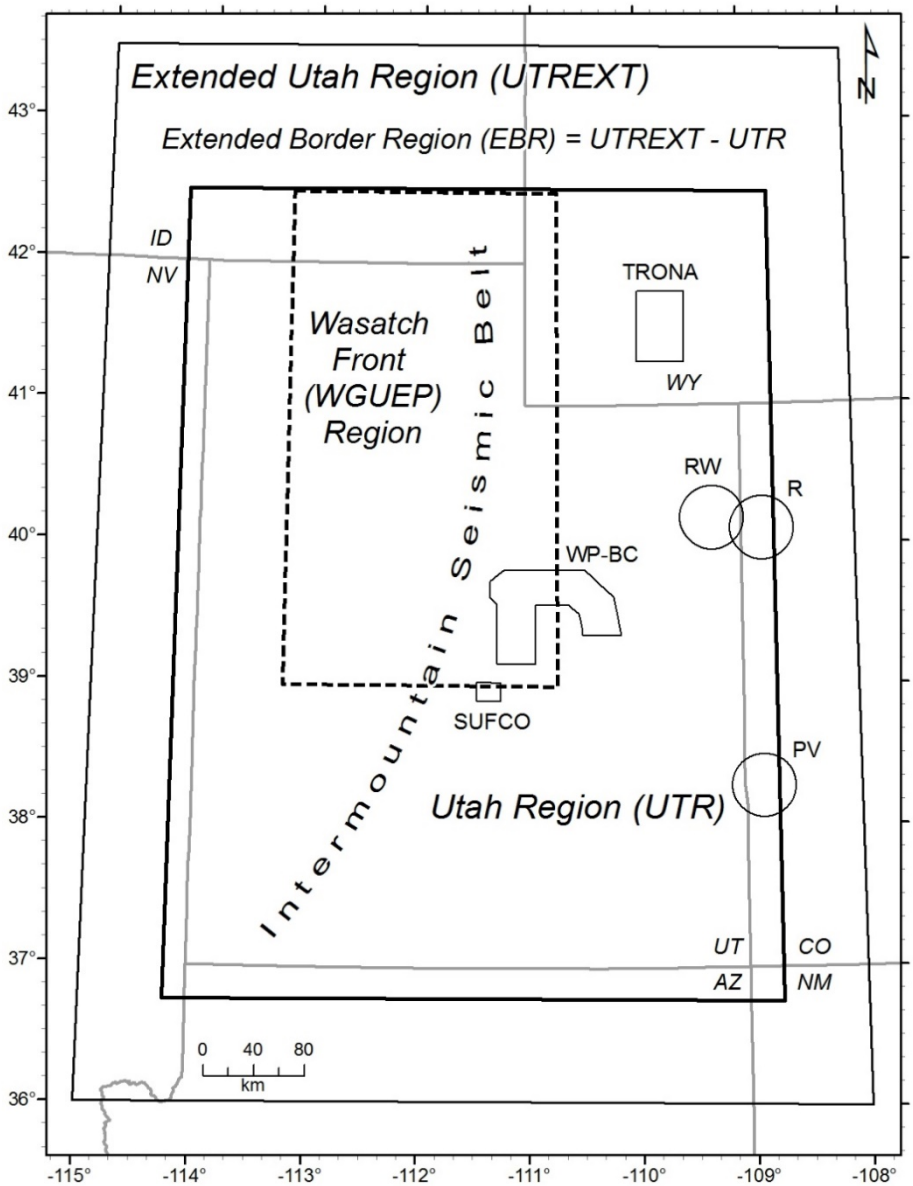

Figure E-1. *Location map. Boundaries of the major catalog domains (table E-1) are shown for the Extended Utah Region, the Utah Region, and the Wasatch Front (WGUEP) Region. Also shown are the outlines of areas demarcated for the removal of non-tectonic and human-triggered seismic events: PV = Paradox Valley, R = Rangely oil field, RW = Red Wash oil field, SUFCO = Southern Fuel Company coal-mining area, TRONA = trona mining district, WP-BC = Wasatch Plateau-Book Cliffs coal-mining region. The general location of the Intermountain Seismic Belt, which transects the study region, is also indicated.*

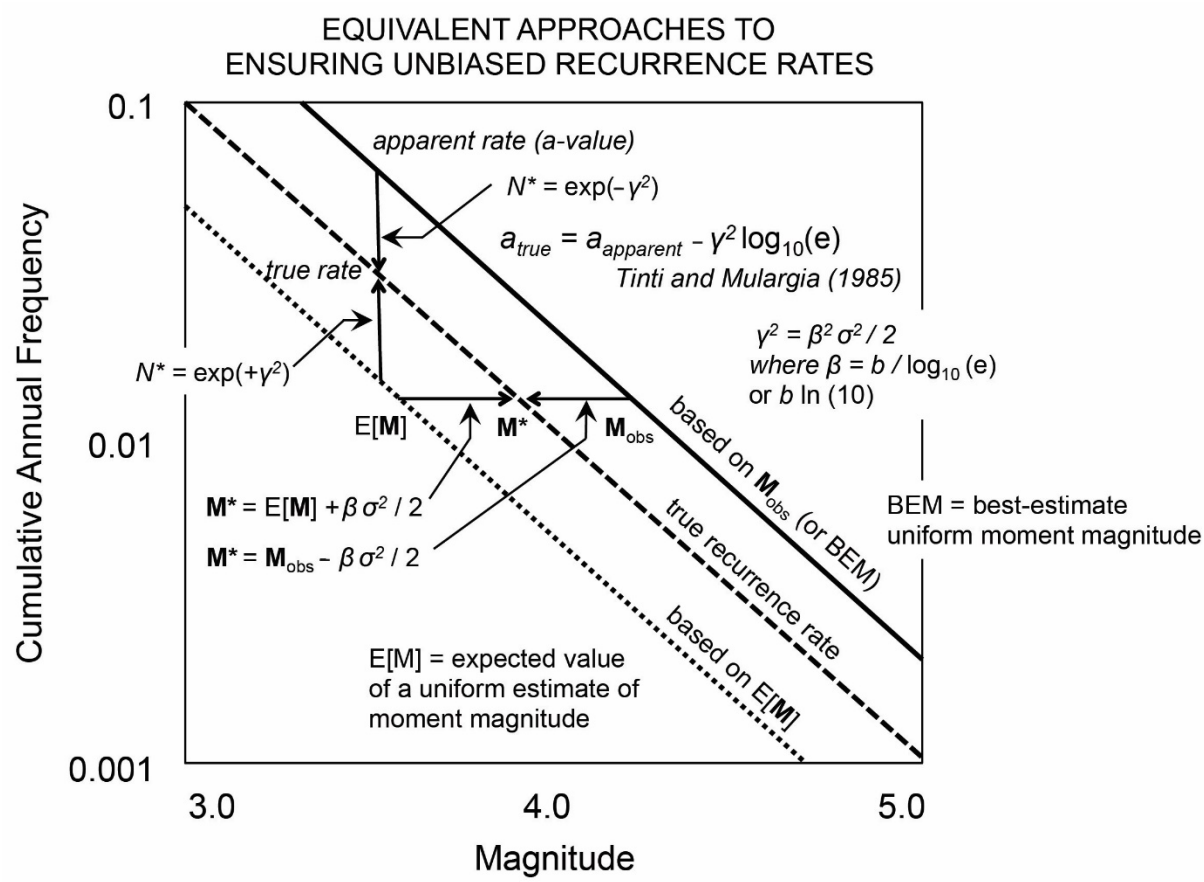

Figure E-2. *Schematic frequency-magnitude diagram showing how unbiased ("true") recurrence rates can be determined by making appropriate corrections in either the x-direction in terms of magnitude,* **M**, *or in the y-direction in terms of rate, expressed here as the cumulative annual rate, a, of earthquakes* ≥ **M**. *Adapted from EPRI/DOE/NRC (2012). N* as defined on the figure is the equivalent count assigned to an individual earthquake.*

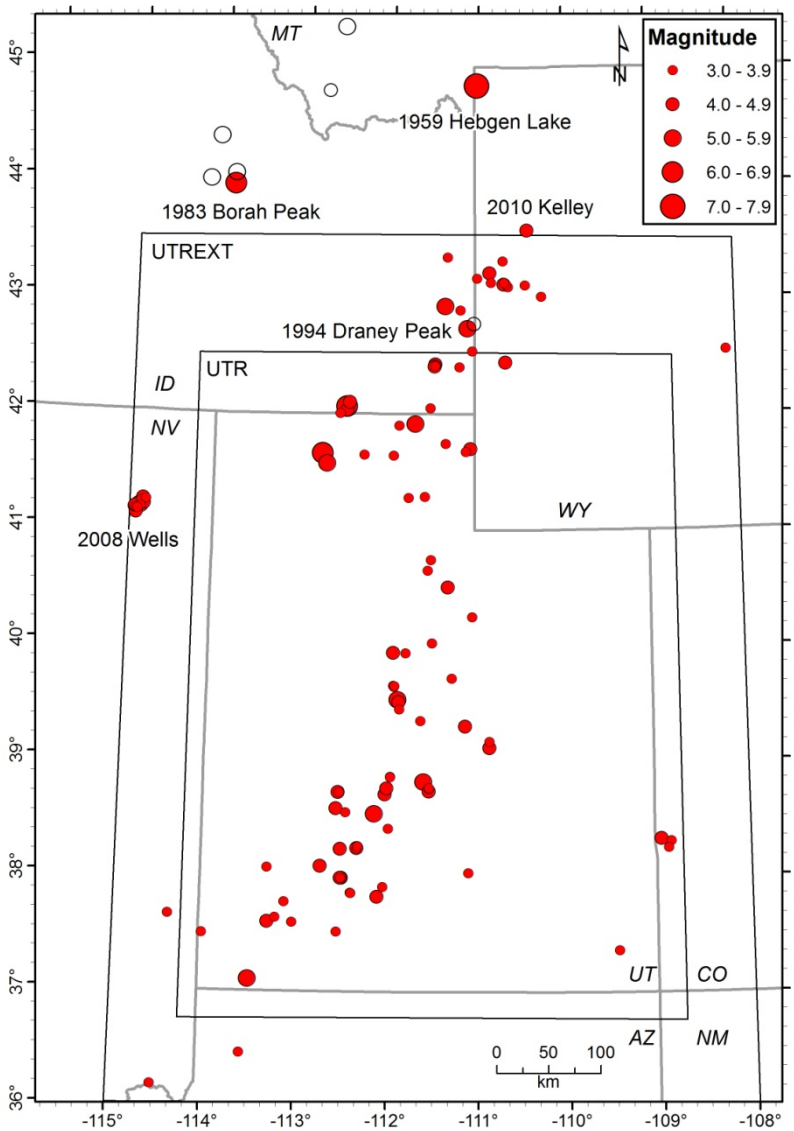

Figure E-3. *Map showing the locations of 114 earthquakes (red dots) for which reliable moment magnitudes were compiled for this study. Boundaries of the UTR and UTREXT as in figure E-1. Magnitudes for the five labeled earthquakes outside the UTR were used to augment data sets for some magnitude conversion relationships developed for the UTR. Data pairs used by Pechmann and Whidden (2013) for regressing* $\boldsymbol{M}_{obs}$ *on* M_L *UU and/or* M_C *UU included data from various earthquakes indicated by red dots plus data from six supplementary earthquakes whose locations are shown by uncolored circles.*

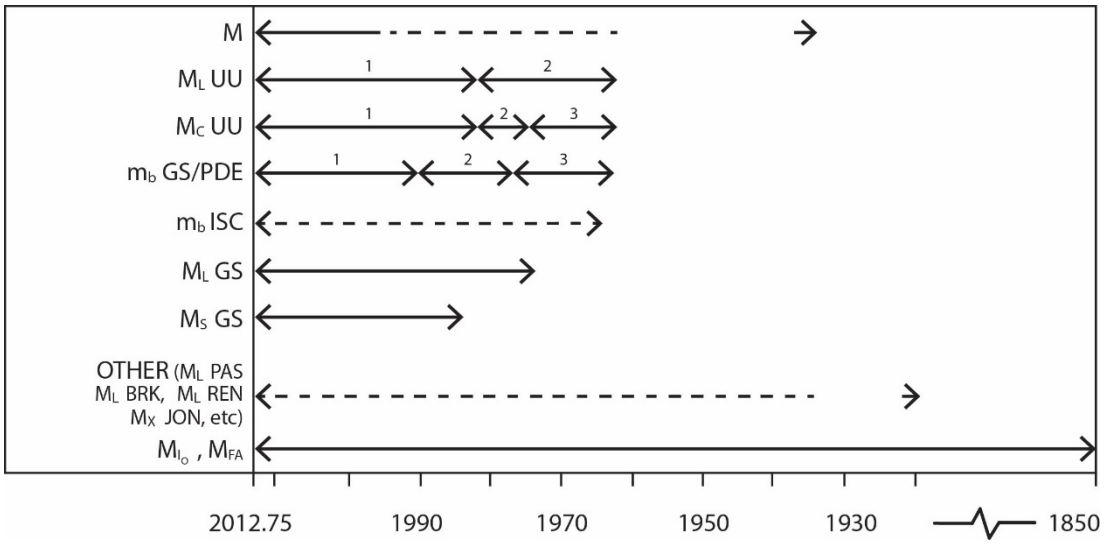

Figure E-4. *Overview of magnitude types reported in the merged source catalogs for the UTREXT. Segmented, numbered timeline for a given magnitude scale (keyed to notation in tables E-8 and E-9) implies time-varying changes in data and/or methods used by a particular agency. Dashed timeline indicates intermittent or sparse data.*

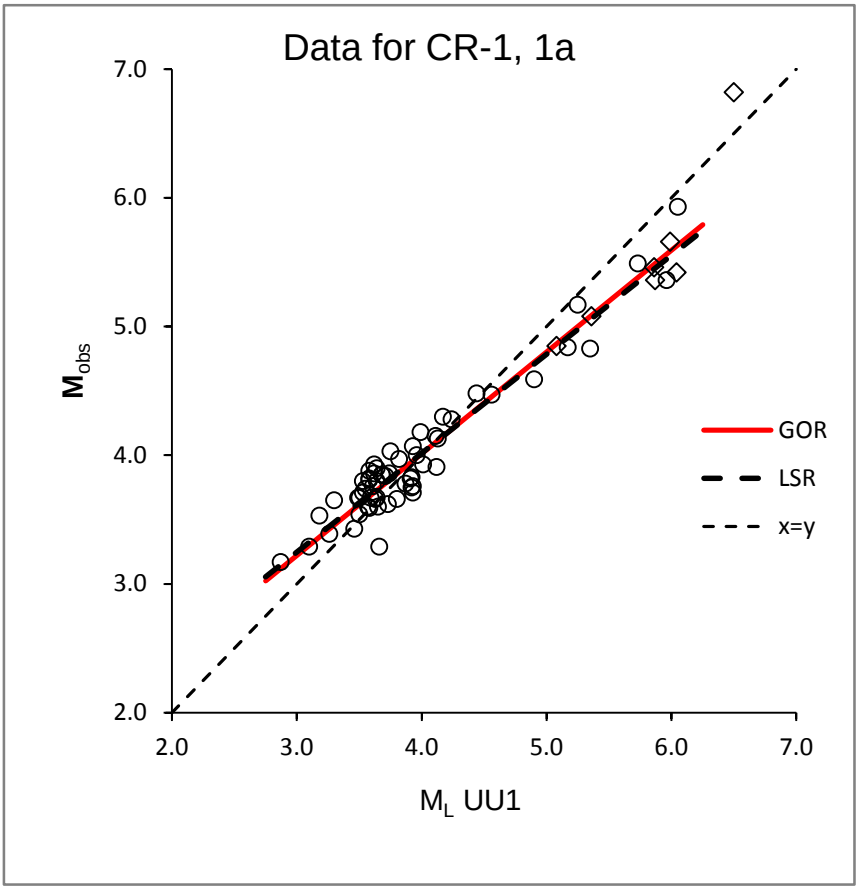

Figure E-5. *Data for general orthogonal regression (GOR) of* $\boldsymbol{M}_{obs}$ *on* M_L *UU1. Least squares regression (LSR) shown for comparison. Modified from original figure of Pechmann and Whidden (2013). Diamonds = non-UUSS* $\boldsymbol{M}_{obs}$.

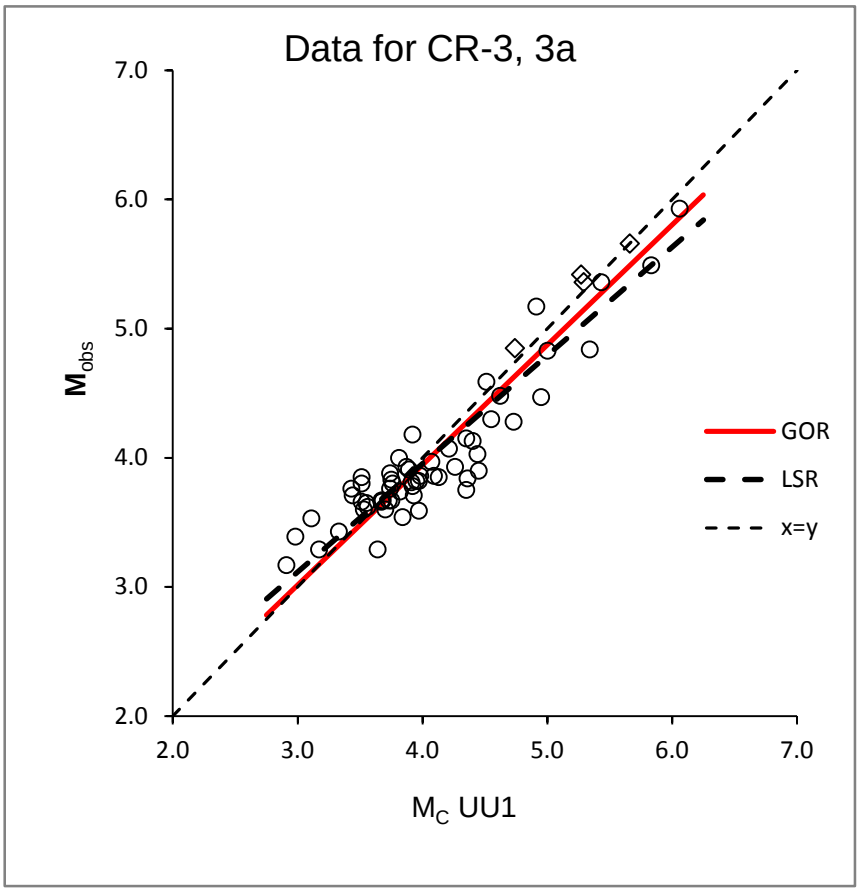

Figure E-6. *Data for general orthogonal regression (GOR) of* $\boldsymbol{M}_{obs}$ *on* M_C *UU1. Least squares regression (LSR) shown for comparison. Modified from original figure of Pechmann and Whidden (2013). Diamonds = non-UUSS* $\boldsymbol{M}_{obs}$.

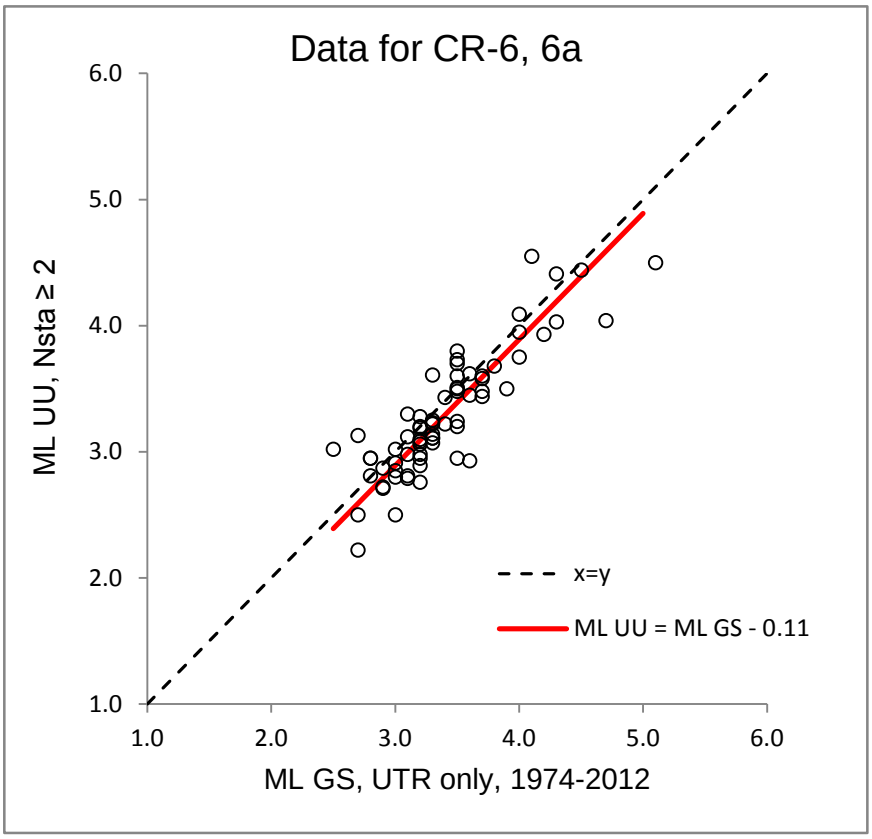

Figure E-7. *Data for the first step of conversion relationships CR-6 (and CR- 6a). Regression, assuming a slope of 1, of M_L UU on M_L GS in the UTR, 1974–2012. Red line shows the offset fit to the data.*

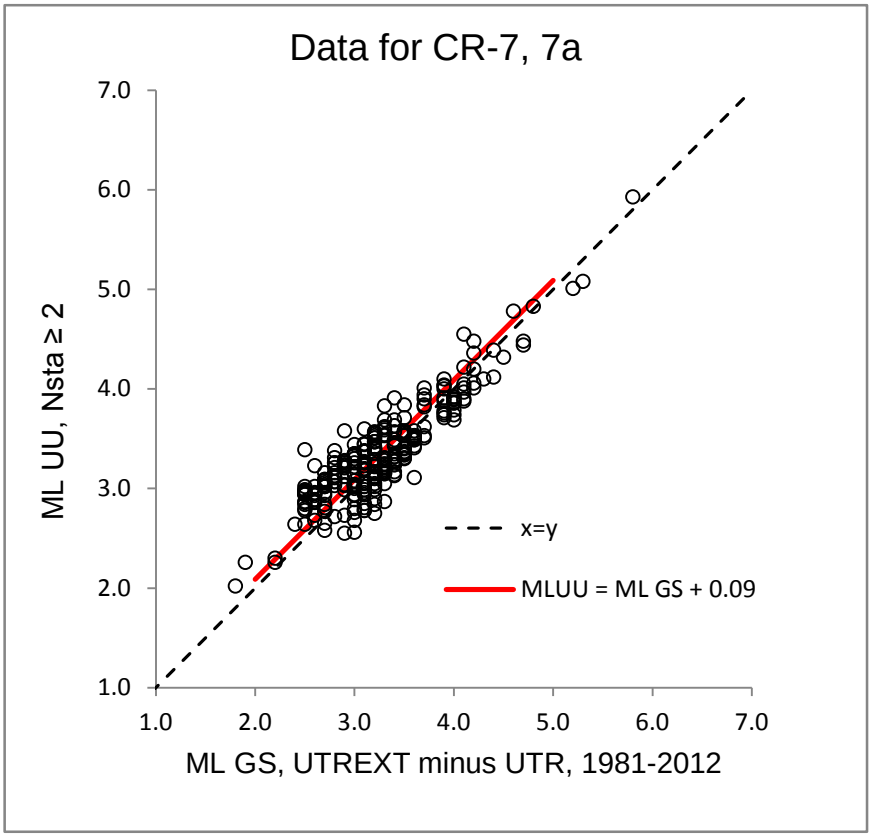

Figure E-8. *Data for the first step of conversion relationship CR-7 (and CR-7a). Regression, assuming a slope of 1, of M_L UU on M_L GS for the Extended Border Region (UTREXT minus UTR), 1981–2012. Red line shows the offset fit to the data.*

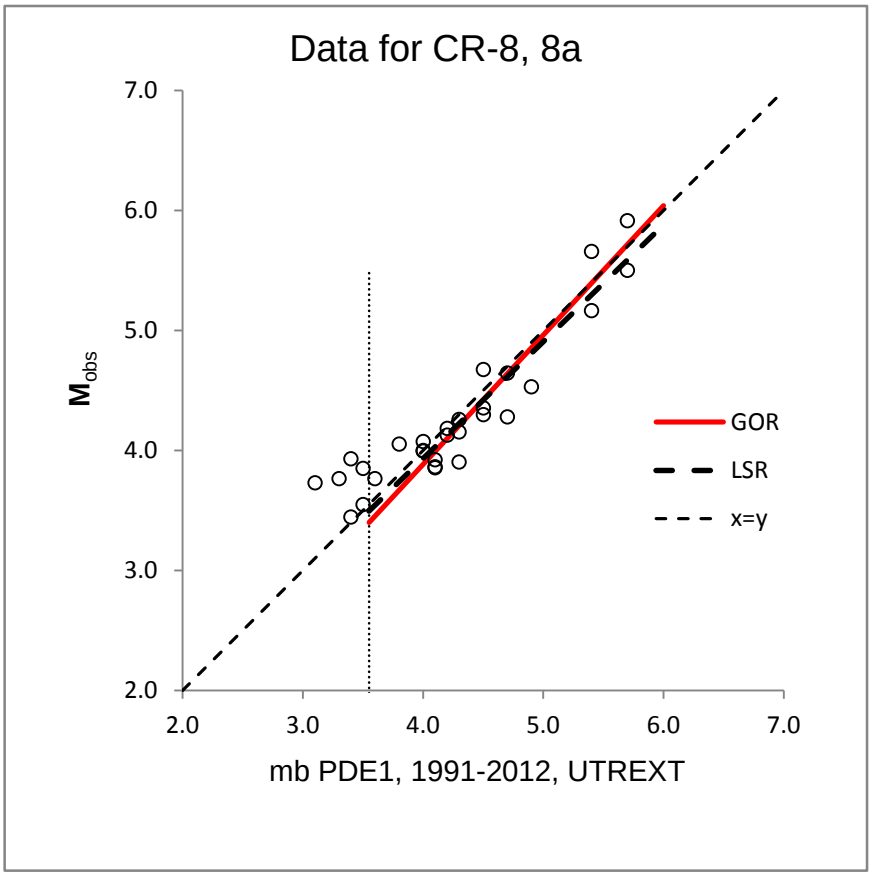

Figure E-9. *Data for general orthogonal regression (GOR) of* $\boldsymbol{M}_{obs}$ *on* m_b *PDE1 > 3.5 in the UTREXT, 1991–2012. Least squares regression (LSR) shown for comparison.*

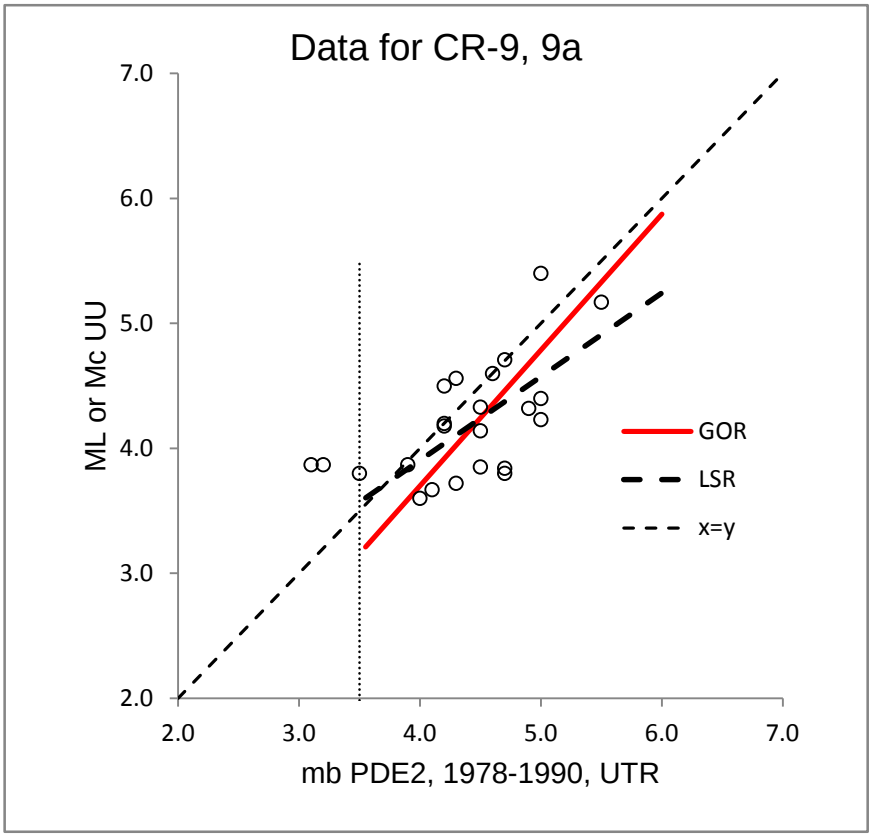

Figure E-10. *Data for the first step of conversion relationship CR-9 (and CR-9a). General orthogonal regression (GOR) of M_L or M_C UU on m_b PDE2 ≥ 3.5 in the UTR, 1978–1990. Least squares regression (LSR) shown for comparison.*

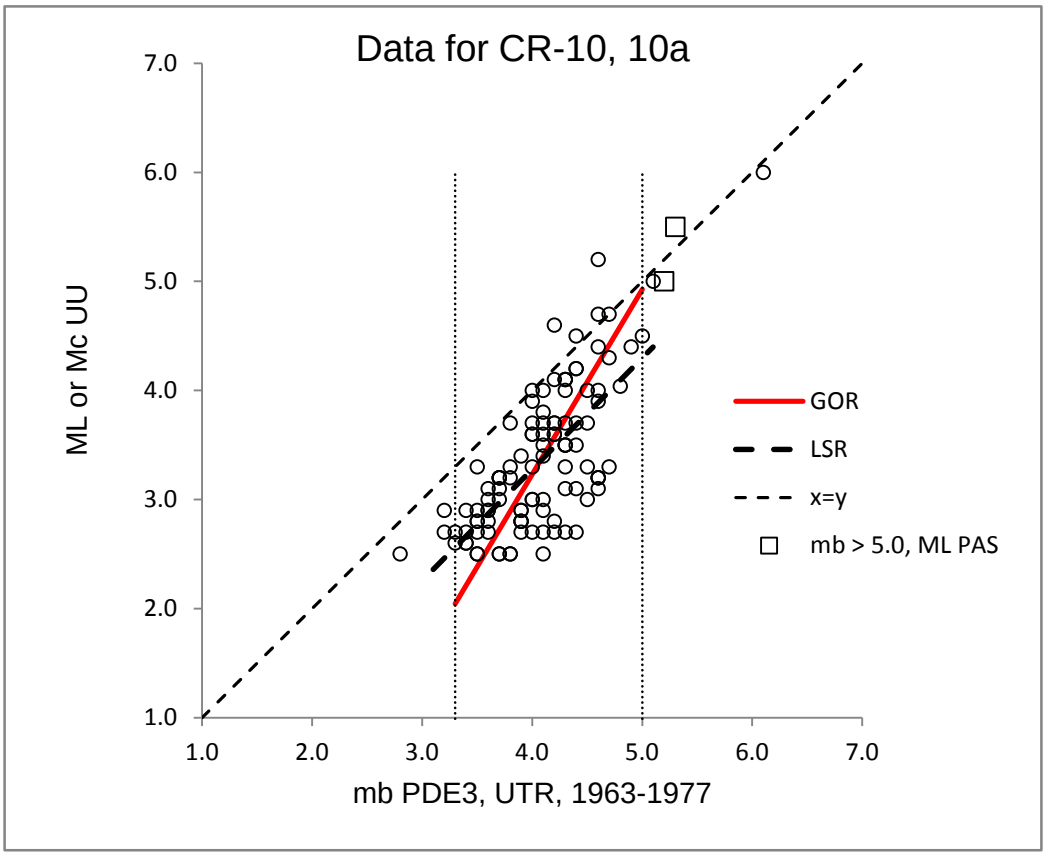

Figure E-11. *Data for the first step of conversion relationship CR-10 (and CR-10a). General orthogonal regression (GOR) of M_L or M_C UU on m_b PDE3 (3.3–5.0) in the UTR, 1963–1977. Least squares regression (LSR) shown for comparison. Squares indicate two earthquakes larger than m_b 5.0 for which the plotted y-value is an M_L from Pasadena.*

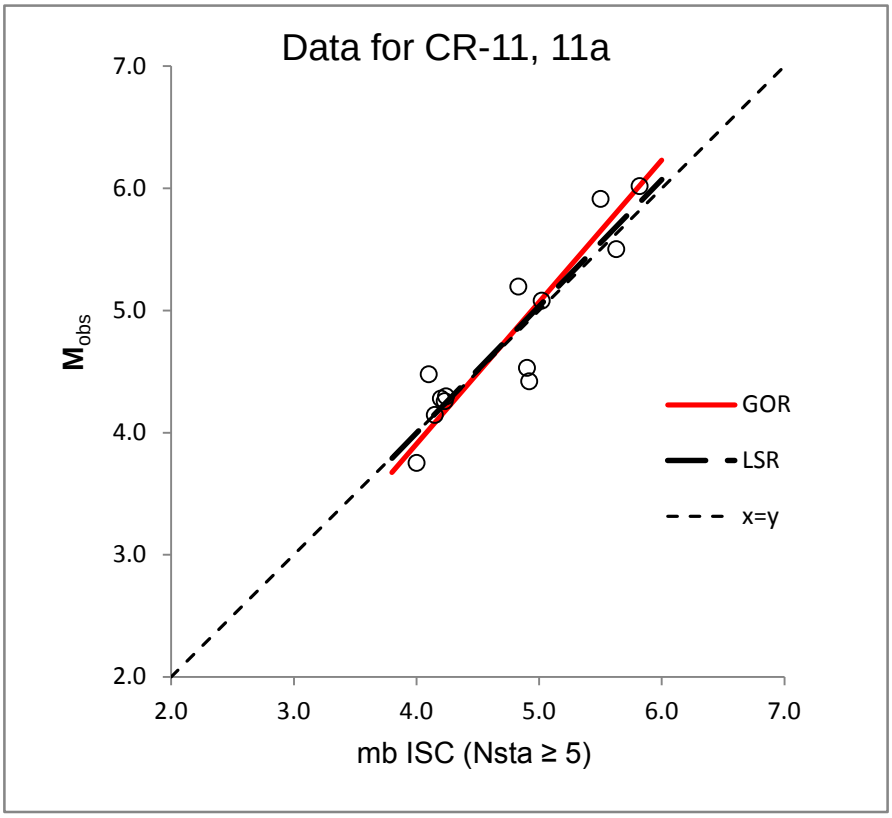

Figure E-12. *Data for general orthogonal regression (GOR) of* $\boldsymbol{M}_{obs}$ *on* m_b *ISC computed from five or more stations. Least squares regression (LSR) shown for comparison.*

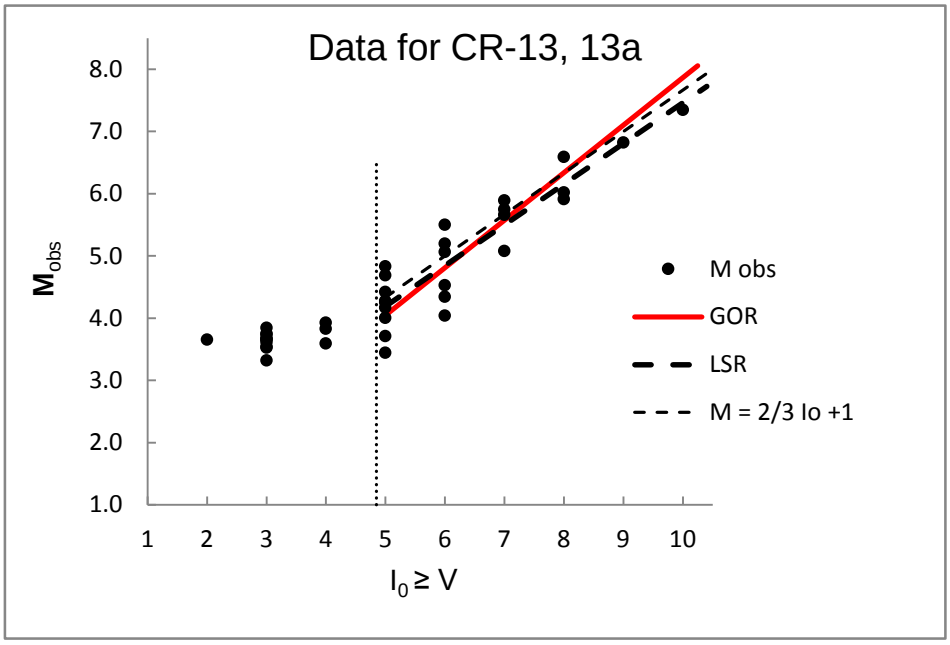

Figure E-13. *Data for conversion relationships CR-13 and CR-13a. Regression of* $\boldsymbol{M}_{obs}$ *on* $I_0 \geq V$*. GOR = general orthogonal regression, LSR = least squares regression. Also shown for reference is Gutenberg and Richter's (1956) relationship,* $M = 2/3\ I_0 + 1$*.*

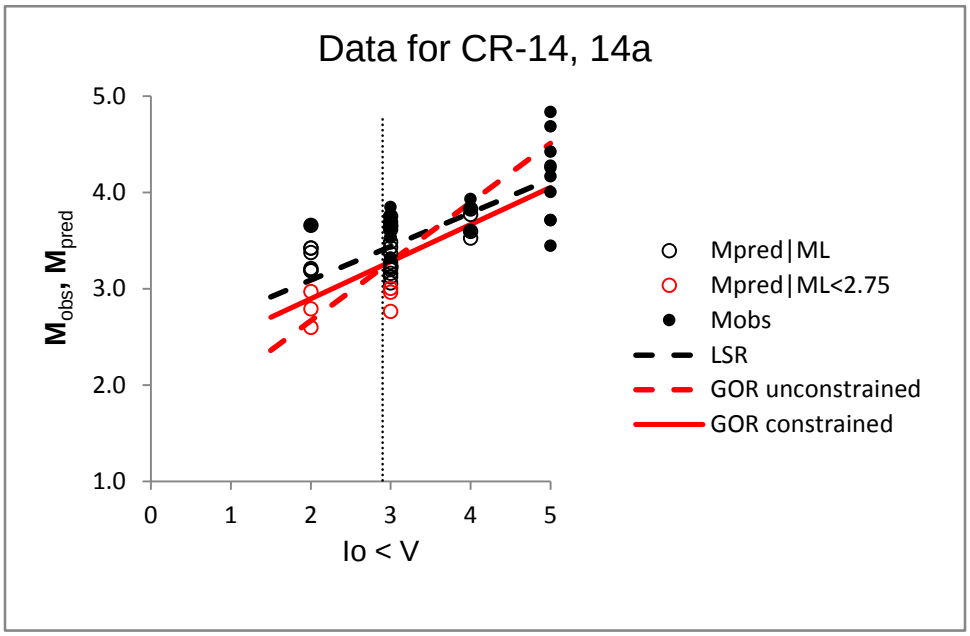

Figure E-14. *Data for provisional conversion relationships CR-14 and CR-14a for $I_o < V$. Regression of $\boldsymbol{M}_{obs}$ and $\boldsymbol{M}_{pred}$ on $I_0 \leq 5$. The regressions exclude data below $I_0 = 3$ and also data based on $\boldsymbol{M}_{pred}|M_L < 2.75$ (red circles); the latter data and the extrapolation of regression lines below $I_0 = 3$ are shown for illustration only. GOR = general orthogonal regression, LSR = least squares regression. The regression for "GOR constrained" was constrained to pass through the same $\boldsymbol{M}_{pred}$ value for $I_0 = 5$ as that for CR-13 for $I_o \geq V$.*

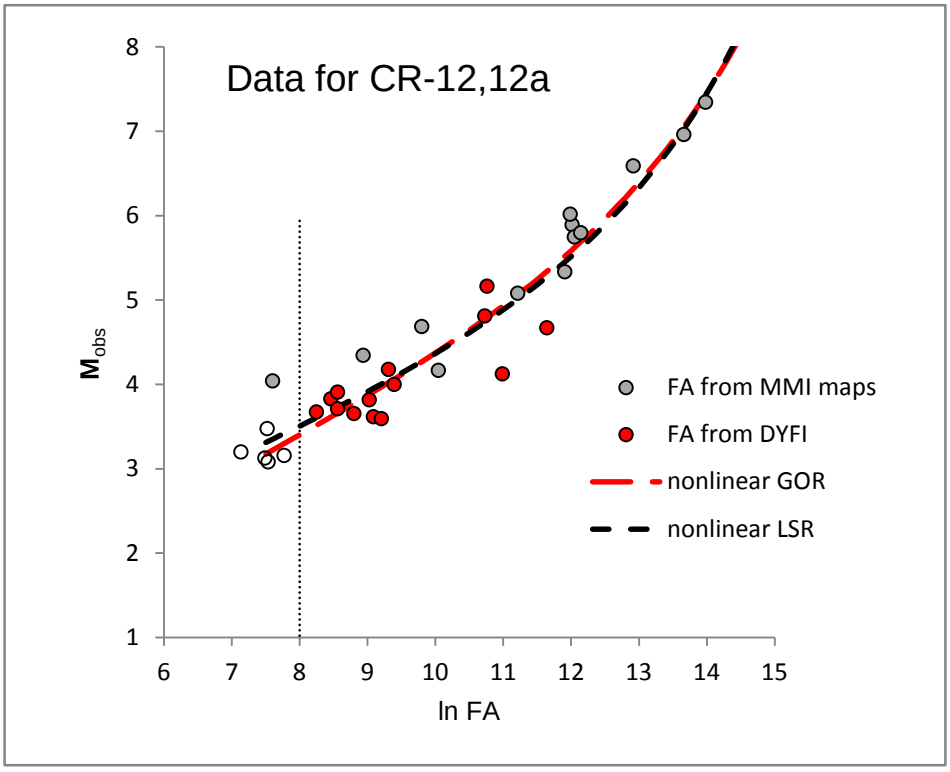

Figure E-15. *Data for conversion relationships CR-12 and CR-12a. Regression of* $\boldsymbol{M}_{obs}$ *on ln(FA) > 8, where FA is in km*^{2}*. GOR = general orthogonal regression, LSR = least squares regression, MMI = Modified Mercalli Intensity, DYFI = Did You Feel It. Data points below ln(FA) = 8 (dotted line) were not used in the regressions and are shown for illustration only; for the open circles, ln(FA) is from DYFI data and the y-value is* $\boldsymbol{M}_{pred}$ *from* M_L *UU using CR-1.*

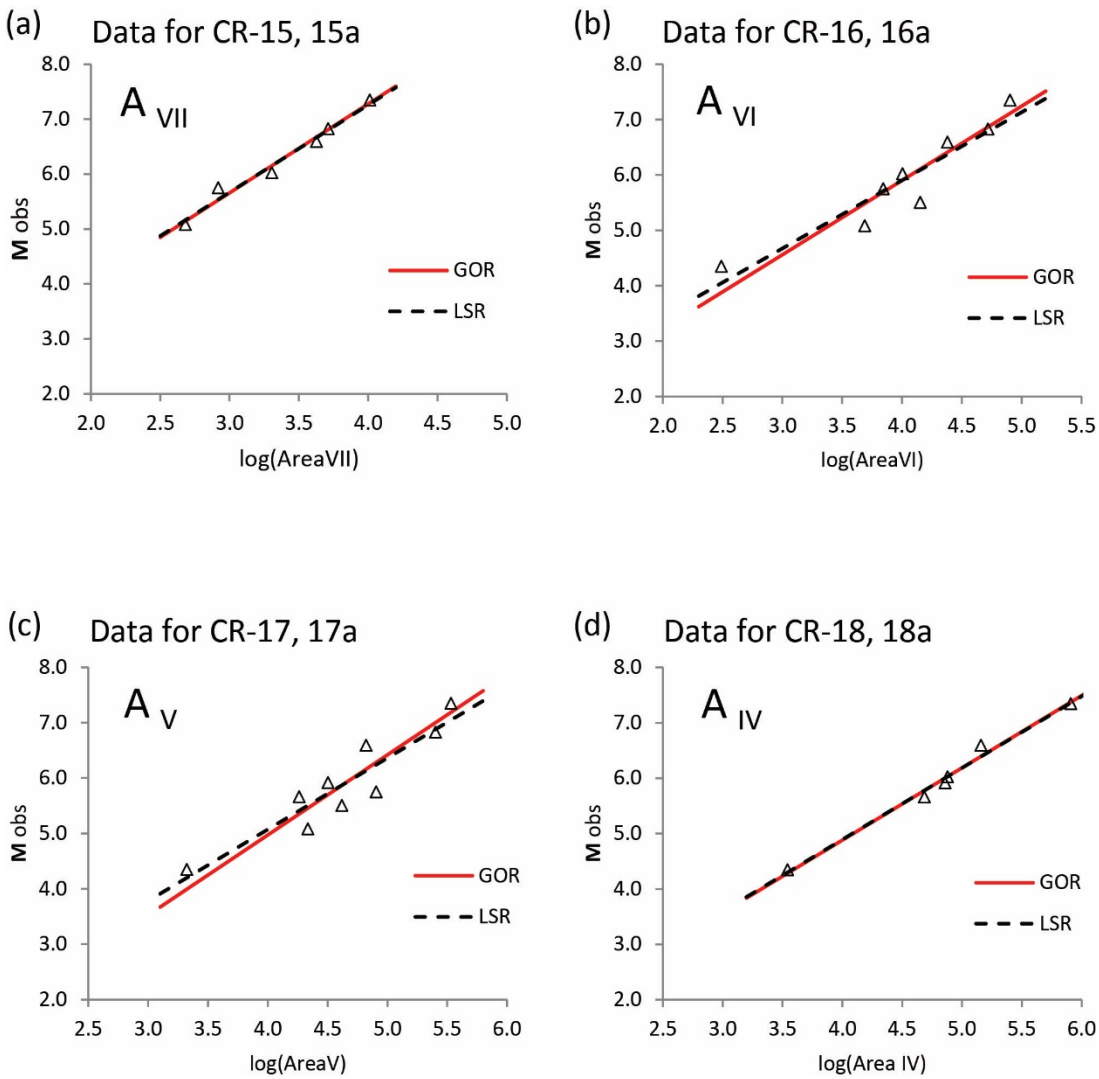

Figure E-16. *Data from general orthogonal regression (GOR) of* $\mathbf{M}_{obs}$ *on the logarithm of the extent of area shaken, in km*^{2}*, at or greater than MMI IV* (A_{IV}) *to MMI VII* (A_{VII})*. Least squares regression (LSR) shown for comparison.*

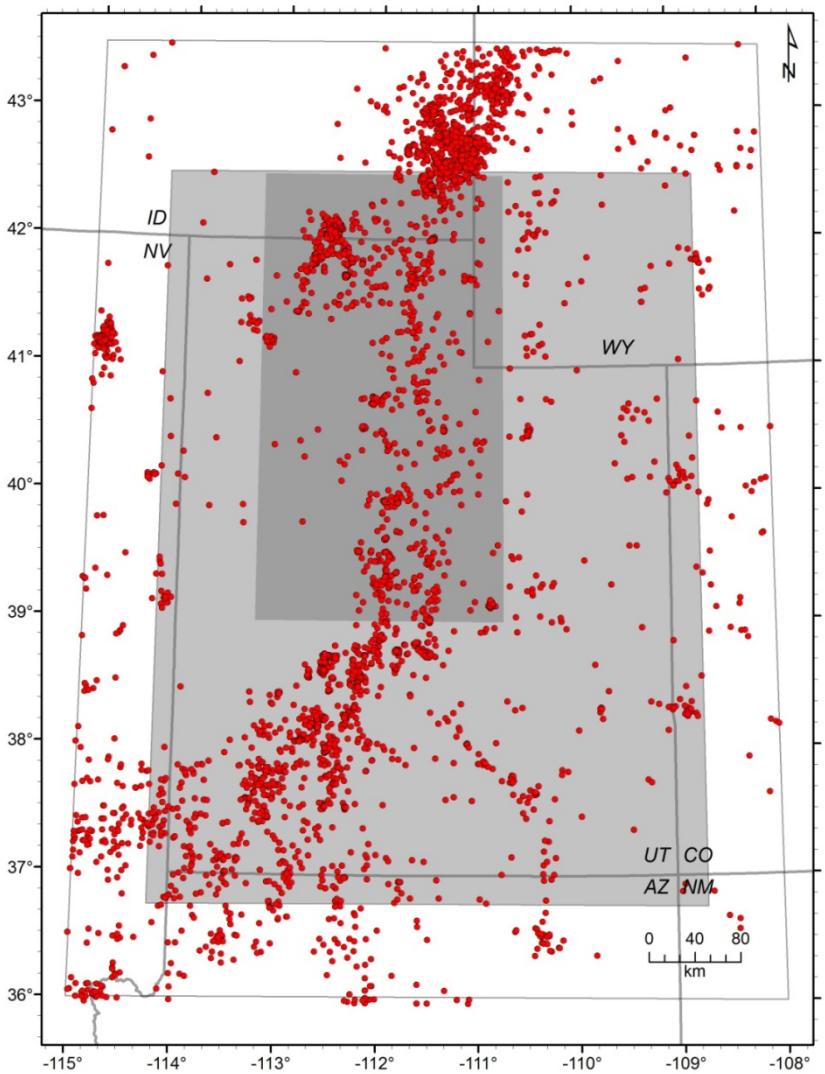

Figure E-17. *Epicenter map of all earthquakes (clustered) in the BEM catalog, 1850 through September 2012, for the entire Extended Utah Region. The WGUEP and Utah regions are shaded in darker and lighter gray, respectively.*

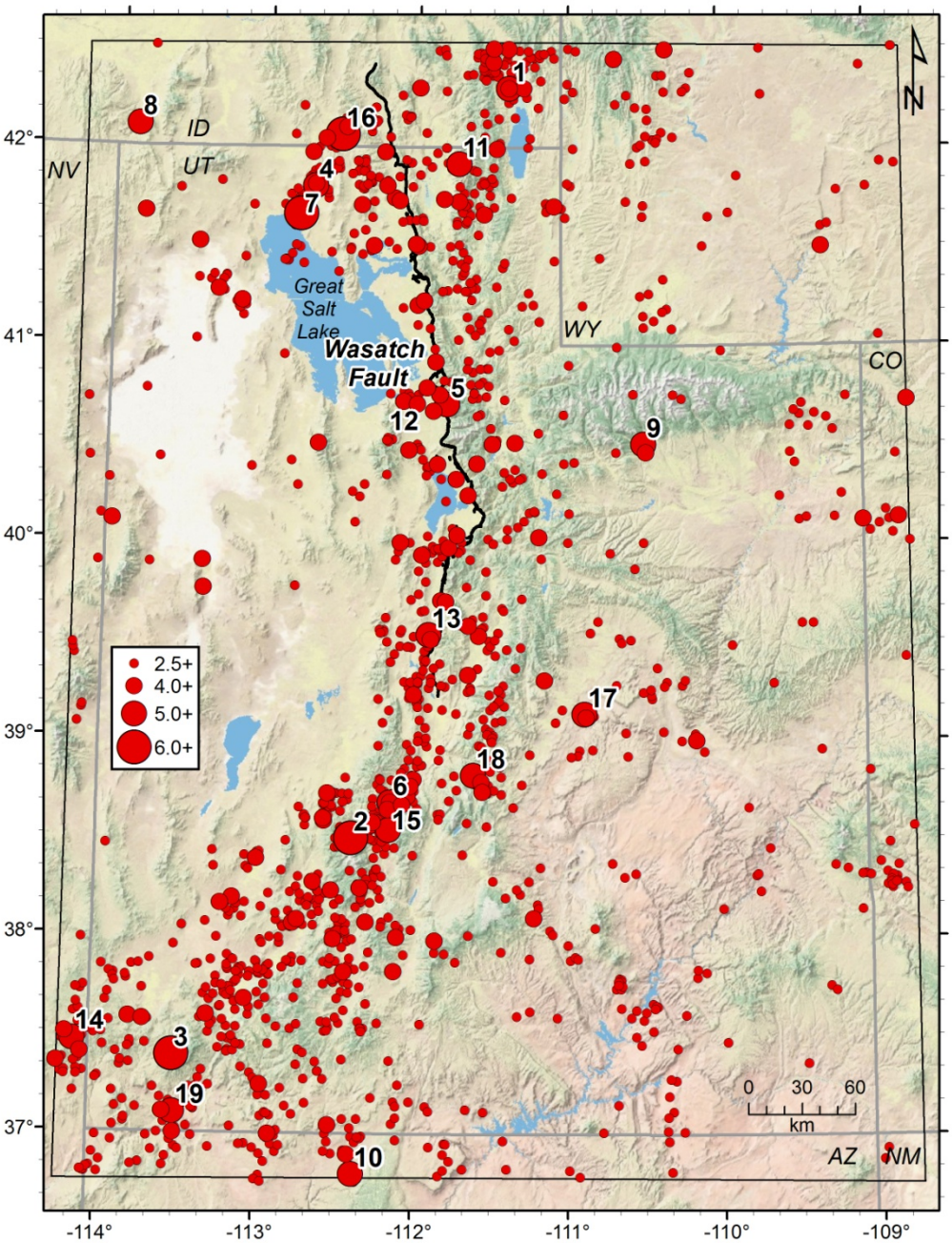

Figure E-18. *Epicenter map of independent mainshocks in the Utah Region, 1850 through September 2012 (BEM catalog, declustered). Epicenters scaled by magnitude. Numbered epicenters (keyed to table E-14) are for earthquakes with* ***M*** *≥ 4.85. Wasatch fault shown for reference.*

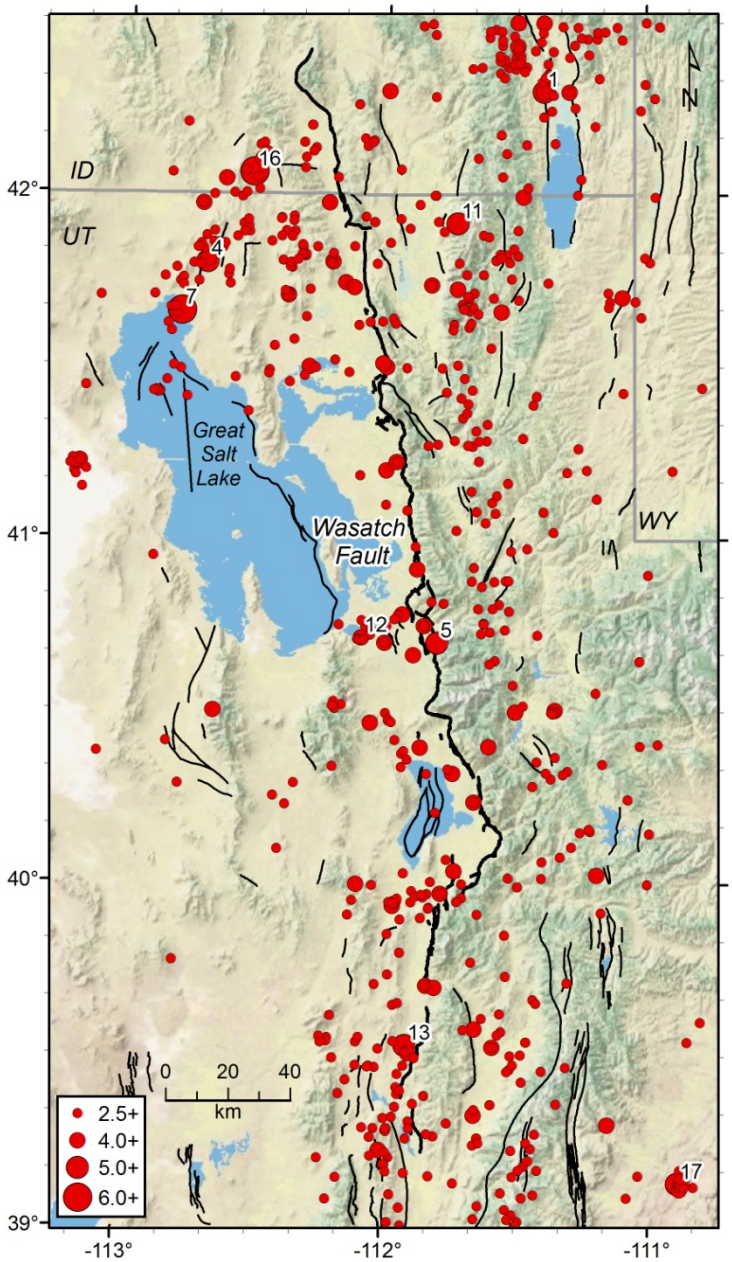

Figure E-19. *Epicenter map of independent mainshocks in the WGUEP Region, 1850 through September 2012 (BEM catalog, declustered). Epicenters scaled by magnitude. Numbered epicenters (keyed to table E-14) are for earthquakes of $M \geq 4.85$). Quaternary faults, after Black and others (2003), shown for reference; Wasatch fault bolded.*

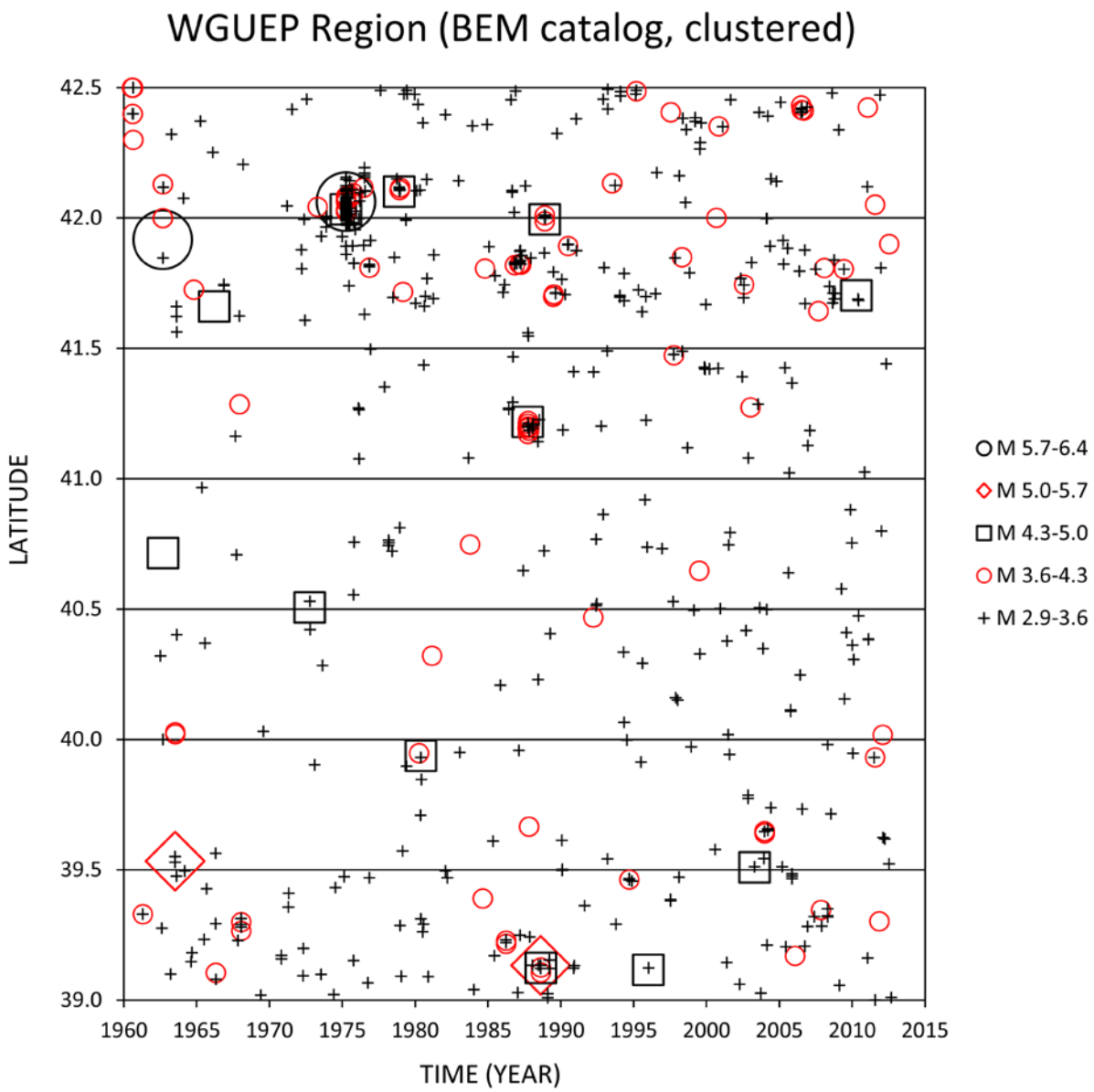

Figure E-20. *Space-time diagram (latitude vs. time since 1960) showing the distribution of earthquakes in the WGUEP Region of* ***M*** *≥ 2.9 (2.85), differentiated by magnitude bins, for the clustered version of the BEM catalog.*

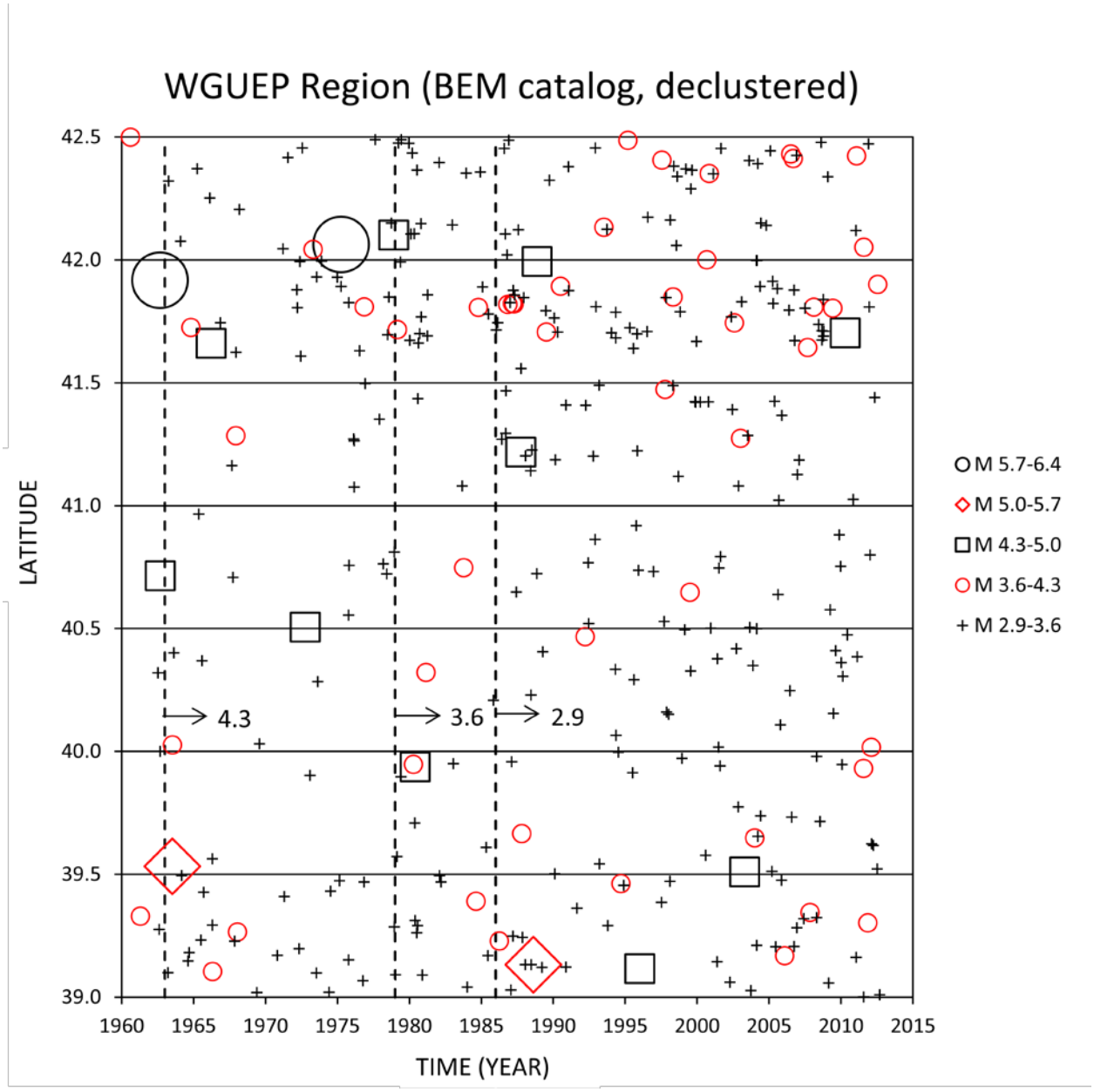

Figure E-21. *Space-time diagram (latitude vs. time since 1960) showing the distribution of mainshocks in the WGUEP Region of* ***M*** *≥ 2.9 (2.85), differentiated by magnitude bins, for the declustered version of the BEM catalog. Vertical dashed lines indicate the start of completeness periods for* ***M*** *≥ 4.3 (1963),* ***M*** *≥ 3.6 (1979), and* ***M*** *≥ 2.9 (1986).*

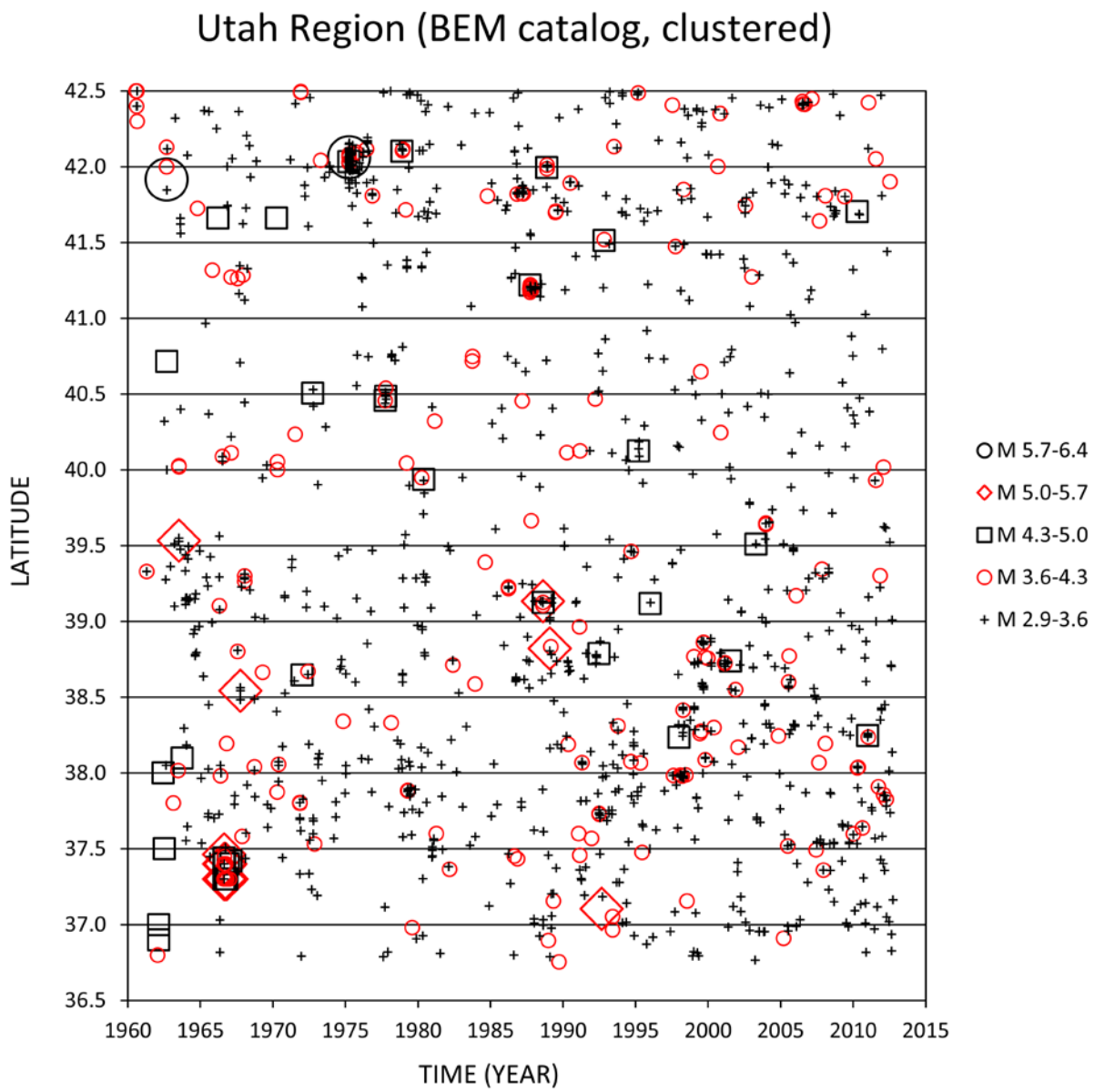

Figure E-22. *Space-time diagram (latitude vs. time since 1960) showing the distribution of earthquakes in the Utah Region of* ***M*** *≥ 2.9 (2.85), differentiated by magnitude bins, for the clustered version of the BEM catalog. Injection-induced earthquakes (table E-4) are excluded.*

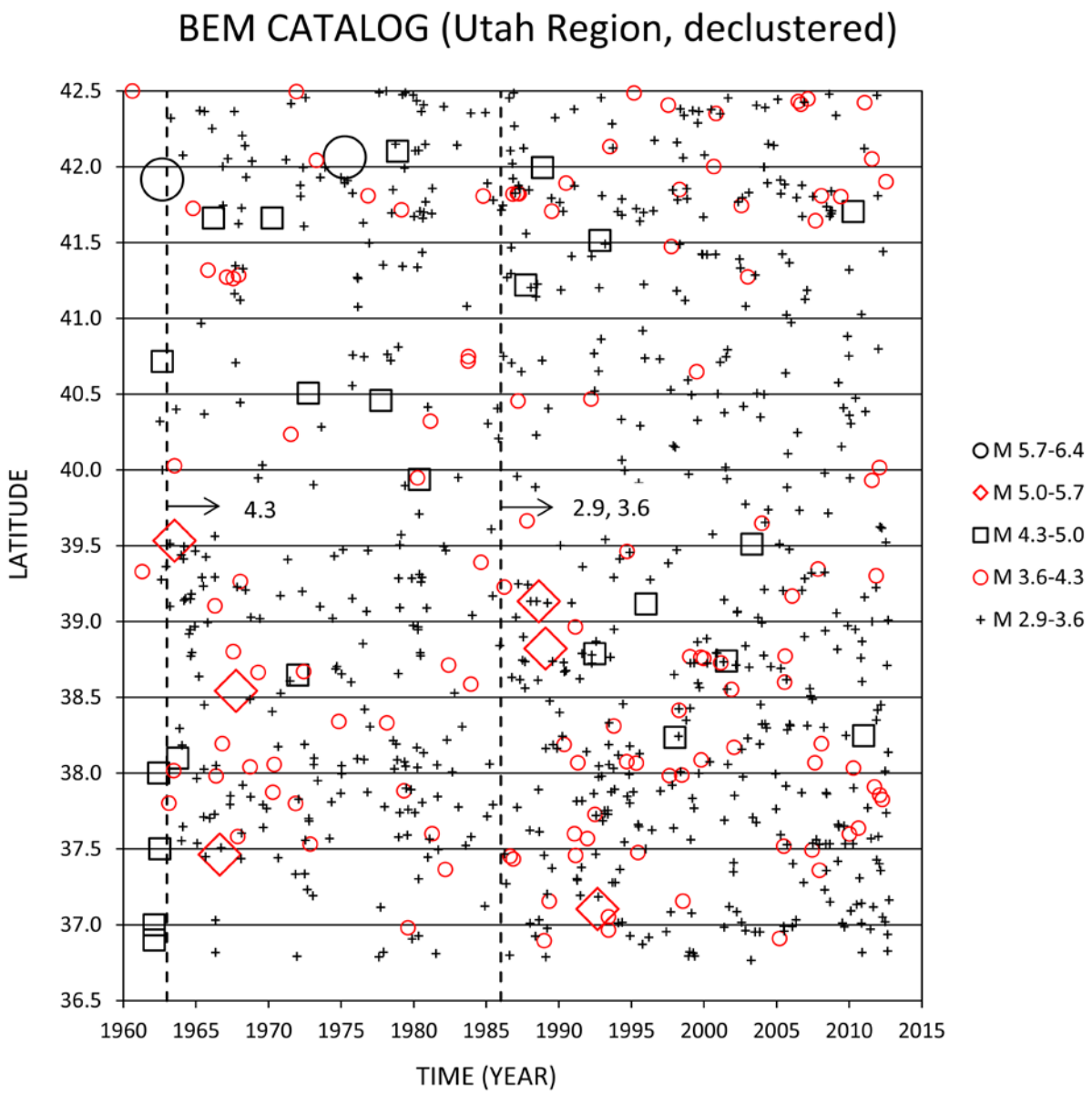

Figure E-23. *Space-time diagram (latitude vs. time since 1960) showing the distribution of mainshocks in the Utah Region of* ***M*** *≥ 2.9 (2.85), differentiated by magnitude bins, for the declustered version of the BEM catalog. Injection-induced earthquakes (table E-4) are excluded. Vertical dashed lines indicate the start of completeness periods in 1963 for* ***M*** *≥ 4.3 (4.25) and in 1986 for both* ***M*** *≥ 3.6 (3.55) and* ***M*** *≥ 2.9 (2.85).*

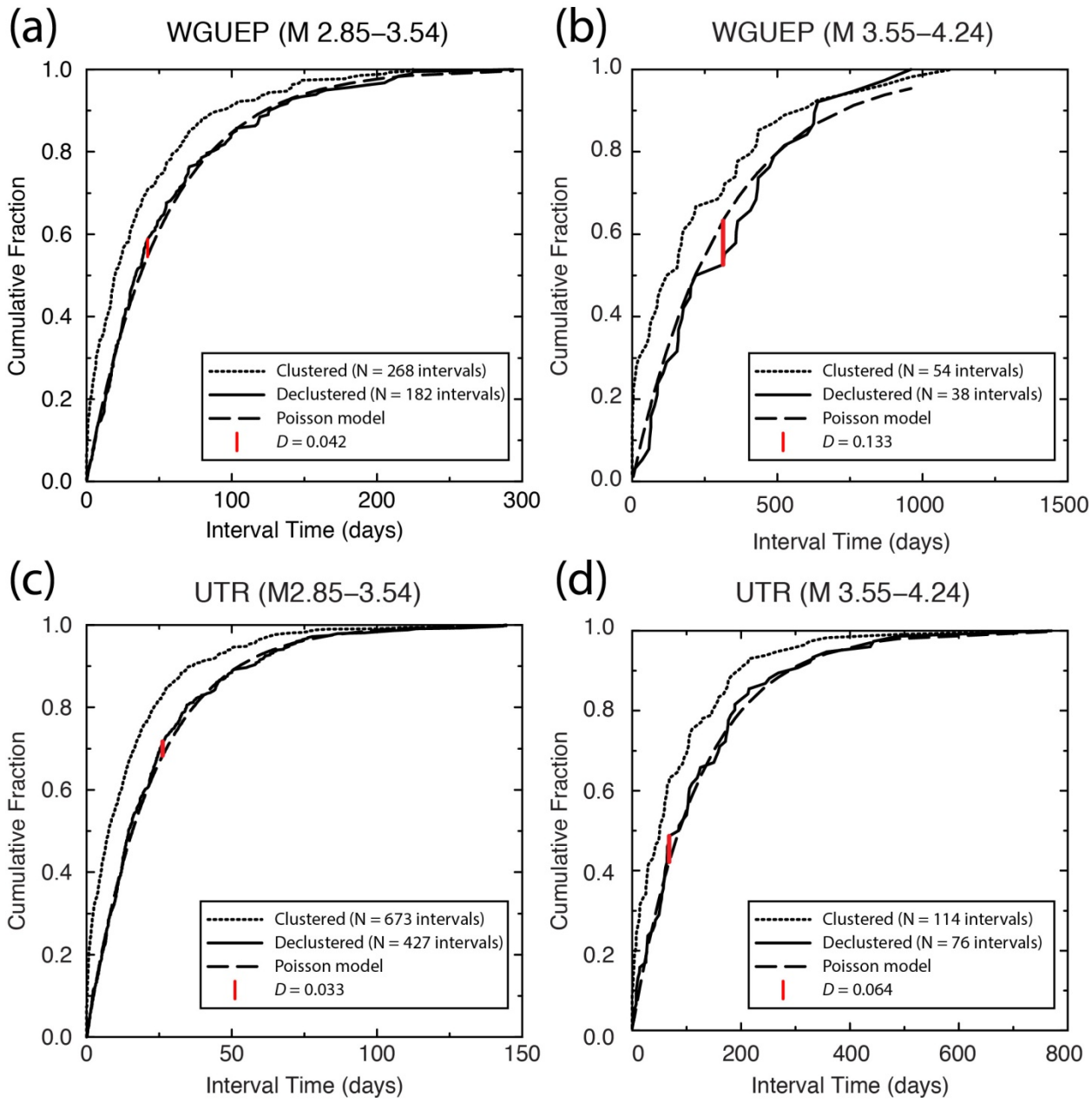

Figure E-24. *Cumulative distribution functions (CDFs) of interval (inter-event) times for earthquakes in selected magnitude bins in the WGUEP Region (a, b) and the Utah Region (c, d). In each panel, CDFs are shown for both the clustered and declustered cases. Data are restricted to the applicable periods of completeness. For the declustered case, the CDF is compared to that expected for a Poisson distribution; the largest absolute difference between the compared CDFs is the K-S statistic, D.*

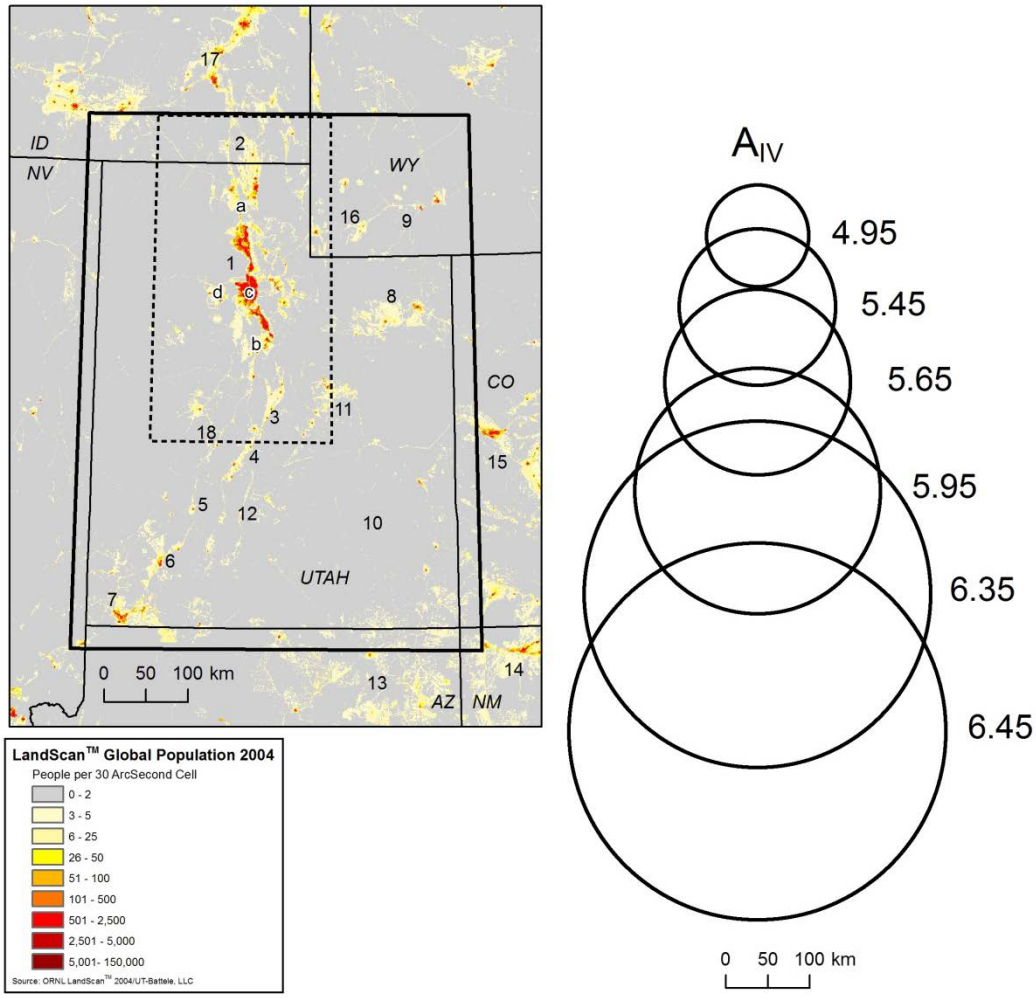

Figure E-25. *(left) Population density map of the Extended Utah Region in 2004 (source: Oak Ridge National Laboratory LandScan™ 2004/UT-Batelle, LLC); one 30 ArcSecond Cell = approx. 0.6 km^2. The WGUEP and Utah regions are outlined by dashed and bold lines, respectively as in figure E-1. Numbered localities are discussed in the text. For reference, a = Brigham City, b = Payson, c = Salt Lake Valley, d= Tooele Valley. (right) Circles showing the expected area shaken at or greater than MMI IV (A_{IV}) for earthquakes of various magnitudes from* ***M*** *4.95 to* ***M*** *6.45 (radii are given in table E-17).*

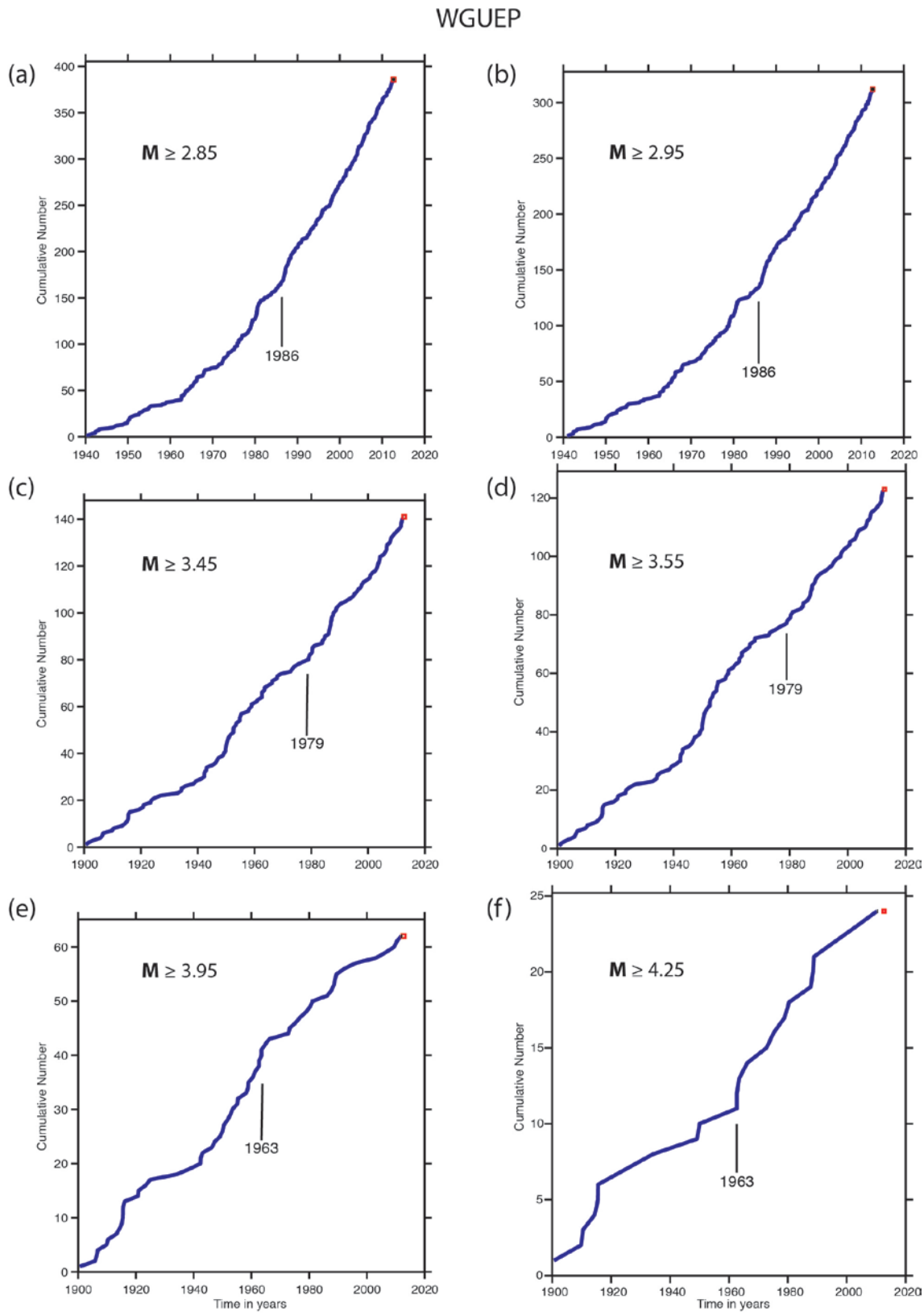
WGUEP
(a)
M ≥ 2.85
1986
(b)
M ≥ 2.95
1986
(c)
M ≥ 3.45
1979
(d)
M ≥ 3.55
1979
(e)
M ≥ 3.95
1963
(f)
M ≥ 4.25
1963
Cumulative Number
Time in years

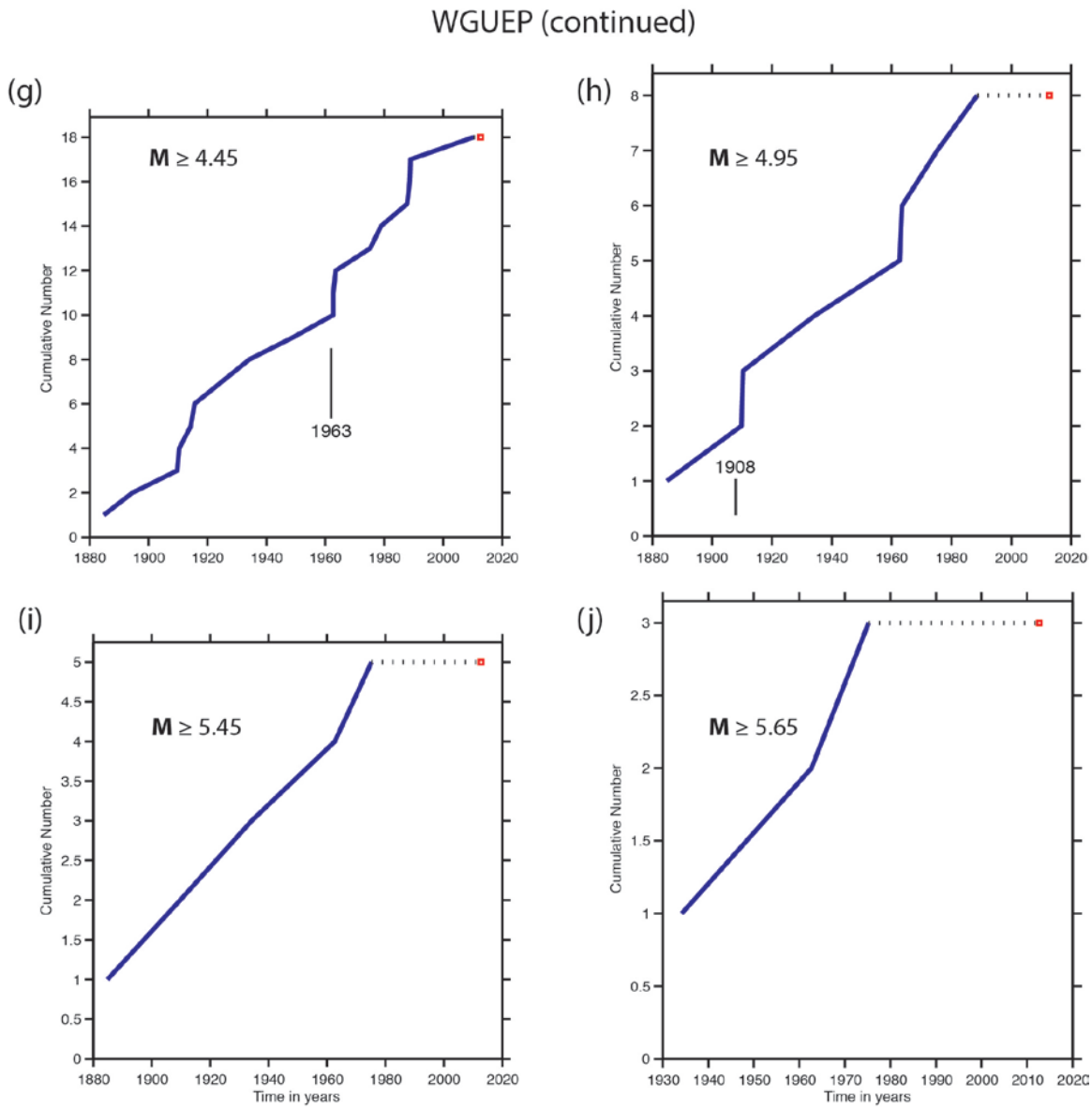

Figure E-26. *Cumulative recurrence curves (CRCs) for declustered earthquakes in the WGUEP Region (BEM catalog) for incremental magnitude thresholds listed in table E-16 from* ***M*** *2.85 to* ***M*** *5.65. Labeled vertical lines in panels (a) to (g) indicate the selected start date of a period of completeness picked from the CRC; that for 1908 in panel (h) is based on other arguments.*

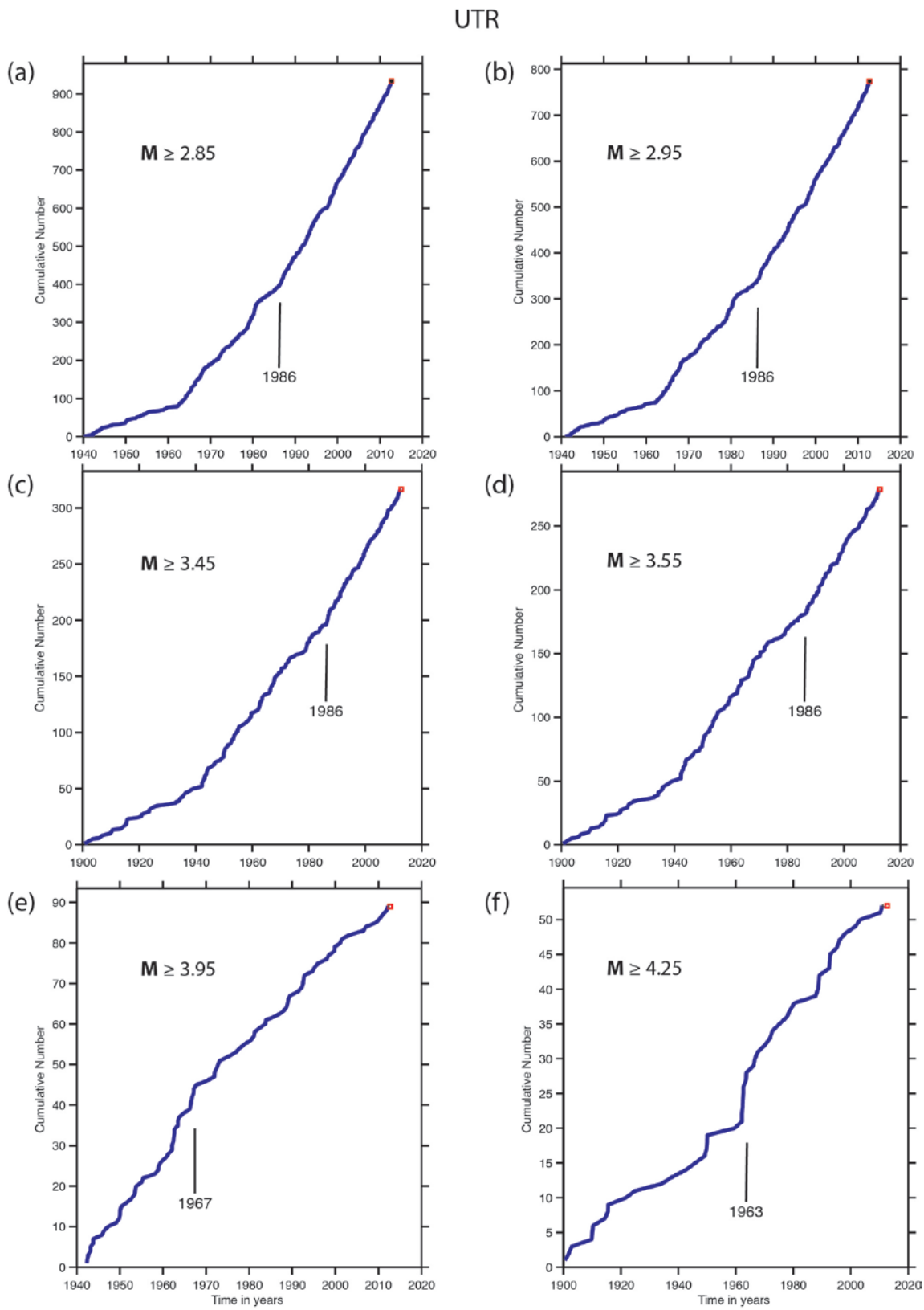
UTR
(a)
M ≥ 2.85
1986
(b)
M ≥ 2.95
1986
(c)
M ≥ 3.45
1986
(d)
M ≥ 3.55
1986
(e)
M ≥ 3.95
1967
(f)
M ≥ 4.25
1963
Cumulative Number
Time in years

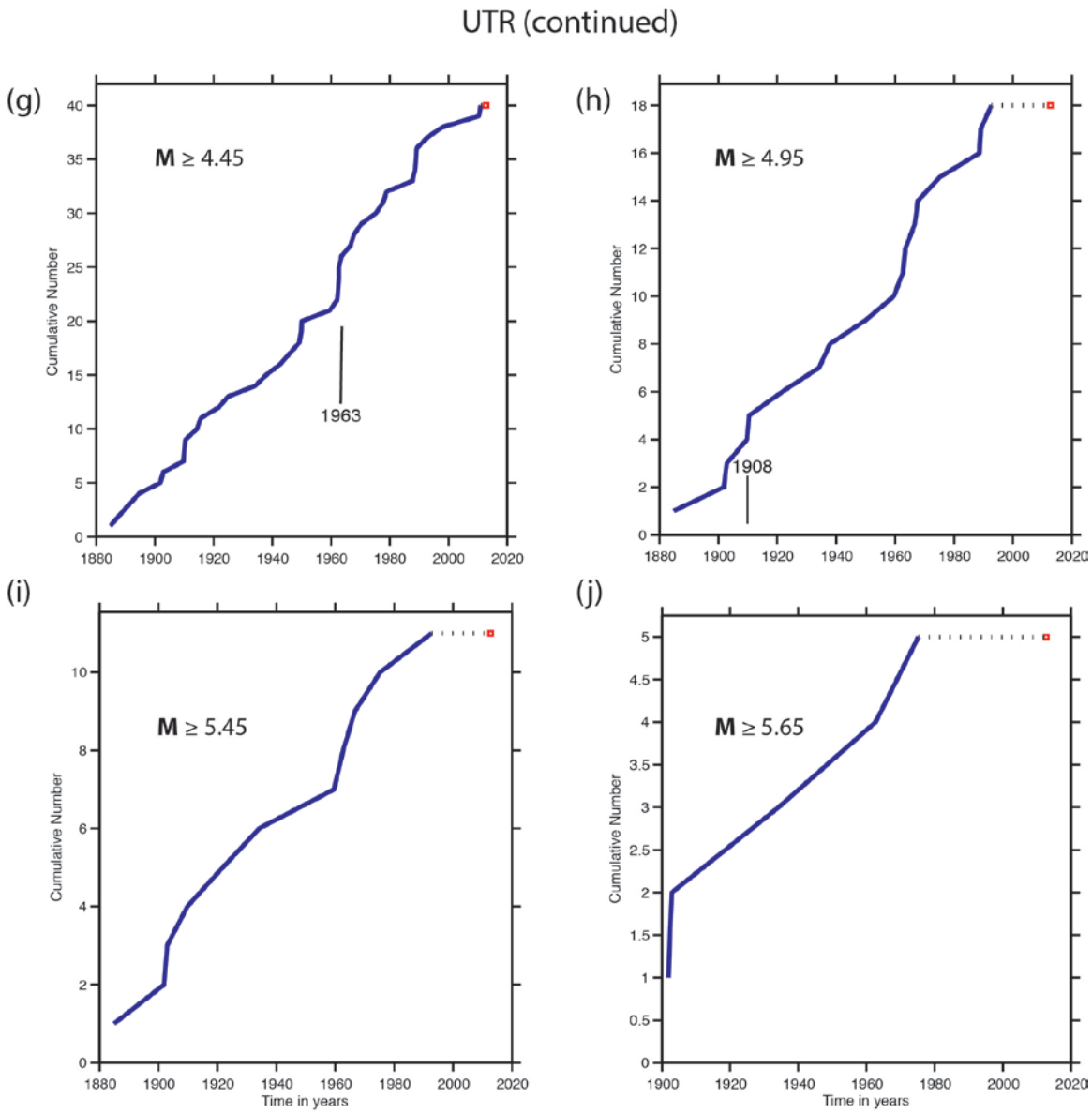

Figure E-27. *Cumulative recurrence curves (CRCs) for declustered earthquakes in the Utah Region (BEM catalog) for incremental magnitude thresholds listed in table E-16 from* ***M*** *2.85 to* ***M*** *5.65. Labeled vertical lines in panels (a) to (g) indicate the selected start date of a period of completeness picked from the CRC; that for 1908 in panel (h) is based on other arguments.*

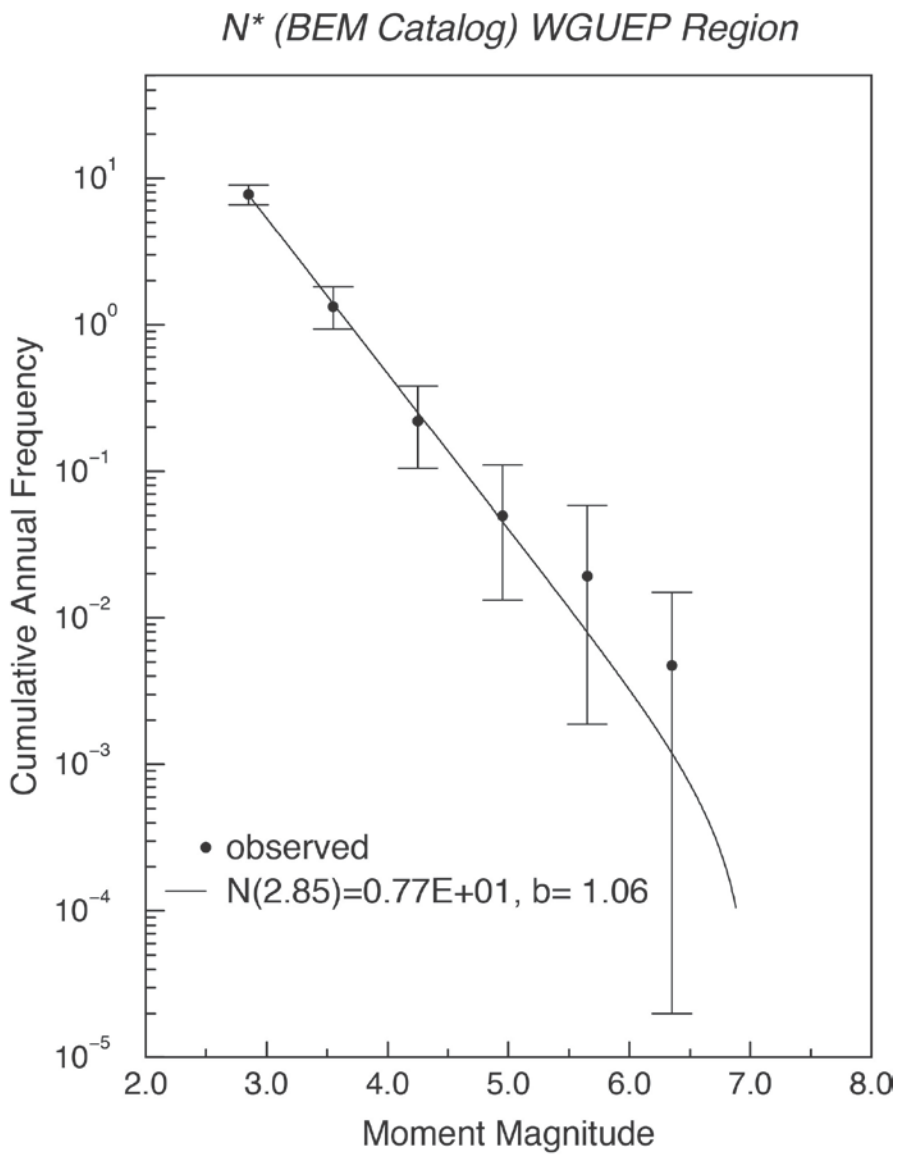

Figure E-28. *Background earthquake model for the WGUEP Region. Frequency-magnitude distribution of independent mainshocks (**M** ≥ 2.85), corrected for magnitude uncertainty and calculated using the maximum-likelihood algorithm of Weichert (1980).*

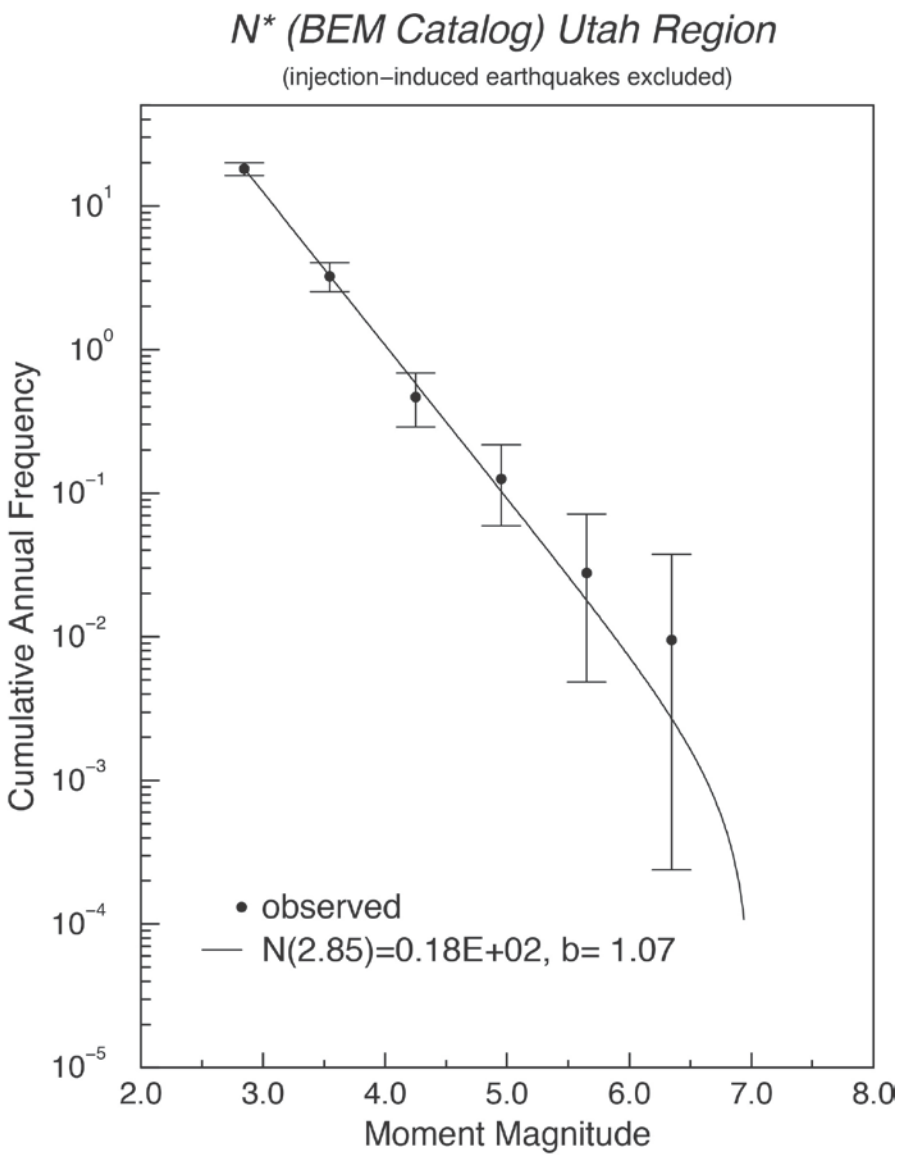

Figure E-29. *Background earthquake model for the Utah Region. Frequency-magnitude distribution of independent mainshocks (**M** ≥ 2.85), corrected for magnitude uncertainty and calculated using the maximum-likelihood algorithm of Weichert (1980). Injection-induced earthquakes listed in table E-4 are excluded from the rate calculation.*